Verhalten linearer 3d-Metall(I)-Komplexe gegenüber C/N-Mehrfachbindungen und aromatischen Systemen

Kumulative Dissertation

Zur Erlangung des akademischen Grades eines
Doktors der Naturwissenschaften
(Dr. rer. Nat.)

dem
Fachbereich Chemie der Philipps-Universität Marburg

vorgelegt von

Igor Müller, M. Sc.
aus Barnaul (Russland)

Erstgutachter: Dr. Gunnar Werncke
Zweitgutachter: Prof. Dr. Jörg Sundermeyer

Marburg 2020
Hochschulkennziffer 1180

Verhalten linearer 3d-Metall(I)-Komplexe gegenüber C/N-Mehrfachbindungen und aromatischen Systemen

Kumulative Dissertation

Zur Erlangung des akademischen Grades eines
Doktors der Naturwissenschaften
(Dr. rer. Nat.)

dem
Fachbereich Chemie der Philipps-Universität Marburg

vorgelegt von

Igor Müller, M. Sc.
aus Barnaul (Russland)

Erstgutachter: Dr. Gunnar Werncke
Zweitgutachter: Prof. Dr. Jörg Sundermeyer

Marburg 2020
Hochschulkennziffer 1180

Dissertation angenommen am: 05.02.2021 Tag der mündlichen Prüfung: 09.02.2021

Erklärung

Ich erkläre, dass eine Promotion noch an keiner anderen Hochschule als der Philipps-Universität Marburg, Fachbereich Chemie, versucht wurde.

Hiermit versichere ich, dass ich die vorliegende Dissertation

„Verhalten linearer 3d-Metall(I)-Komplexe gegenüber C/N-Mehrfachbindungen und aromatischen Systemen“

selbstständig, ohne unerlaubte Hilfe Dritter angefertigt und andere als die in der Dissertation angegebenen Hilfsmittel nicht benutzt habe. Alle Stellen, die wörtlich oder sinngemäß aus veröffentlichten oder unveröffentlichten Schriften entnommen sind, habe ich als solche kenntlich gemacht. Dritte waren an der inhaltlich-materiellen Erstellung der Dissertation nicht beteiligt; insbesondere habe ich hierfür nicht die Hilfe eines Promotionsberaters in Anspruch genommen. Kein Teil dieser Arbeit ist in einem anderen Promotions- oder Habilitationsverfahren verwendet worden. Mit dem Einsatz von Software zur Erkennung von Plagiaten bin ich einverstanden.

Wetter, den _____

Igor Müller

Die vorliegende Arbeit wurde in der Zeit von Januar 2017 bis Dezember 2020 unter der Leitung von Herrn Dr. Gunnar Werncke am Fachbereich Chemie der Philipps-Universität Marburg angefertigt.

„Unsere größte Schwäche liegt im Aufgeben.
Der sicherste Weg zum Erfolg ist immer,
es doch noch einmal zu versuchen.“
Thomas Alva Edison

I. Inhaltsverzeichnis

II Abbildungsverzeichnis

III Verzeichnis der Schemata

IV Abkürzungsverzeichnis

[2.2.2]Kryptand	4,7,13,16,21,24-Hexaoxa-1,10-diazabicyclo[8.8.8]hexacosan
18-c-6 ([18]Krone-6)	1,4,7,10,13,16-Hexaoxacyclooctadecan
Ar	Aryl-Rest
Bipy	2,2'-Bipyridin
^{n}Bu	^{n}Butyl
^{t}Bu	^{t}Butyl
Bn	Benzyl
cAAC	zyklische Alkylaminocarbene
CV	Zyklovoltammetrie
CVD	*engl.* Chemical Vapour Deposition
d	Tag(e)
Dipp	2,6-Di-iso-propylphenyl
DMAP	4-(Dimethylamino)-pyridin
DME	1,2-Dimethoxyethan
DMF	Dimethylformamid
ESI	Elektrospray-Ionisation
Et	Ethyl
Et_2O	Diethylether
eq	Äquivalent(e)
FV	Feinvakuum
h	Stunde(n)
hmds	Hexamethyldisilazanid, $-N(SiMe_3)_2$
IPr	1,3-Bis(2,4,6-trimethylphenyl)imidazolinium
IR	Infrarot
Kat./cat.	Katalysator
konz.	konzentriert
Lsg.	Lösung
Lut	3,5-Lutidin

Me	Methyl
MeCN	Acetonitril
Mes	2,4,6-Trimethylbenzyl, Mesityl
min	Minute(n)
MS	Massenspektrometrie
nacnac	β-Diketiminato
NHC	*N*-heterocyclisches Carben
NMR	*engl.* Nuclear Magnetic Resonance Spectroscopy
Ph	Phenyl
Phen	Phenanthrolin
Phpy	2-Phenylpyridin
Py	Pyridin
R	Rest
RT	Raumtemperatur
T	Temperatur
THF (thf)	Tetrahydrofuran
TMS	Trimethylsilyl

1 Einleitung

1.1 Lineare 3d-Metall(II)-Komplexe (M = Cr – Co)

Seit der Entwicklung der Koordinationstheorie durch WERNER vor über einem Jahrhundert, wonach die Übergangsmetallionen in Komplexen eine charakteristische Koordinations- und Ligandenzahl aufweisen können, kann eine typische Koordinationssphäre (oktaedrisch, tetraedrisch oder quadratisch planar) genau definiert werden, was für die Koordinationschemie von zentraler Bedeutung ist.[1] Die Bindungstheorien entwickelten sich für diese klassischen Komplexe überwiegend aufgrund einfacher Moleküle oder Ionen als Liganden, deren Bindungsatom(e) als Quelle für die negative Ladungsdichte fungieren, auf welche ein Metallkation gerichtet ist.[2-6] Beispiele für solche Liganden sind: CO, CN^-, PR_3, NO^{2-}, Ethylendiamin, NH_3, Pyridin, NCS^-, H_2O, O_2, Oxalat, OH^-, N_3^- oder SCN^-. Diese Liganden haben gemeinsam, dass sie recht klein sind und somit einen geringen sterischen Anspruch besitzen, wodurch bis zu sechs Liganden (oktaedrisch) an ein Übergangsmetallion der ersten Reihe koordinieren können.[6-8] Ende der 1950er und 1960er Jahre arbeiteten einige Arbeitsgruppen an der systematischen Untersuchung der Auswirkungen einer Erhöhung der Sterik im Ligandensystem von Übergangsmetallkomplexen. Daraus resultierten Übergangsmetallalkoxide und -amide unter der Verwendung von Substituenten wie $–O^tBu$ oder $–NMe_2$ welche niedrigere Koordinationszahlen aufweisen.[9-11] Schließlich konnten BÜRGER und WANNAGAT die sperrige Silylamidogruppe $–N(SiMe_3)_2$ (hmds) als Ligand für 3d-Metallkomplexe einführen und die Komplexe $[M(hmds)_2]$ (M = Cr – Ni) darstellen (**Abbildung 1**), in dem sie MI_2 (M = Cr – Ni) mit Na(hmds) in THF bei Raumtemperatur umgesetzt haben.[12,13] Die Metall(II)-Komplexe (M = Cr – Co) werden in der vorliegenden Arbeit als Ausgangsverbindungen für die Synthese der Metall(I)-Komplexe genutzt.

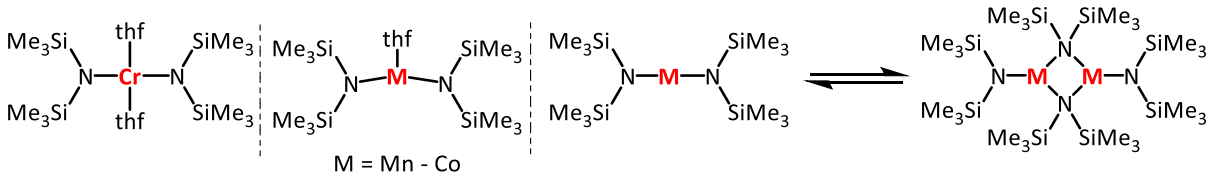

Abbildung 1. Von BÜRGER und WANNAGAT dargestellte Metall(II)-Komplexe $[M(hmds)_2]$ mit M = Cr – Co.[12-16]

Aufgrund ihrer hohen Reaktivität stellte sich die Synthese und Charakterisierung dieser linearen Übergangsmetallkomplexe als schwierig und langwierig heraus, weshalb die erste strukturelle Charakterisierung eines linearen Komplexes im Festkörper erst 1985 von POWER durchgeführt werden konnte. POWER führte seine Synthesen im Gegensatz zu BÜRGER und WANNAGAT in Diethylether (Et_2O) durch und zeigte, dass die Komplexe $[M(hmds)_2]$ (M = Cr – Co) im Festkörper als Dimere vorliegen und keine Addukte bilden (**Abbildung 1**).[14-16]

In der Koordinationschemie gehören stabile und offenschalige (d^1 – d^9lineare Übergangsmetallkomplexe zu den mit am seltensten und wenigsten untersuchten Komplexen. Für die Isolierung der zweifach-koordinierten Übergangskomplexe bei Raumtemperatur sind sterisch anspruchsvolle Liganden notwendig. Dies gelingt mit einer Vielzahl verschiedener, zumeist monoanionischer Liganden, welche zum Beispiel aus Alkyl-, Aryl-, Amido-, Alkoxido- oder Thiolato-Liganden bestehen. Aufgrund der koordinativ ungesättigten Natur des Metallions sind diese Verbindungen zum größten Teil höchst wasser- und luftempfindlich, wodurch die Isolierung dieser Komplexe erschwert wird. In der Vergangenheit zeigten Reaktivitätsstudien, dass die zweifach-koordinierten Komplexe schnell und leicht mit kleinen Molekülen wie beispielsweise O_2, N_2O und CO reagieren können oder mit Lewis-Basen wie Tetrahydrofuran (THF), Pyridin, Phosphinen und verschiedenen ein- oder mehratomige Anionen Komplexe bilden.[14-17]

Trotz dieser Schwierigkeiten, lineare Übergangsmetallkomplexe zu isolieren, ziehen sie eine große Aufmerksamkeit auf sich. Ein Grund dafür ist, dass die Übergangsmetalle durch nur zwei Atome komplexiert werden und dadurch ein unbesetztes oder einfach besetztes Valenzorbital aufweisen können. Dies erleichtert eine große Vielzahl an Substitutions-, Additions- oder Oxidationsreaktionen. Außerdem zeigten sich lineare Eisenkomplexe als nützliche synthetische Vorläufer für die Synthese von Nanomaterialien und Katalysatoren. Darüber hinaus sind lineare Komplexe aufgrund ihrer magnetischen Eigenschaften sehr interessant.[18-21] EABORN und SMITH veröffentlichten die Synthese und Struktur von $[Mn(C(SiMe_3)_3)_2]$, in der das Manganatom linear streng koordiniert ist (**Abbildung 2**).[22]

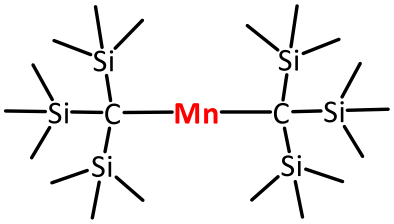

Abbildung 2. Struktur von $[Mn(C(SiMe_3)_3)_2]$.[22]

Die vollständige Charakterisierung und Strukturaufklärung der Metall(II)$(hmds)_2$-Komplexe erfolgte durch BRADLEY (1972) und ANDERSEN (1987) erst einige Jahre später.[10,23] Weitere Untersuchungen zeigten, dass die Metall(II)-Komplexe (M = Mn – Co) Dimere im Festkörper bilden können. Die Komplexe mit einem Chrom- bzw. Kobalt-Zentralatom können durch THF stabilisiert und dargestellt werden.[23-27] In den 1970er und 1980er Jahren wurden die Arbeiten an niedrig-koordinierten und offenschaligen Übergangsmetallkomplexen stark auf dreifach-koordinierte Komplexe fokussiert. Insbesondere wurde dazu der sperrige hmds-Ligand von BRADLEY und Mitarbeitern für die Stabilisierung von trigonalen Komplexen einiger Übergansmetalle und Lanthanide genutzt.[28-31] Des Weiteren wurden in den 1990er Jahren eine Vielzahl an trigonalen Komplexen mit sterisch anspruchsvollen Amido-, Aryloxido-, Triorganosiloxido- und Arylthiolato-Liganden dargestellt. Diese führten auch zur Synthese zahlreicher neuer dreifach-koordinierter Komplexe der Gruppe 5, 6, 8 und 9. Die dreifach-koordinierten schweren Elemente der Gruppe 5 und 6 zeigten eine sehr vielseitige Chemie, da diese Komplexe in der Lage sind, zahlreich kleine Moleküle einschließlich N_2 und CO zu aktivieren.[31-33]

1.2 Eigenschaften von linearen 3d-Metall(II)-Komplexen

Im elektronischen Grundzustand sind in Komplexen mit linearer Koordination am zentralen Metall(II)-Atom die Liganden entlang einer Achse (konventionell die Z-Achse) angeordnet. Das magnetische Orbitalmoment erster Ordnung ergibt sich aus einer ungeraden Anzahl von Elektronen in d_{x2-y2}, d_{xy} oder d_{xz}. Der d_{yz}-Orbitalsatz kann aufgrund der fehlenden Interaktion mit Orbitalen der Liganden und einem schwachen Ligandenfeld behindert werden, wodurch in bestimmten Fällen freier Ionenmagnetismus beobachtet wird. Dies wird belegt durch magnetische Messungen, die das Vorhandensein sehr hoher interner Magnetfelder zeigen. Ein hoher Drehimpuls kann einen wesentlichen Beitrag zur Nullfeldaufspaltung leisten, sodass die Energiebarriere für die Umkehrung der Magnetisierung in den Molekülen beeinflusst werden kann.[18-21,36]

Unter der sehr vereinfachten Annahme für die Ligandenfeldtheorie, dass nur Metall/Ligand-σ-Wechselwirkungen stattfinden, können die d^1-d^9-Elektronenkonfigurationen zusammen mit ihren Grundzuständen beschrieben werden (**Abbildung 3**).[34,35] In allen Fällen wird eine High-Spin-Konfiguration und ein geringes Ligandenfeld angenommen, welches experimentell durch magnetische Messungen bestätigt wurde.[18]

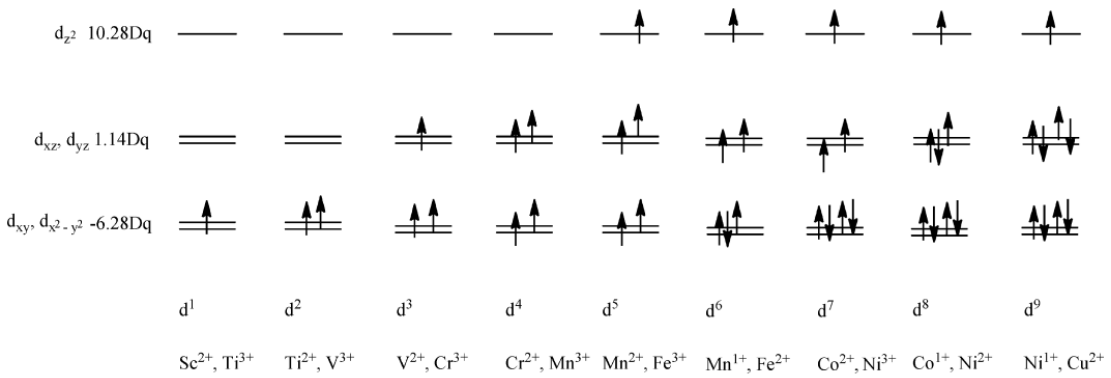

Abbildung 3. Grundzustände und d-Orbitalaufspaltung (d^1 – d^9) in einem einfachen, linearen Kristallfeld.[18]

Die Mehrheit der derzeit bekannten stabilen Komplexe hat im festen Zustand eine nicht-lineare zentrale Bindungsachse. ATANASOV berechnete für einfache Metall(II)-Komplexe (z.B. $M(CH_3)_2$), dass durch den RENNER-TELLER-Effekt mit Ausnahme von Mangan die Moleküle eine leichte gewinkelte Koordination bevorzugen, aber durch die sterisch anspruchsvollen Liganden werden diese in die Linearität gezwungen.[18] Bei einigen linearen Komplexen wird die Linearität durch die Einkristallstrukturanalyse bestimmt, da bei dieser Charakterisierungsmethode mehrere Faktoren zum einen gemittelt werden und zum anderen wird die strikte Linearität durch oftmals ein Inversionszentrum erzeugt.

1.3 Lineare 3d-Metall(I)-Komplexe

Schwerpunkt der hier dargelegten Arbeit ist die Untersuchung des Verhaltens von linearen 3d-Metall(I)-Komplexen (M = Cr – Co) gegenüber C/N-Mehrfachbindungen und aromatischen Systemen. Lineare Metall(I)-Komplexe sind eine recht junge Verbindungsklasse und mit Ausnahme von Kupfer(I)-Komplexen erst seit 2007 bekannt. Die Eigenschaften und das Reaktionsverhalten von Metall(I)-Komplexen (M = Cr – Ni) sind erst wenig erforscht. Im Gegensatz zu Verbindungen mit zweifach-koordinierten Metall(II)-Ionen, welche aufgrund der nahezu ausschließlichen Verwendung von anionischen Liganden neutral sind, finden für monovalente Gegenstücke auch Neutralliganden wie hauptsächlich *N*-heterozyklische-Carbene (NHC´s) und cyclische Alkylaminocarbene (cAAC´s)) Verwendung. Ein Übergangsmetall-Ion der 3d-Block-Elementreihe wird von zwei gleichen (homoleptisch) oder zwei verschiedenen (heteroleptisch) Liganden koordiniert, wodurch je nach verwendeten Liganden geladene oder neutrale Komplexe erhalten werden.

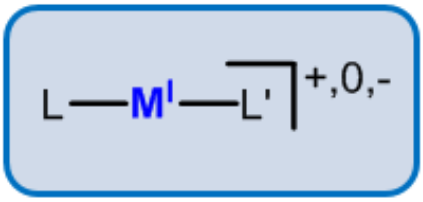

Abbildung 4. Strukturmotiv von einem linearen Metall(I)-Komplex.

Die ungewöhnliche Geometrie und Oxidationsstufe machen die linearen Metall(I)-Komplexe im Hinblick auf die weitere Reaktivität sehr Interessant, aber gleichzeitig auch hochempfindlich. Dadurch wird die Isolierung der Komplexe erschwert und es werden sterisch anspruchsvolle und/oder elektronisch stabilisierende Liganden wie NHC´s, Aryle, Phosphine oder Amide benötigt.

1.3.1 Lineare, heteroleptische 3d-Metall(I)-Komplexe

POWER gelang es 2007 den ersten heteroleptischen Metall(I)-Komplex darzustellen. Er konnte einen neutralen Chrom(I)-Komplex mit einem Phosphinliganden und einem sterisch anspruchsvollen Aryl-Liganden isolieren (**Abbildung 5** (links)), in dem er den (3,5-$^{i}Pr_2$-Ar)CrCl Vorläufer mit KC_8 in PMe_3 umgesetzt hatte.[37] Nur ein Jahr später konnte HILLHOUSE durch die Umsetzung von $(IPrNi(\mu\text{-}Cl))_2$ und Na(hmds) die Synthese eines Ni(I)-Komplexes bestehend aus einem anionischen Amid-Donorliganden und einem neutralen NHC-Liganden darstellen (**Abbildung 5** (rechts)).[38] Für die Nickel(I)-Verbindungen ist zu beachten, dass die Oxidationsstufe +1 insbesondere im Vergleich zu den jeweils leichteren 3d-Metallen (M = Cr – Co) relativ stabil ist.[38]

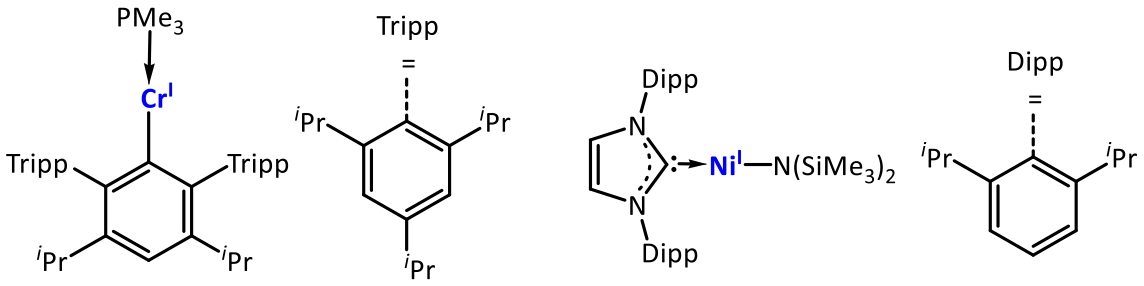

Abbildung 5. Die ersten bekannten heteroleptischen, linearen Chrom(I)-Komplex (POWER, links) und der Nickel(I)-Komplex (HILLHOUSE, rechts).[37,38]

In den nächsten Jahren konnten auch lineare Eisen(I)- und Kobalt(I)-Komplexe aus der 3d-Elementreihe von TILLEY (Eisen)[39] und JONES (Kobalt)[40] synthetisch dargestellt werden. TILLEY deprotonierte $Fe(N(Dipp)(SiMe_3))_2$ mit Diethylaminhydrochlorid in THF und gab 1,3-Bis(2,6-diisopropylphenyl)imidazolinium (IPr) hinzu und reduzierte *in-situ* den Komplex mit KC_8. JONES reduzierte den Kobalt-Komplex-Vorläufer ($[((SiPh_3)(Ar)N)Co(thf)(\mu\text{-}Cl)]_2$) zunächst mit KC_8 in Benzol und isolierte die Zwischenstufe ($[((SiPh_3)(Ar)N)Co(\eta^6\text{-}C_6H_6)]$), die er weiter mit einem Carben umsetzte, um den Kobalt(I)-Komplex darstellen zu können. **Abbildung 6**

zeigt den Eisenkomplex (rechts) und den Kobaltkomplex (links). HILLHOUSE konnte weitere Nickel(I)-Komplexe darstellen, die in der Lage waren, benzylische C–H-Bindungen zu aktivieren.[41]

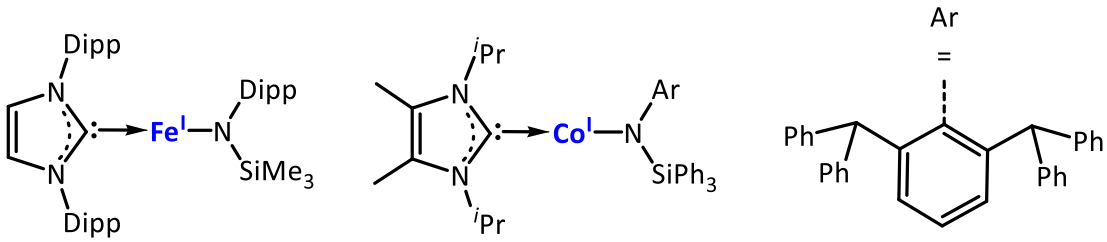

Abbildung 6. Lineare heteroleptische Metall(I)-Komplexe mit Eisen (TILLEY, links) und Kobalt (JONES, rechts).[39,40]

TILLEYS Reaktivitätsstudien des Eisen(I)-Komplexes (**Abbildung 6,** (links)) gegenüber verschiedenen Alkinen zeigten erstmals eine katalytische Anwendung von Metall(I)-Komplexen. Der beschriebene Komplex ([Fe(NHC)(N(Dipp)(SiMe$_3$))] konnte als Katalysator für die Trimerisierung verschiedenster Alkine eingesetzt werden (**Schema 1**). TILLEY konnte später zeigen, dass das NHC dekoordiniert und sich ein verbrückender Eisen-Alkin-Komplex bildet.[39]

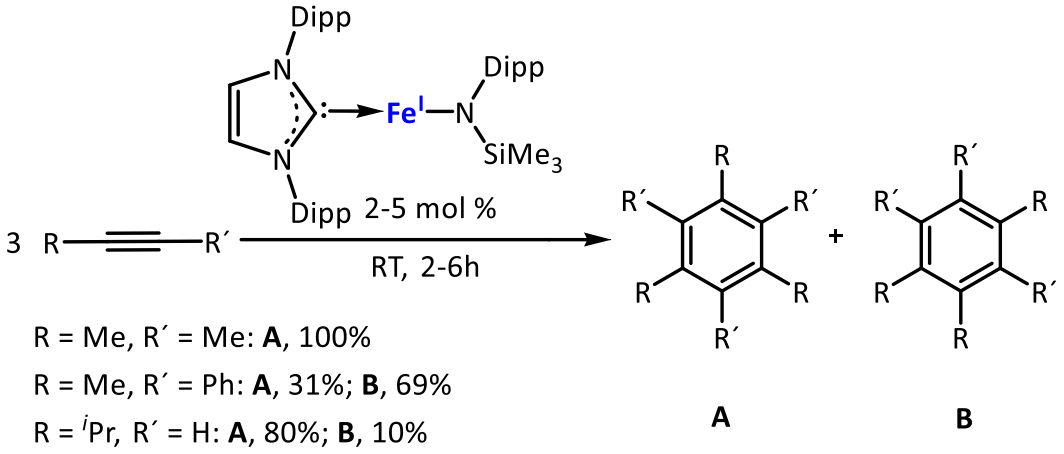

Schema 1. Katalytische Zyklotrimerisierung verschiedener Alkine durch den gezeigten Eisen(I)-Komplex.[39]

1.3.2 Lineare, homoleptische 3d-Metall(I)-Komplexe

Die erst seit 2012 bekannten monovalenten homoleptischen 3d-Übergangsmetall-Komplexe (M = Cr – Ni) werden hauptsächlich durch die Reduktion eines linearen Vorläufers oder durch eine Halogenidabstraktion von einem dreifach-koordinierten Bis(Carben)metall(I)-Halogenid erhalten. Das Metallion wird durch sterisch anspruchsvolle –C(SiMe$_3$)$_3$- und -N(Ar)(SiR$_3$)-Liganden oder durch elektronisch stabilisierende Carbene (besonderes zyklische Alkylaminocarbene, cAAC) stabilisiert.[42-48]

Die Arbeitsgruppe von DENG konnte so 2013 den ersten homoleptischen, kationischen Kobalt(I)-Komplex mit NHC-Liganden darstellen (**Abbildung 7**). Dieser Kobalt(I)-Komplex weist bei Raumtemperatur ein hohes magnetisches Moment von μ_{eff} = 3.65 μ_B (μ_{so} = 2.83 μ_B S=1) auf. Weiterhin zeigt er eine verlangsamte Relaxation der Magnetisierung bei tiefen Temperaturen (τ_0 = 6.6 x 10^{-6} s) und ist damit der erste Einzelion-Magnet mit einer d^8-Elektronenkonfiguration.[43,48] Kurz darauf berichteten drei Arbeitsgruppen um PETERS, ROESKY und DENG unabhängig voneinander von analogen Verbindungen des Eisens unter Verwendung von cAAC-Liganden (**Abbildung 7**). Hierbei konnten wiederum interessante magnetische Eigenschaften aber auch die weitere Reduktion zu nullvalenten Verbindungen beobachtet werden.[45,46,48]

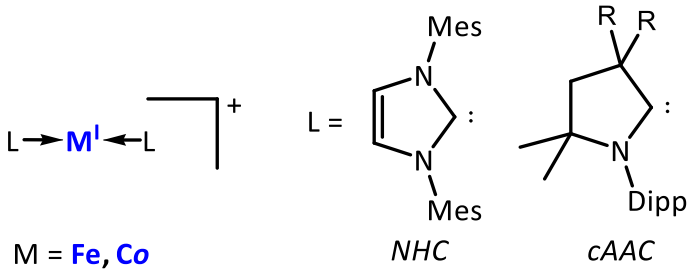

Abbildung 7. Allgemeine Struktur von kationischen, homoleptischen Metall(I)-Komplexen (M = Fe – Co).[43-48]

2013 folgten die ersten anionischen, homoleptischen Übergangsmetall(I)-Komplexe fast zeitgleich und unabhängig voneinander aus den Arbeitsgruppen TILLEY und LONG. Beide reduzierten jeweils lineare Metall(II)-Vorläufer-Komplexe mit KC_8, um die entsprechenden Metall(I)-Komplexe zu erhalten. In beiden Fällen wurde eine Komplexierungshilfe für das Kaliumion, im Fall von TILLEY ein Kronenether (18-c-6) und bei LONG ein [2.2.2]Kryptand, genutzt. Die isolierte Verbindung [K[2.2.2]Kryptand][$Fe^{I}(C(SiMe_3)_3)_2$] (**Abbildung 8** (rechts)) von LONG zeigt die höchste Relaxationsbarriere von 226 cm^{-1} für mononukleare Einzelmolekülmagnete auf Basis von 3d-Übergangsmetallen, die zu der Zeit beobachtet werden konnte. TILLEY synthetisierte zunächst den Nickel(I)-Komplex (**Abbildung 8** (links)) mit dem (N(Dipp)($SiMe_3$))-Ligand gefolgt von einem Chrom(I)-Komplex, während POWER und WERNCKE die gezeigte Reihe vervollständigen konnten.[42-50]

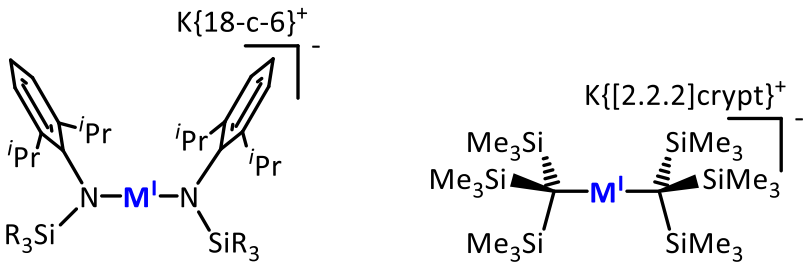

M = **Cr** (R = ^{i}Pr)
M = **Mn - Ni** (R = Me)

M = **Mn**, **Fe**

Abbildung 8. Beispiele für die ersten anionischen, homoleptischen Metall(I)-Komplexe (M = Cr – Ni).[42-50]

WERNCKE konnte durch eine Reduktion mit KC_8 und in Anwesenheit von 18-c-6 die bereits bekannten Verbindungen $[M^{II}(hmds)_2]$ (M = Cr – Co), von BÜRGER und WANNAGAT, reduzieren. Diese Reduktion ist auch von Addukten (z. B. PCy_3) in THF möglich. Der Mangan(I)-Komplex bildet im Festkörper ein Dimer aus und ist nicht langzeitstabil, wodurch WERNCKE diesen nur durch Röntgenstrukturanalyse, *in-situ* ^{1}H-NMR-Spektroskopie und magnetische Messung nach der Methode von EVANS untersuchen konnte. Die Röntgenstrukturanalyse zeigt, dass eine dimere Verbindung mit einem seltenem Fall einer nicht ligandengestützten Mn—Mn-Bindung (2.721 Å)[49] vorliegt. Die Verbindung disproportionierte schnell unter Bildung von [K{18-c-6][Mn(hmds)$_3$)], [K{18-c-6][hmds], und Mangan-Metall. Bei Verwendung der Metalle Chrom, Eisen und Kobalt konnten die Verbindungen vollständig charakterisiert werden (**Schema 2**).[50,51]

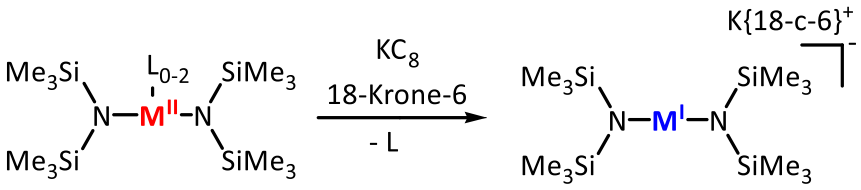

M: **Cr**, **Fe**, **Co**
L: thf

M = **Cr**, **Fe**, **Co**

Schema 2. Synthese der $M^{I}(hmds)_2$-Komplexe (M = Cr, Fe, Co).[50,51]

WERNCKES Untersuchungen der linearen Metall(I)-Amide hinsichtlich ihrer magnetischen Eigenschaften zeigen, dass sich alle Komplexe im High-Spin-Zustand befinden, während ein starker Orbitalbeitrag in den Eisen- und Kobalt-Komplexen zum magnetischen Moment beobachtet wird (**Abbildung 9** (links)). Zusätzlich kann gezeigt werden, dass das d_{z2}-Orbital der Metall(I)-Ionen im Vergleich zu den Metall(II)-Komplexen (**Abbildung 3**) energetisch stark abgesenkt wird.[50,51] In **Abbildung 9** (rechts) wird das Orbitalschema von dem Komplex

K[2.2.2]Kryptand][Fe^{I}(C(SiMe$_3$)$_3$)$_2$] von LONG gezeigt. Dieser zeigt im Vergleich zu den Metall(I)-Amide von WERNCKE, dass die Orbitale energetisch höher liegen, wodurch die höhere Relaxationsbarriere für Einzelmolekülmagnete erklärt werden kann. Es wird gezeigt, dass keine Aufspaltung der d_{xz}- und d_{yz}-Orbitale stattfindet und dass die theoretische Barriere gleich ist.[47]

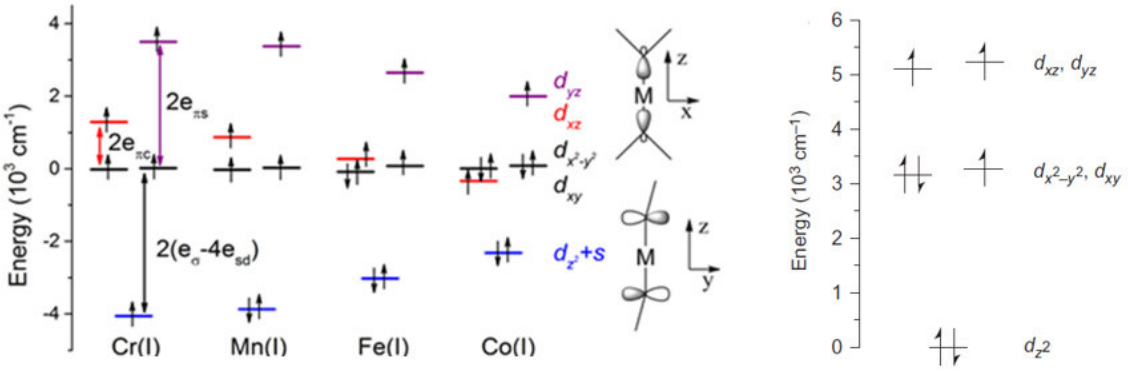

Abbildung 9. Grenzorbitaldiagramm für [K{18-c-6}][M^{I}(hmds)$_2$] (links) (Mangan wurde anhand des Eisenkomplexes berechnet) und [K[2.2.2]Kryptand][Fe^{I}(C(SiMe$_3$)$_3$)$_2$] (rechts).[47,50,51]

1.4 Reaktivität von linearen Metall(I)-Komplexen

Die durch Übergangsmetalle vermittelte Aktivierung kleiner Moleküle und starker Bindungen, spielt eine entscheidende Rolle bei zahlreichen synthetischen, industriellen oder biologischen Transformationen. Die jeweiligen Metallspezies können eine ungewöhnliche (niedrige) Oxidationsstufe und/oder besondere Koordinationsumgebung aufweisen, wobei die Natur der aktiven Schlüsselintermediate während katalytischer Prozesse, zum Beispiel für die eisenkatalysierte Kreuzkupplung, oft nicht bekannt sind.[52,53] Aufgrund der jungen Geschichte isolierbarer linearen Metall(I)-Komplexe ist wenig über deren Reaktivität bekannt. Die Verbindungen weisen durch die Kombination von geringer Koordination und Wertigkeit auf ein hohes chemisches Reaktivitätspotential hin. Die wenigen bisher durchgeführten Reaktivitätsstudien beziehen sich lediglich auf die Aktivierung von Kohlenstoff-Halogenid-Bindungen auf Basis von Nickel(I)-Komplexen (**Abbildung 8**).[42] Die Arbeitsgruppe um TILLEY konnte mit dem von ihnen erhaltenen Nickel(I)-Komplex (K[Ni(N(Dipp)(SiMe$_3$)]) zeigen, dass dieser durch Methyliodid unter Bildung einer Nickel(III)-Alkyl-Spezies oxidiert werden kann (**Schema 3**).[54]

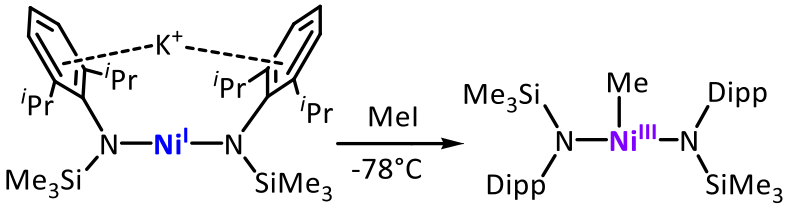

Schema 3. Methylierung von Nickel(I)-Komplexen durch Methyliodid.[54]

DITTRICH konnte anhand eines $[Mn^{I}(cAAC)_2]$-Komplexes molekularen Wasserstoff (H_2) bei Raumtemperatur spalten und durch eine weitere Ein-Elektronen(e^-)-Reduktion des $[M^{I}(cAAC)_2]^+$ (M = Fe, Co) zu $M^0(cAAC)_2$ reduzieren, wobei in beiden Fällen die Elektronen-Akzeptor Eigenschaften des Carbenliganden eine entscheidende Rolle spielen (**Schema 4**).[44,46]

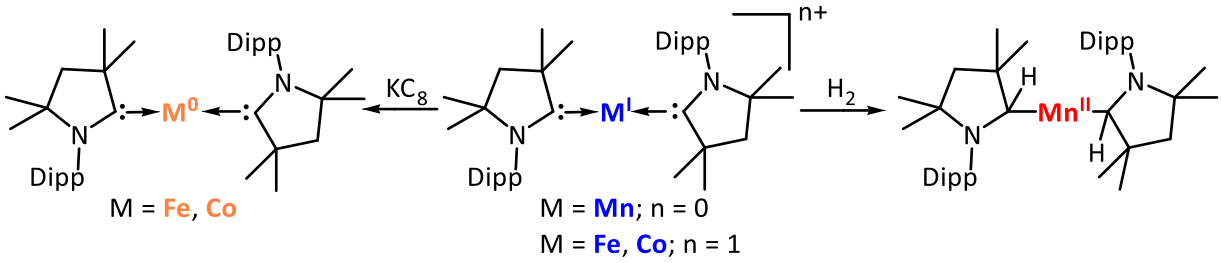

Schema 4. Reaktivitätsstudie von linearen $[M^{I}(cAAC)_2]$-Komplexen (M = Mn – Co).[44,46]

Die Arbeitsgruppe von DENG berichtete kürzlich über die Reaktivität eines kationischen Bis(Carben)eisen(I)-Komplexes gegenüber dem Lösungsmittel THF, wobei ein dreifach-koordiniertes T-förmiges Addukt erhalten wurde. Der Bis(Carben)eisen(I)-Komplex wurde durch die Reduktion von Eisen(II)-Dihalogeniden durch KC_8 in Gegenwart der entsprechenden NHC-Liganden und anschließender Halogenid-Abstraktion mit $NaB(Ph)_4$ dargestellt. Untersuchungen der Lösungseigenschaften durch Absorptionsspektroskopie und Zyklovoltammetrie deuten darauf hin, dass der Eisen(I)-Komplex in THF-Lösung seine entsprechende Zweifach- und Dreifach-Koordinationsform beibehält und ein THF-Molekül reversibel koordinieren kann, um vermutlich die T-förmige Spezies $[(sIMes)_2Fe(THF)][BAr^F_4]$ zu bilden (**Abbildung 10**).[48]

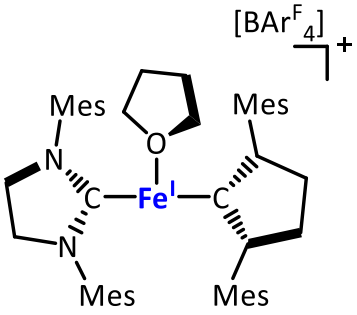

Abbildung 10. T-förmiger Metall(I)-Komplex $[(sIMes)_2Fe(THF)][BAr^F_4]$.[48]

Wie bereits erwähnt wurde, gibt es nur wenige Berichte über die Reaktivität linearer Metall(I)-Komplexe. Daher können auch verwandte lineare Metall(I)-Fragmente, obwohl sie weiterhin durch schwach koordinierende Stickstoff-(N_2) oder Arenliganden maskiert sind, ver-

gleichsweise gut den Fall von Metall(I)-β-Diketiminato-Komplexen beschreiben. In diesen Verbindungen wird das Metallion durch den β-Diketiminato-Chelatliganden (nacnac) stabilisiert und trigonal koordiniert, wodurch die dritte und freie Koordinationsstelle von einem weiteren labilen Liganden wie N_2 oder Arenen abgesättigt wird oder zur Substrataktivierung verwendet werden kann (**Abbildung 11**).[55-61]

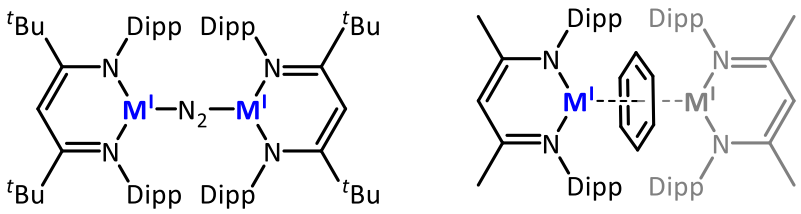

M = **Cr**; *side-on*-N_2
M = **Fe**, **Co**, **Ni**; *end-on*-N_2

mononuklear: M = **Fe**
dinuklear: M = **Cr**, **Ni**

Abbildung 11. Maskierte lineare Metall(I)(nacnac)-Komplexe.[55-61]

HOLLAND konnte Pyridin an einem Eisen(I)-nacnac-Komplex koordinieren und reduktiv kuppeln. Darüber hinaus zeigte HOLLAND, dass das Pyridin formal über eine Ein-Elektronen-Reduktion reduziert wird (**Schema 5**). Dabei handelt es sich bei dem resultierenden Pyridylradikalanionen-Komplex um eine schwer isolierbare Spezies, die spontan dimerisiert (**Schema 5**).[62]

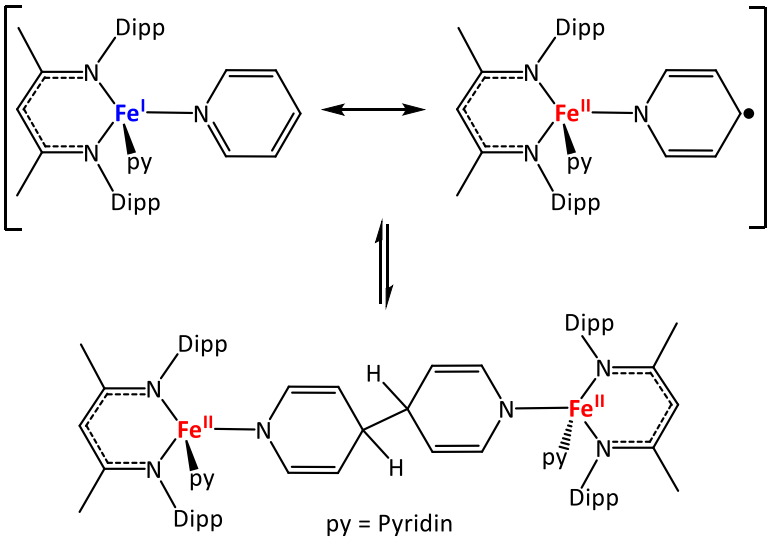

Schema 5. Elektronenübertrag von einem niedervalenten Eisen(I)-nacnac-Komplex auf das Pyridin.[62]

1.4.1 Reaktivität linearer Metall(I)-Komplexe gegenüber C/C-Mehrfachbindungen

Die Wechselwirkung von niedervalenten 3d-Metallen mit Alkinen ist in der metallorganischen Chemie von fundamentaler Bedeutung. Sie nimmt eine entscheidende Rolle bei

wichtigen katalytischen Reaktionen, wie beispielsweise Alkin-Trimerisierung der für die Synthese von nicht funktionalisiertem Benzol, der Bindungsmetathese oder Zyklisierungs- und Oligomerisierungsreaktionen ein.[67-71] Durch die vielen Anwendungsgebiete ist die Kenntnis der Alkin-Metall-Wechselwirkung von sehr großer Bedeutung, um die Reaktionswege vorhersagen und steuern zu können. Bei elektronenreichen Übergangsmetall-Alkin-Komplexen sind an der Metall-Alkin-Bindung die Rückbindung der gefüllten d-Orbitale zum π^*-Orbital des Alkins sowie eine elektrostatische Wechselwirkung beteiligt.[77-81] Für elektronenarme Übergangsmetalle, wie Titan, lassen sich diese Alkin-Komplexe am besten als Metallozyklopropene mit zwei kovalenten Metall-Kohlenstoff-Bindungen beschreiben.[72-76]

Das DEWAR-CHATT-DUNCANSON-Modell ist ein Modell in der metallorganischen Chemie, durch welches die Art der chemischen Bindung zwischen einem Alkin, Alken, CO, etc. und einem Metall in vielen metallorganischen Verbindungen erklärt werden kann. Die Bindungsbeschreibung zeigt, dass die Alkine höchst vielseitig in ihren Bindungsmodi sein können. Das Alkin besitzt zwei π-Orbitale (a_1 und b_1), wobei das a_1 eine σ-Donor-Bindung eingeht. Dabei wirkt das Alkin als 2-Elektronen-Neutralligand, während das andere Alkin-π-Orbital (b_1) senkrecht dazu steht und gegebenenfalls eine π-Donor-Bindung eingehen kann. Dies geschieht nur wenn leere d-Metall-Orbitale von π-Symmetrie zur Verfügung stehen, dabei wirkt das σ,π-Alkin als 4-Elektronen-Neutralligand. Das leere Alkin-π^*-Orbital empfängt Elektronendichte über eine Metall-Ligand Rückbindung und ist in jedem Fall ein stark π-azider Ligand. Das Metall wird oxidiert und das Alkin formal zu $(RCCR)^{2-}$ reduziert, wenn die Rückbindung extrem stark ausgeprägt ist. Das Dianion $(RCCR)^{2-}$ kann als σ,π-6-Elektronen-Donor angesehen werden. Die δ-Bindung (a_2) wird durch eine schwache Rückbindung an den zwei Knotenebenen dargestellt (**Abbildung 12**).[63-66]

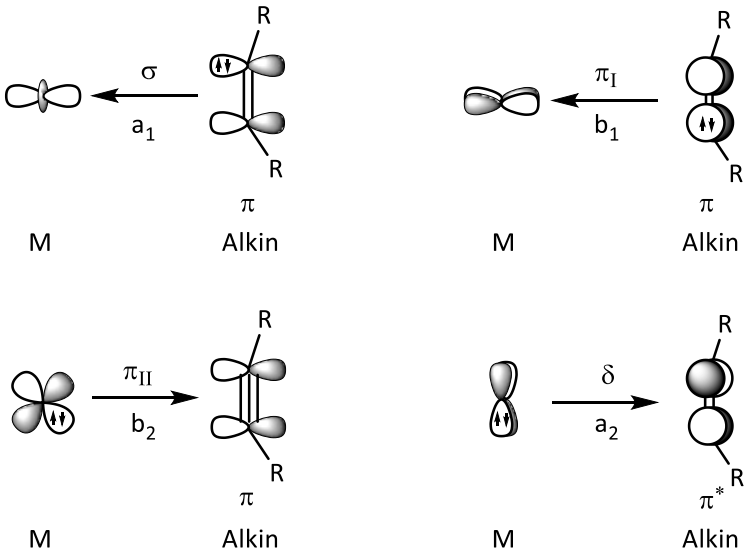

Abbildung 12. Wichtige Orbital-Interaktionen bei geschlossenschaligen Übergangsmetallkomplexen mit teilweise gefüllten Schalen (DEWAR-CHATT-DUNCANSON-Modell).

Neben der *side-on*-Koordination lassen sich für Alkine eine große Vielfalt und Variationsbreite an weiteren Koordinationsmodi beobachten (**Abbildung 13**), wobei diese Einteilung von den jeweiligen Bindungstypen abhängt und deshalb nicht immer eindeutig ist.[66]

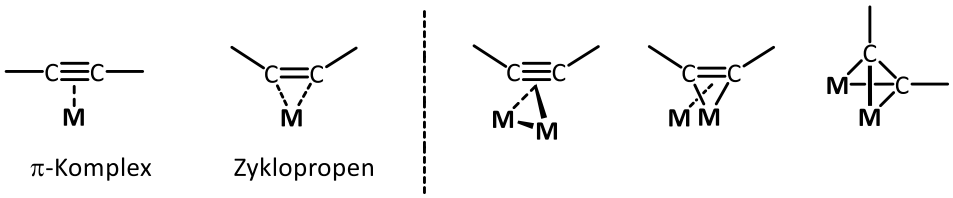

Abbildung 13. Verschiedene Koordinationsformen der Metall-Alkin-Komplexe.[66]

Die überwiegende Mehrheit der in der Literatur bekannten Alkin-Komplexe aus der mittleren 3d-Metallreihe (M = Cr – Co) verfügt über Carbonyl-, Phosphin- und/oder Cyclopentadienylliganden. Von diesen Liganden ist bekannt, dass sie ein niedervalentes Metallatom stabilisieren können.[82-99] Diese Liganden weisen ein starkes Ligandenfeld auf und besitzen, in Verbindung mit hohen Koordinationszahlen ihrer jeweiligen Metallkomplexe, typischerweise eine Low-Spin-Elektronenkonfiguration. Über die Wechselwirkung von Alkinen mit niedrig-koordinierten 3d-Metallionen und einer High-Spin-Konfiguration ist nur wenig bekannt. Für die Metallzentren von Chrom bis Kobalt konnte nur eine geringe Anzahl niedrig-koordinierter Alkinkomplexe (Koordinationszahl ≤ 4) mittels Einkristallstrukturanalyse aufgeklärt werden. THEOPOLD konnte in seiner Arbeitsgruppe die ersten niedervalenten Chrom(I)-Alkin-Komplexe synthetisieren (**Abbildung 14**). Die Acetylenfragmente in den Chrom(I)-Alkin-Komplexen zeigen,

dass eine zweifache Reduktion des Alkins stattgefunden hat, da diese Fragmente eine Bindungslängen- und –winkelaufweitung in Richtung eines Alkens zeigen. Die strukturellen Veränderungen in den Acetylenfragmenten und die Tatsache, dass ein effektives magnetisches Moment von 3,9 μ_B vorliegt, legen nahe, dass sich Chrom mit entsprechender zweifacher Reduktion des Diphenylacetylenliganden im Oxidationszustand +III befindet, was zu einer angemesseneren Beschreibung als Metallazyklopropen führt.[100-102]

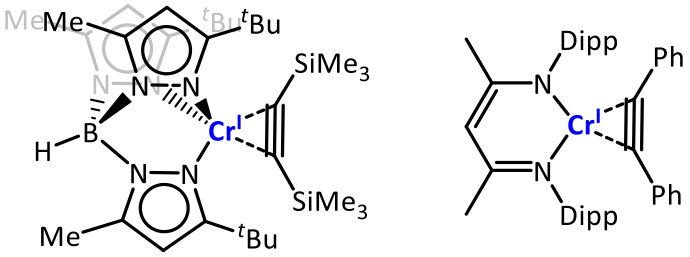

Abbildung 14. Die ersten Chrom(I)alkin-Komplexe.[100-102]

Hinsichtlich Mangan gibt es in der Literatur nur sehr wenige Beispiele für Alkin-Komplexe wie [Mn(η-C_5H_5)(CO)$_2$(PhCCPh)] und keine niedrig-koordinierten Verbindungen der Koordinationszahl ≤4. Diese haben oft Carbonylgruppen oder sterisch sehr anspruchsvolle Carbene als Liganden.[87-90] Für Eisen konnten die Arbeitsgruppen um HOLLAND, CHIRIK und DENG fast zeitgleich die ersten niedervalenten Eisen-Alkin-Komplexe synthetisieren und charakterisieren, wobei alle drei Arbeitsgruppen nacnac und/oder Carbene als Liganden nutzten (**Abbildung 15**).[103-106]

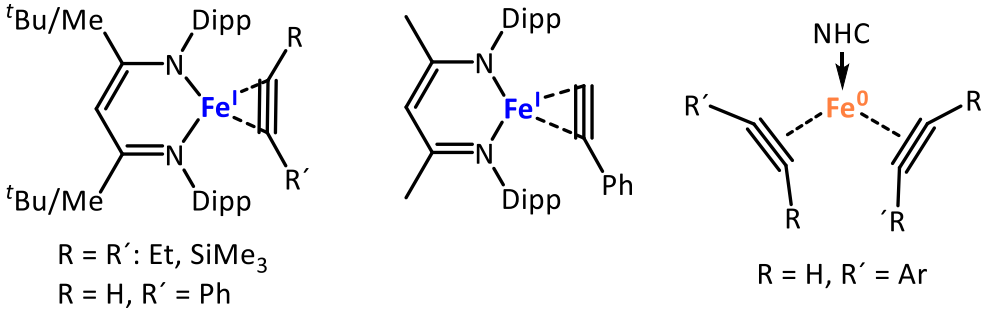

Abbildung 15. Die ersten niedervalenten Eisen-Alkin-Komplexe von CHIRIK (links), HOLLAND (mitte) und DENG (rechts).[103-106]

Für Kobalt gelang es DENG und WALTER die ersten niedervalenten Kobalt-Alkin-Komplexe ihrer Art darzustellen. Wie bei Mangan und Eisen nutzten beide sterisch anspruchsvolle Carbene für die Darstellung der niedervalenten Kobalt-Komplexe (**Abbildung 16**).[107-109]

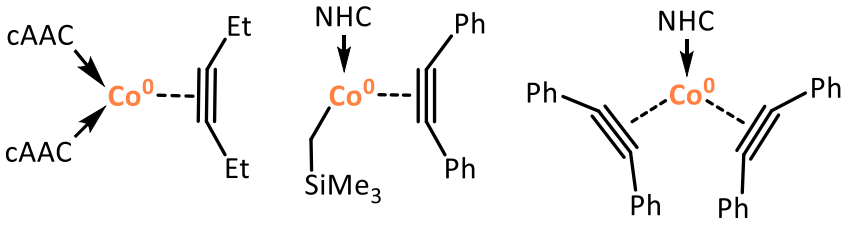

Abbildung 16. Die ersten niedervalenten Kobalt-Alkin-Komplexe von DENG (links, mitte) und WALTER (rechts).[107-109]

Wie schon zuvor bei den niedrig-koordinierten Alkin-Komplexen ist nur sehr wenig über anloge, niedervalente Metallalken-Komplexe bekannt. Die Koordination eines Alkens an ein 3d-Metallatom kann als Metall-π-Komplex angesehen werden. Die Bindungsverhältnisse in Alken-Komplexen können mittels DEWAR-CHATT-DUNCANSON-Modell, wie schon bereits bei den Alkin-Komplexen, beschrieben werden. Hierbei lassen sich ähnlich zu Alkinen diese je nach Metall als π-Komplexe oder Metallcyclopropane auffassen.[66] Die drei Arbeitsgruppen um THEOPOLD (Chrom)[110], HOLLAND (Eisen)[105] und DENG (Kobalt)[111] konnten die ersten niedrig-koordinierten Metallalken-Komplexe darstellen (**Abbildung 17**). Niedervalente Mangan-Alken-Komplexe sind in der Literatur nicht bekannt.

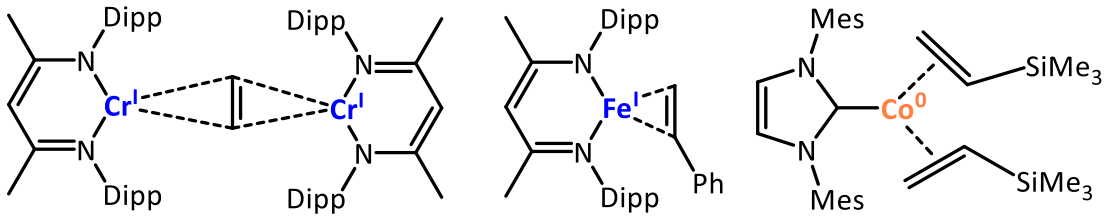

Abbildung 17. Die ersten niedervalenten Metall(I)-Alken-Komplexe (M = Cr, Fe, Co) von THEOPOLD (links), HOLLAND (mitte) und DENG (links).[105,110,111]

2 Motivation und Aufgabenstellung

Wie in der Einleitung bereits erwähnt, wurde das Reaktivitätsverhalten von linearen Metall(I)-Komplexen (M = Cr – Co) erst wenig erforscht. Durch diesen Aspekt motiviert befasst sich die vorliegende Arbeit mit dem Verhalten von linearen 3d-Metall(I)-Komplexen gegenüber C/N-Mehrfachbindungen und aromatischen Systemen. Dabei wird die Arbeit in vier Teile aufgeteilt.

Im ersten Teil sollten die linearen anionischen 3d-Metall(I)-Silylamide (M = Cr – Co)[50,51] mit 2,2'-Bipyridin (bipy) umgesetzt werden (**Schema 6**). Aufgrund des hohen negativen Reduktionspotentials werden ihre Fähigkeiten, Substrate unter Koordination reduzieren zu können, untersucht. Die dargestellten Komplexe sollen hinsichtlich ihrer elektronischen Eigenschaften bzw. Struktur untersucht werden (**Schema 6**).

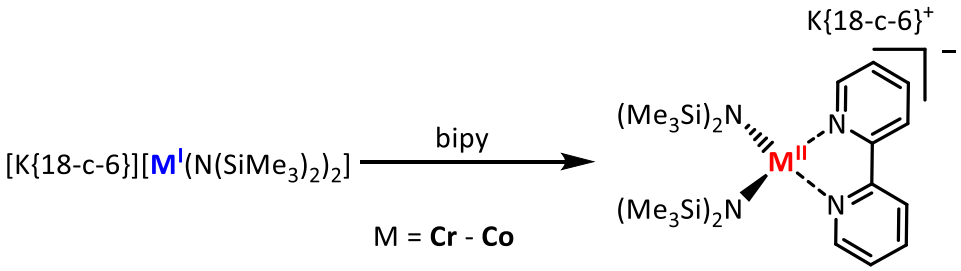

Schema 6. Reaktionspfad für die Synthese der reduzierten Metall(II)-(bipy)-Komplexe.

Alternativ wird getestet, ob die Produkte auch über einen anderen Syntheseweg erhalten werden können, ob es möglich ist, die in der Literatur bekannten neutralen Metall(II)(bipy)-Komplexe (M = Cr – Fe)[112,113] durch KC_8 in Anwesenheit von 18-c-6 zu reduzieren und die Reihe durch Kobalt(II)- und Zink(II)-Komplexe zu vervollständigen (**Schema 7**). Des Weiteren sollen beide Syntheseansätze mit einander verglichen werden, um Rückschlüsse auf die Oxidationsstufe und die elektronische Struktur zu ziehen.

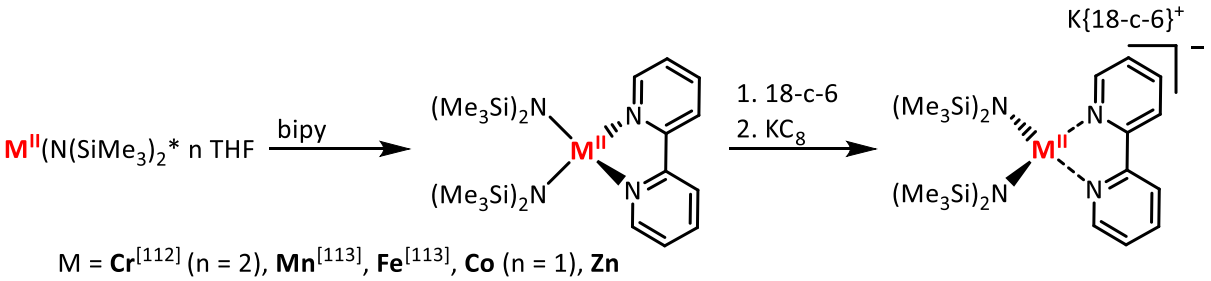

Schema 7. Allgemeiner Syntheseansatz der bekannten neutralen Metall(II)-(bipy)-Komplexe (M = Cr – Fe) sowie deren anschließende Reduktion.[110,111]

Im zweiten Teil soll die Arbeit von HOLLAND[62] aufgegriffen werden, in welcher er von einem Elektronenübergang eines Metall(I)-Komplexes auf Pyridin berichtet (**Schema 5**). In der vorliegenden Ausarbeitung werden die schon gezeigten Metall(I)-Silylamide (M = Cr – Co)[50,51] mit Pyridin umgesetzt, wobei die Änderung der elektronischen Struktur untersucht und der Koordinationsmodus des Pyridins ermittelt wird (**Schema 8**).

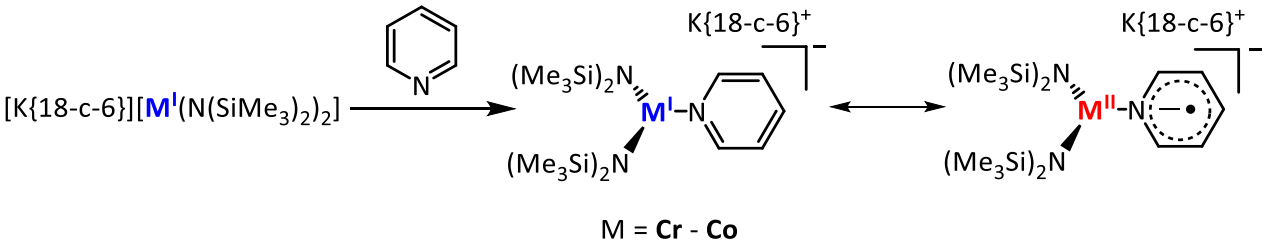

Schema 8. Allgemeiner Syntheseansatz für die Umsetzung von Pyridin mit [K{18-c-6}][M(I)-Silylamiden] (M = Cr – Co).

Anschließend werden die niedervalenten Metall-Pyridin-Komplexe auf das Vorliegen eines Pyridinradikalanions untersucht. Zusätzlich soll geprüft werden, ob eine Substitution der Pyridine einen Einfluss auf die Reaktivität hat.

Der dritte Teil dieser Arbeit befasst sich mit der Reaktivität aliphatischer und aromatischer Alkine gegenüber linearen Metall(I)-Silylamiden (M = Cr – Co)[50,51] (**Schema 9**). In diesem Kontext soll der erste niedrig-koordinierte Mangan-Alkin-Komplex erzeugt werden.

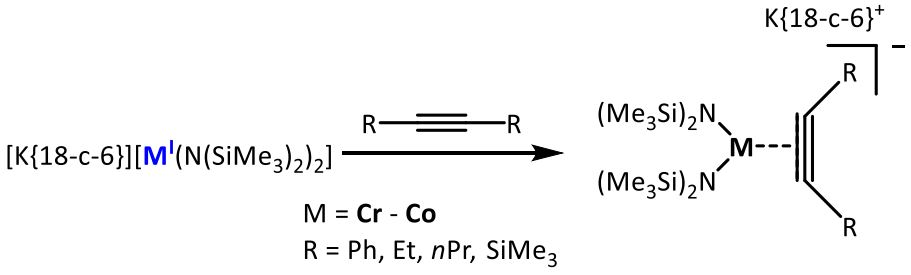

Schema 9. Synthese für niedrig-koordinierte Metall-Alkin-Komplexe.

Dabei soll die Wechselwirkung von Alkinen mit linearen Metallkomplexen in Abhängigkeit vom Metall-Zentrum und den Alkinsubstituenten untersucht werden. Eine quantenchemisch gestützte Analyse unter der Verwendung von DFT- und CASSCF-Methoden soll eine Aufklärung darüber geben, welcher Bindungsmodi zwischen dem Metallatom und dem Alkin vorliegt (**Schema 10**).

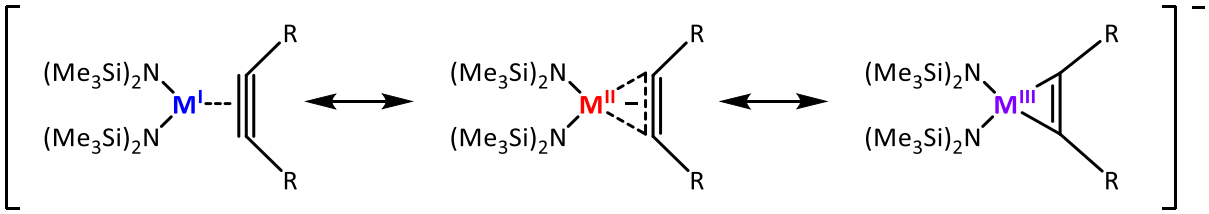

Schema 10. Mögliche Resonanzstrukturen der niedrig-koordinierten Metall-Alkin-Komplexe.

Im vierten Abschnitt der Arbeit soll die Untersuchung zu internen Alkinen auf terminale Alkine ausgeweitet werden und die terminalen Alkine sollen gegenüber linearen Eisen(I)-Silylamiden [K{18-c-6}][Fe(hmds)$_2$] untersucht werden (**Schema 11**). Dabei soll geschaut werden, ob terminale Alkine genauso wie interne Alkine reagieren und den gleichen Bindungsmodus eingehen können. Unter anderem soll der Einfluss des Restes am Alkin untersucht werden und ob dieser den Bindungsmodus, die Komplexbildung oder eine katalytische Transformation beeinflussen kann.

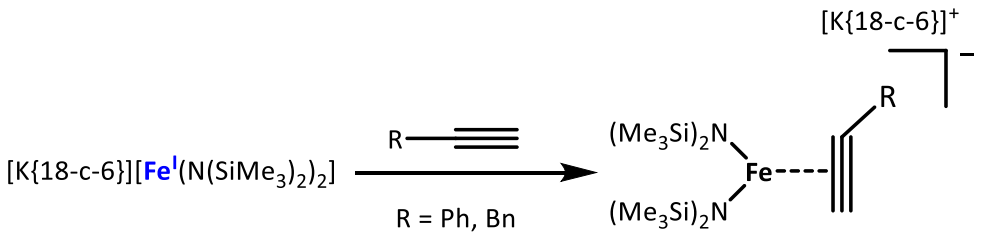

Schema 11. Syntheseansatz für terminale Alkine und Eisen(I)-Silylamide.

Anschließend werden die niedervalenten Eisen-Alkin-Komplexe spektroskopisch untersucht und mit den internen Alkin-Komplexen verglichen.

Der letzter Teil der Arbeit befasst sich mit der Reaktivität aromatischer Alkene gegenüber linearen Metall(I)-Silylamiden (M = Cr – Co)[50,51] (**Schema 12**).

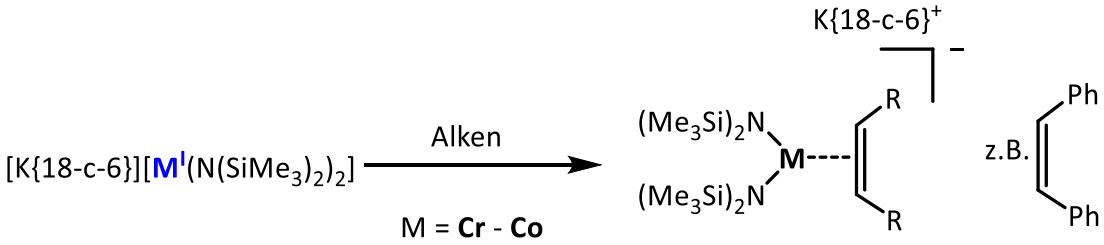

Schema 12. Synthese für niedrig-koordinierte Metall-Alken-Komplexe.

In diesem Kontext soll der erste niedrig-koordinierte Mangan-Alken-Komplex erzeugt werden. Dabei soll die Wechselwirkung von Alkenen mit linearen Metallkomplexen in Abhängigkeit vom Metall-Zentrum und den Alkensubstituenten untersucht werden.

3 Kumulativer Teil

Die Forschungsarbeiten im Rahmen dieser Doktorarbeit haben zur Erstellung von vier Veröffentlichungen geführt. Diese Veröffentlichungen werden im folgenden Kapitel der Dissertation vorgestellt. Der Hauptteil des kumulativen Teils wurde zudem um ein Kapitel mit unveröffentlichten Ergebnissen erweitert (Kapitel 4 *Unveröffentlichte Ergebnisse*), welche sich thematisch an die bisher publizierten Ergebnisse anschließen. Dieses Kaptiel umfasst insbesondere die Arbeiten zu den Alkenen.

3.1 „Reduction of 2,2´-Bipyridine by Quasi-Linear 3d-Metal(I) Silylamides – A Structural and Spectroscopic Study"

Igor Müller, Christian Schneider, Clemens Pietzonka, Florian Kraus und C. Gunnar Werncke, *Inorganics* **2019**, *7*, 117.

3.2 „Reductive coupling of (Fluoro)-Pyridines by Quasi-Linear 3d-Metal(I) Silylamides of Cr – Co: A Tale of C–C bond formation, C–F bond cleavage and pyridyl radical anions"

Igor Müller und C. Gunnar Werncke, *Chem. Eu. J.* **2020**, *eingereichtes Manuskript*.

3.3 „Reactions of Alkynes with Quasilinear 3d-Metal(I) Silylamides of Chromium to Cobalt – A Comparative Study"

Igor Müller, Dominik Munz und C. Gunnar Werncke, *Inorg. Chem.* **2020**, *59*, 9521.

3.4 „Reactions of Terminal Alkyne with Quasilinear Iron(I) Silylamides – A Comparative Study"

Igor Müller und C. Gunnar Werncke, *Manuskript in der Vorbereitung*.

3.5 „ The ambiguous behaviour of diphosphines towards the quasilinear iron(I) complex $[Fe(N(SiMe_3)_2)_2]^-$ between inertness, P–C bondcleavage and C–C double bond isomerisation"

C. Gunnar Werncke und Igor Müller, *Chem. Commun.* **2020**, *56*, 2268.

3.1 „Reduction of 2,2´-Bipyridine by Quasi-Linear 3d-Metal(I) Silylamides – A Structural and Spectroscopic Study"

Igor Müller, Christian Schneider, Clemens Pietzonka, Florian Kraus und C. Gunnar Werncke, *Inorganics* **2019**, *7*, 117.

Abstract: Quasi-linear anionic 3d-metal(I) silylamides are a new and promising class of molecules. Due to their highly negative reduction potential we wanted to test their capability to reduce substrates under coordination of their monoanionic radicaloid form. In a proof of principle studies, we present the results of the reaction of metal(I) silylamides of chromium to cobalt with 2,2´-bipyridine (bipy), the redox non-innocence and reducibility of which was already established. In the course of these studies complexes of the type K{18-crown-6}[M(hmds)$_2$(bipy)] (hmds = –N(SiMe$_3$)$_2$) were obtained. These compounds were isolated and thoroughly characterized to confirm the electron transfer onto the bipyridine ligand, which now acts as a radical monoanion. For comparison of the structural changes of the bipyridine ligand, the analogous zinc complexes were also synthesized. Overall our results indicate that anionic metal(I) silylamides are capable of reducing and ligating substrates, even when the electrochemical reduction potential of the latter is by up to 1 V higher.

Zusammenfassung: Das Manuskript beschäftigt sich mit der Reaktivität von quasi-linearen, anionischen 3d-Metall(I)-Silylamiden (M = Cr – Co) gegenüber dem Substrat 2,2´-Bipyridin (bipy). Aufgrund ihres hohen negativen Reduktionspotentials wurde ihre Fähigkeit, Substrate unter Koordination ihrer monoanionischen Radikaloidform zu reduzieren, getestet. Im Verlauf dieser Untersuchungen wurden Komplexe des Typs [K{18-Krone-6}][M(N(SiMe$_3$)$_2$)$_2$(bipy)] erhalten. Diese Verbindungen wurden in guten Ausbeuten isoliert und vollständig charakterisiert. Dadurch konnte der Elektronentransfer auf den Bipyridinliganden bestätigt werden, der nun als Radikalanion wirkt. Zum Vergleich der Strukturänderungen wurden auch die analogen Zink-Komplexe dargestellt. Zusammengefasst zeigen die im Manuskript dargestellten Ergebnisse, dass anionische Metall(I)-Silylamide Substrate, wie 2,2´-Bipyridin, reduzieren und binden können, selbst wenn deren elektrochemisches Reduktionspotential um bis zu 1 V höher ist als das von 2,2´-Bipyridin.

Eigener Anteil: Alle Synthesen der Verbindungen **1** – **4** und **8** – **10** wurden von mir geplant und durchgeführt, sowie deren analytischen Daten aufgenommen und ausgewertet. PPMS-Messungen wurden von Clemens Pietzonka aus dem Arbeitskreis Kraus der Universität Marburg durchgeführt und ausgewertet. Christian Schneider war verantwortlich für die Aufnahme und Auswertung der Zyklovoltammogramme. ^{1}H-NMR-Experimente wurden sowohl von mir als auch unter Anleitung von Dr. Xiulan Xie in der zentralen NMR-Abteilung des Fachbereichs Chemie an der Philipps-Universität Marburg durchgeführt. Ebenfalls habe ich die UV/VIS- und IR-Messungen selbst durchgeführt. Die Einkristallstrukturanalysen der Verbindungen **3**, **4** und **10** wurden durch die zentrale Abteilung für Kristallstrukturanalyse am Fachbereich Chemie an der Philipps-Universität Marburg unter der Leitung von Dr. Klaus Harms durchgeführt. Die Datensätze wurden jedoch von mir gelöst und verfeinert. Bei den Verbindungen **1** – **2** und **8** – **9** war ich selbst sowohl für die Messung als auch für das Lösen und die Verfeinerung verantwortlich. Das Manuskript wurde von mir und Dr. C. Gunnar Werncke verfasst.

inorganics

MDPI

Article

Reduction of 2,2′-Bipyridine by Quasi-Linear 3d-Metal(I) Silylamides—A Structural and Spectroscopic Study

Igor Müller, Christian Schneider, Clemens Pietzonka, Florian Kraus and C. Gunnar Werncke *

Fachbereich Chemie, Philipps-Universität Marburg, Hans-Meerwein-Straße 4, D-35037 Marburg, Germany; muellera@chemie.uni-marburg.de (I.M.); christian.schneider@chemie.uni-marburg.de (C.S.); pietzonka@staff.uni-marburg.de (C.P.); f.kraus@chemie.uni-marburg.de (F.K.)

* Correspondence: gunnar.werncke@chemie.uni-marburg.de; Tel.: +49-6421-282-5627

Received: 14 August 2019; Accepted: 20 September 2019; Published: 25 September 2019

Abstract: Quasi-linear anionic 3d-metal(I) silylamides are a new and promising class of molecules. Due to their highly negative reduction potential we wanted to test their capability to reduce substrates under coordination of their monoanionic radicaloid form. In a proof of principle study, we present the results of the reaction of metal(I) silylamides of chromium to cobalt with 2,2′-bipyridine (bipy), the redox non-innocence and reducibility of which was already established. In the course of these studies complexes of the type K{18-crown-6}[M(hmds)$_2$(bipy)] (hmds = –N(SiMe$_3$)$_2$) were obtained. These compounds were isolated and thoroughly characterized to confirm the electron transfer onto the bipyridine ligand, which now acts as a radical monoanion. For comparison of the structural changes of the bipyridine ligand, the analogous zinc complexes were also synthesized. Overall our results indicate that anionic metal(I) silylamides are capable of reducing and ligate substrates, even when the electrochemical reduction potential of the latter is by up to 1 V higher.

Keywords: oxidation state +1; 3d-metals; two-coordinate complexes; electron transfer; N-ligands

1. Introduction

Complexes with two-coordinate 3d-metal(I) ions are a rare class of molecules in coordination chemistry [1–13]. They combine an uncommon coordination motif with an, for these metals, unusual oxidation state (with the exception of Cu and to a certain extent nickel). Their scarcity can be explained by the difficulties of stabilizing the electronically and coordinatively unsaturated metal ion. Thus, their isolation usually relies on the use of sterically encumbering and/or electronically stabilizing ligands, such as bulky amides or N-heterocyclic carbenes. Given their only recent history, little is known about their physical properties as well as chemical behavior towards substrates and small molecules. However, first reports indicate a high potential thereof. For example, in case of iron complexes, they can exhibit extraordinary single molecule magnetic behavior, which can be directly connected to the linear ligand arrangement as well as the oxidation state +1 [6,8]. Further, such complexes can mediate the cleavage of H_2 [12] and C–halide bonds [14] or the trimerization of alkynes [15].

We recently showed that it is possible to obtain quasi-linear 3d-metal(I) complexes K{18c6}[M^{I}(hmds)$_2$] (M = Cr, Fe, Co; 18c6 = 18-crown-6) using the comparably unencumbering hmds ligand set (hmds = –N(SiMe$_3$)$_2$) [6,13]. As a result of the sterically uncongested metal center, the labile manganese complex K{18c6}[Mn^{I}(hmds)$_2$], which is supposedly monomeric in solution, forms a metal−metal bonded dimer in the solid state (Scheme 1). Despite the highly accessible metal sites of these metal(I) complexes, they seem surprisingly inert towards Lewis bases such as phosphines, phosphites, NHCs or THF (exemplarily shown for iron) [6], which is in contrast to the behavior of other two-coordinate

metal(I) fragments [1,16–21]. Given this observed reluctance to obtain further electron density upon Lewis base coordination, we were interested in the formal transfer of an electron from the metal(I) ion onto substrates to form metal(II) complexes bearing an anionic radicaloid ligand. In addition, we were interested in elaborating the synthetic usability of the elusive manganese(I) silylamide $[Mn^{I}(hmds)_2]^-$ (Scheme 1), which cannot be isolated due to its extreme sensitivity.

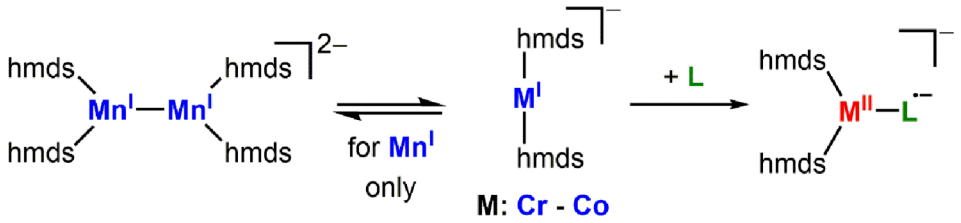

Scheme 1. Metal(I) hexamethyldisilazanides (hmds = $-N(SiMe_3)_2$)$_2$ and their expected use for reduction and ligation of a substrate L.

In a proof of principle study we thus chose 2,2′-biypyridine (bipy), which is widely used as a chelating donor ligand [22]. Further, it can act as a π-acceptor that can take up one or two electrons to form either the 2,2′-bipyridine radical monoanion $[bipy]^{\cdot-}$ or the diamagnetic dianion $[bipy]^{2-}$ when subjected to highly reducing agents such as alkaline metals. This has been shown for the alkali metal salts of 2,2′- as well as 4,4′-bipyridine [23,24] and more importantly for 2,2′-bipyridine containing metal complexes [25–31]. Within these complexes the exact determination of the electronic structure of the [M(bipy)] unit is usually not trivial leading to the generally accepted classification of 2,2′-bipyridine as a redox non-innocent ligand [32,33]. Thereby, it has been shown that the structural features of the central C–C bond within the bipyridine ligand can be a strong indicator of its redox state [32,34,35]. This has been showcased for four-coordinate $[M(mes)_2(bipy)]$ (mes = 2,4,6-trimethylphenyl), where reduction with potassium graphite in the presence of either 18-crown-6 or crypt.222 led to a mainly bipyridine-based reduction and formation of K{L}$[M(mes)_2(bipy)]$ (L = 18-crown-6 or crypt.222) [34,35].

Given this background, we were curious if and how the above-mentioned two-coordinate metal(I) silylamides coordinate 2,2′-bipyridine. Thereby it is important to note that the reported reduction potential of the free $bipy^0/bipy^{\cdot-}$-redox couple is fairly negative ($E_{1/2}$ = −2.53 V vs Fc/Fc^+ in MeCN) [36] in comparison to those of the two-coordinate metal(I) complexes (E_{pc} of −1.5 V for Co to −2.5 V for Mn) [6,13]. We herein report on the reaction of K{18c6}$[M^{I}(hmds)_2]$ (M = Cr–Co) with 2,2′-bipyridine, which leads to the formation of the respective bipyridine complexes K{18c6}$[M(hmds)_2(bipy)]$. These complexes were examined by single-crystal X-ray diffraction analysis and ^{1}H-NMR/UV–Vis spectroscopy and for their magnetic as well as electrochemical properties. In comparison with their neutral metal(II) counterparts and the additional synthesis of the zinc derivatives, the anionic complexes are overall best described as $[M^{II}(hmds)_2(bipy^{\cdot-})]^-$.

2. Results

2.1. Synthesis and Structural Characterisation

The respective metal(I) hmds complex (Cr–Co), either isolated (Fe and Co) or synthesized in situ (Cr and Mn), was treated with one equivalent of 2,2′-bipyridine in Et_2O. In all cases an immediate reaction was visible by a change of color to intense dark green (Cr, Fe and Co) or red (Mn). These mixtures were filtered, layered with pentane and stored at −35 °C. After a few days crystalline samples of the complexes (**1** (Cr^-), **2** (Mn^-), **3** (Fe^-) and **4** (Co^-)) were obtained in moderate to good yields (Scheme 2).

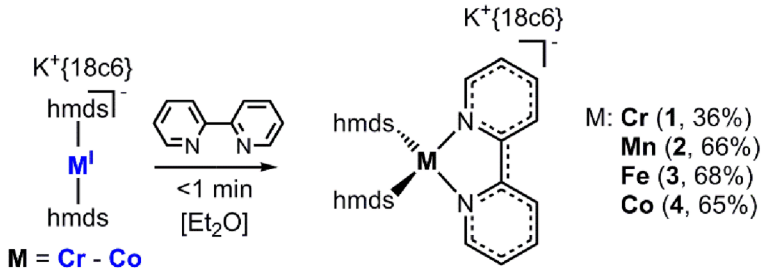

Scheme 2. General synthetic approach for the complexes **1**–**4** (18c6 = 18-crown-6).

X-ray diffraction analysis confirmed their structural identity (Figure 1). Important structural parameters of the complexes **1**–**4** in the solid state are summarized in Table 1.

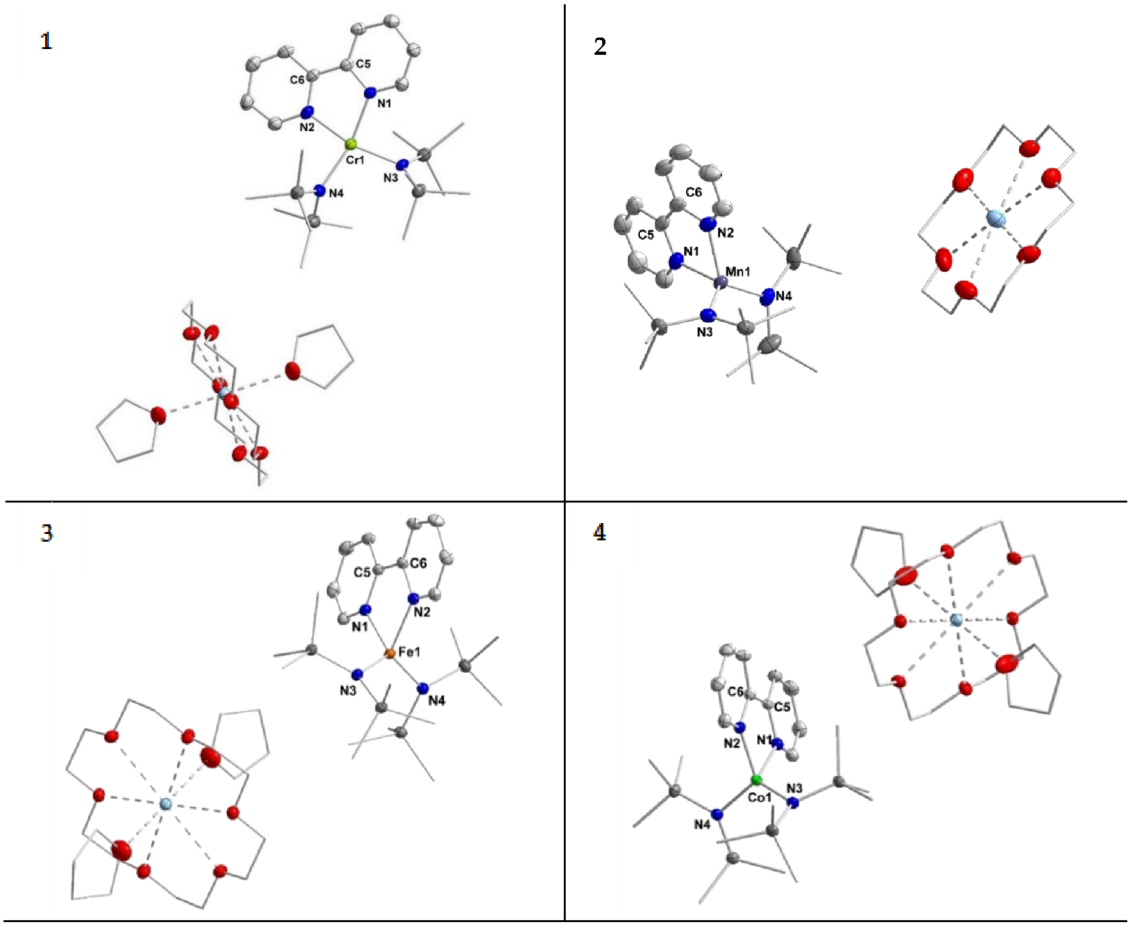

Figure 1. Molecular structures of compounds **1**–**4**. H atoms are omitted for clarity and ellipsoids are shown at 50% probability.

In the solid state the complex anions of compounds **1**–**4** exhibit a four-coordinate metal ion which is ligated by two hmds units and the bipyridine ligand. For the chromium compound **1** the torsion angle between the planes defined by N3–M1–N4 and N1–M1–N2 amounts to 23°. Given the respective τ'_4-parameter of 0.26, this complex is best described as distorted square planar. From a ligand field perspective this indicates a chromium(II) ion (d^4 configuration), which usually prefers a square planar ligand environment such as in $[Cr(hmds)_2(thf)_2]$ or $[CrCl_4]^{2-}$ [37–39]. For the manganese, iron and cobalt complexes the torsion angle amounts to 67.06° (**2** (Mn^-)), 73.98° (**3** (Fe^-)) and 75.3° (**4** (Co^-)). Together with the respective τ'_4-parameters of 0.78, 0.77 and 0.81 these complexes are overall best described as distorted tetrahedral.

Table 1. Important structural metrics of the complex anions of the compounds **1**–**4**.

Compound	1 (Cr^{-})	2 (Mn^{-})	3 (Fe^{-})	4 (Co^{-})
Bond Length/Å				
M–N1 (bipy)	2.089(3)	2.140(4)	2.0808(10)	1.9980(16)
M–N2 (bipy)	2.073(3)	2.168(3)	2.0763(11)	1.9966(16)
M–N3 (hmds)	2.102(3)	2.083(3)	2.0146(10)	2.0037(16)
M–N4 (hmds)	2.076(3)	2.063(3)	2.0109(10)	2.0079(16)
N1–C1	1.342(5)	1.347(7)	1.358(2)	1.359(2)
N1–C5	1.395(5)	1.359(6)	1.384(2)	1.385(2)
C5–C6	1.417(6)	1.422(9)	1.425(2)	1.432(3)
N2–C6	1.403(5)	1.384(7)	1.385(2)	1.379(2)
N2–C10	1.336(6)	1.357(7	1.353(2)	1.357(2)
Angles/°				
N1–M–N2	77.21(14)	76.16(13)	77.17(4)	80.63(6)
N3–M–N4	102.44(12)	121.84(11)	126.28(4)	121.91(6)
N3–M–N4/ N1–M–N3	23.28°	67.06°	73.98	75.3
$\tau_{4'}$	0.26	0.78	0.77	0.81

The $M–N_{hmds}$ bond lengths get slightly shorter along the series from chromium (2.09 Å) to cobalt (2.00 Å). For the $M–N_{bipy}$ distances a contraction is also observed from manganese (2.15 Å) to cobalt (2.00 Å), whereas for chromium a distance of 2.08 Å is observed. This behavior is in general agreement with the ion radii of the respective metal(II) ion. The lengths of the central C–C bond of the bipyridine ligand increases slightly from 1.417(6) Å for chromium to 1.432(3) Å for cobalt. The C–C bond lengths are thereby in the range of ligated 2,2′-bipyridine radical anions within isolable complexes [32,34,35,40,41].

To further substantiate the presence of a bipyridine radical anion in the complexes **1**–**4** on a structural level, we compared their structural features to those of their neutral counterparts, $[M^{II}(hmds)_2(bipy)]$. For the chromium (**5**) [42], manganese (**6**) [43] and iron (**7**) [43] complexes the synthesis and solid state structures were already described in the literature. As further analysis of their spectroscopic properties was lacking, their synthesis was reproduced by the reaction of the respective hmds salt with 2,2′-bipyridine in Et_2O. Analogously, the missing cobalt derivative **8** was obtained as a dark red crystalline solid in moderate yield (Scheme 3; Figure 2, left). Further, we sought the isolation of the respective zinc complexes, as for zinc the reduction of the metal ion is highly unlikely due to the high stability of the +2 oxidation state. $Zn(hmds)_2$ was thus reacted with 2,2′-bipyridine, giving $[Zn(hmds)_2(bipy)]$ (**9**) as pale-yellow crystals (63% yield; Figure 2, middle).

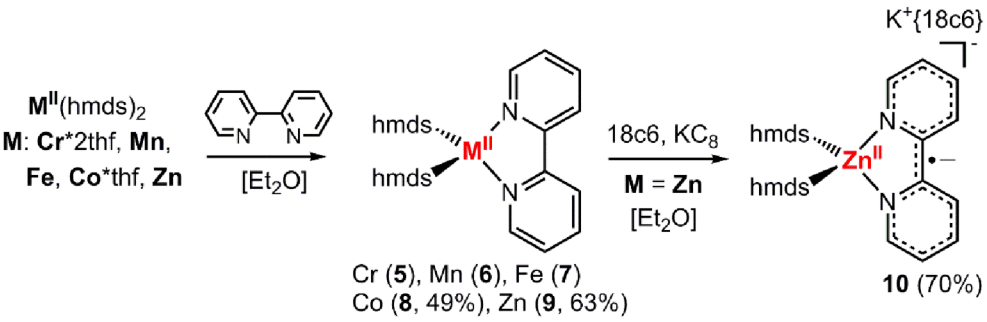

Scheme 3. General synthetic approach for the neutral complexes **5**–**9** (known for Cr, Mn and Fe) as well as the reduced zinc complex **10** (Zn^{-}).

The reduction of compound **9** (Zn) with one equivalent KC_8 in the presence of 18-crown-6 lead to the isolation of rose crystals of K{18c6}[Zn(hmds)$_2$(bipy)] (**10**; Figure 2, right). Similarly, compounds **1**–**4** could also be obtained by reduction of the respective, preformed [M(hmds)$_2$(bipy)] complex.

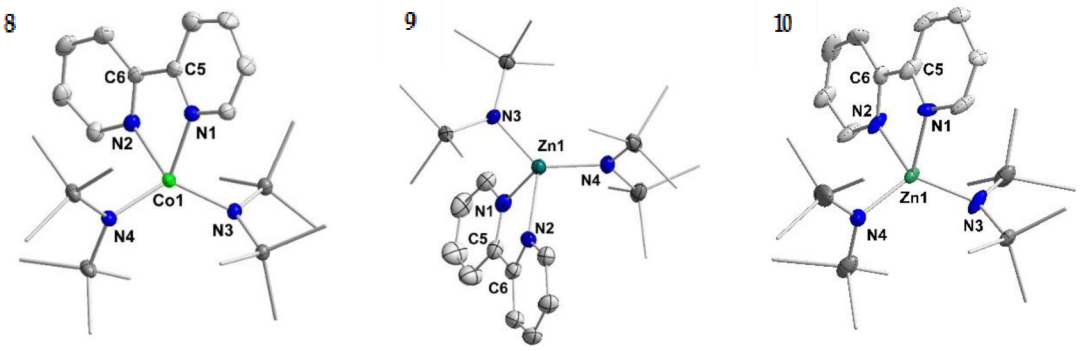

Figure 2. Molecular structure of compounds **8**–**10**. H atoms are omitted for clarity and ellipsoids are shown at 50% probability. The K{18c6}-cation is not shown for **10**.

Important structural features of **5**–**10** are given in Table 2. The structure of **10** suffers from disorder of the complex over two positions. Structural metrics are given for one of the molecules and should be treated with care. For the neutral metal(II) compounds **5**–**9** the following trends are observed: The respective metal nitrogen distances of bipyridine and the hmds ligands shorten along the series, similar to observations made for the reduced complexes. The central C–C bond of the bipyridine ligand also shortens from 1.502(8) Å for the manganese complex **6** (Mn) to 1.474(7) Å for the zinc complex **9** (Zn). The chromium complex **5** (Cr) shows again deviations from this trend with a C–C bond length of 1.481(3) Å. Further, for all neutral complexes but chromium a distorted tetrahedral coordination environment is observed with a torsion angle that increases from 65° to 73° for the manganese to zinc complex. In contrast, the chromium complex **5** (Cr) is better described as distorted square planar with a torsion angle of 20°.

Table 2. Important structural metrics of compounds **5**–**9** as well as of the complex anion of K{18c6}[Zn(hmds)$_2$bipy], **10**.

Compound	5 (Cr) [42] *	6 (Mn) [43]	7 (Fe) [43] *	8 (Co)	9 (Zn)	10 (Zn^-) #
Bond Length/Å						
M–N1 (bipy)	2.159(2)	2.267(5)	2.208(7)	2.121(3)	2.173(4)	2.090(11)
M–N2 (bipy)	2.157(2)	2.253(5)	2.159(8)	2.099(3)	2.174(4)	2.095(12)
M–N3 (hmds)	2.057(2)	2.045(4)	1.971(6)	1.961(3)	1.939(3)	1.979(6)
M–N4 (hmds)	2.052(2)	2.050(4)	1.979(7)	1.959(3)	1.942(3)	1.969(8)
N1–C1	1.343(2)	1.337(8)	1.335(12)	1.335(4)	1.334(6)	1.379(19)
N1–C5	1.356(2)	1.352(7)	1.357(11)	1.349(4)	1.356(5)	1.379(15)
C5–C6	1.481(3)	1.502(8)	1.491(14)	1.479(5)	1.474(7)	1.419(9)
N2–C6	1.350(2)	1.363(7)	1.404(12)	1.346(4)	1.344(6)	1.413(6)
N2–C10	1.342(2)	1.352(8)	1.316(13)	1.338(4)	1.333(6)	1.336(17)
Angles/°						
N1–M–N2	75.15(6)	72.9(2)	75.8(3)	80.6(3)	75.4(14)	78.8(6)
N3–M–N4	105.57(6)	128.24(17)	127.4(3)	124.53(11)	129.93(15)	122.7(3)
N1–M–N2/N3–M–N4	20.145(5)	65.5(2)	69.5(3)	71.8(3)	72.98(11)	77.43(3)
$\tau_{4'}$	0.28	0.74	0.76	0.81	0.74	0.83

* Contains two independent molecules per unit cell with very similar structural metrics of which one was chosen for comparison. # The asymmetric unit contains one molecule of **10** which is disordered over two positions, of which one was chosen for representation of the structural parameters.

In comparison with the neutral compounds, the central C–C bond lengths of the bipyridine ligand are shorter by between 0.05 Å (Zn) and 0.08 Å (Mn) in the reduced complexes. In addition, the reduced complexes exhibit shorter M–N_{bipy} bond lengths, whereas those of the M–N_{hmds} bonds are slightly elongated. Otherwise, the general coordination geometry around the metal are largely the same for the neutral and the reduced complexes. Given these geometric features, the anionic complexes **1**–**4** and **10** (Zn^-) are likely to contain a monoanionic 2,2′-bipyridine ligand.

2.2. ^{1}H-NMR Spectroscopic Features

To gain insights into changes of the electronic situation of the anionic complexes, we turned to the ^{1}H NMR spectroscopic features of the reduced as well as the neutral complexes (Table 3). Providing their mostly paramagnetic nature, the proton signals of the hmds as well as the bipyridine ligands might be indicative of changes in the electronic properties of the metal center. Thereby it has to be noted that the respective proton NMR features of the literature known compounds **5** (Cr), **6** (Mn) and **7** (Fe) were not reported.

Table 3. ^{1}H-NMR spectroscopic features of the compounds **1**–**10** in THF-d_8 (500 MHz).

Complex	δ ($SiMe_3$)/ppm ($w_{\frac{1}{2}}$/Hz)	δ (bipy)/ppm ($w_{\frac{1}{2}}$/Hz)
1 (Cr^-)	No useful signal attribution possible	
5 (Cr)	40.7 (2539 Hz)	53.7, 46.85, 16.4, −70.9
2 (Mn^-)	19.9 (2312 Hz)	No useful signal attribution possible
6 (Mn)	29.5 (5723 Hz)	No useful signal attribution possible
3 (Fe^-)	1.73	268.08 (711 Hz), 178.22 (478 Hz), 77.87 (1534 Hz), 64.49 (154 Hz),
7 (Fe)	10.95 (425 Hz)	64.09 (114 Hz), 52.13 (129 Hz), −19.13 (62 Hz)
4 (Co^-)	2.47 (83 Hz)	155.75 (100 Hz), 143.95 (85 Hz), 104.35 (749 Hz), 50.26 (25 Hz)
8 (Co)	8.11 (68 Hz)	59.68 (253 Hz), 50.94 (25 Hz), 42.65 (31 Hz), −21.01 (27 Hz)
9 (Zn)	−0.11 (2 Hz)	8.91 (d), 8.43 (d), 8.17 (d), 7.73 (d),
10 (Zn^-)	0.54 (234 Hz)	8.62 (34.9 Hz), 8.48 (30.3 Hz), 7.81 (37.5 Hz), 7.29 (36.3 Hz)

For the manganese (**2** (Mn^-) and **6** (Mn)) and chromium complexes (**1** (Cr^-) and **5** (Cr)) the proton NMR spectra showed, if at all, very broad and overlapping signals, which rendered their spectra uninformative (for spectra see Supplementary Materials). The iron complex **3** (Fe^-) is represented by four signals at −268.1, 178.2, 77.9 and 64.5 ppm for the bipyridine ligand (Figure 3, top). The position of the $SiMe_3$ signal is very broad and positioned at approximately 3.58 ppm and is overlapped by the signals belonging to the used solvent (THF-d_8) and 18-crown-6. In comparison, the ^{1}H-NMR spectrum of the neutral iron(II) complex **7** (Fe) shows rather sharp signals at 10.95 ppm for the $SiMe_3$ unit and at 64.09, 52.13 and −19.13 ppm for the bipyridine ligand (Figure 3, bottom).

The expected fourth signal of the bipyridine ligand could not be located in the region between ±400 ppm. It is probably subject to large line broadening and/or may be located beneath other signals. The cobalt complex **4** (Co^-) shows four strongly low-field shifted ^{1}H-NMR signals for the bipyridine ligand at 155.8, 143.95, 104.3 and 50.26 ppm (Figure 4, top). The signal for the $SiMe_3$ groups is situated at 2.47 ppm whereas the one belonging to the crown-ether is approximately at its diamagnetic position. The neutral cobalt complex **8** (Co) exhibits sharper and less paramagnetically shifted signals at 59.7, 50.94, 42.65 and −21.01 ppm for the bipyridine ligand. The signal belonging to the $SiMe_3$ protons is shifted further away (8.11 ppm) from its diamagnetic position (Figure 4, bottom) in comparison with complex **4** (Co^-).

The proton signals of the bipyridine ligand of the reduced Zn complex **10** (Zn^-) are shifted to a higher field in comparison to their position found for the diamagnetic, neutral derivative **9** (Zn). The signals are moderately broadened and show reduced intensity.

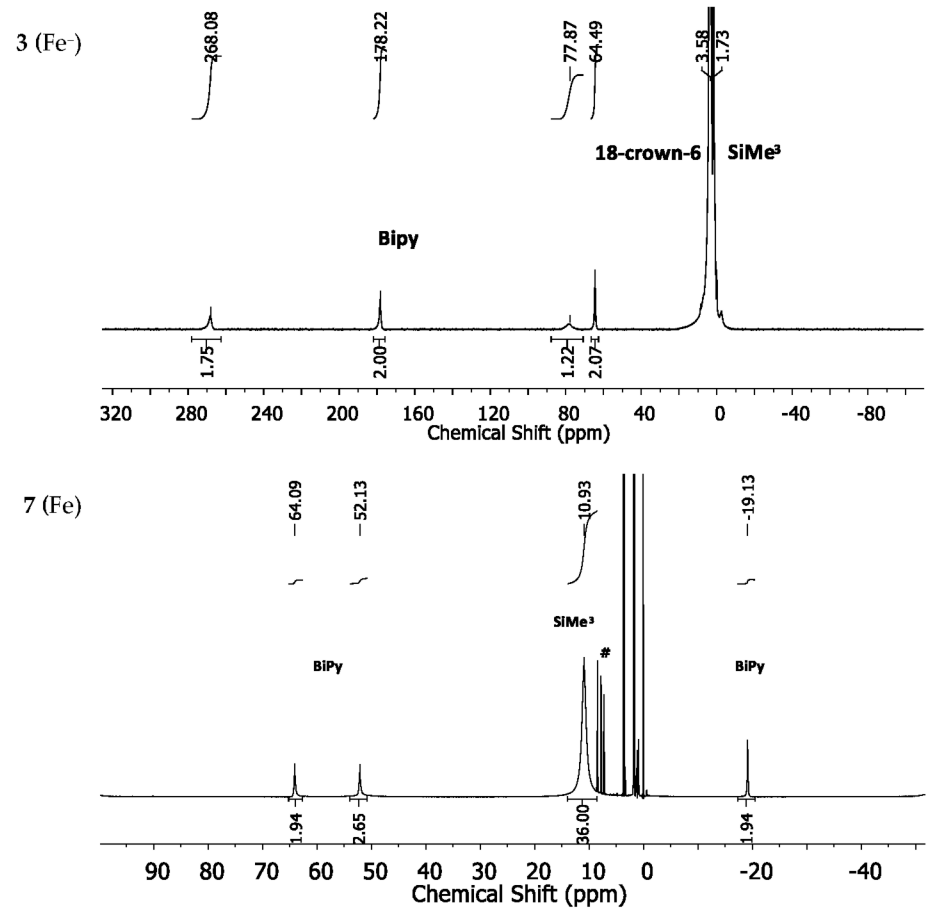

Figure 3. ^{1}H-NMR spectra of the iron complexes **3** (Fe^{-}) (top) and **7** (Fe) (bottom) in THF-d_8. # denotes free 2,2′-bipyridine as an impurity.

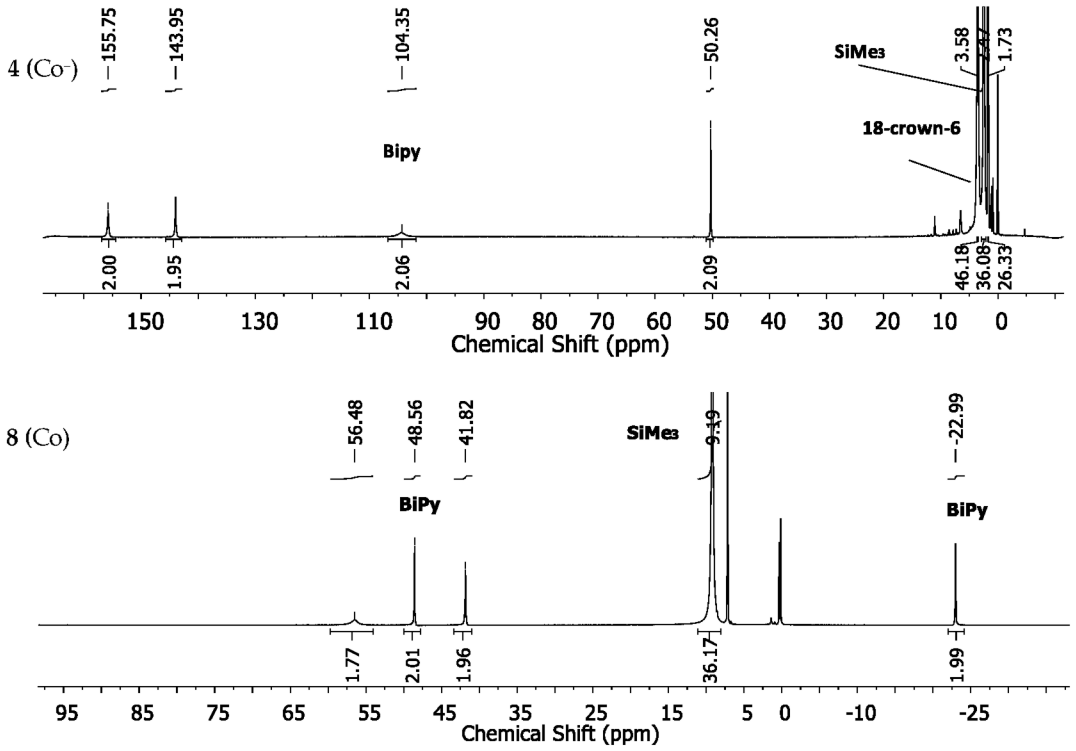

Figure 4. ^{1}H-NMR spectra of the cobalt complexes **4** (Co^{-}) (top) and **8** (Co) (bottom) in THF-d_8.

The signal belonging to the $SiMe_3$ groups is also considerably shifted by approximately 0.6 ppm to a lower field and exhibits a surprisingly large line width of 234 Hz, surpassing the ones found for the more paramagnetic cobalt complexes. Overall, for the anionic complexes, larger paramagnetic shifts and line-broadening are observed for the bipyridine protons in comparison with the respective neutral complexes. In contrast, for the hmds protons for each metal, diverging trends were observed.

2.3. UV/Vis-Spectroscopic Features

To get further insights into the electronic structure of the reduced complexes **1**–**4** and **10**, their UV/Vis spectra were recorded together with those of their non-reduced counterparts. The presence of reduced 2,2-bipyridine can be deducted from two strong bands at 532 and 562 nm and three bands between 700 and 1000 nm, as shown for in situ generated Na(bipy) in THF [44]. For 2,2-bipyridyl radical anion containing metal complexes the situation is similar although the two high-energy bands are often not resolved [30,31,41,45]. The high energy transitions are tentatively assigned to a $\pi \rightarrow \pi^*$-based transition whereas the ones in the low energy region are due to a $\pi^* \rightarrow \pi^*$ centered transition [44]. To corroborate the UV/Vis-spectroscopic signature of the 2,2-bipyridyl radical anion under our reaction conditions, we attempted the reduction of 2,2′-bipyridine with KC_8 in Et_2O in the absence of any 3d-metal complex. However, no change of color was observed. This is in contrast to the reports of isolation of the monopotassium salt of 2,2-bipyridine by the group of Goicoechea and is presumably due to stabilizing effects of the used ethylene diamine solvent in their case. When the reduction of 2,2-bipyridine is performed in the presence of 18-crown-6 the instant formation of a violet solution was observed. The isolation of the presumed K{18-crown-6} stabilized 2,2′-bipyridyl anion failed in our hands, as rapid discoloring of the solution was observed within 60 s. Nonetheless, an immediately recorded UV/Vis spectrum showed two sharp bands at 542 and 577 nm and some very weak bands in the low energy region between 800 and 1000 nm. The position of the signals are similar to those of Na(bipy) in THF, although in our case the low-energy bands were substantially weaker in relative intensity.

Given this background, we started with the zinc derivatives, as in this case the bipyridine centered reduction is highly plausible. The neutral zinc(II) complex **9** (Zn) shows only a weak absorption band around 350 nm, which reflects its pale yellow color (Figure 5). In the case of the reduced zinc complex **10** (Zn^-) this band is more pronounced. Furthermore, two distinct sharp bands at 505 and 535 nm and three broad bands in the range of 700−1000 nm were observed, which can be attributed to the bipyridyl radical anion (Table 4). At 914 nm an additional small band was detected which was already observed in the case of the neutral complex **9** (Zn).

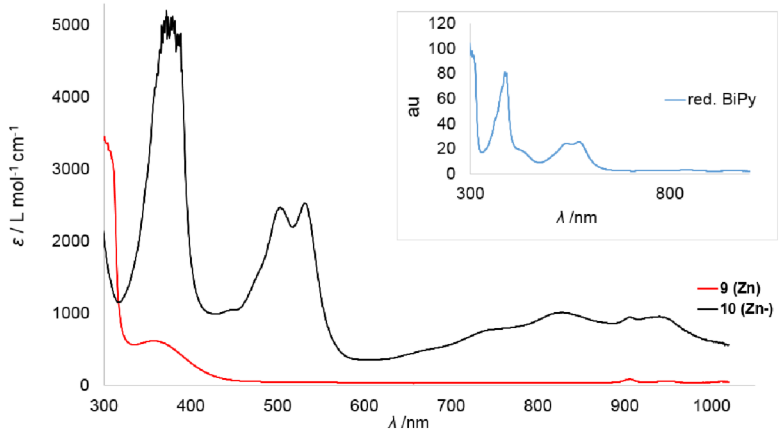

Figure 5. Overlay of the UV/Vis spectra of the Zn complexes **9** (Zn) and **10** (Zn^-) in Et_2O. The inset belongs to the in situ spectrum of 2,2′-bipyridine reduced by KC_8 in the presence of 18-crown-6 in Et_2O after approximately 3 min.

Table 4. UV/Vis spectroscopic features of complexes **1**–**10** in Et_2O. Bold numbers highlight the two optical bands attributed to the π→π*-based transition of the reduced bipyridine ligand.

Complex	λ/nm (ε/L·mol^{-1}·cm^{-1})
"K{18c6}[bipy]"	391, 428, **540**, **576**
1 (Cr^-) **5** (Cr)	359 (*5698*), **488** (*2833*), **525** (*2301*), 656 (*1365*), 912 (*1443*), 959 (*1256*) 373 (*5698*), 520 (*4443*), 914 (*1434*)
2 (Mn^-) **6** (Mn)	366 (*5781*), **487** (*3126*), **523** (*2164*), 713 (*965*), 815 (*1706*), 916 (*1841*) 382 (*878*), 913 (*74*)
3 (Fe^-) **7** (Fe)	337 (*2155*), 372 (*2105*), 428 (*1061*), **460** (*926*), **497** (*842*), 914 (*491*) 387 (*2174*), 622 (*264*), 908 (*115*), 941 (*97*)
4 (Co^-) **8** (Co)	405 (*2659*), 566 (*418*), 648 (*308*), 754 (651), 903 (*125*) 356 (*4276*), 461 (*2843*), 660 (*1219*), 742 (*1555*), 917 (*847*)
9 (Zn) **10** (Zn^-)	374 (*559*), 917 (*57*) 373 (*4894*), **505** (*2248*), **535** (*2328*), 750 (*784*), 807 (*951*), 931 (*949*)

Overall, the coordination of the supposed bipyridine radical anion to the zinc ion lead to a slight blue-shift of the two high-energy bands with only marginal change in the separation in between them (Δλ ≈ 30 nm). The bands in the region of 700–1000 nm are more pronounced than for "K{18c6}[bipy]" and their intensity is in line with the reports on Na(bipy).

Next, we examined the compounds **1**–**8** whose main optical transitions are shown in Table 4.

For the reduced manganese and chromium complexes **2** (Mn^-) (Figure 6) and **1** (Cr^-) (see Supplementary Materials for spectrum) the two high energy bands were somewhat blue-shifted (Mn: 487 and 523 nm, Δλ ≈ 35 nm; Cr: 488 and 525 nm, Δλ ≈ 35 nm). For the iron complex **3** (Fe^-) the intensity of these bands is reduced, which impeded their identification (460 and 497 nm, Δλ ≈ 30 nm), whereas for compound **4** (Co^-) (see Supplementary Materials for spectra) no clear assignment was possible. The low-energy region between 700 and 1000 nm shows pronounced bands for complexes **2** (Mn^-) and **4** (Co^-), whereas the spectra of compounds **1** (Cr^-) and **3** (Fe^-) reveal only a broad absorption.

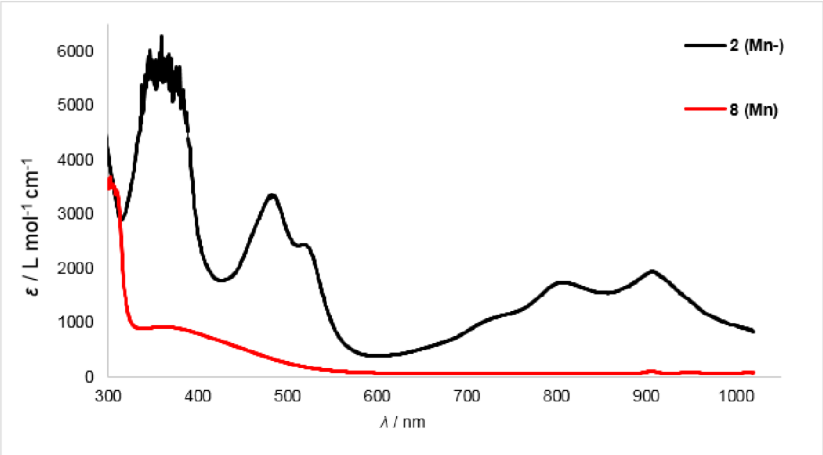

Figure 6. Overlay of UV/Vis spectra of the manganese complexes **2** (Mn^-) and **6** (Mn).

2.4. Magnetic Properties

Given the paramagnetic nature of the anionic complexes, their magnetic properties in solid state were evaluated using a physical properties measurement system and in solution via the Evans method [46,47]. The structural and UV/Vis spectroscopic features of the anionic complexes already hinted to their likely formulation as a [M^{II}/bipy·$^-$] system. As such, two limiting cases can be assumed:

First, a metal(II) ion that is strongly ferromagnetically coupled to the unpaired electron of the bipyridyl radical anion, which gives $S_{tot} = S_M + S_{1/2}$ as the upper limit. On the other hand, antiferromagnetic coupling leads to $S_{tot} = S_M - S_{1/2}$. Further, the absence of significant coupling between the spin centers would give $S_{tot} = S_M \times S_{1/2}$, with a value for the magnetic susceptibility that lies between those limiting cases. For the metal(II) ions a high-spin configuration is assumed, given the low-coordinate and rather weak ligand field environment of these complexes. The magnetic susceptibilities of compounds **1**–**4** and **10** (Zn^-) were measured in the solid state in a field of H = 1 T in a temperature range of 3–300 K (Figure 7). The magnetic data were corrected for diamagnetic contributions from the sample holder and the diamagnetic susceptibility of the respective compound using Pascal constants. The paramagnetic susceptibility χ_{para} was fitted using the Curie-Weiss Law $\chi_{CW} = \left(\frac{N_A \mu_B^2 n_{eff}}{3k_B}\right)^2 \frac{1}{T-\theta}$ (n_{eff} = effective magnetic moment in Bohr's magnetons per formula unit, Θ = Weiss temperature) with contributions from a temperature independent paramagnetism χ_{TIP} using the overall equation $\chi_{para}T = (\chi_{TIP} + \chi_{CW})T$. Obtained results (Table 5) are thus discussed within the simplified framework of the presented limiting cases with a focus on the room-temperature χT values and the general curvature of the χT vs T slopes. A more detailed description of this spin-system would necessitate more experimental magnetic data which lay beyond the scope of this study.

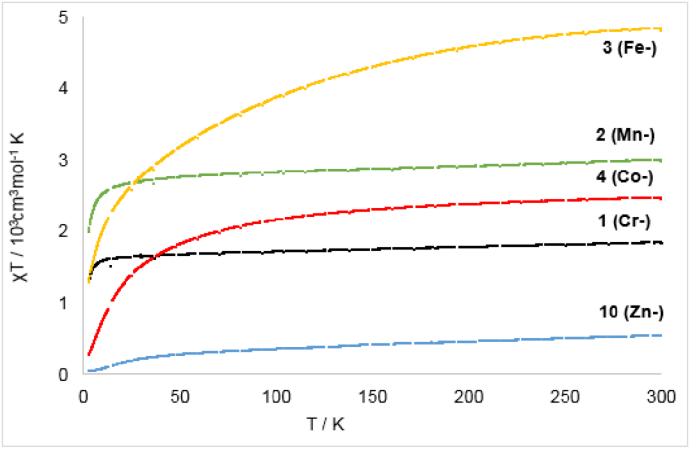

Figure 7. Temperature magnetic susceptibility (χT vs T) of the complexes **1**–**4** and **10** from 3 K to 300 K at 1 T.

Table 5. Calculated Θ and χ_{TIM} values for the anionic complexes **1**–**4** and **10** obtained from fitting of their variable temperature magnetic data to the Curie–Weiss Law.

Complex	mol. weight (g/mol)	Diamagn. corr./10^{-4} emu·mol^{-1}	μ_{eff}/μ_B (300 K)	Θ/K	$\chi_{TIM}/10^{-4}$ emu·mol^{-4}	χ_T/cm^3·mol^{-1}·K (300 K)
1 (Cr^-)	832.37	−2.87	3.66	−0.634	5.75	1.84
2 (Mn^-)	835.32	−2.85	4.71	−1.13	7.43	2.98
3 (Fe^-)	836.22	−2.87	6.67	−43.87	0.0	4.80
4 (Co^-)	839.31	−2.83	4.61	−23.56	0.0	2.45
10 (Zn^-)	845.76	−2.86	1.72	−28.85	6.78	0.54

For the zinc complex **10** (Zn^-) the χT vs T slope showed a gradual increase when going from 3 K to 50 K, after which the curve flattens, reaching a value of 0.54 cm^3·mol^{-1}·K at 300 K (1.72 μ_B). The value is close to the measured magnetic moment of 1.81 μ_B in solution using the Evans method and is in line with a $S = \frac{1}{2}$ system. The slight, steady increase from 50 K to 300 K can be explained by contributions from a temperature independent paramagnetism, whereas the decrease below 50 K is unexpected for an isolated $S = \frac{1}{2}$ system. This can be reasoned by significant intermolecular magnetic coupling between the ligating bipyridyl radical anions whose phenyl rings are in proximity in the solid state

(minimum C–C distance of 3.99 Å). Such an intermolecular interaction is known for purely organic radicals, which can also exhibit intermolecular ferro- as well as antiferromagnetic coupling [48–50].

For the chromium complex **1** (Cr^-) the slope increased rapidly from 2 K to 20 K, where it reaches a plateau at a χT value of 1.84 $cm^3 \cdot mol^{-1} \cdot K$ (300 K, μ_{eff} = 3.66 μ_B). The value at room temperature fits well the magnetic moment in solution (μ_{eff} = 3.60 μ_B, Evans method). It is far off the one for a possible formulation as a chromium(I) complex for which a spin-only value of 5.97 (S = 5/2) is likely, as observed for the chromium(I) precursor $[Cr(hmds)_2]^-$ [13]. Thus, the observed value is best explained by a strongly antiferromagnetically coupled [Cr^{II}/bipy$\cdot^-$]. The slope of the manganese complex **2** (Mn^-) shows similar behavior. Its effective magnetic moment of 4.71 μ_B in solid state is slightly higher than the one in solution (4.46 μ_B) which might be indicative of a paramagnetic impurity. Nonetheless, the value fits best for the description for complex **2** (Mn^-) as a strongly antiferromagnetically coupled ([Mn^{II}/bipy$\cdot^-$]) system.

The χT(T) slope of the reduced iron and cobalt complexes **3** (Fe^-) and **4** (Co^-) increased steadily and merely plateaued at 300 K, reaching 4.80 $cm^3 \cdot mol^{-1} \cdot K$ (μ_{eff} = 6.67 μ_B) for complex **3** (Fe^-) and 2.45 $cm^3 \cdot mol^{-1} \cdot K$ (μ_{eff} = 4.61 μ_B) for complex **4** (Co^-). These very high values are suspicious as they exceed those of their respective quasi-linear metal(I) precursor complexes, which already show free ion behavior with significant spin-orbit coupling [6,13]. Together with the significantly lower magnetic susceptibilities in solution at ambient temperatures (**3** (Fe^-): μ_{eff} = 4.12 μ_B; **4** (Co^-): μ_{eff} = 3.52 μ_B), this points to the presence of a superparamagnetic impurity. A similar observation of unrealistically high χT(T) values was already made for the used two-coordinate iron(I) precursor, which could be attributed to an otherwise undetectable paramagnetic impurity [6]. Given the magnetic moments in solution for complexes **3** (Fe^-) and **4** (Co^-), they also contain most likely high-spin metal(II) ions antiferromagnetically coupled to the 2,2′-bipyridine radical anion [23].

2.5. Electrochemistry

Additional information on the electron transfer onto the bipyridine ligand was sought using electrochemical means. When the reduced complexes **1**–**4** and **10** are subjected to cyclovoltammetric measurements (1 mM, THF, 500 mV/s, 0.1 M NBu_4PF_6, vs Fc/Fc^+), no clear redox event is observed in the expected region between −1 V to −3 V (exemplarily shown for **2** (Mn^-) in Figure 8, see Supplementary material for further details). This is surprising, as bipyridine complexes can exhibit a rich electrochemistry with reversible redox events in this region (see the introduction). Upon examination of the neutral complexes **6**–**9**, each showed a reversible redox event between $E_{1/2}$ = −2.48 V (**6** (Mn)) and −2.81 V (**9** (Zn), Table 6). In contrast, the chromium complex **5** (Cr) showed no comparable redox event. As the reported $E_{1/2}$ = −2.3 V of the bipy/$bipy^-$ redox couple of free 2,2′-bipyridine is low in comparison with that of compounds **6**–**9**, we analyzed 2,2′-bipyridine under our conditions, which gave $E_{1/2}$ = −2.67 V. Thus, the measured values for $E_{1/2}$ of complexes **6**–**9** vary only little with respect to the identity of the metal of the employed $[M(hmds)_2(bipy)]$ complex and are close to the value of free 2,2′-bipyridine. This indicates a bipyridine centered reduction for these compounds. Compounds **6**–**8** show a second irreversible reduction around −3.0 V. This reduction wave is also rather unaffected by the identity of the metal in those complexes and is presumably due to a second bipyridine centered reduction, which would lead to the diamagnetic bipyridyl dianion [23].

Table 6. Cyclovoltammetric data for compounds **6**–**9** and 2,2′-bipyridine.

Compound	6 (Mn)	7 (Fe)	8 (Co)	9 (Zn)	bipy
$E_{1/2}$/V	−2.48	−2.74	−2.50	−2.81	−2.67
ΔE_{Peak}/V	0.096	0.111	0.095	0.131	0.187
E_{red2}/V	−2.94	−3.14	−3.04	-	-

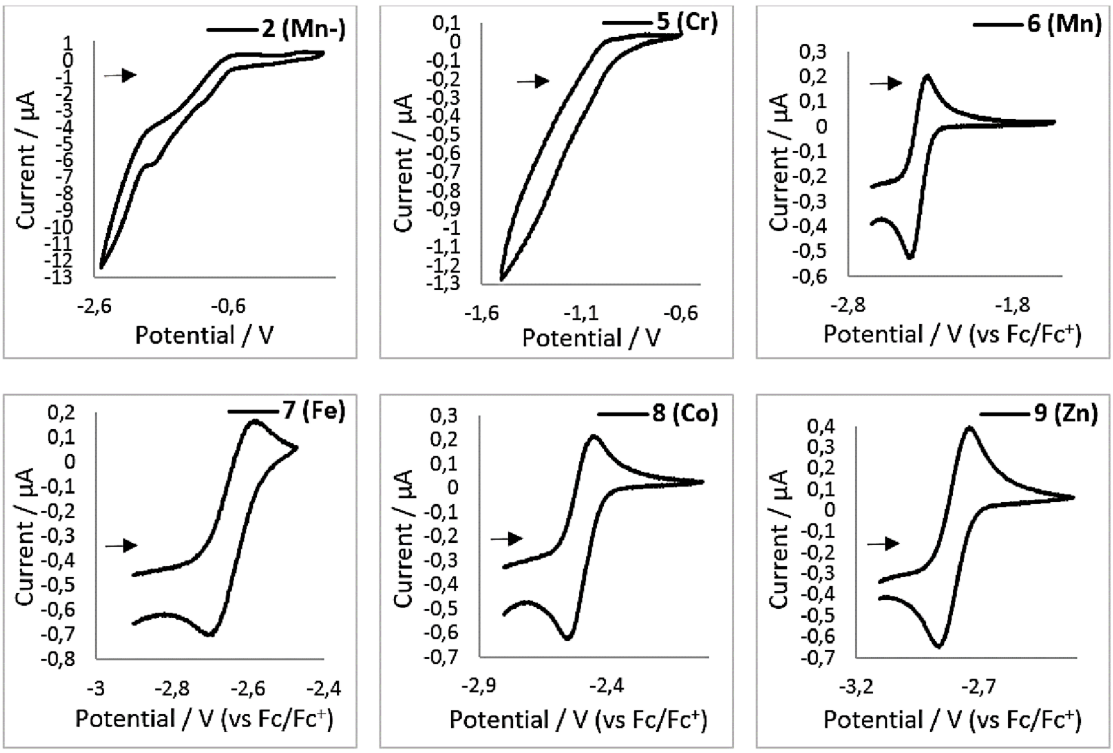

Figure 8. Cyclic voltammograms for complexes **2**, **5**–**9** in THF (1 mM, 500 mV/s, 0.1 M $[NBu_4][PF_6]$).

3. Discussion

The quasi-linear metal(I) complexes K{18c6}[M(hmds)$_2$] reacted instantaneously with 2,2-bipyridine, giving four-coordinate complexes of the type K{18c6}[M(hmds)$_2$(bipy)]. This is remarkable given the high reduction potential of free 2,2′-bipyridine ($E_{1/2}$ = −2.3 V vs Fc/Fc^+). Within complexes the reduction of bipyridine is usually found to occur in a range between −0.8 V and −2.5 V depending on the metal and the charge of the complex [30,40,51–56]. Thereby, lower potentials are observed mainly for neutral or anionic complexes, such as [Mn(bipy)(CO)$_3$Br] (approximately −2.0 V vs Fc/Fc^+). Our results implicate that, despite the lack of an observable interaction of $[M^I(hmds)_2]^-$ with Lewis bases, as examined exemplarily for iron, an inner-sphere electron transfer mechanism is likely to take place upon temporary bipyridine coordination. The structural features of K{18c6}[M(hmds)$_2$(bipy)], especially those of the central C–C bond of the bipyridine ligand, are indicative of the reduction of the bipyridine to its monoanionic state. This notion is supported by the lack of significant geometric differences around the metal ion in comparison with their neutral, non-reduced counterparts. This holds especially true for the chromium complex, which retains its distorted square planar geometry in the neutral as well as the reduced state, which is typical for four-coordinate chromium(II) ions.

Electrochemical examination of the reduced complexes $[M(hmds)_2(bipy)]^-$ by cyclovoltammetry surprisingly showed no redox event between −1 V and −3 V (vs. Fc/Fc^+), which is the expected range of bipyridyl radical anion containing complexes (see the introduction). This may be the result of the highly sensitive nature of these compounds. In contrast, their neutral counterparts **6**–**9**, (with the exception of **5** (Cr)) exhibit a reversible redox event in the range of $E_{1/2}$ = −2.48 V (**2** (Mn)) and $E_{1/2}$ = −2.81 V (**9** (Zn)), which can be attributed to the $[M(hmds)_2(bipy)]^0/[M(hmds)_2(bipy)]^{-1}$ redox pair. As the redox events are largely independent from the identity of the metal and similar to the one of free 2,2′-bipyridine ($E_{1/2}$ = −2.67 V), it is highly indicative of a largely bipyridine centered reduction in these complexes. It is important to note that these $E_{1/2}$ values are partially more negative than the ones of the respective quasi-linear metal(I) silylamides (E_{pc} = −2.45 V (Mn^I), −1.98 V (Fe^I) and −1.47 V (Co^I)) [6,13]. For chromium no clear redox event is visible in the examined region.

^{1}H-NMR spectroscopic examination of compounds **1**–**8** revealed highly paramagnetically influenced signals for all those complexes, whereas those of chromium (**1** (Cr^-) and **5** (Cr)) and manganese (**2** (Mn^-) and **6** (Mn)) are mostly uninformative due to the extent of the paramagnetism. For the iron and cobalt complexes **3** (Fe^-) and **4** (Co^-) generally larger isotropic shifts and line broadening for the bipyridine protons are observed in comparison to their respective neutral counterparts **7** (Fe) and **8** (Co). Whereas the zinc complex **9** (Zn) is diamagnetic with well resolved proton signals; in the reduced zinc complex **10** (Zn^-) these signals are subject to an isotropic shift and significant line broadening. For the signals of the $SiMe_3$ protons of the complexes, no comparable trend is observed for each complex pair. Generally a higher unpaired electron count is connected to a more paramagnetically distorted ^{1}H-NMR spectrum for otherwise structurally identical compounds [57], as for example seen for the metal(I) precursors [6,13] or the [M(hmds)$_2$(bipy)] complexes themselves (vide supra). In the hypothetical case of a largely metal-based reduction, this would lead to an overall reduction of the respective spin state, which generally gives sharper and lesser isotropic shifted proton signals. Therefore, in the reduced complexes the bipyridine protons likely experience not only the presence of the paramagnetic metal center but also the proximity of the electron of the bipyridyl radical anion. However, one has to bear in mind that this is only a simplified approach as the exact extent of magnetic relaxation as well as that the isotropic shift is dependent on the orientation of the d-orbital towards the respective proton to which the electron is added (pseudocontact shift) and the change in the hyperfine coupling between the protons and the unpaired electrons of metal (contact shift) [58].

UV/Vis spectroscopy showed for most reduced complexes (**1** (Cr^-), **2** (Mn^-), **10** (Zn^-) and to a lesser extent for **3** (Fe^-)) two distinct bands between 450 and 550 nm. These can also be found for the free 2,2′-bipyridine radical anion and are attributed to a pi–pi* transition [44]. Further, complexes **2** (Mn^-), **4** (Co^-) and **10** (Zn^-) show strong additional absorption bands in the range of 700 to 1000 nm, which originate from a pi–pi* transition within the bipyridyl radical anion. This means that for all reduced complexes UV/Vis spectroscopy reveals the presence of a bipyridyl radical anion. Thereby, its signature is most pronounced for the manganese (**2** (Mn^-)) and zinc (**2** (Zn^-)) derivatives. It indicates in these cases a mainly electrostatic interaction between the metal ion and the radical anion. For cobalt, iron and chromium, the respective transitions belonging to the bipyridine radical anion are broader and less pronounced, which might be attributed to additional orbital interactions with the d-metal ion.

The examination of the magnetic features of the anionic complexes in the solid state show for the chromium (**1** (Cr^-)) and manganese (**2** (Mn^-)) complexes that these systems are best described as strongly antiferromagnetically coupled metal(II) bipyridine radical anions. This is consistent with the situation found for the respective [M(mes)$_2$(bipy)]$^-$ complexes (M = Cr and Mn) [35]. For the cobalt and iron complexes **3** (Fe^-) and **4** (Co^-) the situation is more complicated, as solid state magnetic measurements of otherwise analytically pure samples gave rather high χT(T) values at room temperature, which are materially higher than those found in solution by Evan's method. This indicates an inseparable superparamagnetical impurity, which makes the solid state measurements ambiguous. The magnetic susceptibility in solution for complexes **3** (Fe^-) and **4** (Co^-) amount to 4.12 μ_B and 3.57 μ_B. These values are indicative of a strongly antiferromagnetically coupled [M^{II}(hmds)$_2$(bipy$\cdot^-$)]$^-$ system ($\mu_{theor.}$(S = |2 − 1/2|) = 3.87 μ_B for **3** (Fe^-); $\mu_{theor.}$ (S = |3/2 − 1/2|) = 2.83 μ_B for **4** (Co^-)) with additional orbital contributions [34]. The room temperature magnetic susceptibility of **3** (Fe^-) is in line with that found for [Fe(mes)$_2$(bipy)]$^-$ [34], whereas the value found for complex **4** (Co^-) is significantly higher than the one obtained for the pseudo square-planar [Co(mes)$_2$(bipy)]$^-$ (μ_{eff} = 1.88 μ_B). For the latter, a mixture of a singlet and a triplet state was assumed [35]. The comparable high value found for complex **4** (Co^-) is probably due to a different complex geometry (distorted tetrahedral) giving the presence of a high spin cobalt(II) ion. Thereby, the difference in geometry between [Co(mes)$_2$(bipy)]$^-$ and **4** (Co^-) can be attributed to the higher ligand field imposed by the mesityl groups.

Taken together, the reduced complexes [M(hmds)$_2$(bipy)]$^-$ are best described as metal(II) complexes bearing a monoanionic bipyridine radical, which is deducted from the combined use of a variety of analytical techniques. The outcome is in line with a study on related [M(mes)$_2$(bipy)]$^-$

complexes (M = Cr–Ni; mes = 2,4,6-trimethylbenzyl), which, however, were obtained from a reduction of the preformed [M(mes)$_2$(bipy)] parent complexes with KC_8 in the presence of crypt.222 [34,35].

4. Materials and Methods

All manipulations were carried out in a glovebox under a dry argon atmosphere, unless indicated otherwise. Used solvents were dried by continuous distillation over sodium metal for several days, degassed via three freeze-pump cycles and stored over molecular sieves 4 Å. Deuterated solvents were used as received, degassed via three freeze-pump cycles and stored over molecular sieves 4 Å. The ^{1}H-NMR spectra were recorded on a Bruker AV 500 or a Bruker HD 500 NMR spectrometer (Bruker Corporation, Billerica, MA, USA). Chemical shifts are reported in ppm relative to the residual proton signals of the solvent (for ^{1}H) or relative to the signal of the solvent itself (^{13}C). $w_{1/2}$ is the line width of a signal at half its maximum intensity. Integrals of the broad signals of the hmds units were obtained directly or by peak fitting (in case of overlapping signals) using the MestreNova software package (Mestrelab, Santiago de Compostela, Spain). IR measurements were conducted on a Bruker Alpha ATR-IR spectrometer (Bruker Corporation, Billerica, MA, USA). Elemental analyses were performed by the "in-house" service of the Chemistry Department of the Philipps University Marburg, Germany using a CHN(S) analyzer vario MICRO Cube (Elementar Analysensysteme GmbH, Langenselbold, Germany). UV/Vis-spectra were recorded on an AnalytikJena Specord S600 diode array spectrometer (AnalytikJena, Jena, Germany). The dc susceptibility data was obtained in a range of 3 K to 300 K at 1 T on a physical properties measurement system from LQT/QD (Quantum Design, San Diego, CA, USA). The samples were mounted in a plastic sample holder. The Curie-Weiss Law was used for fitting the magnetic data, whereas the diamagnetic correction was obtained using tabulated pascal constants as well as experimental data for the sample holder. Cyclic voltammograms were recorded on a RHD Instruments measuring cell of the type Microcell HC and a Pt electrode (RHD Instruments GmbH, Darmstadt, Germany). The potentiostat is a Methrom autolab type PGStat 204 (Methrom AG, Herisau, Switzerland). Cyclic voltammetry measurements were carried out under Argon at 500 mV/s scan rate in THF/0.1 M [NBu_4][PF_6]. Potentials are referenced to Fc/Fc^+, which was added after the respective measurement. 2,2′-bipyridine and Nbu_4PF_6 were obtained commercially and used as received, unless noted otherwise. Nbu_4PF_6 was dried in vacuo at 100 °C for several hours prior to use. [M(N(SiMe$_3$)$_2$)$_2$] (Mn and Fe) [59,60], [Cr(N(SiMe$_3$)$_2$)$_2$(thf)$_2$] [61], [Co(N(SiMe$_3$)$_2$)$_2$(thf)] [59], K{18c6}[M(N(SiMe$_3$)$_2$)$_2$] (Fe and Co) [6,13] and [M(N(SiMe$_3$)$_2$)$_2$(bipy)] (Cr–Fe) [43,62], were prepared according to literature procedures. K{18c6}[M(N(SiMe$_3$)$_2$)$_2$] (Cr and Mn) were synthesized in situ according the published procedure for K{18c6}[Mn(N(SiMe$_3$)$_2$)$_2$] and used as such [13].

4.1. Synthesis of Complexes

[K{18c6}][Cr(N(SiMe$_3$)$_2$)$_2$(bipy)] (1): [Cr(N(SiMe$_3$)$_2$)$_2$*(THF)$_2$] (103.4 mg, 0.20 mmol, 1.0 equivalent) and 18-crown-6 (60.6 mg, 0.2 mmol, 1.0 equivalent) were dissolved in 3 mL of Et_2O. The addition of KC_8 (27.0 mg. 0.2 mmol, 1.0 equivalent) led to an immediate color change to dark orange. After stirring for 5 min, the mixture was filtered, and the filtrate was given to 2,2′-bipyridine (31.2 mg, 0.20 mmol, 1.0 equivalent), this led to an immediate color change to dark green. The solution was stirred for 5 min and layered with 3 mL of pentane. Storing the solution at −35 °C for days yielded a dark green crystalline solid. The solution was removed via a Pasteur pipette. Washing of the residue with 2 × 5 mL of pentane and drying it under reduced pressure afforded compound **1** as a dark green crystalline solid (60.2 mg, 0.072 mmol, 36%). ^{1}H-NMR ([D8]THF, 500.1 MHz, 298 K, ppm): No useful signal attribution possible; IR (ATR, cm^{-1}): ν = 2939 (w), 2892 (m), 1492 (m), 1350 (w), 1231 (m), 1104 (vs), 1004 (vs), 961 (s), 890 (m), 869 (m), 819 (vs), 716 (m), 654 (m), 604 (w), 465 (w), 425 (w); elemental analysis calculated ($C_{34}H_{68}CrKN_4O_6Si_4$ 832.37 g/mol) C 49.06 H 8.23 N 6.26; experimental C 49.01 H 8.15 N 6.36. μ_{eff} = 3.60 μ_B ([D8]THF). Crystals, suitable for X-ray diffraction analysis, were obtained from a pentane layered solution of compound **1** in Et_2O at −35 °C.

[K{18c6}][Mn(N(SiMe$_3$)$_2$)$_2$(bipy)] (2): Mn(N(SiMe$_3$)$_2$)$_2$ (75.1 mg, 0.20 mmol, 1.0 equivalent) and 18-crown-6 (63.7 mg, 0.2 mmol, 1.05 equivalent) were dissolved in 3 mL of Et_2O. The addition of KC_8 (32.4 mg. 0.2 mmol, 1.5 equivalent) led to an immediate color change to dark purple. After stirring for 5 min, the mixture was filtered, and the filtrate was given to 2,2´-bipyridine (31.2 mg, 0.20 mmol, 1.0 equivalent), leading to an immediate color change to dark red. The solution was stirred for 5 min and layered with 3 mL of pentane. Storing the solution at −35 °C for days yielded a dark red crystalline solid. The solution was removed via a Pasteur pipette. The residue was washed with 2 × 5 mL of pentane and dried under reduced pressure to afford compound **2** as a dark red crystalline solid (110.9 mg, 0.13 mmol, 66%). ^{1}H-NMR ([D8]THF, 500.1 MHz, 298 K, ppm): δ = 3.62 (s, 24H, $w_{\frac{1}{2}}$ = 29 Hz, OCH_2), 19.90 (s, 36H, $w_{\frac{1}{2}}$ = 2312 Hz, Si(CH_3)$_3$); IR (ATR, cm^{-1}): ν = 2940 (w), 2889(w), 1453 (m), 1351 (m), 1232 (s), 1001 (s), 961 (s), 890 (m), 869 (m), 819 (vs), 771 (vs), 724 (m), 703 (m), 659 (m), 604 (w), 528 (w), 449 (w), 415 (w); elemental analysis calculated ($C_{34}H_{68}MnKN_4O_6Si_4$ 832.37 g/mol) C 48.89 H 8.21 N 6.71; experimental C 47.61 H 8.09 N 6.35. A lower carbon value of 1% was consistently observed upon several attempts (>5), despite using different, freshly prepared crystalline batches of **8**. We attribute this to possible carbide formation. M_{eff} = 3.46 μ_B ([D8]THF). Crystals, suitable for X-ray diffraction analysis, were obtained from a pentane layered solution of compound **2** in Et_2O at −35 °C.

[K{18c6}][Fe(N(SiMe$_3$)$_2$)$_2$(bipy)] (3): [K{18c6}][Fe(N(SiMe$_3$)$_2$)$_2$] (135.9 mg, 0.20 mmol, 1.0 equivalent) and 2,2´-bipyridine (31.2 mg, 0.20 mmol, 1.0 equivalent) were dissolved in 3 mL of Et_2O, which led to an immediate color change from brownish green to dark green. After stirring for 5 min the solution was layered with 3 mL of pentane. Storing the solution at −35 °C for days yielded a dark green crystalline solid. The solution was removed via a Pasteur pipette. Washing of the residue with 2 × 5 mL of pentane and drying it under reduced pressure afforded compound **3** as a dark green crystalline solid (113.8 mg, 0.14 mmol, 68%). ^{1}H-NMR ([D8]THF, 500.3 MHz, 298 K, ppm): δ = 1.73 (s, 36H, Si(CH_3)$_3$), 3.58 (s, 24H, OCH_2) 64.49 (s, 2H, $w_{\frac{1}{2}}$ = 154 Hz, CH_{bipy}), 77.87 (s, 2H, $w_{\frac{1}{2}}$ = 1534 Hz, CH_{bipy}), 178.22 (s, 2H, $w_{\frac{1}{2}}$ = 478 Hz, CH_{bipy}), 268.08 (s, 2H, $w_{\frac{1}{2}}$ = 711 Hz, CH_{bipy}); IR (ATR, cm^{-1}): ν = 2941 (w), 2890 (w), 1536 (w), 1493 (m), 1350 (m), 1229 (m), 1001 (s), 961 (s), 889 (m), 869 (m), 820 (vs), 774 (m), 728 (m), 703 (m), 640 (m), 601 (w), 528 (w), 455(w), 417 (w); elemental analysis calculated ($C_{34}H_{68}FeKN_4O_6Si_4$ 836.22 g/mol) C 48.84 H 8.20 N 6.70; experimental C 48.63 H 8.06 N 6.96. μ_{eff} = 4.12 μ_B ([D8]THF). Crystals, suitable for X-ray diffraction analysis, were obtained from a pentane layered solution of compound **3** in Et_2O at −35 °C.

[K{18c6}][Co(N(SiMe$_3$)$_2$)$_2$(bipy)] (4): [K{18c6}][Co(N(SiMe$_3$)$_2$)$_2$] (68.3 mg, 0.10 mmol, 1.0 equivalent) and 2,2´-bipyridine (15.6 mg, 0.10 mmol, 1.0 equivalent) were dissolved in 3 mL of Et_2O, which led to an immediate color change from pale yellow-green to dark green. After stirring for 5 min the solution was layered with 3 mL of pentane. Storing the solution at −35 °C for days yielded a dark green crystalline solid. The solution was removed via a Pasteur pipette. Washing of the residue with 2 × 5 mL of pentane and drying it under reduced pressure afforded compound **4** as a dark green crystalline solid (54.8 mg, 0.065 mmol, 65%). ^{1}H-NMR ([D8]THF, 500.1 MHz, 298 K, ppm): δ = 2.47 (bs, 36H, $w_{\frac{1}{2}}$ = 83 Hz, Si(CH_3)$_3$), 3.58 (s, 24H, $w_{\frac{1}{2}}$ = 29 Hz, OCH_2), 50.26 (s, 2H, $w_{\frac{1}{2}}$ = 25 Hz, CH_{bipy}), 104.35 (bs, 2H, $w_{\frac{1}{2}}$ = 749 Hz, CH_{bipy}), 143.95 (s, 2H, $w_{\frac{1}{2}}$ = 85 Hz, CH_{bipy}), 155.75 (s, 2H, $w_{\frac{1}{2}}$ = 100 Hz, CH_{bipy}); IR (ATR, cm^{-1}): ν = 2940 (m), 2887 (m), 1565 (w), 1552 (w), 1503 (m), 1470 (m), 1451 (m), 137 (w), 1350 (m), 1293 (m), 1227 (m), 1103 (vs), 1009 (s), 958 (s), 866 (m), 817 (vs), 687 (m), 653 (w), 605 (m), 528 (m), 462 (w), 419 (w); elemental analysis calculated ($C_{34}H_{68}CoKN_4O_6Si_4$ 839.31 g/mol) C 48.66 H 8.17 N 6.68; experimental C 48.98 H 7.79 N 6.83. μ_{eff} = 3.52 μ_B ([D8]THF). Crystals, suitable for X-ray diffraction analysis, were obtained from a pentane layered solution of compound **4** in Et_2O at −35 °C.

[Cr(N(SiMe$_3$)$_2$)$_2$(bipy)] (5) [42]: [Cr(N(SiMe$_3$)$_2$)$_2$*(THF)$_2$] (206.8 mg, 0.4 mmol, 1.0 equivalent) and 2,2´-bipyridine (62.5 mg, 0.4 mmol, 1.0 equivalent) were dissolved in 3 mL of Et_2O, which led to an immediate color change from orange to dark violet. After stirring for 5 min the solution was layered with 3 mL of pentane. Storing the solution at −35 °C for days yielded a dark violet crystalline solid. The solution was removed via a Pasteur pipette. Washing of the residue with 2 × 5 mL of pentane and drying it under reduced pressure afforded compound **5** as a dark violet crystalline solid (184.0 mg,

0.35 mmol, 87%). ^{1}H-NMR ([D8]THF, 500.1 MHz, 300 K, ppm): δ = −71.19 (s, 2H, $w_{\frac{1}{2}}$ = 931 Hz, CH_{bipy}), 16.47 (s, 2H, $w_{\frac{1}{2}}$ = 258 Hz, CH_{bipy}), 40.78 (s, 36H, $w_{\frac{1}{2}}$ = 2539 Hz, $Si(CH_3)_3$), 47.05 (s, 2H, $w_{\frac{1}{2}}$ = 979 Hz, CH_{bipy}), 53.82 (s, 2H, $w_{\frac{1}{2}}$ = 1415 Hz, CH_{bipy}); IR (ATR, cm^{-1}): ν = 2939 (m), 2892 (w), 1601 (m), 1572 (w), 1466 (w), 1441 (m), 1305 (w), 1249 (s), 1234 (s), 1152 (w), 986 (vs), 886 (m), 864 (m), 813 (vs), 761 (vs), 733 (vs), 657 (s), 606 (m), 419 (m).

[Mn(N(SiMe$_3$)$_2$)$_2$(bipy)] (6) [43]: $Mn(N(SiMe_3)_2)_2$ (150.3 mg, 0.4 mmol, 1.0 equivalent) and 2,2´-bipyridine (62.5 mg, 0.4 mmol, 1.0 equivalent) were dissolved in 3 mL of Et_2O, which led to an immediate color change from colorless to dark orange. After stirring for 5 min the solution was layered with 3 mL of pentane. Storing the solution at −35 °C for days yielded a dark orange crystalline solid. The solution was removed via pipette. Washing of the residue with 2 × 5 mL of pentane and drying it under reduced pressure afforded compound **6** as a light orange crystalline solid (194.0 mg, 0.36 mmol, 92%). ^{1}H-NMR ([D8]THF, 500.1 MHz, 300 K, ppm): δ = 29.54 (s, 36H, $w_{\frac{1}{2}}$ = 5723 Hz, $Si(CH_3)_3$), no further useful signal attribution is possible; IR (ATR, cm^{-1}): ν = 2942 (m), 2890 (w), 1596 (m), 1441 (m), 1235 (s), 1155 (w), 993 (vs), 888 (w), 866 (s), 814 (vs), 775 (m), 756 (s), 736 (m), 703 (w), 662 (s), 625 (w) 610 (m).

[Fe(N(SiMe$_3$)$_2$)$_2$(bipy)] (7) [43]: $Fe(N(SiMe_3)_2)_2$ (149.9 mg, 0.4 mmol, 1.0 equivalent) and 2,2´-bipyridine (62.5 mg, 0.4 mmol, 1.0 equivalent) were dissolved in 3 mL of Et_2O, which led to an immediate color change from pale to dark green. After stirring for 5 min the solution was layered with 3 mL of pentane. Storing the solution at −35 °C for days yielded a dark green crystalline solid. The solution was removed via a Pasteur pipette. Washing of the residue with 2 × 5 mL of pentane and drying it under reduced pressure afforded compound **7** as a dark green crystalline solid (198.0 mg, 0.37 mmol, 93%). ^{1}H-NMR ([D8]THF, 500.1 MHz, 300 K, ppm): δ = −19.13 (s, 2H, $w_{\frac{1}{2}}$ = 61 Hz, CH_{bipy}), 10.93 (s, 36H, $w_{\frac{1}{2}}$ = 425 Hz, $Si(CH_3)_3$), 52.13 (s, 2H, $w_{\frac{1}{2}}$ = 128 Hz, CH_{bipy}), 64.09 (s, 2H, $w_{\frac{1}{2}}$ = 113 Hz, CH_{bipy}), the fourth signal belonging to the bipyridine ligand was not observed, which is attributed to its paramagnetism; IR (ATR, cm^{-1}): ν = 2942 (m), 2890 (w), 1597 (w), 1441 (m), 1236 (s), 974 (vs), 888 (m), 862 (m), 820 (vs), 779 (s), 755 (s), 708 (s), 662 (s), 621 (w), 610 (w).

[Co(N(SiMe$_3$)$_2$)$_2$(bipy)] (8): $[Co(N(SiMe_3)_2)_2{*}thf]$ (460.0 mg, 1.0 mmol, 1.0 equivalent) and 2,2´-bipyridine (156.12 mg, 1.0 mmol, 1.0 equivalent) were dissolved in 3 mL of Et_2O, which led to an immediate color change from pale green to dark red. After stirring for 5 min the solution was layered with 3 mL of pentane. Storing the solution at −35 °C for days yielded a dark red crystalline solid. The solution was removed via a Pasteur pipette. Washing of the residue with 2 × 5 mL of pentane and drying it under reduced pressure afforded compound **8** as a dark red crystalline solid (263.0 mg, 0.49 mmol, 49%). ^{1}H-NMR ([D8]THF, 500.1 MHz, 300 K, ppm): δ = −21.01 (s, 2H, $w_{\frac{1}{2}}$ = 27 Hz, CH_{bipy}), 8.11 (s, 36H, $w_{\frac{1}{2}}$ = 68 Hz, $Si(CH_3)_3$), 42.65 (s, 2H, $w_{\frac{1}{2}}$ = 31 Hz, CH_{bipy}), 50.94 (s, 2H, $w_{\frac{1}{2}}$ = 25 Hz, CH_{bipy}), 59.68 (s, 2H, $w_{\frac{1}{2}}$ = 253 Hz, CH_{bipy}); IR (ATR, cm^{-1}): ν = 2941 (w), 2890 (m), 1598 (m), 1441 (m), 1235 (s), 1154 (m), 976 (vs), 888 (w), 860 (vs), 660 (m), 609 (w); elemental analysis calculated ($C_{22}H_{44}CoN_2Si_4$ 535.19 g/mol) C 49.31 H 8.28 N 10.46; experimental C 48.65 H 8.20 N 10.50. A lower carbon value of 1% was consistently observed upon several attempts (>5), despite using different, freshly prepared crystalline batches of **8**. We attribute this to possible carbide formation. LIFDI mass calc. ($C_{22}H_{44}CoN_2Si_4$ 535.1975 *m/z*); exp. ($C_{22}H_{44}CoN_2Si_4$ 535.1958 *m/z*). Crystals, suitable for X-ray diffraction analysis, were obtained from a pentane layered solution of compound **8** in Et_2O at −35 °C.

[Zn(N(SiMe$_3$)$_2$)$_2$(bipy)] (9): $Zn(N(SiMe_3)_2)_2$ (154.2 mg, 0.4 mmol, 1.0 equivalent) and 2,2´-bipyridine (62.5 mg, 1.0 mmol, 1.0 equivalent) were dissolved in 3 mL of Et_2O, which led to an immediate color change from colorless to pale yellow. After stirring for 5 min the solution was layered with 3 mL of pentane. Storing the solution at −35 °C for days yielded a light yellow crystalline solid. The solution was removed via a Pasteur pipette. Washing of the residue with 2 × 5 mL of pentane and drying it under reduced pressure afforded compound **9** as a light yellow crystalline solid (136.3 mg, 0.25 mmol, 63%). ^{1}H-NMR ([D8]THF, 500.1 MHz, 300 K, ppm): δ = 0.11 (s, 36H, $w_{\frac{1}{2}}$ = 2 Hz, $Si(CH_3)_3$), 7.64–7.85 (m, 2H, CH_{bipy}), 8.17 (t, ^{3}J =7.5 Hz, 2H, CH_{bipy}), 8.44 (d, ^{3}J =8.1 Hz, 2H, CH_{bipy}),

9.92 (d, ^{3}J = 4.7 Hz, 2H, CH_{bipy}); IR (ATR, cm^{-1}): ν = 2942 (m), 2892 (w), 1597 (m), 1474 (m), 1236 (s), 1154 (m), 984 (vs), 894 (m), 868 (s), 821 (vs), 757 (s), 737 (s), 662 (s), 609 (w), 427 (w); elemental analysis calculated ($C_{22}H_{44}ZnN_2Si_4$ 542.34 g/mol) C 48.72 H 8.18 N 10.33; experimental C 48.26 H 7.89 N 10.43. HR-LIFDI-MS (calculated for $C_{22}H_{44}ZnN_2Si_4$: 540.1935 *m/z*) = 540.1932 *m/z*. Crystals, suitable for X-ray diffraction analysis, were obtained from a pentane layered solution of compound **9** in Et_2O at −35 °C.

[K{18c6}][Zn(N(SiMe$_3$)$_2$)$_2$(bipy)] (10): Compound **9** (54.2 mg, 0.10 mmol, 1.0 equivalent), 18-crown-6 (26.4 mg, 0.1 mmol, 1.0 equivalent) and KC_8 (20.3 mg, 0.1 mmol, 1.5 equivalent) were dissolved in 3 mL of Et_2O, which led to an immediate color change from pale yellow to dark purple. After stirring for 5 min the solution was layered with 3 mL of pentane. Storing the solution at −35 °C for days yielded a dark red crystalline solid. The solution was removed via a Pasteur pipette. Washing of the residue with 2 × 5 mL of pentane and drying it under reduced pressure afforded compound **10** as a dark red crystalline solid (59.5 mg, 0.07 mmol, 70%). ^{1}H-NMR ([D8]THF, 500.1 MHz, 298 K, ppm): δ = 0.53 (bs, 36H, $w_{\frac{1}{2}}$ = 139 Hz, $Si(CH_3)_3$), 3.63 (s, 24H, $w_{\frac{1}{2}}$ = 6 Hz, OCH_2), 4.18 (s, 2H, $w_{\frac{1}{2}}$ = 20 Hz, CH_{bipy}), 4.95 (bs, 2H, $w_{\frac{1}{2}}$ = 20 Hz, CH_{bipy}), 5.81 (s, 2H, $w_{\frac{1}{2}}$ = 24 Hz, CH_{bipy}), 6.72 (s, 2H, $w_{\frac{1}{2}}$ = 18 Hz, CH_{bipy}); IR (ATR, cm^{-1}): ν = 2941 (m), 2893 (m), 1570 (w), 1486 (m), 1473 (w), 1454 (w), 1351 (m), 1283 (w), 1233 (s), 1104 (vs), 989 (vs), 961 (s), 870 (s), 823 (vs), 780 (w), 748(m), 716 (m), 658 (m), 608 (m), 529 (m), 452 (w), 415 (w); elemental analysis calculated ($C_{34}H_{68}ZnKN_4O_6Si_4$ 845.75 g/mol) C 48.28 H 8.10 N 6.62; experimental C 48.49 H 7.86 N 6.59. μ_{eff} = 1.82 μ_B ([D8]THF). Crystals, suitable for X-ray diffraction analysis, were obtained from a pentane layered solution of compound **10** in Et_2O at −35 °C.

4.2. X-ray Diffraction Data

Data for compounds **3** (CCDC 1918204), **4** (CCDC 1918205) and **10** (CCDC 1918207) were collected at 100 K on a Bruker Quest D8 diffractometer (Bruker Corporation, Billerica, MA, USA) using a graphite-monochromated Mo Kα radiation and equipped with an Oxford Instrument Cooler Device (Oxford Instruments, Abingdon, UK). Data for compounds **8** (CCDC 1918202), **1** (CCDC 1918208) and **9** (CCDC 1918206) were collected at 100 K on a STOE IPDS2 diffractometer (STOE & Cie GmbH, Darmstadt, Germany) and data for compound **2** (CCDC 1918203) were collected at 100 K on a STOE IPDS2T diffractometer using a graphite-monochromated Mo Kα radiation (λ = 0.71073 Å) and equipped with an Oxford Cryosystems Cryostream Cooler Device (Oxford Instruments, Abingdon, UK). The structures have been solved using either OLEX SHELXT V2014/1 [63] and refined by means of least-squares procedures on an F^2 with the aid of the program SHELXL-2016/6 [64] included in the software package WinGX version 1.63 [65] or using CRYSTALS [66]. The atomic scattering factors were taken from International Tables for X-ray Crystallography [67]. All non-hydrogen atoms were refined anisotropically. All hydrogens atoms were refined by using a riding model. Absorption corrections were introduced by using the MULTISCAN and X-Red programs [68,69]. Drawings of molecules are performed with the program DIAMOND (Crystal Impact, Bonn, Germany) with 50% probability displacement ellipsoids for non-H atoms. Depiction of H atoms is omitted for clarity.

Crystal Data for **1** ($C_{42}H_{84}CrKN_4O_8Si_4$ x $(thf)_2$, 976.59 g/mol): Triclinic, space group P−1, a = 11.6269(2) Å, b = 21.5546(4) Å, c = 21.8560(4) Å, α = 95.633(2)°, β = 89.8920(10)°, γ = 90.377(2)°, V = 5450.83(17) Å^3, Z = 4, T = 100.0 K, μ(Mo Kα) = 0.710 mm^{-1}, ρ_{calc} = 1.190 g/cm^3, 88,325 reflections measured (3.504° ≤ 2Θ ≤ 50.0°), 19,148 unique (R_{int} = 0.0630, R_{sigma} = 0.0368), which were used in all calculations. The final R_1 was 0.0512 ($I > 2\sigma(I)$) and wR_2 was 0.1323 (all data).

Crystal data for **2** ($C_{34}H_{68}MnKN_4O_6Si_4$, 835.32 g/mol): Monoclinic, space group C2, a = 34.8403(17) Å, b = 18.4715(11) Å, c = 14.5302(8) Å, α = 90.0, β = 96.555(4)°, γ = 90.0°, V = 9289.8(9) Å^3, Z = 8, T = 100.0 K, μ(Mo Kα) = 0.710 mm^{-1}, ρ_{calc} = 1.194 g/cm^3, 52,126 reflections measured (3.668° ≤ 2Θ ≤ 54.998°), 21354 unique (R_{int} = 0.0285, R_{sigma} = 0.0488), which were used in all calculations. The final R_1 was 0.0376 ($I > 2\sigma(I)$) and wR_2 was 0.0815 (all data).

Crystal data for **3** ($C_{42}H_{84}FeKN_4O_8Si_4$ x $(thf)_2$, 978.61 g/mol): Triclinic, space group P−1, a = 10.8613(5) Å, b = 13.2627(6) Å, c = 19.8669(9) Å, α = 77.5970(10)°, β = 80.062(2)°, γ = 83.452(2)°, V = 2744.3(2) Å^3, Z = 2, T = 100.0 K, μ(Mo-Kα) = 0.710 mm^{-1}, ρ_{calc} = 1.184 g/cm^3, 103,782 reflections

measured (4.646 ° ≤ 2Θ ≤ 55.124°), 12,642 unique (R_{int} = 0.0332, R_{sigma} = 0.0201), which were used in all calculations. The final R_1 was 0.0279 ($I > 2\sigma(I)$) and wR_2 was 0.0658 (all data).

Crystal data for **4** ($C_{42}H_{84}CoKN_4O_8Si_4$ x $(thf)_2$, 978.61 g/mol): Triclinic, space group P−1, a = 10.8097(5) Å, b = 13.2648(6) Å, c = 19.9051(10) Å, α = 77.712 (2)°, β = 80.199(2)°, γ = 83.606(2)°, V = 2739.7(2) Å^3, Z = 2, T = 100.0 K, μ(Mo Kα) = 0.710 mm^{-1}, ρ_{calc} = 1.192 g/cm^3, 89,930 reflections measured (4.238° ≤ 2Θ ≤ 55.058°), 12,549 unique (R_{int} = 0.0853, R_{sigma} = 0.0565) which were used in all calculations. The final R_1 was 0.0420 ($I > 2\sigma(I)$) and wR_2 was 0.0831 (all data).

Crystal data for **8** ($C_{22}H_{44}CoKN_4Si_4$, 535.90 g/mol): Orthorhombic, space group P$ca2_1$, a = 18.7674(9) Å, b = 18.1030(8) Å, c = 17.5930(7) Å, $\alpha = \beta = \gamma$ = 90.0°, V = 5977.2(5) Å^3, Z = 8, T = 100.0 K, μ(Mo Kα) = 0.710 mm^{-1}, ρ_{calc} = 1.191 g/cm^3, 31,013 reflections measured (3.88° ≤ 2Θ ≤ 52.0°), 10,939 unique (R_{int} = 0.0280, R_{sigma} = 0.0312), which were used in all calculations. The final R_1 was 0.0280 ($I > 2\sigma(I)$) and wR_2 was 0.0689 (all data).

Crystal data for **9** ($C_{22}H_{44}ZnKN_4Si_4$, 542.34 g/mol): Orthorhombic, space group P$ca2_1$, a = 18.8806(12) Å, b = 18.0560(13) Å, c = 17.6133(17) Å, $\alpha = \beta = \gamma$ = 90.0°, V = 6004.5(8) Å^3, Z = 8, T = 100.0 K, μ(Mo Kα) = 0.710 mm^{-1}, ρ_{calc} = 1.200 g/cm^3, 52,603 reflections measured (4.314° ≤ 2Θ ≤ 51.996°), 11,789 unique (R_{int} = 0.0737, R_{sigma} = 0.0589), which were used in all calculations. The final R_1 was 0.0340 ($I > 2\sigma(I)$) and wR_2 was 0.0718 (all data).

Crystal data for **10** ($C_{38}H_{78}MZnKN_4O_7Si_4$ x (Et_2O), 919.87 g/mol): Monoclinic, space group P$2_1/c$, a = 12.1899(7) Å, b = 18.4365(10) Å, c = 22.8273(13) Å, α = 90.0, β = 95.432(2)°, γ = 90.0°, V = 5107.2(5) Å^3, Z = 4, T = 100.0 K, μ(Mo Kα) = 0.710 mm^{-1}, ρ_{calc} = 1.196 g/cm^3, 96,672 reflections measured (4.268° ≤ 2Θ ≤ 49.998°), 8987 unique (R_{int} = 0.0946, R_{sigma} = 0.0427) which were used in all calculations. The final R_1 was 0.1288 ($I > 2\sigma(I)$) and wR_2 was 0.2616 (all data).

5. Conclusions

We presented the facile reaction of two-coordinate 3d-metal(I) silylamides (Cr−Co) with 2,2′-bipyridine. Obtained complexes of the form K{18-crown-6}[M$(hmds)_2$(bipy)] were structurally and spectroscopically characterized. Thereby, the isolation of the manganese complex [Mn$(hmds)_2$(bipy)]$^-$ shows that the so-far elusive monomeric manganese(I) hexamethyldisilazide [Mn$(hmds)_2$]$^-$ can be trapped in synthetically acceptable yields. The anionic complexes were examined with respect to their structural features in solid state as well as their ^{1}H-NMR and UV/Vis spectroscopic and electrochemical signatures in conjunction with their magnetic properties. Comparisons with their neutral, not-reduced counterparts are drawn. Overall, the obtained anionic complexes are described best as [$M^{II}(hmds)_2$(bipy$^{\cdot-}$)]$^-$; 2,2′-bipyridine is thus reduced to a certain extent upon coordination, even if the reduction potentials of the employed metal(I) complexes can be lower by up to 1 V than the one of free 2,2′-bipyridine (as in case of cobalt). This indicates that, although the used metal(I) complexes are reluctant to coordinate donor ligands, electron transfer to a substrate and its persistent coordination in a reduced state is possible. Ongoing studies now focus on the use of these metal(I) complexes as a valuable tool to obtain and stabilize more unusual organic radical anions.

Supplementary Materials: The following are available online at http://www.mdpi.com/2304-6740/7/10/117/s1: The CIF and the checkCIF output files. ^{1}H-NMR spectra, UV/Vis spectra and cyclovoltammograms of all compounds. Magnetic susceptibility data of compounds **1**–**4** and **10**.

Author Contributions: Conceptualization, C.G.W.; Data curation, I.M., C.S., C.P., C.G.W.; Formal analysis, I.M., C.P., C.G.W.; Funding acquisition, C.G.W.; Investigation, I.M., C.S., C.G.W.; Project administration, C.G.W.; Resources, F.K., C.G.W.; Validation, C.G.W.; Visualization, I.M., C.S., C.G.W.; Writing—original draft, I.M., C.G.W.; Writing—review & editing, I.M., C.S., C.P., F.K., C.G.W.

Funding: This research was funded by the Deutsche Forschungsgemeinschaft (DFG), grant number WE 5627/4-1.

Acknowledgments: The authors thank the Department of Chemistry of the Philipps University for support.

Conflicts of Interest: The authors declare no conflict of interest.

References

1. Power, P.P. Stable two-coordinate, open-shell (d^1-d^9) transition metal complexes. *Chem. Rev.* **2012**, *112*, 3482–3507. [PubMed]
2. Ung, G.; Rittle, J.; Soleilhavoup, M.; Bertrand, G.; Peters, J.C. Two-Coordinate Fe^0 and Co^0 Complexes Supported by Cyclic (alkyl) (amino) carbenes. *Angew. Chem. Int. Ed.* **2014**, *53*, 8427–8431.
3. Roy, S.; Mondal, K.C.; Roesky, H.W. Cyclic Alkyl (amino) Carbene Stabilized Complexes with Low Coordinate Metals of Enduring Nature. *Acc. Chem. Res.* **2016**, *49*, 357–369. [PubMed]
4. Mo, Z.; Ouyang, Z.; Wang, L.; Fillman, K.L.; Neidig, M.L.; Deng, L. Two- and three-coordinate formal iron(I) compounds featuring monodentate aminocarbene ligands. *Org. Chem. Front.* **2014**, *1*, 1040–1044.
5. Samuel, P.P.; Mondal, K.C.; Amin Sk, N.; Roesky, H.W.; Carl, E.; Neufeld, R.; Stalke, D.; Demeshko, S.; Meyer, F.; Ungur, L.; et al. Electronic Structure and Slow Magnetic Relaxation of Low-Coordinate Cyclic Alkyl(amino) Carbene Stabilized Iron(I) Complexes. *J. Am. Chem. Soc.* **2014**, *136*, 11964–11971. [PubMed]
6. Werncke, C.G.; Bunting, P.C.; Duhayon, C.; Long, J.R.; Bontemps, S.; Sabo-Etienne, S. Two-coordinate iron(I) complex $[Fe\{N(SiMe_3)_2\}_2]^-$: Synthesis, properties, and redox activity. *Angew. Chem. Int. Ed.* **2015**, *54*, 245–248.
7. Lin, C.-Y.; Fettinger, J.C.; Grandjean, F.; Long, G.J.; Power, P.P. Synthesis, Structure, and Magnetic and Electrochemical Properties of Quasi-Linear and Linear Iron(I), Cobalt(I), and Nickel(I) Amido Complexes. *Inorg. Chem.* **2014**, *53*, 9400–9406. [PubMed]
8. Zadrozny, J.M.; Xiao, D.J.; Atanasov, M.; Long, G.J.; Grandjean, F.; Neese, F.; Long, J.R. Magnetic blocking in a linear iron(I) complex. *Nat. Chem.* **2013**, *5*, 577–581.
9. Lipschutz, M.I.; Yang, X.; Chatterjee, R.; Tilley, T.D. A Structurally Rigid Bis (amido) Ligand Framework in Low-Coordinate Ni(I), Ni(II), and Ni(III) Analogues Provides Access to a Ni(III) Methyl Complex via Oxidative Addition. *J. Am. Chem. Soc.* **2013**, *135*, 15298–15301.
10. Cai, I.C.; Lipschutz, M.I.; Tilley, T.D. A bis (amido) ligand set that supports two-coordinate chromium in the +1, +2, and +3 oxidation states. *Chem. Commun.* **2014**, *50*, 13062–13065.
11. Samuel, P.P.; Neufeld, R.; Chandra Mondal, K.; Roesky, H.W.; Herbst-Irmer, R.; Stalke, D.; Demeshko, S.; Meyer, F.; Rojisha, V.C.; De, S.; et al. Cr(I)Cl as well as Cr^+ are stabilised between two cyclic alkyl amino carbenes. *Chem. Sci.* **2015**, *6*, 3148–3153. [PubMed]
12. Samuel, P.P.; Mondal, K.C.; Roesky, H.W.; Hermann, M.; Frenking, G.; Demeshko, S.; Meyer, F.; Stückl, A.C.; Christian, J.H.; Dalal, N.S.; et al. Synthesis and Characterization of a Two-Coordinate Manganese Complex and its Reaction with Molecular Hydrogen at Room Temperature. *Angew. Chem. Int. Ed.* **2013**, *52*, 11817–11821.
13. Werncke, C.G.; Suturina, E.; Bunting, P.C.; Vendier, L.; Long, J.R.; Atanasov, M.; Neese, F.; Sabo-Etienne, S.; Bontemps, S. Homoleptic Two-Coordinate Silylamido Complexes of Chromium(I), Manganese(I), and Cobalt(I). *Chem. Eur. J.* **2016**, *22*, 1668–1674. [CrossRef] [PubMed]
14. Werncke, C.G.; Pfeiffer, J.; Müller, I.; Vendier, L.; Sabo-Etienne, S.; Bontemps, S. C–Halide bond cleavage by a two-coordinate iron(I) complex. *Dalton Trans.* **2019**, *48*, 1757–1765. [CrossRef] [PubMed]
15. Lipschutz, M.I.; Tilley, T.D. Carbon–Carbon Cross-Coupling Reactions Catalyzed by a Two-Coordinate Nickel(II)-Bis (amido) Complex via Observable Ni^I, Ni^{II}, and Ni^{III} Intermediates. *Angew. Chem. Int. Ed.* **2014**, *53*, 7290–7294.
16. Lipschutz, M.I.; Chantarojsiri, T.; Dong, Y.; Tilley, T.D. Synthesis, characterization, and alkyne trimerization catalysis of a heteroleptic two-coordinate Fe(I) complex. *J. Am. Chem. Soc.* **2015**, *137*, 6366–6372. [CrossRef] [PubMed]
17. Ouyang, Z.; Du, J.; Wang, L.; Kneebone, J.L.; Neidig, M.L.; Deng, L. Linear and T-Shaped Iron(I) Complexes Supported by N-Heterocyclic Carbene Ligands: Synthesis and Structure Characterization. *Inorg. Chem.* **2015**, *54*, 8808–8816. [CrossRef]
18. Hicks, J.; Jones, C. Low-Coordinate Cobalt(I) Complexes Stabilized by an Extremely Bulky Amide Ligand. *Organometallics* **2015**, *34*, 2118–2121. [CrossRef]
19. Pfirrmann, S.; Limberg, C.; Herwig, C.; Stösser, R.; Ziemer, B. A dinuclear nickel(I) dinitrogen complex and its reduction in single-electron steps. *Angew. Chem. Int. Ed.* **2009**, *48*, 3357–3361. [CrossRef]
20. MacLeod, K.C.; Lewis, R.A.; DeRosha, D.E.; Mercado, B.Q.; Holland, P.L. C-H and C-N Activation at Redox-Active Pyridine Complexes of Iron. *Angew. Chem. Int. Ed.* **2017**, *56*, 1069–1072. [CrossRef]

21. Dugan, T.R.; Sun, X.; Rybak-Akimova, E.V.; Olatunji-Ojo, O.; Cundari, T.R.; Holland, P.L. A Masked Two-Coordinate Cobalt(I) Complex That Activates C–F Bonds. *J. Am. Chem. Soc.* **2011**, *133*, 12418–12421. [CrossRef] [PubMed]
22. Constable, E.C. Homoleptic Complexes of 2,2′-Bipyridine. In *Advances in Inorganic Chemistry*, 1st ed.; Sykes, A.G., Ed.; Academic Press: Cambridge, MA, USA, 1989; Volume 34, pp. 1–63.
23. Gore-Randall, E.; Irwin, M.; Denning, M.S.; Goicoechea, J.M. Synthesis and characterization of alkali-metal salts of 2,2′- and 2,4′-bipyridyl radicals and dianions. *Inorg. Chem.* **2009**, *48*, 8304–8316. [CrossRef] [PubMed]
24. Denning, M.S.; Irwin, M.; Goicoechea, J.M. Synthesis and characterization of the 4,4′-bipyridyl dianion and radical monoanion. A structural study. *Inorg. Chem.* **2008**, *47*, 6118–6120. [CrossRef] [PubMed]
25. Bock, H.; Lehn, J.-M.; Pauls, J.; Holl, S.; Krenzel, V. Sodium Salts of the Bipyridine Dianion: Polymer $[(bpy)^{2-}\{Na^{+}(dme)\}_2]_\infty$, Cluster $[(Na_8O)^{6+}Na^{+}{}_6(bpy)_6{}^{2-}(tmeda)_6]$, and Monomer $[(bpy)^{2-}\{Na^{+}(pmdta)\}_2]$. *Angew. Chem. Int. Ed.* **1999**, *38*, 952–955. [CrossRef]
26. Roitershtein, D.; Domingos, A.; Pereira, L.C.J.; Ascenso, J.R.; Marques, N. Coordination of 2,2′-bipyridyl and 1,10-phenanthroline to yttrium and lanthanum complexes based on a scorpionate ligand. *Inorg. Chem.* **2003**, *42*, 7666–7673. [CrossRef] [PubMed]
27. Bellavance, P.L.; Corey, E.R.; Corey, J.Y.; Hey, G.W. Synthesis and characterization of complexes of aluminum halide with 2,2′-bipyridine, 1,10-phenanthroline and 2,2′,2′′-terpyridine in acetonitrile. *Inorg. Chem.* **1977**, *16*, 462–467. [CrossRef]
28. Nikiforov, G.B.; Roesky, H.W.; Noltemeyer, M.; Schmidt, H.-G. Reactivity of $Ti(bipy)_3$ and preparation of the $Li(THF)_4[Al(bipy)_2]$ complex with the dinegative bipy ligand. *Polyhedron* **2004**, *23*, 561–566. [CrossRef]
29. Jacquot, L.; Xémard, M.; Clavaguéra, C.; Nocton, G. Multiple One-Electron Transfers in Bipyridine Complexes of Bis (phospholyl) Thulium. *Organometallics* **2014**, *33*, 4100–4106. [CrossRef]
30. Ortu, F.; Liu, J.; Burton, M.; Fowler, J.M.; Formanuik, A.; Boulon, M.-E.; Chilton, N.F.; Mills, D.P. Analysis of Lanthanide-Radical Magnetic Interactions in Ce(III) 2,2′-Bipyridyl Complexes. *Inorg. Chem.* **2017**, *56*, 2496–2505. [CrossRef]
31. Ortu, F.; Zhu, H.; Boulon, M.-E.; Mills, D. Synthesis and Reactivity of a Cerium(III) Scorpionate Complex Containing a Redox Non-Innocent 2,2′-Bipyridine Ligand. *Inorganics* **2015**, *3*, 534–553. [CrossRef]
32. Scarborough, C.C.; Wieghardt, K. Electronic structure of 2,2′-bipyridine organotransition-metal complexes. Establishing the ligand oxidation level by density functional theoretical calculations. *Inorg. Chem.* **2011**, *50*, 9773–9793. [CrossRef] [PubMed]
33. Wolff, C.; Gottschlich, A.; England, J.; Wieghardt, K.; Saak, W.; Haase, D.; Beckhaus, R. Molecular and Electronic Structures of Mononuclear and Dinuclear Titanium Complexes Containing π-Radical Anions of 2,2′-Bipyridine and 1,10-Phenanthroline: An Experimental and DFT Computational Study. *Inorg. Chem.* **2015**, *54*, 4811–4820. [CrossRef] [PubMed]
34. Irwin, M.; Jenkins, R.K.; Denning, M.S.; Kramer, T.; Grandjean, F.; Long, G.J.; Herchel, R.; McGrady, J.E.; Goicoechea, J.M. Experimental and computational study of the structural and electronic properties of Fe^{II}(2,2′-bipyridine)$(mes)_2$ and $[Fe^{II}$(2,2′-bipyridine)$(mes)_2]^{-}$, a complex containing a 2,2′-bipyridyl radical anion. *Inorg. Chem.* **2010**, *49*, 6160–6171. [CrossRef] [PubMed]
35. Irwin, M.; Doyle, L.R.; Krämer, T.; Herchel, R.; McGrady, J.E.; Goicoechea, J.M. A homologous series of first-row transition-metal complexes of 2,2′-bipyridine and their ligand radical derivatives: Trends in structure, magnetism, and bonding. *Inorg. Chem.* **2012**, *51*, 12301–12312. [CrossRef] [PubMed]
36. Tokel-Takvoryan, N.E.; Hemingway, R.E.; Bard, A.J. Electrogenerated chemiluminescence. XIII. Electrochemical and electrogenerated chemiluminescence studies of ruthenium chelates. *J. Am. Chem. Soc.* **1973**, *95*, 6582–6589. [CrossRef]
37. Bradley, D.C.; Hursthouse, M.B.; Newing, C.W.; Welch, A.J. Square planar and tetrahedral chromium (II) complexes; crystal structure determinations. *Chem. Commun.* **1972**, 567. [CrossRef]
38. Cotton, F.A.; Rice, C.E.; Rice, G.W. The crystal and molecular structures of bis (2,4-pentanedionato) chromium. *Inorg. Chim. Acta* **1977**, *24*, 231–234. [CrossRef]
39. Babar, M.A.; Ladd, M.F.C.; Larkworthy, L.F.; Povey, D.C.; Proctor, K.J.; Summers, L.J. The crystal structures of propane-1,3-diammonium tetrachlorochromate(II), a sheet ferromagnet, and bis (dimethylammonium) tetrachlorochromate(II) an antiferromagnetic compound containing isolated $[Cr_3Cl_{12}]^{6-}$ units. *Chem. Commun.* **1981**, 1046. [CrossRef]

40. Scarborough, C.C.; Sproules, S.; Weyhermüller, T.; DeBeer, S.; Wieghardt, K. Electronic and molecular structures of the members of the electron transfer series $[Cr(^{t}bpy)_3]^n$ (n = 3+, 2+, 1+, 0): An X-ray absorption spectroscopic and density functional theoretical study. *Inorg. Chem.* **2011**, *50*, 12446–12462. [CrossRef]
41. Schultz, M.; Boncella, J.M.; Berg, D.J.; Tilley, T.D.; Andersen, R.A. Coordination of 2,2′-Bipyridyl and 1,10-Phenanthroline to Substituted Ytterbocenes: An Experimental Investigation of Spin Coupling in Lanthanide Complexes. *Organometallics* **2002**, *21*, 460–472. [CrossRef]
42. Zhou, W.; Desnoyer, A.N.; Bailey, J.A.; Patrick, B.O.; Smith, K.M. Direct synthesis of ligand-based radicals by the addition of bipyridine to chromium(II) compounds. *Inorg. Chem.* **2013**, *52*, 2271–2273. [CrossRef] [PubMed]
43. Margraf, G.; Schödel, F.; Sänger, I.; Bolte, M.; Wagner, M.; Lerner, H.-W. Eine elektrochemische und strukturelle Studie an den Eisensilylamiden $Fe[N(SiMe_3)_2]_2$ und $Fe[N(SiMe_3)_2]_3$ / An Electrochemical and Structural Study of the Iron Silylamides $Fe[N(SiMe_3)_2]_2$ and $Fe[N(SiMe_3)_2]_3$. *Z. Naturforsch. B Chem. Sci.* **2012**, *67*, 549–556. [CrossRef]
44. König, E.; Kremer, S. The lower excited electronic states of singly and doubly reduced 2,2′-bipyridine. *Chem. Phys. Lett.* **1970**, *5*, 87–90. [CrossRef]
45. Da Re, R.E.; Kuehl, C.J.; Brown, M.G.; Rocha, R.C.; Bauer, E.D.; John, K.D.; Morris, D.E.; Shreve, A.P.; Sarrao, J.L. Electrochemical and spectroscopic characterization of the novel charge-transfer ground state in diimine complexes of ytterbocene. *Inorg. Chem.* **2003**, *42*, 5551–5559. [CrossRef]
46. Schubert, E.M. Utilizing the Evans method with a superconducting NMR spectrometer in the undergraduate laboratory. *J. Chem. Educ.* **1992**, *69*, 62. [CrossRef]
47. Evans, D.F. 400. The determination of the paramagnetic susceptibility of substances in solution by nuclear magnetic resonance. *J. Chem. Soc.* **1959**, 2003. [CrossRef]
48. Awaga, K.; Maruyama, Y. Ferromagnetic and antiferromagnetic intermolecular interactions of organic radicals, α-nitronyl nitroxides. II. *Phys. Chem. Chem. Phys.* **1989**, *91*, 2743–2747. [CrossRef]
49. Fujita, W.; Awaga, K. Room-Temperature Magnetic Bistability in Organic Radical Crystals. *Science* **1999**, *286*, 261–263. [CrossRef]
50. Eusterwiemann, S.; Doerenkamp, C.; Dresselhaus, T.; Janka, O.; de Oliveira, M.; Daniliuc, C.G.; Eckert, H.; Neugebauer, J.; Pöttgen, R.; Studer, A. Strong intermolecular antiferromagnetic verdazyl-verdazyl coupling in the solid state. *Phys. Chem. Chem. Phys. PCCP* **2017**, *19*, 15681–15685. [CrossRef]
51. Roffia, S.; Marcaccio, M.; Paradisi, C.; Paolucci, F.; Balzani, V.; Denti, G.; Serroni, S.; Campagna, S. Electrochemical reduction of (2,2′-bipyridine)- and bis ((2-pyridyl) pyrazine) ruthenium(II) complexes used as building blocks for supramolecular species. Redox series made of 8, 10, and 12 redox steps. *Inorg. Chem.* **1993**, *32*, 3003–3009. [CrossRef]
52. Margel, S. Electrochemistry of 2,2′-Bipyridine Complexes of Cobalt in the Presence of Acrylonitrile. *J. Electrochem. Soc.* **1978**, *125*, 241. [CrossRef]
53. Braterman, P.S.; Song, J.I.; Peacock, R.D. Electronic absorption spectra of the iron(II) complexes of 2,2′-bipyridine, 2,2′-bipyrimidine, 1,10-phenanthroline, and 2,2′:6′,2′′-terpyridine and their reduction products. *Inorg. Chem.* **1992**, *31*, 555–559. [CrossRef]
54. De Bruin, B.; Bill, E.; Bothe, E.; Weyhermüller, T.; Wieghardt, K. Molecular and Electronic Structures of Bis (pyridine-2,6-diimine) metal Complexes $[ML_2](PF_6)_n$ (n = 0, 1, 2, 3; M = Mn, Fe, Co, Ni, Cu, Zn). *Inorg. Chem.* **2000**, *39*, 2936–2947. [CrossRef] [PubMed]
55. Bourrez, M.; Molton, F.; Chardon-Noblat, S.; Deronzier, A. [Mn(bipyridyl)$(CO)_3$Br]: An Abundant Metal Carbonyl Complex as Efficient Electrocatalyst for CO_2 Reduction. *Angew. Chem. Int. Ed.* **2011**, 9903–9906. [CrossRef] [PubMed]
56. Sullivan, B.P.; Bolinger, C.M.; Conrad, D.; Vining, W.J.; Meyer, T.J. One- and two-electron pathways in the electrocatalytic reduction of CO_2 by fac-Re(bpy)$(CO)_3$Cl (bpy = 2,2′-bipyridine). *Chem. Commun.* **1985**, 1414–1416. [CrossRef]
57. La Mar, G.N.; Horrocks, W.D.; Holm, R.H. *NMR of Paramagnetic Molecules: Principles and Applications*; Elsevier Science: Burlington, NJ, USA, 1973.
58. Bertini, I.; Luchinat, C.; Parigi, G.; Pierattelli, R. NMR spectroscopy of paramagnetic metalloproteins. *Chembiochem* **2005**, *6*, 1536–1549. [CrossRef] [PubMed]
59. Bürger, H.; Wannagat, U. Silylamido-Derivate von Eisen und Kobalt. *Monatsh. Chem.* **1963**, *94*, 1007–1012. [CrossRef]

60. Bürger, H.; Wannagat, U. Silylamido-Verbindungen von Chrom, Mangan, Nickel und Kupfer. *Monatsh. Chem.* **1964**, *95*, 1099–1102. [CrossRef]
61. Conley, M.P.; Delley, M.F.; Siddiqi, G.; Lapadula, G.; Norsic, S.; Monteil, V.; Safonova, O.V.; Copéret, C. Polymerization of Ethylene by Silica-Supported Dinuclear Cr^{III} Sites through an Initiation Step Involving C–H Bond Activation. *Angew. Chem. Int. Ed.* **2014**, *53*, 1872–1876. [CrossRef]
62. Dalvit, C.; Invernizzi, C.; Vulpetti, A. Fluorine as a hydrogen-bond acceptor: Experimental evidence and computational calculations. *Chem. Eur. J.* **2014**, *20*, 11058–11068. [CrossRef]
63. Dolomanov, O.V.; Bourhis, L.J.; Gildea, R.J.; Howard, J.A.K.; Puschmann, H. OLEX2: A complete structure solution, refinement and analysis program. *J. Appl. Crystallogr.* **2009**, *42*, 339–341. [CrossRef]
64. Sheldrick, G.M. Crystal structure refinement with *SHELXL*. *Acta Cryst. C* **2015**, *71*, 3–8. [CrossRef] [PubMed]
65. Farrugia, L.J. WinGX suite for small-molecule single-crystal crystallography. *J. Appl. Crystallogr.* **1999**, *32*, 837–838. [CrossRef]
66. Betteridge, P.W.; Carruthers, J.R.; Cooper, R.I.; Prout, K.; Watkin, D.J. CRYSTALS version 12: Software for guided crystal structure analysis. *J. Appl. Crystallogr.* **2003**, *36*, 1487. [CrossRef]
67. International Union of Crystallography. *International Tables for Crystallography*, 1st ed.; Springer: Chester, UK; New York, NY, USA, 2006.
68. Bruker AXS Inc. *SADABS*; 2016/2; Bruker AXS Inc.: Madison, WI, USA, 2016.
69. STOE&Cie GmbH. *X-Area*; X.-R. 1.6.1.0; STOE&Cie GmbH: Darmstadt, Germany, 2016.

3.2 „Reductive coupling of (Fluoro)-Pyridines by Quasi-Linear 3d-Metal(I) Silylamides of Cr – Co: A Tale of C–C bond formation, C–F bond cleavage and pyridyl radical anions"

Igor Müller und C. Gunnar Werncke, *Chem. Eu. J.* **2020**, eingereichtes Manuskript.

Abstract: In this manuscript the facile reductive coupling of pyridine (and derivatives) by two-coordinate metal(I) silylamides of chromium to iron but not cobalt is disclosed. This leads to highly labile binuclear metal(II) complexes bearing a 4,4'-dihydropyridyl ligand via dimerisation of an elusive monomeric metal(II) pyridyl radical anion complex. Its presence was proven via its H atom abstraction capability as well as reaction with the trityl radical (Gomberg dimer). In due process, the blue radical anion of 2-phenylpyridine could also be structurally identified. Employing perfluoropyridine C–F bond cleavage takes place under formation of rare trigonal metal(II) fluoride complexes of manganese, iron and cobalt as well as the homocoupling or reductive degradation of the substrate. For lesser fluorinated pyridines C–F bond cleavage but no homocoupling is observed.

Zusammenfassung: In diesem Manuskript wird die reduktive Kopplung von Pyridin (und Derivaten) durch zweifach-koordinierte Metall(I)-Silylamide von Cr–Fe, mit Ausnahme von Kobalt, offengelegt. Dies führt, durch Dimerisierung eines schwer fassbaren monomeren Metall(II)-Pyridylradikalanionkomplexes, zu hochlabilen binuklearen Metall(II)-Komplexen, die einen 4,4'-Dihydropyridylliganden tragen. Seine Anwesenheit wurde durch seine Fähigkeit zur Abstraktion von H-Atomen sowie durch die Reaktion mit dem Tritylradikal (GOMBERG-Dimer) nachgewiesen. Zudem konnte erstmals das Radikalanion eines einfachen Pyridins auch strukturell identifiziert werden. Die Spaltung der C–F-Bindung von Perfluorpyridin erfolgt unter Bildung seltener trigonaler Metall(II)-Fluorid-Komplexe von Mangan, Eisen und Kobalt sowie unter Homo-Kopplung oder reduktivem Abbau des Substrats. Bei weniger fluorierten Pyridinen wird eine C–F-Bindungsspaltung, aber keine Homo-Kupplung beobachtet.

Eigener Anteil: Alle Synthesen der Verbindungen **1** – **4d** wurden von mir geplant und durchgeführt, sowie deren analytischen Daten aufgenommen und ausgewertet. ^{1}H-NMR-Experimente wurden sowohl von mir als auch unter Anleitung von Dr. Xiulan Xie in der zentralen NMR-Abteilung des Fachbereichs Chemie an der Philipps-Universität Marburg durchgeführt.

Ebenfalls habe ich die UV/VIS- und IR-Messungen selbst durchgeführt. Die Einkristallstruktur-analyse für die Verbindungen **2c**, **2b** und **4b** wurde durch die zentrale Abteilung für Kristall-strukturanalyse am Fachbereich Chemie an der Philipps-Universität Marburg unter der Leitung von Dr. Klaus Harms und Dr. Sergei Ivlev durchgeführt. Die Datensätze wurden jedoch von mir gelöst und verfeinert. Bei den Verbindungen **1**, **2c**, **3a**, **3c**, **4a**, **4c** und **4d** war ich selbst sowohl für die Messung als auch das Lösen und Verfeinern verantwortlich. Das Manuskript wurde von mir und Dr. C. Gunnar Werncke verfasst.

FULL PAPER

Reductive Coupling of (Fluoro)-Pyridines by Quasi-Linear 3d-Metal(I) Silylamides of Cr – Co: A Tale of C–C Bond Formation, C–F Bond Cleavage and Pyridyl Radical Anions

I. Müller,[a] C. G. Werncke*[a]

[a] Igor Müller, Dr. Christian Gunnar Werncke
Fachbereich Chemie/Department of Chemistry
Philipps-Universität Marburg
Hans-Meerwein-Straße 4, D-35037 Marburg, Germany
E-mail: gunnar.werncke@chemie.uni-marburg.de

Supporting information for this article is given via a link at the end of the document.

Abstract: In this manuscript the facile reduction of pyridine (and derivatives) by two-coordinate metal(I) silylamides of chromium to iron is disclosed. This results in intermolecular C−C coupling dinuclear giving dinuclear metal(II) complexes bearing a bridging 4,4'-dihydropyridyl ligand. For iron we demonstrate that the C−C coupling is reversible in solution, either directly or by reaction with substrates. In due process the isomerisation of 1,4-cyclohexadiene is observed, leading to benzene, cyclohexadiene and 1,3-cyclohexadiene.Further, the deliberate formation and structural characterisation of a pyridyl radical anion is presented, which is not 3d-metal bound. Employing perfluoropyridine C−F bond cleavage takes place under formation of metal(II) fluoride complexes of manganese, iron and cobalt as well as the homocoupling or reductive degradation of the substrate. In case of cobalt, lesser fluorinated pyridines are briefly examined as substrates giving C−F bond cleavage but no homocoupling. Overall, we give insights how multifaceted simple (fluoro)pyridines can behave in the presence of moderately to highly reducing metal complexes.

Introduction

Polypyridines such as bipyridine or phenanthroline are a versatile class of donor ligands.[1,2] It has been shown, that they can be reduced in the coordination sphere of the metal, often in a reversible fashion.[3] This halts also true for monopyridine based ligands, in which the pyridine is part of a larger conjugated system (e.g. mono- or diiminopyridines).[4,5–7] The redox-non-innocent behaviour of such ligands has been exploited in numerous cases in (photo)-redox-chemistry as well as bond and small molecule activation.[2,5–7,8] As a further consequence of the reduction of the polypyridine – especially in case of highly reducing actinide or divalent rare earth metal complexes – the formed metal-bound radical anion can react under intra- or intermolecular C−C coupling.[9] In few instances the C−C bond formation can be also reversible so that as a consequence the electron is formally not stored in the polypyridine as a radical anion but within the formed bond,[10] a phenomenon that has also been observed for other related nitrogen based ligands.[11]

The corresponding reduction of the parent pyridine is considerably less common due to its higher cathodic potential of −2.7 V (vs. SCE[12]). Few examples of metal mediated 1e⁻ reduction and coupling of pyridine are known and rely on the highly reducing capabilities of low-valent rare-earth metal complexes of scandium, thulium and samarium as well as of thorium.[13] Examples of reductive coupling of pyridine by d-block transition metal complexes are restricted to a titanium(II) synthon,[14] and an iron(I) nacnac system (nacnac = N,N'-2,6-diisopropylphenyl-ß-diketiminate) of Holland and co-workers (**Figure 1**).[15,16] They could also observe the reversibility of C−C bond formation in solution with the monomeric iron pyridine species bearing partial radical anionic character of the pyridine ligand.

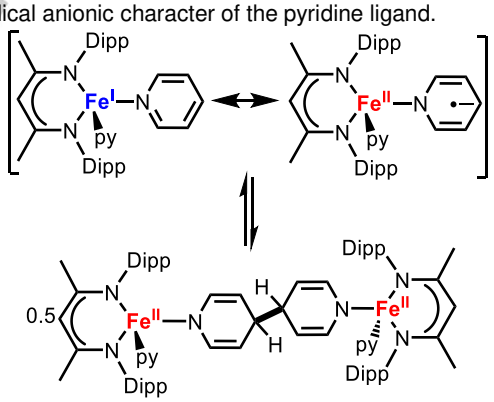

Figure 1. Reversible C–C bond formation by an iron pyridine complex (py = pyridine).[16]

Recently, we reported on quasi-linear 3d-metal(I) hexamethyldisilazanide complexes $[K\{18c6\}][M^{I}(NR_2)_2]$ (M = Cr − Co; 18c6 = 18-crown-6; R = $SiMe_3$).[17,18] Despite of an easily accessible metal ion, these silylamides complexes are surprisingly inert towards Lewis bases such as phosphines and NHCs.[19] This contrasts the usual Lewis acidic behaviour of other low-coordinate metal(I) compounds,[20,21] and became obvious in case of the reaction of $[K\{18c6\}][Fe^{I}(NR_2)_2]$

with an ethylene bridged diphosphine whereas coordination to the ethylene backbone and not the phosphines was preferred.[19] Given this background we started to elaborate the behaviour metal(I) silylamides towards substrates which, to a certain extent, can be reduced.[22,23]

Here we report on the reaction of 3d metal(I) complexes (M = Cr − Co) with pyridine and selected derivatives. This led in case of chromium, manganese and iron to the reductive C−C coupling of the substrate and formation of binuclear metal(II) complexes, which were isolated and characterized. For iron it could be demonstrated that the C−C coupling is reversible. Further, a pyridyl radical anion could be further identified via X-Ray diffraction analysis as well as UV/Vis spectroscopy, that is free of 3d-metal coordination. Employing perfluoropyridine as substrate the instantaneous C−F bond cleavage takes place und formation of rare trigonal metal(II) fluoride complexes of manganese, iron and cobalt as well as the homocoupling or reductive degradation of the substrate. For lesser fluorinated pyridines C−F bond cleavage but no homocoupling is observed, as demonstrated in case of cobalt.

Results and Discussion

The respective metal(I) silylamide complex (Cr−Co), either isolated (Fe and Co) or synthesized *in-situ* (Cr and Mn),[17,18] was treated with one equivalent of pyridine (py) in Et_2O. This resulted in an immediate colour change for iron (greenish brown -> light yellow), manganese (dark violet -> light yellow) and chromium (red orange to bright orange), whereas for cobalt no conversion was observed. The reaction mixtures were filtered, layered with pentane and stored at −35 °C. After a few days crystalline samples of the complexes **1** (Crpy) and **3a** (Fepy), (Scheme **1**)) were obtained in moderate yields. Compound **2a** (Mnpy) could not be isolated in an analytically pure fashion due to the parallel formation of the manganese(II) trisamide $[Mn^{II}(NR_2)_3]^-$, the decomposition product of the labile $[Mn^{I}(NR_2)_2]^-$ starting compound.[17] Solid state analysis of compounds **1**, **2a** and **3a** (**Figure 2**) revealed the formation of dinuclear dianions. The two metal ions are bridged by a 4,4'-dihydrobipyridyl, stemming from the formal dimerization of an elusive metal pyridine adduct at the 4-position of the pyridine. The bond metrics of the bipyridyl ligand revealed a loss of aromaticity with now localized single and double bonds (

Table 1). For **2a** and **3a** the coordination sphere of each metal(II) ion is completed by the two silylamide ligands giving it a trigonal coordination geometry. In case of the chromium compound **1** an additional, unreduced pyridine ligand coordinates to the metal ion, leading to a square planar coordination environment (τ'_4-parameter of 0.26). This supports the notion of divalent compounds, as chromium(II) compounds prefer such a complex geometry.[24] This behaviour might also reason why chromium is facilitating the pyridine reduction whereas cobalt is not, despite having a similar reduction potential (E_{ox} = −1.47 V (Co) vs. −1.30 V (Cr), vs Fc/Fc^+).[17]

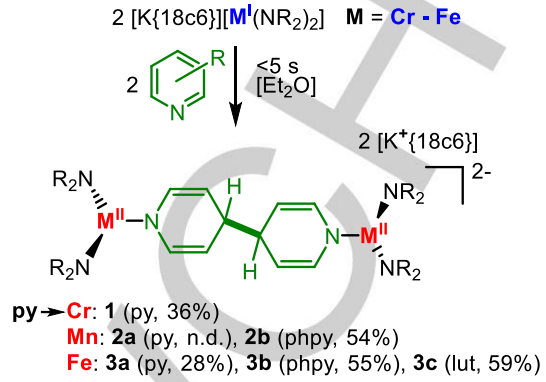

Scheme 1. Reaction of metal(I) silylamides with pyridines (R = $SiMe_3$, py = pyridine, phpy = 2-phenylpyridine, lut = 2,6-dimethylpyridine, 18c6 = 18-crown-6, n.d. = not determined).

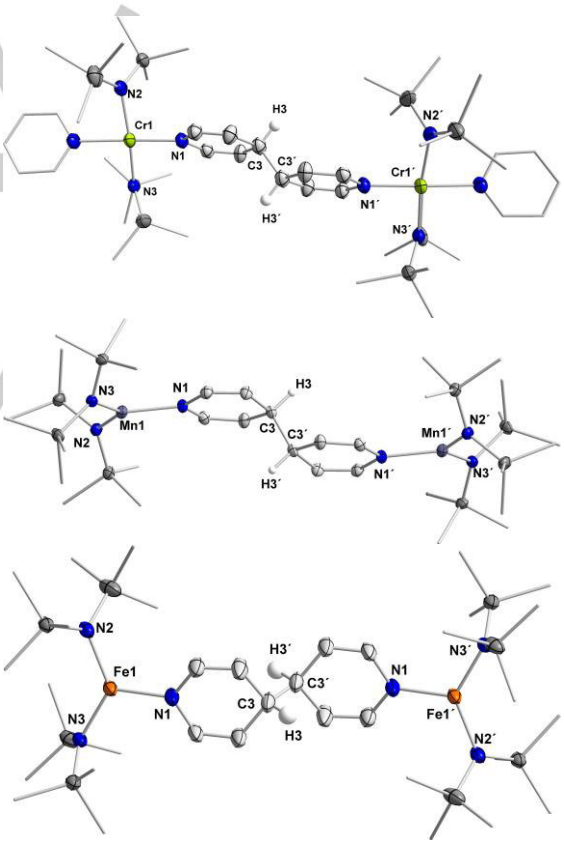

Figure 2. Molecular structure of compounds **1** (top), **2a** (middle) and **3a** (bottom). H atoms are omitted for clarity and ellipsoids are shown at 50% probability. The K{18c6} cations are not shown.

Table 1. Important structural metrics of the complex anions of the compounds **1-3c**.

Compound	**1** (Crpy)	**2a** (Mnpy)	**2b** (Mnphpy)	**3a** (Fepy)	**3b** (Fephpy)	**3c** (Felut)
Bond Length / Å						
M−N1 (py)	2.057(3)	2.053(1)	2.053(7)	1.990(3)	2.008(3)	1.966(4)
M−N2 (hmds)	2.090(3)	2.045(1)	2.073(7)	1.959(3)	1.969(3)	1.972(4)
M−N3 (hmds)	2.095(2)	2.047(1)	2.041(6)	1.960(3)	1.959(3)	1.971(4)
N1−C1	1.372(3)	1.385(2)	1.399(1)	1.404(5)	1.393(5)	1.407(5)
N1−C5	1.376(3)	1.394(2)	1.397(1)	1.371(5)	1.394(5)	1.406(6)
C1−C2	1.348(3)	1.345(2)	1.331(1)	1.337(6)	1.331(6)	1.337(6)
C3−C3´	1.558(5)	1.568(3)	1.550(2)	1.548(1)	1.569(8)	1.588(6)
C4-C5	1.339(3)	1.339(2)	1.346(1)	1.345(6)	1.360(6)	1.338(6)
Bond Angles / °						
N1−M−N2	175.23(8)	114.70(5)	110.60(3)	116.90(1)	110.86(1)	116.8(2)
N2−M−N3	171.58(7)	125.31(5)	124.90(3)	127.41(1)	121.08(1)	128.1(2)

The $M-N_{hmds}$ bond lengths become shorter from chromium (2.09 Å) to iron (1.96 Å) reflecting a general contraction of the ion radii when going along the series. The same trend is observed for the bond lengths of $M-N_{py}$ (chromium 2.06 Å − iron 1.99 Å), which are in the general range found for metal bound amides. Next, we wanted to get insights into factors that govern the formation of elusive metal bound pyridyl radical anions (such as $[M^{II}(NR_2)_2(py^{\bullet-})]^-$ and subsequent C−C bond coupling formation. If the 4-position of pyridine is blocked by a nitrogen or carbon based substituent (^{t}Bu or NMe_2) no dimerization or even simple coordination was evidenced by ^{1}H NMR spectroscopy and recrystallization of the starting compounds. This is in contrast with observations made by Holland and co-workers (**Figure 1**) and indicated that substrate reduction is necessary prior or during coordination to the metal ion. To rule out simple steric effects, 3,5-lutidine (lut) was reacted with K{18c6}[$Fe(NR_2)_2$] but also gave a dimeric 4,4'-dihydrobipyridyl complex (**3c**) (**Figure 3**). Next we employed 2-phenylpyridine (phpy) to possibly stabilize the radical character over a larger aromatic system and thus favour a monomeric complex bearing a pyridyl radical anion. This lead again to dimeric systems for manganese (**2b**) and iron (**3b**). The bond lengths and bond angles of these complexes do not differ significantly from the before mentioned reduced pyridine complexes. Intriguingly, during the synthesis of **2b**, a pale yellow compound, a bright blue solution was obtained, which hinted to the presence of a radical anion. Upon careful crystallization small amounts of brownish violet crystals could be observed as a by-product of **2b**. X-Ray diffraction analysis revealed the formation of compound **4** (**Figure 3**) in which a 2-phenylpyridine unit is sandwiched between two K{18c6} cations, and an additional $[M^{II}(NR_2)_2)_3]^-$ counter anion. The potassium cations are pulled out of the plane defined by the crown-ethers oxygen atoms and are oriented towards the 2-phenylpyridine. The shortest K···C distance (~3.05 Å) is slightly shorter than those of reported interactions between K{18c8} cations and reduced aromatic hydrocarbons.[25] Together with the almost co-planar orientation of both aromatic rings (2.7(4)°), that contrast the slightly twisted orientation of 2-phenylpyridine units (10−20°),[26] suggested the presence of a pyridyl radical anion with delocalisation of the unpaired spin over both rings. This becomes more obvious looking at the C−C bond lengths within and between both aromatic rings of the 2-phenylpyridine unit (**Scheme 2**). The interring C−C bond amounts to 1.429(4) Å which is markedly shorter that comparable bond of 2-phenylpyridine units that range between 1.47 and 1.50 A. Further, the C−C bonds within the aromatic rings vary between 1.373(4) and 1.434(4) A which is consistent with those of the related potassium bipyridyl radical anion complexes[27,28]. Reports on structurally characterized pyridine radical anions are rare, due to their obvious tendency for dimerization as already shown above and in the seminal report of Anderson in 1870, followed by others.[29] Only in recent years the isolation of pyridine based radical anions could be achieved using boron based substituents.[30] The presence of the $[Mn(NR_2)_3]^-$ counter ion indicated that the formation of **4** was probably result of the parallel decomposition of the manganese(I) starting complex $[Mn(NR_2)_2]^-$.[17] Indeed, independent reduction of phpy with KC_8 in the presence of 18c6 and the manganese(II) trisamide K{18c6}[$Mn(NR_2)_3$] gave a dark blue solution, from which larger amounts of **4** were obtained (**Scheme 2**). These were extremely sensitive and decomposed quickly upon attempts for their isolation, and eluded so far further characterisation.

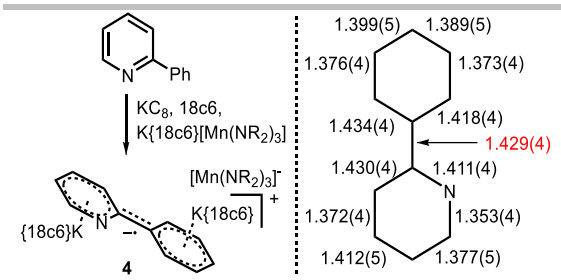

Scheme 2. Left: Reduction of 2-phenylpyridine in the presence of K{18c6}[Mn(NR$_2$)$_3$]. Right: Bond metrics of the phpy radical anion.

Interestingly, the formation of the pyridyl radical anion [2-phpy]$^-$ is not observed in the absence of the manganese trisamide and the provided additional K{18c6}$^+$ cation. It implicated that the sandwich-like structure seen in **4** helped in stabilizing the radical anion [2-phpy]$^-$. *In-situ* UV/Vis spectroscopic examination of mixtures containing **4** revealed two broad, overlapping absorption maxima at 560 and 590 . Their position are similar to those of the related 2,2'-bipyridyl radical anion (540 and 576 nm), and can be assigned to intramolecular π->π* transitions.[22,27] Having acquired the UV/Vis-spectroscopic signature of the 2-phenylpyridyl radical anion, the respective dimeric pyridine complexes were re-examined accordingly, to detect the possible presence of their monomeric form which would likely consists of a metal(II) bound radical anion. However no corresponding absorption bands were observed.

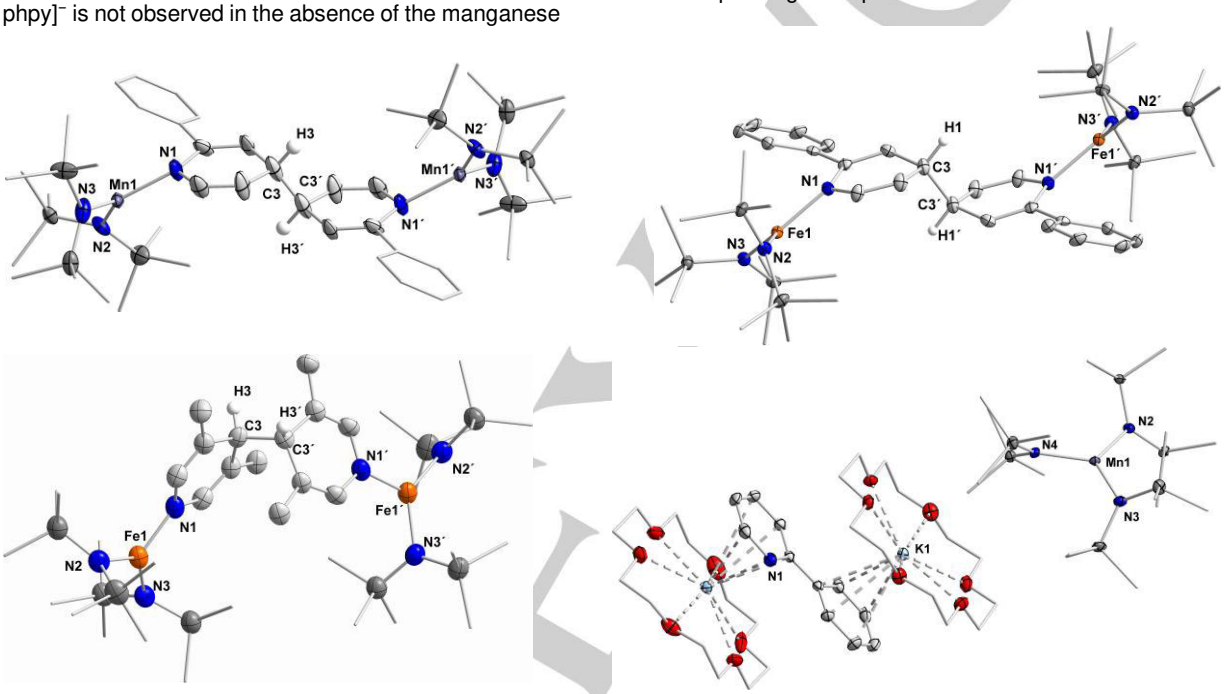

Figure 3. Molecular structure of compounds **2b** (top left), **3b** (top right) **3c** (bottom left), and **4** (bottom right). H atoms are omitted for clarity and ellipsoids are shown at 50% probability. The K{18c6}-cations are not shown for all compounds except from **4**.

To get further insights into the solution behaviour of the pyridine complexes, we looked at their ^{1}H-NMR spectroscopic features. For the chromium (**1** (Crpy) and manganese (**2a** (Mnpy) and **2b** (Mnphpy)) complexes the proton NMR spectra in THF-d showed very broad and uninformative signals due to the compounds' highly paramagnetic character. For the iron complex **3a** the proton signal attributed to the SiMe$_3$ units was found at −4.50, whose position corresponds well with other anionic trigonal iron(II) silylamide complexes bearing an anionic ligand.[31] **3a** (Fepy) is represented further by three signals at 12.5, 15.7 and 198.6 ppm for the pyridine ligand. Thereby, the signals belonging to the pyridyl unit could only be observed via *in-situ* formation of **3a** using five equivalents of pyridine, which indicated an equilibrium with the starting iron(I) complex. Such an equilibrium became obvious in case of the isolated compounds **3b** (Fephpy) and **3c** (Felut). Their ^{1}H NMR spectra showed mostly the initial iron(I) complex [Fe(NR$_2$)$_2$]$^-$ as well as minor signals tentatively attributed to the provided **3b** and **3c**, respectively. The addition of 2-phenylpyridine and 3,5-lutidine, respectively, slightly shifted the equilibrium in solution to **3b** or **3c**, but also effectuated decomposition to [Fe(NR)$_2$)$_3$]$^-$. Given these observations we wanted to elucidate chemically if the reductive C−C bond formation is also reversible in case of **3a** (**Scheme 3**). Treatment of **3a** with 2,2'-bipyridine (bipy) lead to the partial formation of the known bipyridyl complex [Fe(NR$_2$)$_2$)(bipy$^{\bullet-}$)]$^-$ but also effectuated decomposition (Figure S30).[22] Using the trityl radical •CPh$_3$ (Gomberg dimer) gave an instantaneous colour change to blood red which eventually was attributed to the formation of small amounts of the triphenylmethanide anion. The anion was thereby result

of the reaction of the trityl radical anion with the iron(I) starting complex K{18c6}[Fe(NR$_2$)$_2$], as corroborated by an independent reaction (Figure S43-45). Intriguingly, the treatment of **3a** with 1,4-cyclohexadiene gave rise to 1,3-cyclohexadiene as well as benzene together with equimolar amounts of cyclohexene as evidenced by ^{1}H NMR spectroscopy (Figure S31/32). The impact of the pyridine free [Fe(NR$_2$)$_2$]$^-$ was again verified and indeed showed the complete transfer hydrogenation of 1,4-CHD to benzene and cyclohexene over the course of 12 h (Figure S33-35). No 1,3-CHD was observed in this case, which evidentially had to be mediated by **3a**. The mechanism of both transformations, double bond migration and intermolecular hydrogen transfer, is not clear at this point. Usually metal hydrides are proposed in these bond isomerisation reactions,[32] for which however in our system no evidence could be obtained so far. An alternative mechanistic possibility is the bond isomerisation via reversible H atom abstraction,. This was proposed for the transformation of 1,4-CHD by an iron nitride,[33] and is at least plausible for the pyridine complex **3a**, respectively its monomeric form [**3a**]$^-$. Combining all these results, it showed for **3a** that the pyridine coordination and dimerization is fully reversible whereas both the iron(I) starting compound [Fe^{I}(NR$_2$)$_2$]$^-$ as well as a monomeric pyridyl radical anion complex are responsible for the observed reactivity.

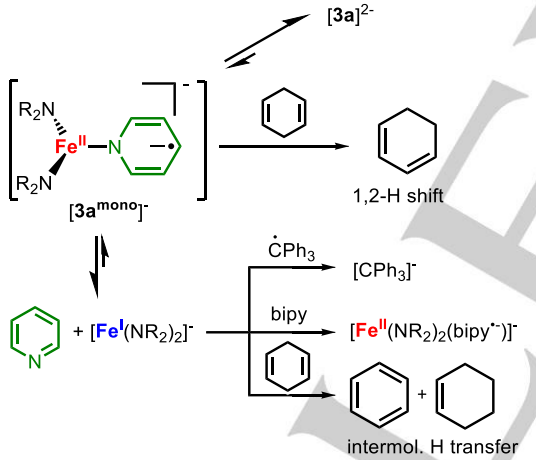

Scheme 3. Chemical examination of the reversibility of the formation of [**3a**]$^{2-}$ via the presumed monomeric form [**3a**^{mono}]$^-$. The K{18c6} cations are not shown.

Having established the reductive coupling of pyridines using the metal(I) silylamides of chromium, manganese and iron we turned back to cobalt. As initially shown, the cobalt(I) complex K{18c6}[Co(NR$_2$)$_2$] did not interact with the examined pyridines which we attributed to its comparably low reduction potential. As such the significantly more electron deficient perfluoropyridine C$_6$F$_5$N (PFP) was employed to facilitate the pyridine reduction (**Scheme 4**). Indeed, its reaction with K{18c6}[Co(NR$_2$)$_2$] led to an instantaneous change of colour from pale to intense green. *In-situ* ^{1}H NMR analysis showed the formation of only one paramagnetic species (δ_{SiMe3} = −15.20 ppm), which was subsequently identified as a rare example of a low-coordinate fluorocobalt(II) complex (K{18c6}[Co(F)(NR$_2$)$_2$], **5**, (**Figure 4** top).[21] The fate of the employed PFP was revealed via *in-situ* ^{19}F NMR spectroscopy upon detection of considerable amounts of 4,4-octafluorobipyridine (4,4'-Fbipy).[34] 4,4'-Fbipy is an uncommon perfluoro derivative of 4,4'-bipyridine and its synthesis can be achieved via copper mediated cross-coupling using zinc organyls under forcing conditions, [35] reaction of PFB with hexaethyltriamidophosphite,[34] or unselective electrochemical reduction of PFB.[36] Given our previous observation of C−F bond cleavage of fluorobenzene by the iron(I) compound K{18c6}[Fe(NR$_2$)$_2$] into an fluoroiron(II) and an aryliron(II) complex,[31] we speculated on a related mechanism in the presented case. However, upon reaction of PFP with two equivalents of K{18c6}[Co(NR$_2$)$_2$] no signal belonging to an aryl cobalt(II) species [Co(R)(NR$_2$)$_2$] was observed with full conversion of the employed cobalt(I) compound. As in this case 4,4'-Fbipy is absent it indicated that the formed 4,4'-Fbipy might have reacted with the excess of cobalt(I). Next, pyridines with lower degree of fluorination were briefly examined, namely 2-fluoropyridine, 2,4-difluoropyridine, 2,4,6-trifluoropyridine, 2,3,6-trifluoropyridine and 2,3,5,6-tetrafluoropyridine. Whereas for the first no conversion was observed, reaction of all pyridines with more than one fluoride substituent with K{18c6}[Co(NR$_2$)$_2$] showed by ^{1}H NMR spectroscopy the formation of the cobalt(II) fluoride **5** (in yields up to 45%), and a second, presumably organocobalt(II) species [Co(R)(NR$_2$)$_2$]), which could however not be isolated or structurally characterized so far. No defluorinative C−C homocoupling of the substrate, that would lead to a purely organic product, was observed in any case.

Given the successful isolation of the cobalt fluoride complex **5** using PFP as the fluorination agent, analogous reactions of PFP with K{18c6}[Fe(NR$_2$)$_2$] and K{18c6}[Mn(NR$_2$)$_2$] were also performed. For the former this gave a dark solution from which the known iron fluoride K{18c6}[Fe(F)(NR$_2$)$_2$], **6a**,[31] was obtained that now could be isolated in a pure fashion.

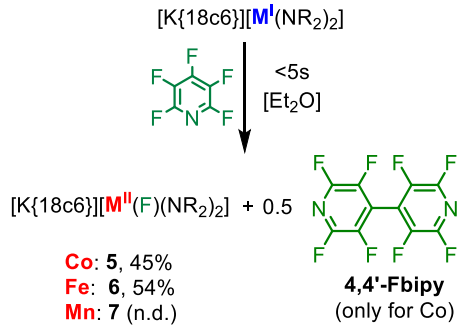

Scheme 4. Synthesis of the three-coordinate fluorido complexes **5, 6** and **7**.

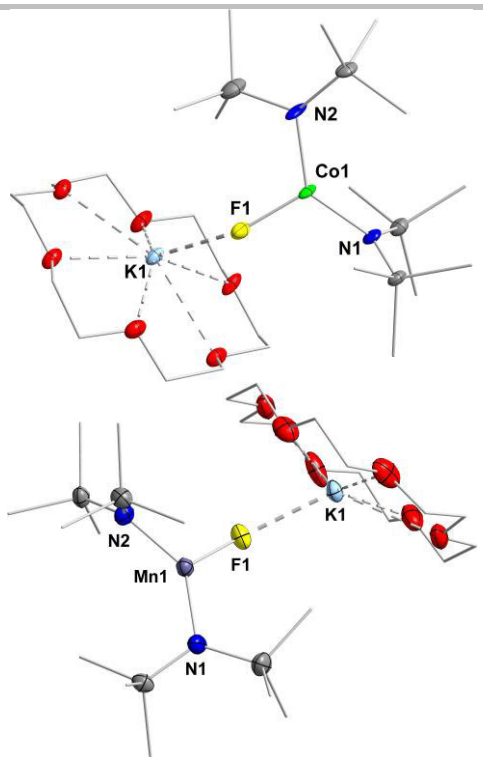

Figure 4. Molecular structure of compounds **5** (top) and **7** (bottom). H atoms are omitted for clarity and ellipsoids are shown at 50% probability. Only one of the three molecules for **5** and **7** in the asymmetric unit are shown. Important bond lengths (Å) and distances (°): **5**) Co−F1 1.885(4), Co−N1 1.938(4), Co−N2 1.935(4), K−F1 2.588(4); N1−Co−N2 133.2(2), N1−Co−F1 111.8(2), N2−Co−F1 114.3(2). **7**) Mn−F1 1.946(3), Mn−N1 2.048(4), Mn−N2 2.048(4), K−F1 2.609(3); N1−Mn−N2 129.8(2), N1−Mn−F1 113.6(2), N2−Mn−F1 116.6(2).

In this case only traces of 4,4'-Fbipy as well as some amounts of $FSiMe_3$ were observed. This can be attributed to total degradation of perfluoropyridine via consequent defluorination reactions, explaining also the blackish reaction mixture. Similar observations were made using the manganese(I) silylamide, yielding the first example of a low-coordinate manganese(II) fluoride ($K\{18c6\}[Mn(F)(NR_2)_2]$, **7**). In solid state the complex anions of compound **5** and **7** exhibit a three-coordinate metal ion in a distorted trigonal planar fashion. Together with the iron complex **6** the bond lengths $M–N_{hmds}$ bonds shorten from manganese (2.05 Å) to cobalt (1.94 Å). The same trend is observed for the M–F bonds (manganese 1.95 Å − cobalt 1.89 Å). In all three structures (**5** – **7**) the potassium atom of the cation is oriented towards the fluorine atom.

Conclusions

Concluding, we presented the facile reductive coupling of pyridines using quasilinear metal(I) silylamides of chromium, manganese and iron ($[M(NR_2)_2]^-$), which lead to dinuclear metal(II) complexes bridged by a 4,4'-dihydrobipyridyl dianion. This is especially remarkable in case of chromium, given a mismatch between the respective reduction potentials of nearly 2 V. In due process we could also give structural evidence of a non-3d-metal ligated pyridyl radical anion sandwiched between two K{18c6} units. For the dimeric iron 4,4'-dihydrobipyridyl complexes it was shown that the C−C bond formation is reversible, also revealing an iron(I) mediated double bond isomerisation by either by an elusive monomeric iron pyridiyl radical anion or the starting iron (I) complex $[Fe(NR_2)_2]^-$. Employing perfluoropyridine as a substrate cleavage of the para-C−F bond under formation of rare metal(II) fluoride complexes could be observed together with the C−C-coupling product of 4,4-perfluorobipyridine or its degradation. For lesser fluorinated pyridines, their exemplary reactions with the cobalt(I) silylamide stops at a mixture of the metal(II) fluoride and the organometal(II) complex. Overall, we showed the multifaceted behaviour of simple (fluoro)pyridines in the presence of reducing metal(I) complexes. Ongoing work concerns the further isolation and characterisation of pyridine and related radical anions, as well as the iron(I) mediated bond isomerisation processes observed herein.

Materials and Methods

Supporting Information. The supporting material contains the synthesis and analysis of all compounds (^{1}H, IR and UV/Vis spectroscopy, combustion analysis), *in-situ* NMR spectra as well as crystallographic details.

AUTHOR INFORMATION

*Dr. C. G. Werncke, Department of Chemistry, Philipps-University Marburg, Hans-Meerwein-Strasse 4, D-35043 Marburg, Germany. E-Mail: gunnar.werncke@chemie.uni-marburg.de

Funding Information

The work was funded by the DFG (grant 5627/4-1 for C. G. Werncke).

ACKNOWLEDGMENTS

We thank the Department of Chemistry of the Philipps-University for support and A. Schwabauer for assistance.

References

[1] a) A. P. Sadimenko, *Adv. Heterocycl. Chem.* **2007**, *93*, 179; b) L. Tong, L. Duan, A. Zhou, R. P. Thummel, *Coord. Chem. Rev.* **2020**, *402*, 213079; c) C. Kaes, A. Katz, M. W. Hosseini, *Chem.*

Rev. **2000**, *100*, 3553; d) P. G. Sammes, G. Yahioglu, *Chem. Soc. Rev.* **1994**, *23*, 327; e) W. W. Brandt, F. P. Dwyer, E. D. Gyarfas, *Chem. Rev.* **1954**, *54*, 959.

[2] N. Elgrishi, M. B. Chambers, X. Wang, M. Fontecave, *Chem. Soc. Rev.* **2017**, *46*, 761.

[3] a) A. C. Bowman, J. England, S. Sproules, T. Weyhermüller, K. Wieghardt, *Inorg. Chem.* **2013**, *52*, 2242; b) B. de Bruin, E. Bill, E. Bothe, T. Weyhermüller, K. Wieghardt, *Inorg. Chem.* **2000**, *39*, 2936; c) C. C. Scarborough, S. Sproules, T. Weyhermüller, S. DeBeer, K. Wieghardt, *Inorg. Chem.* **2011**, *50*, 12446; d) C. C. Scarborough, K. Wieghardt, *Inorg. Chem.* **2011**, *50*, 9773; e) C. Wolff, A. Gottschlich, J. England, K. Wieghardt, W. Saak, D. Haase, R. Beckhaus, *Inorg. Chem.* **2015**, *54*, 4811.

[4] a) C. C. Lu, T. Weyhermüller, E. Bill, K. Wieghardt, *Inorg. Chem.* **2009**, *48*, 6055; b) C. C. Lu, E. Bill, T. Weyhermüller, E. Bothe, K. Wieghardt, *J. Am. Chem. Soc.* **2008**, *130*, 3181; c) C. C. Lu, S. DeBeer George, T. Weyhermüller, E. Bill, E. Bothe, K. Wieghardt, *Angew. Chem. Int. Ed.* **2008**, *47*, 6384; d) Q. Knijnenburg, S. Gambarotta, P. H. M. Budzelaar, *Dalton Trans.* **2006**, 5442; e) Di Zhu, I. Thapa, I. Korobkov, S. Gambarotta, P. H. M. Budzelaar, *Inorg. Chem.* **2011**, *50*, 9879; f) B. Butschke, K. L. Fillman, T. Bendikov, L. J. W. Shimon, Y. Diskin-Posner, G. Leitus, S. I. Gorelsky, M. L. Neidig, D. Milstein, *Inorg. Chem.* **2015**, *54*, 4909; g) E. Peris, R. H. Crabtree, *Chem. Soc. Rev.* **2018**, *47*, 1959; h) M. J. C. Dawkins, A. N. Simonov, C. Jones, *Dalton Trans.* **2020**, *49*, 6627.

[5] P. J. Chirik, K. Wieghardt, *Science* **2010**, *327*, 794.

[6] Z. Flisak, W.-H. Sun, *ACS Catal.* **2015**, *5*, 4713.

[7] M. D. Ward, J. A. McCleverty, *J. Chem. Soc., Dalton Trans.* **2002**, 275.

[8] a) B. Pashaei, S. Karimi, H. Shahroosvand, P. Abbasi, M. Pilkington, A. Bartolotta, E. Fresta, J. Fernandez-Cestau, R. D. Costa, F. Bonaccorso, *Chem. Soc. Rev.* **2019**, *48*, 5033; b) V. T. Annibale, D. Song, *RSC Adv.* **2013**, *3*, 11432; c) S. Blanchard, E. Derat, M. Desage-El Murr, L. Fensterbank, M. Malacria, V. Mouriès-Mansuy, *Eur. J. Inorg. Chem.* **2012**, *2012*, 376.

[9] a) A. Jaoul, Y. Yang, N. Casaretto, C. Clavaguéra, L. Maron, G. Nocton, *Chem. Commun.* **2020**, *56*, 11875; b) W. Ren, W. W. Lukens, G. Zi, L. Maron, M. D. Walter, *Chem. Sci.* **2013**, *4*, 1168; c) M. E. Garner, S. Hohloch, L. Maron, J. Arnold, *Organometallics* **2016**, *35*, 2915; d) G. Nocton, C. H. Booth, L. Maron, L. Ricard, R. A. Andersen, *Organometallics* **2014**, *33*, 6819; e) G. Nocton, C. H. Booth, L. Maron, R. A. Andersen, *Organometallics* **2013**, *32*, 1150.

[10] a) G. Nocton, W. W. Lukens, C. H. Booth, S. S. Rozenel, S. A. Medling, L. Maron, R. A. Andersen, *J. Am. Chem. Soc.* **2014**, *136*, 8626; b) G. Nocton, L. Ricard, *Chem. Commun.* **2015**, *51*, 3578.

[11] a) M. J. Monreal, P. L. Diaconescu, *J. Am. Chem. Soc.* **2010**, *132*, 7676; b) C. Camp, V. Guidal, B. Biswas, J. Pécaut, L. Dubois, M. Mazzanti, *Chem. Sci.* **2012**, *3*, 2433; c) C. Camp, V. Mougel, P. Horeglad, J. Pécaut, M. Mazzanti, *J. Am. Chem. Soc.* **2010**, *132*, 17374; d) B. A. Frazier, P. T. Wolczanski, E. B. Lobkovsky, T. R. Cundari, *J. Am. Chem. Soc.* **2009**, *131*, 3428; e) C. C. H. Atienza, C. Milsmann, S. P. Semproni, Z. R. Turner, P. J. Chirik, *Inorg. Chem.* **2013**, *52*, 5403; f) B. Liu, T. Yoshida, X. Li, M. Stępień, H. Shinokubo, P. J. Chmielewski, *Angew. Chem. Int. Ed.* **2016**, *55*, 13142.

[12] *CRC handbook series in inorganic electrochemistry*, CRC Pr, Boca Raton, Fla., **1988**.

[13] a) S. Labouille, F. Nief, X.-F. Le Goff, L. Maron, D. R. Kindra, H. L. Houghton, J. W. Ziller, W. J. Evans, *Organometallics* **2012**, *31*, 5196; b) I. L. Fedushkin, V. I. Nevodchikov, M. N. Bochkarev, S. Dechert, H. Schumann, *Russ. Chem. Bull.* **2003**, *52*, 154; c) F. Jaroschik, F. Nief, X.-F. Le Goff, L. Ricard, *Organometallics* **2007**, *26*, 3552; d) A. Formanuik, F. Ortu, J. Liu, L. E. Nodaraki, F. Tuna, A. Kerridge, D. P. Mills, *Chem. Eur. J.* **2017**, *23*, 2290.

[14] J. R. Aguilar-Calderón, J. Murillo, A. Gomez-Torres, C. Saucedo, A. Jordan, A. J. Metta-Magaña, M. Pink, S. Fortier, *Organometallics* **2020**, *39*, 295.

[15] R. A. Lewis, K. C. MacLeod, B. Q. Mercado, P. L. Holland, *Chem. Commun.* **2014**, *50*, 11114.

[16] T. R. Dugan, E. Bill, K. C. MacLeod, G. J. Christian, R. E. Cowley, W. W. Brennessel, S. Ye, F. Neese, P. L. Holland, *J. Am. Chem. Soc.* **2012**, *134*, 20352.

[17] C. G. Werncke, E. Suturina, P. C. Bunting, L. Vendier, J. R. Long, M. Atanasov, F. Neese, S. Sabo-Etienne, S. Bontemps, *Chem. Eur. J.* **2016**, *22*, 1668.

[18] C. G. Werncke, P. C. Bunting, C. Duhayon, J. R. Long, S. Bontemps, S. Sabo-Etienne, *Angew. Chem. Int. Ed.* **2015**, *54*, 245.

[19] C. G. Werncke, I. Müller, *Chem. Commun.* **2020**, *56*, 2268.

[20] a) S. Pfirrmann, C. Limberg, C. Herwig, R. Stösser, B. Ziemer, *Angew. Chem. Int. Ed.* **2009**, *48*, 3357; b) K. C. MacLeod, R. A. Lewis, D. E. DeRosha, B. Q. Mercado, P. L. Holland, *Angew. Chem. Int. Ed.* **2017**, *56*, 1069; c) M. I. Lipschutz, T. Chantarojsiri, Y. Dong, T. D. Tilley, *J. Am. Chem. Soc.* **2015**, *137*, 6366; d) Y. Gao, G. Li, L. Deng, *J. Am. Chem. Soc.* **2018**, *140*, 2239; e) J. Hicks, C. Jones, *Organometallics* **2015**, *34*, 2118; f) R. Wolf, M. Brynda, C. Ni, G. J. Long, P. P. Power, *J. Am. Chem. Soc.* **2007**, *129*, 6076.

[21] T. R. Dugan, X. Sun, E. V. Rybak-Akimova, O. Olatunji-Ojo, T. R. Cundari, P. L. Holland, *J. Am. Chem. Soc.* **2011**, *133*, 12418.

[22] I. Müller, C. Schneider, C. Pietzonka, F. Kraus, C. G. Werncke, *Inorganics* **2019**, *7*, 117.

[23] I. Müller, D. Munz, C. G. Werncke, *Inorg. Chem.* **2020**, *59*, 9521.

[24] a) D. C. Bradley, M. B. Hursthouse, C. W. Newing, A. J. Welch, *Chem. Commun.* **1972**, 567; b) F. A. Cotton, C. E. Rice, G. W. Rice, *Inorg. Chim. Acta* **1977**, *24*, 231; c) M. A. Babar, M. F. C. Ladd, L. F. Larkworthy, D. C. Povey, K. J. Proctor, L. J. Summers, *Chem. Commun.* **1981**, 1046.

[25] a) R. Wolf, E.-M. Schnöckelborg, *Chem. Commun.* **2010**, *46*, 2832; b) W. Huang, P. M. Abukhalil, S. I. Khan, P. L. Diaconescu, *Chem. Commun.* **2014**, *50*, 5221; c) I. Korobkov, S. Gambarotta, G. P. A. Yap, *Angew. Chem. Int. Ed.* **2003**, *42*, 4958; d) P. B. Hitchcock, M. F. Lappert, A. V. Protchenko, *J. Am. Chem. Soc.* **2001**, *123*, 189.

[26] a) T. J. Donohoe, J. F. Bower, D. B. Baker, J. A. Basutto, L. K. M. Chan, P. Gallagher, *Chem. Commun.* **2011**, *47*, 10611; b) Q. Cao, Y. Xie, J. Jia, X.-W. Hong, *Acta crystallographica. Section E, Structure reports online* **2009**, *65*, o3182; c) D. E. Stephens, J. Lakey-Beitia, J. E. Burch, H. D. Arman, O. V. Larionov, *Chem. Commun.* **2016**, *52*, 9945.

[27] M. S. Denning, M. Irwin, J. M. Goicoechea, *Inorg. Chem.* **2008**, *47*, 6118.

[28] E. Gore-Randall, M. Irwin, M. S. Denning, J. M. Goicoechea, *Inorg. Chem.* **2009**, *48*, 8304.

[29] a) C. R. Smith, *J. Am. Chem. Soc.* **1924**, *46*, 414; b) V. Kalyanaraman, C. N. R. Rao, M. V. George, *J. Chem. Soc. B* **1971**, 2406; c) T. Anderson, *Liebigs Ann. Chem.* **1870**, *154*, 270.

[30] a) J. Schröder, D. Himmel, D. Kratzert, V. Radtke, S. Richert, S. Weber, T. Böttcher, *Chem. Commun.* **2019**, *55*, 1322; b) N. Yuan, W. Wang, Z. Wu, S. Chen, G. Tan, Y. Sui, X. Wang, J. Jiang, P. P. Power, *Chem. Commun.* **2016**, *52*, 12714.

[31] C. G. Werncke, J. Pfeiffer, I. Müller, L. Vendier, S. Sabo-Etienne, S. Bontemps, *Dalton Trans.* **2019**, *48*, 1757.

[32] a) G. J. Balaich, I. P. Rothwell, *J. Am. Chem. Soc.* **1993**, *115*, 1581; b) M. B. Fischer, E. J. James, T. J. McNeese, S. C. Nyburg, B. Posin, W. Wong-Ng, S. S. Wreford, *J. Am. Chem. Soc.* **1980**, *102*, 4941; c) K. J. Karel, M. Brookhart, R. Aumann, *J. Am. Chem. Soc.* **1981**, *103*, 2695; d) A. J. Pearson, *Acc. Chem. Res.* **1980**, *13*, 463; e) J. E. Arnet, R. Pettit, *J. Am. Chem. Soc.* **1961**, *83*, 2954; f) M. Orchin, *16*, 1; g) B. F. Hallam, P. L. Pauson, *J. Chem. Soc.* **1958**, 642; h) J. X. Mao, R. T. Mathers,

K. Damodaran, *J. Organomet. Chem.* **2013**, *741-742*, 15; i) K. R. Sawyer, E. A. Glascoe, J. F. Cahoon, J. P. Schlegel, C. B. Harris, *Organometallics* **2008**, *27*, 4370; j) J. E. Lyons, *J. Chem. Soc. D* **1969**, *0*, 564; k) M. Green, T. A. Kuc, *J. Chem. Soc., Dalton Trans.* **1972**, 832.

[33] W.-T. Lee, R. A. Juarez, J. J. Scepaniak, S. B. Muñoz, D. A. Dickie, H. Wang, J. M. Smith, *Inorg. Chem.* **2014**, *53*, 8425.

[34] A. V. Gutov, E. B. Rusanov, A. B. Ryabitskii, A. N. Chernega, *J. Fluor. Chem* **2010**, *131*, 278.

[35] A. S. Vinogradov, V. E. Platonov, *Russ. J. Org. Chem.* **2015**, *51*, 1388.

[36] R. D. Chambers, W. Musgrave, C. R. Sargent, F. G. Drakesmith, *Tetrahedron* **1981**, *37*, 591.

Entry for the Table of Contents

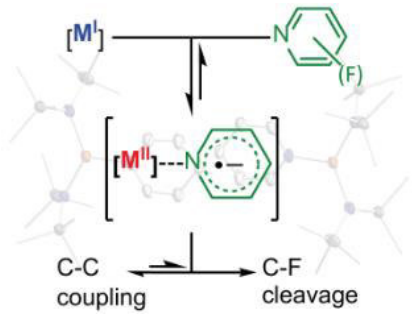

The reaction of two-coordinate metal(I) complexes (M = Cr − Fe) with simple pyridines lead to reductive coupling of the substrates via intermolecular C−C bond formation, which is reversible in case of iron. For fluoropyridines the C−F bond cleavage is preferred, giving rare low-coordinate metal(II) fluorides. Further, an rare case of a 3d-metal free pyridyl radical anion is presented.

Institute and/or researcher Twitter usernames: @wernckegunnar

3.3 „Reactions of Alkynes with Quasilinear 3d-Metal(I) Silylamides of Chromium to Cobalt – A Comparative Study"

Igor Müller, Dominik Munz und C. Gunnar Werncke, *Inorg. Chem*. **2020**, *59*, 9521.

Abstract: This report describes a series of rare low-coordinate 3d-transition metal alkyne complexes resulting from the reaction of quasilinear metal(I) silylamides, [K{18c6}][MX_2] (18-c-6 = 18-crown-6; X = –$N(SiMe_3)_2$, –N(Dipp)$SiMe_3$; Dipp = 2,6-di-*iso*-propylphenyl), of chromium, manganese, iron and cobalt with aliphatic and aromatic alkynes. We evaluated the interaction of alkynes with quasilinear metal complexes in dependence of the metal and the alkyne substituents. Whereas only a weak and reversible alkyne coordination is observed for cobalt, the formation of side-on alkyne complexes of the type [$M(L_2)(\eta^2$-RCCR)]$^-$ takes place readily for iron. In case of manganese, we report the first example of a low-coordinate manganese alkyne complexes and, depending on the substrate, unique examples for the manganese mediated reduction of the alkyne to their dianions or even alkyne trimerisation. For chromium, also alkyne coordination or reduction to the respective alkyne dianions is observed. Computational analysis of the series of [$M(N(SiMe_3)_2)_2(\eta^2$-PhCCPh)]$^-$ complexes (M = Cr – Co) using DFT and CASSCF methods reveals a partial reduction of the alkyne by the metal. This leads to the description of the electronic situation of all these complexes as formal metal(II) bound alkynyl radical anions. In case of chromium, indication for further contributions of a metal(III) cyclopropene resonance structure were found. The computational analysis rationalises the facile reduction to bis-metallated alkene dianions due to the radical anion character of the alkyne π-complexes.

Zusammenfassung: Dieser Bericht beschreibt eine Reihe seltener niedrigkoordinierter 3d-Übergangsmetall-Alkin-Komplexe, die aus der Reaktion von quasilinearen Metall(I)-Silylamiden [K{18-c-6}][MX_2] (18-c-6 = 18-Krone-6; X = –$N(SiMe_3)_2$, –N(Dipp)$SiMe_3$; Dipp = 2,6-Di-*iso*-propylphenyl) (M = Cr – Co) mit aliphatischen und aromatischen Alkinen resultieren. Dabei wurde die Wechselwirkung zwischen Komplex und Substrat durch Variation beider Komponenten untersucht. Während für Kobalt nur eine schwache und reversible Alkin-Koordination beobachtet wurde, bildeten sich stabile *side-on* Alkin-Komplexe vom Typ [$M(L_2)(\eta^2$-RCCR)]$^-$ im Fall von Eisen. Bei der Verwendung von Mangan wird über die ersten niedrig-koordinierten Mangan-Alkin-Komplexe berichtet. Je nach Substrat können einzigartige Beispiele für die

Mangan vermittelte Reduktion des Alkins zu Dianionen oder sogar zur Alkintrimerisierung führen. Für Chrom wird ebenfalls eine Alkin-Koordination oder -Reduktion zu den jeweiligen Alkin-Dianionen, vergleichbar zu den Mangan-Komplexen, beobachtet. Eine Computeranalyse der Komplex-Reihe $[M(N(SiMe_3)_2)_2(\eta^2\text{-PhCCPh})]^-$ (M = Cr – Co) unter Verwendung von DFT- und CASSCF-Methoden zeigt eine teilweise Reduktion des Alkins durch das Metall. Dadurch kann die elektronische Situation dieser Komplexe als formal Metall(II) gebundene Alkinylradikalanionen beschrieben werden. Im Fall von Chrom wurden weitere Hinweise auf Beiträge einer Metall(III)-cyclopropenresonanzstruktur gefunden. Die quantenchemische Analyse erklärt die einfache Reduktion zu bis-metallierten Alkendianionen aufgrund des Radikalanionencharakters der Alkin-π-Komplexe.

Eigener Anteil: Alle Synthesen der Verbindungen **1** – **6b** wurden von mir geplant und durchgeführt, sowie deren analytischen Daten aufgenommen und ausgewertet. ^{1}H-NMR-Experimente wurden sowohl von mir als auch unter Anleitung von Dr. Xiulan Xie in der zentralen NMR-Abteilung des Fachbereichs Chemie an der Philipps-Universität Marburg durchgeführt. Ebenfalls habe ich die UV/VIS- und IR-Messungen selbst durchgeführt. Die DFT- und CASSCF-Rechnungen wurden von Dr. Dominik Munz am Fachbereich Chemie der Universität Saarbücken durchgeführt und interpretiert. Die Einkristallstrukturanalyse für die Verbindungen **1**, **2a**, **3a**, **3b**, **4a**, **4c** und **4d** wurde durch die zentrale Abteilung für Kristallstrukturanalyse am Fachbereich Chemie an der Philipps-Universität Marburg unter der Leitung von Dr. Klaus Harms und Dr. Sergei Ivlev durchgeführt. Die Datensätze wurden jedoch von mir gelöst und verfeinert. Bei den Verbindungen **2c**, **2b**, **4b**, **6a** und **6b** war ich selbst sowohl für die Messung als auch das Lösen und Verfeinern verantwortlich. Das Manuskript wurde von mir, Dr. Dominik Munz und Dr. C. Gunnar Werncke verfasst.

Inorganic Chemistry

pubs.acs.org/IC Article

Reactions of Alkynes with Quasi-Linear 3d Metal(I) Silylamides of Chromium to Cobalt: A Comparative Study

Igor Müller, Dominik Munz, and C. Gunnar Werncke*

Cite This: *Inorg. Chem.* 2020, 59, 9521−9537 Read Online

ACCESS | Metrics & More | Article Recommendations | Supporting Information

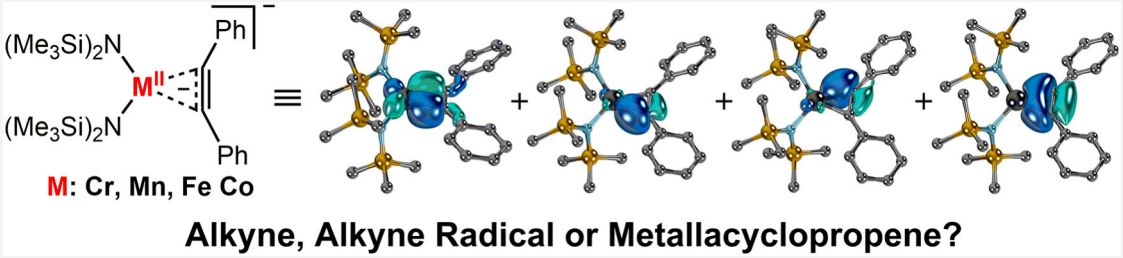

ABSTRACT: This report describes a series of rare low-coordinate 3d transition metal alkyne complexes resulting from the reaction of quasi-linear metal(I) silylamides, K{18c6}[MX_2] (18c6 = 18-crown-6; X = −N($SiMe_3$)$_2$), −N(Dipp)$SiMe_3$; Dipp = 2,6-diisopropylphenyl), of chromium, manganese, iron, and cobalt with aliphatic and aromatic alkynes. We evaluated the interaction of alkynes with quasi-linear metal complexes in dependence of the metal and the alkyne substituents. Whereas only a weak and reversible alkyne coordination is observed for cobalt, the formation of side-on alkyne complexes of the type [M(L_2)(η^2-RCCR)]$^-$ takes place readily for iron. In the case of manganese, we report the first example of a low-coordinate manganese alkyne complexes and, depending on the substrate, unique examples for the manganese mediated reduction of the alkyne to their dianions or even alkyne trimerization. For chromium, alkyne coordination or reduction to the respective alkyne dianions is also observed. Computational analysis of the series of [M(N($SiMe_3$)$_2$)$_2$(η^2-PhCCPh)]$^-$ complexes (Cr−Co) using DFT and CASSCF methods reveals a partial reduction of the alkyne by the metal. This leads to the description of the electronic situation of all these complexes as formal metal(II) bound alkynyl radical anions. In the case of chromium, indications for further contributions of a metal(III) cyclopropene resonance structure were found. The computational analysis rationalizes the facile reduction to bis-metalated alkene dianions due to the radical anion character of the alkyne π-complexes.

INTRODUCTION

The interaction of low-valent 3d metals with alkynes is fundamental to organometallic chemistry. It plays a crucial role in important catalytic transformations including oligomerization and cyclization reactions, bond metathesis (e.g., [2 + 2 + 1] cyclization for cyclopentenone synthesis (Pauson−Khand reaction))[1,2] or alkyne trimerization for the synthesis of functionalized benzene (and related pyridine) derivatives.[3−5] Thereby, the knowledge of the alkyne−metal interaction is crucial to predict and control the reactions. For early transition metals, such as titanium, these alkyne complexes are best described as metallacyclopropenes with two covalent metal−carbon bonds.[6−10] In late transition metal alkyne complexes, the metal alkyne bond is dominated by back-bonding of the filled d-orbitals into the antibonding π^* orbitals of the alkyne as well as electrostatic interactions.[11−15] The vast majority of complexes of the middle 3d metals (chromium to cobalt) reported in the literature use carbonyl, phosphine, and/or cyclopentadienyl ligands, which are known to stabilize a low-valent metal center.[16−33] These ligands exhibit a strong ligand field, and in conjunction with high coordination numbers, their respective metal complexes are typically of a low-spin electron configuration. Much less is known about the interaction of alkynes with low-coordinate 3d metal ions, which often give rise to high-spin configurations. For chromium to cobalt, only a small number of low-coordinate alkyne complexes (coordination number ≤ 4) were structurally characterized (Cr: 2,[34,35] Fe 5[36−39] and Co: 3,[40−42] Scheme 1). Manganese alkyne complexes are generally scarce,[21−24] and examples for low-coordinate manganese complexes remain elusive to the best of our knowledge.

Recently, the synthesis and properties of the two-coordinate 3d metal(I) hexamethyldisilazanide complexes K{18c6}[M^I(N($SiMe_3$)$_2$)$_2$] of chromium to cobalt were reported (18c6 = 18-crown-6).[43,44] Given the fairly accessible metal center, and its

Received: February 5, 2020
Published: June 30, 2020

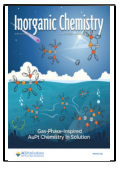

https://dx.doi.org/10.1021/acs.inorgchem.0c00365
Inorg. Chem. 2020, 59, 9521−9537

Scheme 1. Previously Reported Low-Coordinate 3d Metal Alkyne Complexes of Middle 3d-Transition Metals and Related Complexes Presented in This Study

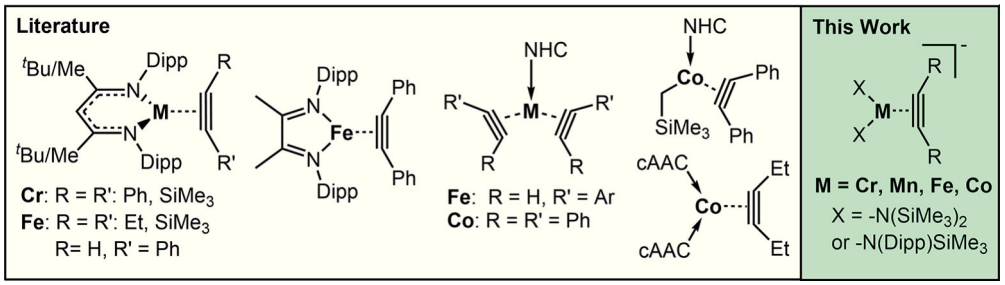

reactivity in bond activation and cleavage processes[45−48] we were fundamentally interested in the behavior of such quasi-linear metal(I) complexes toward alkynes. Using the same silyl amide ligand set, we thereby wanted to elaborate the impact of the metal ion onto the activation mode of alkynes in an otherwise similar ligand environment. The potential of low-coordinate metal(I) complexes to promote the conversion of alkynes was recently demonstrated by Tilley and co-workers, who used the mixed NHC/amide ligated iron(I) complex [Fe(N(Dipp)SiMe$_3$)(Idipp)] (Idipp = 1,3-bis(2,6-diisopropyl-phenyl)-imidazolin-2-ylidene, Dipp = 2,6-diisopropylphenyl) for the catalytic trimerization of alkynes. As intermediates, these invoked a side-on bound alkyne and a metallocyclopentadiene although they did not observe such species. Herein we present the isolation as well as structural and spectroscopic characterization of a variety of rare low-coordinate side-on alkyne complexes of chromium to cobalt, among others the first for manganese, using quasi-linear metal(I) silylamides. Furthermore, substrate reduction to stilbene dianions in the cases of manganese and chromium or alkyne trimerization in the case of manganese can be observed. Computational analysis of the side-on alkyne complexes reveals the partial reduction of the alkyne, leading to a description of metal(II) complexes with a covalently bound alkyne with some radical character at the ligand.

RESULTS

Cobalt. The synthesis of low-valent cobalt complexes with alkynes is comparably well-developed, although these complexes rely almost exclusively on the use of stabilizing carbonyl, phosphine, and/or cyclopentadienyl ligands. The few examples of structurally characterized low-coordinate cobalt alkyne compounds are either NHC ligated cobalt(0) or mixed alkyl/NHC ligated cobalt(I) complexes (Scheme 1).[42] The reaction of K{18c6}[Co(N(SiMe$_3$)$_2$)$_2$] with diphenylacetylene (tolane) led to the formation of K{18c6}[Co(η^2-PhCCPh)(N(SiMe$_3$)$_2$)$_2$], **1** (Scheme 2), as proven by single-crystal diffraction analysis. In the solid state, the cobalt ion is coordinated by two −N(SiMe$_3$)$_2$ units as well as a side-on bound tolane ligand with Co−C distances of around 1.93 Å (Figure 1).

Scheme 2. Synthesis of Low-Coordinate Cobalt Alkyne Complex 1

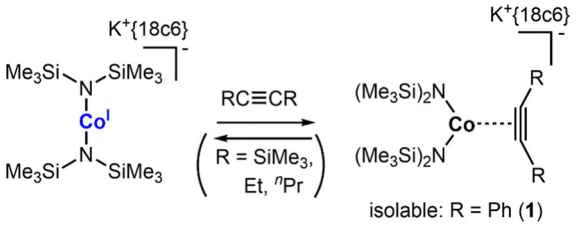

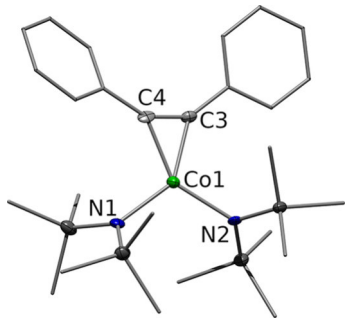

Figure 1. Molecular structure of **1**. The K$^+${18c6} counterion as well as H atoms are omitted for clarity. The asymmetric unit contains two molecules of **1**, of which one was chosen for structural discussions. Selected bond lengths (Å) and angles (deg): Co1−C3 1.931(6), Co1−C4 1.932(6), C3−C4 1.284(8), Co1−N1 1.980(5), Co1−N2 1.979(5); N1−Co1−N2 111.3(2), C3−C4−C$_{Ph}$ 146.8(6), C4−C3−C$_{Ph}$ 145.4(6), (N1,Co1,N2)−(C3,Co1,C4) 13.9(3).

The alkyne ligand is arranged in a nearly coplanar fashion toward the plane defined by cobalt and the −N(SiMe$_3$)$_2$ ligands ((N1−Co1−N2)−(C3−Co1−C4) 13.9(3)°). The length of the central carbon−carbon bond amounts to 1.284(8) Å and is elongated in comparison to free tolane (∼1.20 Å) which indicates a significant amount of metal-to-ligand back-bonding. The C−C bond length is similar to the one in the low-valent cobalt(I) complex [Co^{I}(Iad)(CH$_2$SiMe$_3$)(η^2-PhCCPh)] (1.271(3) Å),[42] which also exhibits a pseudo-square-planar-coordinated cobalt ion (counting the alkyne as a bidentate ligand to account for the alkyne orientation). Other low-valent cobalt complexes such as [Co^{0}(I^{t}Bu)$_2$)(η^2-PhCCPh)] or [Co^{I}(PMe$_3$)$_3$(η^2-PhCCPh)]$^+$ also show comparable bond elongation of the substrate (1.27−1.28 Å).[29,30,40,49] The IR spectrum of **1** revealed a weak band at 1820 cm^{-1}, which can be attributed to the symmetric C−C stretching mode. In comparison with free tolane (2225 cm^{-1}),[50] the stretching mode is shifted by 405 cm^{-1} to lower frequencies. This is comparable to the shifts reported for [Co^{I}(Pme$_3$)$_3$(η^2-PhCCPh)]$^+$ (445 cm^{-1}) and for a side-on bound phenyl acetylene bound (nacnac)iron(I) complex (393 cm^{-1}, Scheme 1).[33,38]

^{1}H NMR spectroscopic examination of an isolated sample of **1** showed, in addition to paramagnetically shifted signals (−7.67, −5.39, 8.54, and 26.05 ppm), the presence of free tolane and the cobalt(I) reactant (Figure 2). This indicated, despite the

https://dx.doi.org/10.1021/acs.inorgchem.0c00365
Inorg. Chem. 2020, 59, 9521−9537

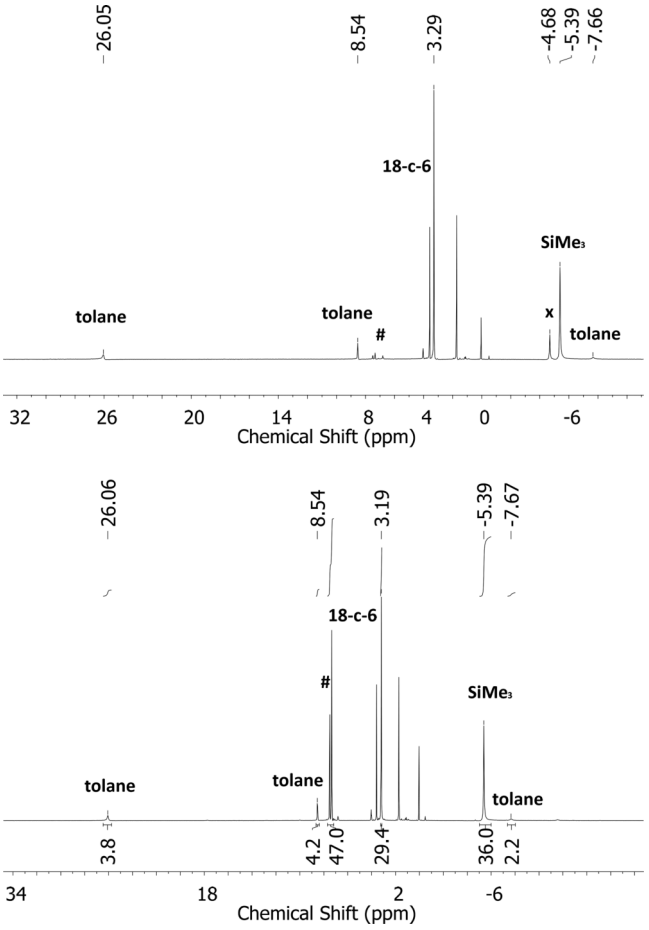

Figure 2. ^{1}H NMR spectrum of isolated [K{18c6}][Co(N-(SiMe$_3$)$_2$)$_2$(η^2-PhCCPh)], **1**, (top) and in the presence of 5 equiv of PhCCPh (bottom) in THF-d_8 (500.1 MHz). (#) denotes free tolane (PhCCPh) and (*x*) denotes free [Co(N(SiMe$_3$)$_2$)$_2$]$^-$.

elongated C−C bond in the solid state, a weak cobalt(I)−alkyne interaction in solution, which seems reasonable in sight of the anionic nature of the cobalt(I) precursor. Upon addition of five additional equivalents of tolane the equilibrium was shifted toward **1** (see the Supporting Information). A larger excess of substrate (>10 equiv) thereby effectuated the decomposition of **1**. Upon cooling a solution of **1** in THF-d_8 to −80 °C a shift of the equilibrium toward **1** is also observed via variable-temperature (VT) ^{1}H NMR spectroscopy. Given the educt/product equilibrium, direct measurement of the magnetic susceptibility of **1** in solution using the Evans method was not feasible. Therefore, 5 equiv of tolane were added to shift the equilibrium essentially quantitatively toward **1**. This gave a magnetic susceptibility of μ_{eff} = 3.2 μ_B for **1** that is slightly higher than the spin-only value for a high-spin d^8 system ($\mu_{s.o.}$(S = 1) = 2.83 μ_B). It is significantly smaller than the value observed for the quasi-linear cobalt(I) precursor complex [Co^I(N(SiMe$_3$)$_2$)$_2$]$^-$ (μ_{eff} = 4.18 μ_B) which experiences strong spin−orbit coupling due to the complex's linearity.[43] To evaluate the influence of the acetylene substituents K{18c6}[Co(N(SiMe$_3$)$_2$)$_2$] was reacted with more electron-rich bisalkylated and silylated acetylene derivates (namely, 4-octyne, 3-hexyne, and bis(trimethylsilyl)-acetylene (btmsa)). An immediate color change to brownish red was observed for all substrates in solution as was the case for tolane, hinting at coordinative interactions. However, the *in situ* ^{1}H NMR spectroscopic analysis of the reaction mixtures showed only the cobalt(I) starting complex. Attempts to isolate the corresponding alkyne complexes by crystallization at −35 °C gave only the cobalt(I) precursor in quantitative yield, even when employing an excess of the respective alkyne.

Iron. When K{18c6}[Fe(N(SiMe$_3$)$_2$)$_2$] was treated with 1 equiv of an alkyne (tolane, 3-hexyne, or 4-octyne) in diethyl ether, an immediate color change from greenish brown to red violet was observed (Scheme 3). Upon layering the obtained solutions with pentane and storing them at −35 °C for several days, dark red crystals were obtained for tolane (**2a**), hexyne (**2b**), and octyne (**2c**).

Scheme 3. Synthesis of Low-Coordinate Iron Alkyne Complexes 2a−c

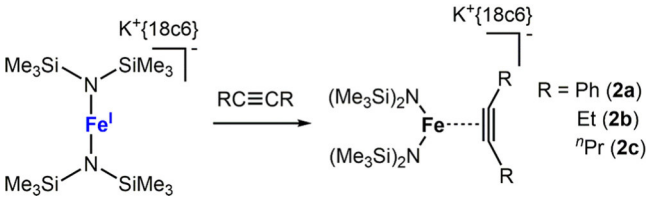

X-ray diffraction analysis of suitable single crystals of **2a**, **2b**, and **2c** revealed the presence of alkyne iron complexes (Figure 3). Important bond lengths and angles are given in Table 1. In each complex, the respective alkyne coordinates in a side-on fashion with a Fe−C$_{alkyne}$ distance between 1.947(3) Å (**2a**) and 1.966(2) Å (**2c**). The central C−C bonds of the coordinated alkynes are moderately elongated to 1.269(5) Å (**2a**), 1.283(6) Å (**2b**), and 1.272(3) Å (**2c**) in comparison to the free alkyne (reference for **2b** and **2c**: ^{t}BuCC^{t}Bu (1.202(2) Å)).[51] For **2a**, the C−C bond length of 1.269(5) Å is similar to the one observed for the cobalt tolane complex **1** (1.284(8) Å). The torsion angle between the planes defined by the diamido iron unit (N1,Fe1,N1′/N2) and the iron acetylene fragment (C$_{alkyne}$,Fe1,C′$_{alkyne}$) unit are found to vary between 26.9(3)° (**2b**) and 48.3(2)° (**2a**). This is in contrast to the situation found in cobalt complex **1** and the related 1,3-β-diketiminato based [(nacnac)Fe^I(η^2-alkyne)] complexes, where the respective metal ion experiences a rather pseudo-square-planar ligand sphere.[38]

In **2a−c**, the angles between the central C−C bond and the substituent on the respective alkyne amount to approximately 150° which is similar to those of **1** and other iron alkyne complexes (140−150°).[38,52,53] IR spectroscopic analysis of the iron alkyne complexes revealed the symmetric C−C stretching frequency bands at 1787 cm^{-1} (**2a**), 1824 cm^{-1} (**2b**; free 3-hexyne $\nu_{C\equiv C}$ = 2256 cm^{-1}),[54] and 1820 cm^{-1} (**2c**; free 4-octyne $\nu_{C\equiv C}$ = 2270 cm^{-1}).[55] In iron tolane complex **2a**, the elongation is slightly enhanced in comparison to the cobalt analogue **1** (1820 cm^{-1}). In the case of **2b**, the C−C stretching frequency is slightly less shifted than that of the related nacnac based iron 3-hexyne complex from Yu et al. (1802 cm^{-1}; Scheme 1).[38]

^{1}H NMR spectroscopic examination of iron compounds **2a−c** gave paramagnetically shifted signals for each compound, whereas the signal belonging to the −N(SiMe$_3$)$_2$ unit is located at −1.88 ppm (**2a**, Figure 4), −3.31 ppm (**2b**), and −3.26 ppm (**2c**), respectively. The positions are similar to the ones observed in the related [Fe(dppee)(N(SiMe)$_3$)$_2$)$_2$]$^-$ complexes (*cis*-dppee: −2.66 ppm, *trans*-dppee: −4.53 ppm; dppee = 1,2-bis(diphenylphosphino) ethylene).[47]

https://dx.doi.org/10.1021/acs.inorgchem.0c00365
Inorg. Chem. 2020, 59, 9521−9537

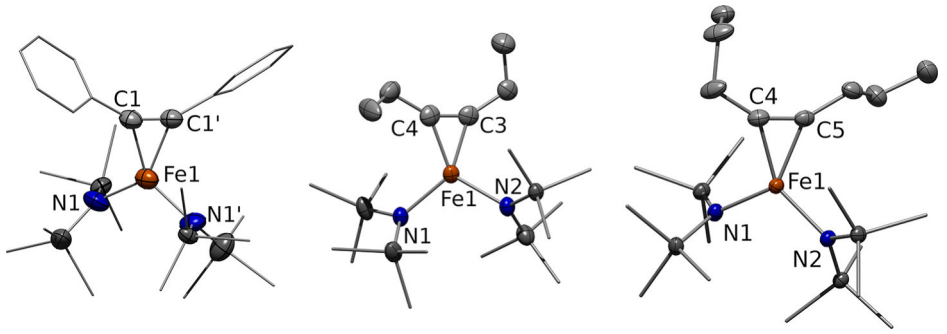

Figure 3. Molecular structure of **2a** (left), **2b** (middle), and **2c** (right) in the solid state. The K^+{18c6} counterions as well as H atoms are omitted for clarity. Structure of **2a** and **2b** suffers from disorder of the whole anion (not depicted) from which one was chosen for structure discussion.

Table 1. Selected Bond Metrics of Compounds 2a–c

compound	**2a** (tolane)	**2b** (hexyne)	**2c** (octyne)
	Bond Lengths/Å		
Fe1–C_{alkyne}	1.947(3)	1.938(5)	1.966(2)
Fe1–C'_{alkyne}	1.947(3)	1.952(5)	1.957(2)
C≡C	1.269(5)	1.283(6)	1.272(3)
Fe1–N1	1.973(3)	1.999(2)	2.006(2)
Fe1–N2	1.973(3)	2.011(8)	1.990(2)
	Bond Angles/deg		
N1–Fe1–N2	117.74(15)	117.3(6)	113.23(7)
alkyne torsion angle (N1,Fe,N2)–(C_{alkyne},Fe,C'_{alkyne})	48.3(2)	26.9(3)	38.08(11)
C≡C–C_R	151.3(4)	147.1(4)	149.2(2)
	151.3(4)	150.6(5)	148.0(2)

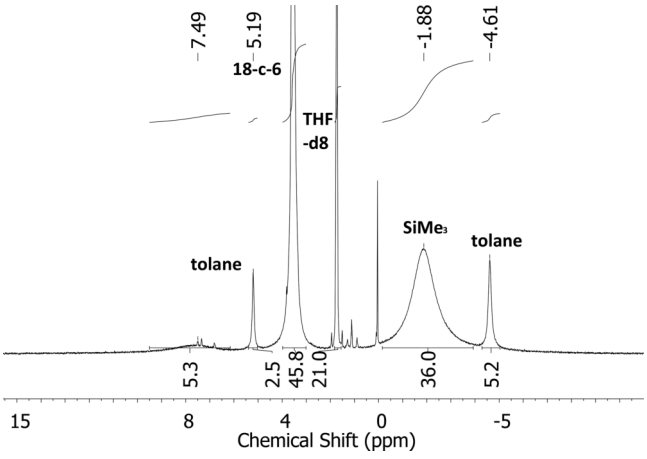

Figure 4. ^{1}H NMR spectrum of [K{18c6}][Fe(N(SiMe$_3$)$_2$)$_2$(PhCCPh)], **2a**, in THF-d_8 (500.1 MHz). The signal of 18c6 and the second signal of THF overlap.

When subjecting either **2a** to an excess of 3-hexyne (5 equiv) or **2b** with an excess of tolane, no exchange of the alkyne ligand was observed, implicating a fairly strong interaction between the metal(I) fragment and the alkyne. Determination of the magnetic moment in solution by the Evans method gave values which varied between $\mu_{eff} = 4.97\ \mu_B$ (**2a**), $\mu_{eff} = 5.08\ \mu_B$ (**2b**), and $\mu_{eff} = 6.18\ \mu_B$ (**2c**). With the exception of the latter, these values are similar to the one of the iron(I) precursor ($\mu_{eff} = 5.12\ \mu_B$).[44]

Manganese. Next, we turned our attention to manganese. Given the labile nature of the manganese(I) silylamide [Mn(N(SiMe$_3$)$_3$)$_2$]$^-$, we first examined the related, isolable complex K{18c6}[Mn(N(Dipp)SiMe$_3$)$_2$].[43] Its reaction with tolane in THF led to an immediate color change from dark violet to brownish yellow (Scheme 4). Layering the reaction mixture

Scheme 4. Synthesis of Low-Coordinate Manganese Alkyne Complexes 3a and 3b

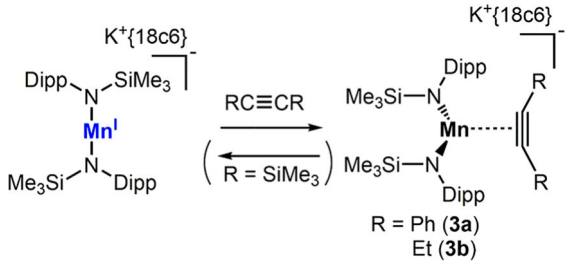

with pentane gave crystalline K{18c6}[Mn(N(Dipp)SiMe$_3$)$_2$(η^2-PhCCPh)], **3a** (Figure 5, left). Analogously, the reaction with 3-hexyne led to K{18c6}[Mn(N(Dipp)SiMe$_3$)$_2$(η^2-EtCCEt)], **3b** (Figure 5, right). For btmsa, a color change to reddish violet was observed upon exposure to K{18c6}[Mn(N(Dipp)SiMe$_3$)$_2$], indicating coordinative interactions. *In situ* ^{1}H NMR spectroscopy indeed revealed the consumption of the starting material as well as new paramagnetic signals. However, attempts to isolate the presumed alkyne complex via crystallization led to the recurrence of the starting manganese(I) complex.

In **3a** and **3b**, the manganese ion is surrounded by the two silylamides as well as the alkyne ligand, the latter in the expected side-on fashion. The alkyne is positioned nearly orthogonal to the plane span by the manganese ion and the two amide nitrogen atoms (**3a**: 82.12(16)°; **3b**: 77.045(1)°). The N–Mn bond lengths are found in a range of 2.039(2)–2.073(1) Å. The bond lengths of the C–C multiple bond of the alkyne are 1.271(4) Å (**3a**) and 1.274(1) Å (**3b**).

The IR spectrum of **3a** showed a weak band at 1789 cm^{-1}, whereas for **3b** no such band could be identified. The value

https://dx.doi.org/10.1021/acs.inorgchem.0c00365
Inorg. Chem. 2020, 59, 9521–9537

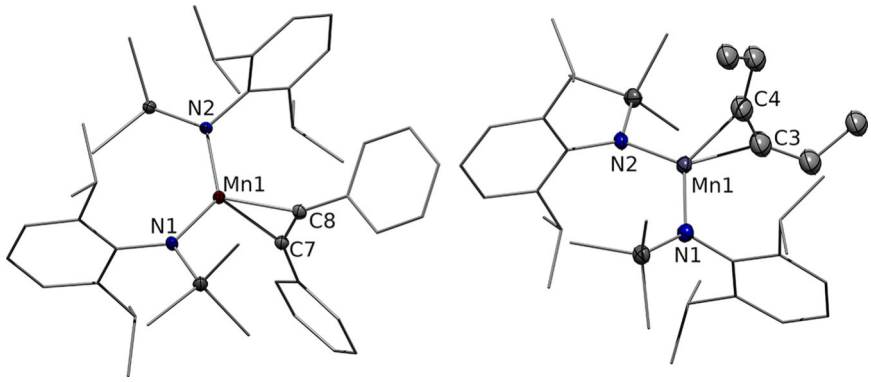

Figure 5. Molecular structure of **3a** and **3b**. The $K^+\{18c6\}$ counterions as well as H atoms are omitted for clarity. For **3b**, a disorder of one methyl group of the 3-hexyne ligand is not depicted. Selected bond lengths (Å) and angles (deg): **3a**: Mn1−C7 2.081(2), Mn1−C8 2.037(3), C7−C8 1.271(4), Mn1−N1 2.039(2), Mn1−N2 2.046(2); N1−Mn1−N2 132.86(8), C7−C8−C_{Ph} 142.8(3) C8−C7−C_{Ph} 132.86(6), (N1−Mn1−N2)−(C7−Mn1−C8) 82.12(16). **3b**: Mn1−C3 2.0458(1), Mn1−C4 2.0540(1), C3−C4 1.2739(1), Mn1−N1 2.0729(1), Mn1−N2 2.0524(1); N1−Mn1−N2 124.739(6), C3−C4−CEt 144.273(9), C4−C3−CEt 143.036(9), (N1,Mn1,N2)−(C3,Mn1,C4) 77.045(1).

found for **3a** is thereby similar to the cobalt (**1**) and iron (**2a**) congeners. Overall, this implicated only a moderate degree of C−C triple bond activation for these first examples of low-coordinate manganese alkyne complexes. **3a** and **3b** showed broad ^{1}H NMR spectroscopic features which could not be unambiguously assigned to the respective protons of the $-N(Dipp)SiMe_3$ ligand set. Compound **3a** exhibited a magnetic moment in solution of 4.63 μ_B, whereas for **3b**, a value of μ_{eff} = 3.28 μ_B was found. These values are lower, especially in the case of **3b**, than the spin-only value of an initially presumed high-spin d^6 complex ($\mu_{s.o.}(S = 2)$ = 4.90 μ_B) as well as the experimental value found for the manganese(I) precursor (μ_{eff} = 4.98 μ_B), pointing to a more complicated electronic situation. Upon attempts to substitute the alkyne in **3a** and **3b** with 3-hexyne or tolane, respectively, interactions were observed via ^{1}H spectroscopy leading to other, hitherto unidentified species. In combination with the reversible interaction with btmsa, this indicated a weak and reversible alkyne coordination to a quasi-linear manganese(I) ion.

Given the successful isolation of complexes **3a** and **3b**, we became interested in the behavior of the related, labile $K\{18c6\}[Mn(N(SiMe_3)_2)_2]$, which is dimeric in the solid state but is presumed to take a monomeric form in solution.[43] Treatment of $K\{18c6\}[Mn(N(SiMe_3)_2)_2]$ with different alkynes led to rapid color changes to reddish violet. However, identification of the products proved challenging due to the highly sensitive nature of these complexes, lack of useful ^{1}H NMR spectroscopic features, and the formation of inseparable $K\{18c6\}[Mn(N(SiMe_3)_2)_3]$, **5**, which is the main decomposition product of the starting compound $K\{18c6\}[Mn(N(SiMe_3)_2)_2]$.[43] In due course of these studies, several reactions products could be identified via X-ray diffraction analysis, which despite unsuccessful attempts for their isolation, gave nonetheless intriguing insights into unusual alkyne activation modes. When *in situ* generated $K\{18c6\}[Mn(N(SiMe_3)_2)_2]$ was subjected to $Me_3SiCCSiMe_3$ (btmsa) (Scheme 5), crystallization gave a mixture of **5**, $K[18c6\}[N(SiMe_3)_2)]$ and dark red crystals.

The latter were identified as the dinuclear manganese complex $K\{18c6\}[(Mn(N(SiMe_3)_2)_2(\mu\text{-}N(SiMe_3)_2)(\mu\text{-}\eta^2\text{:}\eta^2\text{-}Me_3SiCCSiMe_3]$, **4a**, via X-ray diffraction analysis (Figure 6). In this complex, two manganese ions are ligated each by an $-N(SiMe_3)_2$ ligand and connected via a bridging $-N(SiMe_3)_2$ unit as well as the alkyne. The latter binds in a *syn*-μ-η^2:η^2 fashion

Scheme 5. Formation of 4a via Reaction of $[Mn(N(SiMe_3)_2)_2]^-$ with Bis(trimethylsilyl)acetylene

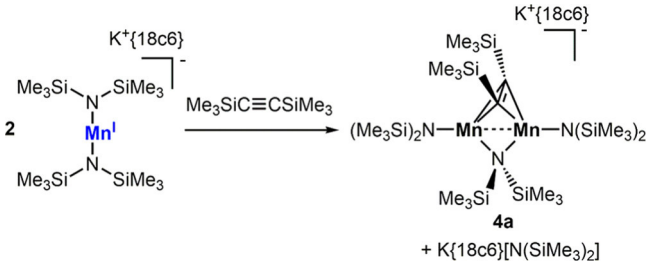

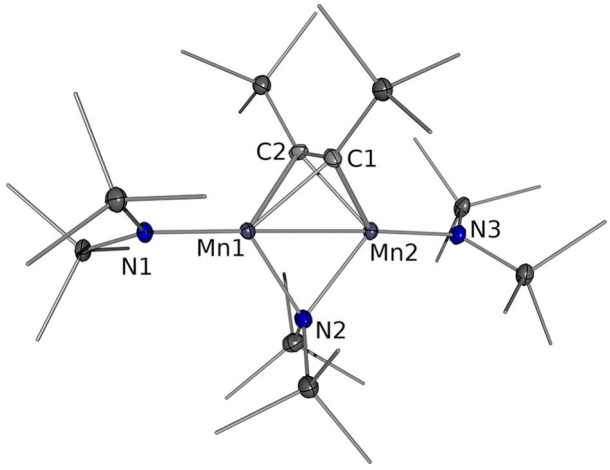

Figure 6. Molecular structure of **4a**. The $K^+\{18c6\}$ counterion as well as H atoms are omitted for clarity. Selected bond lengths (Å) and angles (deg): Mn1−Mn2 2.6699(4), Mn1−N1 2.035(2), Mn1−N2 2.196(2), Mn2−N2 2.227(2), Mn2−N3 2.052(2), Mn1−C1 2.125(2), Mn1−C2 2.085(2), Mn2−C1 2.081(2), Mn2−C2 2.138(2), C1−C2 1.353(3); C1−C2−Si 134.8(2), C2−C1−Si 133.1(2).

with the C−C bond oriented perpendicular to the Mn−Mn axis. The central C−C bond lengths of the substrate amounts to 1.353(3) Å with a C1−C2−$SiMe_3$ bond angle of around 134°. In comparison with the bond lengths found for free btmsa ($d_{C\equiv C}$ = 1.208(3) Å)[56] as well as for a 1,2-dialuminacyclobutene obtained from reaction of an Al(I) dimer with btmsa (1.362(3) Å),[57] the bonding situation for btmsa moiety in **4a** can be

https://dx.doi.org/10.1021/acs.inorgchem.0c00365
Inorg. Chem. 2020, 59, 9521−9537

understood as a *cis*-alkene-1,2-diyl ligand bound to two manganese(II) ions.

The Mn1−Mn2 distance of 2.6699(4) Å is rather short in comparison with other dimeric manganese complexes and is indicative of bonding interactions.[58,59] The formation of **4a** is likely to occur via reaction of an intermittent manganese alkyne complex that is reduced by a second equivalent of $[Mn(N(SiMe_3)_2)_2]^-$ under formal two-electron reduction of the alkyne. This is accompanied by release of $K\{18c6\}[N(SiMe_3)_2]$, whose presence was corroborated via X-ray diffraction of colorless crystals found in the crystalline mixture.

When $K\{18c6\}[Mn^I(N(SiMe_3)_2)_2]$ in diethyl ether was added to tolane, an instantaneous color change from violet to red was observed (Scheme 6). From the reaction mixture, highly

Scheme 6. Proposed Reaction Cascade from the Reaction of $[Mn(N(SiMe_3)_2)_2]^-$ with Tolane Leading to Complexes 4b, 4c, and 4d

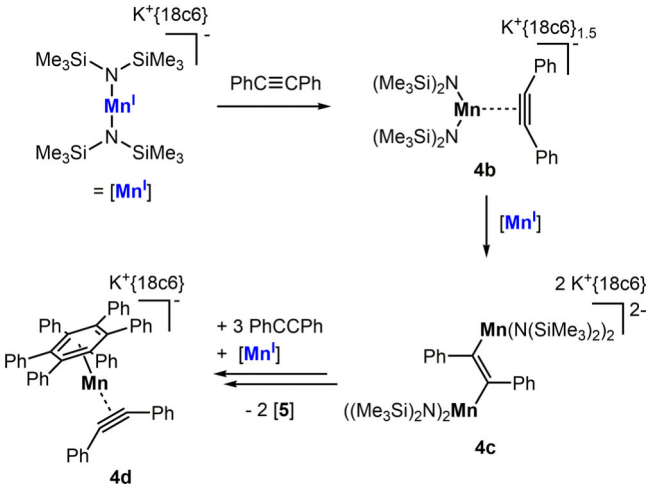

sensitive dark red crystals (besides colorless **5**) were obtained after layering the solution with pentane and storage at −35 °C. These were identified by X-ray diffraction analysis as $(K\{18c6\}_{1.5})[Mn(N(SiMe_3)_2)_2(\eta^2\text{-PhCCPh})]$, **4b**.

4b (Figure 7 left) structurally resembles the NDippTMS analogues **3a** and **3b**. In **4b**, the central C−C bond length of the side-on bound substrate amounts to 1.305(7) Å, which is slightly longer than those found for **3a** and **3b**. Furthermore, the alkyne is twisted by 25.2(3)° with respect to the plane span by the manganese amide unit. This is significantly less than in cases of **3a**/**b** (82.12(16) and 77.045(1)°) and is presumably a result of the smaller amide ligand set. Accordingly, the coordination sphere around the manganese ion in **4b** can be best described as distorted square planar.

Besides **4b** and **5**, small amounts of bright yellow crystals were also observed in the crystalline mixture, which turned out to be the dinuclear compound $(K\{18c6\})_2[Mn(N(SiMe_3)_2)_2(\mu\text{-}\kappa^1(C):\kappa^1(C)\text{-PhCCPh})]$, **4c** (Figure 7 right). In **4c**, the substrate bridges two metal amide moieties which are situated in *trans*-position of the central C−C bond of the former alkyne. Bearing in mind the moderate crystallographic data, the C−C bond length amounts to 1.411(13) Å which is in the range of a carbon−carbon double bond with bond angles around the two carbon atoms in the range of 112−121°. Together with the fact that low-coordinate manganese(II) silylamide complexes are mostly colorless,[43,60] the bond situation in **4c** is best described as two manganese(II) ions bridged by a stilbene dianion in the trans position. The formation of **4c** likely proceeds via an attack of a second manganese(I) amide to **4b** from the opposing side of the C−C multiple bond. Such a 2-fold triple bond metalation by metal complexes is remarkable and was previously only observed in the case of reactions of internal alkynes with dimeric aluminum(II) or magnesium(I) species which acted as synchronous $2e^-$ reductants.[61−63]

When $K\{18c6\}[Mn^I(N(SiMe_3)_2)_2]$ was reacted with tolane and left to crystallize at ambient temperatures, black crystals were obtained among others. The X-ray diffraction analysis revealed the formation of $(K\{18c6\})[Mn(C_6Ph_6)(\eta^2\text{-PhCCPh})]$, **4d** (Figure 8). Lacking any amide ligands, the anion of **4d** contains a metal-bound arene, stemming from substrate trimerization, as well as a side-on bound tolane. The metal atom is situated 1.5371(8) Å above the centroid of the arene. The central C−C bond of the alkyne is elongated to 1.346(7) Å, which is longer than any other η^2-alkyne metal(I) complex presented in this study and approaches the value of a C−C double bond. As such, complex **4d** could be described as a manganese(I) metallacyclopropene. For the structurally similar iron derivative $[Fe(C_6Ph_6)(\eta^2\text{-PhCCPh})]^-$ reported by Wolf et

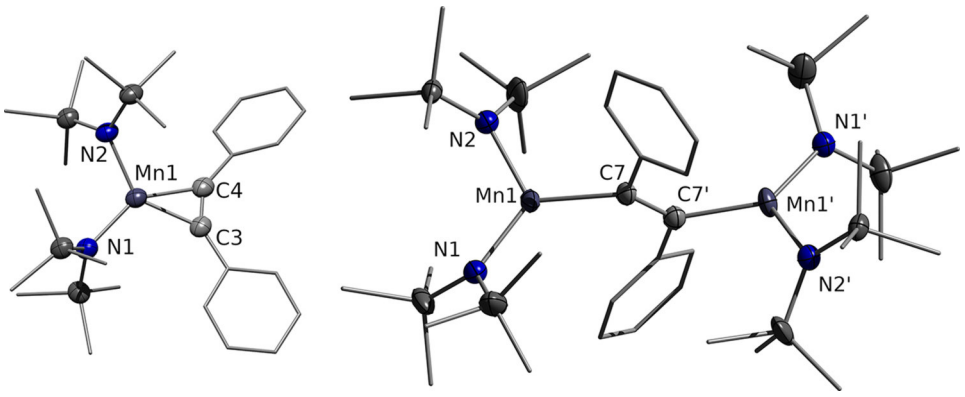

Figure 7. Molecular structures of **4b** (left) and **4c** (right). The $K^+\{18c6\}$ counterion, H atoms, and disorders are omitted for clarity. **4c** exhibits a disorder of the whole dianion which is not depicted. Selected bond lengths (Å) and angles (deg): **4b**: Mn1−C3 2.022(5), Mn1−C4 2.044(5), Mn1−N1 2.054(4), Mn1−N2 2.042(4), C3−C4 1.305(7); C3−C4−C_{Ph} 148.0(5), (Mn1−N2−Mn2)−(C1−C2) 25.1(3). **4c**: Mn1−N1 2.075(11), Mn1−N2 2.077(9), Mn1−C7 2.226(11), C7−C7′ 1.411(13); N1−Mn1−N2 116.8(4), N1−Mn1−C7 120.5(4), N2−Mn1−C7 118.1(5), C7−C7′−C_{Ph} 116.1(7).

https://dx.doi.org/10.1021/acs.inorgchem.0c00365
Inorg. Chem. 2020, 59, 9521−9537

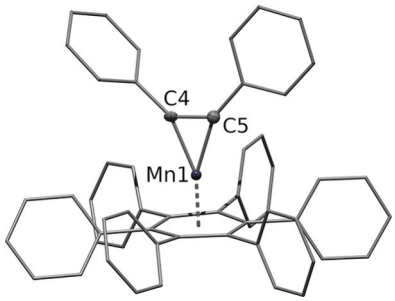

Figure 8. Molecular structure of **4d**. The $K^+\{18c6\}(thf)_2$ counterion as well as H atoms (except H8) are omitted for clarity. Selected bond lengths (Å) and angles (deg): Mn1−Arene 1.5371(8), M1−C4 1.905(5), M1−C5 1.893(5), C4−C5 1.346(7); C4−C5−C_{Ph} 134.4(5).

al.,[64] a formal −I oxidation state was calculated. Accordingly, **4d** could also be seen as a manganese(−I) alkyne complex, whereas in comparison with **3a** the subvalent oxidation state would lead to a stronger elongation of the central C−C bond of the alkyne due to enhanced metal-to-ligand back-bonding. Unfortunately, the unambiguous determination of the oxidation state was not possible due to the lack of an analytically pure sample of **4d**. Attempts to deliberately obtain **4d** by adjusting the stoichiometry of the reactants as well as by varying the reaction temperature proved unsuccessful. In any case, the formation of a formal manganese(−I) ion could be explained by redox disproportionation and amide ligand transfer under concomitant formation of the manganese trisamide **5**. The presence of the latter was indeed confirmed by structural identification of the known $K\{18c6\}[Mn(N(SiMe_3)_2)_3]$ (**5**) and $K\{18c6\}N(SiMe_3)_2$ from the reaction mixtures.

Complex **4d** is interesting for several reasons: It shows (a) the feasibility of substrate trimerization, (b) the ready redox disproportionation of $[Mn^I(N(SiMe_3)_2)_2]^-$, and (c) the feasibility of displacement of the amido ligands, reflecting the labile nature of the nonchelating silylamide ligands. In addition, complexes **4a−c** pose potential snapshots in the stepwise construction of the benzene derivate **4d**. Thereby, two metal ions are cooperating during the alkyne reduction and transformation.

Chromium. For chromium, the reaction of *in situ* formed $K\{18c6\}[Cr(N(SiMe_3)_2)_2]$ with btmsa led to the isolation of side-on alkyne complex **6a** (Scheme 7), whose structure was confirmed by X-ray diffraction analysis of suitable single crystals (Figure 9, left).

The side-on coordinate alkyne in **6a** is oriented nearly orthogonal to the chromium amide unit (Cr1−N2−Cr2)−(C1−C2) 88.3(4)°). The central alkyne C−C bond is elongated to 1.312(8) Å with a C−C−Si bond angle of 139.3(5)°. These structural features are in agreement with the only other low-coordinate chromium alkyne system, namely, [(nacnac)Cr(η^2-alkyne)] (tolane, btmsa) from Theopold and co-workers.[34,35] In the IR spectrum, a band at 1978 cm^{-1} (free BTMSA: 2109 cm^{-1})[65] is observed which was initially assigned to the C−C triple bond stretching frequency. However, the comparably small shift of the stretching frequency of only 131 cm^{-1} contrasts the very large C−C bond elongation and might be the result of other, unresolved interactions. **6a** showed no useful ^1H NMR signatures. Its magnetic moment in solution amounted to μ_{eff} = 3.44 μ_B which is significantly lower than the value of the high-spin chromium(I) precursor (μ_{eff} = 5.99, S = 5/2). The observed value for **6a** is thus better in agreement with a formulation as a

Scheme 7. Formation of Complexes 6a and 6b from the Reaction of $K\{18c6\][Cr(N(SiMe_3)_2)_2]$ with Bis(trimethylsilyl)acetylene and Tolane

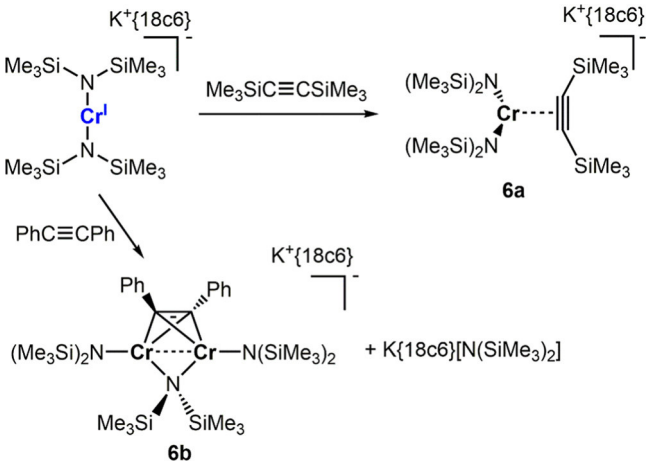

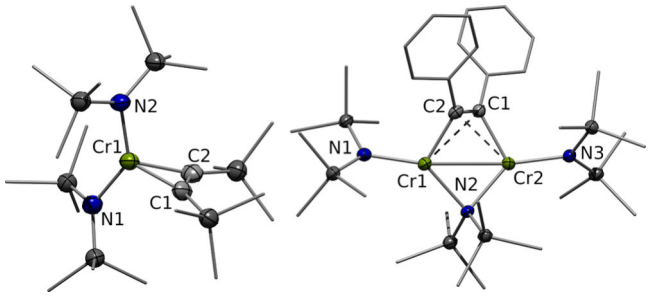

Figure 9. Molecular structure of **6a** (left) and **6b** (right) in the solid state. For **6b**, three independent molecules are found in the asymmetric unit of which one was chosen as representative. The K{18c6} cation and H atoms are omitted for clarity. Selected bond length and angles: **6a**: Cr1−C1 2.029(6), Cr1−C2 2.029(6), C1−C2 1.312(8), Cr1−N1 2.0315(5), Cr1−N2 2.034(5); N1−Cr1−N2 136.4(2), C1−C2−Si 140.3(5), C2−C1−Si 139.3(5), (Cr1−N2−Cr2)−(C1−C2) 88.3(4). **6b**: Cr1−Cr2 2.7968(9), Cr1−C1 1.984(5), Cr2−C2 1.976(2), Cr1−N1 1.997(2), Cr1−N2 2.0971(19), Cr2−N2 2.090(2), Cr2−N3 2.003(2), C1−C2 1.389(3), (Cr1−N2−Cr2)−(C1−C2) 46.16(12).

chromium(III) metalla-cyclopropene ($\mu_{s.o.}(S = 3/2) = 3.87\ \mu_{eff}$), similar to the [(nacnac)Cr(η^2-alkyne)] complexes.[34,35]

For tolane, substrate-bridged compound **6b** was obtained (Scheme 7, Figure 9 right), which resembles manganese complex **4a**. However, the substrate now binds in a μ_2-κ^1C:κ^1C′-bridging fashion, with the substrate oriented approximately 45° with respect to the central Cr−Cr axis. The C−C bond length of the coordinated tolane ligand is found to be 1.389(3) Å, which is a clear indication of the presence of a C−C double bond. Thus the chromium ions are supposedly in a +2 oxidation state, which would also reason the substrate orientation as four-coordinate chromium(II) ions prefer a square planar complex geometry.[66−70] **6b** showed no useful ^1H NMR spectroscopic features. Its magnetic moment amounted to μ_{eff} = 2.86 μ_B. Together with the short Cr−Cr distance of 2.7968(9) Å, this indicates a bonding interaction between the two metal ions.

Computational Analysis. Next, we sought to explore the intricate electronic structure of this unique series of alkyne complexes by computations. Despite of the importance of alkyne complexes in catalysis, there is only scarce precedence in the literature for a detailed computational analysis of open-shell

https://dx.doi.org/10.1021/acs.inorgchem.0c00365
Inorg. Chem. 2020, 59, 9521−9537

alkyne complexes.[71,72] However, diamagnetic alkyne complexes were studied in much detail, including an energy decomposition analysis of low-spin alkyne complexes of the groups 6, 8, and 10[13,73] by Frenking and co-workers and Grimme's investigation of ancillary ligand effects in d^{10} configured nickel(0) alkyne complexes.[74] Also the electronic structure of alkyne complexes of the early transition metals with a formal d-electron count of 0 (i.e., metalla-cyclopropenes) was assessed computationally.[75,76] For all diamagnetic compounds, the bonding interaction between alkyne and transition metal is understood with the Dewar−Chatt−Duncanson model (Figure 10).[14,15]

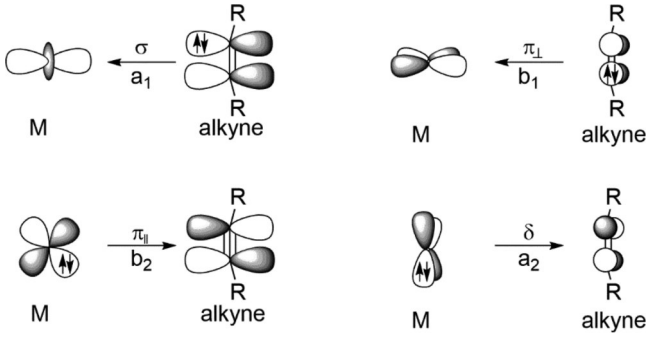

Figure 10. Most important orbital interactions for closed-shell transition metal complexes with partially filled d-orbitals.

Although not including alkyne ligands, a very detailed experimental/computational study was reported for π-adducts of nickel bisphosphine complexes by Love and Kennepohl.[77] The authors concluded that these complexes are best understood as d^{10}-configured nickel(0) complexes but furthermore suggested that electron-deficient and hence π-acidic olefins partially oxidize the metal due to enhanced back-bonding from the metal, resulting in up to 1/3 of partial nickel(I) and 1/10 of even nickel(II) character.

The structural parameters of alkyne complexes **1**, **2a**, **4b**, and **6a** and, for comparison the tolane chromium hexamethyldisilazide complex $[Cr(N(SiMe_3)_2)_2)(\eta^2\text{-PhCCPh})$ **6c***, were optimized using the density functionals BP86, B3LYP, PBE0, and B3PW91 (def-TZVP basis set for the metal, def2-SVP basis set for all other atoms, dispersion correction D3BJ) and the composite methods PBEh-3c and B97-3c.[78,79] The B3LYP method[80−83] proved most robust and afforded the best agreement with the parameters obtained by the XRD analysis and the alkyne C−C bond stretching frequencies (Table S13). Using the B3LYP geometric parameters, the analysis of the complexes' electronic structure was then performed by single-point calculations with the def2-TZVPP basis set. One GGA functional (BP86) and (meta-) hybrid density functionals with varying amount of HF exchange (TPSSh: 10%; B3LYP: 20%; PBE0:25%; M06:27%; ωB97X-D3: variable) were used. Furthermore, in sight of moderate to fairly high fractional occupancy density (FOD)[84,85] values (N^{FOD}: **1**: 1.37; **2a**: 1.13; **4b**: 0.65; **6a**: 0.94; **6c***: 1.01) CASSCF/NEVPT2 calculations were performed. For the DFT calculations, we investigated Knizia's localized[86,87] intrinsic bond orbitals (IBOs)[88] as well as Neese's quasi-restricted orbitals (QROs).[89] Scalar relativistic calculations using the zeroth-order approximation (ZORA) gave essentially equivalent results. Also, test calculations with (in sight of the complexes' anionic nature) diffuse functions (ma-def2-TZVPP) gave consistent results, albeit at the expense of tremendously increased computational cost.

We start with the analysis of the electronic structure of **4b**, which shows the lowest N^{FOD} of 0.65. The CAS(10,9) single-point calculations (Figure 11) reveal that the HONO (highest

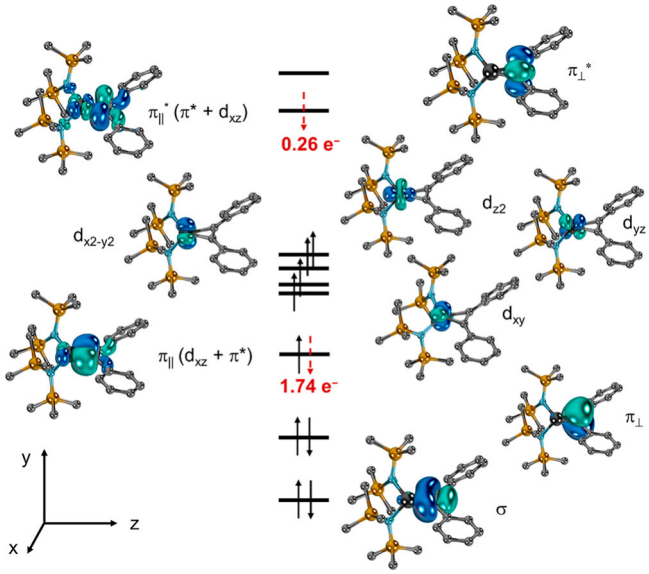

Figure 11. Frontier orbitals of manganese complex **4b** as calculated by CASSCF(10,9). Hydrogen atoms are omitted for clarity.

occupied natural orbital) through HONO−3 relate to essentially nonbonding, singly occupied d-orbitals (i.e., a high-spin electron configuration of the metal). HONO−4, which is occupied by two electrons, shows mixing of the metal's d_{xz} orbital with the in-plane, antibonding π^*-orbital of the alkyne (Mn: 70%; CC: 30%). This molecular orbital reflects a covalent interaction and relates to the back-bonding $\pi_{\parallel}$ orbital. The calculations predict an occupancy of only 1.74 electrons, whereas the remaining 0.26 electrons populate the corresponding antibonding and of course rather ligand centered orbital ($\pi_{\parallel}$*, LUNO). Overall, this description coincides with partial oxidation of the metal (reduction of the alkyne, respectively) beyond formally manganese(I) as well as partial anionic character of the alkyne ligand.

Turning to DFT, repeated attempts to obtain broken-symmetry wave functions with an antiferromagnetically coupled radical located at the alkyne ligand did not meet with success. Nevertheless, the analysis of the unrestricted, magnetic corresponding orbitals, which showed 95% overlap, suggests that the compound seems to share at least some antiferromagnetic character. Indeed, also the Löwdin population analysis[90] of **4b** with $S = 4/2$ using the B3LYP functional, which leads to a small spin contamination of $\langle S^2\rangle = 6.15$ (ideal value for $S = 4/2$: 6), suggests considerable spin density (overall more than −0.20 e^-) at the acetylene ligand. The population analysis using canonical orbitals as was applied to Wolf's related iron(Cp*) complexes[91] did not help to further understand the population of the metal's five valence d-orbitals due to fractional occupancy (e.g., B3LYP: reduced orbital charges: 5 × 1.2 a.u.; reduced orbital spin population: 1 × 0.9, 2 × 0.8, and 2 × 0.7 e^-). Instead, localized orbitals such as IBOs (Figure 11; Tables S15−S19) or QROs (Table S20, Figure S23), obtained by any of the investigated DFT methods, clearly suggest a d^5 electron configuration for **4b** (Figure 12). Thereby, the α IBOs corroborate an electronic structure composed of four singly occupied, essentially nonbonding d-orbitals ($d_{x^2-y^2}$, d_{z^2}, d_{yz}, d_{xy})

https://dx.doi.org/10.1021/acs.inorgchem.0c00365
Inorg. Chem. 2020, 59, 9521−9537

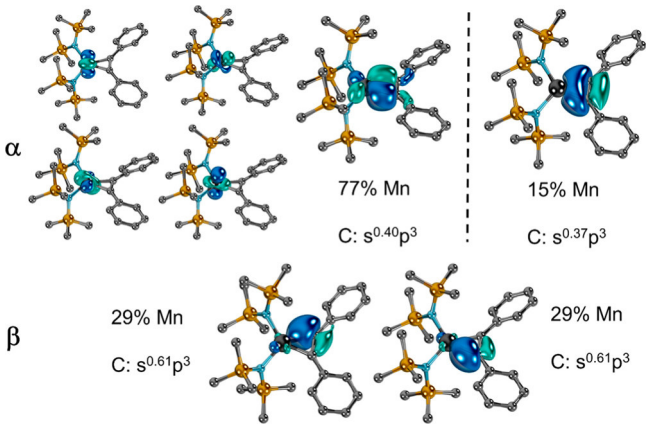

Figure 12. Covalent IBOs of **4b** with considerable metal character (B3LYP). Hydrogen atoms are omitted for clarity.

and a covalent $\pi_{\parallel}$ interaction between the d_{xz} and the in-plane π^*-orbital of the alkyne. This results in a formal d^5-electron configuration. Furthermore, two ligand-centered, covalent σ-type IBOs are obtained. In detail, these two β-orbitals are composed each of 29% d_{xy}(Mn), 11% s(C), and 56% p(C) contributions, which translate formally into a $s^{0.61}p^3$ hybridization of the carbon atoms. This value is fairly close to the $sp^{2.68}$ ($s^{0.89}p^3$, respectively) hybridization of the vinylic carbon atoms in cyclopropene.[92] Eventually, one α-IBO of σ-symmetry shows only 15% metal (mainly s-orbital) contribution, which translates into only low covalency for the σ-donation from the alkyne. We conclude that both methods indicate that the alkyne ligand formally oxidizes the metal by one electron to d^5, Mn^{II}, hence leading to considerable metalla-cyclopropene and alkyne radical-anion character.

In order to put this result into perspective to the previously studied bisphosphine-nickel complexes, we evaluated the complex obtained from π-coordination of tolane to bis-(dimethylphosphosphino)ethane nickel (i.e., [Ni(dmpe)(η^2-PhCCPh)]). In agreement with the previous findings, the IBOs obtained from an unrestricted calculation predict a d^{10} electron configuration (Table 2; i.e., nickel(0) with four nonbonding, doubly occupied d-orbitals) and likewise one covalent interaction associated with the $\pi_{\parallel}$ orbital (75% metal character).

In agreement with the magnetic data obtained by Evans' method, the DFT calculations predict overall multiplicities of S = 2/2, 3/2, 4/2, and 3/2 for the cobalt (**1**), iron (**2a**), manganese (**4b**), and chromium complexes (**6a**, **6c***), respectively. The electronic structures of the complexes **1** and **2a** are essentially equivalent to the electronic structure of **4b**, except that further electrons are added to the nonbonding d-orbitals (Table S15–S20). This leads to a d^6 electron configuration for the iron- and a d^7 electron configuration for the cobalt complex. Following the position of the transition metals in the periodic table and hence their electronegativity, a slight increase of population of the rather ligand-based, antibonding LUNO (**1**: 0.25 e^-, **2a**: 0.26 e^-, **4b**: 0.27 e^-) is predicted by the CASSCF method. This trend goes in line with the length of the C−C multiple bond of the acetylene ligands (**1**: 1.291 Å, **2a**: 1.300 Å, **4b**: 1.312 Å, **6c***: 1.334 Å), the C−C−Ph angle (**1**: 149°, **2a**: 148°, **4b**: 144°, **6c***: 137°), the calculated C−C bond stretching frequencies (**1**: 1840 cm^{-1}, **2a**: 1802 cm^{-1}, **4b**: 1743 cm^{-1}), the metal contribution to the $\pi_{\parallel}$ orbital (**1**: 82%, **2a**: 81%, **4b**: 77%), and the increasing s-character of the associated β-IBOs (**1**: $s^{0.50}p^3$, **2a**: $s^{0.54}p^3$, **4b**: $s^{0.61}p^3$). Overall, we conclude that the earlier and less noble the metal, the more covalently and stronger it binds and activates the alkyne ligand.

Nevertheless, for chromium compounds **6a** and **6c***, the picture seems more ambiguous. Optimizing the structural parameters of **6c*** with the B3LYP functional[93] suggests an S = 3/2 ground state with the alkyne ligand in perpendicular arrangement in agreement with the structure in the solid state (Scheme 8). Moderate spin delocalization is found on the ligand (0.12 e^- for both **6a** and **6c***; $\langle S^2 \rangle$ = 3.83). However, the in-plane S = 3/2 isomer is essentially isoenergetic (ΔE = +1 kJ mol^{-1}), and the S = 5/2 state with a ligand-centered radical is close in energy (B3LYP, adiabatic: + 59 kJ mol^{-1}).[94] Of course, this electronic structure is very well in line with the experimentally observed dimerization of **6c***.

The picture is similar for **6a**, although there the perpendicular arrangement of the alkyne ligand is significantly more stable than the planar isomer (ΔE^{B3LYP} = +44 kJ mol^{-1}); we hence conclude that the steric bulk of the trimethylsilyl-groups as well as the absence of a conjugated phenyl group stabilizes **6a** in the monomeric form.

The CASSCF calculations predict a similar electronic structure for the ground state of chromium complexes **6a** and **6c*** as was found for **4b**. In detail, three nonbonding, singly occupied valence d-orbitals and one further covalent interaction by two shared electrons between the metal and the alkyne ($\pi_{\parallel}$ orbital) were found. The antibonding $\pi_{\parallel}$* orbital showed a comparable low occupation of 0.21 e^- for **6a** and 0.16 e^- for **6c***, nevertheless indicating overall a d^4 electron configuration. In contrast, the IBOs as obtained by DFT showed two σ-type

Table 2. Calculated Electronic Structures of Compounds 1, 2a, 4b, 6a, and 6c* in Comparison with the Known Nickel Alkyne Complex [Ni(dmpe)(η^2-PhCCPh)]

	[Ni(dmpe)(η^2-PhCCPh)]	**1** (Co)	**2a** (Fe)	**4b** (Mn)	**6a** (Cr)	**6c*** (Cr)
S	0	2/2	3/2	4/2	3/2	3/2
d-orbital population (QROs, IBOs)	d^{10}	d^7	d^6	d^5	d^4	d^4
C−C bond length [Å]	1.299	1.291	1.300	1.312	1.328	1.334
C−C−Ph angle [deg][a]	147	149	148	144	139	137
C−C bond stretching frequency [cm^{-1}]	1800	1840	1802	1743	1616	1647
metal character $\pi_{\parallel}$ α-IBO[b]	75%	82%	81%	77%	(53%, 40%)	(47%, 40%)[c]
metal character σ-type interaction, β-IBOs[a]	75%[d]	45%	39%	31%	33%	33%
hybridization C, σ-type interaction, β-IBOs[a]	$s^{0.38}p^3$	$s^{0.50}p^3$	$s^{0.54}p^3$	$s^{0.61}p^3$	$s^{0.82}p^3$	$s^{0.73}p^3$
CASSCF: metal character $\pi_{\parallel}$ (population in e^-)	n.a.	78% (1.78)	75% (1.76)	70% (1.74)	64% (1.81)	61% (1.86)

[a]Averaged value. [b]Only contributions from the metal and alkyne ligand. [c]Two orbitals of σ-symmetry and comparable shape with considerable extension onto the phenyl ligands were found. [d]α- and β-IBOs equivalent.

https://dx.doi.org/10.1021/acs.inorgchem.0c00365
Inorg. Chem. 2020, 59, 9521−9537

Scheme 8. Three Isomers (Planar and Perpendicular Position of Alkyne Ligand) Of Complex 6c* Are Predicted to Have Similar Energies

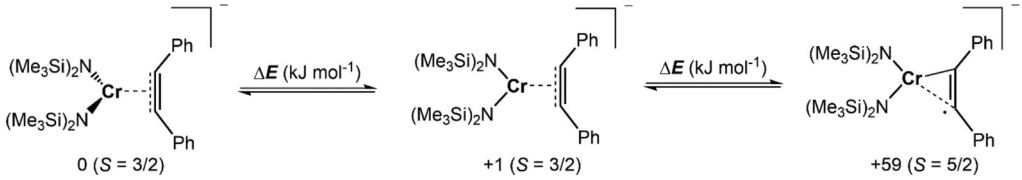

bonding interactions with each α- or β-spin with overall 4 electrons relating to an overlap of the chromium's d_{xy} orbital with two hybrid orbitals of the acetylene's carbon atoms (Figure 13).

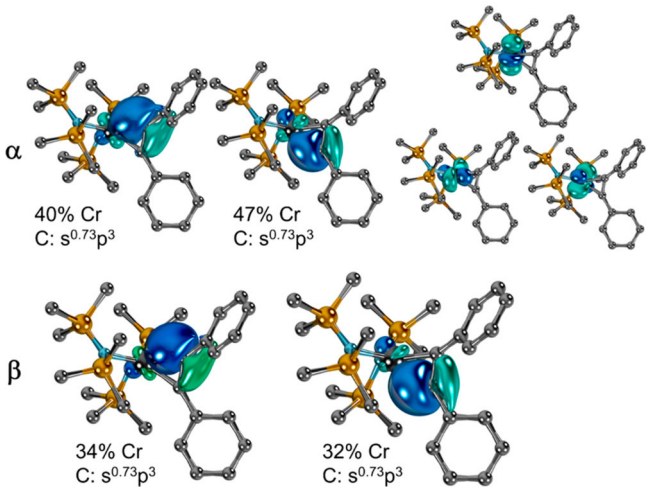

Figure 13. IBOs of **6c*** with considerable metal character (B3LYP). Hydrogen atoms are omitted for clarity.

These two hybrid orbitals at the carbon atoms are described as formally $s^{0.73}p^3$ hybridized and are very covalent (metal contribution: 32−47%). The BP86, PBE0, TPSSh, M06, and ωB97X-D3 functionals afford similar degrees of covalency with metal contributions in the range of 31−48% for **6c*** (Tables S15 − S20). In total, we tentatively assign the electronic structure of the metals in these complexes as d^4, chromium(II). However, in contrast to **1**, **2a**, and **4b**, the alkyne ligands in chromium complexes **6a** and **6c*** seem to share considerable bisanionic character, further leading to some d^3 chromium(III) character.

DISCUSSION

The reaction of anionic quasi-linear metal(I) silylamides with alkynes give in the first instance complexes with a side-on coordinated alkyne. The elongation of the central C−C bond is moderate for each alkyne complex (Table 3). Thereby, the degree of the elongation seems similar in the cases of cobalt, iron, and manganese and is slightly larger for chromium. The bond elongation is also reflected by the observation of a redshift of the corresponding stretching frequency for these complexes via IR spectroscopy. In the case of **3b**, such a band was not observed. This is not necessarily surprising given that the C≡C stretching frequency itself is IR-forbidden and can only be seen when the bond symmetry is lifted upon coordination or if it is coupled to another vibration (e.g., C≡C−C). In the case of chromium compound **6a**, a strong band was found at 1978 cm^{-1}. This would speak only for a slight C≡C bond activation for **6a** which contradicts structural data in solid state as well as the computational analysis. The origin of this IR band is thus unclear so far.

Obtained complexes are paramagnetic as indicated by their ^{1}H NMR spectroscopic signatures, which is corroborated by the determination of their magnetic susceptibility. Insights into the electronic structure of these complexes were gained by the computational analysis of the diphenylacetylene complexes of chromium to cobalt using DFT methods and CASSCF calculations. They suggest four nonbonding molecular orbitals centered at the metals ($d_{x^2-y^2}$, d_{z^2}, d_{yz}, d_{xy}) and one covalent interaction between the d_{xz}-orbital and the in-plane π^*-orbital of the alkyne. Depending on the nature of the metal, these nonbonding orbitals are sequentially occupied by six (Co), five (Fe), four (Mn), or three (Cr) electrons corroborating the observed paramagnetism of the presented complexes. Thus, an increase of the number of d-electrons populating these nonbonding orbitals has only a moderate impact on the C≡C bond activation, in agreement with structural and IR spectroscopic data. Thereby, a clear trend is found with an elongation of the C≡C bond and redshift of the corresponding IR band when going from cobalt to chromium. This is only partially reflected by the experimental data which can be attributed to solid state effects as well as the limited sample size. The back-bonding $\pi_{\|}$ orbital, which is composed of the d_{xz} orbital of the metal and the in-plane π^*-orbital of the alkyne, is covalent. It shows 70−82% metal contribution depending on the type of metal (Mn, Fe, and Co) as well as the computational method (DFT, CASSCF). CASSCF calculations predict only partial occupancy of the $\pi_{\|}$ and significant population of the antibonding, alkyne-centered $\pi_{\|}^*$ orbital by about one-fourth electron (cf., Table 2). Overall, the electronic structure could be

Table 3. Comparison of the Bond Length and Stretching Frequencies of the Side-On Bound Alkynes Found for Selected Metal(I) Alkyne Complexes in This Report[a]

compound	**1** (tolane)	**2a** (tolane)	**2b** (3-hexyne)	**2c** (4-octyne)	**3a** (tolane)	**3b** (3-hexyne)	**6a** (btmsa)
$d_{C\equiv C}$ (Å)	1.284(8)	1.269(5)	1.283(6)	1.272(3)	1.271(4)	1.2739(1)	1.312(8)
$\Delta d_{C\equiv C}$ (Å)	0.08	0.07	0.08	0.07	0.07	0.07	0.10
$\nu_{C\equiv C}$ (cm^{-1})	1820	1787	1824	1820	1789	n.d.	(1978)
$\Delta\nu_{C\equiv C}$ (cm^{-1})	405	438	401	450	436	n.d.	(131)

[a]n.d. = not detected.

https://dx.doi.org/10.1021/acs.inorgchem.0c00365
Inorg. Chem. 2020, 59, 9521−9537

Scheme 9. Important Resonance Structures of the Presented Metal Alkyne Complexes

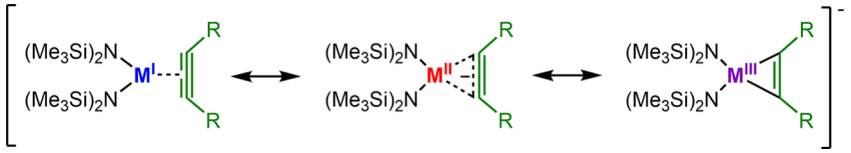

understood as metal(II) ions bound to an anionic alkyne ligand with moderate radical character at the alkyne ligand. In the case of chromium, this situation becomes more pronounced, with very covalent $\pi_{\parallel}$ and $\pi_{\parallel}$ * interactions and accordingly non-negligible contributions from a metal(III) cyclopropene description. Comparative calculations conducted for an alkyne coordinate nickel bisphosphine complex [Ni(dmpe)(η^2-PhCCPh)] corroborate for this also previously studied case a d^{10} electron configuration without formal reduction of the alkyne ligand.

In light of these results, it becomes clear that for these complexes strong back-bonding goes in line with high covalency and considerable population of the antibonding $\pi_{\parallel}$* orbital. Overall, this picture corresponds to formal $1e^-$ reduction of the alkyne ligands. Thus, in the much simplified language of resonance structures, the electronic situation of the covalently bound alkyne ligands in these silyl amide complexes seems to share some three-center−three-electron ($3c-3e^-$) character (Scheme 9; cf., Figures 11−13 and Scheme 8) leading to radical reactivity at the alkyne ligand (cf., Figure 11). Depending on the metal and alkyne substituents, the delocalization of spin density on the alkyne can however accumulate up to the point of the formation of a vinyl radical or even beyond (i.e., considerable metallacyclopropene character).

These findings highlight the continuum between formally anionic ("X-type") as well as formally neutral ("L-type") ligands for alkynes. Furthermore, they rationalize the radical reactivity at the alkyne ligand as well as the facile loss of the anionic silylamide ligands and the subsequent redox state redistributions. Eventually, we conclude that the covalent nature of the metal/alkyne bond does not necessarily transfer to its stability, as for the manganese and cobalt complexes the swift dissociation of the alkyne was observed.

CONCLUSION

In conclusion, using quasi-linear, anionic metal(I) silylamides as precursors we synthesized and characterized a variety of rare (Cr, Fe, and Co) and, in the case of manganese first, examples of low-coordinate metal alkyne complexes. The elongation of the central C−C bond of the alkyne ligands is moderate, ranging from 1.31 Å for chromium to 1.27 Å for iron. For cobalt, the metal−alkyne interaction is very weak, and an equilibrium between the starting metal(I) compound $[Co^{I}(N(SiMe_3)_2)_2]^-$ and the respective cobalt alkyne complex is obtained. In contrast, the analogous iron alkyne complexes are thermodynamically stable. For a sterically encumbered manganese silylamide ($[Mn(N(Dipp)SiMe_3)_2]^-$), labile alkyne coordination is observed, whereas the smaller manganese(I) hexamethyldisilazanide $[Mn(N(SiMe_3)_2)_2]^-$ effectuated a variety of C−C triple bond activation processes. These range from side-on coordination, $2e^-$ reduction of the alkyne to alkyne trimerization. This happens under oxidation state redistribution of the employed manganese(I) hexamethyldisilazanide as well as ligand exchange, stressing the lability of manganese(I) hexamethyldisilazide. For the chromium(I) complex $[Cr(N(SiMe_3)_2)_2]^-$, the reaction with alkynes gave either a side-on complex or 2-fold substrate reduction.

Computational assessment of the side-on complexes indicate that the alkynes are covalently bound to the metals in their +II oxidation state and share alkynyl radical anion character due to the partial population of the in-plane π* orbital. This differs from the classical dichotomy of the description as either π-alkyne or cyclopropane complexes and seems to be a result of the high-spin character of these complexes. The radical anion character found for the metal bound alkyne explains the formation of bismetalated products and overall hints at new opportunities to use alkynes as building blocks in organic synthesis. Ongoing studies focus on further spectroscopic examination as well as synthetic exploitation of this activation mode.

EXPERIMENTAL SECTION

Materials and Methods. All manipulations were carried out in a glovebox under a dry argon atmosphere, unless indicated otherwise. Used solvents were dried by continuous distillation over sodium metal for several days, degassed via three freeze−pump−thaw cycles and stored over 4 Å molecular sieves. Deuterated solvents were used as received, degassed via three freeze−pump cycles, and stored over 4 Å molecular sieves. ^{1}H NMR spectra were recorded on a Bruker AV 500, a Bruker HD 500, or a Bruker HD 300 NMR spectrometer (Bruker Corporation, Billerica, USA). Chemical shifts are reported in ppm relative to the residual proton signals of the solvent (for ^{1}H). $w_{1/2}$ is the line width of a signal at half its maximum intensity. Integrals of the broad signals of the $N(SiMe_3)_2$ units were obtained directly or by peak-fitting (in the case of overlapping signals) using the MestreNova software package (Mestrelab, Santiago de Compostela, Spain). Solution magnetic susceptibilities were determined by the Evans method.[95,96] IR measurements were conducted on a Bruker Alpha ATR-IR spectrometer (Bruker Corporation, Billerica, USA). The UV/vis measurements were recorded on an AnalytikJena Specord S600 using WinASPECT software. Elemental analyses were performed by the "in-house" service of the Chemistry Department of Philipps-University Marburg, Germany, using a CHN(S) analyzer vario MICRO Cube (Elementar Analysensysteme GmbH, Langenselbold, Germany). $[Mn(N(SiMe_3)_2)_2]$,[97] $[Cr(N(SiMe_3)_2)_2(thf)_2]$,[98] and K{18c6}[M(N-$(SiMe_3)_2)_2$] (Fe and Co)[43,44] were prepared according to literature procedures. K{18c6}$[M(N(SiMe_3)_2)_2]$ (Cr and Mn) was synthesized according to the published procedure for K{18c6}$[Mn(N(SiMe_3)_2)_2]$ and reacted *in situ* with the respective alkynes without intermittent isolation.[43]

Synthesis and Characterization. *[K{18c6}][Co(N(SiMe$_3$)$_2$)$_2$(η^2-PhCCPh)] (1).* [K{18c6}][Co(N(SiMe$_3$)$_2$)$_2$] (68.3 mg, 0.10 mmol, 1.0 equiv) was dissolved in 3 mL of Et_2O. Addition of diphenylacetylene (17.8 mg, 0.10 mmol, 1.0 equiv) led to an immediate color change from pale green to dark red. After stirring for 5 min, the solution was layered with 3 mL of pentane. Storing the solution at −35° for days yielded a dark red crystalline solid. The supernatant solution was removed via a Pasteur pipet. Washing of the residue with 2 × 5 mL of pentane and drying under reduced pressure afforded **1** as a dark red crystalline solid (79.7 mg, 0.093 mmol, 93%). ^{1}H NMR (THF-d_8, 300.1 MHz, 298 K, ppm): δ = −7.62 (bs, 2H, $w_{1/2}$ = 54 Hz, CH_{tolane}), −5.39 (s, 36H, $w_{1/2}$ = 16 Hz, Si(CH_3)$_3$), 3.19 (s, 24H, $w_{1/2}$ = 5 Hz, OCH_2), 8.54 (s, 4H, $w_{1/2}$ = 73 Hz, CH_{tolane}), 26.06 (s, 4H, $w_{1/2}$ = 35 Hz, CH_{tolane}). IR (ATR, cm^{-1}): ν = 2941 (m), 2887 (m), 1819 (w, $\delta_{C\equiv C}$), 1589 (w), 1472 (m), 1453 (m), 1365 (m), 1351 (m), 1231 (s), 1107 (vs), 961 (s), 886 (s), 866

https://dx.doi.org/10.1021/acs.inorgchem.0c00365
Inorg. Chem. 2020, 59, 9521−9537

(s), 822 (vs), 775 (m), 755 (m), 697 (m), 655 (m), 607 (m), 544 (w). Elemental analysis calcd ($C_{38}H_{70}CoKN_2O_6Si_4$ 861.36 g/mol) C 52.99, H 8.19, N 3.25. Exp C 52.94, H 7.94, N 3.52. As the magnetic moment in solution could not be directly determined due the solution equilibrium between complex **1** and the cobalt(I) precursor, the measurement was performed in the presence of additional 5 equiv of tolane. μ_{eff} = 3.16 μ_B (Evans, THF-d_8 + 1% TMS, 500.1 MHz, 300 K, 5 equiv of tolane). $\mu_{s.o.}(S = 1)$ = 2.82 μ_B. Crystals suitable for X-ray diffraction analysis were obtained from a pentane-layered solution of **1** in Et_2O at −35 °C.

*[K{18c6}][Fe(N(SiMe$_3$)$_2$)$_2$(η^2-PhCCPh)] (**2a**).* [K{18c6}][Fe(N(SiMe$_3$)$_2$)$_2$] (68.0 mg, 0.10 mmol, 1.0 equiv) was dissolved in 3 mL of Et_2O. Addition of diphenylacetylene (17.8 mg, 0.10 mmol, 1.0 equiv) led to an immediate color change from brownish green to dark red. After stirring for 5 min, the solution was layered with 3 mL of pentane. Storing the solution at −35 °C for days yielded a dark red crystalline solid. The supernatant solution was removed via a Pasteur pipet. Washing of the residue with 2 × 5 mL of pentane and drying it under reduced pressure afforded compound **2a** as a dark red crystalline solid (53.8 mg, 0.06 mmol, 61%). ^{1}H NMR (THF-d_8, 500.3 MHz, 298 K, ppm): δ = −4.61 (s, 4H, $w_{1/2}$ = 45 Hz, CH_{tolane}), −1.88 (bs, 36H, $w_{1/2}$ = 363 Hz Si(CH_3)$_3$), 3.58 (s, 24H, OCH_2), 5.19 (s, 2H, $w_{1/2}$ = 24 Hz, CH_{tolane}), 7.49 (bs, 4H, $w_{1/2}$ = 787 Hz, CH_{tolane}). IR (ATR, cm^{-1}): ν = 2941 (m), 2888 (m), 2825 (w), 1787 (w, $\delta_{C\equiv C}$), 1589 (m), 1484 (w), 1472 (w), 1453 (m), 1351 (w), 1283 (w), 1231 (s), 1104 (vs), 1063 (w), 962 (vs), 887 (vs), 822 (m), 776 (m), 762 (m), 706 (m), 695 (m), 657 (s), 608 (m), 529 (w). Elemental analysis calcd ($C_{40}H_{76}FeKN_2O_6Si_4$ 836.22 g/mol) C 53.18, H 8.22, N 3.26. Exp C 52.69, H 7.92, N 3.41. μ_{eff} = 4.97 μ_B (Evans, THF-d_8 + 1% TMS, 300.1 MHz, 300 K). $\mu_{s.o.}(S = 3/2)$ = 3.87 μ_B. Crystals suitable for X-ray diffraction analysis were obtained from a pentane-layered solution of compound **2a** in Et_2O at −35 °C.

*[K{18c6}][Fe(N(SiMe$_3$)$_2$)$_2$(η^2-EtCCEt)] (**2b**).* K{18c6}][Fe(N(SiMe$_3$)$_2$)$_2$] (68.0 mg, 0.10 mmol, 1.0 equiv) was dissolved in 3 mL of Et_2O. Addition of 3-hexyne (8.1 mg, 0.10 mmol, 1.0 equiv) led to an immediate color change from brownish green to dark red. After stirring for 5 min, the solution was layered with 3 mL of pentane. Storing the solution at −35 °C for days yielded a dark red crystalline solid. The supernatant solution was removed via a Pasteur pipet. Washing of the residue with 2 × 5 mL of pentane and drying it under reduced pressure afforded compound **2b** as a light red crystalline solid (56.7 mg, 0.074 mmol, 74%). ^{1}H NMR (THF-d_8, 500.3 MHz, 298 K, ppm): δ = −6.46 (s, 6H, $w_{1/2}$ = 232 Hz, CH_{hex}), −3.31 (s, 36H, $w_{1/2}$ = 326 Hz, Si(CH_3)$_3$), 3.58 (s, 24H, OCH_2), 24.46 (s, 4H, $w_{1/2}$ = 708 Hz, CH_{hex}). IR (ATR, cm^{-1}): ν = 2941 (m), 2903 (m), 2827 (w), 1824 (w, $\delta_{C\equiv C}$), 1474 (w), 1454 (w), 1433 (m), 1351 (w), 1284 (w), 1229(s), 1103 (vs), 1005 (vs), 962 (vs), 892 (w), 870 (m), 819 (vs), 774 (m), 749 (m), 706 (w), 656 (s), 606 (m), 529 (w). Elemental analysis calcd ($C_{30}H_{70}FeKN_2O_6Si_4$ 762.18 g/mol) C 47.28, H 9.11, N 3.68. Exp C 46.82, H 8.95, N 3.63. μ_{eff} = 5.08 μ_B (Evans, THF-d_8 + 1% TMS, 500.1 MHz, 300 K). $\mu_{s.o.}(S = 3/2)$ = 3.87 μ_B. Crystals suitable for X-ray diffraction analysis were obtained from a pentane-layered solution of compound **2b** in Et_2O at −35 °C.

*[K{18c6}][Fe(N(SiMe$_3$)$_2$)$_2$(η^2-^{n}PrCC^{n}Pr)] (**2c**).* K{18c6}][Fe(N(SiMe$_3$)$_2$)$_2$] (68.0 mg, 0.10 mmol, 1.0 equiv) was dissolved in 3 mL of Et_2O. Addition of 4-octyne (11.0 mg, 0.10 mmol, 1.0 equiv) led to an immediate color change from brownish green to dark red. After stirring for 5 min, the solution was layered with 3 mL of pentane. Storing the solution at −35 °C for days yielded a dark red crystalline solid. The supernatant solution was removed via a Pasteur pipet. Washing of the residue with 2 × 5 mL of pentane and drying it under reduced pressure afforded compound **2c** as a dark red crystalline solid (43.3 mg, 0.055 mmol, 55%). ^{1}H NMR (THF-d_8, 500.3 MHz, 298 K, ppm): δ = −3.26 (s, 36H, $w_{1/2}$ = 312 Hz, Si(CH_3)$_3$), −0.12 (s, 2H, $w_{1/2}$ = 39 Hz, CH_{oct}), 0.89 (s, 2H, $w_{1/2}$ = 39 Hz, CH_{oct}), 1.30 (s, 2H, $w_{1/2}$ = 57 Hz, CH_{oct}), 3.58 (s, 24H, OCH_2), 14.38 (s, 2H, $w_{1/2}$ = 700 Hz, CH_{oct}). IR (ATR, cm^{-1}): ν = 2938 (m), 2895 (m), 2821 (w), 1820 (w, $\delta_{C\equiv C}$), 1472 (w), 1454 (w), 1350 (w), 1283 (w), 1228 (s), 1104 (vs), 1005 (s), 962 (s), 890 (m), 868 (m), 820 (vs), 774 (m), 748 (m), 706 (w), 656 (s), 607 (m), 530 (w). Elemental analysis calcd ($C_{32}H_{74}FeKN_2O_6Si_4$ 790.36 g/mol) C 48.64, H 9.44, N 3.55. Exp C 48.00, H 9.01, N 3.50. μ_{eff} = 6.18 μ_B (Evans, THF-d_8 + 1% TMS, 500.1 MHz, 300 K). $\mu_{s.o.}(S = 3/2)$ = 3.87 μ_B. Crystals suitable for X-ray diffraction analysis were obtained from a pentane-layered solution of compound **2c** in Et_2O at −35 °C.

*[K{18c6}][Mn(N(Dipp)(SiMe$_3$))$_2$(η^2-PhCCPh)] (**3a**).* K{18c6}][Mn(N(Dipp)(SiMe$_3$))$_2$] (42.76 mg, 0.05 mmol, 1.0 equiv) was dissolved in in 3 mL of THF. Addition of diphenylacetylene (8.90 mg, 0.05 mmol, 1.0 equiv) led to an immediate color change from dark violet to dark yellow. After stirring for 5 min, the solution was layered with 3 mL of pentane. Storing the solution at −35 °C for days yielded a dark yellow crystalline solid. The solution was removed via a Pasteur pipet. Washing of the residue with 2 × 5 mL of pentane and drying it under reduced pressure afforded compound **3a** as a dark yellow crystalline solid (33.7 mg, 0.033 mmol, 65%). ^{1}H NMR (THF-d_8, 300.3 MHz, 298 K, ppm): No useful signal attribution possible. IR (ATR, cm^{-1}): ν = 3039 (w), 2949 (w), 2911 (w), 2861 (w), 1789 (w, $\delta_{C\equiv C}$), 1586 (m), 1471 (w), 1420 (m), 1351 (m), 1283 (m), 1236 (s), 962 (s), 880 (m), 829 (vs), 774 (m), 761 (m), 736 (m), 695 (m), 662 (w), 613 (w), 568 (w), 528 (w) 500 (w), 435 (m). Elemental analysis calcd ($C_{56}H_{86}MnKN_2O_6Si_2$ 1033.52 g/mol) C 65.08, H 8.39, N 2.71. Exp C 64.73, H 8.14, N 3.27. μ_{eff} = 4.63 μ_B (Evans, THF-d_8 + 1% TMS, 500.1 MHz, 300 K). $\mu_{s.o.}(S = 2)$ = 4.89 μ_B. Crystals suitable for X-ray diffraction analysis were obtained from a pentane-layered solution of compound **3a** in THF at −35 °C.

*[K{18c6}][Mn(N(Dipp)(SiMe$_3$))$_2$(η^2-EtCCEt)] (**3b**).* [K{18c6}][Mn(N(Dipp)(SiMe$_3$))$_2$] (42.76 mg, 0.05 mmol, 1.0 equiv) and 3-hexyne (4.05 mg, 0.05 mmol, 1.0 equiv) were dissolved in 3 mL of THF, which led to an immediate color change from dark violet to dark red. After stirring for 5 min, the solution was layered with 3 mL of pentane. Storing the solution at −35 °C for days yielded a dark red crystalline solid. The solution was removed via a Pasteur pipet. Washing of the residue with 2 × 5 mL of pentane and drying it under reduced pressure afforded compound **3b** as a dark red crystalline solid (19.0 mg, 0.02 mmol, 41%). ^{1}H NMR (THF-d_8, 300.3 MHz, 298 K, ppm): No useful signal attribution possible. IR (ATR, cm^{-1}): ν = 2947 (w), 2889 (w), 1582 (w), 1453 (w), 1417 (m), 1351 (m), 1313 (m), 1235 (s), 1194 (w), 1104 (vs), 988 (w), 961 (m), 921 (m), 828 (s), 773 (s), 738 (m), 663 (m), 615 (w), 530 (w) 500 (w), 428 (w). Elemental analysis calcd ($C_{48}H_{86}MnKN_2O_6Si_2$ 937.43 g/mol) C 61.50, H 9.25, N 2.99. Exp C 58.13 H 8.90, N 2.50. No matching C value could be obtained, even when using freshly prepared, crushed crystals. An approximately 3.5% lower value was always observed (>4 tries). μ_{eff} = 3.28 μ_B (Evans, THF-d_8 + 1% TMS, 500.1 MHz, 300 K). $\mu_{s.o.}(S = 2)$ = 4.89 μ_B. Crystals suitable for X-ray diffraction analysis were obtained from a pentane-layered solution of compound **3b** in THF at −35 °C.

*[K{18c6}]$_2$[Mn$_2$(N(SiMe$_3$)$_2$)$_2$(μ-N(SiMe$_3$)$_2$)(μ-η^2-Me$_3$SiCCSiMe$_3$)] (**4a**).* Mn(N(SiMe$_3$)$_2$)$_2$ (37.6 mg, 0.10 mmol, 1.0 equiv) and 18-crown-6 (31.8 mg, 0.105 mmol, 1.05 equiv) were dissolved in 3 mL of Et_2O. Addition of KC_8 (20.2 mg. 0.15 mmol, 1.5 equiv) led to an immediate color change to dark violet. After stirring for 5 min, the mixture was filtered, and the filtrate was added to bis(trimethylsilyl)acetylene (17.8 mg, 0.10 mmol, 1.0 equiv), leading to an immediate color change to dark red. The solution was stirring for 5 min and layered with 3 mL of pentane. Storing the solution at −35° for days yielded a dark red crystalline solid. The supernatant solution was removed via pipet. Washing of the residue with 2 × 5 mL of pentane and drying it afforded **4a** as a dark red crystalline solid. Determination of the yield of **4a** and further analysis was not possible because of complex sensitivity and presence of (decomposition) products **5** and [K{18c6}][N(SiMe$_3$)$_2$]. Crystals suitable for X-ray diffraction analysis were directly obtained from the reaction mixture.

*[K{18c6}$_{1.5}$][Mn(N(SiMe$_3$)$_2$)$_2$(η^2-PhCCPh)] (**4b**).* Mn(N(SiMe$_3$)$_2$)$_2$ (37.6 mg, 0.10 mmol, 1.0 equiv) and 18-crown-6 (31.8 mg, 0.105 mmol, 1.05 equiv) were dissolved in 3 mL of Et_2O. Addition of KC_8 (20.2 mg. 0.15 mmol, 1.5 equiv) led to an immediate color change to dark violet. After stirring for 5 min, the mixture was filtered and the filtrate was added to diphenylacetylene (17.8 mg, 0.10 mmol, 1.0 equiv), leading to an immediate color change to dark red. The solution was stirred for 5 min and layered with 3 mL of pentane. Storing the solution at −35° for days yielded a mixture of colorless (**5**) and dark red

https://dx.doi.org/10.1021/acs.inorgchem.0c00365
Inorg. Chem. 2020, 59, 9521−9537

(**4b**) crystals. Determination of the yield of **4b** and further analysis was not possible because of complex sensitivity and presence of decomposition product **5**. Crystals suitable for X-ray diffraction analysis were directly obtained from the reaction mixture. During crystallization, small amounts of yellowish crystals were observed, which were identified as $[K\{18c6\}]_2[(Mn(N(SiMe_3)_2)_2)_2(\mu\text{-}PhCCPh\text{-}1\kappa C^1{:}2\kappa C^2)]$, **4c**.

*[K{18c6}][Mn(η⁶-Ph₆C₆)(η²-PhCCPh)] (**4d**).* $Mn(N(SiMe_3)_2)_2$ (37.6 mg, 0.10 mmol, 1.0 equiv) and 18-crown-6 (31.8 mg, 0.105 mmol, 1.05 equiv) were dissolved in 3 mL of Et_2O. Addition of KC_8 (20.2 mg. 0.15 mmol, 1.5 equiv) led to an immediate color change to dark violet. After stirring for 5 min, the mixture was filtered, and the filtrate was added to diphenylacetylene (17.8 mg, 0.10 mmol, 1.0 equiv), leading to an immediate color change to dark red. The solution was stirred for 5 min and layered with 3 mL of pentane. After storing the mixture at room temperature for a few days, a mixture of colorless (**5**) and dark red (**4d**) crystals could be obtained. Determination of the yield of **4d** and further analysis was not possible because of complex sensitivity and presence of (decomposition) product **5**.

*[K{18c6}][Mn(N(SiMe₃)₂)₃] (**5**).* $Mn(N(SiMe_3)_2)_2$ (37.6 mg, 0.10 mmol, 1.0 equiv), 18-crown-6 (26.3 mg, 0.10 mmol, 1.0 equiv), and $K(N(SiMe_3))$ (19.9 mg. 0.1 mmol, 1.0 equiv) were dissolved in 3 mL of Et_2O. After stirring for 5 min, the mixture was filtered and layered with 3 mL of pentane. Storing the solution at −35° for days yielded a clear colorless crystalline solid. The solution was removed via a Pasteur pipet. Washing of the residue with 2 × 5 mL of pentane and drying under reduced pressure afforded **5** as a colorless crystalline solid (56.9 mg, 0.07 mmol, 70%). ^{1}H NMR (THF-d_8, 300.1 MHz, 298 K, ppm): No useful signal attribution possible. IR (ATR, cm^{-1}): ν = 2941 (w), 2894 (w), 1472 (w), 1454 (w), 1350 (w), 1283 (w), 1233 (m), 1105 (vs), 1056 (w), 1000 (vs), 963 (s), 869 (m), 822 (vs), 774 (m), 748 (m), 702 (m), 659 (m), 607 (m), 529 (w). Elemental analysis calcd ($C_{29}H_{75}MnKN_3O_6Si_4$824.48 g/mol) C 42.25, H 9.17, N 5.10. Exp C 42.69, H 9.06, N 4.87. μ_{eff} = 5.66 μ_B (Evans, THF-d_8 + 1% TMS, 500.1 MHz, 298 K). $\mu_{s.o.}(S = 5/2)$ = 5.91 μ_B.

*[K{18c6}][Cr(N(SiMe₃)₂)₂(η²-Me₃SiCCSiMe₃)] (**6a**).* $Cr(N(SiMe_3)_2)_2$*$(THF)_2$ (51.7 mg, 0.10 mmol, 1.0 equiv) and 18-crown-6 (31.8 mg, 0.105 mmol, 1.05 equiv) were dissolved in 3 mL of Et_2O. Addition of KC_8 (20.2 mg. 0.15 mmol, 1.5 equiv) led to an immediate color change to dark greenish orange. After stirring for 5 min, the mixture was filtered, and the filtrate was added to bis(trimethylsilyl)-acetylene (17.1 mg, 0.10 mmol, 1.0 equiv), leading to an immediate color change to dark red. The solution was stirred for 5 min and layered with 3 mL of pentane. Storing the solution at −35° for days yielded a dark red crystalline solid. The supernatant solution was removed via pipet. Washing of the residue with 2 × 5 mL of pentane and drying it afforded **6a** as a dark red crystalline solid (37.8 mg, 0.045 mmol, 45%). ^{1}H NMR (THF-d_8, 300.1 MHz, 298 K, ppm): No useful signal attribution possible. IR (ATR, cm^{-1}): ν = 2944 (w), 2887 (w), 1978 (w, $\delta_{C\equiv C}$), 1473 (w), 1453 (w), 1351 (m), 1284 (m), 1233 (m), 1104 (vs), 995 (m), 960 (m), 918 (m), 820 (vs), 749 (m), 683 (m), 657 (m), 601 (w), 529 (w), 461 (w). Elemental analysis calcd ($C_{32}H_{78}CrKN_2O_6Si_4$ + Et_2O 920.71 g/mol) C 46.96, H 9.63, N 3.04. Exp C 46.55, H 8.83, N 2.94. μ_{eff} = 3.44 μ_B (Evans, THF-d_8 + 1% TMS, 500.1 MHz, 298 K). Crystals suitable for X-ray diffraction analysis were obtained from a pentane-layered solution of **6a** in Et_2O at −35 °C.

*[K{18c6}]₂[Cr₂(N(SiMe₃)₂)₂(μ-N(SiMe₃)₂)(μ-PhCCPh-1κC¹,2κC²)] (**6b**).* $[Cr(N(SiMe_3)_2)_2$*$(thf)_2]$ (51.7 mg, 0.10 mmol, 1.0 equiv) and 18-crown-6 (31.8 mg, 0.105 mmol, 1.05 equiv) were dissolved in 3 mL of Et_2O. Addition of KC_8 (20.2 mg. 0.15 mmol, 1.5 equiv) led to an immediate color change to dark orange. After stirring for 5 min, the mixture was filtered, and the filtrate was added to diphenylacetylene (17.8 mg, 0.10 mmol, 1.0 equiv), leading to an immediate color change to dark red. The solution was stirred for 5 min and layered with a few drops of pentane. Storing the solution at −35 °C for days yielded a dark red crystalline solid. The solution was removed via a Pasteur pipet. Washing of the residue with 2 × 5 mL of pentane and drying it under reduced pressure afforded compound **6b** as a dark red crystalline solid (12.5 mg, 0.012 mmol, 23%). The low yield is due to the use of only small of amounts of pentane in order to avoid the concomitant crystallization of either **5** or $K\{18c6\}[N(SiMe_3)_2]$. ^{1}H NMR (THF-d_8, 300.1 MHz, 298 K, ppm): No useful signal attribution possible. IR (ATR, cm^{-1}): ν = 2937 (m), 2890 (m), 1581 (w), 1470 (m), 1453 (w), 1351 (m), 1282 (m), 1236 (m), 1102 (vs), 960 (s), 881 (vs), 815 (m), 764 (m), 669 (m), 649 (m), 601 (m), 529 (w). Elemental analysis calcd ($C_{44}H_{88}Cr_2KN_3O_6Si_6$ 1066.80 g/mol) C 49.54, H 8.31, N 3.94. Exp C 49.40, H 7.98, N 3.49. μ_{eff} = 2.86 μ_B (Evans, THF-d_8 + 1% TMS, 500.1 MHz, 298 K).). Crystals suitable for X-ray diffraction analysis were obtained from a pentane-layered solution of compound **6b** in Et_2O at −35 °C.

X-ray Diffraction Analysis. Data for compounds **1** (CCDC 1979591), **3a** (CCDC 1979598), **3b** (CCDC 1979601), **4a** (CCDC 1979603), **4c** (CCDC 1979627), and **4d** (CCDC 1979655) were collected at 100 K on a Bruker Quest D8 diffractometer (Bruker Corporation, Billerica, USA) using Incoatec Microfocus Source Mo Kα radiation and equipped with an Oxford Instrument Cooler Device (Oxford Instruments, Abingdon, UK) and Photon 100 detector. Data for compounds **4b** (CCDC 1979606) and **6b** (CCDC 1979685) were collected at 100 K on a STOE IPDS2 diffractometer (STOE & Cie GmbH, Darmstadt, Germany), and data for compound **2b** (CCDC 1979595), **2c** (CCDC 1979596), and **6a** (CCDC 1979663) were collected at 100 K on a STOE IPDS2T diffractometer using graphite-monochromated Mo Kα radiation (λ = 0.71073 Å) and equipped with an Oxford Instrument Cooler Device (Oxford Instruments, Abingdon, UK). Data for compound **2a** (CCDC 1979594) were collected at 100 K on a STOE StadiVari diffractometer using Xenocs Microfocus Source Cu Kα radiation (λ = 1.54186 Å) equipped with an Oxford Instrument Cooler Device (Oxford Instruments, Abingdon, UK) and a Dectris Pilatus 300 K. The structures have been solved using either OLEX SHELXT V2014/1[99] and refined by means of least-squares procedures on an F^2 with the aid of the program SHELXL-2016/6[100] included in the software package WinGX version 1.63[101] or using CRYSTALS.[102] The atomic scattering factors were taken from International Tables for X-ray Crystallography.[103] All non-hydrogen atoms were refined anisotropically. All hydrogens atoms were refined by using a riding model. Absorption corrections were introduced by using the MULTI-SCAN and X-Red programs.[104,105] Drawings of molecules are performed with the program DIAMOND (Crystal Impact, Bonn, Germany) with 50% probability displacement ellipsoids for non-H atoms. Additional details are given in the Supporting Information.

Calculations. All calculations were performed with ORCA v. 4.0.1.[78,79] The structural parameters were optimized with the B3LYP,[80−83,106] B3PW91,[80,81] BP86,[81,107] PBEh-3c,[108] and B97-3c[109] functionals starting from the solid-state geometries (**6c*** from **6a**) using the def2-TZVP basis set for the metals and the def2-SVP basis set for all other atoms.[110] Dispersion effects were accounted for, where applicable, by Grimme's D3 correction with Becke−Johnson (BJ) damping.[111] The optimized geometric parameters were verified as true minima by the absence of negative eigenvalues in the harmonic vibrational frequency analysis. The B3LYP functional gave the best fit with the experimental structures in the solid state (Table S13) and a good fit with the experimental CC bond stretching frequencies. Stretching frequencies reported in the manuscript are scaled by 0.959 as suggested by Truhlar,[112] whereas the values reported in the Supporting Information are unscaled. Test calculations using the ma-def2-SVP (ma-def2-TZVP on the metals, respectively) basis set[113] suggest that additional diffuse functions do not to improve the fit with the experimental solid-state structures, whereas a moderate improvement was observed for the CC stretching frequency (Table S14). The RIJCOSX approximation[114,115] with the related auxiliary basis set def2/J was used to speed up the calculations.[116] Tighter-than-default scf ("*tightscf*") and optimization ("*tightopt*") criteria were chosen in conjunction with finer-than-default grid values ("*grid6*"; "*nofinalgrid*"). The B3LYP optimized structural parameters were used for further single-point calculations (functional/def2-TZVPP//B3LYP-D3BJ/def2/SVP) in order to obtain the intrinsic bond orbitals (IBOs)[88] and quasi-restricted orbitals (QROs).[89] The compositions of the IBOs and QROs were assessed by the reduced Löwdin[90] scheme. The B3LYP, B3PW91, BP86, M06,[117,118] TPSSh,[119] and ωB97XD3[120] functionals were evaluated (Tables S15−S19). The CASSCF

https://dx.doi.org/10.1021/acs.inorgchem.0c00365
Inorg. Chem. 2020, 59, 9521−9537

calculations were also performed with the def2-TZVPP basis set on all atoms. The active spaces were chosen according to Figure 11 to include all d-orbitals and ligand based orbitals related to the Dewar-Chatt-Duncanson model (i.e., CAS(12,9) for **1**, CAS(11,9) for **2a**, CAS(10,9) for **4b**, and CAS(9,9) for **6a** and **6b**). All reported energies were corrected by second-order perturbation theory (NEVPT2)[121] without the frozen core approximation ("*nofrozencore*"). Inclusion of scalar relativistic effects with the "zeroth-order regular approximation" (ZORA)[122,123] with the related basis- and auxiliary basis set (ZORA-def2-TZVPP; SARC/J) led to essentially equivalent energies (ΔE < 0.003 eV) of the five energetically lowest states. In order to evaluate the energetic order of the various spin states, state-averaged calculations (**1**: s, t, q; 1, 5, 5 roots; **2a**: d, q, s: 3, 5, 5 roots; **4b**: s, t, q, s: 3, 5, 5, 1 roots; **6a**, **6b**: d, q, s: 3, 5, 5 roots) were performed. The orbitals shown in Figure 11 relate to the ground state only. Molecular orbitals were visualized with IBOView[88] and Chemcraft (https://www.chemcraftprog.com).

■ ASSOCIATED CONTENT

Supporting Information

The Supporting Information is available free of charge at https://pubs.acs.org/doi/10.1021/acs.inorgchem.0c00365.

^{1}H NMR, IR, and UV/vis spectra of all isolated compounds as well as crystallographic and computational details (PDF)

Cartesian coordinates (XYZ)

Accession Codes

CCDC 1979591, 1979594−1979596, 1979598, 1979601, 1979603, 1979606, 1979627, 1979655, 1979663, and 1979685 contain the supplementary crystallographic data for this paper. These data can be obtained free of charge via www.ccdc.cam.ac.uk/data_request/cif, or by emailing data_request@ccdc.cam.ac.uk, or by contacting The Cambridge Crystallographic Data Centre, 12 Union Road, Cambridge CB2 1EZ, UK; fax: +44 1223 336033.

■ AUTHOR INFORMATION

Corresponding Author

C. Gunnar Werncke − *Department of Chemistry, Philipps-University Marburg, 35043 Marburg, Germany;* orcid.org/0000-0002-9963-8391; Email: gunnar.werncke@chemie.uni-marburg.de

Authors

Igor Müller − *Department of Chemistry, Philipps-University Marburg, 35043 Marburg, Germany*

Dominik Munz − *Inorganic Chemistry: Coordination Chemistry, Saarland University, 66123 Saarbrücken, Germany; Inorganic and General Chemistry, Friedrich-Alexander University Erlangen-Nürnberg, 91058 Erlangen, Germany;* orcid.org/0000-0003-3412-651X

Complete contact information is available at: https://pubs.acs.org/10.1021/acs.inorgchem.0c00365

Author Contributions

I.M. performed the synthetic studies, D.M. carried out the computations, and C.G.W. designed and supervised the project. The manuscript was written through contributions of all authors. All authors have given approval to the final version of the manuscript.

Funding

The work was funded by the DFG (grant 5627/4−1 for C.G.W.).

Notes

The authors declare no competing financial interest.

■ ACKNOWLEDGMENTS

We acknowledge the Department of Chemistry of Philipps-University for support. We thank K. Beuthert for assistance. D.M. thanks the Fonds der Chemischen Industrie for a Liebig fellowship, K. Meyer for his continuous support, and the RRZ Erlangen for computational resources.

■ REFERENCES

(1) Gibson, S. E.; Stevenazzi, A. The Pauson-Khand reaction: the catalytic age is here! *Angew. Chem., Int. Ed.* **2003**, *42*, 1800−1810.

(2) Khand, I. U.; Knox, G. R.; Pauson, P. L.; Watts, W. E. A cobalt induced cleavage reaction and a new series of arenecobalt carbonyl complexes. *J. Chem. Soc. D* **1971**, 36a.

(3) Broere, D.; Ruijter, E. Recent Advances in Transition-Metal-Catalyzed [2 + 2+2]-Cyclo(co)trimerization Reactions. *Synthesis* **2012**, *44*, 2639−2672.

(4) Varela, J. A.; Saá, C. Construction of pyridine rings by metal-mediated 2 + 2 + 2 cycloaddition. *Chem. Rev.* **2003**, *103*, 3787−3801.

(5) Reppe, W.; Schweckendiek, W. J. Cyclisierende Polymerisation von Acetylen. III Benzol, Benzolderivate und hydroaromatische Verbindungen. *Ann. Chem. Pharm.* **1948**, *560*, 104−116.

(6) Fachinetti, G.; Floriani, C.; Marchetti, F.; Mellini, M. Structure and properties of carbonylbis(η-cyclopentadienyl)(η-diphenyl-acetylene) titanium: the first titanium complex containing a two-carbon η-bonded ligand. *J. Chem. Soc., Dalton Trans.* **1978**, 1398−1403.

(7) Shur, V. B.; Burlakov, V. V.; Vol'pin, M. E. Complex of titanocene with tolane. Isolation, spectral characteristics, reactivity. *J. Organomet. Chem.* **1988**, *347*, 77−83.

(8) Burlakov, V. V.; Polyakov, A. V.; Yanovsky, A. I.; Struchkov, Y. T.; Shur, V. B.; Vol'pin, M. E.; Rosenthal, U.; Görls, H. Novel acetylene complexes of titanocene and permethyltitanocene without additional ligands. Synthesis spectral characteristics and X-ray diffraction study. *J. Organomet. Chem.* **1994**, *476*, 197−206.

(9) Varga, V.; Mach, K.; Polášek, M.; Sedmera, P.; Hiller, J.; Thewalt, U.; Troyanov, S. I. Titanocene-bis(trimethylsilyl)acetylene complexes: effects of methyl substituents at the cyclopentadienyl ligands on the structure of thermolytic products. *J. Organomet. Chem.* **1996**, *506*, 241−251.

(10) Wijeratne, G. B.; Zolnhofer, E. M.; Fortier, S.; Grant, L. N.; Carroll, P. J.; Chen, C.-H.; Meyer, K.; Krzystek, J.; Ozarowski, A.; Jackson, T. A.; Mindiola, D. J.; Telser, J. Electronic Structure and Reactivity of a Well-Defined Mononuclear Complex of Ti(II). *Inorg. Chem.* **2015**, *54*, 10380−10397.

(11) Rosenthal, U.; Oehme, G.; Burlakov, V. V.; Petrovskii, P. V.; Shur, V. B.; Vol'pin, M. E. 13C1H NMR studies of selected transition metal alkyne complexes. *J. Organomet. Chem.* **1990**, *391*, 119−122.

(12) Martín, C.; Sierra, M.; Alvarez, E.; Belderrain, T. R.; Pérez, P. J. Hydrotris(3-mesitylpyrazolyl)borato-copper(I) alkyne complexes: synthesis, structural characterization and rationalization of their activities as alkyne cyclopropenation catalysts. *Dalton Trans.* **2012**, *41*, 5319−5325.

(13) Nechaev, M. S.; Rayón, V. M.; Frenking, G. Energy Partitioning Analysis of the Bonding in Ethylene and Acetylene Complexes of Group 6, 8, and 11 Metals: (CO)5TM-C2Hx and Cl4TM-C2Hx (TM = Cr, Mo, W), (CO)4TM-C2Hx (TM = Fe, Ru, Os), and TM+-C2Hx (TM = Cu, Ag, Au). *J. Phys. Chem. A* **2004**, *108*, 3134−3142.

(14) Chatt, J.; Duncanson, L. A. 586. Olefin co-ordination compounds. Part III. Infra-red spectra and structure: attempted preparation of acetylene complexes. *J. Chem. Soc.* **1953**, 2939.

(15) Dewar, M. A review of π Complex Theory. *Bull. Soc. Chem. Fr* **1951**, *18*, C79.

(16) Adams, C. J.; Bartlett, I. M.; Connelly, N. G.; Harding, D. J.; Hayward, O. D.; Martín, A. J.; Guy Orpen, A.; Quayle, M. J.; Rieger, P. H. Redox routes to arenechromium complexes of two-, three- and four-electron alkynes; structure and bonding in paramagnetic [Cr(CO)L(η-

RC≡CR)(η-arene)]+. *J. Chem. Soc., Dalton Trans.* **2002**, *6*, 4281−4288.
(17) Salt, J. E.; Girolami, G. S.; Wilkinson, G.; Motevalli, M.; Thornton-Pett, M.; Hursthouse, M. B. Synthesis and characterisation of 1,2-bis(dimethylphosphino)ethane (dmpe) complexes of chromium-(0) and -(IV): X-ray crystal structures of trans-Cr(N2)2(dmpe)2, cis-Cr(CO)2(dmpe)2, Cr(C2Ph2)2(dmpe), and CrH4(dmpe)2. *J. Chem. Soc., Dalton Trans.* **1985**, 685.
(18) Danopoulos, A. A.; Wilkinson, G.; Sweet, T. K. N.; Hursthouse, M. B. Pentamethylcyclopentadienyl imido compounds of chromium. *J. Chem. Soc., Dalton Trans.* **1996**, 271.
(19) Wink, D. J.; Creagan, B. T. Synthesis of simple CrL4(alkyne) complexes by displacement of a labile cyclooctadiene ligand. *J. Am. Chem. Soc.* **1990**, *112*, 8585−8586.
(20) Wink, D. J.; Fox, J. R.; Cooper, N. J. One- and two-electron reduction of a chromium(0) alkyne complex and isolation of the chromium(1-) product. *J. Am. Chem. Soc.* **1985**, *107*, 5012−5014.
(21) Ortin, Y.; Coppel, Y.; Lugan, N.; Mathieu, R.; McGlinchey, M. J. Dynamic equilibration of eta 1-carbene and eta 2-alkyne moieties within an alkynylcarbene dimanganese complex. *Chem. Commun.* **2001**, 1690−1691.
(22) Cash, G. G.; Pettersen, R. C. Synthesis and crystal structure of [{Mn(η-C 5 H 4 Me)(CO) 2 } 2 {μ-(2−3-η:4−5-η)-MeC≡CC≡Me}], a manganese-conjugated diacetylene complex. *J. Chem. Soc., Dalton Trans.* **1979**, 1630−1633.
(23) Ortin, Y.; Sournia-Saquet, A.; Lugan, N.; Mathieu, R. Electrocatalytic dimerisation of non-heteroatom-substituted manganese alkynylcarbene complexes. *Chem. Commun.* **2003**, 1060−1061.
(24) Casey, C. P.; Dzwiniel, T. L.; Kraft, S.; Guzei, I. A. Synthesis of Cyclic cis -Enediynes from Manganese Carbyne Complexes and α,ω-Diynes. *Organometallics* **2003**, *22*, 3915−3920.
(25) Akita, M.; Kakuta, S.; Sugimoto, S.; Terada, M.; Tanaka, M.; Moro-Oka, Y. Nucleophilic Addition to the η 2 -Alkyne Ligand in [CpFe(CO) 2 (η2-R-C⋮C-R)]+. Dependence of the Alkenyl Product Stereochemistry on the Basicity of the Nucleophile. *Organometallics* **2001**, *20*, 2736−2750.
(26) Barrow, M.; Cromhout, N. L.; Cunningham, D.; Manning, A. R.; McArdle, P. The photolysis of Fe(CO)3{P(OPh)3}2 and reaction of the photoproduct with alkynes: crystal structures of Fe(CO)2{P-(OPh)3}2(η2-PhCCPh), Fe(CO)2{P(OPh)3}2{η1:η1-C(O)C(Me)-C[CH(OEt)2]C(O)} and Fe2(CO)4{P(OPh)3}2(PhCCH)2. *J. Organomet. Chem.* **2000**, *612*, 61−68.
(27) Reger, D. L.; Klaeren, S. A.; Lebioda, L. Iron.eta.2-alkyne complexes. Crystal and molecular structures of [CpFeCO[P(OPh)3]-(.eta.2-MeC.tplbond.CPh)]SbF6 and [CpFeCO[P(OPh)3](.eta.2-MeC.tplbond.CMe)]SbF6. *Organometallics* **1988**, *7*, 189−193.
(28) Fox, J. R.; Gladfelter, W. L.; Geoffroy, G. L.; Tavanaiepour, I.; Abdel-Mequid, S.; Day, V. W. Reaction of H2FeRu3(CO)13 with alkynes. Preparation and characterization of isomeric FeRu3(CO)12-(RC.ident.CR′) clusters. A definitive structural characterization of the.mu.4-.eta.2-bonding mode for substituted alkynes. *Inorg. Chem.* **1981**, *20*, 3230−3237.
(29) Hoffmann, F.; Wagler, J.; Roewer, G. Die Molekül- und Kristallstrukturen von (η5-Cyclopentadienyl)bis-(triphenylphosphan)cobalt(I)−(Hexan/Toluol) (2/1), (η5-Cyclopentadienyl)-{1,1′-[(1,2-η)-ethin-1,2-diyl]bis(benzol)}-(triphenylphosphan)cobalt(I) und (η5-Cyclopentadienyl)(1,2,3,4-tetraphenyl-buta-1,3-dien-1,4-diyl)(triphenyl-Phosphan)cobalt(I). *Z. Anorg. Allg. Chem.* **2008**, *634*, 1133−1139.
(30) Mokhtarzadeh, C. C.; Rheingold, A. L.; Figueroa, J. S. Dinitrogen binding, P4-activation and aza-Büchner ring expansions mediated by an isocyano analogue of the CpCo(CO) fragment. *Dalton Trans.* **2016**, *45*, 14561−14569.
(31) Sly, W. G. The Molecular Configuration of Dicobalt Hexacarbonyl Diphenylacetylene. *J. Am. Chem. Soc.* **1959**, *81*, 18−20.
(32) Baert, F.; Guelzim, A.; Poblet, J. M.; Wiest, R.; Demuynck, J.; Benard, M. Dynamic, static, and theoretical electron deformation density for binuclear transition-metal complexes: dicobalt hexacarbonyl acetylene. *Inorg. Chem.* **1986**, *25*, 1830−1841.
(33) Capelle, B.; Dartiguenave, M.; Dartiguenave, Y.; Beauchamp, A. L. (Trimethylphosphine)cobalt(I) complexes. 2. Reactivity with diphenylacetylene: chemical and structural evidence for alkyne ligand as variable-electron donor in tris(trimethylphosphine)-(diphenylacetylene)(acetonitrile)cobalt tetraphenylborate and tris-(trimethylphosphine)(diphenylacetylene)cobalt tetraphenylborate. *J. Am. Chem. Soc.* **1983**, *105*, 4662−4670.
(34) Monillas, W. H.; Young, J. F.; Yap, G. P. A.; Theopold, K. H. A well-defined model system for the chromium-catalyzed selective oligomerization of ethylene. *Dalton Trans.* **2013**, *42*, 9198−9210.
(35) Dai, F.; Yap, G. P. A.; Theopold, K. H. The direct oxidative addition of O2 to a mononuclear Cr(I) complex is spin forbidden. *J. Am. Chem. Soc.* **2013**, *135*, 16774−16776.
(36) Stoian, S. A.; Yu, Y.; Smith, J. M.; Holland, P. L.; Bominaar, E. L.; Münck, E. Mössbauer, electron paramagnetic resonance, and crystallographic characterization of a high-spin Fe(I) diketiminate complex with orbital degeneracy. *Inorg. Chem.* **2005**, *44*, 4915−4922.
(37) Bart, S. C.; Hawrelak, E. J.; Lobkovsky, E.; Chirik, P. J. Low-Valent α-Diimine Iron Complexes for Catalytic Olefin Hydrogenation. *Organometallics* **2005**, *24*, 5518−5527.
(38) Yu, Y.; Smith, J. M.; Flaschenriem, C. J.; Holland, P. L. Binding affinity of alkynes and alkenes to low-coordinate iron. *Inorg. Chem.* **2006**, *45*, 5742−5751.
(39) Cheng, J.; Chen, Q.; Leng, X.; Ye, S.; Deng, L. Three-Coordinate Iron(0) Complexes with N-Heterocyclic Carbene and Vinyltrimethylsilane Ligation: Synthesis, Characterization, and Ligand Substitution Reactions. *Inorg. Chem.* **2019**, *58*, 13129−13141.
(40) Enachi, A.; Baabe, D.; Zaretzke, M.-K.; Schweyen, P.; Freytag, M.; Raeder, J.; Walter, M. D. (NHC)CoR2: pre-catalysts for homogeneous olefin and alkyne hydrogenation. *Chem. Commun.* **2018**, *54*, 13798−13801.
(41) Du, J.; Chen, W.; Chen, Q.; Leng, X.; Meng, Y.-S.; Gao, S.; Deng, L. Reactivity of a Two-Coordinate Cobalt(0) Cyclic (Alkyl)(amino)-carbene Complex. *Organometallics* **2020**, *39*, 729−739.
(42) Mo, Z.; Xiao, J.; Gao, Y.; Deng, L. Regio- and stereoselective hydrosilylation of alkynes catalyzed by three-coordinate cobalt(I) alkyl and silyl complexes. *J. Am. Chem. Soc.* **2014**, *136*, 17414−17417.
(43) Werncke, C. G.; Suturina, E.; Bunting, P. C.; Vendier, L.; Long, J. R.; Atanasov, M.; Neese, F.; Sabo-Etienne, S.; Bontemps, S. Homoleptic Two-Coordinate Silylamido Complexes of Chromium(I), Manganese(I), and Cobalt(I). *Chem. - Eur. J.* **2016**, *22*, 1668−1674.
(44) Werncke, C. G.; Bunting, P. C.; Duhayon, C.; Long, J. R.; Bontemps, S.; Sabo-Etienne, S. Two-coordinate iron(I) complex [Fe{N(SiMe3)2}2](−): Synthesis, properties, and redox activity. *Angew. Chem., Int. Ed.* **2015**, *54*, 245−248.
(45) Müller, I.; Schneider, C.; Pietzonka, C.; Kraus, F.; Werncke, C. G. Reduction of 2,2′-Bipyridine by Quasi-Linear 3d-Metal(I) Silylamides—A Structural and Spectroscopic Study. *Inorganics* **2019**, *7*, 117.
(46) Werncke, C. G.; Pfeiffer, J.; Müller, I.; Vendier, L.; Sabo-Etienne, S.; Bontemps, S. C-Halide bond cleavage by a two-coordinate iron(i) complex. *Dalton Trans.* **2019**, *48*, 1757−1765.
(47) Werncke, C. G.; Müller, I. The ambiguous behaviour of diphosphines towards the quasilinear iron(i) complex Fe(N(SiMe3)-2)2- - between inertness, P-C bond cleavage and C-C double bond isomerisation. *Chem. Commun.* **2020**, *56*, 2268−2271.
(48) Reckziegel, A.; Pietzonka, C.; Kraus, F.; Werncke, C. G. C-H Bond Activation by an Imido Cobalt(III) and the Resulting Amido Cobalt(II) Complex. *Angew. Chem., Int. Ed.* **2020**, *59*, 8527.
(49) Capelle, B.; Beauchamp, A. L.; Dartiguenave, M.; Dartiguenave, Y. Diphenylacetylene as a variable electron donor: syntheses and X-ray crystal structures of [Co(C2Ph2)(MeCN)(PMe3)3]BPh4 and [Co-(C2Ph2)(PMe3)3]BPh4. *J. Chem. Soc., Chem. Commun.* **1982**, 566.
(50) Abramczyk, H.; Kołodiejski, M.; Waliszewska, G. Vibrational relaxation of diphenylacetylene at low temperatures. *Chem. Phys.* **1998**, *228*, 313−322.
(51) Boese, R.; Bläser, D.; Latz, R.; Bäumen, A. 2,2,5,5-Tetramethylhex-3-yne at 281K. *Acta Crystallogr., Sect. C: Cryst. Struct. Commun.* **1999**, *55*, IUC9900016.

https://dx.doi.org/10.1021/acs.inorgchem.0c00365
Inorg. Chem. 2020, 59, 9521−9537

(52) Bart, S. C.; Lobkovsky, E.; Chirik, P. J. Preparation and molecular and electronic structures of iron(0) dinitrogen and silane complexes and their application to catalytic hydrogenation and hydrosilation. *J. Am. Chem. Soc.* **2004**, *126*, 13794−13807.
(53) Burcher, B.; Sanders, K. J.; Benda, L.; Pintacuda, G.; Jeanneau, E.; Danopoulos, A. A.; Braunstein, P.; Olivier-Bourbigou, H.; Breuil, P.-A. R. Straightforward Access to Stable, 16-Valence-Electron Phosphine-Stabilized Fe 0 Olefin Complexes and Their Reactivity. *Organometallics* **2017**, *36*, 605−613.
(54) Crowder, G. A.; Blankenship, P. Vibrational assignment for 3-hexyne and evidence for free internal rotation. *J. Mol. Struct.* **1987**, *156*, 147−150.
(55) Müller, N.; Brückner, L.; Motzkus, M. Invited Article: Coherent Raman and mid-IR microscopy using shaped pulses in a single-beam setup. *APL Photonics* **2018**, *3*, 092406.
(56) Bruckmann, J.; Krüger, C. Bis(trimethylsilyl)acetylene. *Acta Crystallogr., Sect. C: Cryst. Struct. Commun.* **1997**, *53*, 1845−1846.
(57) Cui, C.; Li, X.; Wang, C.; Zhang, J.; Cheng, J.; Zhu, X. Isolation of a 1,2-dialuminacyclobutene. *Angew. Chem., Int. Ed.* **2006**, *45*, 2245−2247.
(58) Lewis, R. A.; Morochnik, S.; Chapovetsky, A.; Wu, G.; Hayton, T. W. Synthesis and characterization of M2(N = CtBu2)5- (M = Mn, Fe, Co): metal ketimide complexes with strong metal-metal interactions. *Angew. Chem., Int. Ed.* **2012**, *51*, 12772−12775.
(59) Duncan Lyngdoh, R. H.; Schaefer, H. F.; King, R. B. Metal-Metal (MM) Bond Distances and Bond Orders in Binuclear Metal Complexes of the First Row Transition Metals Titanium Through Zinc. *Chem. Rev.* **2018**, *118*, 11626−11706.
(60) Werncke, C. G.; Vendier, L.; Sabo-Etienne, S.; Sutter, J.-P.; Pichon, C.; Bontemps, S. Crystal Structure and Magnetic Characterization of Three-Coordinate [M{N(SiMe 3) 2 } 2 (PCyp 3)] Complexes with M = Mn II, Fe II, and Co II (Cyp = Cyclopentyl). *Eur. J. Inorg. Chem.* **2017**, *2017*, 1041−1406.
(61) Zhao, Y.; Liu, Y.; Lei, Y.; Wu, B.; Yang, X.-J. Activation of alkynes by an α-diimine-stabilized Al-Al-bonded compound: insertion into the Al-Al bond or cycloaddition to AlN2C2 rings. *Chem. Commun.* **2013**, *49*, 4546−4548.
(62) Hofmann, A.; Lamprecht, A.; González-Belman, O. F.; Dewhurst, R. D.; Jiménez-Halla, J. O. C.; Kachel, S.; Braunschweig, H. Dialumination of unsaturated species with a reactive bis-(cyclopentadienyl) dialane. *Chem. Commun.* **2018**, *54*, 1639−1642.
(63) Dange, D.; Gair, A. R.; Jones, D. D. L.; Juckel, M.; Aldridge, S.; Jones, C. Acyclic 1,2-dimagnesioethanes/-ethene derived from magnesium(i) compounds: multipurpose reagents for organometallic synthesis. *Chem. Sci.* **2019**, *10*, 3208−3216.
(64) Wolf, R.; Ghavtadze, N.; Weber, K.; Schnöckelborg, E.-M.; de Bruin, B.; Ehlers, A. W.; Lammertsma, K. P-C dichotomy: divergent iron(-I)-mediated alkyne and phosphaalkyne cycloligomerisations. *Dalton Trans.* **2010**, *39*, 1453−1456.
(65) Moses, D. G.; Baglin, F. G. A Raman scattering study of the liquid-state dynamics of a high-torque molecular liquid. *J. Phys. Chem.* **1987**, *91*, 1942−1947.
(66) Deng, Y.-F.; Han, T.; Wang, Z.; Ouyang, Z.; Yin, B.; Zheng, Z.; Krzystek, J.; Zheng, Y.-Z. Uniaxial magnetic anisotropy of square-planar chromium(II) complexes revealed by magnetic and HF-EPR studies. *Chem. Commun.* **2015**, *51*, 17688−17691.
(67) Babar, M. A.; Ladd, M. F. C.; Larkworthy, L. F.; Povey, D. C.; Proctor, K. J.; Summers, L. J. The crystal structures of propane-1,3-diammonium tetrachlorochromate(II), a sheet ferromagnet, and bis(dimethylammonium) tetrachlorochromate(II) an antiferromagnetic compound containing isolated [Cr3Cl12]6? units. *J. Chem. Soc., Chem. Commun.* **1981**, 1046.
(68) Glavee, G. N.; Jagirdar, B. R.; Schneider, J. J.; Klabunde, K. J.; Radonovich, L. J.; Dodd, K. Synthesis, chemistry, and structures of mono-.eta.6-arene complexes of chromium(II) bearing trichlorosilyl and carbon monoxide ligands. *Organometallics* **1992**, *11*, 1043−1050.
(69) Latreche, S.; Schaper, F. Highly symmetrical chromium(II) bisdiketiminate complexes. *Inorg. Chim. Acta* **2011**, *365*, 49−53.
(70) Bradley, D. C.; Hursthouse, M. B.; Newing, C. W.; Welch, A. J. Square planar and tetrahedral chromium(II) complexes; crystal structure determinations. *J. Chem. Soc., Chem. Commun.* **1972**, 567.
(71) Sodupe, M.; Bauschlicher, C. W. Theoretical study of the bonding of the first- and second-row transition-metal positive ions to acetylene. *J. Phys. Chem.* **1991**, *95*, 8640−8645.
(72) Frenking, G.; Fröhlich, N. The nature of the bonding in transition-metal compounds. *Chem. Rev.* **2000**, *100*, 717−774.
(73) Massera, C.; Frenking, G. Energy Partitioning Analysis of the Bonding in L 2 TM-C 2 H 2 and L 2 TM-C 2 H 4 (TM = Ni, Pd, Pt; L 2 = (PH 3) 2, (PMe 3) 2, H 2 PCH 2 PH 2, H 2 P(CH 2) 2 PH 2) †. *Organometallics* **2003**, *22*, 2758−2765.
(74) Piacenza, M.; Rakow, J.; Hyla-Kryspin, I.; Grimme, S. Theoretical Study of the Effects of Phosphane Substituents on the Bonding Properties of Acetylene with Ni(PR3)2 (R = H, CH3, F, CF3, C6H5). *Eur. J. Inorg. Chem.* **2006**, *2006*, 213−221.
(75) Jemmis, E. D.; Roy, S.; Burlakov, V. V.; Jiao, H.; Klahn, M.; Hansen, S.; Rosenthal, U. Are Metallocene-Acetylene (M = Ti, Zr, Hf) Complexes Aromatic Metallacyclopropenes? ||. *Organometallics* **2010**, *29*, 76−81.
(76) Lee, Y. K.; Manceron, L.; Pápai, I. An IR Matrix Isolation and DFT Theoretical Study of the First Steps of the Ti(0) Ethylene Reaction: Vinyl Titanium Hydride and Titanacyclopropene. *J. Phys. Chem. A* **1997**, *101*, 9650−9659.
(77) Desnoyer, A. N.; He, W.; Behyan, S.; Chiu, W.; Love, J. A.; Kennepohl, P. The Importance of Ligand-Induced Backdonation in the Stabilization of Square Planar d10 Nickel π-Complexes. *Chem. - Eur. J.* **2019**, *25*, 5259−5268.
(78) Neese, F. Software update: the ORCA program system, version 4.0. *Wiley Interdiscip. Rev.: Comput. Mol. Sci.* **2018**, *8*, 8.
(79) Neese, F. The ORCA program system. *Wiley Interdiscip. Rev.: Comput. Mol. Sci.* **2012**, *2*, 73−78.
(80) Becke, A. D. Density-functional thermochemistry. III. The role of exact exchange. *J. Chem. Phys.* **1993**, *98*, 5648−5652.
(81) Becke. Density-functional exchange-energy approximation with correct asymptotic behavior. *Phys. Rev. A: At., Mol., Opt. Phys.* **1988**, *38*, 3098−3100.
(82) Vosko, S. H.; Wilk, L.; Nusair, M. Accurate spin-dependent electron liquid correlation energies for local spin density calculations: a critical analysis. *Can. J. Phys.* **1980**, *58*, 1200−1211.
(83) Stephens, P. J.; Devlin, F. J.; Chabalowski, C. F.; Frisch, M. J. Ab Initio Calculation of Vibrational Absorption and Circular Dichroism Spectra Using Density Functional Force Fields. *J. Phys. Chem.* **1994**, *98*, 11623−11627.
(84) Bauer, C. A.; Hansen, A.; Grimme, S. The Fractional Occupation Number Weighted Density as a Versatile Analysis Tool for Molecules with a Complicated Electronic Structure. *Chem. - Eur. J.* **2017**, *23*, 6150−6164.
(85) Grimme, S.; Hansen, A. A practicable real-space measure and visualization of static electron-correlation effects. *Angew. Chem., Int. Ed.* **2015**, *54*, 12308−12313.
(86) Vidossich, P.; Lledós, A. The use of localised orbitals for the bonding and mechanistic analysis of organometallic compounds. *Dalton Trans.* **2014**, *43*, 11145−11151.
(87) Thom, A. J. W.; Sundstrom, E. J.; Head-Gordon, M. LOBA: a localized orbital bonding analysis to calculate oxidation states, with application to a model water oxidation catalyst. *Phys. Chem. Chem. Phys.* **2009**, *11*, 11297−11304.
(88) Knizia, G. Intrinsic Atomic Orbitals: An Unbiased Bridge between Quantum Theory and Chemical Concepts. *J. Chem. Theory Comput.* **2013**, *9*, 4834−4843.
(89) Neese, F. Importance of direct spin-spin coupling and spin-flip excitations for the zero-field splittings of transition metal complexes: a case study. *J. Am. Chem. Soc.* **2006**, *128*, 10213−10222.
(90) Löwdin, P.-O. On the Non-Orthogonality Problem Connected with the Use of Atomic Wave Functions in the Theory of Molecules and Crystals. *J. Chem. Phys.* **1950**, *18*, 365−375.
(91) Schnöckelborg, E.-M.; Khusniyarov, M. M.; de Bruin, B.; Hartl, F.; Langer, T.; Eul, M.; Schulz, S.; Pöttgen, R.; Wolf, R. Unraveling the

https://dx.doi.org/10.1021/acs.inorgchem.0c00365
Inorg. Chem. 2020, 59, 9521−9537

electronic structures of low-valent naphthalene and anthracene iron complexes: X-ray, spectroscopic, and density functional theory studies. *Inorg. Chem.* **2012**, *51*, 6719−6730.
(92) Allen, F. H. The geometry of small rings—IV. *Tetrahedron* **1982**, *38*, 645−655.
(93) BP86, PBE0, B3PW91, B97-3c, and PBEh-3c give consistent results.
(94) The vertical sextet/quartet gap is given for the structural parameters for $S = 6/2$ as obtained by DFT.
(95) Schubert, E. M. Utilizing the Evans method with a superconducting NMR spectrometer in the undergraduate laboratory. *J. Chem. Educ.* **1992**, *69*, 62.
(96) Evans, D. F. 400. The determination of the paramagnetic susceptibility of substances in solution by nuclear magnetic resonance. *J. Chem. Soc.* **1959**, 2003.
(97) Bürger, H.; Wannagat, U. Silylamido-Verbindungen von Chrom, Mangan, Nickel und Kupfer. *Monatsh. Chem.* **1964**, *95*, 1099−1102.
(98) Conley, M. P.; Delley, M. F.; Siddiqi, G.; Lapadula, G.; Norsic, S.; Monteil, V.; Safonova, O. V.; Copéret, C. Polymerization of Ethylene by Silica-Supported Dinuclear Cr III Sites through an Initiation Step Involving C−H Bond Activation. *Angew. Chem., Int. Ed.* **2014**, *53*, 1872−1876.
(99) Dolomanov, O. V.; Bourhis, L. J.; Gildea, R. J.; Howard, J. A. K.; Puschmann, H. OLEX2: a complete structure solution, refinement and analysis program. *J. Appl. Crystallogr.* **2009**, *42*, 339−341.
(100) Sheldrick, G. M. Crystal structure refinement with SHELXL. *Acta Crystallogr., Sect. C: Struct. Chem.* **2015**, *71*, 3−8.
(101) Farrugia, L. J. WinGX suite for small-molecule single-crystal crystallography. *J. Appl. Crystallogr.* **1999**, *32*, 837−838.
(102) Betteridge, P. W.; Carruthers, J. R.; Cooper, R. I.; Prout, K.; Watkin, D. J. CRYSTALS version 12: software for guided crystal structure analysis. *J. Appl. Crystallogr.* **2003**, *36*, 1487.
(103) *International Tables for Crystallography*; International Union of Crystallography; Springer: Chester, England, 2006.
(104) *SADABS-2016/2*; Bruker, 2016.
(105) *X-Area*, 1.6.1.0; STOE & Cie GmbH, Darmstadt, Germany, 2016.
(106) Lee, C.; Yang, W.; Parr, R. G. Development of the Colle-Salvetti correlation-energy formula into a functional of the electron density. *Phys. Rev. B: Condens. Matter Mater. Phys.* **1988**, *37*, 785−789.
(107) Perdew. Density-functional approximation for the correlation energy of the inhomogeneous electron gas. *Phys. Rev. B: Condens. Matter Mater. Phys.* **1986**, *33*, 8822−8824.
(108) Grimme, S.; Brandenburg, J. G.; Bannwarth, C.; Hansen, A. Consistent structures and interactions by density functional theory with small atomic orbital basis sets. *J. Chem. Phys.* **2015**, *143*, 054107.
(109) Brandenburg, J. G.; Bannwarth, C.; Hansen, A.; Grimme, S. B97-3c: A revised low-cost variant of the B97-D density functional method. *J. Chem. Phys.* **2018**, *148*, 064104.
(110) Weigend, F.; Ahlrichs, R. Balanced basis sets of split valence, triple zeta valence and quadruple zeta valence quality for H to Rn: Design and assessment of accuracy. *Phys. Chem. Chem. Phys.* **2005**, *7*, 3297−3305.
(111) Grimme, S.; Ehrlich, S.; Goerigk, L. Effect of the damping function in dispersion corrected density functional theory. *J. Comput. Chem.* **2011**, *32*, 1456−1465.
(112) Alecu, I. M.; Zheng, J.; Zhao, Y.; Truhlar, D. G. Computational Thermochemistry: Scale Factor Databases and Scale Factors for Vibrational Frequencies Obtained from Electronic Model Chemistries. *J. Chem. Theory Comput.* **2010**, *6*, 2872−2887.
(113) Zheng, J.; Xu, X.; Truhlar, D. G. Minimally augmented Karlsruhe basis sets. *Theor. Chem. Acc.* **2011**, *128*, 295−305.
(114) Neese, F.; Wennmohs, F.; Hansen, A.; Becker, U. Efficient, approximate and parallel Hartree−Fock and hybrid DFT calculations. A 'chain-of-spheres' algorithm for the Hartree−Fock exchange. *Chem. Phys.* **2009**, *356*, 98−109.
(115) Izsák, R.; Neese, F. An overlap fitted chain of spheres exchange method. *J. Chem. Phys.* **2011**, *135*, 144105.
(116) Weigend, F. Accurate Coulomb-fitting basis sets for H to Rn. *Phys. Chem. Chem. Phys.* **2006**, *8*, 1057−1065.
(117) Zhao, Y.; Truhlar, D. G. Density functionals with broad applicability in chemistry. *Acc. Chem. Res.* **2008**, *41*, 157−167.
(118) Zhao, Y.; Truhlar, D. G. The M06 suite of density functionals for main group thermochemistry, thermochemical kinetics, noncovalent interactions, excited states, and transition elements: two new functionals and systematic testing of four M06-class functionals and 12 other functionals. *Theor. Chem. Acc.* **2008**, *120*, 215−241.
(119) Staroverov, V. N.; Scuseria, G. E.; Tao, J.; Perdew, J. P. Comparative assessment of a new nonempirical density functional: Molecules and hydrogen-bonded complexes. *J. Chem. Phys.* **2003**, *119*, 12129−12137.
(120) Chai, J.-D.; Head-Gordon, M. Long-range corrected hybrid density functionals with damped atom-atom dispersion corrections. *Phys. Chem. Chem. Phys.* **2008**, *10*, 6615−6620.
(121) Angeli, C.; Cimiraglia, R.; Evangelisti, S.; Leininger, T.; Malrieu, J.-P. Introduction of n -electron valence states for multireference perturbation theory. *J. Chem. Phys.* **2001**, *114*, 10252−10264.
(122) van Lenthe, E.; Baerends, E. J.; Snijders, J. G. Relativistic regular two-component Hamiltonians. *J. Chem. Phys.* **1993**, *99*, 4597−4610.
(123) van Wüllen, C. Molecular density functional calculations in the regular relativistic approximation: Method, application to coinage metal diatomics, hydrides, fluorides and chlorides, and comparison with first-order relativistic calculations. *J. Chem. Phys.* **1998**, *109*, 392−399.

https://dx.doi.org/10.1021/acs.inorgchem.0c00365
Inorg. Chem. 2020, 59, 9521−9537

3.4 „Catalytic Transformation of Alkynes by Low-Coordinate Iron Silylamides and the Surprising Role of Potassium"

Igor Müller und C. Gunnar Werncke, *Manuskript in der Vorbereitung*.

Abstract: The iron catalysed transformation of alkynes is presented. Linear iron(I) silylamides are capable to catalytically trimerise internal alkynes to arenes or transformation of a terminal alkyne to either an allene or an internal alkyne complex. Similarly, a trigonal iron(II) silylamide can mediate the terminal alkyne/allene conversion. Ultimately, also the simple potassium hexamethyldisilazanide can catalyzed the triple bond shift.

Zusammenfassung: Die eisenkatalysierte Umwandlung von Alkinen wird vorgestellt. Lineare Eisen(I)-Silylamide sind in der Lage, interne Alkine katalytisch zu Arenen zu trimerisieren oder ein terminales Alkin entweder in ein Alken oder einen internen Alkin-Komplex umzuwandeln. In ähnlicher Weise kann ein trigonales Eisen(II)-Silylamid die Umwandlung von terminalem Alkin zu Alken vermitteln. Letztlich kann auch das einfache Kaliumhexamethyldisilazanid die Dreifachbindungsverschiebung katalysieren.

Eigener Anteil: Beide Synthesen der Verbindungen **1** und **2** wurden von mir geplant und durchgeführt, sowie deren analytischen Daten aufgenommen und ausgewertet. ^{1}H-NMR-Experimente wurden sowohl von mir als auch unter Anleitung von Dr. Xiulan Xie in der zentralen NMR-Abteilung des Fachbereichs Chemie an der Philipps-Universität Marburg durchgeführt. Ebenfalls habe ich die UV/VIS- und IR-Messungen selbst durchgeführt. Die Einkristallstrukturanalyse für die Verbindungen **2** wurde durch die zentrale Abteilung für Kristallstrukturanalyse am Fachbereich Chemie an der Philipps-Universität Marburg unter der Leitung von Dr. Sergei Ivlev durchgeführt. Die Datensätze wurden jedoch von mir gelöst und verfeinert. Bei der Verbindung **1** war ich selbst sowohl für die Messung als auch das Lösen und Verfeinern verantwortlich. Das Manuskript wurde von mir und Dr. C. Gunnar Werncke verfasst.

COMMUNICATION

Catalytic Transformation of Alkynes by Low-Coordinate Iron Silylamides and the Surprising Role of Potassium

Igor Müller[a] and C. Gunnar Werncke[a,*]

Received 00th January 20xx,
Accepted 00th January 20xx

DOI: 10.1039/x0xx00000x

The iron catalysed transformation of alkynes is presented. Linear iron(I) silylamides are capable to catalytically trimerisee internal alkynes to arenes or transformation of a terminal alkyne to either an allene or an internal alkyne complex. Similarly, a trigonal iron(II) silylamide can mediate the terminal alkyne/allene conversion. Ultimately, also the simple potassium hexamethyldisilazanide can catalyzed the triple bond shift.

3d-transition metals complexes play a vital role in catalytic bond transformation. In contrast to compounds with second or third row metals complexes with earth abundant first-row metals, being generally more benign and abundant, and are often found in an open-shell configuration with higher spin state.[1–12] This explains their tendency to undergo one-electron process, which makes their use challenging but also can give rise to novel catalytic conversions.[13] In recent years the use of low-coordinate metal complexes has gained interest, given the coordinatively and electronically unsaturated state of the metal ion, whereas iron has proven to be very versatile.[14–17] In a seminal example Tilley presented the trimerisation of internal alkynes using a two-coordinate iron(I) complex ([Fe(N(Dipp)SiMe$_3$)(IPr)], which catalyses the trimerisation of alkynes to benzene derivatives via an unprecedented binuclear mechanism. Others could show the trimerisation of internal alkynes using Fe(N(SiMe$_3$)$_2$)$_2$, whereas the hmds functions acted as an internal base and the catalytic conversion was attributed to in-situ formed iron(0) particles. In all these cases low-valent iron ions are found and thought to be crucial in engaging pi-interactions and subsequent bond transformations. Recently, we observed, that the iron(I) complex K{18c6}[Fe(N(SiMe$_3$)$_2$)$_3$], **A**, mediated cis->trans bond isomerisation of a 1,2-bisphosphine substituted ethylene cis-diphosphine, even on a catalytic scale.[18] Thereby the bond isomerisation was proposed to the proceed via intermittent 1e$^-$ reduction of the C–C double bond by the highly reducing metal(I) ion. Such a possibility was supported by a further study on the electronic structure of related metal(I) complexes bearing internal alkynes.[19] We wanted now to survey the possibility of bond transformations of internal alkynes, versatile building blocks in organic chemistry, by **A** or the sterically slightly more encumbered K{18c6}[Fe(Ndipp)SiMe$_3$)$_2$], **B**.

Using 1 mol% **A** or **B** in THF-d$_8$ internal alkynes were tested first using 3-hexyne, diphenyl acetylene and 1-phenylpropyne as representatives. Whereas no conversion was observed for any substrate using **A**, **B** mediated the trimerisation of diphenyl acetylene to the hexaphenyl benzene, that precipitated directly from the reaction mixture (isolated yield 95 %). The reactivity difference between both complexes is remarkable as a) both compounds initially form π-complexes in stoichiometric conversions and b) **A** should be more reactive due to lesser steric shielding.[19,20] Stoichiometric trimerisation was already observed in case of the formally neutral analogue of **A**, [KFe(NDipp)SiMe$_3$)$_2$], under redox and ligand distribution to [Fe(arene)(η^2-PhCCPh) (arene = C$_6$Ph$_6$).[20] A similar transformation might be in play for **A** in the presence of an excess of substrate. This was supported by the disappearance of the ^{1}H NMR signature of **A** or **B**, respectively, in case of all substrates and the appearance of other paramagnetically shifted proton signals. Next, we turned to terminal alkynes with an alkyl (1-hexyne), aryl (phenyl acetylene) and benzylic substituent (3-phenylpropyne). Whereas 1-hexyne or phenyl acetylene were unaffected using 1mol% of catalyst, substrate conversion was observed in case of the benzylic alkyne by ^{1}H NMR spectroscopy. Surprisingly, no trimerisation but bond migration and H atom shifts were detected. In case of **A** the substrate is converted instantaneously (<5 min, >99%) to the internal alkyne 1-phenylpropyne. For **B** the slow conversion of the same substrate to phenyl allene took place over the course of 1 week with no signs of (consecutive) formation of the internal alkyne.

[a] *Fachbereich Chemie, Philipps-Universität Marburg, Hans-Meerwein-Straße 4, D-35032 Marburg, Germany, gunnar.werncke@chemie.uni-marburg.de*

Electronic Supplementary Information (ESI) available: Synthesi and characterisation of compounds 1 and 2. Details of catalysis (conditions, spectra). See DOI: 10.1039/x0xx00000x

Scheme 1. Iron mediated bond isomerisation of terminal alkynes.

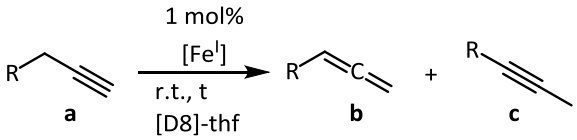

Table 1. Iron mediated bond isomerisation of terminal alkynes.

Substituent R	Precatalyst	Time	ratio		
			a	**b**	**c**
Ph	**A**	5 min	0	0	**>99**
	B	5 min	95	5	0
		7 d	67	33	0
	C	5 min	30	70	0
		7d	5	**95**	0
	Fe(hmds)$_2$	7d	100	0	0
–CH_2Ph	**A**	5 min	42	58	0
–OPh	**A**	7d	No conversion		
–NMe_2	**A**	7d	Isomerisation/polymerisation		

For insight into this conversion stoichiometric reactions of 3-phenyl propyne with **A** and **B** were performed. For **A** this led to complex **1** with a symmetrically bound η_2-Ph–C≡C–**CH_3** ligand, supporting the iron(I) mediated triple bond migration. The central C≡C bond length amounts to 1.262(3) Å). This is in agreement with previous examples of related alkyne complexes and speaks to a moderate activation of the triple bond.[19] **1** can also be directly obtained using Ph–C≡C–**CH_3**. For the analogous reaction of 3-phenyl propyne with **B**, work-up yielded only the starting compound **B** in quantitative yield. NMR spectroscopic analysis of the supernatant showed phenyl allene. Given the observation of phenyl allene in case of **B**, its intermediacy was also likely for **A**. Indeed subjecting **A** to phenyl allene yielded the internal alkyne. As such it is plausible to assume that the increased sterics in case of **B** might block allene coordination and thus supress the second H-atom shift. Aliphatic terminal alkynes were also unaffected which held also mostly true for terminal alkynes with heteroatoms in the *ß*-position. Only for 4-phenyl butyne 50% conversion to the terminal allene was observed whereas in case of Me_2N–CH_2CCH a variety of olefinic signals were detected, which pointed to the formation of an allene and its subsequent oligomerisation. The complete triple bond shift in case of **A** remarkable as isomerisation of terminal alkynes by transition metal complexes is known to give predominantly allenes,[21] vinylidenes,[22–24] and to a lesser extent 1,3-dienes.[25] Thereby the intermittent formation of a metal hydride is found to be important, which we deemed unlikely in our system.[23,26–28] Reports on the metal complex mediated complete triple bond shift from terminal to internal alkynes are restricted to magnesium and involves the deprotonation of the alkyne.[29] Due to the basic nature of the silylamide ligands such a mechanism could be in play here, but deemed highly likely as it would somewhat involve a highly unstable two-coordinate iron(I) amide/acetylide complex. To elaborate on the bonding situation of **A** with a terminal alkyne, phenyl acetylene was used to prevent bond migration which gave the η_2-complex **2**.

Scheme 2. Reaction of **A** with phenyl acetylene and 3-phenyl-propyne (R = $SiMe_3$

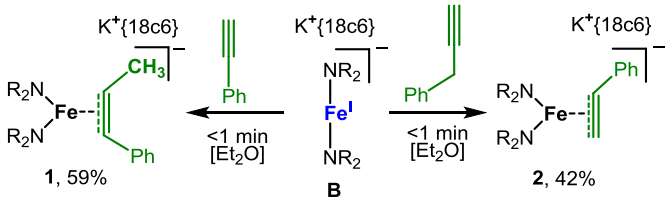

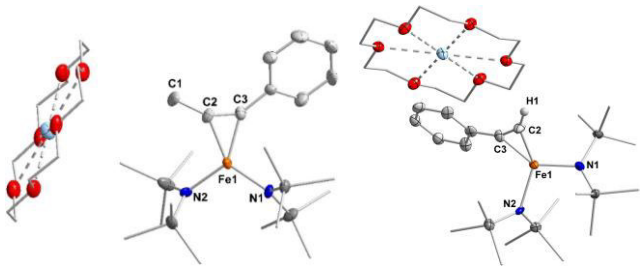

Figure 1. Molecular structure of **1** (left) and **2** (right). Unneccessary H atoms are omitted. Important bond lengths (Å) and angles (°): **1**) Fe1–C2 1.976(8), Fe1–C3 1.959(7), Fe1–N1 1.976(6), Fe1–N2 1.990(6), C3–C2 1.261(10), C3–C2–C1 141.2(8), C2–C3–CPh 143.2(8); **2**) Fe1–C2 1.962(5), Fe1–C3 1.918(5), Fe1–N1 1.988(4), Fe1–N2 2.085(8), C2–C3 1.262(3), C2–C3–C_{Ph} 151.7(5).

The bond metrics of the bound phenyl acetylene ligand unit itself ($d_{C≡C}$: 1.262(3) Å, $<_{Ph–C≡C}$: 151.7(5)°) is in line with those of **1** and comparable 3d-metal compounds.[30–34] However, the alkyne binds asymmetrically with M–C_{Ph} (1.918(5) Å) being significantly shorter than M–C_H (1.962(5) Å). This is in contrast to the usual observation of either equidistant M–C_{alkyne}[33,34] or shorter M–C_H bonds.[35,36] Such an assymetric alkyne coordination was already found as an energetically higher spin isomer in case of internal alkyne binding to two-coordinate chromium(I), with a ligand centered radical on the distal alkyne carbon.[19] Such a situation is likely enhanced by the assymetric alkyne substitution found here for iron. The ligand centered radical could then facilitate a 1,3-sigmatropic H shift leading to the allene and subsequently the internal alkyne. However, a deprotonative mechanism cannot be ruled out at this point.

Scheme 3. Postulated mechanism for iron(I) mediated triple bond isomerisation.

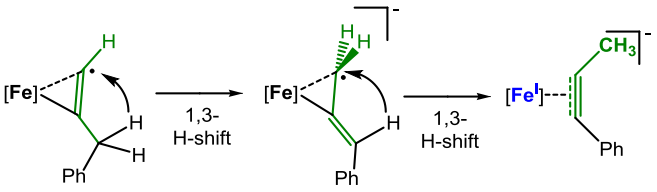

Attempts to obtain an metal allene π-complex failed so far. To delineate the possible impact of the oxidation state we also examined divalent Fe(hmds)$_2$ and K{1c86}[Fe(hmds)$_3$ (**C**) using 3-phenyl-1-propyne as substrate. Its reaction with 1 mol% Fe(hmds)$_2$ in thf-d_8 (giving Fe(hmds)$_2$*thf in solution) yielded no substrate conversion – beeing it bond isomerisation or trimerisation as reported for aryl acetylenes (**Table 2**).[37] In

contrast, for the anionic iron(II) trisamide **C** allene formation was observed although needing 7 d for completion under these conditions. In this case a more classic deprotonation pathway is plausible, as in the before mentioned magnesium example.[29] This has been shown as the initial step for related alkyne isomerisation reactions using rare earth hexamethyldisilazanides, which however needed elevated temperatures and yielded different products such as 2,3,4 hexatriene.[29,38,39] Thereby the terminal alkyne is deprotonated and then rearranges to the allene which gets re-protonated due to its significantly higher basicity. As such the stoichiometric reaction of K{18c6}[Fe(hmds)$_3$] did not lead the isolation of a terminal acetylide complex, but yielded the free allene. Using phenyl acetylene also no deprotonation was occurred.

Scheme 4. Metal amide mediated bond isomerisation of terminal alkynes.

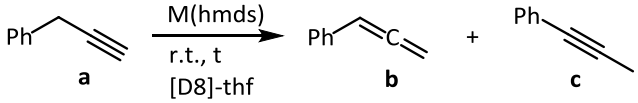

Table 2. Alkali metal amide mediated bond isomerisation of terminal alkynes.

Precatalyst	Amount	Time	ratio		
			a	**b**	**c**
Khmds	10 mol%	5 min	0	0	**>99**
Lihmds	10 mol%	5 min	0	81	19
		24 h	0	57	43
		7 d	0	19	81

Nonetheless, given the presumption of a deprotonative mechanism we fathomed the simple potassium hexamethyldisilizanide as a catalyst (w and w/o 18c6). As it turned out, Khmds also effectuated rapid substrate isomerisation to 1-phenyl-propyne (1mol%, r.t. <5 min). This contrast reports on the reverse reaction using stoichiometric amounts of lithium or potassium bases, that predominantly transform internal to terminal alkynes ("Zipper" reaction). [40–43] The preference for the thermodynamically less favoured terminal alkyne is thereby attributed to the formation of insoluble alkali metal acetylenides.[44] For Lihmds the respective reaction proceeded significantly slower, but showed intermittent allene formation. In view of the high reactivity of Khmds the selective formation of allene in case of K{18c6}[Fe(hmds)$_3$] implicated modulation of the reactivity of Khmds via its reversible binding to Fe(hmds)$_2$. During all these catalytic reactions reaction solutions became highly colored (reddish/violet), whereas stoichiometric reactions of the metal amide only gave reoccurring alkali metal hexamethydisilazanide.

Overall we presented the use of low-valent, low-coordinate iron hexamethyldisilazanides as catalysts for the transformation of alkynes. For internal alkynes it was shown that an iron(I) complex can effectuate their catalytic trimerisation to a benzene derivative whereas this is so far restricted to diphenyl acetylene. The examination of terminal alkynes revealed that for a benzylic alkyne, namely 3-phenyl propyne, [Fe(N(SiMe$_3$)$_2$)$_2$]$^-$ catalyzes the instantaneous triple bond shift to the thermodynamically more stable internal alkyne. This could be retraced on a stoichiometric level, indicating a homogeneous reaction. The mechanism remains unclear at this point but we tentatively assume it to proceed via partial substrate reduction to a radical anion. For the more bulky [Fe(N(Dipp)SiMe$_3$)$_2$]$^-$ the reaction is slower and stops at the allene state, the intermediate of the complete triple bond shift. The related trigonal iron(II) trisamide [Fe(N(SiMe$_3$)$_2$)$_3$]$^-$ also effectuates the isomerisation to phenyl allene, likely attributed to a deprotonation/reprotonation mechanism. Ultimately, we could also expand this to the simple, commercially available potassium hexamethyldisilazanide which also catalyses the isomerisation of terminal to a internal alkynes. Thereby in all cases the bond shift is restricted to the bond adjacent to the terminal alkyne function. On-going work concerns the scope of this simple and effective alkyne isomerisation, especially in case of widely avalaible alkali metal amides, as well as the acquisition of deeper mechanistic insights.

Conflicts of interest

"There are no conflicts to declare".

Notes and references

Experimental details, spectra and Cif-files are given in the Electronic Supporting Information.

[1] Sherry, B. D.; Fürstner, A. *Acc. Chem. Res.* **2008**, *41*, 1500–1511.
[2] Zweig, J. E.; Kim, D. E.; Newhouse, T. R. *Chem. Rev.* **2017**, *117*, 11680–11752.
[3] Du, X.; Huang, Z. *ACS Catal.* **2017**, *7*, 1227–1243.
[4] Chirik, P. J. *Angew. Chem. Int. Ed.* **2017**, *56*, 5170–5181.
[5] Webster, R. L. *Dalton Trans.* **2017**, *46*, 4483–4498.
[6] Su, B.; Cao, Z.-C.; Shi, Z.-J. *Acc. Chem. Res.* **2015**, *48*, 886–896.
[7] Buñuel, E.; Cárdenas, D. J. *Chem. Eur. J.* **2018**, *24*, 11239–11244.
[8] Sears, J. D.; Neate, P. G. N.; Neidig, M. L. *J. Am. Chem. Soc.* **2018**, *140*, 11872–11883.
[9] Riener, K.; Haslinger, S.; Raba, A.; Högerl, M. P.; Cokoja, M.; Herrmann, W. A.; Kühn, F. E. *Chem. Rev.* **2014**, *114*, 5215–5272.
[10] Wei, D.; Darcel, C. *Chem. Rev.* **2019**, *119*, 2550–2610.
[11] Bézier, D.; Sortais, J.-B.; Darcel, C. *Adv. Synth. Catal.* **2013**, *355*, 19–33.
[12] Misal Castro, L. C.; Li, H.; Sortais, J.-B.; Darcel, C. *Green Chem.* **2015**, *17*, 2283–2303.
[13] Chirik, P. J.; Wieghardt, K. *Science* **2010**, *327*, 794–795.
[14] Taylor, L. J.; Kays, D. L. *Dalton Trans.* **2019**, *48*, 12365–12381.
[15] Roy, S.; Mondal, K. C.; Roesky, H. W. *Acc. Chem. Res.* **2016**, *49*, 357–369.
[16] Power, P. P. *Chem. Rev.* **2012**, *112*, 3482–3507.
[17] Danopoulos, A. A.; Simler, T.; Braunstein, P. *Chem. Rev.* **2019**, *119*, 3730–3961.

[18] Werncke, C. G.; Müller, I. *Chem. Commun.* **2020**, *56*, 2268–2271.
[19] Müller, I.; Munz, D.; Werncke, C. G. *Inorg. Chem.* **2020**, *59*, 9521–9537.
[20] R. Weller, C. Duhayon, S. Sabo-Etienne, S. Bontemps, C. G. Werncke **2020**, *manuscript in preparation*.
[21] Krause, N.; Hashmi, A. S., Eds. *Modern allene chemistry*; Wiley-VCH: Weinheim, 2004.
[22] Puerta, M.; Valerga, P. *Coord. Chem. Rev.* **1999**, *193-195*, 977–1025.
[23] Bruneau, C.; Dixneuf, P. H. *Acc. Chem. Res.* **1999**, *32*, 311–323.
[24] Wakatsuki, Y.; Koga, N.; Yamazaki, H.; Morokuma, K. *J. Am. Chem. Soc.* **1994**, *116*, 8105–8111.
[25] Shintani, R.; Duan, W.-L.; Park, S.; Hayashi, T. *Chem. Commun.* **2006**, 3646–3647.
[26] Otsuka, M.; Tsuchida, N.; Ikeda, Y.; Kimura, Y.; Mutoh, Y.; Ishii, Y.; Takano, K. *J. Am. Chem. Soc.* **2012**, *134*, 17746–17756.
[27] Wakatsuki, Y. *J. Organomet. Chem.* **2004**, *689*, 4092–4109.
[28] Larionov, E.; Li, H.; Mazet, C. *Chem. Commun.* **2014**, *50*, 9816–9826.
[29] Rochat, R.; Yamamoto, K.; Lopez, M. J.; Nagae, H.; Tsurugi, H.; Mashima, K. *Chem. Eur. J.* **2015**, *21*, 8112–8120.
[30] Stoian, S. A.; Yu, Y.; Smith, J. M.; Holland, P. L.; Bominaar, E. L.; Münck, E. *Inorg. Chem.* **2005**, *44*, 4915–4922.
[31] Linden, A.; Llovera, L.; Herrera, J.; Dorta, R.; Agrifoglio, G.; Dorta, R. *Organometallics* **2012**, *31*, 6162–6171.
[32] Yu, Y.; Smith, J. M.; Flaschenriem, C. J.; Holland, P. L. *Inorg. Chem.* **2006**, *45*, 5742–5751.
[33] Chan, C.; Carpenter, A. E.; Gembicky, M.; Moore, C. E.; Rheingold, A. L.; Figueroa, J. S. *Organometallics* **2019**, *38*, 1436–1444.
[34] Bonrath, W.; Pörschke, K. R.; Wilke, G.; Angermund, K.; Krüger, C. *Angew. Chem. Int. Ed.* **1988**, *27*, 833–835.
[35] Martín, C.; Sierra, M.; Alvarez, E.; Belderrain, T. R.; Pérez, P. J. *Dalton Trans.* **2012**, *41*, 5319–5325.
[36] Titov, A. A.; Larionov, V. A.; Smol'yakov, A. F.; Godovikova, M. I.; Titova, E. M.; Maleev, V. I.; Shubina, E. S. *Chem. Commun.* **2019**, *55*, 290–293.
[37] Brenna, D.; Villa, M.; Gieshoff, T. N.; Fischer, F.; Hapke, M.; Jacobi von Wangelin, A. *Angew. Chem. Int. Ed.* **2017**, *56*, 8451–8454.
[38] Brinkmann, C.; Barrett, A. G. M.; Hill, M. S.; Procopiou, P. A.; Reid, S. *Organometallics* **2012**, *31*, 7287–7297.
[39] Barrett, A. G. M.; Crimmin, M. R.; Hill, M. S.; Hitchcock, P. B.; Lomas, S. L.; Procopiou, P. A.; Suntharalingam, K. *Chem. Commun.* **2009**, 2299–2301.
[40] Brown, C. A.; Yamashita, A. *J. Am. Chem. Soc.* **1975**, *97*, 891–892.
[41] Ma, S.; He, Q. *Angew. Chem. Int. Ed.* **2004**, *43*, 988–990.
[42] Maercker, A.; Fischenich, J. *Tetrahedron* **1995**, *51*, 10209–10218.
[43] Jacobs, T. L.; Akawie, R.; Cooper, R. G. *J. Am. Chem. Soc.* **1951**, *73*, 1273–1276.
[44] Avocetien, K.; Li, Y.; O'Doherty, G. A. *The Alkyne Zipper Reaction in Asymmetric Synthesis*. In *Modern alkyne chemistry: Catalytic and atom-economic transformations*; Trost, B. M., Li, C.-J., Eds.; Wiley-VCH Verlag GmbH & Co. KGaA: Weinheim, Germany, 2015; pp 365–394.

3.5 „The ambiguous behaviour of diphosphinestowards the quasilinear iron(I) complex $[Fe(N(SiMe_3)_2)_2]^-$ between inertness, P–C bondcleavage and C–C double bond isomerisation"

C. Gunnar Werncke und Igor Müller, *Chem. Commun.,* **2020**, *56*, 2268.

Abstract: Chelating phosphines are widely used as robust and reliable ligands in catalysis. We show, that the anionic iron(I) complex $[Fe^{I}(N(SiMe_3)_2)_2]^-$ is able to selectively cleave a P-aryl bond of 1,2-bis(diphenylphosphino)benzene. Further, the related *cis*-1,2-bis(diphenylphosphino)-ethylene (dppee) binds not by the P donors but by the ethylene unit, and is (catalytically) transformed to the *trans*-isomer.

Zusammenfassung: Chelatbildende Phosphine sind als robuste und zuverlässige Liganden in der Katalyse weit verbreitet. Wir zeigen, dass der anionische Eisen(I)-Komplex $[Fe^{I}(N(SiMe_3)_2)_2]^-$ in der Lage ist, selektiv eine P-Aryl-Bindung von 1,2-Bis(diphenylphosphino)benzol zu spalten. Außerdem bindet das verwandte *cis*-1,2-Bis(diphenylphosphino)-ethylen (dppee) nicht durch die P-Donoren, sondern durch die Ethyleneinheit und wird (katalytisch) in das *trans*-Isomer umgewandelt.

Eigener Anteil: Alle Synthesen der Verbindungen **2** – **5** wurden von Dr. C. Gunnar Werncke geplant und durchgeführt, sowie deren analytischen Daten aufgenommen und ausgewertet. ^{1}H-NMR-Experimente wurden sowohl von Dr. C. Gunnar Werncke als auch unter Anleitung von Dr. Xiulan Xie in der zentralen NMR-Abteilung des Fachbereichs Chemie an der Philipps-Universität Marburg durchgeführt. Ebenfalls hat Dr. C. Gunnar Werncke die IR-Messungen durchgeführt. Die Einkristallstrukturanalyse für die Verbindungen **2** – **5** wurde durch die zentrale Abteilung für Kristallstrukturanalyse am Fachbereich Chemie an der Philipps-Universität Marburg unter der Leitung von Dr. Klaus Harms durchgeführt. Die Datensätze wurden jedoch von mir gelöst und verfeinert. Das Manuskript wurde von Dr. C. Gunnar Werncke verfasst.

COMMUNICATION

The Ambiguous Behaviour of Diphosphines Towards the Quasilinear Iron(I) Complex $[Fe(N(SiMe_3)_2)_2]^-$ – Between Inertness, P–C Bond Cleavage and C–C Double Bond Isomerisation

Received 00th January 20xx,
Accepted 00th January 20xx

DOI: 10.1039/x0xx00000x

Christian Gunnar Werncke,*[a] and Igor Müller[a]

Chelating phosphines are widely used as robust and reliable ligands in catalysis. We show, that the anionic iron(I) complex $[Fe^{I}(N(SiMe_3)_2)_2]^-$ is able to selectively cleave a P-aryl bond of 1,2-bis(diphenylphosphino)benzene. Further, the related *cis*-1,2-bis(diphenylphosphino)-ethylene (dppee) binds not by the P donors but by the ethylene unit, and is (catalytically) transformed to the *trans*-isomer.

Tertiary phosphines are common ligands in organometallic chemistry that are mainly used to stabilize metal centres in medium to low oxidation states. They are usually seen as robust spectator ligands that can be easily modified concerning its electronic and steric properties. As such they are widely used as co-ligands in many catalytic transformations.[1] However, the cleavage and/or scrambling of the P–aryl and to a lesser extent P–alkyl bonds in ligating phosphines is sometimes observed and can pose an unwanted deactivation pathway in catalysis.[2,3] This is mainly the case for 2nd and 3rd row transition metals (especially Pd).[4] For 3d-metals less is known about P–C bond cleavage, and is mainly observed for metal carbonyls upon prolonged heating.[3,5] Rare exceptions for reported conversions under mild conditions involve (di)cobalt,[6,7] diiron[8] and dinickel[7,9] carbonyl compounds and the bis(diphenylphosphino)methane ligand resulting in bridged phosphide complexes. P–C bond cleavage for carbonyl free 3d-metal systems was only seen in case of a nickel complex.[10]

Recently we reported on the synthesis of the quasi-linear iron(I) complex K{18-crown-6}[$Fe(N(SiMe_3)_2)_2$], **1**.[11] Despite a sterically unhindered metal centre, preliminary examinations showed that it is unaffected by monodentate lewis bases like PPh_3, PCy_3, $P(OEt)_3$ or the N-hetero cyclic carbene IMes. This behaviour is peculiar for two-coordinate metal(I) ions,[12] and might be result of the anionic state of the complex anion in **1**. We were thus interested if the observed inertness of compound **1** towards pure Lewis bases holds true for a variety of commonly used (chelating) Lewis base additives used in catalysis, especially diphosphines. This would shed light onto the behaviour of these additives towards low-coordinate, low-valent 3d-metal species observed or postulated in a variety of catalytic transformations, especially those where anionic metallates are likely such as in Grignard based C–C cross-coupling.[13]

When compound **1** is subjected to regular O- or N-Donors such as simple ethers (THF, dimethoxy ethane), N-methyl-2-pyrrolidone (NMP), amines (NEt_3, TMEDA) or pyridine derivatives (4-dimethylaminopyridine, 4-tert-butylpyridine) no reaction is observed. This holds also true for carbenes (IDipp, SIMes, SIDipp), PEt_3 and larger monodentate phosphines as well as chelating phosphines like Xanthphos, 1,2-bis(diethylphosphino)ethane or 1,2-bis(diphenylphosphino) methane/ethane as well as propane. This implicates, that low-coordinate, low-valent *anionic* iron complexes might display only weak interactions with mono- and bidentate phosphines, which is emphasized by the lack of respective complexes.[14]

Employing 1,2-bis(diphenylphosphino) *benzene* (dppbz), a further commonly used ligand framework, it reacted with complex **1** under formation of a dark red solution within 30 minutes. Workup afforded a mixture of colourless as well as blood red crystals. The former turned out to be K{18c6}[$Fe^{II}(N(SiMe_3)_2)_3$], **2**, (18c6 = 18-crown-6) whereas the latter is the tetrahedral phenyliron(II) complex **3** (Scheme 1), whose equimolar formation was shown by ^{1}H NMR spectroscopy. The phenyl group is result of the P–C bond cleavage of one P–Ph units of the dppbz ligand which now acts as an anionic phosphine/phosphanide ligand (ppbz* = 1-(diphenylphosphino)-2-(phenylphosphido)benzene)). The Fe1–P1 and Fe1–P2 bond lengths amount 2.4557(6) Å and 2.4096(5) which reflects the difference between the phosphine and phosphide unit. Together with the tetrahedral geometry of the phosphide moiety, whereas the free lone pair points away from the iron ion, it indicates the absence of significant double bond character of the iron-phosphide bond.

[a] *Dr. C. Gunnar Werncke, Igor Müller, Fachbereich Chemie, Philipps-University Marburg, Hans-Meerwein-Straße, D-35043 Marburg, Germany, e-mail: gunnar.werncke@chemie.uni-marburg.de*

Electronic Supplementary Information (ESI) available: Experimental details and crystallographic details, NMR and UV/Vis spectra. See DOI: 10.1039/x0xx00000x

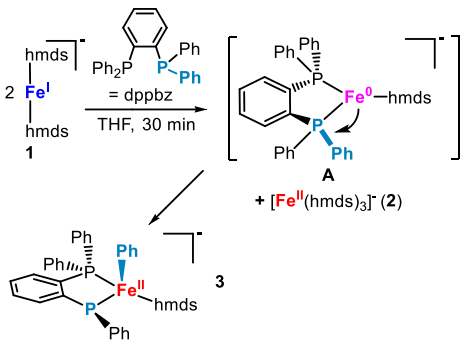

Scheme 1. Reaction of **1** with 1,2-bis(diphenylphosphino)benzene (dppbz) and proposed iron(0) intermediate responsible for the P–aryl bond cleavage. K$^+${18c6} was omitted.

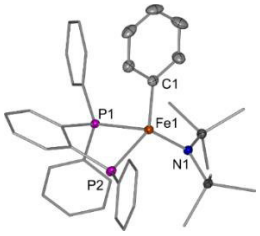

Figure 1. Section of the crystal structure of complex **3**. The K{18c6} cation was omitted. Selected bond lengths (Å) and angles (°): Fe1–P1 2.4557(6), Fe1–P2 2.4096(5), Fe1–N1 1.9886(13), Fe1–C1 2.068(2), P1–Fe1–P2 77.32(2), P1–Fe1–C1 101.15(5), P1–Fe1–N1 114.47(4), P2–Fe1–C1 117.93(5), P2–Fe1–N1 115.16(4), C1–Fe1–N1 120.75(6).

Complex **3** exhibits a number of paramagnetic ^{1}H NMR signals owing to the asymmetric nature of the formed ppbz* ligand. The magnetic susceptibility of compound **3** of μ_{eff} = 5.29 μ_B is expected for a high spin iron(II) complex. This example of an iron mediated P–aryl bond cleavage at mild conditions is rare (vide supra). Moreover, the use of the asymmetric ppbz* as a ligand is unknown so far and its parent protonated form was only detected as a side product in the unselective reaction of dppbz with alkali metals.[15] The inertness of **1** towards other aryl phosphines, and the stability of the related complexes [Fe^{I}(dppbz)$_2$(X)] (X = Br, Cl, *p*-tolyl)[16] implicated that the presence of an iron(I) ion is not necessarily sufficient in P–aryl bond rupture. Thus, we hypothesized that the formation of **3** is result of a disproportionation of **1** into the observed iron(II) complex **2** as well as the proposed iron(0) species **A** via formal e$^-$/hmds exchange (Scheme 1) which is triggered by dppbz, due to the additional presence of the unsaturated ligand backbone. **A** would then facilitate the formal intramolecular oxidative addition of a P–Aryl unit to the iron centre. This behaviour is similar the one of the nickel(0) complex [Ni^0(IMe$_4$)$_2$(PPh$_3$)] which rapidly transforms into [Ni^{II}(IMe$_4$)$_2$(Ph)(PPh$_2$)] (IMe$_4$=l,3,4,5- tetramethylimidazol-2-ylidene) and contrasts the behaviour of phosphine stabilized iron(0) species which prefer cyclometallation via adjacent C–H bonds of the phosphine substituents, especially in case of aryl groups.[17]

Given the observed reactivity of dppbz with **1**, which contrasts the inertness of arylated diphosphines with a saturated backbone such as dppe, we speculated about some degree of back donation or partial electron transfer from the metal to the ligand backbone that might initiate redox disproportionation and formation of **3**. As such we turned our attention to *cis*-1,2-bis(diphenylphosphino) *ethylene* (dppee). Reaction of dppee with complex **1** in THF gave a rapid colour change to brown. After stirring over night the reaction mixture was filtered and then layered with pentane to give reddish violet crystals after storage at −40°C for a few days (Scheme 2). X-Ray diffraction analysis revealed the presence of the dppee iron complex **4** (Figure 2). The iron centre, besides two hmds ligands, exhibits a diphosphine ligand, which astonishingly binds *not* via the phosphine atoms but solely by the C–C double bond of the backbone. This behaviour is unprecedented for any mononuclear transition metal complex with dppee or a related diphosphine ligand. Such an ethylene coordination was only observed for binuclear complexes where the ethylene bridged diphosphine already coordinated to a second metal ion via the P donor atoms or when it is enforced by the backbone of the diphosphine.[18] Further, in complex **4** the phosphine atoms are situated in a *trans*-arrangement, revealing a *cis*–>*trans* double bond isomerisation. The C1–C2 bond length amounts to 1.438(2) Å which is between the values of free dppee (1.334(4) Å)[19] and 1,2-bis(diphenylphosphino) ethane (1.521(7) Å).[20] The planes span by N1–Fe1–N2 and C1–Fe1–C2 are twisted by approximately 26° towards each other.

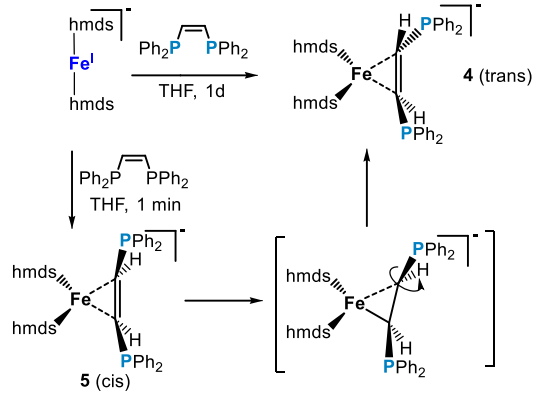

Scheme 2. Synthesis of complexes **4** and **5** and proposed isomerisation mechanism.

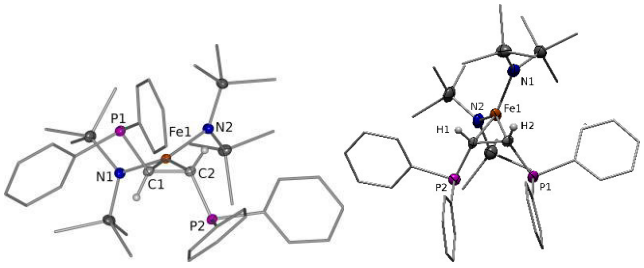

Figure 2. Sections of the crystal structure of complexes **4** and **5**. K{18c6} cations, disorders and hydrogen atoms are omitted (with the exception of the ethylene H atoms). Selected bond lengths (Å) and angles (°): (**4**) Fe1–C1 2.085(2), Fe1–C2 2.064(2), Fe1–N1 2.009(2), Fe1–N2 2.000(2); C1–C2 1.438(3), N1–Fe1–N2 116.33(7). (**5**) Fe1–C1 2.153(12), Fe1–C2 2.1187(12), Fe1–N1 2.001(6), Fe1–N2 1.998(6), C1–C2 1.463(15); N1–Fe1–N2 116.4(2).

The ^{1}H NMR spectrum of isolated **4**, which can also directly be obtained when reacting **1** with *trans*-dppee, shows one set of paramagnetically shifted signals, with the signal attributed for the hmds protons at −4.53 ppm which is similar to the value observed for iron(II) bound hmds ligands.[21] The magnetic

susceptibility of compound **4** amounts to μ_{eff} = 4.38 μ_B and corresponds to the values of other low-coordinate iron(I) alkene complexes.[22] However, given the strong elongation of the C=C double bond it implicates significant charge transfer from iron to the alkyne.

An immediately recorded ^{1}H-NMR spectrum of the reaction of compound **1** with *cis*-dppee gave a single set of paramagnetic signals attentively attributed to the *cis*-isomer **5** (δ_{hmds} = −2.67 ppm), which transformed completely to compound **4** over the course of three days (45% after 16 h). The identity of the *cis*-dppee complex **5** was confirmed by X-ray diffraction analysis. In complex **5** The C1−C2 bond length of the iron bound dppee amounts to 1.463(15) Å which is even more elongated than in case of the *trans*-complex **4**. The planes spanned by N1−Fe1−N2 and C1−Fe1−C2 are also more twisted (56.6(7)°), which is probably due to the different steric demand of *cis*-dppee.

The observed metal mediated *cis*–>*trans* C−C double bond isomerisation is rather unexpected. It is commonly seen during olefin metathesis, mediated by a metal hydride via 1,2-addition to a C−C double bond or scrambling of a metal (hydride) bound allylic species.[23] However, in our case such possibilities can be excluded due to the absence of a metal hydride species or allylic substrate positions. The only comparable example is an iron mediated stilbene isomerisation, although the mechanism and the identity of the iron species remained elusive.[24] As in complex **5** the C=C bond of *cis*-dppee is significantly elongated this very bond could be sufficiently weakened to allow for the rotation of the substituents. A more speculative mechanism would be a reversible formal 1e$^-$-transfer from the metal(I) ion to the substrate (similar to complex **1** mediated irreversible reduction of 2,2'-bipyridine)[25] under intermittent formation of a formally metal(II) ion bound η_1-*cis*-alkenyl radical anion. Alkenyl radical anions are calculated to exhibit no rotational barrier, however were so far not observed in the proximity of a metal ion.[26] As the C=C isomerisation is an electroneutral process, we aspired a catalytic transformation. Indeed, when employing 10% of compound **1** *cis*-dppee is slowly isomerized over the course of several days, (66%, r.t. 6 d, Scheme 3). However, the catalysis is limited by simultaneous decomposition of complex **1** within this timeframe.

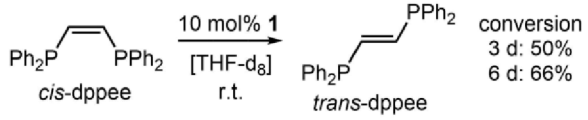

Scheme 3. Catalytic *cis*->*trans* isomerisation of *cis*-dppee mediated by complex **1**.

Concluding, we presented the peculiar behaviour of the two-coordinate iron(I) complex **1** towards commonly used phosphine and diphosphine ligands. Thereby it shows, that most phosphines (as well as various N/O donor ligands) do *not* interact with the anionic iron(I) complex **1**, despite its accessible metal ion. However, in case of dppbz the facile rupture of a P−Aryl bond is observed leading to the formation of an iron(II) phenyl complex ligated by a novel bidentate mixed phosphine/phosphide ligand. For *cis*-dppee the unprecedented sole coordination via the C=C bond of the ethylene linker but not the phosphorous atoms is observed. Further, an unusual *cis*–>*trans* isomerisation of this very bond took place, that involved no apparent metal hydride or allyl species, and could be performed on a catalytic scale. Overall, it shows that for low-coordinate, anionic iron complexes (and potentially of other metals) the role of phosphines as a simple and robust P donor ligand should not be readily assumed.

Conflicts of interest

There are no conflicts to declare.

Notes and references

1 a) R. Martin and S. L. Buchwald, *Acc. Chem. Res.*, 2008, **41**, 1461–1473; b) T. J. Colacot, *Chem. Rev.*, 2003, **103**, 3101–3118; c) L. M. Pignolet, *Homogeneous Catalysis with Metal Phosphine Complexes*, Springer, New York, NY, 2013; d) C. A. Tolman, *Chem. Rev.*, 1977, **77**, 313–348; e) R. H. Crabtree, *J. Organomet. Chem.*, 2005, **690**, 5451–5457; f) L. C. Misal Castro, H. Li, J.-B. Sortais and C. Darcel, *Green Chem.*, 2015, **17**, 2283–2303;

2 a) A. W. Parkins, *Coord. Chem. Rev.*, 2006, **250**, 449–467; b) P. W.N.M. van Leeuwen, *Applied Catalysis A: General*, 2001, **212**, 61–81; c) E. Igartúa-Nieves, A. J. Rivera-Brown and J. E. Cortés-Figueroa, *Inorg. Chem. Commun.*, 2012, **21**, 43–46;

3 P. E. Garrou, *Chem. Rev.*, 1985, **85**, 171–185.

4 a) D. K. Morita, J. K. Stille and J. R. Norton, *J. Am. Chem. Soc.*, 1995, **117**, 8576–8581; b) T. Rünzi, U. Tritschler, P. Roesle, I. Göttker-Schnetmann, H. M. Möller, L. Caporaso, A. Poater, L. Cavallo and S. Mecking, *Organometallics*, 2012, **31**, 8388–8406; c) W. H. Watson, G. Wu and M. G. Richmond, *Organometallics*, 2006, **25**, 930–945; d) F. E. Goodson, T. I. Wallow and B. M. Novak, *J. Am. Chem. Soc.*, 1997, **119**, 12441–12453; e) W. H. Watson, S. Kandala and M. G. Richmond, *J. Organomet. Chem.*, 2007, **692**, 1648–1652;

5 a) A. G. Abatjoglou and D. R. Bryant, *Organometallics*, 1984, **3**, 932–934; b) N. M. Doherty, G. Hogarth, S. A.R. Knox, K. A. Macpherson, F. Melchior, D. A.V. Morton and A.G. Orpen, *Inorganica Chim. Acta*, 1992, **198-200**, 257–270; c) R. A. Dubois and P. E. Garrou, *Organometallics*, 1986, **5**, 466–473; d) N. M. Doherty, G. Hogarth, S. A. R. Knox, K. A. Macpherson, F. Melchior and A. G. Orpen, *Chem. Commun.*, 1986, 540–542; e) R. A. Dubois, P. E. Garrou, K. D. Lavin and H. R. Allcock, *Organometallics*, 1984, **3**, 649–650;

6 a) H. Xu, P. G. Williard and W. H. Bernskoetter, *Organometallics*, 2013, **32**, 798–806; b) S. Ahmed, D. G.

Holah, A. N. Hughes and R. T. Markewich, *Polyhedron*, 1993, **12**, 1101–1102;

7 D. J. Elliot, D. G. Holah, A. N. Hughes, H. A. Mirza and E. Zawada, *Chem. Commun.*, 1990, **85**, 32–33.

8 a) G. Hogarth, *J. Organomet. Chem.*, 1991, **407**, 91–95; b) G. Hogarth, S. A. R. Knox and M. L. Turner, *Chem. Commun.*, 1990, **85**, 145–146;

9 M. Itazaki, N. Tsuchida, Y. Shigesato, K. Takano and H. Nakazawa, *Dalton Trans.*, 2016, **45**, 19216–19220.

10 a) S. Sabater, M. J. Page, M. F. Mahon and M. K. Whittlesey, *Organometallics*, 2017, **36**, 1776–1783; b) J. Cao, X. Huang and L. Wu, *Chem. Commun.*, 2013, **49**, 7747–7749; c) D. R. Fahey and J. E. Mahan, *J. Am. Chem. Soc.*, 1976, **98**, 4499–4503;

11 C. G. Werncke, P. C. Bunting, C. Duhayon, J. R. Long, S. Bontemps and S. Sabo-Etienne, *Angew. Chem. Int. Ed.*, 2015, **54**, 245–248.

12 a) S. Pfirrmann, C. Limberg, C. Herwig, R. Stösser and B. Ziemer, *Angew. Chem. Int. Ed.*, 2009, **48**, 3357–3361; b) T. R. Dugan, X. Sun, E. V. Rybak-Akimova, O. Olatunji-Ojo, T. R. Cundari and P. L. Holland, *J. Am. Chem. Soc.*, 2011, **133**, 12418–12421; c) K. C. MacLeod, R. A. Lewis, D. E. DeRosha, B. Q. Mercado and P. L. Holland, *Angew. Chem. Int. Ed.*, 2017, **56**, 1069–1072; d) M. I. Lipschutz, T. Chantarojsiri, Y. Dong and T. D. Tilley, *J. Am. Chem. Soc.*, 2015, **137**, 6366–6372; e) Y. Gao, G. Li and L. Deng, *J. Am. Chem. Soc.*, 2018, **140**, 2239–2250; f) J. Hicks and C. Jones, *Organometallics*, 2015, **34**, 2118–2121; g) R. Wolf, M. Brynda, C. Ni, G. J. Long and P. P. Power, *J. Am. Chem. Soc.*, 2007, **129**, 6076–6077;

13 a) R. Shang, L. Ilies, S. Asako and E. Nakamura, *J. Am. Chem. Soc.*, 2014, **136**, 14349–14352; b) K. Gao and N. Yoshikai, *Acc. Chem. Res.*, 2014, **47**, 1208–1219; c) J. A. Garduño, A. Arévalo and J. J. García, *Dalton Trans.*, 2015, **44**, 13419–13438; d) R. B. Bedford, P. B. Brenner, E. Carter, P. M. Cogswell, M. F. Haddow, J. N. Harvey, D. M. Murphy, J. Nunn and C. H. Woodall, *Angew. Chem. Int. Ed.*, 2014, **53**, 1804–1808;

14 G. T. Sazama and T. A. Betley, *Inorg. Chem.*, 2014, **53**, 269–281.

15 J. A. van Doom, J. H. G. Frijns and N. Meijboom, *Recl. Trav. Chim. Pays-Bas*, 1991, **110**, 441–449.

16 C. J. Adams, R. B. Bedford, E. Carter, N. J. Gower, M. F. Haddow, J. N. Harvey, M. Huwe, M. Á. Cartes, S. M. Mansell, C. Mendoza, D. M. Murphy, E. C. Neeve and J. Nunn, *J. Am. Chem. Soc.*, 2012, **134**, 10333–10336.

17 a) S. D. Ittel, C. A. Tolman, P. J. Krusic, A. D. English and J. P. Jesson, *Inorg. Chem.*, 1978, **17**, 3432–3438; b) H. Azizian and R. H. Morris, *Inorg. Chem.*, 1983, **22**, 6–9; c) G. Hata, H. Kondo and A. Miyake, *J. Am. Chem. Soc.*, 1968, **90**, 2278–2281; d) F. Mohr, S. H. Privér, S. K. Bhargava and M. A. Bennett, *Coord. Chem. Rev.*, 2006, **250**, 1851–1888;

18 a) G. B. Robertson, P. A. Tucker and P. O. Whimp, *Inorg. Chem.*, 1980, **19**, 2307–2315; b) B. J. Barrett and V. M. Iluc, *Inorg. Chem.*, 2014, **53**, 7248–7259; c) P. Binger, B. Biedenbach, R. Mynott, R. Benn, A. Rufińska, P. Betz and C. Krüger, *J. Chem. Soc., Dalton Trans.*, 1990, **98**, 1771–1777; d) Z. Qiu, L. Deng and Z. Xie, *J. Organomet. Chem.*, 2013, **747**, 225–228;

19 S. J. Berners-Price, L. A. Colquhoun, P. C. Healy, K. A. Byriel and J. V. Hanna, *J. Chem. Soc., Dalton Trans.*, 1992, 3357.

20 C. Pelizzi and G. Pelizzi, *Acta. Cryst. B*, 1979, **35**, 1785–1790.

21 C. G. Werncke, J. Pfeiffer, I. Müller, L. Vendier, S. Sabo-Etienne and S. Bontemps, *Dalton Trans.*, 2019, **48**, 1757–1765.

22 Y. Yu, J. M. Smith, C. J. Flaschenriem and P. L. Holland, *Inorg. Chem.*, 2006, **45**, 5742–5751.

23 a) E. Larionov, H. Li and C. Mazet, *Chem. Commun.*, 2014, **50**, 9816–9826; b) M. Hassam, A. Taher, G. E. Arnott, I. R. Green and W. A. L. van Otterlo, *Chem. Rev.*, 2015, **115**, 5462–5569; c) G. Li, J. L. Kuo, A. Han, J. M. Abuyuan, L. C. Young, J. R. Norton and J. H. Palmer, *J. Am. Chem. Soc.*, 2016, **138**, 7698–7704; d) E. H. P. Tan, G. C. Lloyd-Jones, J. N. Harvey, A. J. J. Lennox and B. M. Mills, *Angew. Chem. Int. Ed.*, 2011, **50**, 9602–9606; e) A. Kapat, T. Sperger, S. Guven and F. Schoenebeck, *Science*, 2019, **363**, 391–396; f) A. Schmidt, A. R. Nödling and G. Hilt, *Angew. Chem. Int. Ed.*, 2015, **54**, 801–804; g) G. Hilt, *ChemCatChem*, 2014, **6**, 2484–2485; h) S. H. Hong, D. P. Sanders, C. W. Lee and R. H. Grubbs, *J. Am. Chem. Soc.*, 2005, **127**, 17160–17161; i) K. J. Ivin and J. C. Mol, *Olefin Metathesis and Metathesis Polymerization*, Elsevier professional, s.l., 2nd edn., 1997;

24 M. Mayer, A. Welther and A. Jacobi von Wangelin, *ChemCatChem*, 2011, **3**, 1567–1571.

25 I. Müller, C. Schneider, C. Pietzonka, F. Kraus and C. G. Werncke, *Inorganics*, 2019, **7**, 117.

26 a) H. C. Wang, G. Levin and M. Szwarc, *J. Am. Chem. Soc.*, 1977, **99**, 2642–2647; b) J. E. Gano, E. J. Jacob, P. Sekher, G. Subramaniam, L. A. Eriksson and D. Lenoir, *J. Org. Chem.*, 1996, **61**, 6739–6743;

4 Unveröffentlichte Ergebnisse

Im folgenden Kapitel werden neue Verbindungen vorgestellt, die noch nicht publiziert und vollständig charakterisiert wurden, aber relevant für das Promotionsprojekt sind. Die in diesem Kapitel aufgeführten Ergebnisse befassen sich mit der Reaktivität ausgewählter aromatischer Alkene gegenüber linearen Metall(I)-Silylamiden (M = Cr – Co)[50,51]. Die Diskussion der Ergebnisse wird von der Einkristallstrukturanalyse gestützt.

4.1 Reaktivität linearer Metall(I)-Komplexe (M = Cr – Co) gegenüber Alkenen

Zunächst wurden terminale Alkene (Styrol und 1,1-Diphenylethylen) mit linearen Metall(I)-Silylamiden $[K\{18\text{-c-}6\}][MX_2]$ (18-c-6 = 18-Krone-6; X = $-N(SiMe_3)_2$) (M = Cr – Co) bei Raumtemperatur in Et_2O umgesetzt. Während für Kobalt, durch die Färbung der Reaktionslösung von grün nach rot, nur eine schwache und reversible Alken-Koordination beobachtet wurde, konnte quantitativ nur der Kobalt(I)-Komplex erhalten werden. Im Fall von Eisen bildete sich bei der Reaktion von Styrol und $[K\{18\text{-c-}c6\}][Fe^I(hmds)_2]$ in Et_2O bei Raumtemperatur ein stabiler *side-on* Alken-Komplex vom Typ $[M(L_2)(\eta^2\text{-}RCHCH_2)]^-$ (**Schema 13**). Bei der Reaktion für das Substrat 1,1-Diphenylethylen konnte nur eine Färbung der Reaktionslösung von grüngelb nach rot beobachtet, aber keine Einkristalle erhalten werden.

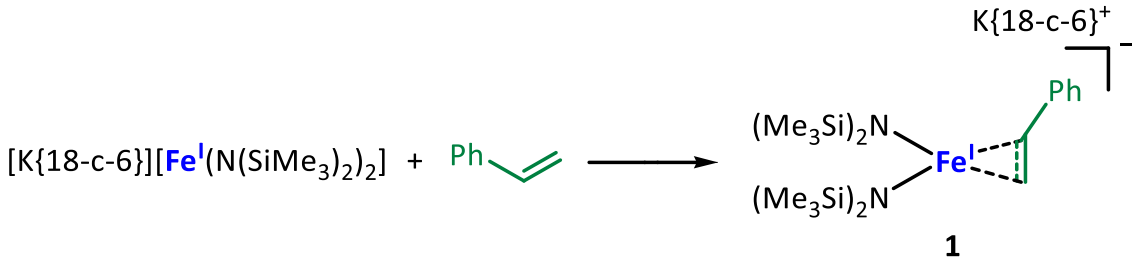

Schema 13. Darstellung von $[K\{18\text{-c-}c6\}][Fe^I(hmds)_2(\eta^2\text{-styrol})]$ (**1**).

Die Molekülstruktur von **1** aus der Einkristallstrukturanalyse zeigt eine *side-on* Koordination des Alkens im Komplex (**Abbildung 18**). Dabei wird die Doppelbindung zwischen C1 und C2 (1.422 Å) aufgeweitet und liegt im Bereich einer Einfach- und Doppelbindung[117]. Die Bindungslängen von Fe-C1 und Fe-C2 betragen 2.051(2) Å und 2.078(2) Å.

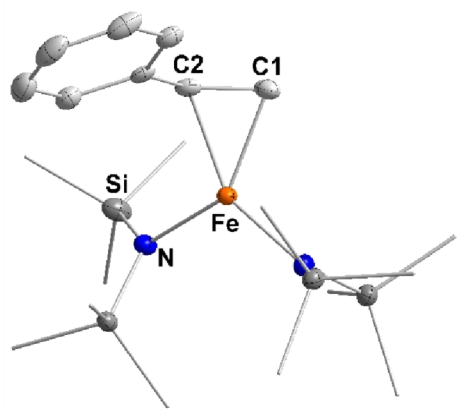

Abbildung 18. Molekülstruktur von **1**. Wasserstoffatome und das Kation $K\{18\text{-c-}6\}^+$ wurden der Übersicht halber nicht dargestellt.

Zusätzliche wurde $[K\{18\text{-c-}c6\}][Fe^{I}(hmds)_2]$ mit 4-Allylanisol in Et_2O bei Raumtemperatur für die Untersuchung einer potentiellen 1,3-Verschiebung der Doppelbindung umgesetzt. Die Arbeit von KAPAT stellt dar, dass es möglich ist, mit einem Nickel-Katalysator über eine Nickel-Hydrid-Spezies, eine 1,3-Verschiebung der Doppelbindung durchzuführen.[116] Jedoch zeigt die Molekülstruktur des Komplexes $[K\{18\text{-c-}c6\}][Fe^{I}(hmds)_2(\eta^2\text{-allylanisol})]$ (**2**), dass keine Verschiebung der Doppelbindung stattgefunden hat (**Abbildung 29**). Auf dieser Grundlage wurden keine weiteren Untersuchungen der Verschiebung der Doppelbindung getätigt.

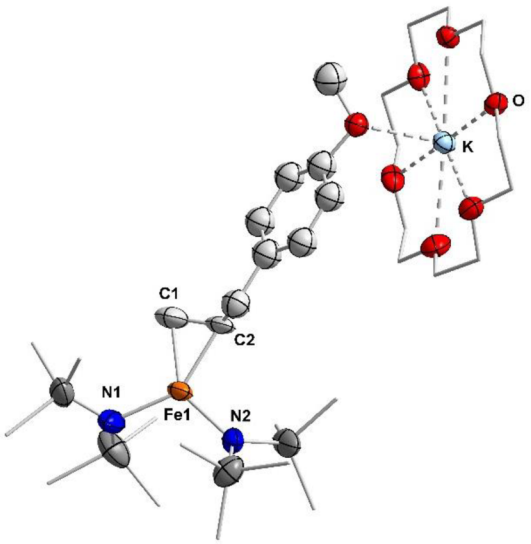

Abbildung 19. Molekülstruktur von **2**. Wasserstoffatome wurden der Übersicht halber nicht dargestellt. Ausgewählte Bindungslängen (Å) und –winkel (°): Fe1-C1 2.040(1), Fe1-C2 2.050(9), Fe1-N1 1.996(9), Fe1-N2 1.992(8), C1-C2 1.372(2), C1-C2-C_{ph} 120.5(10), N1-Fe1-N2 114.1(3).

Im Fall von Mangan und der Umsetzung mit dem Substrat 1,1-Diphenylethylen und [K{18-c-c6}][$Mn^{I}(hmds)_2$] in Et_2O bei Raumtemperatur kann, wie schon zuvor beschrieben, bei der Reaktion mit dem Chrom(I)-Komplex, eine reduktive Kupplung des Substrates zu einem Butandianion beobachtet werden (**Schema 14**). Die Bindungslängen zwischen den Kohlenstoffatomen C1 und C4 liegen im Bereich einer Einfachbindung[117].

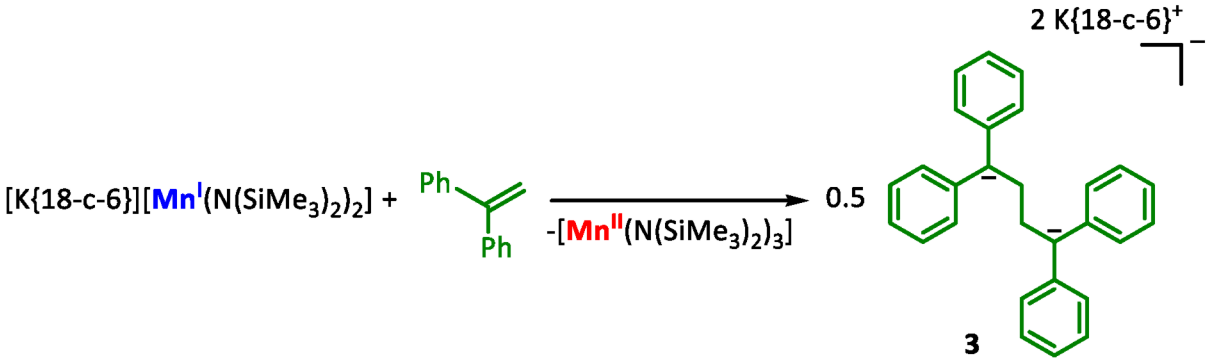

Schema 14. Reaktionsverlauf von 1,1-Diphenylethylen mit dem $[Mn^{I}(hmds)_2]^{-}$-Komplex.

Die Bildung von **3** kann durch die formale Reduktion des Substrats zum Radikalanion sowie durch dessen Dimerisierung erklärt werden. Eine Bindung an den eingesetzten Mangan(I)-Komplex wird überraschenderweise nicht beobachtet und lässt sich eventuell mit durch sterische Gründe erklären. Die Molekülstruktur von **3** zeigt, dass das 1,1-Diphenylethylen reduktiv zu einem Dianion gekuppelt wurde und kein Mangan mehr in der Struktur vorhanden ist (**Abbildung 20**).

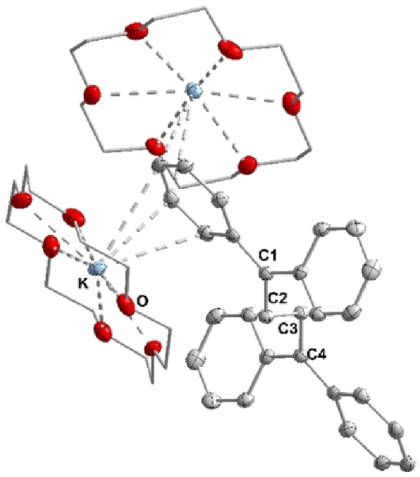

Abbildung 20. Molekülstruktur von **3**. Wasserstoffatome wurden der Übersicht halber nicht dargestellt. Ausgewählte Bindungslängen (Å): C1-C2 1.521(3), C2-C3 1.549(3), C3-C4 1.521(3).

Chrom zeigte eine interessante Reaktivität, denn unter der Abspaltung eines hmds-Liganden werden die Substrate (Styrol und 1,1-Diphenylethylen) jeweils reduktiv gekuppelt und es entsteht eine Art Fünfring mit dem Chrom-Komplex (**Schema 15**). Der abgespaltete hmds-Ligand wird von einem zweiten $[Cr^{I}(hmds)_2]^-$-Komplex, welcher das benötigte zweite Reduktionsäquivalent bereitstellt, unter Bildung eines $[Cr^{II}(hmds)_3]^-$-Komplexes abgefangen.

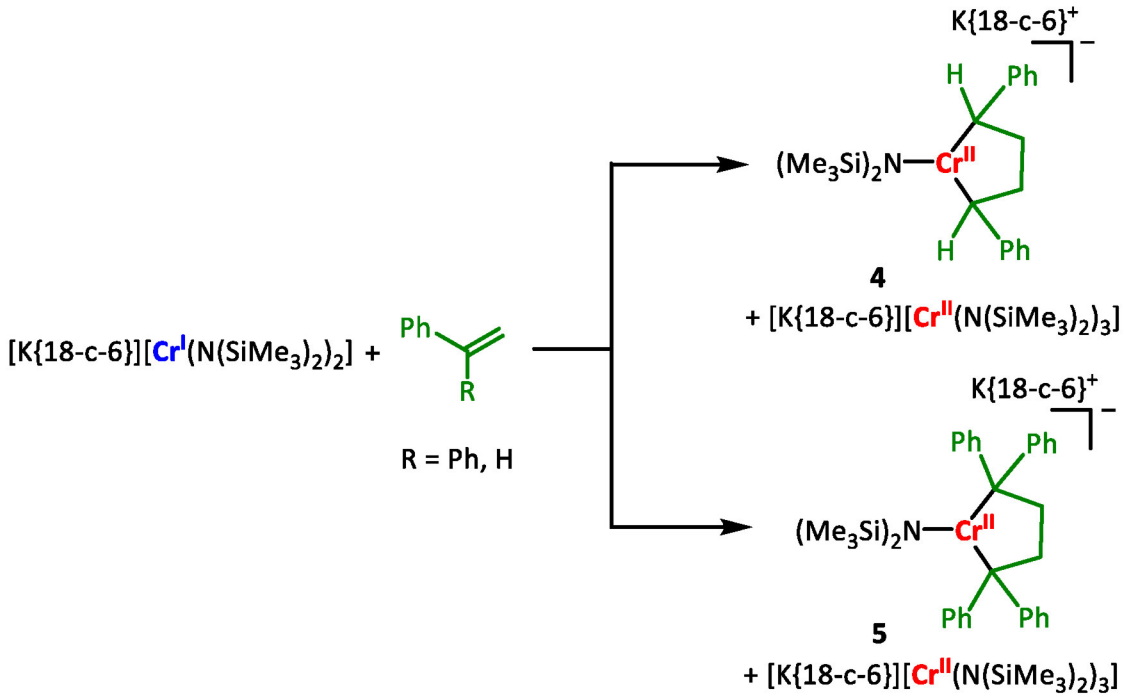

Schema 15. Reaktion der terminalen Alkene (Styrol und 1,1-Diphenylethylen) mit dem $[Cr^{I}(hmds)_2]^-$-Komplex.

Die **Abbildung 19** zeigt die Molekülstruktur von $[K\{18\text{-c-}6\}][Cr(hmds)_2](\eta^2\text{-}(PhCHCH_2CH_2CHPh)]$ (**4**) (links) und $[K\{18\text{-c-}6\}][Cr(hmds)_2](\eta^2\text{-}(Ph_2CCH_2CH_2CPh_2)]$ (**5**) (rechts). Die wichtigsten Bindungslängen und –winkel werden in **Tabelle 1** dargestellt.

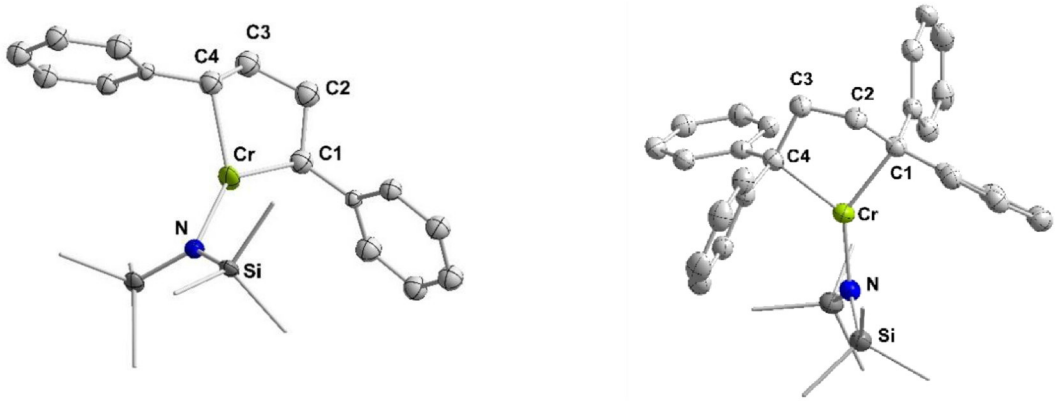

Abbildung 21. Molekülstruktur von **4** (links) und **5** (rechts). Wasserstoffatome und die Kationen $K\{18\text{-c-}6\}^+$ wurden der Übersicht halber nicht dargestellt.

Tabelle 1. Wichtige Bindungslängen und –winkel der Verbindungen **4** und **5**.

Verbindung	**4**	**5**
Bindungslängen/Å		
Cr-N	2.009(7)	2.010(2)
Cr-C1	2.158(7)	2.172(2)
Cr-C4	2.158(7)	2.175(3)
C1-C2	1.513(1)	1.529(4)
C2-C3	1.486(1)	1.524(3)
C3-C4	1.513(1)	1.537(3)
Bindungswinkel/°		
C1-Cr-C4	86.3(4)	86.1(8)
C2-C1-C_{ph}	119.7(6)	113.6(2)

Die Komplexe **4** und **5** sind sehr ähnlich aufgebaut und weisen kaum strukturelle Abweichungen auf. Der größte Unterschied liegt in den Bindungslängen zwischen den Kohlenstoffatomen C2 und C3. Bei dem Komplex **4** ist die Bindungslänge 1.486(1) Å und für den Komplex **5** 1.524(3) Å lang. Die Differenz von 0.038 Å kann zum einen durch das Inversionszentrum von **4** kommen und/oder zum anderen durch den zweiten Phenylring von **5**, der durch die erhöhte Sterik am Fünfring aufgeweitet wird.

Im Anschluss wurden interne Alkine als Substrate untersucht. Dabei wurde *cis*-Stilben und *cis*-β-Methylstyrol auf die Wechselwirkung zwischen der Variation der Metall(I)-Komplexe (M = Cr – Co) untersucht. Die Substrate (*cis*-Stilben und *cis*-β-Methylstyrol) wurden mit den Metall(I)-Silylamiden (M = Cr – Fe) bei Raumtemperatur in Et_2O umgesetzt (**Schema 16**).

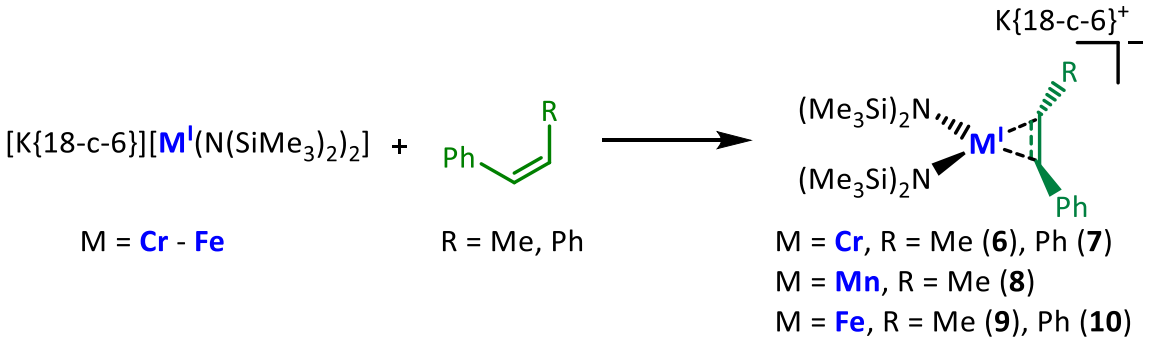

Schema 16. Allgemeiner Syntheseansatz für cis-Stilben und *cis*-β-Methylstyrol gegenüber den Metall(I)-Silylamiden (M = Cr – Fe).

Wie schon zuvor gezeigt wurde, konnte für Kobalt nur eine schwache und reversible Alken-Koordination beobachtet werden. Es konnten mittels Einkristallstrukturanalyse nahezu für alle Metalle *side-on* Alken-Komplexe vom Typ $[M(hmds)_2(\eta^2\text{-RCHCHR})]^-$ (M = Cr – Fe) nachgewiesen werden. Auffällig ist, dass in allen Fällen ein *trans*-Alken vorliegt und damit eine Metall vermittelte *cis* -> *trans* Isomerisierung stattgefunden hat. Die Molekülstrukturen von **8** und **9** werden hier exemplarisch für die Komplexe **6 – 10** gezeigt, da all diese Komplexe vom gleichen Typ sind (**Abbildung 22**). Die wichtigsten Bindungslängen und –winkel werden in **Tabelle 2** dargestellt.

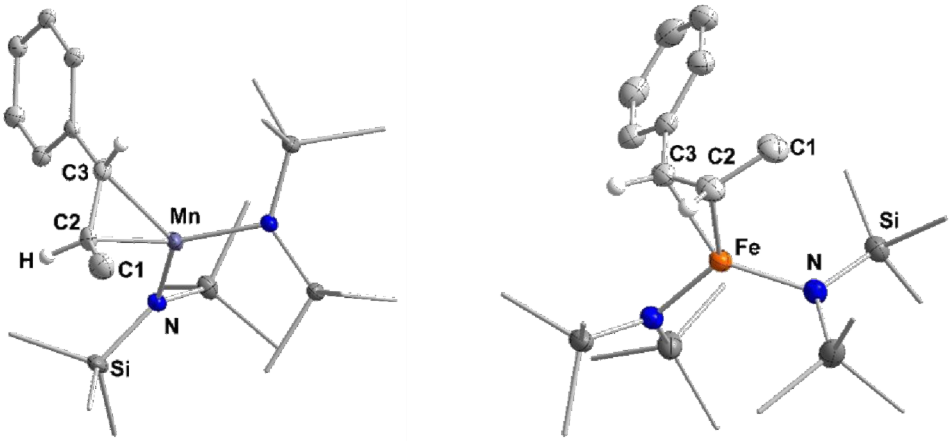

Abbildung 22. Molekülstruktur von dem ersten Mangan-Alken-Komplex **8** (links) und $[K\{18c6\}][Fe(N(SiMe_3)_2)_2(\eta^2\text{-}(cis\text{-}\beta\text{-methylstyrol})]$ (**9**)(rechts). Wasserstoffatome und die Kationen $K\{18\text{-c-}6\}^+$ wurden der Übersicht halber nicht dargestellt.

Tabelle 2. Wichtige Bindungslängen und –winkel der Verbindungen **6 – 10**.

Verbindung	6 (Cr, Me)	7 (Cr, Ph)	8 (Mn, Me)	9 (Fe, Me)	10 (Fe, Ph)
Bindungslängen/Å					
M-N1	2.016(2)	2.023(1)	2.059(2)	1.997(4)	2.016(2)
M-N2	2.028(2)	2.019(1)	2.058(2)	1.981(4)	2.028(2)
M-C2	2.121(2)	2.096(1)	2.111(2)	2.065(2)	2.156(6)
M-C3	2.056(2)	2.108(3)	2.236(2)	2.091(2)	2.142(6)
C2-C3	1.469(3)	1.462(2)	1.430(4)	1.414(3)	1.439(8)
Bindungswinkel/°					
N1-M-N2	122.5(2)	134.6(5)	122.8(5)	118.4(6)	116.7(1)
C1-C2-C3	118.5(2)	121.2(1)	119.2(3)	126.8(2)	124.6(6)

Die zentrale C–C-Bindungslänge beträgt im Falle von Chrom ca. 1.47 Å und liegt damit nahe einer Doppelbindung. Damit lässt sich **6** und **7** als ein Metallzyklopropen auffassen. Magnetische Messungen in Lösung unterstützen dabei das Vorliegen eines Chrom(III)-Komplexes. Die C–C-Bindungslängen nehmen im Falle von Mangan und Eisen zu und spiegeln den Übergang zu einem π-Alken-Komplex wieder. Hierbei ist zu bemerken, dass es sich bei **8** um den ersten niedrig-koordinierten Mangan-Alken-Komplex handelt. Solch eine *Z/E*-Isomerisierung von Stilbenderivaten kann gewöhnlich metallfrei ablaufen, wodurch die Reaktion photochemisch, thermisch oder katalysiert wird.[118] Die Metallkatalyse, *Z/E*-Isomerisierung, ist für allylische Doppelbindungen bekannt, erfolgt jedoch ausschließlich unter Beteiligung von Metall-Hydrid-Spezies. In der Arbeitsgruppe WERNCKE konnte bei der Reaktion von [K{18-c-6}][Fe^{I}(hmds)$_2$] und 1,2-Bis(diphenylphosphino)ethan eine *Z/E*-Isomerisierung beobachtet werden. Dieses Substrat weist ebenfalls keine allylische Doppelbindungen auf.[119] Diese *Z/E*-Isomerisierung kann wahrscheinlich auf der Arbeitsgrundlange von GANO erklärt werden. GANO konnte berechnen, dass für die *Z/E*-Isomerisierung bei neutralen Verbindungen eine sehr hohe Energie nötig ist. Wenn die Verbindungen jedoch anionisch sind, ist die benötigte Energiedifferenz für die *Z/E*-Isomerisierung nahezu null (**Abbildung 23**).[120]

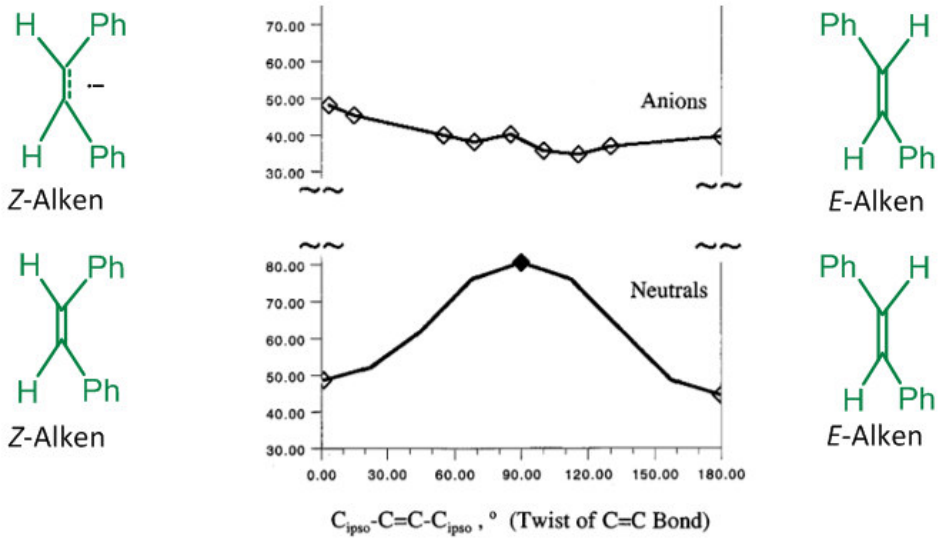

Abbildung 23. Berechnete Energiedifferenz für die *Z/E*-Isomerisierung für neutrale und anionische Alkene.[120]

Werden die gewonnen Erkenntnisse von GANO auf das vorliegende System angewendet, bildet sich im Verlauf der Reaktion eine Radikalmonoanion-Spezies, die die *Z/E*-Isomerisierung energetisch begünstigt (**Schema 17**). Die hier erhaltenen Metall-Alken-Komplexe lassen sich vor dem Hintergrund der entsprechenden Alkin-Verbindungen als Metall(II)-Alkenradikalanion-

Komplexe auffassen. Damit ließe sich eine Rotation um die C–C-Bindung erklären. Die Beteiligung eines initial gebildeten *Z*-Alken-Komplexes **9** konnte im Fall von Eisen und cis-β-Methylstyrol durch Kristallisation gezeigt und nachgewiesen werden (**Abbildung 24** (rechts)).

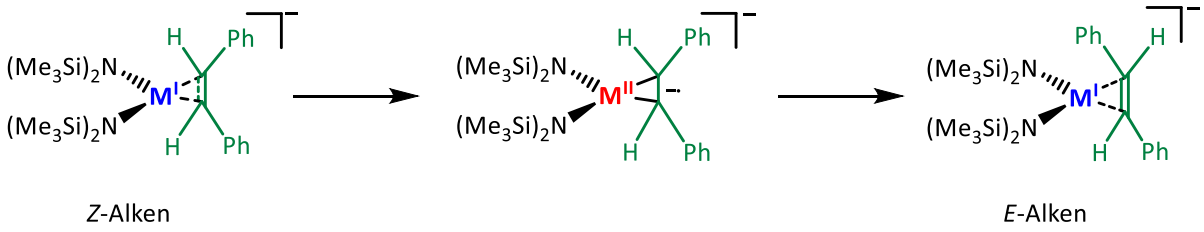

Schema 17. Potentieller Reaktionsverlauf für die *Z/E*-Isomerisierung der Alken-Komplexe.

In Reaktion von *cis*-Stilben mit [K{18-c-6}][Mn^{I}(hmds)$_2$] konnte mittels Einkristallstrukturanalyse das Vorliegen des vermuteten Stilben-Radikalanions **11** nachgewiesen werden (**Abbildung 24**). Die Stilben-Einheit **11** wird von zwei [K{18-c-6}] koordiniert und stabilisiert; als Gegenion liegt [Mn^{II}(hmds)$_3$]$^-$ vor. Auf die Diskussion der Bindungslängen und –winkel wird hier verzichtet, da der Datensatz zum einen nicht optimal ist und zum anderen ist das Stilben-Radikalanion **11** auf der Symmetrieachse fehlgeordnet und mit verschiedenen *constraints* und *restraints* verfeinert worden. Die Anordnung des vermuteten Radikalanions **11** zwischen zwei [K{18-c-6}]-Kationen erinnert dabei an den Fall des zuvor gezeigten 2-Phenylpyridins. Analog zu diesem ist **11** auch wahrscheinlich Produkt der Disproportionierung des Mangan(I)-Vorläufers, jedoch macht es das Vorliegen eines metall(II)gebundenen Radikalanions plausibel.

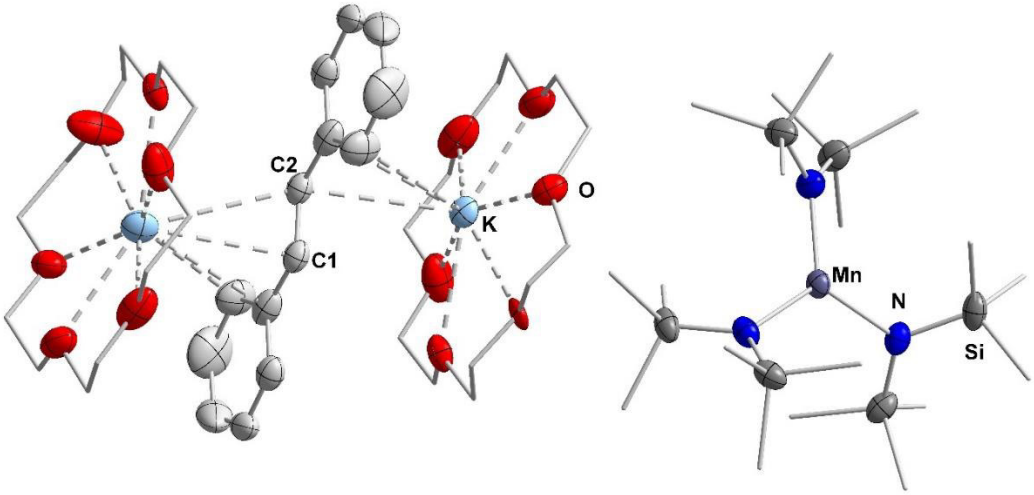

Abbildung 24. Molekülstruktur von dem Stilben-Radikalanion **11**. Wasserstoffatome wurden der Übersicht halber nicht dargestellt.

Im Anschluss wurde 2,3-Dimethylbutadien als konjugiertes Dien mit den Metall(I)-Komplexen [K{18-c-6}][MX_2] (18-c-6 = 18-Krone-6; X = –$N(SiMe_3)_2$) (M = Cr – Co) bei Raumtemperatur in Et_2O umgesetzt. Während für Kobalt keine Reaktivität zu beobachten war, zeigten sich je nach Metall einzigartige und verschiedene Reaktionsmodi (**Schema 18**).

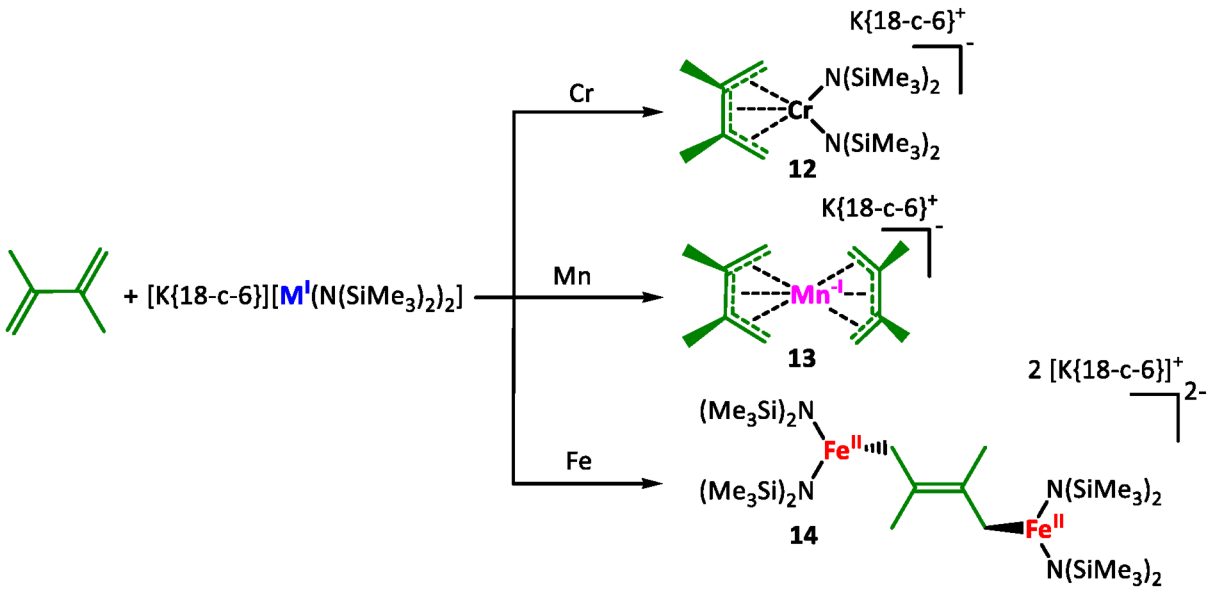

Schema 18. Verschiedene Aktivierungsmodi von 2,3-Dimethylbutadien durch $[M^I(hmds)_2]^-$-Komplexe (M = Cr – Fe).

Für Chrom wird die erwartete *side-on* Koordination erhalten, da das 2,3-Dimethylbutadien über die Kohlenstoffatome C1 bis C4 an das Metallatom koordiniert. Dabei sind beide Doppelbindungen über das System delokalisiert. Die Bindungslängen von C1 bis C4 liegen zwischen 1.403 Å und 1.461 Å, somit sind die Bindungslängen aufgeweitet und liegen zwischen einer Doppel- und Einfachbindung[117] (**Abbildung 25**).

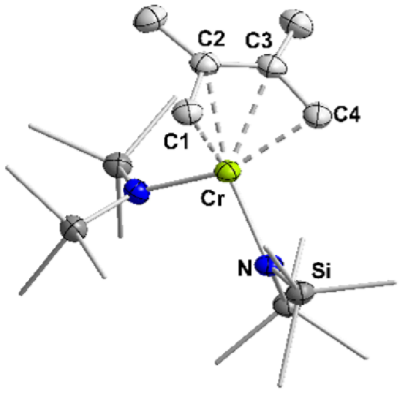

Abbildung 25. Molekülstruktur von **12**. Wasserstoffatome und das Kation $K\{18\text{-c-}6\}^+$ wurden der Übersicht halber nicht dargestellt.

Für Mangan zeigte sich, dass ähnlich zur Reaktion mit Tolan ein Ligandenaustausch und Redoxprozesse stattgefunden haben. Ein formales Mangan(-I)atom wird von zwei 2,3-Dimethylbutadienen und einem Kaliumatom koordiniert (**Abbildung 26**), dadurch hat das Manganatom eine Oxidationsstufe von –I. Die Bindungslängen von C1 bis C4 liegen alle im Bereich zwischen 1.417 Å und 1.456 Å, somit sind die Doppelbindungen des Butadienliganden delokalisiert.

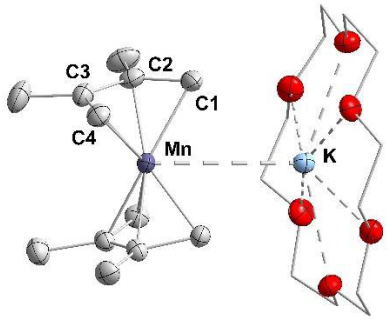

Abbildung 26. Molekülstruktur von **13**. Wasserstoffatome wurden der Übersicht halber nicht dargestellt.

Im Fall von Eisen zeigte sich, dass das Substrat 2,3-Dimethylbutadienen zweifach reduziert wurde und zwei [$Fe^{II}(hmds)_2$]-Einheiten an das Alken an Position C1 und C5 koordinieren (**Abbildung 27**). Dabei konnte beobachtet werden, dass die Bindungslängen zwischen C1-C2 (1.566 Å) und C4-C5 (1.464 Å) eine Einfachbindung und C2-C4 (1.282 Å) eine Doppelbindung geworden sind. Die Bindungslängen zwischen den Eisen- und Kohlenstoffatomen liegen bei 2.052 Å. YANG konnte mit einem Aluminium(II)-Dimer ein ähnliches Koordinationsmuster beobachten.[115]

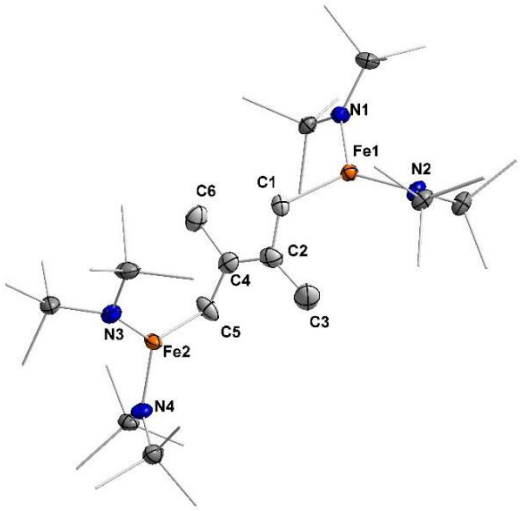

Abbildung 27. Molekülstruktur von **14**. Wasserstoffatome und beide Kationen $K\{18\text{-c-}6\}^+$ wurden der Übersicht halber nicht dargestellt.

5 Zusammenfassung

Im Rahmen dieser Doktorarbeit wurde das Verhalten von linearen 3d-Metall(I)-Silylamiden (M = Cr – Co) [50,51] gegenüber C/N-Mehrfachbindungen und aromatischen Systemen untersucht.

Im ersten Teil der Arbeit konnten die reduzierten Metall(II)-(bipy)-Komplexe (M = Cr – Co, Zn) in guten Ausbeuten erhalten werden. Dabei spielt es keine Rolle, ob der Metall(I)-Komplex mit 2,2´-Bipyridin oder zunächst der Metall(II)-Komplex mit 2,2´-Bipyridin, mit anschließender Reduktion durch KC_8 in Anwesenheit von 18-c-6, umgesetzt wurde (**Schema 19**).

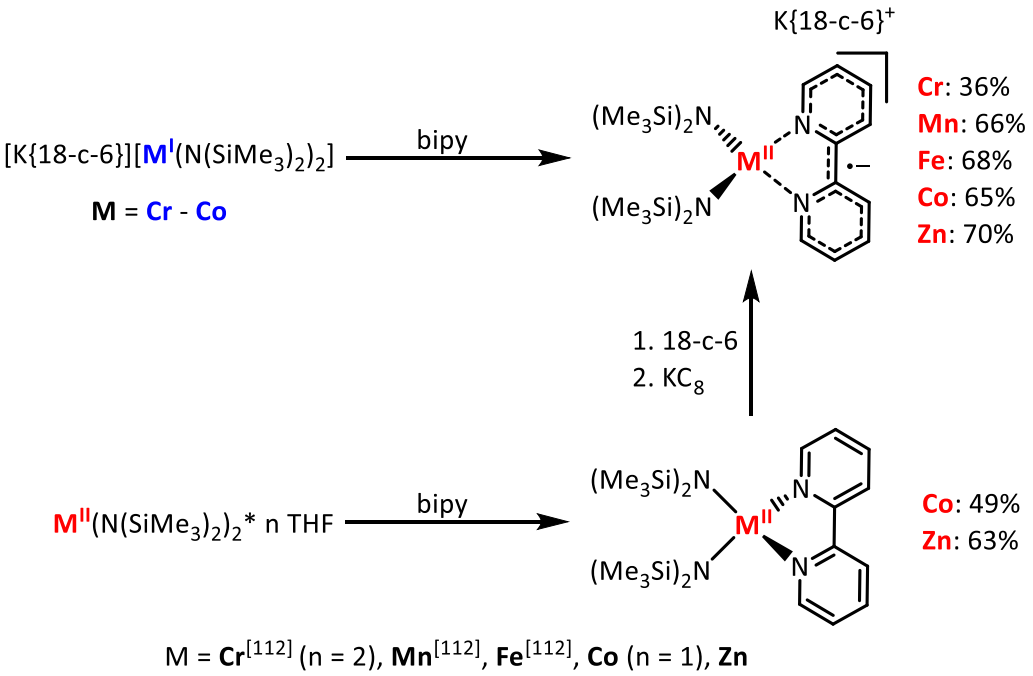

M = **Cr**[112] (n = 2), **Mn**[112], **Fe**[112], **Co** (n = 1), **Zn**

Schema 19. Darstellung der reduzierten Metall(II)-Bipyridylkomplexe (M = Cr – Co, Zn) auf zwei unterschiedlichen Synthesewegen.

2,2´-Bipyridin kann durch Aufnahme von einem und/oder zwei Elektronen zum π-Radikal-Monoanion und diamagnetischen Dianion reduziert werden (**Schema 20**.

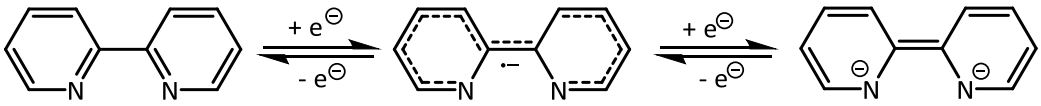

Schema 20. Mögliche Resonanzstrukturen von 2,2-Bipyridin. Bindungslängen zwischen den Pyridinringen: 1.49 Å (Neutralligand), 1.43 Å (π-Radikal-Monoanion), 1.39 Å (diamagnetisches Dianion).[114]

Über verschiedene spektroskopische Methoden und einer Einkristallstrukturanalyse konnte ein Elektronentransfer vom Metall(I)-Komplex auf den Bipyridinliganden bestätigt werden, der nun als Radikalanion wirkt. Zusammengefasst zeigen die anionischen Metall(I)-Silylamid-

Substrate, dass 2,2´-Bipyridin reduziert und gebunden werden kann, selbst wenn deren elektrochemisches Reduktionspotential um bis zu 1 V höher liegt als das von 2,2´-Bipyridin.

Im nächsten Teil dieser Doktorarbeit wurden die Metall(I)-Silylamide (M = Cr – Co)[50,51] mit Pyridin umgesetzt, um Komplexe mit einem Pyridylradikalanion zu erzeugen. Jedoch konnten über die Festkörperanalyse Verbindungen mit einem zweikernigen Dianion ermittelt werden. Die beiden Metallionen sind durch ein Pyridin abgleitendes Dianion (4,4´-Dihydropyridin) verbrückt, welches durch die formale ein-Elektronen Reduktion und Dimerisierung von Pyridin in *para*-Position entstanden ist (**Schema 21**). Die Bindungsmetrik des Dihydrobipyridyls weist einen Verlust der Aromatizität bei nun lokalisierten Einfach- und Doppelbindungen auf. Bei Blockierung der *para*-Position des Pyridins durch einen Substituenten auf Stickstoff- oder Kohlenstoffbasis (NMe_2 oder ^tBu) konnte keine Dimerisierung oder gar einfache Koordination nachgewiesen werden. Für Kobalt konnte in allen Fällen keine Interaktion mit Pyridin oder mit Pyridinderivaten beobachtet werden.

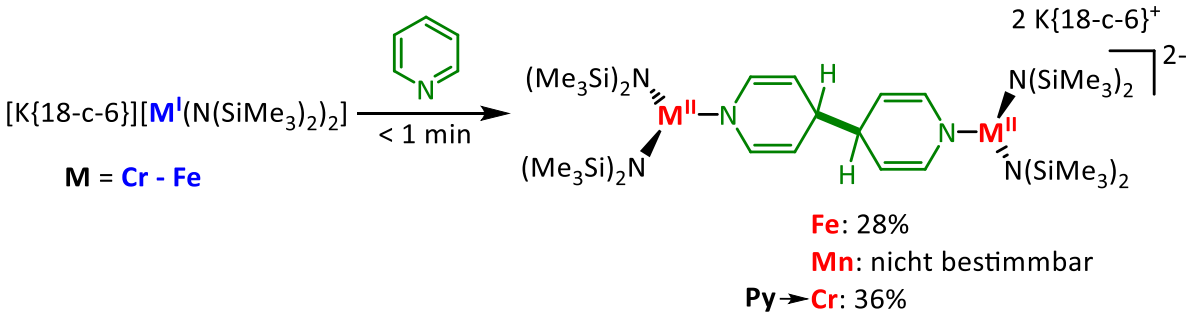

Schema 21. Allgemeiner Syntheseansatz für die Umsetzung von Pyridin mit Metall(I)-Silylamiden (M = Cr – Fe).

Die Reaktion zwischen Pyridin und den Metall(I)-Komplexen zeigte, dass eine Substratreduktion vor oder während der Koordination des Substrats an das Metallzentrum notwendig ist. Um einfache sterische Effekte auszuschließen, wurde 3,5-Lutidin mit den Metall(I)-Silylamiden umgesetzt (**Schema 22**). Jedoch konnte hier ebenfalls eine Dimerisierung beobachtet werden. Um den Radikalcharakter möglicherweise über ein größeres aromatisches System zu stabilisieren, wurde 2-Phenylpyridin ebenfalls getestet (**Schema 22**).

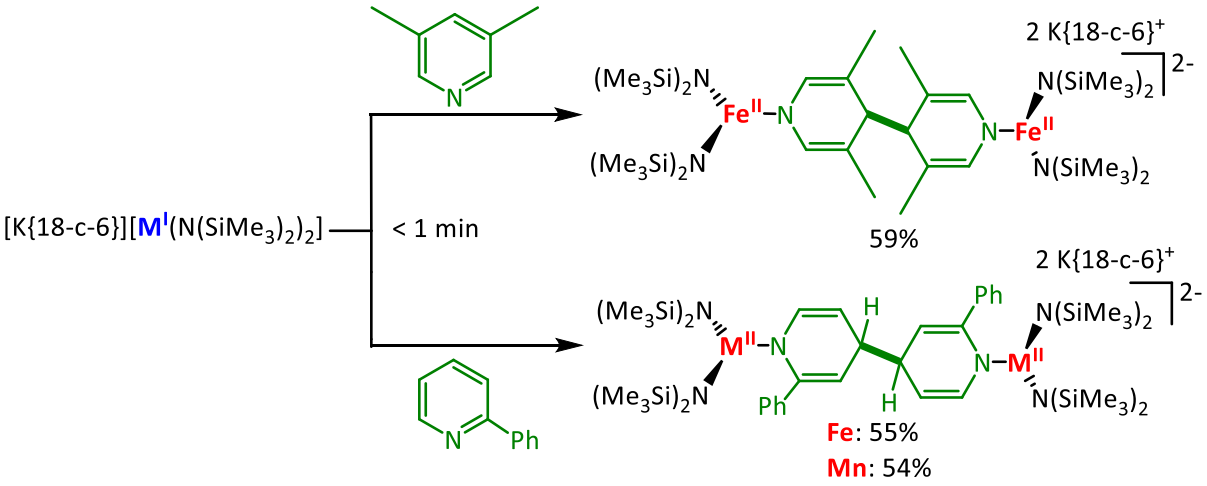

Schema 22. Reaktion der sterisch anspruchsvollen Pyridine (3,5-Lutidin und 2-Phenylpyridin) mit den Metall(I)-Silylamid-Komplexen (Mn und Fe).

Es zeigte sich, dass die Reaktionen mit den Eisen- und Mangan-Komplexen erneut zur Dimerisierung der Pyridine führt. Zusätzlich konnten bei der Reaktion zwischen 2-Phenylpyridin und [K{18-c-6}][Mn^{I}(hmds)$_2$] blaue Kristalle erhalten werden. Durch eine Einkristallstrukturanalyse konnte die Verbindung aus **Abbildung 28** bestätigt werden, in der eine 2-Phenylpyridyl-Einheit zwischen zwei [K{18-c-6}]-Kationen und einem [Mn(hmds)$_3$]$^-$ als Gegenion angeordnet ist. Das Vorhandensein des Gegenions deutet auf ein Pyridylradikalanion hin, dessen Anwesenheit mittels UV-Vis-Spektroskopie bestimmt wurde. Das Pyridylradikalanion konnte durch die direkte Reduktion von 2-Phenylpyridin durch KC_8 in Anwesenheit von [K{18-c-6}][Mn(hmds)$_3$] und 18-c-6 dargestellt und ebenfalls mittels UV-Vis-Spektroskopie bestimmt werden.

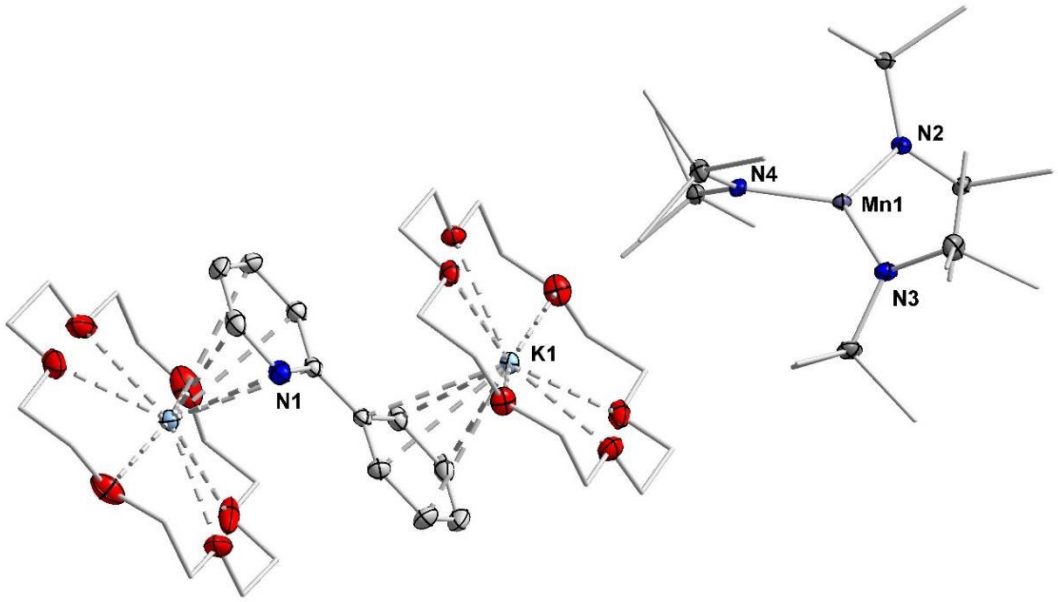

Abbildung 28. Molekülstruktur von [K{18-c-6}]$_2$[Mn(hmds)$_3$][2-Phenylpyridyl]. Wasserstoffatome sind aus Gründen der Übersichtlichkeit nicht dargestellt.

Nachdem die reduktive Kupplung von Pyridinen unter Verwendung von Metall(I)-Silylamiden (M = Cr – Fe), mit der Ausnahme des Kobalt(I)-Komplexes gezeigt wurde, wurden elektronenarme Fluoropyridine mit unterschiedlichen Fluorierungsgraden eingesetzt, um die Reduktion insbesondere im Falle von Kobalt zu erleichtern (**Schema 23**). Das Reduktionspotential des Kobalt(I)-Komplexes gegenüber Pyridinen ist vergleichsweise gering.

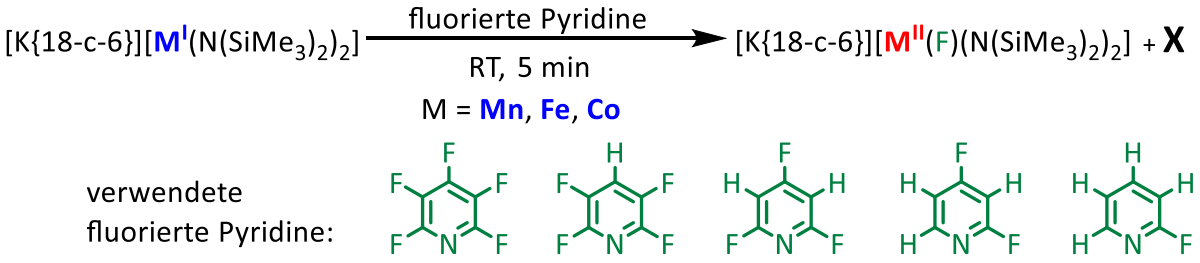

Schema 23. Variation des Fluorierungsgrades des Pyridin-Derivats.

Die Umsetzung zeigte, dass sich immer ein fluorierter Metall-Komplex (M = Mn – Co) und eine oder mehrere unbekannte Spezies unabhängig des eingesetzten Fluoropyridins, bilden (**Schema 23**). Für das Substrat Pentafluoropyridin konnte das Nebenprodukt spektroskopisch als 4,4´-Perfluorobipyridin nachgewiesen werden, welches sich aus einer reduktiven Kupplung unter C–F-Spaltung bildete. Bei der Umsetzung mit 2-Fluorpyridin konnte ein Pyridyl-Komplex als Nebenprodukt mithilfe einer Einkristallstrukturanalyse identifiziert werden (**Schema 24**). Für Mangan konnte der erste strukturell charakterisierte Mangan-Fluorido-Komplex in trigonaler Umgebung dargestellt werden.

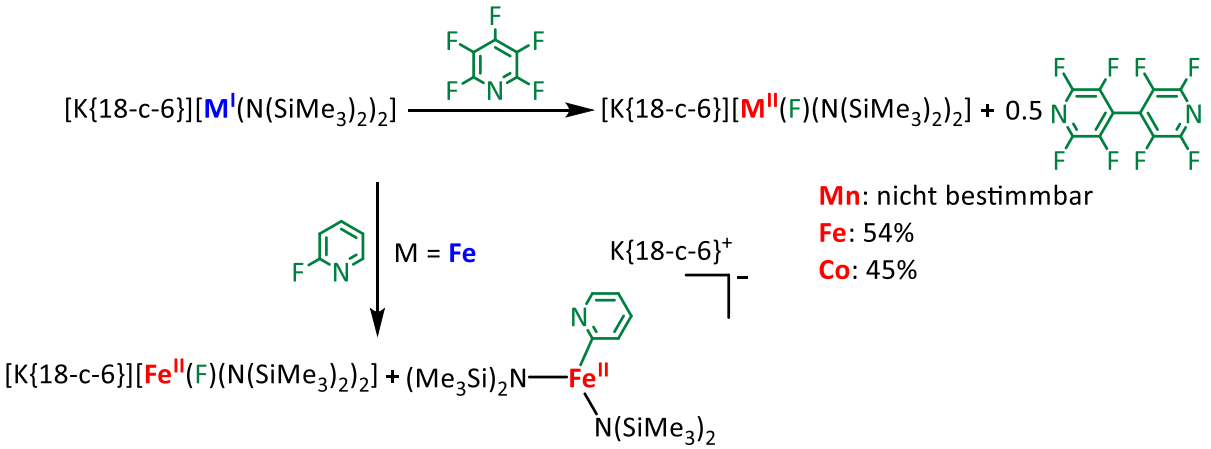

Schema 24. Synthese der niedrig-koordinierten Fluorido-Metall-Komplexe durch Umsetzung von Metall(I)-Silylamiden (M = Mn – Co) mit Perfluorobipyridin und 2-Fluorpyridin.

Neben der Reaktivität von Metall(I)-Komplexen gegenüber 2,2´-Bipyridin und Pyridinen konnte in dieser Arbeit gezeigt werden, dass eine Reihe seltener niedrig-koordinierter 3d-Übergangsmetall-Alkin-Komplexe aus der Reaktion von linearen Metall(I)-Silylamiden [K{18-c-

6}[MX_2] (18-c-6, X = –N($SiMe_3$)$_2$), –N(Dipp)$SiMe_3$; Dipp = 2,6-Di-*iso*-propylphenyl) (M = Cr – Co) mit aliphatischen und aromatischen Alkinen resultieren können (**Schema 25**).

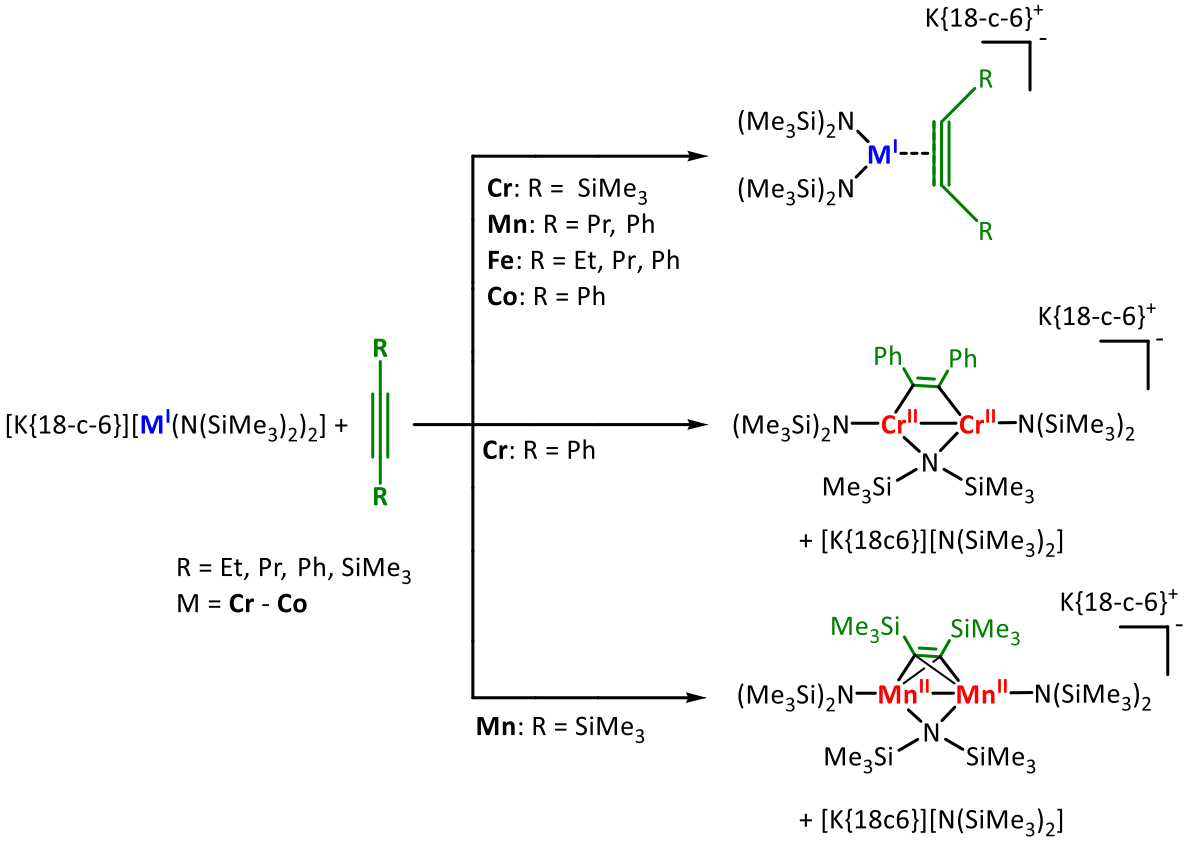

Schema 25. Darstellung von niedrig-koordinierten Metall-Alkin-Komplexen.

Es wurde die Wechselwirkung von Alkinen mit linearen Metall(I)-Komplexen sowohl in Abhängigkeit des Metalls als auch des Alkinsubstituenten untersucht. Während für Kobalt nur eine schwache und reversible Alkin-Koordination beobachtet wird, findet die Bildung von *side-on* Alkin-Komplexen des Typs [M(hmds)$_2$(η^2-RCCR)]$^-$ für Eisen leicht statt. Im Fall von Mangan wurden die ersten niedrig-koordinierten Mangan-Alkin-Komplexe vorgestellt. Je nach Substrat können weiterhin einzigartige Beispiele der Mangan vermittelten Reduktion des Alkins zum Dianion auch die Trimerisierung des Alkins gezeigt werden (**Schema 26**). Für Chrom konnte ebenfalls eine Alkin-Koordination zu den jeweiligen *side-on* Komplexen oder eine Reduktion zum Alkin-Dianion beobachtet werden. Quantenchemische Analysen der Komplex-Reihe [M(hmds)$_2$(η^2-PhCCPh)]$^-$ (M = Cr – Co) unter Verwendung von DFT- und CASSCF-Methoden zeigten eine teilweise Reduktion des Alkins durch das Metallion, sodass durch die elektronischen Situation all dieser Komplexe als formal Metall(II)-gebundenes Alkinylradikalanion beschrieben werden können. Im Fall von Chrom wurden weiterhin signifikante Beiträge einer Metall(III)-Zyklopropenresonanzstruktur quantenchemisch gefunden.

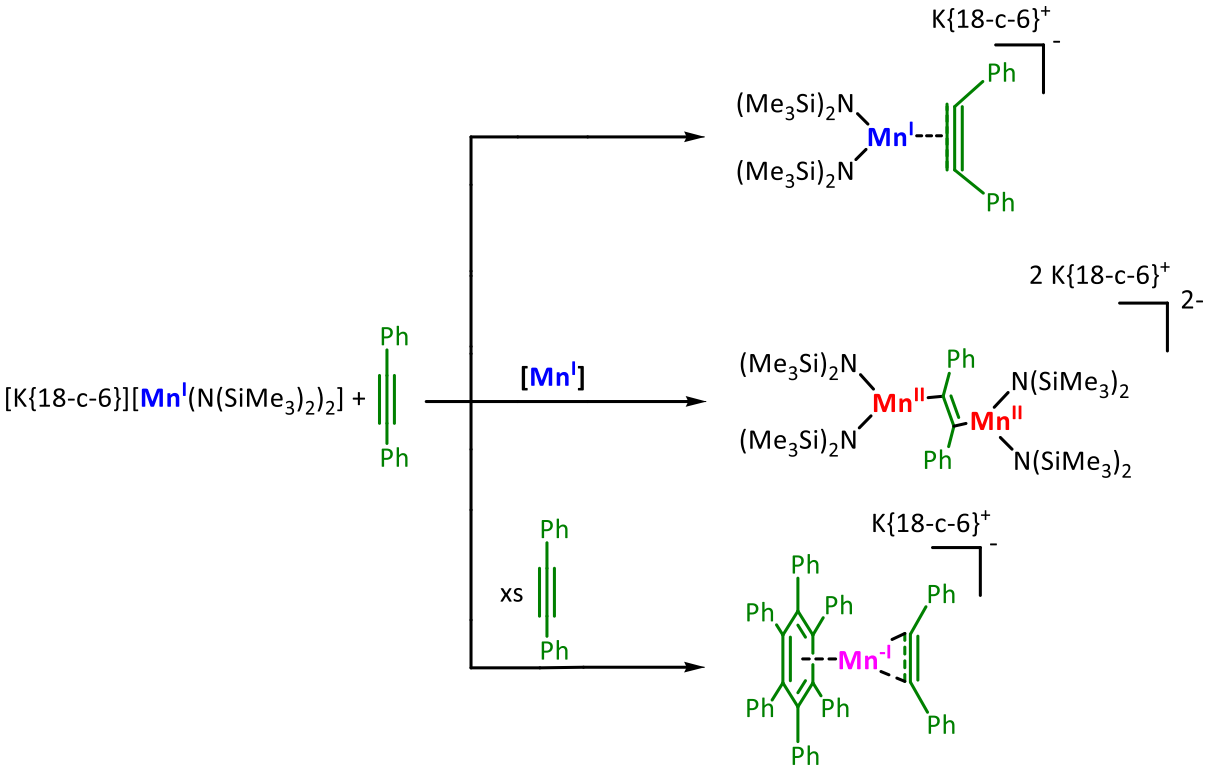

Schema 26. Verschiedene Aktivierungsmodi von Tolan durch [K{18-c-6}][Mn(I)(hmds)$_2$].

Bei den Reaktionen zwischen terminalen Alkinen und linearen Eisen(I)-Silylamiden [K{18-c-6}][Fe(hmds)$_2$] zeigte sich ein sehr ähnliches Koordinationsmuster wie bei den nicht-terminalen Alkinen schon zuvor. In beiden Fällen bildete sich ein *side-on* Komplex mit der Besonderheit bei dem Substrat 3-Phenyl-1-propin. Hier wird zusätzlich eine instantane Umlagerung der Dreifachbindung beobachtet (**Schema 27**).

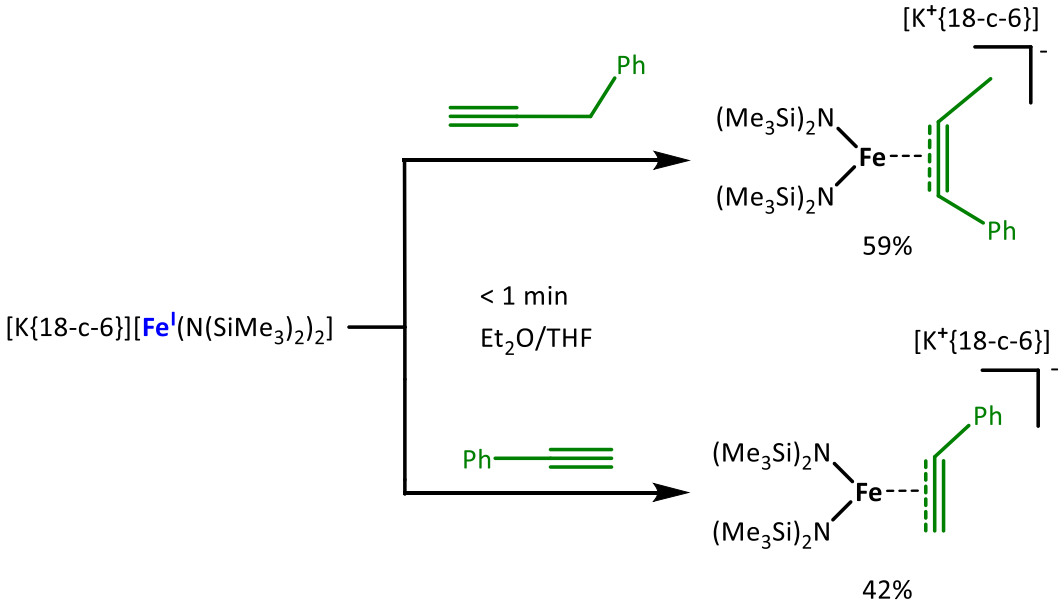

Schema 27. Reaktion der terminalen Alkine (Phenylacetylen und 3-Phenyl-1-propin) mit dem Eisen(I)-Silylamid-Komplex.

Nach der Erkenntnis der Umlagerung der Dreifachbindung bei dem Substrat 3-Phenyl-1-propin im Komplex, wurden für dieses und andere Substrate eine Umlagerung unter Verwendung von katalytischen Mengen an verschiedenen Eisenverbindungen untersucht (**Schema 28**).

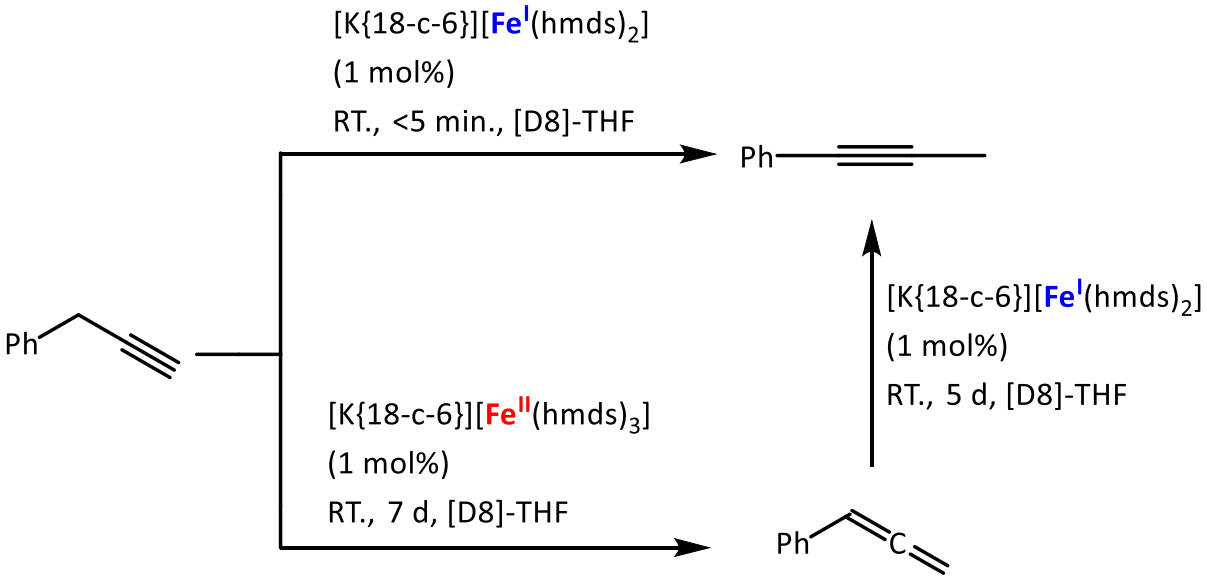

Schema 28. Katalytische Untersuchung von 3-Phenyl-1-propin bei der Verwendung von zwei verschiedenen Katalysatoren.

Hierbei zeigt sich, dass die Umlagerung von 3-Phenyl-1-propin auch im katalytischen Maßstab bei Raumtemperatur unter Verwendung von [K{18-c-6}][Fe(hmds)$_2$] instantan erfolgen kann. K{18-c-6}][Fe(hmds)$_2$] ist weniger aktiv, führt jedoch zur ausschließlichen Bildung von Phenylallen. Der Mechanismus für die Umlagerung der Dreifachbindung ist noch ungeklärt, wobei eine Beteiligung einer Metall-Hydrid-Spezies hier unwahrscheinlich erscheint. Zusätzlich wurden [K{18-c-6}][Fe(hmds)$_3$], K(hmds) und Li(hmds) als Katalysatoren (10 mol%) mit dem Substrat 3-Phenyl-1-propin umgesetzt. Dabei zeigte sich, dass [K{18-c-6}][Fe(hmds)$_3$] die langsame, aber selektive Bildung des Phenylallens herbeiführt, während K(hmds) die sofortige Umlagerung zum internen Alkin vermittelt. Für Li(hmds) wird erst die Bildung des Allens und in Folge die des internen Alkins beobachtet.

Neben der Reaktivität von Metall(I)-Komplexen gegenüber Alkinen konnte in dieser Arbeit gezeigt werden, dass eine Reihe seltener niedrig-koordinierter 3d-Übergangsmetall-Alken-Komplexe aus der Reaktion von quasi-linearen Metall(I)-Silylamiden [K{18-c-6}[MX$_2$] (18-c-6, X = –N(SiMe$_3$)$_2$), hmds, (M = Cr – Co) mit terminalen, internen Alkenen und Dienen resultieren können. Es konnte für Kobalt generell nur eine schwache und reversible Alken-Koordination beobachtet werden.

Für die terminalen Alkene konnte im Fall von Eisen ein *side-on* Alken-Komplex des Typs $[Fe(hmds)_2(\eta^2\text{-PhCHCH})]^-$ dargestellt werden. Während für Chrom und Mangan eine reduktive Kupplung der Substrate beobachtet wurde (**Schema 29**).

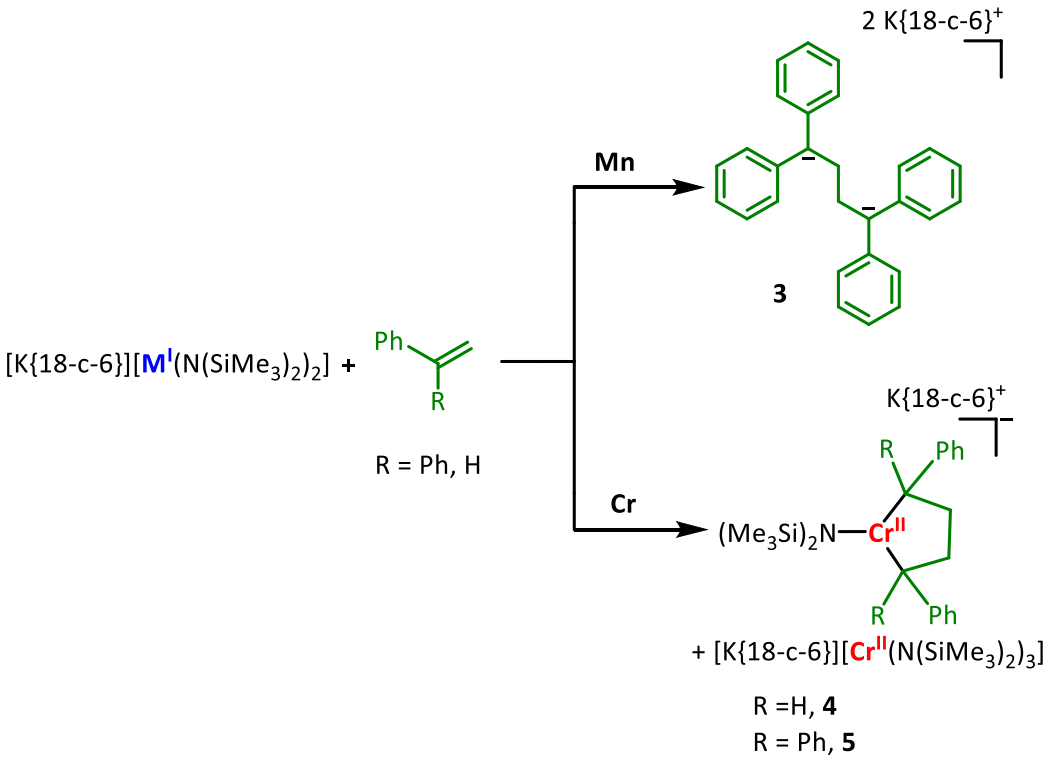

Schema 29. Reaktion der terminalen Alkene (Styrol und 1,1-Diphenylethylen) mit dem $[M^I(hmds)_2]^-$-Komplex (M = Cr und Mn).

Für interne Alkene findet die Bildung von *side-on* Alken-Komplexen des Typs $[M(hmds)_2(\eta^2\text{-PhCHCHR})]^-$ statt. Im Fall von Mangan wurden die ersten niedrig-koordinierten Mangan-Alken-Komplexe vorgestellt. Dabei wurde in allen Fällen eine *Z/E*-Isomerisierung der eingesetzten *cis*-Substrate (Stilben und β-Methylstyrol) beobachtet (**Schema 30**).

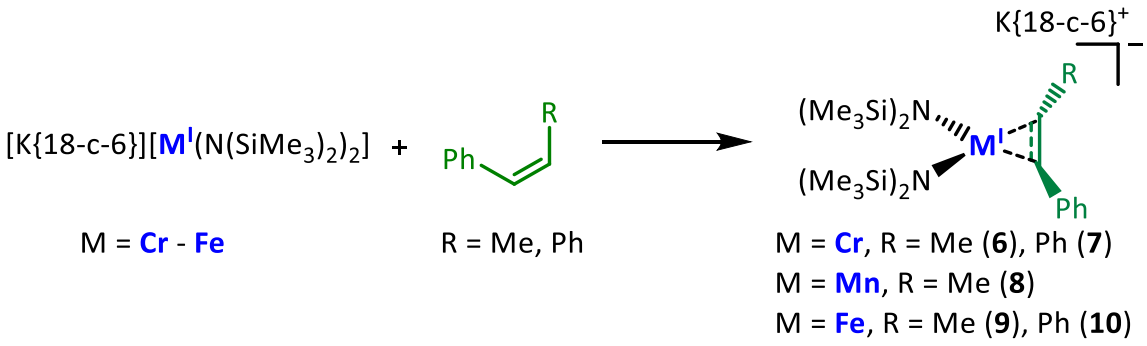

Schema 30. Allgemeiner Syntheseansatz für *cis*-Substrate (Stilben und β-Methylstyrol) gegenüber den Metall(I)-Silylamiden (M = Cr – Fe).

Die *cis/trans*-Isomerisierung findet wahrscheinlich durch das Vorliegen von metallgebundenen Alken-Radikalanion statt. Im Zuge dieser Arbeit konnte daher ein 3d-Metallfreies Alken-Radikalanion strukturell charakterisiert werden.

Zum Schluss wurde die Wechselwirkung von einem Dien (2,3-Dimethylbutadienen) mit quasilinearen Metall(I)-Komplexen in Abhängigkeit des Metalls untersucht (**Schema 31**).

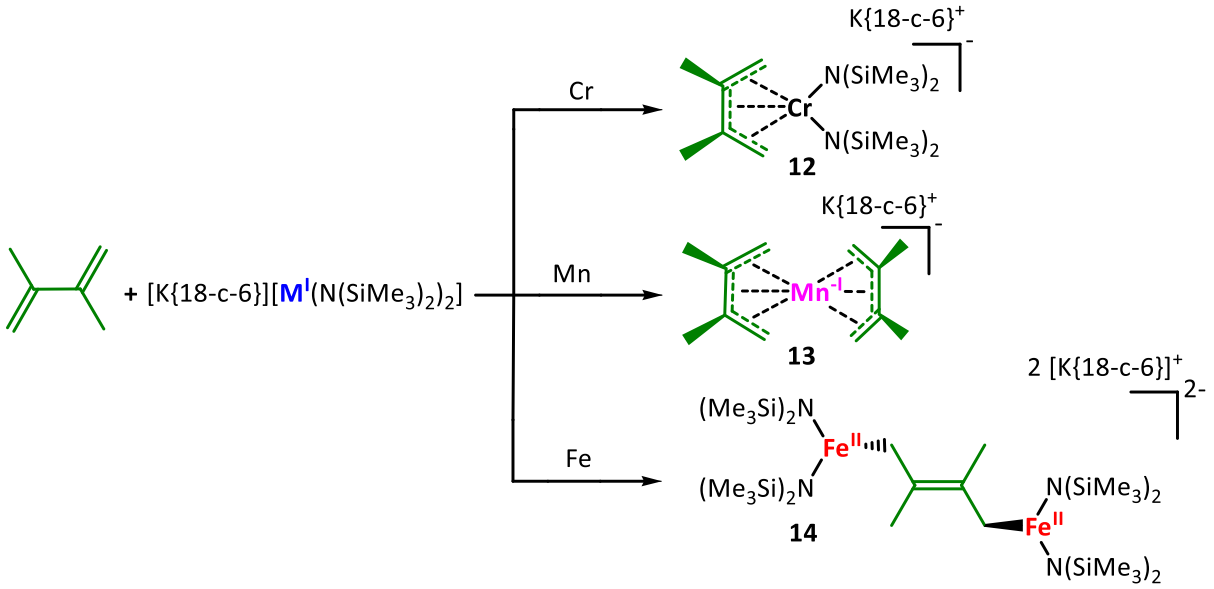

Schema 31. Verschiedene Aktivierungsmodi von 2,3-Dimethylbutadien durch $[M^{I}(hmds)_2]^-$-Komplexe (M = Cr – Fe).

2,3-Dimethylbutadien zeigte eine Vielseitigkeit an verschiedenen Aktivierungsmodi gegenüber der Metall(I)-Komplexe (M = Cr – Fe). Für Chrom konnte ein *side-on* Dien-Komplex dargestellt werden, wobei die zwei Doppelbindungen delokalisiert und über das Substrat verteilt sind. In dem Fall von Mangan fand ein kompletter Ligandenaustausch statt und das formale Mangan wird von zwei 2,3-Dimethylbutadienen koordiniert, wobei Mangan die Oxidationsstufe von –I besitzt. Bei Eisen wurde das Substrat 2,3-Dimethylbutadien zweifach reduziert, während für Kobalt keine Reaktivität gegenüber 2,3-Dimethylbutadien beobachtet werden konnte.

Insgesamt konnten durch diese ersten umfassenden Studien zur Substrataktivierung durch anionische, linear 3d-Metall(I)-Komplexe Einblicke in das ungewöhnliche chemische Verhalten dieser jungen Substanzklasse erhalten werden. Hierbei zeigte sich auch die Möglichkeit zum katalyischen Einsatz solcher Verbindungen, was in Zukunft noch weiter ausgenutzt werden kann.

6 Summary

The scope of this doctoral thesis is the chemical behavior of linear 3d-metal(I) silylamides of the type [K{18-c-6}][M^{I}(hmds)$_2$] (M = Cr – Co)[50,51] towards C/N multiple bonds and aromatic systems.

In the first part of this work it could be shown that the reduced metal(I) complexes reacted readily with 2,2'-bipyridine under substrate reduction and formation of metal(II) complexes bearing a bipyridyl radical anion. Alternatively the metal(II) complexes [M^{II}(hmds)$_2$] (M = Cr – Co, Zn) could be reacted first with 2,2'-bipyridine and subsequently reduced by KC_8 in the presence of {18-c-6} (**Scheme 1**), allowing for the isolation of the zinc derivative.

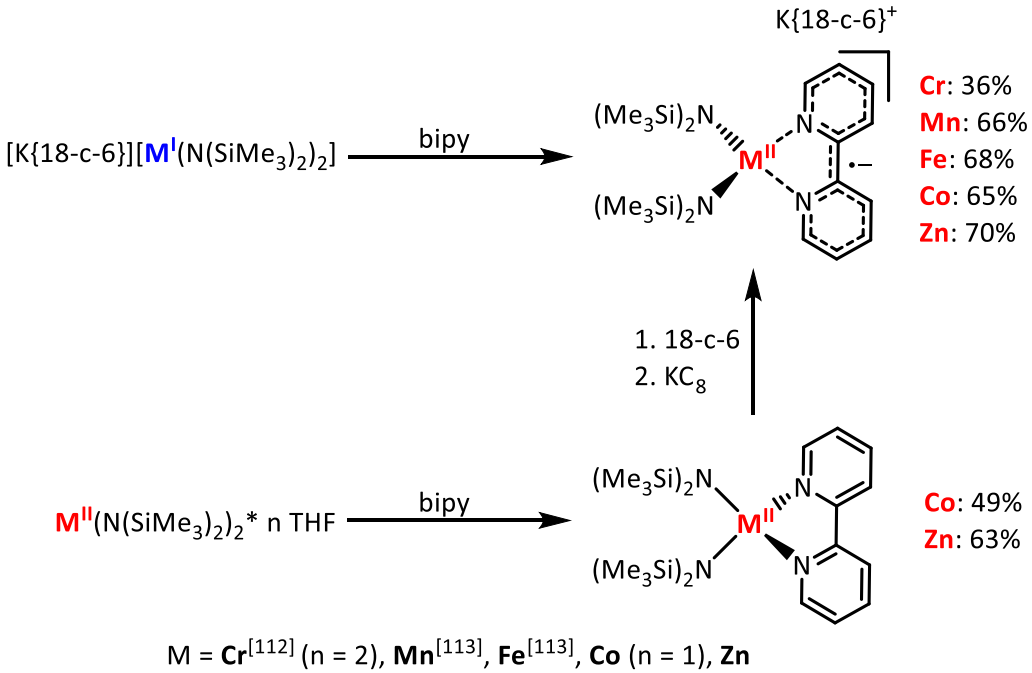

M = **Cr**[112] (n = 2), **Mn**[113], **Fe**[113], **Co** (n = 1), **Zn**

Scheme 1. Synthesis of the reduced metal(II)(bipy) complexes (M = Cr – Co, Zn) using two different synthetic routes.

As 2,2´-bipyridine can be reduced to a radical monoanion, and a diamagnetic dianion by accepting one or two electrons respectively (**Scheme 2**).

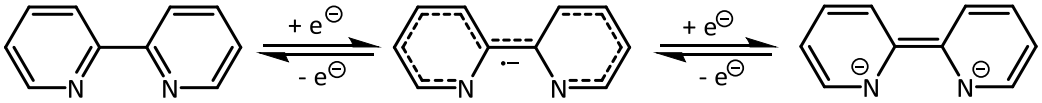

Scheme 2. Resonance structures of 2,2-bipyridine. Bond length between the pyridine rings: 1.49 Å (Neutral ligand), 1.43 Å (π radical monoanion), 1.39 Å (diamagnetic dianion).[114]

Using various spectroscopic methods and single crystal structure analysis, it shows that for all compounds the description as $Mn^{II}(bipy^{*-})$ is valid. This is remarkable, as the reduction potential needed for 2,2'-bipyridine reduction is lower by up to 1 V that provided by the metal(I) complexes.

In order to expand this approach to even more challenging to needed substrates, metal(I) silylamides (M = Cr – Co)[50,51] were reacted with pyridine to possible create metal bound pyridyl radical anions. However, binuclear dianions were found by solid-state analysis. Two metal ions are bridged by a dihydrobipyridyl, originating from the reductive dimerization of pyridine in the *para*-position (**Scheme 3**). The bond metrics of the bipyridyl ligand shows a loss of aromaticity with single and double bonds now being localized. When the *4*-position of pyridine was blocked by a nitrogen- or carbon-based substituent (NMe_2 or ^tBu), no dimerization or coordination was detected. For cobalt, no interaction with pyridine or with pyridine derivatives could be observed in any of these cases.

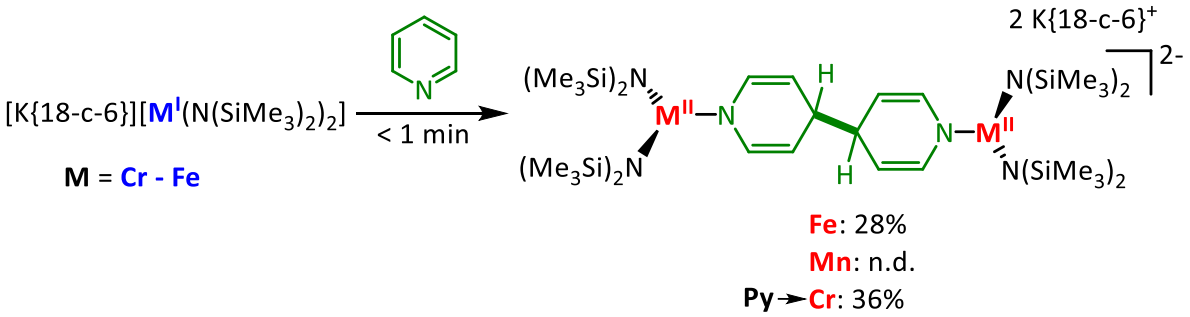

Scheme 3. General synthetic approach for the reaction of pyridine with metal(I) silylamides (M = Cr – Fe).

The reaction between pyridine and metal(I) complexes indicates the necessity of substrate reduction before or during the coordination to the metal center. In order to rule out simple steric effects, 3,5-lutidine was reacted with the metal(I) silylamides (**Scheme 4**). However, dimerization was also observed. In order to possibly stabilize the radical character via a larger aromatic system, 2-phenylpyridine was tested, too (**Scheme 4**), yielding the same outcome for manganese and iron.

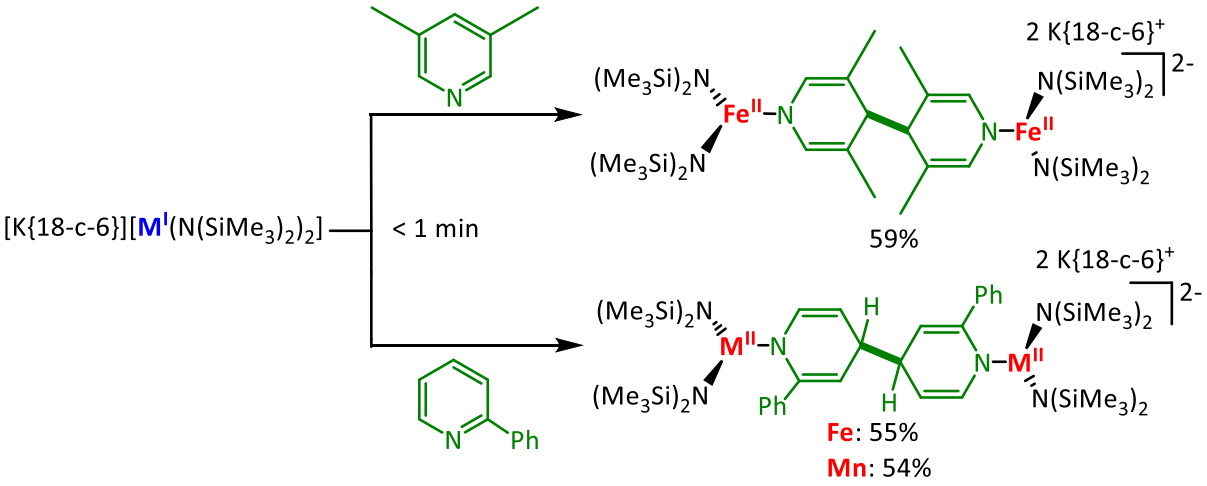

Scheme 4. Reaction of sterically demanding pyridines (2-phenylpyridine and 3,5-lutidine) with metal(I) silylamide complexes (Mn and Fe).

In addition, blue crystals could be obtained by reacting 2-phenylpyridine with the manganese(I) complex as a side product. Single crystal structure analysis revealed the presence of a 2-phenylpyridyl unit, which is sandwiched between two $[K\{18\text{-c-}6\}]^+$ cations (**Figure 1**) with $[Mn(hmds)_3]^-$ acting as counter ion. The counter ion indicates the presence of an unprecedented pyridyl radical anion, which was confirmed using bond metrics as well as UV/vis spectroscopy. Its more selective formation was achieved by reacting 2-phenylpyridine with KC_8 in the presence of 18-c-6 and $[K\{18\text{-c-}6\}][Mn^{II}(hmds)_3]$. The latter is needed to provide the additional stabilizing [K{18-c-6}] cation.

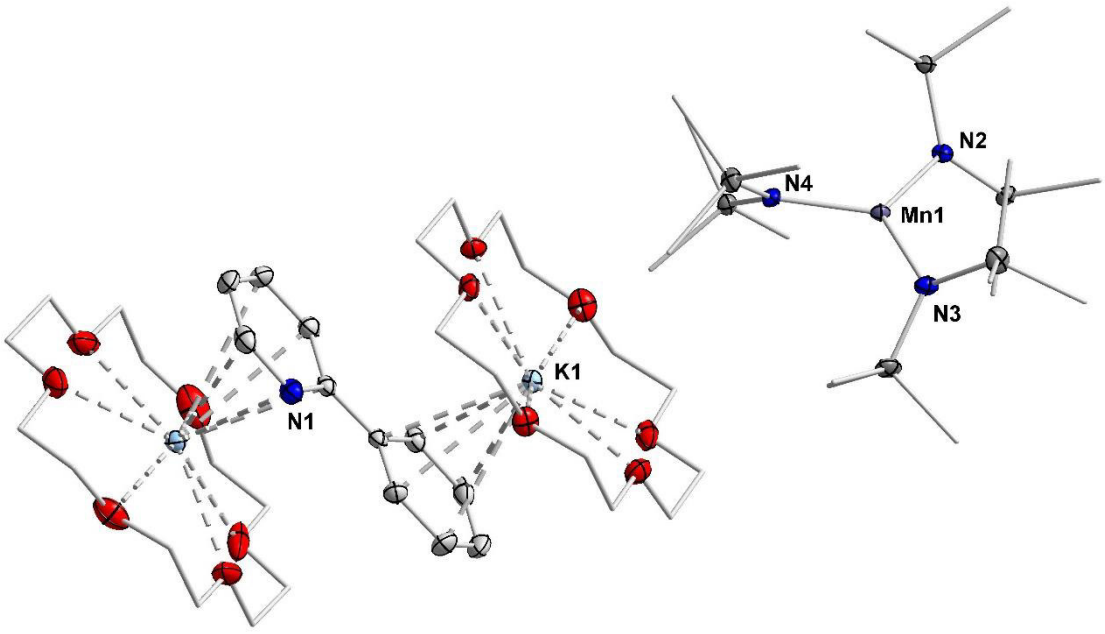

Figure 1. Molecular structure of $[K\{18\text{-c-}6\}]_2[Mn(hmds)_3]$[2-phenylpyridyl]. Hydrogen atoms are omitted for clarity.

Additionally to the just discussed reductive coupling of pyridines, electron-deficient fluoropyridines, bearing variable degrees of fluorination, were used to facilitate the reduction (**Scheme 5**), especially for the so far unreactive cobalt(I) complex $[Co(hmds)_2]^-$. Although reactions took place readily in all instances (except for 2-fluoropyridine with the cobalt(I) complex) no reductive coupling to a dihydropyridyl anion but C–F bond cleavage was observed. This gave very rare three-coordinate metal(II) fluoride of the type $[K\{18\text{-c-}6\}][M^{II}(F)(hmds)_2]$ (M = Mn – Co).

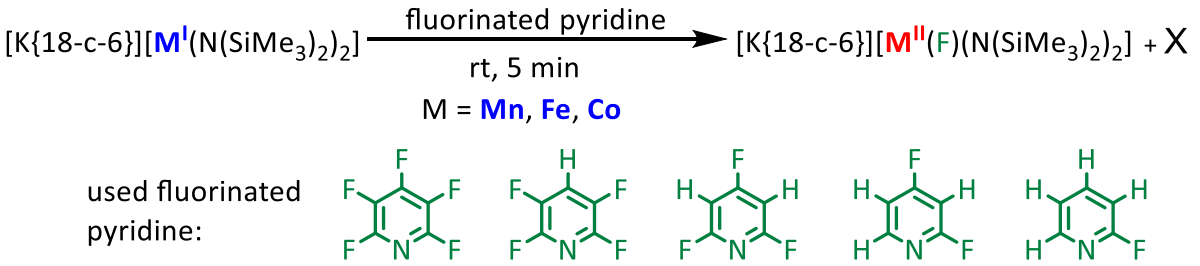

Scheme 5. Variation of the degree of fluorination of the pyridine derivatives and reaction with metal(I) silylamides (M = Mn – Co).

In addition, totally degradation of higher fluorinated pyridines is observed, that act as electron scavenger. Only for the substrate pentafluoropyridine, the by-product could be identified spectroscopically as perfluorobipyridine. In the reaction with 2-fluoropyridine, the pyridyl complex could be identified as a by-product by means of single-crystal structure analysis (**Scheme 6**).

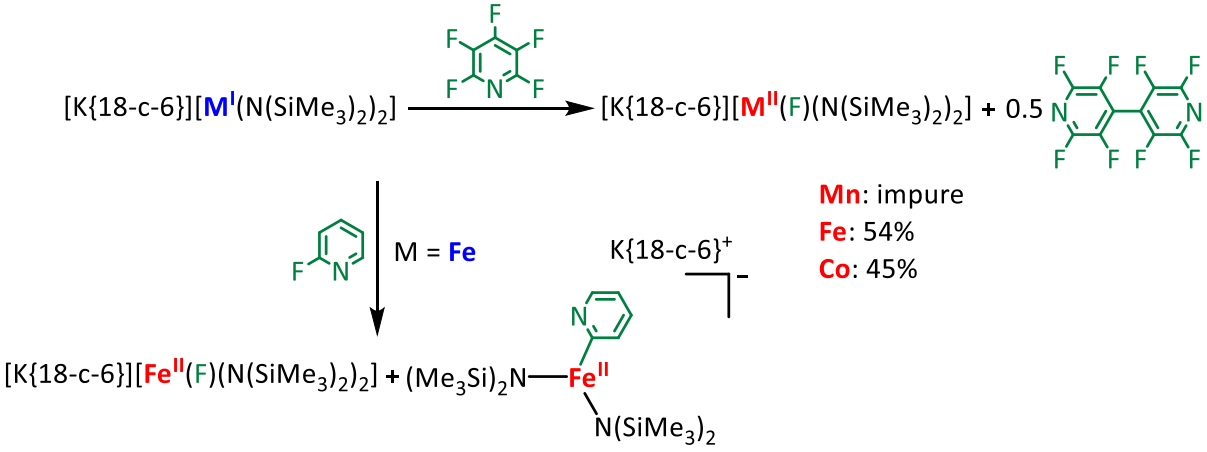

Scheme 6. Synthesis of low-coordinated fluorido metal complexes by reacting metal(I) silylamides (M = Mn – Co) with different fluoropyridines.

In addition to the reactivity of metal(I) complexes towards 2,2´-bipyridine and pyridine, this work could also show the synthesis of low-coordinated 3d-transition metal alkyne complexes resulting from the reaction of quasi-linear metal(I) silylamides $[K\{18\text{-c-}6\}][MX_2]$ (M = Cr

– Co ; X = –N(SiMe$_3$)$_2$), –N(Dipp)SiMe$_3$; Dipp = 2,6-di-*iso*-propylphenyl) with aliphatic and aromatic internal alkynes (**Scheme 7**).

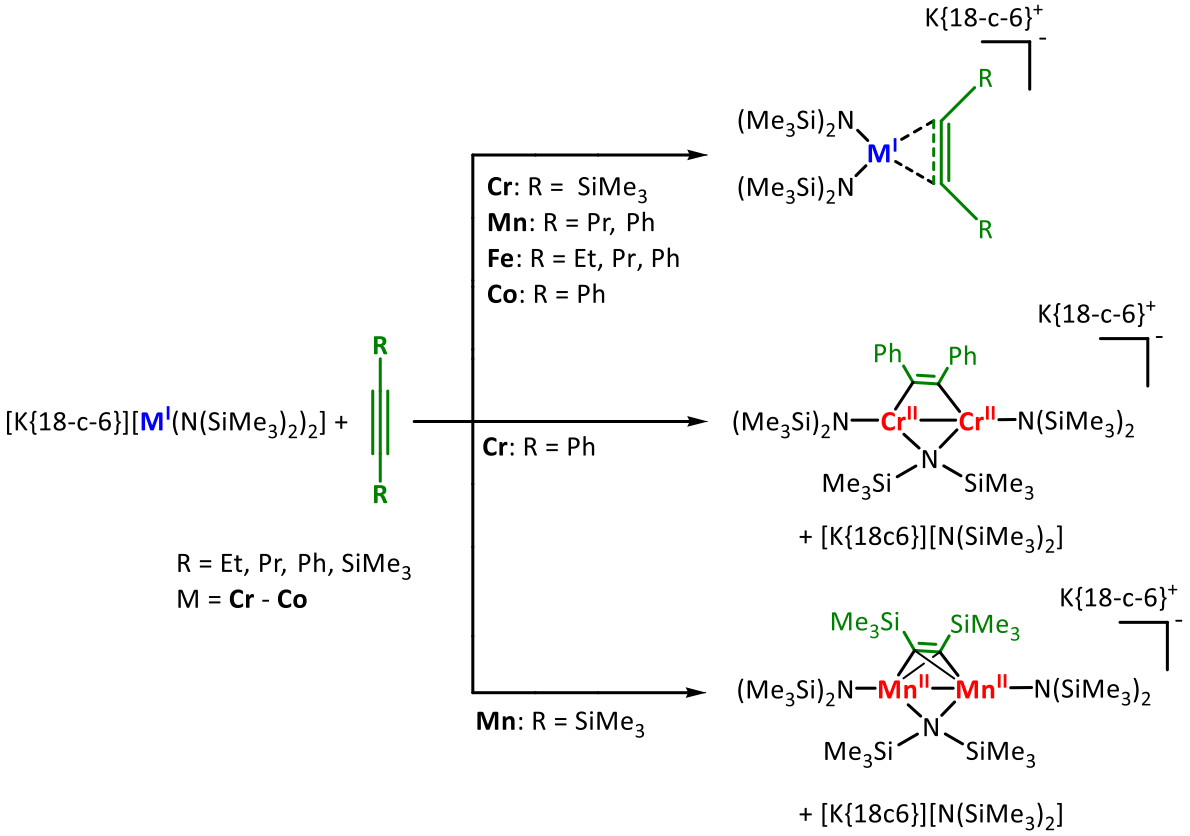

Scheme 7. Synthetic route for low-coordinate metal alkyne complexes.

While only weak and reversible alkyne coordination is observed for cobalt, the formation of anionic *side-on* alkyne complexes of the type [M(hmds)$_2$(η^2-RCCR)]$^-$ for iron occurs easily. In case of manganese, first examples of low-coordinated manganese alkyne complexes and, depending on the substrate, unique examples of the manganese-mediate a reduction of the alkyne to a dianionic structure or even alkyne trimerization were observed (**Scheme 8**). An alkyne coordination or reduction to the alkene dianion could be also observed for chromium. A quantum chemical analysis of the [M(hmds)$_2$(η^2-PhCCPh)]$^-$ complexes (M = Cr – Co) using DFT and CASSCF methods was performed, showed that the electronic situation of all these complexes can be described best as formal metal(II) bound alkynyl radical anions. In case of chromium, evidence of further contributions of a metal(III) cyclopropene resonance structure was found. The computational analysis rationalizes the bimetallic reduction to bis-metalated alkene dianions, a rarely observed phenomenon.

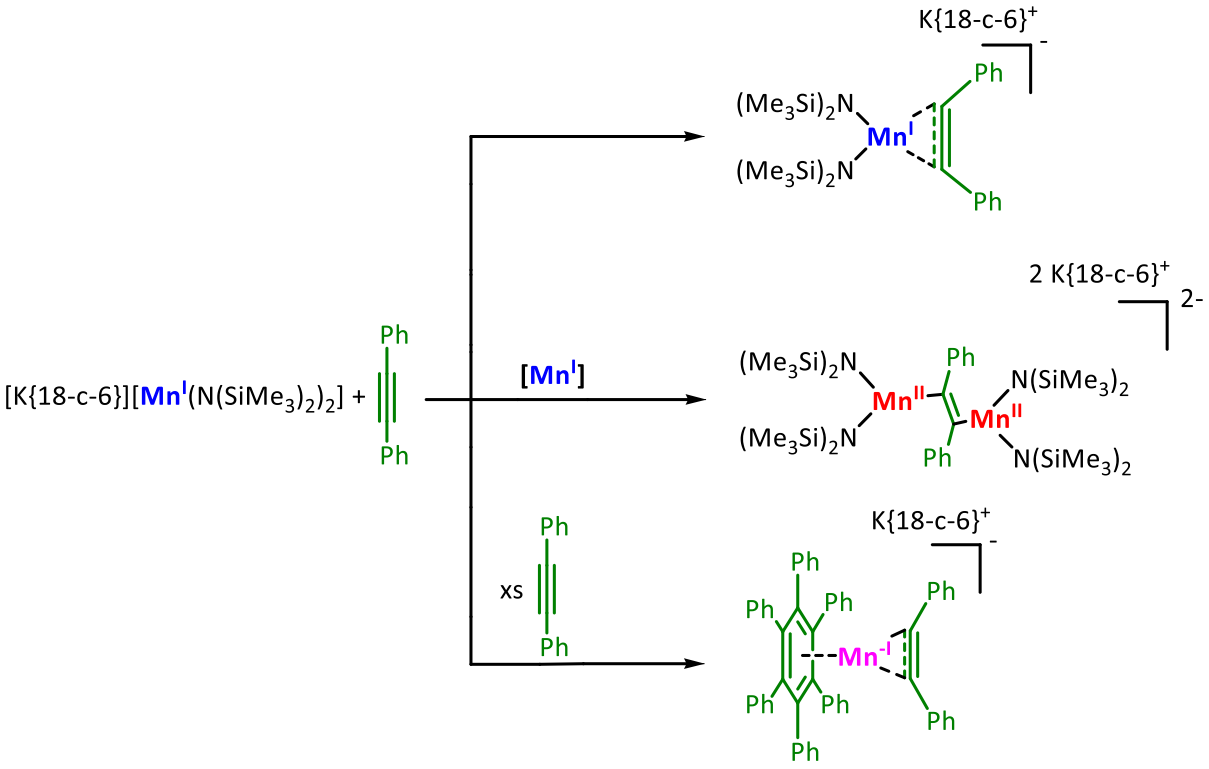

Scheme 8. Different activation modes of tolane by the anionic $[Mn^{I}(hmds)_2]^-$ complex.

Reactions between terminal alkynes and quasi-linear iron(I)-silylamides [K{18-c-6}][Fe(hmds)$_2$] showed a very similar coordination pattern. In both cases, a side-on complex was formed with the particularity of the substrate 3-phenyl-1-propyne, where a shift of the triple bond was additionally observed (**Scheme 9**).

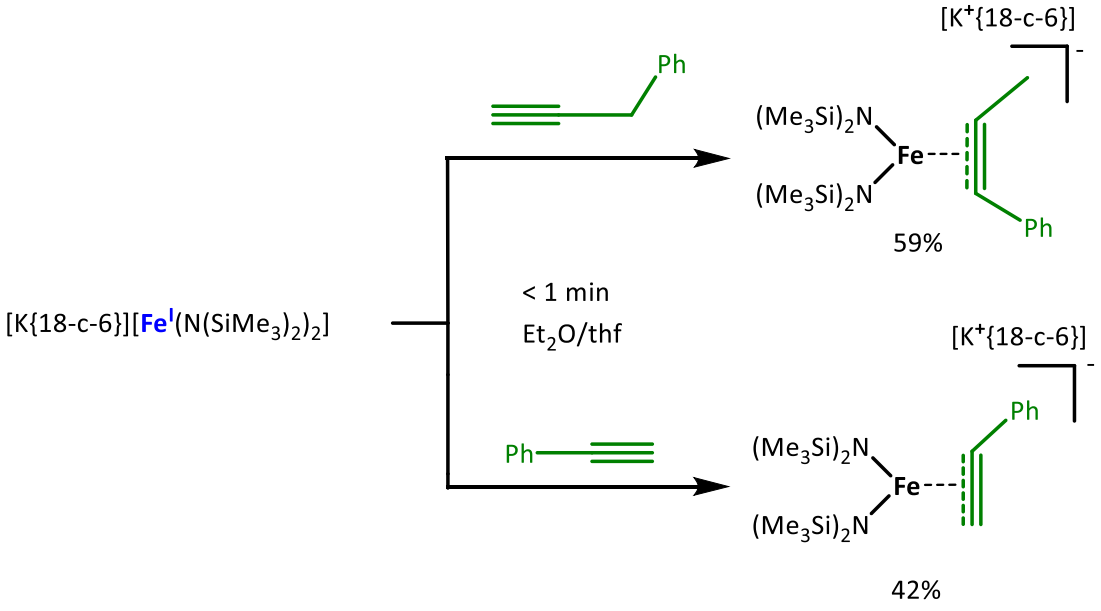

Scheme 9. Reaction of the terminal alkynes (phenylacetylene and 3-phenyl-1-propyne) with the iron(I) silylamide complex $[Fe(hmds)_2]^-$.

After observing this unusual triple bond rearrangement, we attempted the bond isomerisation on a catalytic scale for this and other substrates using different iron complexes (**Scheme 10**).

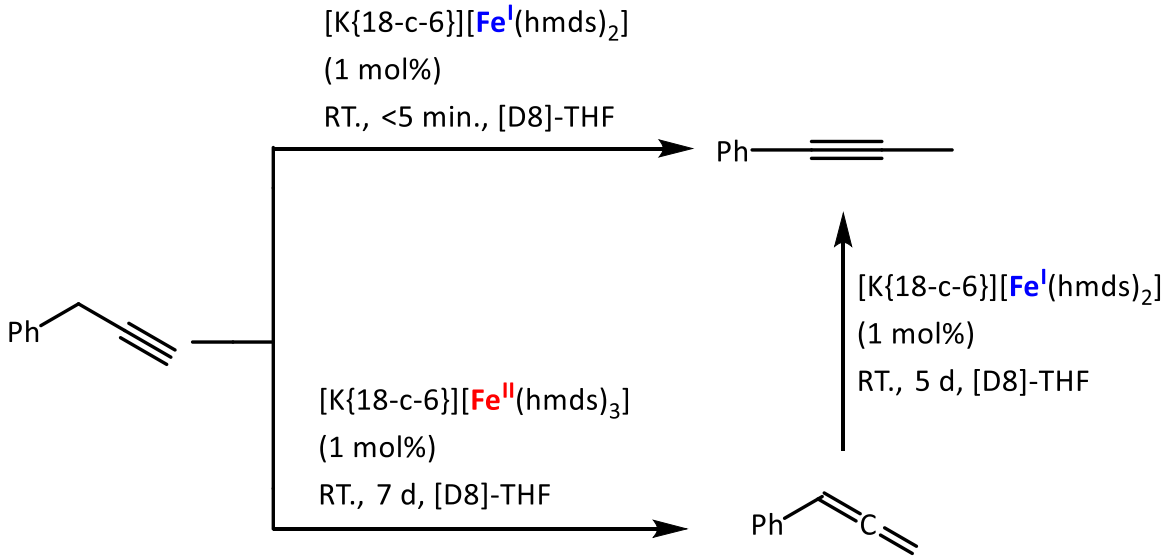

Scheme 10. Catalytic study of 3-phenyl-1-propine using two different catalysts.

Indeed, 1mol% of [K{18-c-6}][Fe(hmds)$_2$] mediated the instantaneous rearrangement of 3-Phenyl-1-propin to the internal alkyne. K{18-c-6}][Fe(N(Dipp(SiMe$_3$)$_2$] is less active but leads to the exclusive formation of phenyl allene. It also rapidly showed, that the substrate scope is fairly limited as only 4-phenyl butyne could also be transformed to the allene using [K{18-c-6}][Fe(hmds)$_2$]. The mechanism of this transformation is unresolved but participation of a metal hydride is unlikely for these systems. In addition [K{18-c-6}][Fe(hmds)$_3$], K(hmds) und Li(hmds) were employed as catalysts (10 mol%). Thereby it showed, that [K{18-c-6}][Fe(hmds)$_3$] mediated the (slow) transformation of 3-Phenyl-1-propin to phenyl allene. Intriguingly, the simple K(hmds) is highly active which yields the internal alkyne, whereas Li(hmds) is slower and by that reveals the stepwise allene and internal alkyne formation.

In addition to the reactivity of metal(I) complexes toward alkynes, this work demonstrated that a number of rare low-coordination 3d transition metal-alkene complexes can result from the reaction of linear metal(I) silylamides [K{18-c-6}[MX$_2$] (18-c-6, X = -N(SiMe$_3$)$_2$), hmds, (M = Cr – Co) with terminal internal alkenes and diene. Only weak and reversible alkene coordination could be observed for cobalt.

For the terminal alkenes, a side-on alkene complex of the type [Fe(hmds)$_2$(η^2-PhCHCH)]$^-$ could be shown in the case of iron. In contrast, for chromium and manganese, reductive coupling of the substituents was observed (**Scheme 11**).

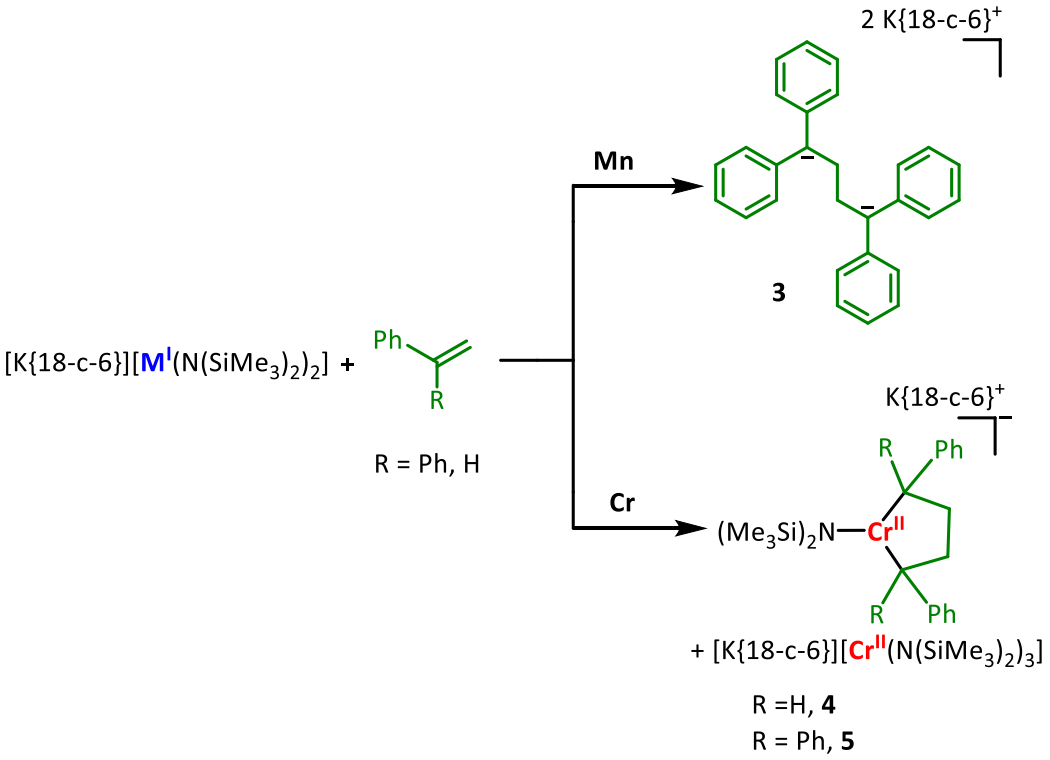

Scheme 11. Reaction of terminal alkenes (styrene and 1,1-diphenylethylene) with the $[M^{I}(hmds)_2]$ complex (M = Cr and Mn).

The interaction of internal alkenes with linear metal(I) complexes as a function of both the metal and the alkene substituent was also studied. The formation of side-on alkene complexes of the type $[M(hmds)_2(\eta^2\text{-PhCHCHR})]^-$ readily takes place. As such, the first low-coordinated manganese-alkene complexes could be obtained. In addition, Z/E isomerization of the *Z*-substrates (stilbene and β-methylstyrene) could be observed (**Scheme 12**).

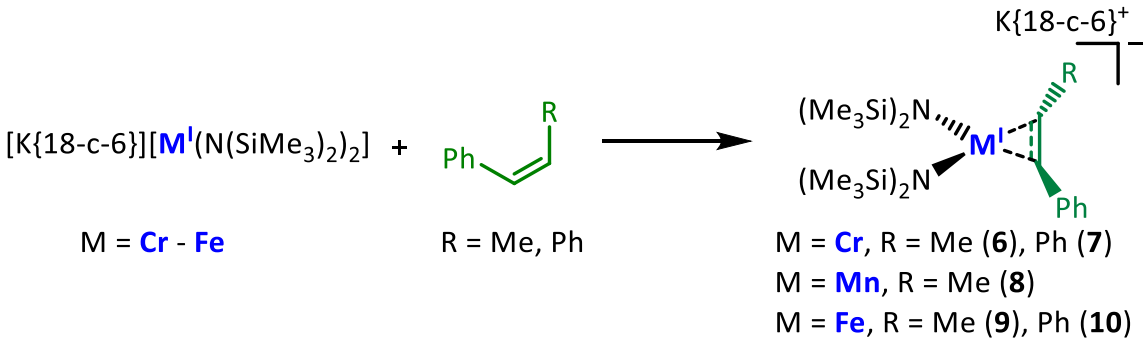

Scheme 12. General synthesis approach for *cis*-substrates (stilbene and β-methylstyrene) towards the metal(I) silylamides (M = Cr – Fe).

The simple *Z/E* isomerization of the substrates is tentatively attributed to the formulation of these compounds as metal(II) stabilized radical anions. The presence of such a species was authenticated by X-Ray diffractometer analysis, however not 3d-metal bound.

Finally, the interaction of a diene (2,3-dimethylbutadiene) with linear metal(I) complexes was studied as a function of metal (**Scheme 13**).

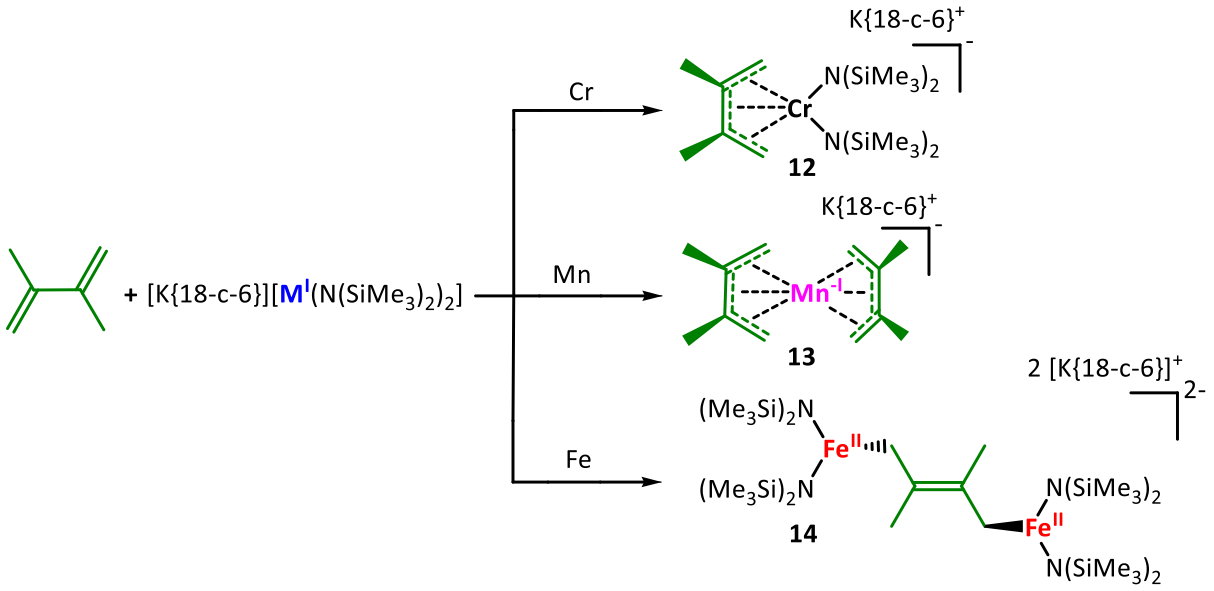

Scheme 13. Different activation modes of 2,3-dimethylbutadiene by $[M^{I}(hmds)_2]^-$ complexes (M = Cr – Fe).

2,3-Dimethylbutadiene showed a versatility of different activation modes towards the metal(I) complexes (M = Cr – Fe). For chromium, a side-on diene complex could be presented, with the two double bonds delocalized and distributed over the substrate. In the case of manganese, a ligand exchange took place and the "naked" manganese is coordinated by two 2,3-dimethylbutadienes, with manganese having the oxidation state of -I. For iron, the substrate 2,3-dimethylbutadiene was twofold reduced and is coordinated by two $[Fe^{II}(hmds)_2]$ complexes. For cobalt, no reactivity towards 2,3-dimethylbutadiene was observed.

Overall, the first comprehensive study on the chemical behaviour of anionic, linear 3d-metall(I) complex was presented revealing unusual results. In addition, the catalytic use of such compounds in some substrate conversions could also be revealed, which will be part of future endeavours.

7 Literaturverzeichnis

[1] A. Z. Werner, *Anorg. Chem.* **1893**, *3*, 267.

[2] H. Ann. Bethe, *Phys.* **1929**, *3*, 135.

[3] R. S. Mulliken, *Phys. Rev*. **1932**, *40*, 55.

[4] J. H. Van Vleck, *Chem. Phys*. **1935**, *3*, 803.

[5] L. Pauling, *The Nature of the Chemical Bond*; Cornell University Press: Ithaca, NY, **1940**.

[6] C. Ballhausen, *Introduction to Ligand Field Theory*; McGraw-Hill: New York, **1962**.

[7] W. Moffitt, C. Ballhausen, *Annu. Rev. Phys. Chem.* **1956**, *7*, 107.

[8] C. K. Jorgensen, *Modern Aspects of Ligand Field Theory*; Elsevier: New York, **1971**.

[9] D. C. Bradley, R. C. Mehrotra, D. P. Gaur, *Metal Alkoxides*; Academic Press: London, **1978**.

[10] D. C. Bradley, *Adv. Inorg. Chem. Radiochem.* **1972**, *15*, 259.

[11] (a) M. F. Lappert, P. P. Power, A. R. Sanger, R. C. Srivastava, *Metal and Metalloid Amides*; Ellis-Horwood: Chichester, **1980**. (b) M. F. Lappert, P. P. Power, A. Protchenko, A. Seeber, *Metal Amide Chemistry*; Wiley: Chichester, **2008**.

[12] H. Bürger, U. Wannagat, *Monatsh*. **1964**, *95*, 1099.

[13] H. Bürger, U. Wannagat, *Monatsh.* **1963**, *94*, 1007.

[14] P. P. Power, *Comments Inorg. Chem*. **1989**, *8*, 177.

[15] P. P. Power, *Chemtracts Inorg*. *Chem*. **1994**, *6*, 181.

[16] D. L. Kays*, Dalton Trans*. **2011**, *40*, 769.

[17] C. Ni, P. P. Power, *Struct. Bonding (Berlin).* **2010**, *136*, 59.

[18] (a) P. P. Power, *Chem. Rev*. **2012**, *112*, 3482. (b) M. Atanasov, J. M. Zadrozny, J. R. Long, F. Neese*, Chem. Sci.*, **2013**, *4*, 139.

[19] W. M. Reiff, A. M. LaPointe, E. H. Witten, *J. Am. Chem. Soc.* **2004**, *126*, 10206.

[20] W. M. Reiff, C. E. Schulz, M. H. Whangbo, J. I. Seo, Y. S. Lee, G. R. Potratz, C. W. Spicer, G. S. Girolami, *J. Am. Chem. Soc.* **2009**, *131*, 404.

[21] W. A. Merrill, T. A. Stich, M. Brynda, G. J. Yeagle, R. De Hont, J. C. , Fettinger, W. M. Reiff, P. P. Power, *J. Am. Chem. Soc.* **2009**, *131*, 12693.

[22] N. H. Buttrus, C. Eaborn, P. B. Hitchcock, A. C. Sullivan, *J. Chem. Soc., Chem. Commun*. **1985**, 1380.

[23] R. A. Andersen, K. Faegri, J. C. Green, A. Haaland, M. F. Lappert, W. P. Leung, K. Rypdal, *Inorg. Chem.* **1988**, *27*, 1782.

[24] D. C. Bradley, M. B. Hursthouse, K. M. A. Malik, R. Moseler, *Trans. Met. Chem*. **1978**, *3*, 253.

[25] B. D. Murray, P. P. Power, *Inorg. Chem.* **1984**, *23*, 4584.

[26] M. M. Olmstead, P. P. Power, S. C. Shoner, *Inorg. Chem.* **1991**, *30*, 2547.

[27] D. C. Bradley, M. B. Hursthouse, C. W. Newing, A. J. Welch, *Chem. Commun*. **1972**, 467.

[28] D. C. Bradley*, Chem. Br.* **1975**, 393.

[29] P. G. Eller, D. C. Bradley, M. B. Hursthouse, D. W. Meek, *Coord. Chem. Rev.* **1977**, *24*, 1.

[30] S. Alvarez, *Coord. Chem. Rev.* **1999**, *13*, 193.

[31] C. C. Cummins, *Prog. Inorg. Chem.* **1998**, *47*, 885.

[32] (a) G. K. Barker, M. F. Lappert, *J. Organomet. Chem.* **1974**, *76*, C45. (b) P. B. Hitchcock, M. F. Lappert, R. G. Smith, R. A. Bartlett, P. P. Power, *J. Chem. Soc., Chem. Commun.* **1988**, 1007.

[33] C. C. Cummins, *Chem. Commun.* **1998**, 1777.

[34] A. L. Companion, M. A. Komarynsky, *J. Chem. Educ.* **1964**, *41*, 257.

[35] R. Krishnamurthy, W. B. Schaap, *J. Chem. Educ*. **1969**, *46*, 799.

[36] R. S. Drago, *Physical Methods in Chemistry;* Saunders: Philadelphia, PA, **1977**; p 478.

[37] R. Wolf, M. Brynda, C. Ni, G. J. Long, P. P. Power, *J. Am. Chem. Soc.* **2007**, *129*, 6076.

[38] a) C. A. Laskowski, G. L. Hillhouse, *J. Am. Chem. Soc.* **2008**, *130*, 13846. b) C. A. Laskowski, D. J. Bungum, S. M. Baldwin, S. A. Del Ciello, V. M. Iluc, G. L. Hillhouse, *J. Am. Chem. Soc.* **2013**, *135*, 18272.

[39] a) M. I. Lipschutz, T. Chantarojsiri, Y. Dong, T. D. Tilley, *J. Am. Chem. Soc.* **2015**, *137*, 6366. b) R. J. Witzke, D. Hait, K. Chakarawet, M. Head-Gordon, T. D. Tilley, *ACS Catal.* **2020**, *10*, 7800.

[40] J. Hicks, C. Jones, *Organometallics* **2015**, *34*, 2118.

[41] C. A. Laskowski, G. R. Morello, C. T. Saouma, T. R. Cundari, G. L. Hillhouse, *Chem. Sci.* **2013**, *4*, 170.

[42] M. I. Lipschutz, X. Yang, R. Chatterjee, T. D. Tilley, *J. Am. Chem. Soc.* **2013**, *135*, 15298.

[43] a) I. C. Cai, M. I. Lipschutz, T. D. Tilley, *Chem. Commun.* **2014**, *50*, 13062; b) C.-Y. Lin, J. C. Fettinger, F. Grandjean, G. J. Long, P. P. Power, *Inorg. Chem.* **2014**, *53*, 9400; c) Z. Mo, D. Chen, X. Leng, L. Deng, *Organometallics* **2012**, *31*, 7040; d) Z. Mo, Z. Ouyang, L. Wang, K. L. Fillman, M. L. Neidig, L. Deng, *Org. Chem. Front.* **2014**, *1*, 1040; e) P. P. Samuel, R. Neufeld, K. Chandra Mondal, H. W. Roesky, R. Herbst-Irmer, D. Stalke, S. Demeshko, F. Meyer, V. C. Rojisha, S. De, P. Parameswaran, A. C. Stückl, W. Kaim, J. H. Christian, J. K. Bindra, N. S. Dalal, *Chem. Sci.* **2015**, *6*, 3148; f) M. I. Lipschutz, T. D. Tilley, *Organometallics* **2014**, *33*, 5566; g) C.-Y. Lin, J. C. Fettinger, N. F. Chilton, A. Formanuik, F. Grandjean, G. J. Long, P. P. Power, *Chem. Commun.* **2015**, *51*, 13275.

[44] P. P. Samuel, K. C. Mondal, H. W. Roesky, M. Hermann, G. Frenking, S. Demeshko, F. Meyer, A. C. Stückl, J. H. Christian, N. S. Dalal, L. Ungur, L. F. Chibotaru, K. Pröpper, A. Meents, B. Dittrich, *Angew. Chem.* **2013**, *125*, 12033.

[45] P. P. Samuel, K. C. Mondal, N. Amin Sk, H. W. Roesky, E. Carl, R. Neufeld, D. Stalke, S. Demeshko, F. Meyer, L. Ungur, L. F. Chibotaru, J. Christian, V. Ramachandran, J. van Tol, N. S. Dalal, *J. Am. Chem. Soc.* **2014**, *136*, 11964.

[46] G. Ung, J. Rittle, M. Soleilhavoup, G. Bertrand, J. C. Peters, *Angew. Chem. Int. Ed.* **2014**, *53*, 8427.

[47] J. M. Zadrozny, D. J. Xiao, M. Atanasov, G. J. Long, F. Grandjean, F. Neese, J. R. Long, *Nature Chem.* **2013**, *5*, 577.

[48] a) Z. Ouyang, J. Du, L. Wang, J. L. Kneebone, M. L. Neidig, L. Deng, *Inorg. Chem.* **2015**, *54*, 8808. b) Z. Mo, Z. Ouyang, L. Wang, K. L. Fillman, M. L. Neidg, L. Deng, *Org. Chem. Front.,* **2014**, *1*, 1040. c) Y.-S. Meng, Z. Mo, B.-W. Wang, Y.-Q. Zhang, L. Deng, S. Gao, *Chem. Sci.* **2015**.

[49] J. Chai, H. Zhu, A. C. Stückl, H. R. Roesky, J. Magull, A. Bencini, A. Caneschi, D. Gatteschi, *J. Am. Chem.Soc.* **2005**, *127*, 9201.

[50] C. G. Werncke, E. Suturina, P. C. Bunting, L. Vendier, J. R. Long, M. Atanasov, F. Neese, S. Sabo-Etienne, S. Bontemps, *Chem. Eur. J.* **2016**, *22*, 1668.

[51] C. G. Werncke, P. C. Bunting, C. Duhayon, J. R. Long, S. Bontemps, S. Sabo-Etienne, *Angew. Chemie - Int. Ed.* **2015**, *54*, 245.

[52] (a) J. K. Kochi, *J. Organomet. Chem.* **2002**, *653*, 11. (b) T. J. Anderson, G. D. Jones, D. A. Vicic, *J. Am. Chem. Soc.* **2004**, *126*, 8100.

[53] B. D. Sherry, A. Fürstner, *Acc. Chem. Res.* **2008**, *41*, 1500.

[54] M. I. Lipschutz, T. D. Tilley, *Angew. Chem.* **2014**, *126*, 7418.

[55] T. R. Dugan, X. Sun, E. V. Rybak-Akimova, O. Olatunji-Ojo, T. R. Cundari, P. L. Holland, *J. Am. Chem. Soc.* **2011**, *133*, 12418.

[56] J. M. Smith, R. J. Lachicotte, K. A. Pittard, T. R. Cundari, G. Lukat-Rodgers, K. R. Rodgers, P. L. Holland, *J. Am. Chem. Soc.* **2001**, *123*, 9222.

[57] K. Ding, A. W. Pierpont, W. W. Brennessel, G. Lukat-Rodgers, K. R. Rodgers, T. R. Cundari, E. Bill, P. L. Holland, *J. Am. Chem. Soc.* **2009**, *131*, 9471.

[58] X. Dai, P. Kapoor, T. H. Warren, *J. Am. Chem. Soc.* **2004**, *126*, 4798.

[59] S. Pfirrmann, C. Limberg, C. Herwig, R. Stößer, B. Ziemer, *Angew. Chem.* **2009**, *121*, 3407.

[60] Y.-C. Tsai, P.-Y. Wang, S.-A. Chen, J.-M. Chen, *J. Am. Chem. Soc.* **2007**, *129*, 8066.

[61] (a) W. H. Monillas, G. P. A. Yap, L. A. MacAdams, K. H. Theopold, *J. Am. Chem. Soc.* **2007**, *129*, 8090. (b) P. L. Holland, T. R. Cundari, L. L. Perez, N. A. Eckert, R. J. Lachicotte, *J. Am. Chem. Soc.* **2002**, *124*, 14416. (c) R. E. Cowley, P. L. Holland, *Inorg. Chem.* **2012**, *51*, 8352. (d) G. Bai, P. Wei, D. W. Stephan, *Organometallics* **2005**, *24*, 5901. (e) J. M. Smith, A. R. Sadique, T. R. Cundari, K. R. Rodgers, G. Lukat-Rodgers, R. J. Lachicotte, C. J. Flaschenriem, J. Vela, P. L. Holland, *J. Am. Chem. Soc.* **2006**, *128*, 756. (f) S. Pfirrmann, S. Yao, B. Ziemer, R. Stösser, M. Driess, C. Limberg, *Organometallics* **2009**, *28*, 6855.

[62] (a) T. R. Dugan, E. Bill, K. C. MacLeod, G. J. Christian, R. E. Cowley, W. W. Brennessel, S. Ye, F. Neese, P. L. Holland, *J. Am. Chem. Soc.* **2012**, *134*, 20352. (b) R. A. Lewis, K. C. MacLeod, B. Q. Mercado, P. L. Holland, *Chem. Commun.* **2014**, *50*, 11114.

[62] J. Chatt, L. A. Duncanson, *J. Chem. Soc.* **1953**, 2939.

[64] M. A Dewar, *Bull. Soc. Chem. Fr* **1951**, *18*, C79.

[65] J. Chatt, L. A. Duncanson, L. M. Venanzi, *J. Chem. Soc.* **1955**, 4456.

[66] C. Elschenbroich: Organometallchemie. 6. A. Wiesbaden: Teubner, **2008**.

[67] S. E. Gibson, A. Stevenazzi, *Angew. Chem. Int. Ed.* **2003**, *42*, 1800.

[68] I. U. Khand, G. R. Knox, P. L. Pauson, W. E. Watts, *J. Chem. Soc. D* **1971**, 36a.

[69] D. Broere, E. Ruijter, *Synthesis* **2012**, *44*, 2639.

[70] J. A. Varela, C. Saá, *Chem. Rev.* **2003**, *103*, 3787.

[71] W. Reppe, W. Schweckendiek, J. *Ann. Chem. Pharm.* **1948**, *560*, 104.

[72] G. Fachinetti, C. Floriani, F. Marchetti, M. Mellini, *J. Chem. Soc., Dalton Trans.* **1978**, 1398.

[73] V. B. Shur, V. V. Burlakov, M. E. Vol'pin, *J. Organomet. Chem.* **1988**, *347*, 77.

[74] V. V. Burlakov, A. V. Polyakov, A. I. Yanovsky, Y. T. Struchkov, V. B. Shur, M. E. Vol'pin, U. Rosenthal, H. Görls, *J. Organomet. Chem.* **1994**, *476*, 197.

[75] V. Varga, K. Mach, M. Polášek, P. Sedmera, J. Hiller, U. Thewalt, S. I. Troyanov, *J. Organomet. Chem.* **1996**, *506*, 241.

[76] G. B. Wijeratne, E. M. Zolnhofer, S. Fortier, L. N. Grant, P. J. Carroll, C.-H. Chen, K. Meyer, J. Krzystek, A. Ozarowski, T. A. Jackson, D. J. Mindiola, J. Telser, *Inorg. Chem.* **2015**, *54*, 10380.

[77] U. Rosenthal, G. Oehme, V. V. Burlakov, P. V. Petrovskii, V. B. Shur, M. E. Vol'pin, *J. Organomet. Chem.* **1990**, *391*, 119.

[78] C. Martín, M. Sierra, E. Alvarez, T. R. Belderrain, P. J. Pérez, *Dalton Trans.* **2012**, *41*, 5319.

[79] M. S. Nechaev, V. M. Rayón, G. Frenking, *J. Phys. Chem.* **2004**, *108*, 3134.

[80] J. Chatt, L. A. Duncanson, *J. Chem. Soc.* **1953**, 2939.

[81] M. Dewar, *Bull. Soc. Chem. Fr.* **1951**, *18*, C79.

[82] C. J. Adams, I. M. Bartlett, N. G. Connelly, D. J. Harding, O. D. Hayward, A. J. Martín, A. Guy Orpen, M. J. Quayle, P. H. Rieger, *J. Chem. Soc., Dalton Trans.* **2002**, *6*, 4281.

[83] J. E. Salt, G. S. Girolami, G. Wilkinson, M. Motevalli, M. Thornton-Pett, M. B. Hursthouse, *J. Chem. Soc., Dalton Trans.* **1985**, 685.

[84] A. A. Danopoulos, G. Wilkinson, T. K. N. Sweet, M. B. Hursthouse, *J. Chem. Soc., Dalton Trans.* **1996**, 271.

[85] D. J. Wink, B. T. Creagan, *J. Am. Chem. Soc.* **1990**, *112*, 8585.

[86] D. J. Wink, J. R. Fox, N. J. Cooper, *J. Am. Chem. Soc.* **1985**, *107*, 5012.

[87] Y. Ortin, Y. Copple, N. Lugan, R. Mathieu, M. McGlinchey, J. *Chem. Commun.* **2001**, 1690.

[88] G. G. Cash, R. C. Pettersen, *J. Chem. Soc., Dalton Trans.* **1979**, 1630.

[89] Y. Ortin, A. Sournia-Saquet, N. Lugan, R. Mathieu, *Chem. Commun.* **2003**, 1060.

[90] C. P. Casey, T. L. Dzwiniel, S. Kraft, I. Guzei, *Organometallics* **2003**, *22*, 3915.

[91] M. Akita, S. Kakuta, S. Sugimoto, M. Terada, M. Tanaka, Y. Moro-oka, *Organometallics* **2001**, *20*, 2736.

[92] M. Barrow, N. L. Cromhout, D. Cunningham, A. R. Manning, P. McArdle, *J. Organomet. Chem.* **2000**, *612*, 61.

[93] D. L. Reger, S. A. Klaeren, L. Lebioda, *Organometallics* **1988**, *7*, 189.

[94] J. R. Fox, W. L. Gladfelter, G. L. Geoffroy, I. Tavanaiepour, S. Abdel-Mequid, V. W. Day, *Inorg. Chem.* **1981**, *20*, 3230.

[95] F. Hoffmann, J. Wagler, G. Roewer, *Z. anorg. allg. Chem.* **2008**, *634*, 1133.

[96] C. C. Mokhtarzadeh, A. L. Rheingold, J. S. Figueroa, *Dalton Trans.* **2016**, *45*, 14561.

[97] W. G. Sly, *J. Am. Chem. Soc.* **1959**, *81*, 18.

[98] F. Baert, A. Guelzim, J. M. Poblet, R. Wiest, J. Demuynck, M. Benard, *Inorg. Chem.* **1986**, *25*, 1830.

[99] B. Capelle, M. Dartiguenave, Y. Dartiguenave, A. L. Beauchamp, *J. Am. Chem. Soc.* **1983**, *105*, 4662.

[100] W. H. Monillas, J. F. Young, G. P. A. Yap, K. H. Theopold, *Dalton Trans.* **2013**, *42*, 9198.

[101] F. Dai, G. P. A. Yap, K. H. Theopold, *J. Am. Chem. Soc.* **2013**, *135*, 16774.

[102] E. S. Akturk, G. P. A. Yap, K. H. Theopold, *Chem. Commun*. **2015**, *51*, 15402

[103] S. A. Stoian, Y. Yu, J. M. Smith, P. L. Holland, E. L. Bominaar, E. Münck, *Inorg. Chem.* **2005**, *44*, 4915.

[104] S. C. Bart, E. J. Hawrelak, E. Lobkovsky, P. J. Chirik, *Organometallics* **2005**, *24*, 5518.

[105] Y. Yu, J. M. Smith, C. J. Flaschenriem, P. L. Holland, *Inorg. Chem.* **2006**, *45*, 5742.

[106] J. Cheng, Q. Chen, X. Leng, S. Ye, L. Deng, *Inorg. Chem.* **2019**, *58*, 13129.

[107] A. Enachi, D. Baabe, M.-K. Zaretzke, P. Schweyen, M. Freytag, J. Raeder, M. D. Walter, *Chem. Commun.* **2018**, *54*, 13798.

[108] J. Du, W. Chen, Q. Chen, X. Leng, Y.-S. Meng, S. Gao, L. Deng, *Organometallics* **2020**, *39*, 729.

[109] Z. Mo, J. Xiao, Y. Gao, L. Deng, *J. Am. Chem. Soc.* **2014**, *136*, 17414.

[110] W. H. Monillas, G. P. A. Yap, L. A. MacAdams, K. H. Theopold, *J. Am. Chem. Soc.* **2007**, 129, 26, 8090.

[111] J. Du, L. Wang, M. Xie, L. Deng, *Angew. Chem. Int. Ed.* **2015**, *54*, 12640.

[112] W. Zhou, A. N. Desnoyer, J. A. Bailey, B. O. Patrick, K. M. Smith, *Inorg. Chem.* **2013**, *52*, 2271.

[113] G. Margraf, F. Schödel, I. Sänger, M. Bolte, M. Wagner, H.-W. Lerner, *Z. Naturforsch. B Chem. Sci.* **2012**, *67*, 549.

[114] (a) M. Irwin, R. K. Jenkins, M. S. Denning, T. Krämmer, F. Grandjean, G. J. Long, R. Herchel, J. E. McGrady, J. M. Goicoechea, *Inorg. Chem.* **2010**, *49*, 6160. (b) M. Irwin, L. R. Doyle, T. Krämer, R. Herchel, J. E. McGrady, J. M. Goicoechea, *Inorg. Chem.* **2012**, *51*, 12301.

[115] Y. Zhao, Y. Lei, Q. Dong, B. Wu, X.-J. Yang, *Chem. Eur. J.* **2013**, *19*, 12059.

[116] A. Kapat, T. Sperger, S. Guven, F. Schoenebeck, *Science* **2019**, *363*, 391.

[117] D. R. Lide, *Tetrahedron Lett.* **1962**, *17*, 125.

[118] Ivan Ernest: *Bindung, Struktur und Reaktionsmechanismen in der organischen Chemie*, Springer-Verlag, **1972**, S.329.

[119] C. G. Werncke, I. Müller, *Chem. Commun.,* **2020**, *56*, 2268.

[120] J. E. Gano, E. J. Jacob, P. Sekher, G. Subramaniam, L. A. Eriksson, D. Lenoir, *J. Org. Chem.* **1996**, *61*, 6739.

[121] D. D. Perrin, W. L. F. Armareg, *Purification of Laboratory Chemicals*, 4. Auflage Butterworth-Heinemann, Oxford, **1997**.

[122] H. E. Gottlieb, V. Kotlyar, A. Nudelman, *J. Org. Chem.* **1997**, *62*, 7512.

[123] (a) D. F. Evans, *J. Chem. Soc*. **2003**, 1959. (b) E. M. Schubert, *J. Chem. Educ.* **1992**, *69*, 62.

[124] *X-Area*, Stoe & Cie GmbH, Darmstadt, Hessen, Germany, **2013**.

[125] O. V. Dolomanov, L. J. Bourhis, R. J. Gildea, J. A. K. Howard, H. Puschann, *J. Apl. Cryst.* **2009**, *42*, 339.

[126] *X-Area, X-Red* 1.63.1.0, Stoe & Cie GmbH, Darmstadt, Hessen, Germany, **2016**.

[127] G. M. Sheldrick, *Acta Crystallogr. A Found Adv* **2015**, *71*, ***3.***

[128] G. M. Sheldrick, *Acta Crystallogr. Section C, Structural chemistry* **2015**, *71*, 3.

[129] K. Brandenburg, *Diamond – Crystal and Molecular Structure Viualization, Crystal Impact* – Dr. H. Putz & Dr. K. Brandenburg GbR, Bonn, Germany, **2014**.

[130] C. B. Hübschle, G. M. Sheldrick, B. Ditrich, Journal of applied crystallography **2011**, *44*, 1281.

[131] *APEX3*, Bruker AXS Inc., Madison, Wisconsin, USA, **2016**.

[132] *SAINT*, Bruker AXS Inc., Madison, Wisconsin, USA, **2015**.

[133] *TWINABS-2012/1*, Bruker AXS Inc., Madison, Wisconsin, USA, **2012**.

8 Anhang

8.1 Supporting Information zur Publikation „Reduction of 2,2´-Bipyridine by Quasi-Linear 3d-Metal(I) Silylamides – A Structural and Spectroscopic Study"

Igor Müller, Christian Schneider, Clemens Pietzonka, Florian Kraus und C. Gunnar Werncke, *Inorganics* **2019**, *7*, 117.

Supplementary Materials: Reduction of 2,2′-Bipyridine by Quasi-Linear 3d-Metal(I) Silylamides—A Structural and Spectroscopic Study

Igor Müller, Christian Schneider, Clemens Pietzonka, Florian Kraus and C. Gunnar Werncke

Table of Contents

1. NMR Spectra

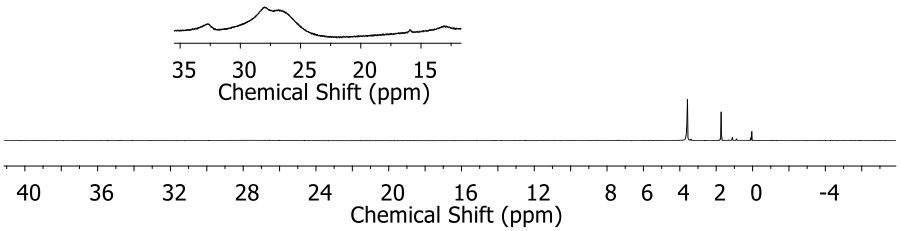

Figure S1. ^{1}H NMR spectrum of [K{18c6}][Cr(N(SiMe$_3$)$_2$)$_2$(bipy)] (**1**) in THF-d$_8$ (500.1 MHz).

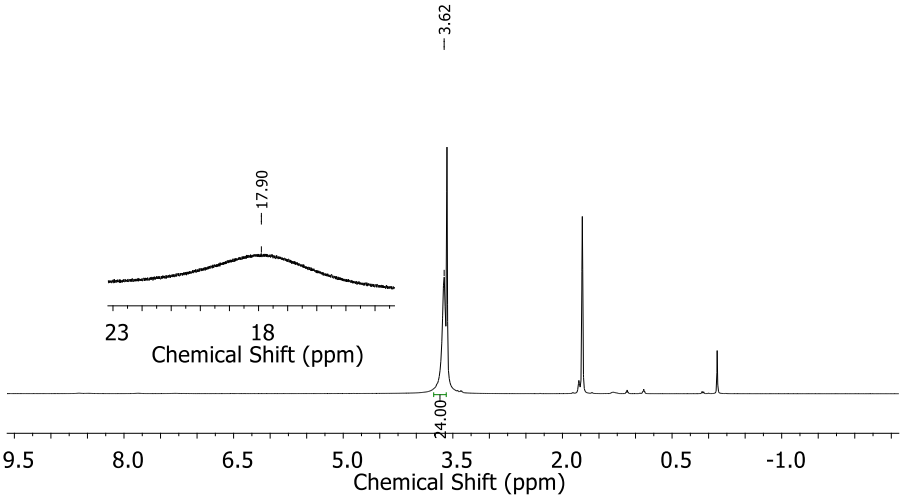

Figure S2. ^{1}H NMR spectrum of [K{18c6}][Mn(N(SiMe$_3$)$_2$)$_2$(bipy)] (**2**) in THF-d$_8$ (500.1 MHz).

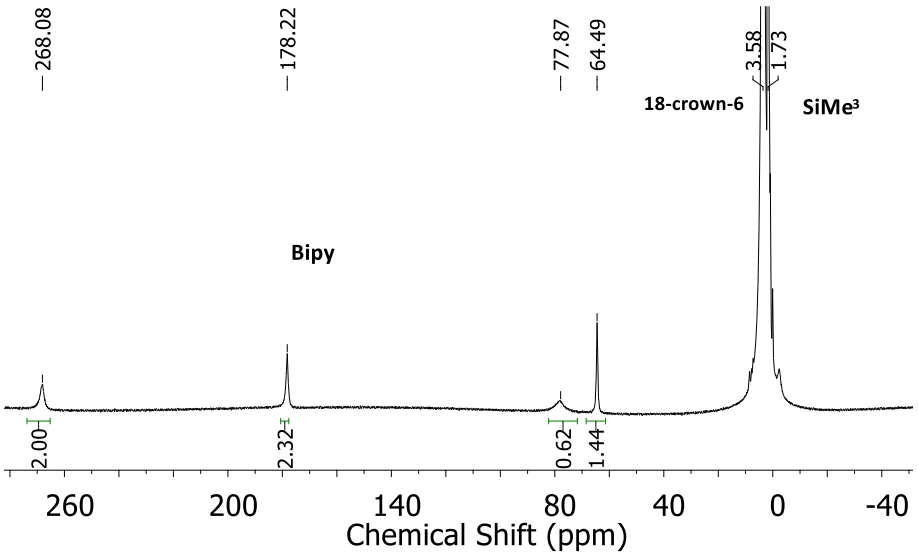

Figure S3. ^{1}H NMR spectrum of [K{18c6}][Fe(N(SiMe$_3$)$_2$)$_2$(bipy)] (**3**) in THF-d$_8$ (500.1 MHz).

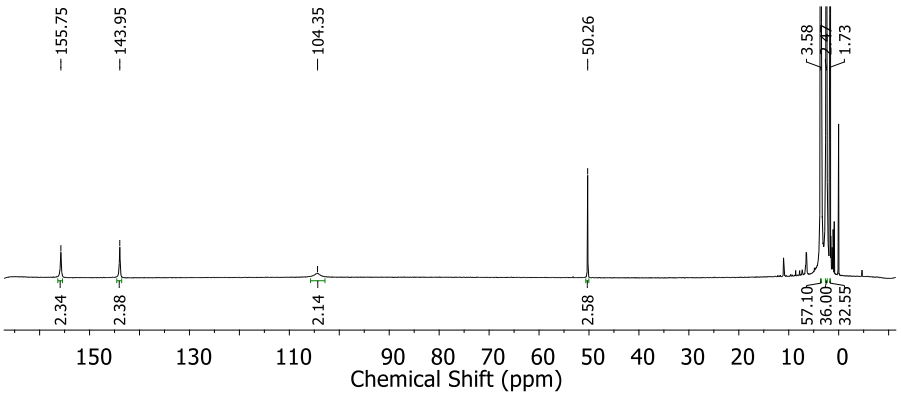

Figure S4. ^{1}H NMR spectrum of [K{18c6}][Co(N(SiMe$_3$)$_2$)$_2$(bipy)] (**4**) in THF-d$_8$ (500.1 MHz).

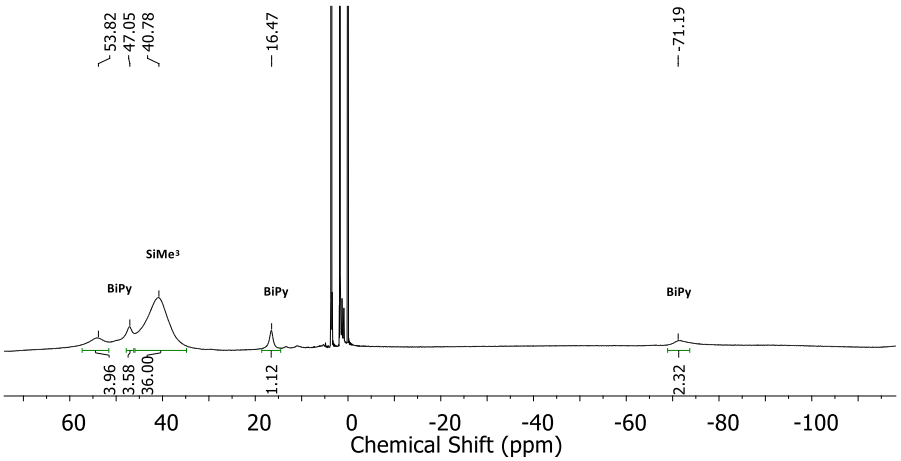

Figure S5. ^{1}H NMR spectrum of [Cr(N(SiMe$_3$)$_2$)$_2$(bipy)] (**5**) in THF-d$_8$ (500.1 MHz).

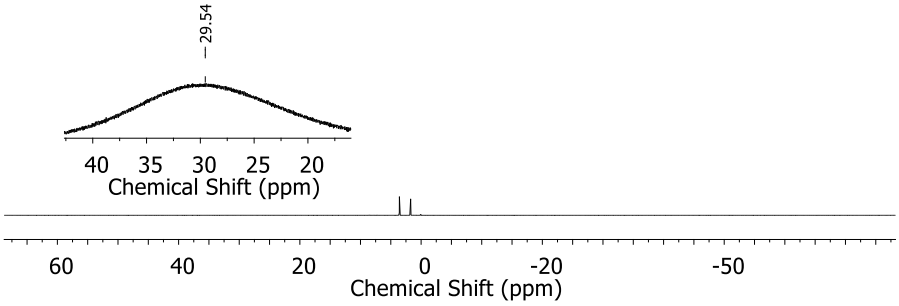

Figure S6. ^{1}H NMR spectrum of [Mn(N(SiMe$_3$)$_2$)$_2$(bipy)] (**6**) in THF-d$_8$ (500.1 MHz).

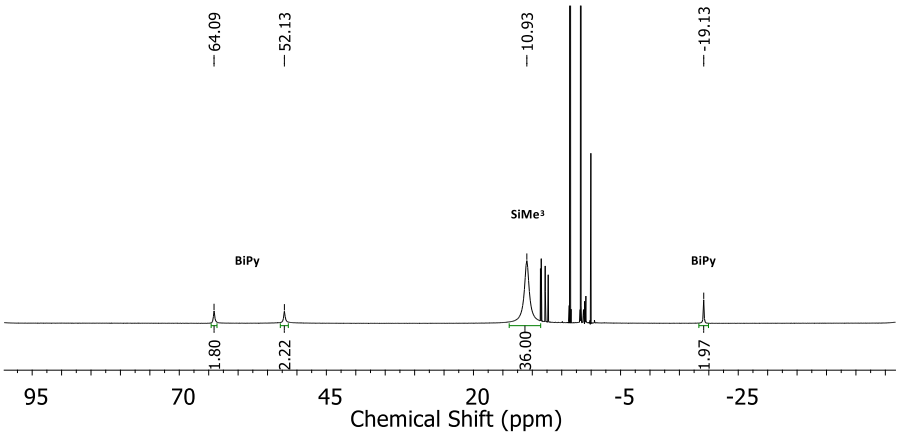

Figure S7. ^{1}H NMR spectrum of [Fe(N(SiMe$_3$)$_2$)$_2$(bipy)] (**7**) in THF-d$_8$ (500.1 MHz).

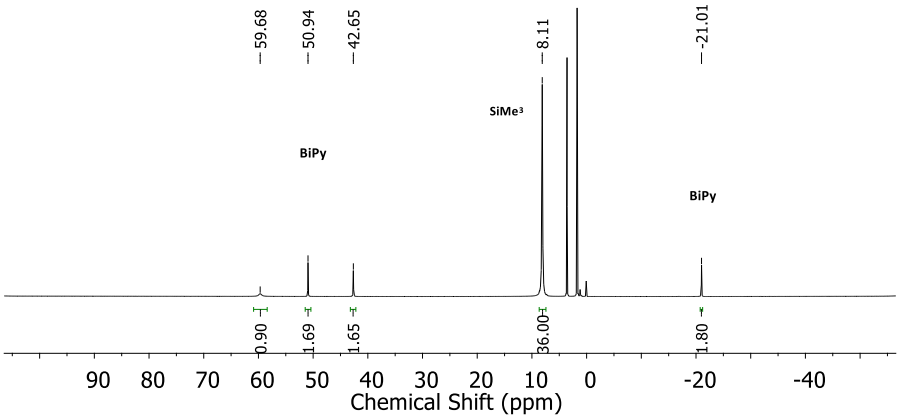

Figure S8. ^{1}H NMR spectrum of [Co(N(SiMe$_3$)$_2$)$_2$(bipy)] (**8**) in THF-d$_8$ (500.1 MHz).

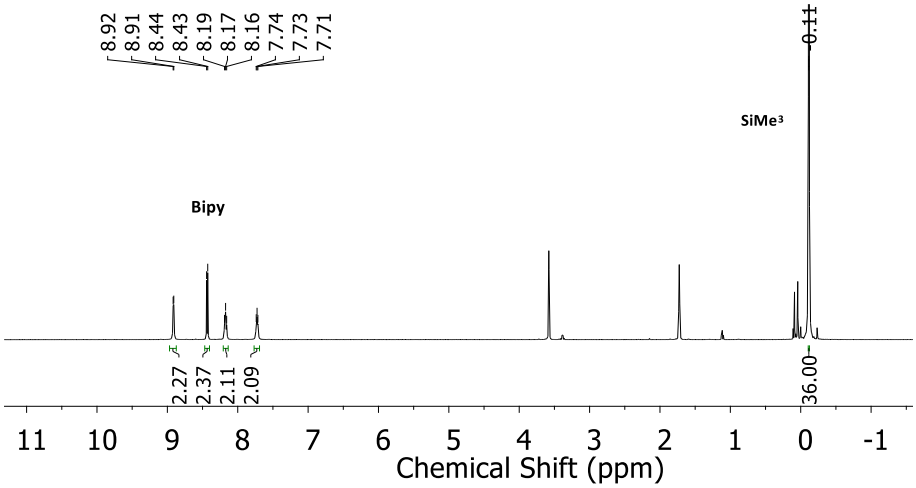

Figure S9. ^{1}H NMR spectrum of [Zn(N(SiMe$_3$)$_2$)$_2$(bipy)] (**9**) in THF-d$_8$ (500.1 MHz).

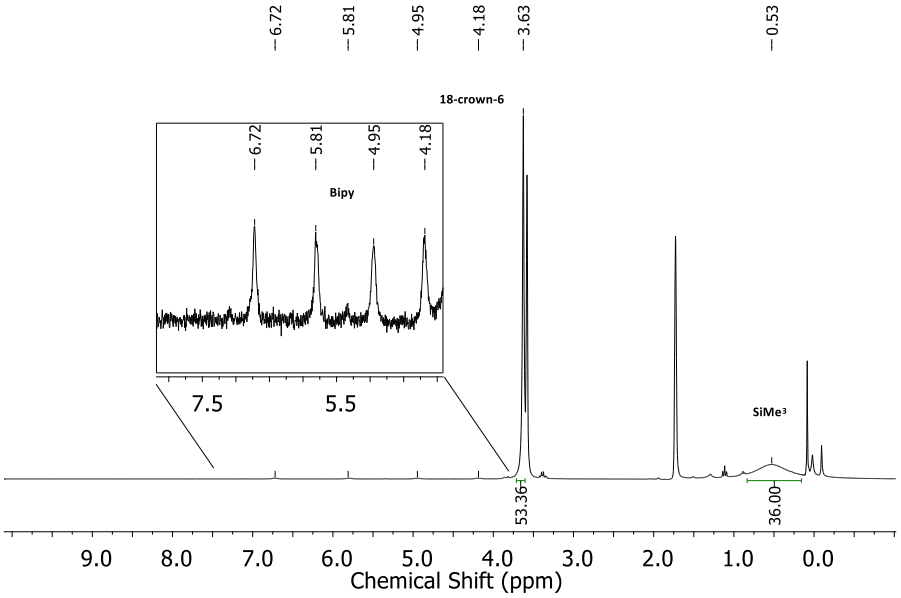

Figure S10. ^{1}H NMR spectrum of [K{18c6}][Zn(N(SiMe$_3$)$_2$)$_2$(BiPy)] (**10**) in THF-d$_8$ (500.1 MHz).

2. IR Spectra

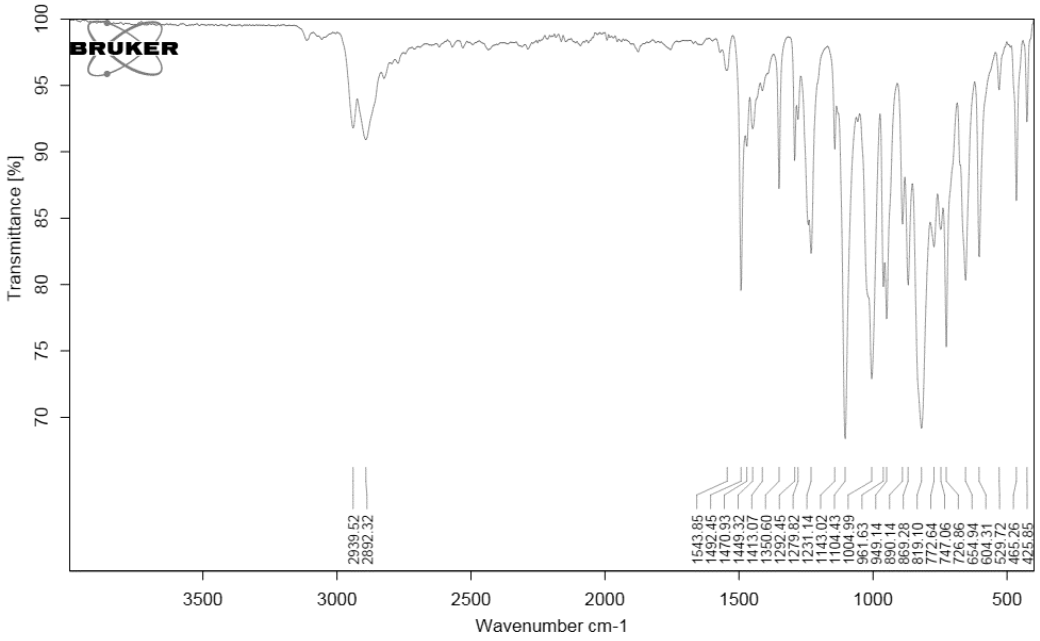

Figure S11. IR spectrum of [K{18c6}][Cr(N(SiMe$_3$)$_2$)$_2$(bipy)] (**1**).

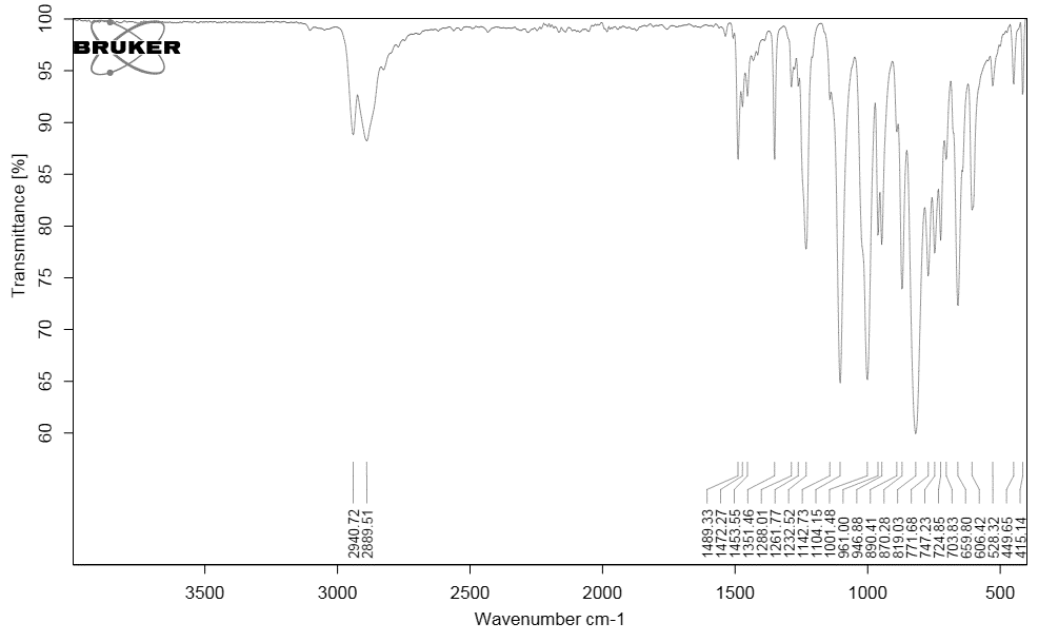

Figure S12. IR spectrum of [K{18c6}][Mn(N(SiMe$_3$)$_2$)$_2$(bipy)] (**2**).

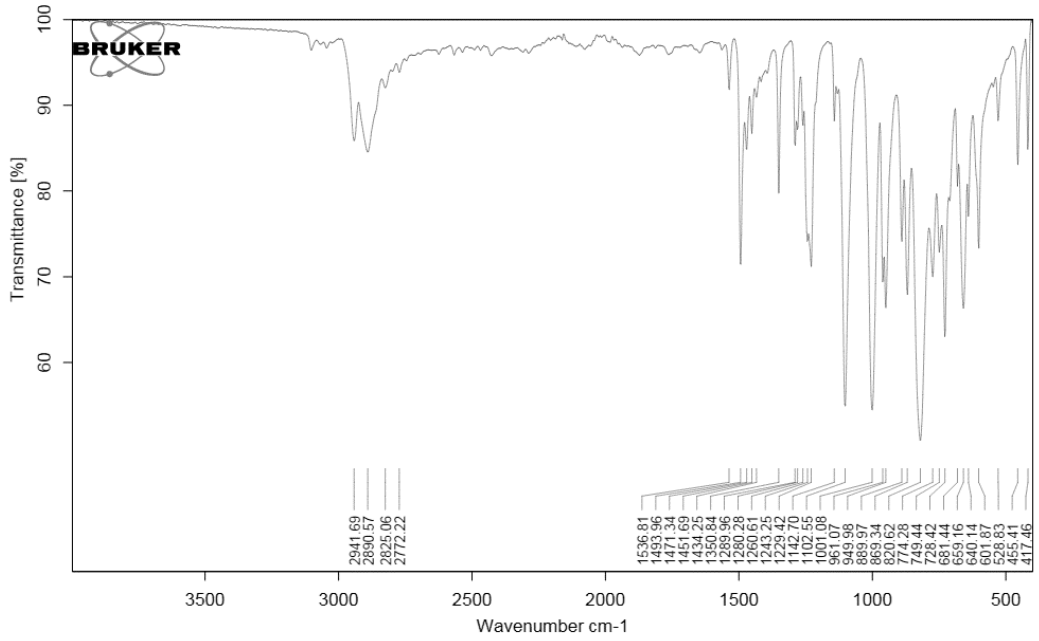

Figure S13. IR spectrum of [K{18c6}][Fe(N(SiMe$_3$)$_2$)$_2$(bipy)] (**3**).

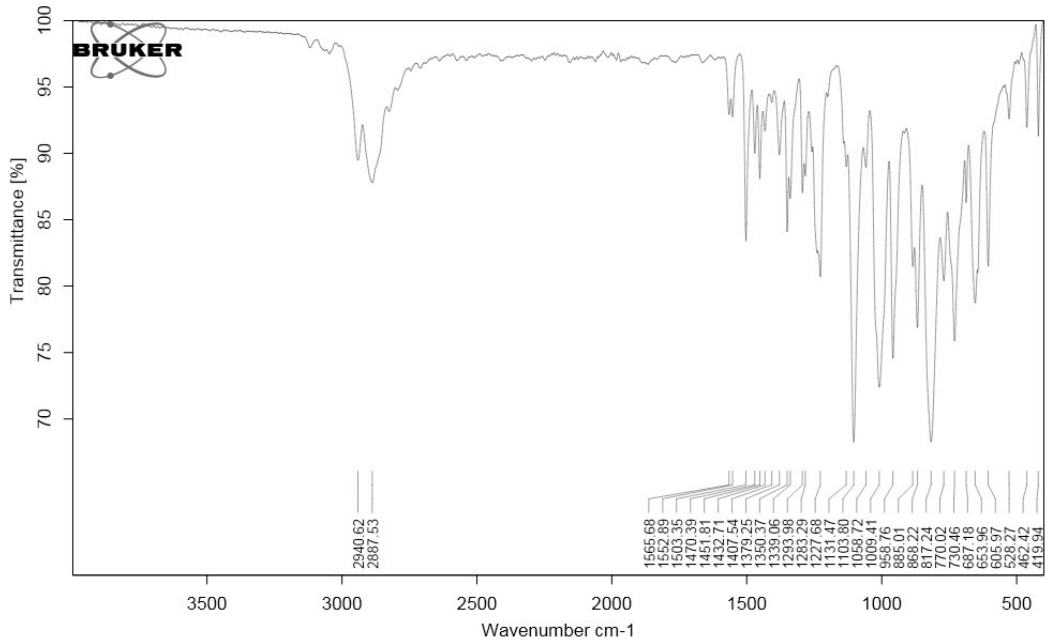

Figure S14. IR spectrum of [K{18c6}][Co(N(SiMe$_3$)$_2$)$_2$(bipy)] (**4**).

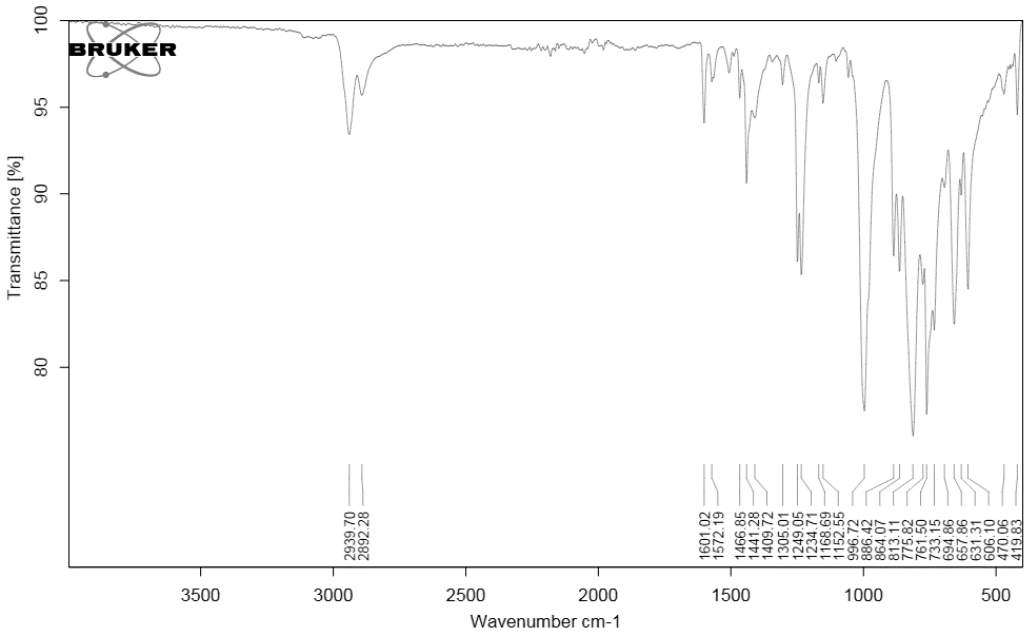

Figure S15. IR spectrum of [Cr(N(SiMe$_3$)$_2$)$_2$(bipy)] (**5**).

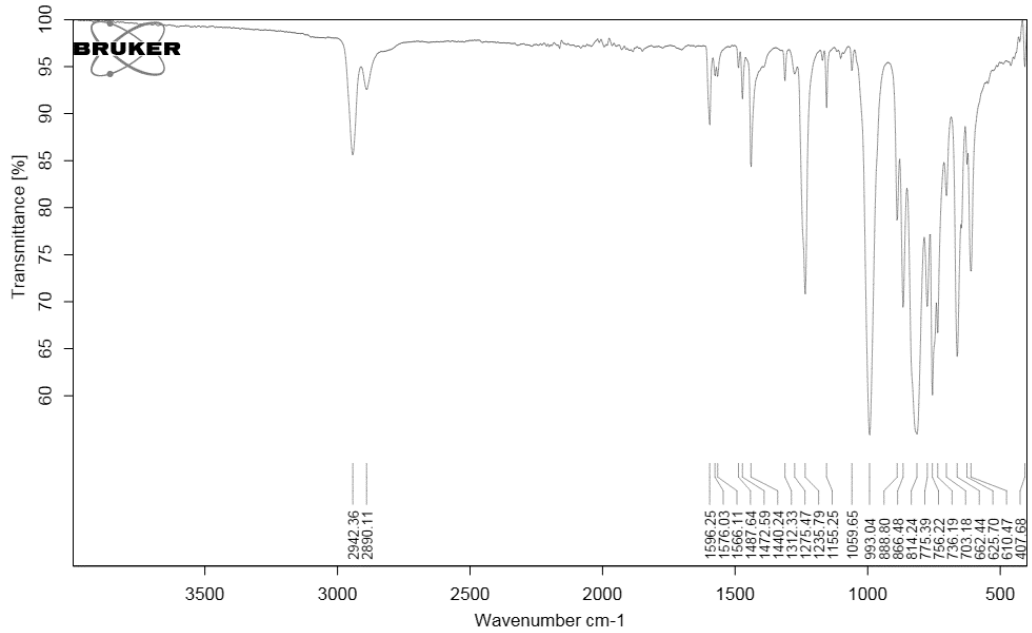

Figure S16. IR spectrum of [Mn(N(SiMe$_3$)$_2$)$_2$(bipy)] (**6**).

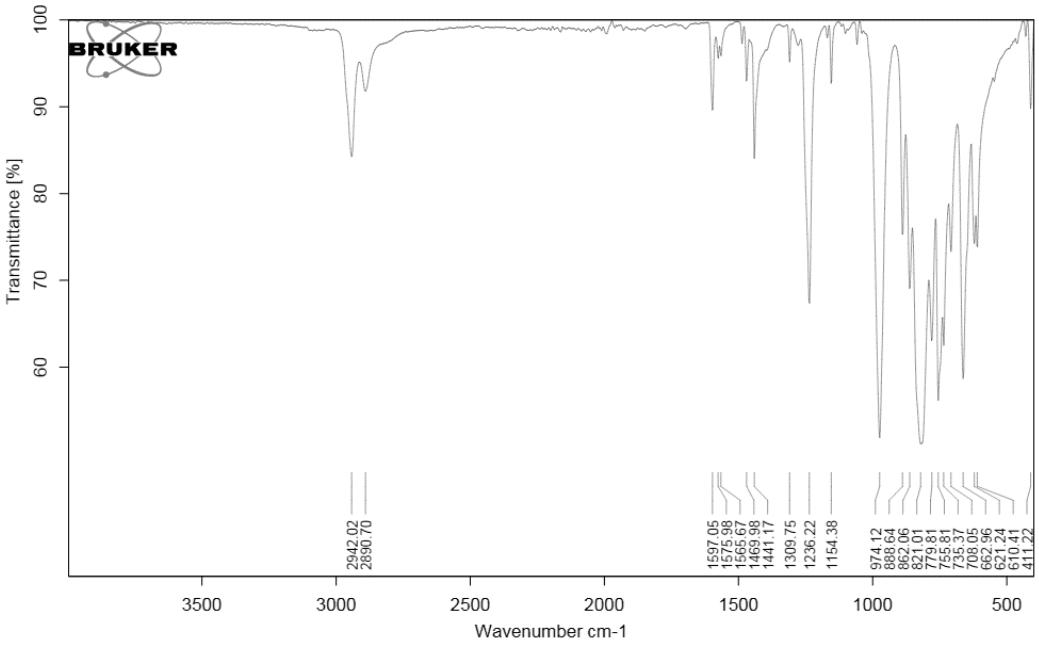

Figure S17. IR spectrum of [Fe(N(SiMe$_3$)$_2$)$_2$(bipy)] (**7**).

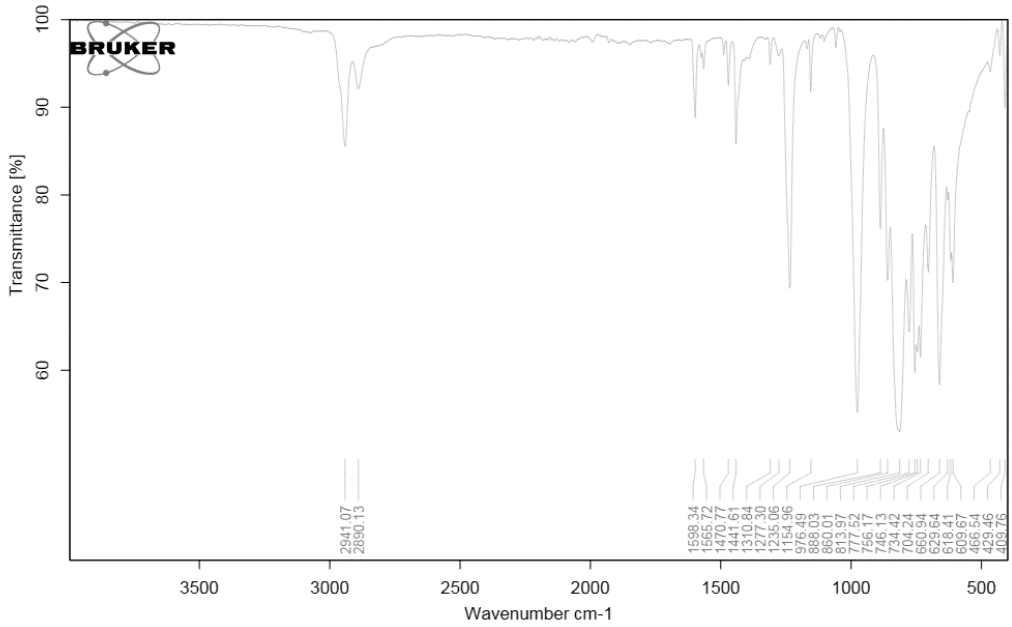

Figure S18. IR spectrum of [Co(N(SiMe$_3$)$_2$)$_2$(bipy)] (**8**).

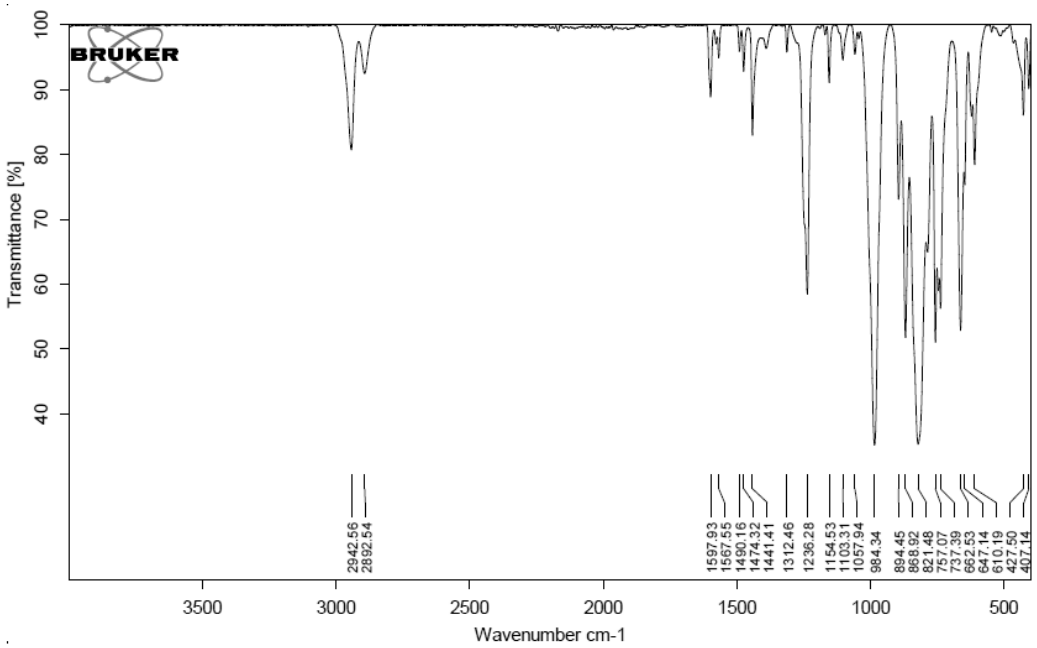

Figure S19. IR spectrum of [Zn(N(SiMe$_3$)$_2$)$_2$(bipy)] (**9**).

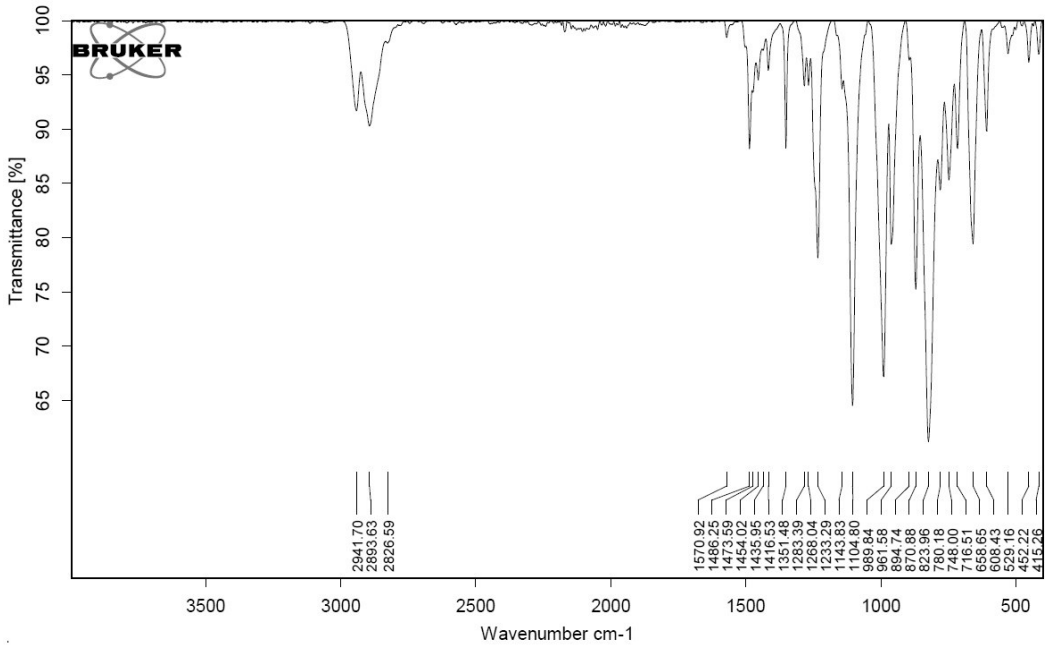

Figure S20. IR spectrum of [K{18c6}][Zn(N(SiMe$_3$)$_2$)$_2$(bipy)] (**10**).

3. UV/Vis Spectra

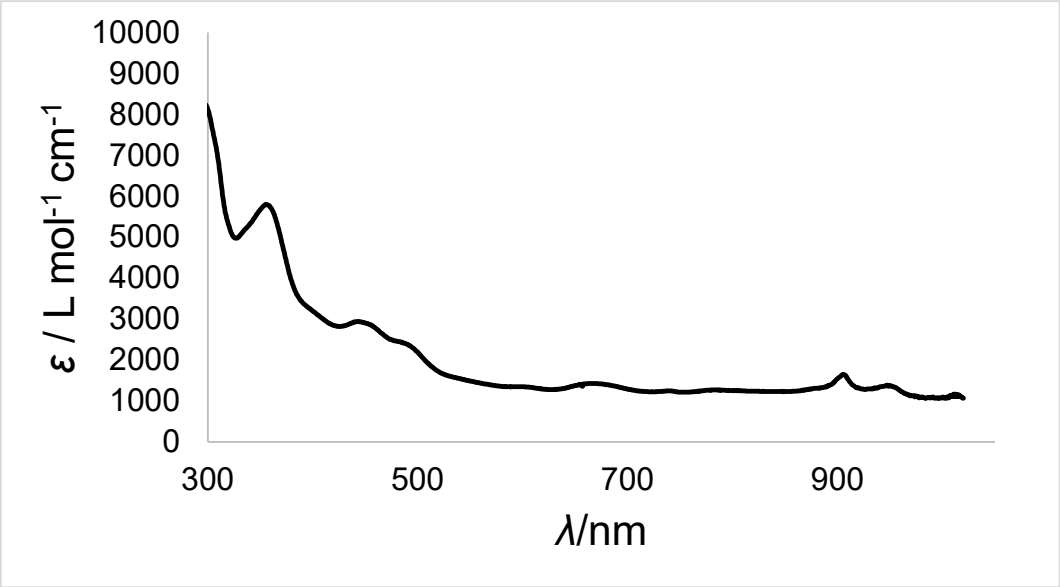

Figure S21. UV/Vis spectrum of [K{18c6}][Cr(N(SiMe$_3$)$_2$)$_2$(bipy)] (**1**) in Et$_2$O.

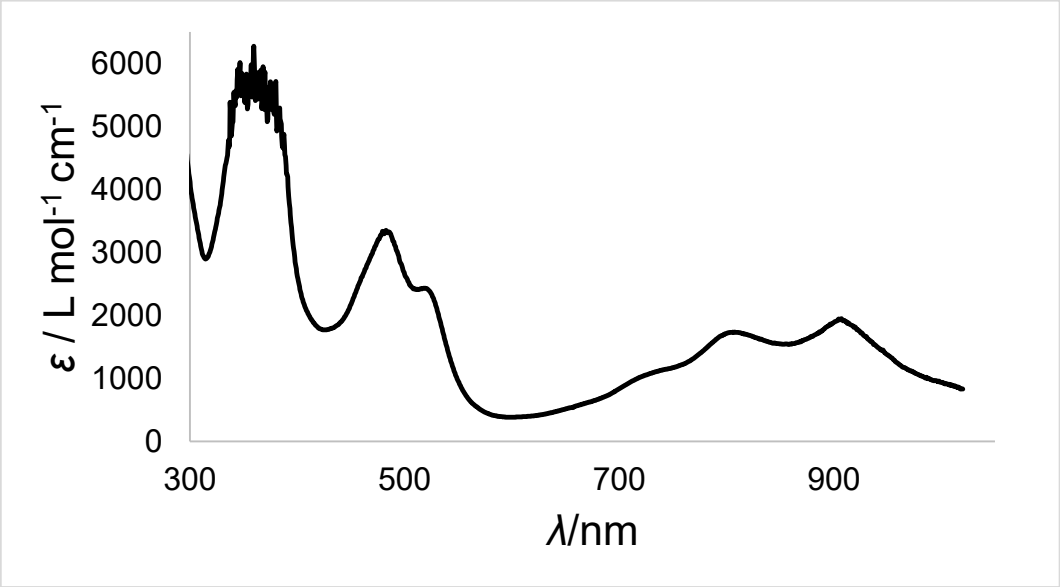

Figure S22. UV/Vis spectrum of [K{18c6}][Mn(N(SiMe$_3$)$_2$)$_2$(bipy)] (**2**) in Et$_2$O.

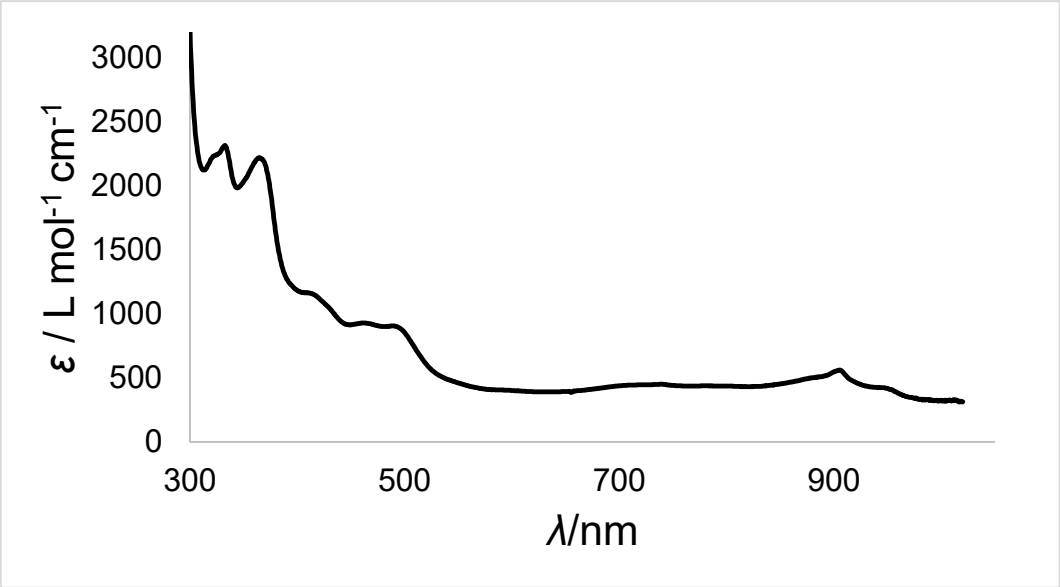

Figure S23. UV/Vis spectrum of [K{18c6}][Fe(N(SiMe$_3$)$_2$)$_2$(bipy)] (**3**) in Et$_2$O.

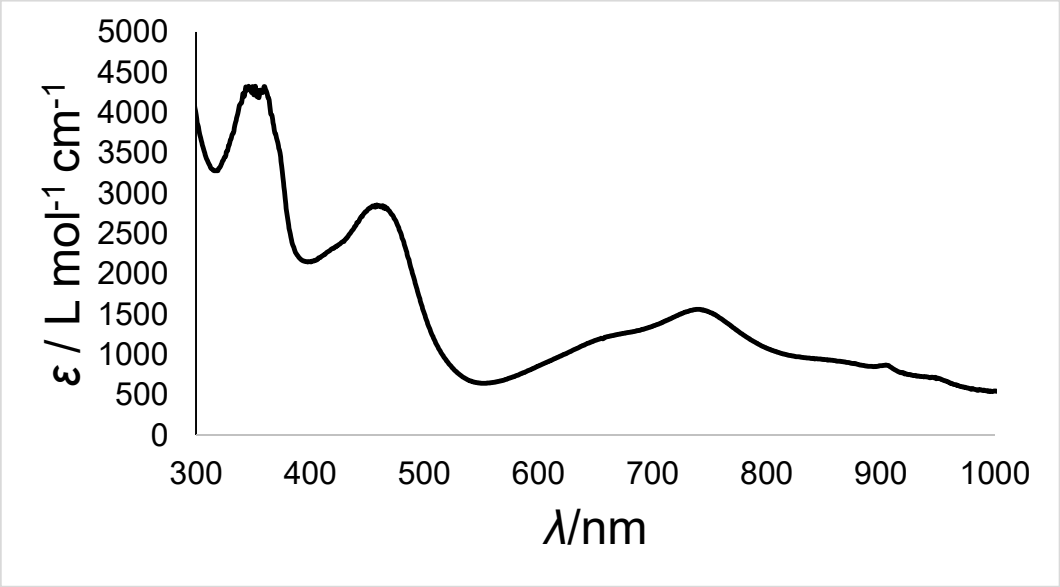

Figure S24. UV/Vis spectrum of [K{18c6}][Co(N(SiMe$_3$)$_2$)$_2$(bipy)] (**4**) in Et$_2$O.

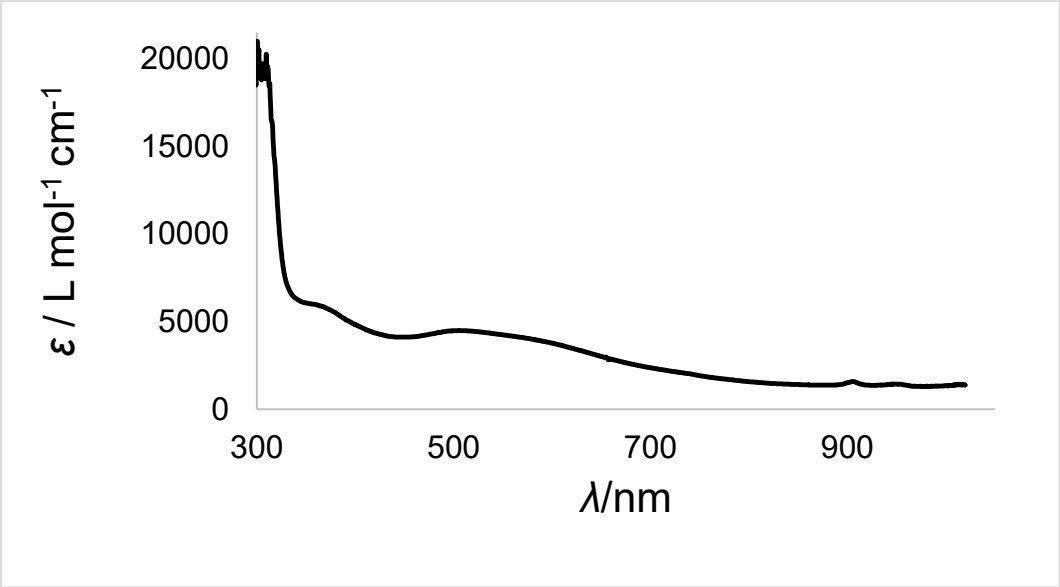

Figure S25. UV/Vis spectrum of [Cr(N(SiMe$_3$)$_2$)$_2$(bipy)] (**5**) in Et$_2$O.

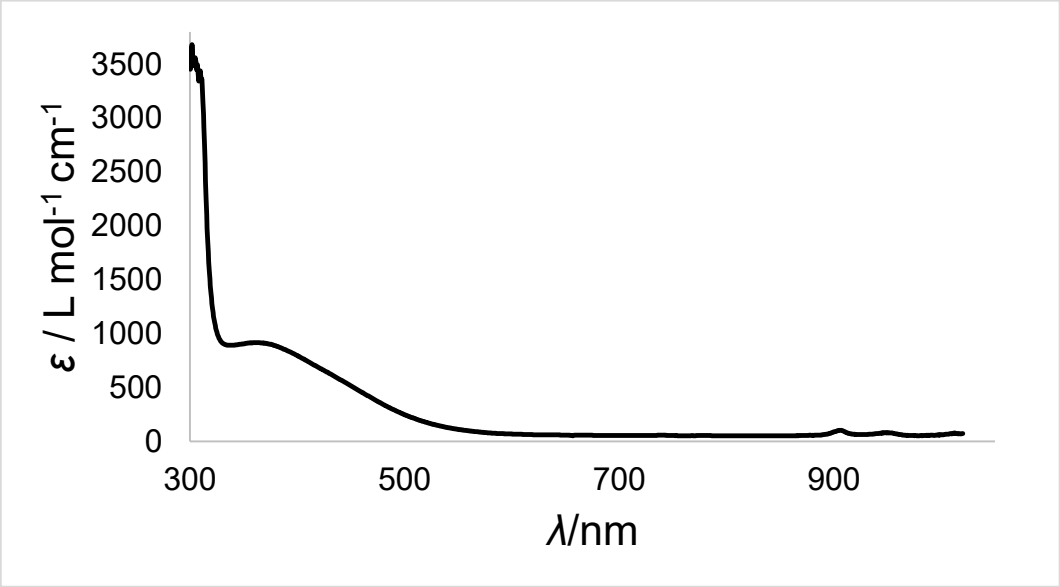

Figure S26. UV/Vis spectrum of [Mn(N(SiMe$_3$)$_2$)$_2$(bipy)] (**6**) in Et$_2$O.

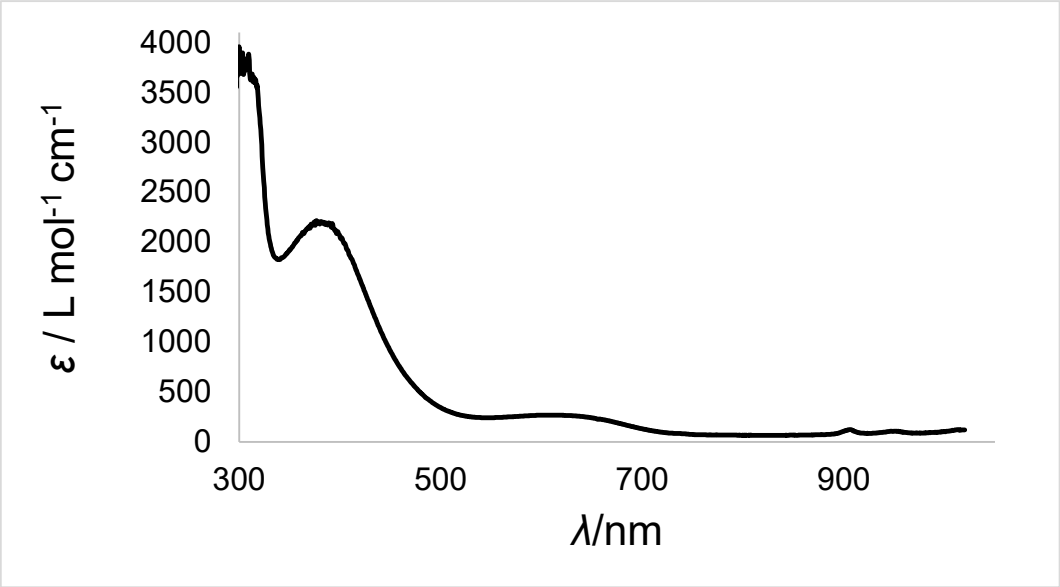

Figure S27. UV/Vis spectrum of [Fe(N(SiMe$_3$)$_2$)$_2$(bipy)] (**7**) in Et$_2$O.

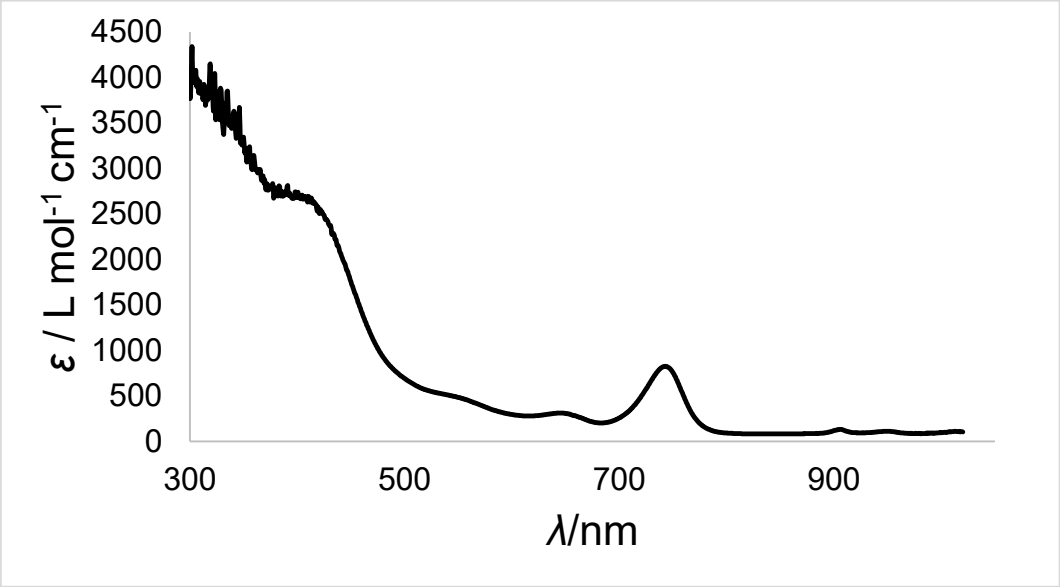

Figure S28. UV/Vis spectrum of [Co(N(SiMe$_3$)$_2$)$_2$(bipy)] (**8**) in Et$_2$O.

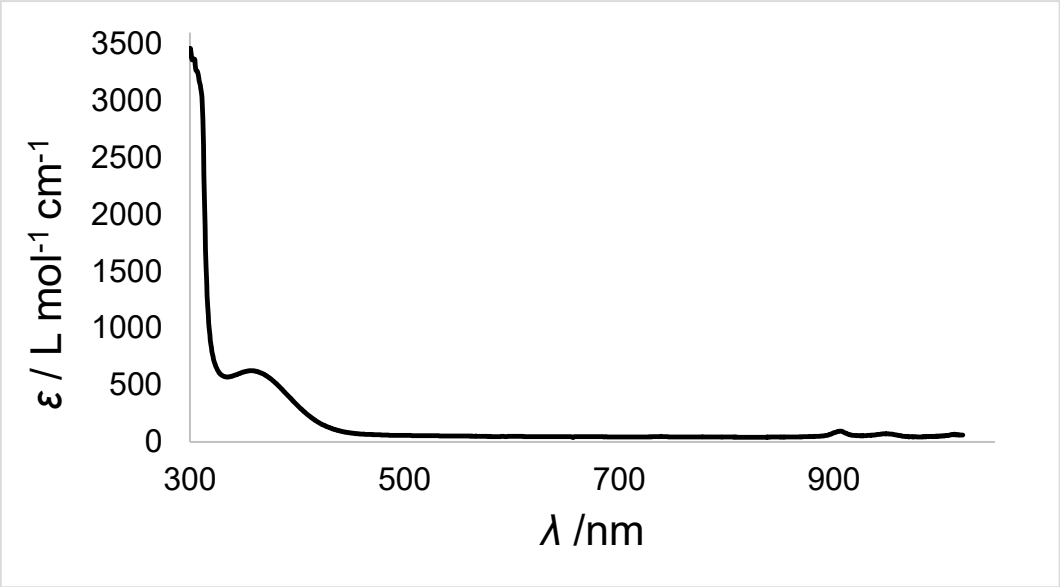

Figure S29. UV/Vis spectrum of [Zn(N(SiMe$_3$)$_2$)$_2$(bipy)] (**9**) in Et$_2$O.

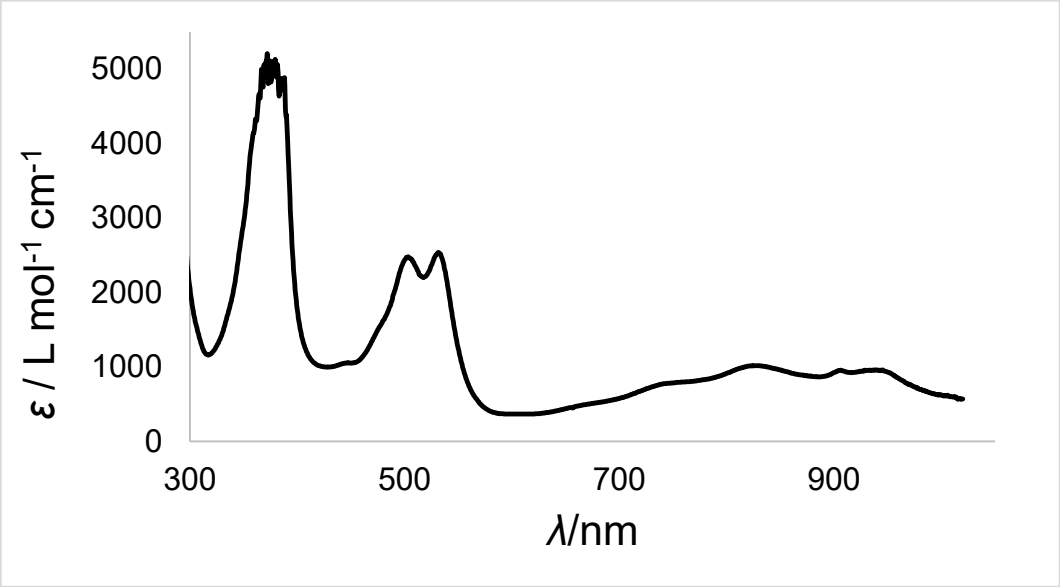

Figure S30. UV/Vis spectrum of [K{18c6}][Zn(N(SiMe$_3$)$_2$)$_2$(bipy)] (**10**) in Et$_2$O.

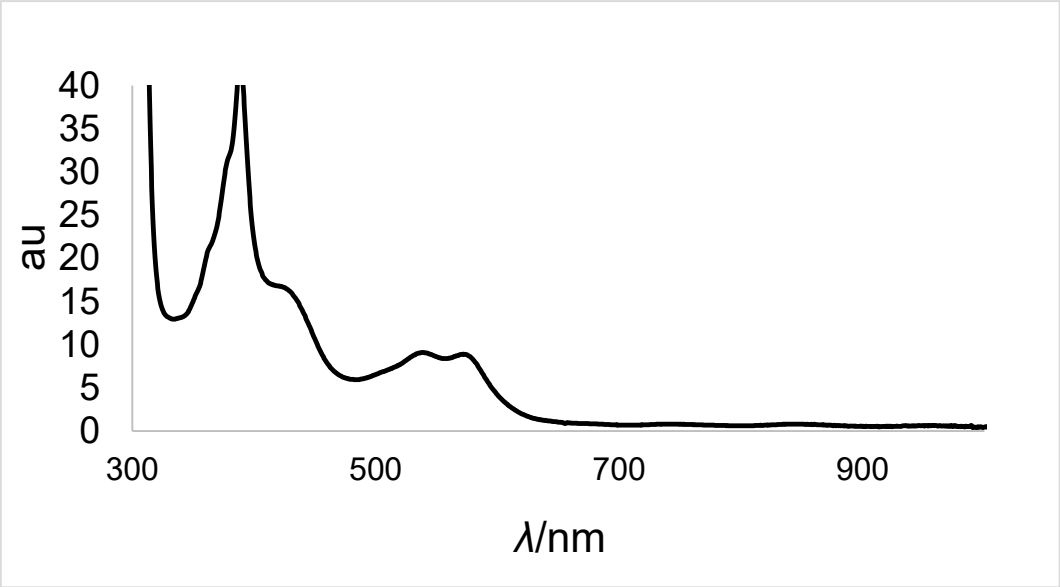

Figure S31. UV/Vis spectrum of [K{18c6}][(bipy)] in Et_2O. [K{18c6}][(bipy)] was obtained in-situ from a reaction of 2,2´-bipyridine with KC_8 in the presence of 18-crown-6 in Et_2O.

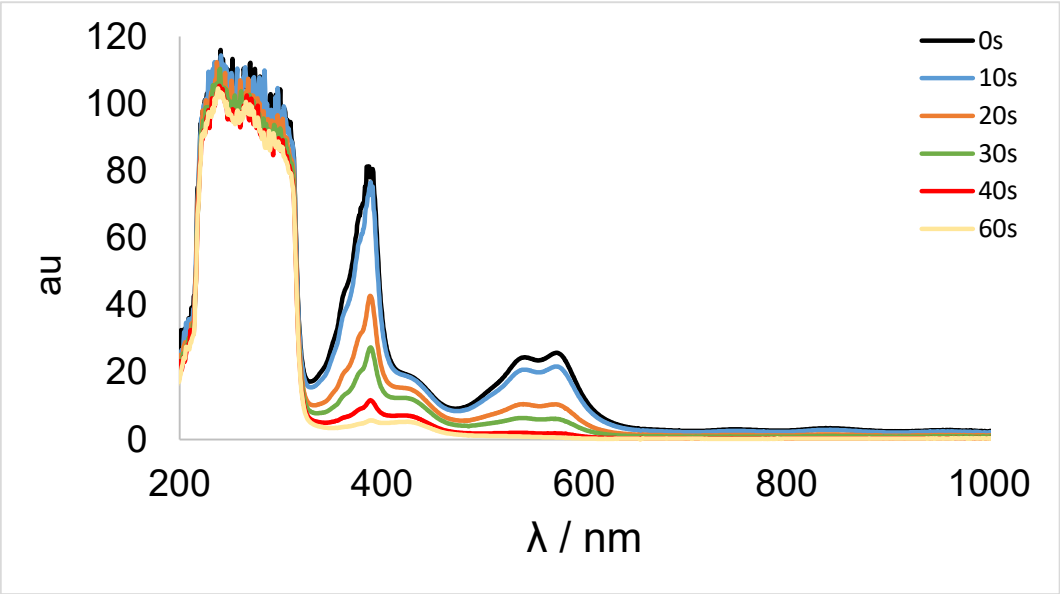

Figure S32. Time-dependent UV/Vis spectra of in-situ synthesized [K{18c6}][(bipy)] in Et_2O.

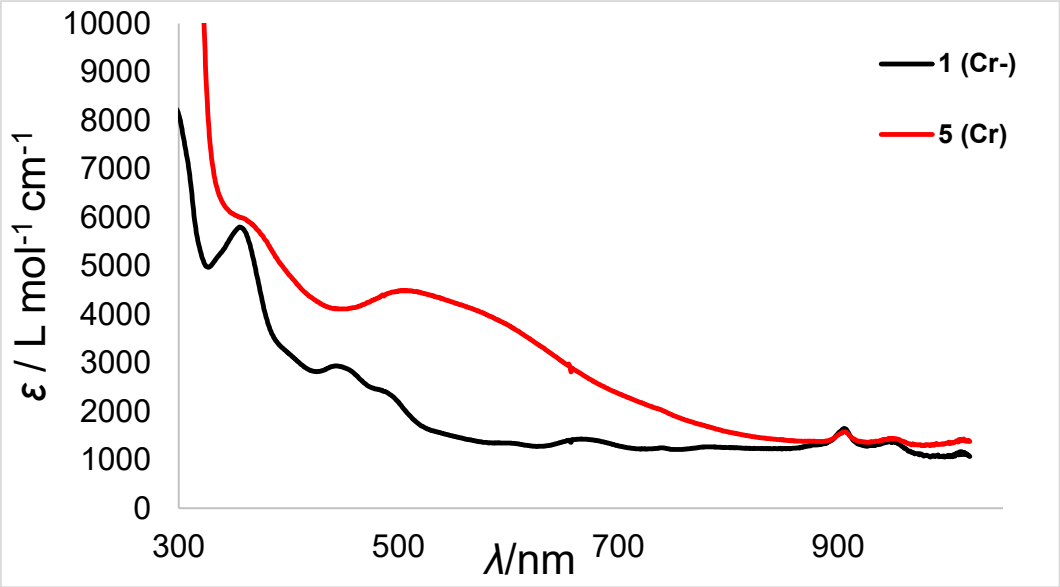

Figure S33. Overlay of UV/Vis spectra of [K{18c6}][Cr(N(SiMe$_3$)$_2$)$_2$(bipy)] (**1**) and [Cr(N(SiMe$_3$)$_2$)$_2$(bipy)] (**5**) in Et$_2$O.

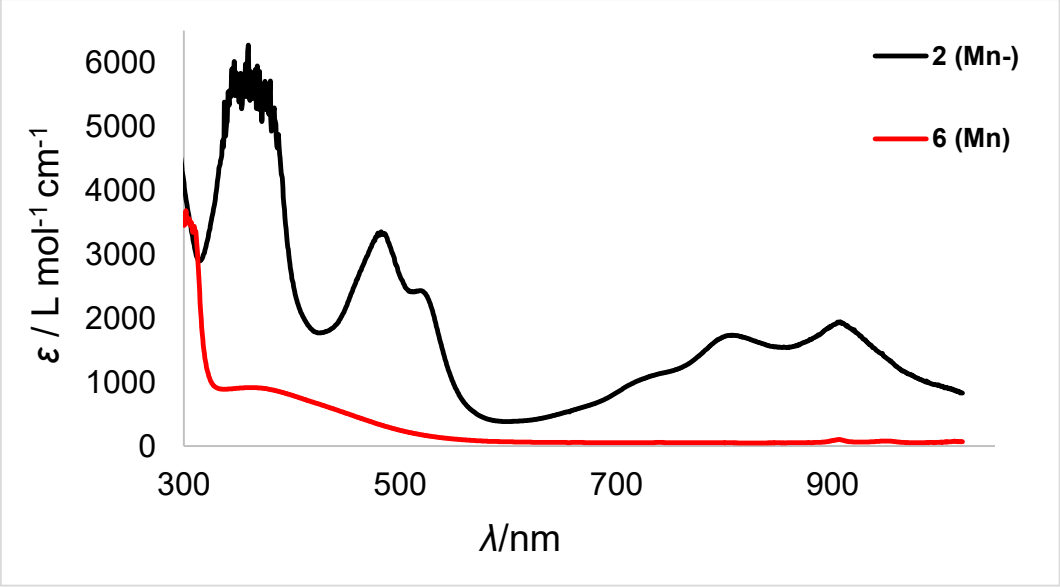

Figure S34. Overlay of UV/Vis spectra of [K{18c6}][Mn(N(SiMe$_3$)$_2$)$_2$(bipy)] (**2**) and [Mn(N(SiMe$_3$)$_2$)$_2$(bipy)] (6) in Et$_2$O.

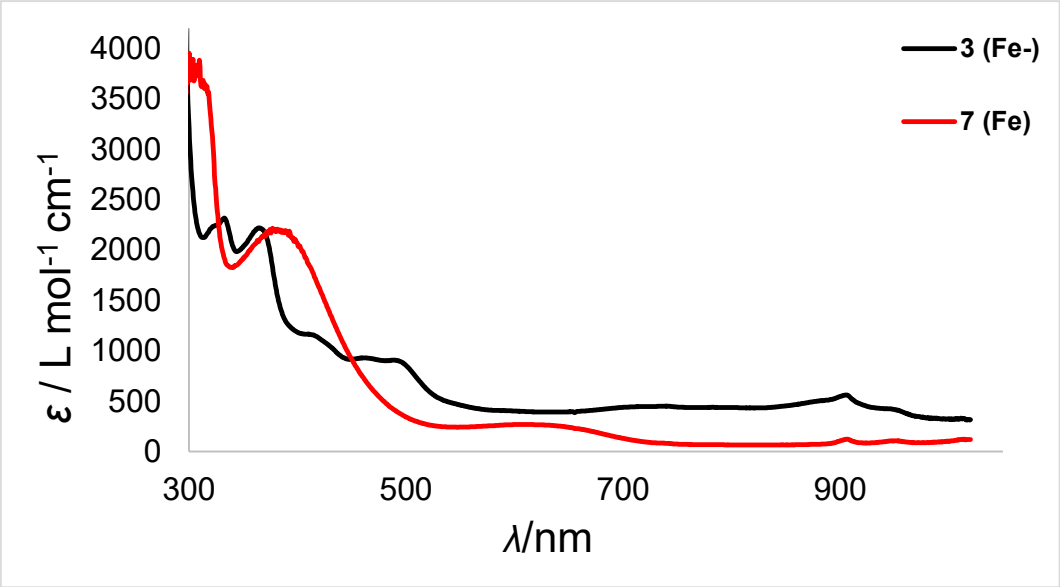

Figure S35. Overlay of UV/Vis spectra of [K{18c6}][Fe(N(SiMe$_3$)$_2$)$_2$(bipy)] (**3**) and [Fe(N(SiMe$_3$)$_2$)$_2$(bipy)](**7**) in Et$_2$O.

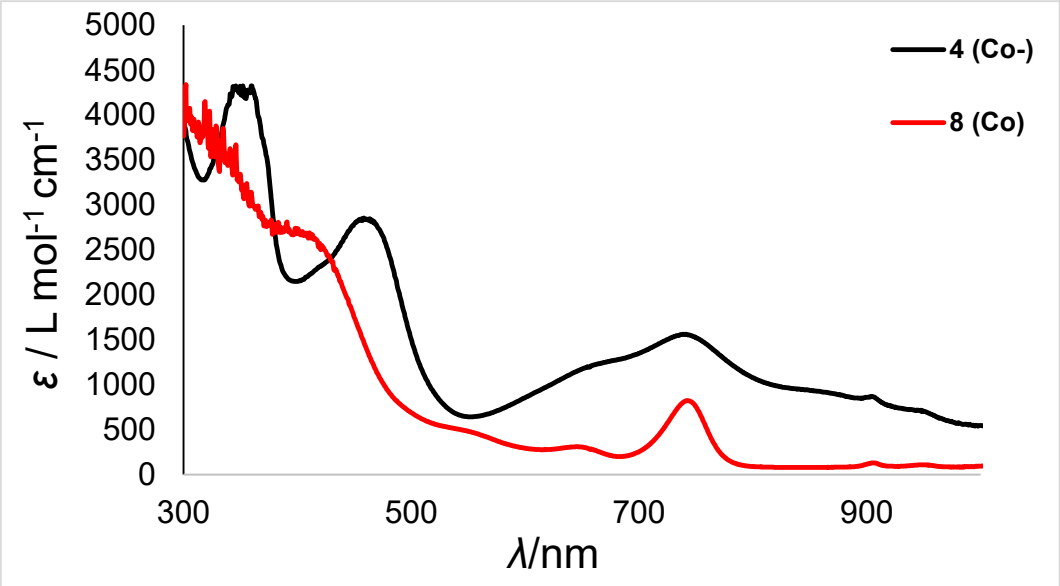

Figure S36. Overlay of UV/Vis spectra of [K{18c6}][Co(N(SiMe$_3$)$_2$)$_2$(bipy)] (**4**) [Co(N(SiMe$_3$)$_2$)$_2$(bipy)] (**8**) in Et$_2$O.

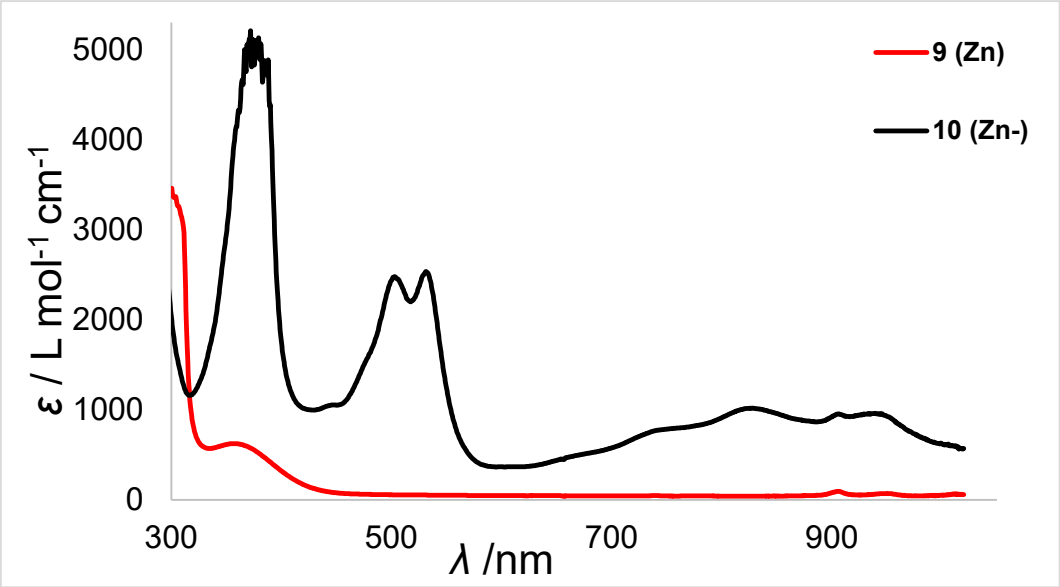

Figure S37. Overlay of UV/Vis spectra of [Zn(N(SiMe$_3$)$_2$)$_2$(bipy)] (**9**) and [K{18c6}][Zn(N(SiMe$_3$)$_2$)$_2$(bipy)] (**10**) in Et$_2$O.

4. Magnetic Data

Magnetic data of compounds **1**–**4** and **10** were recorded on dried crystalline samples and were corrected for diamagnetic contributions from the sample holder and the diamagnetic susceptibility of the respective compound using Pascal constants. Obtained paramagnetic susceptibility χ_{para} was fit using the Curie-Weiss-law $\chi_{CW} = (\frac{N_A \mu_B^2 n_{eff}}{3k_B})^2 \frac{1}{T-\theta}$ (n_{eff} = effective magnetic moment in Bohr's magnetons per formula unit, Θ = Weiss temperature) with contributions from a temperature independent paramagnetism χ_{TIP} using the overall equation $\chi_{para}T = (\chi_{TIP} + \chi_{CW})T$.

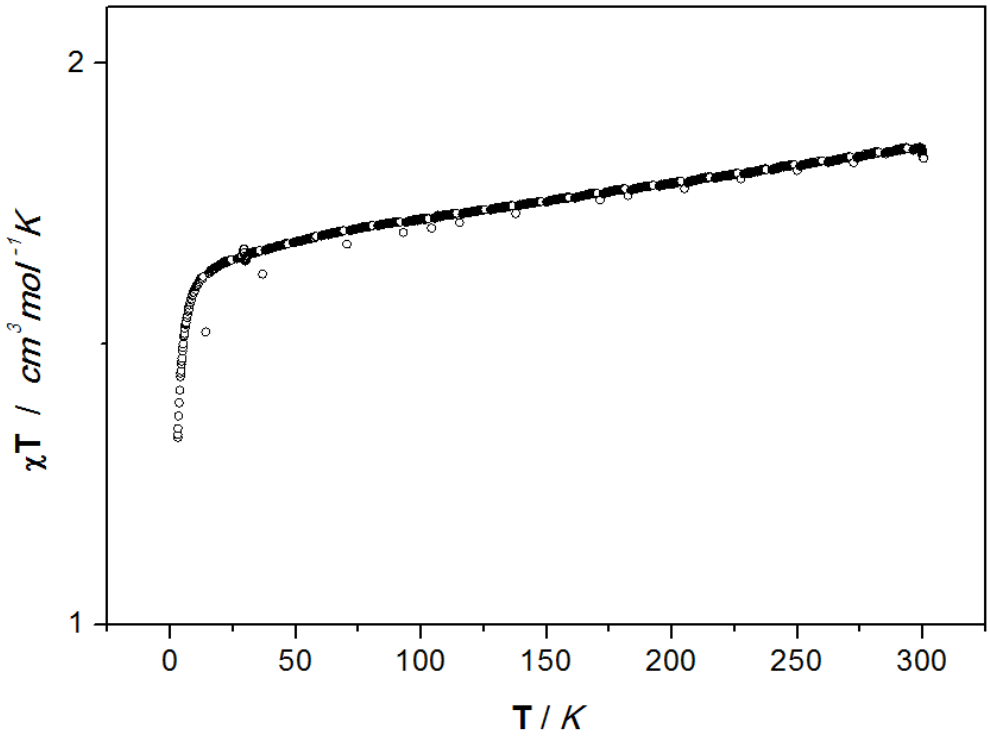

Figure S38. Temperature dependence of the molar magnetic susceptibility times temperature product (χT vs. T) for compound K{18c6}][Cr(N(SiMe$_3$)$_2$)$_2$(bipy)] (**1**). Data were collected under an applied dc field of 1 T in a temperature range of 3 to 300 K.

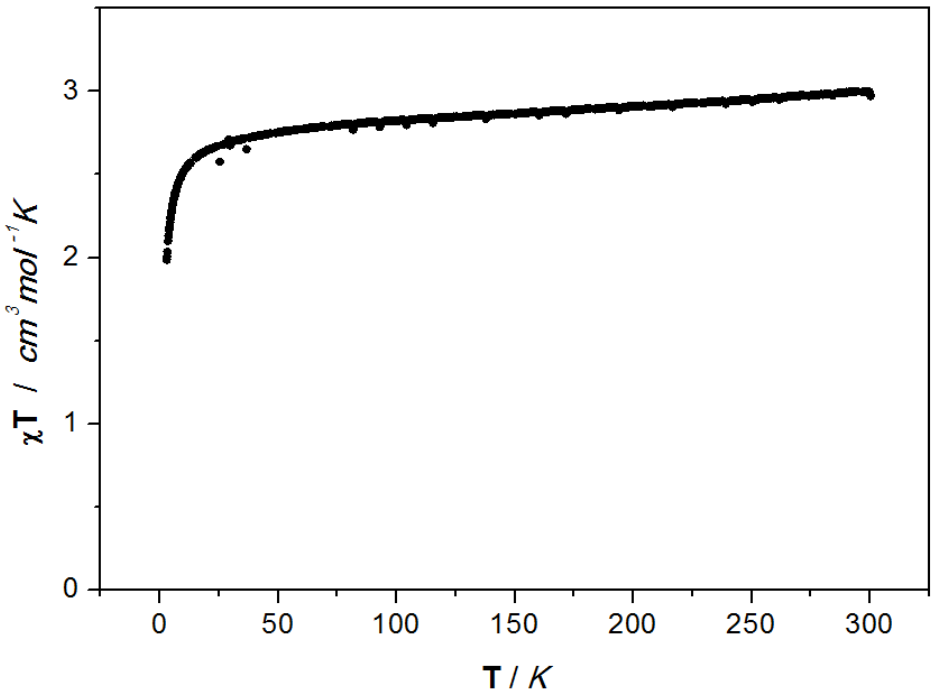

Figure S39. Temperature dependence of the molar magnetic susceptibility times temperature product (χT vs. T) for compound K{18c6}][Mn(N(SiMe$_3$)$_2$)$_2$(bipy)] (**2**). Data was collected under an applied dc field of 1 T in a temperature range of 3 to 300 K.

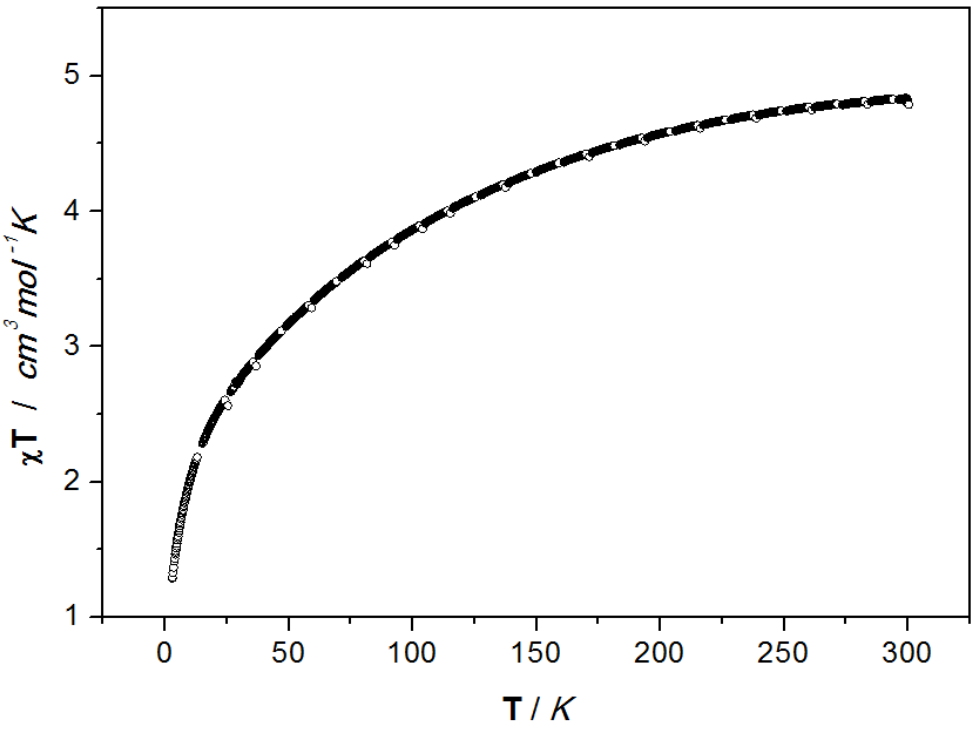

Figure S40. Temperature dependence of the molar magnetic susceptibility times temperature product (χT vs. T) for compound K{18c6}][Fe(N(SiMe$_3$)$_2$)$_2$(bipy)] (**3**). Data was collected under an applied dc field of 1 T in a temperature range of 3 to 300 K.

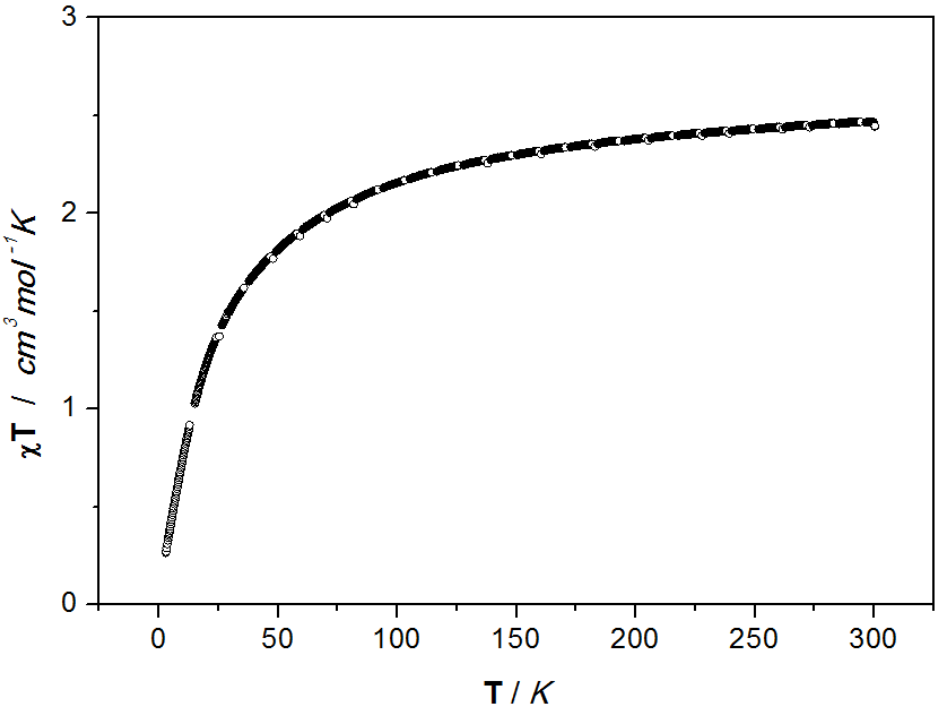

Figure S41. Temperature dependence of the molar magnetic susceptibility times temperature product (χT vs. T) for compound K{18c6}][Co(N(SiMe$_3$)$_2$)$_2$(bipy)] (**4**). Data was collected under an applied dc field of 1 T in a temperature range of 3 to 300 K.

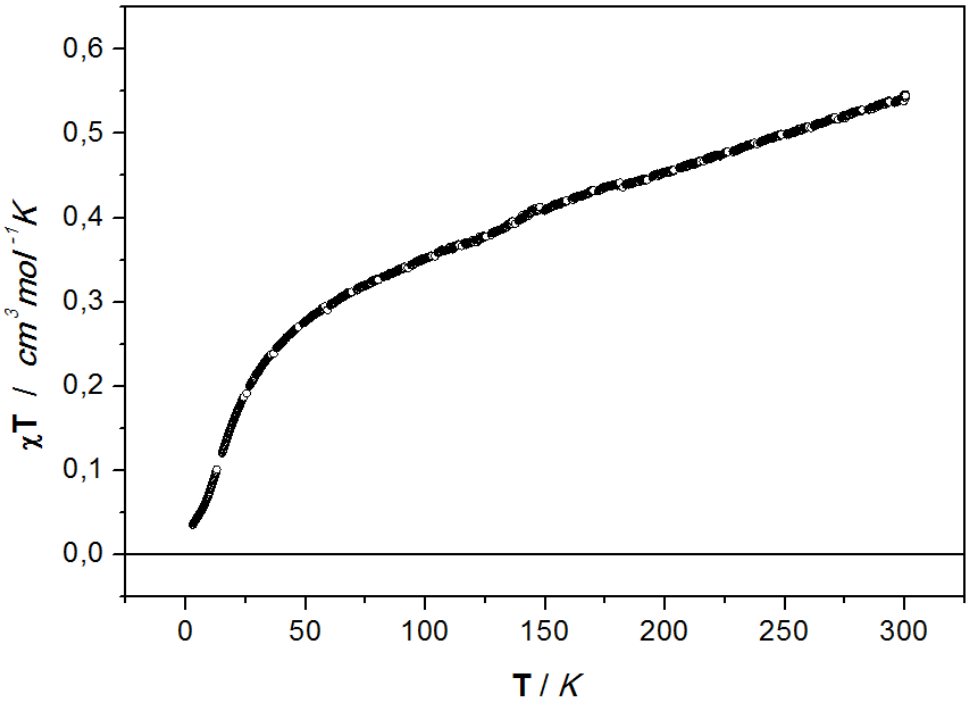

Figure S42. Temperature dependence of the molar magnetic susceptibility times temperature product (χT vs. T) for compound K{18c6}][Zn(N(SiMe$_3$)$_2$)$_2$(bipy)] (**10**). Data was collected under an applied dc field of 1 T in a temperature range of 3 to 300 K.

5. Cyclic Voltammetry

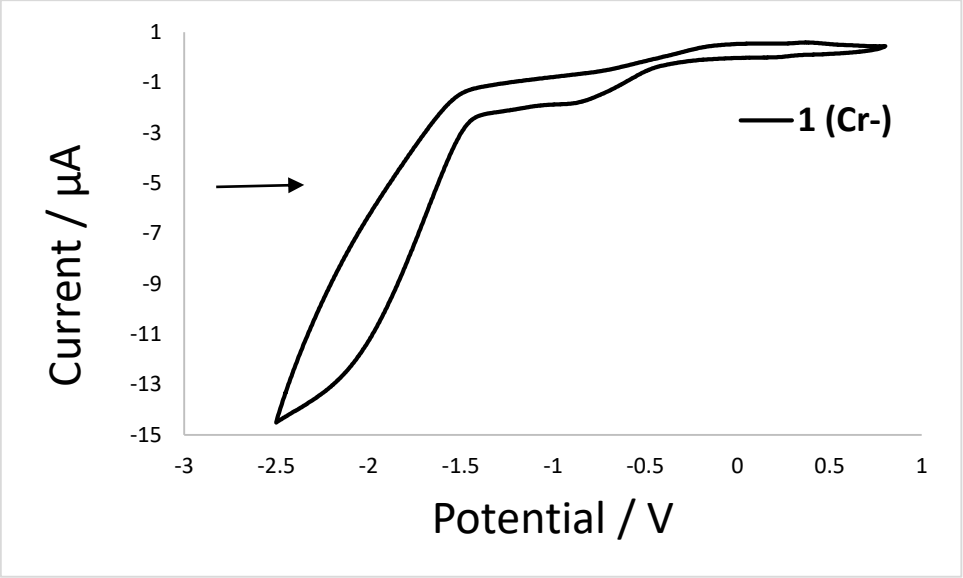

Figure S33. Cyclic voltammogram for complex **1** in THF (1 mM, 500 mV/s, 0.1 M [NBu$_4$][PF$_6$]).

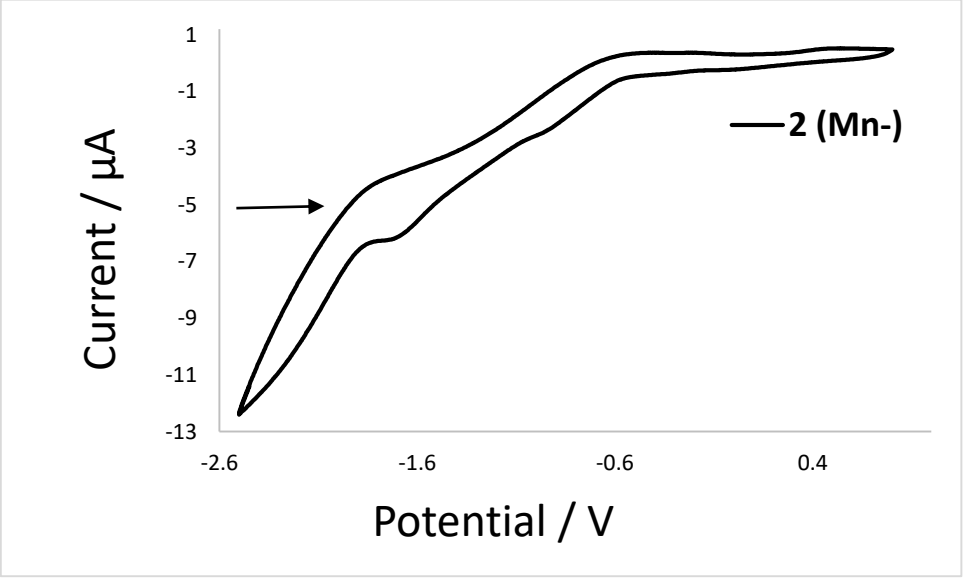

Figure S44. Cyclic voltammogram for complex **2** in THF (1 mM, 500 mV/s, 0.1 M [NBu$_4$][PF$_6$]).

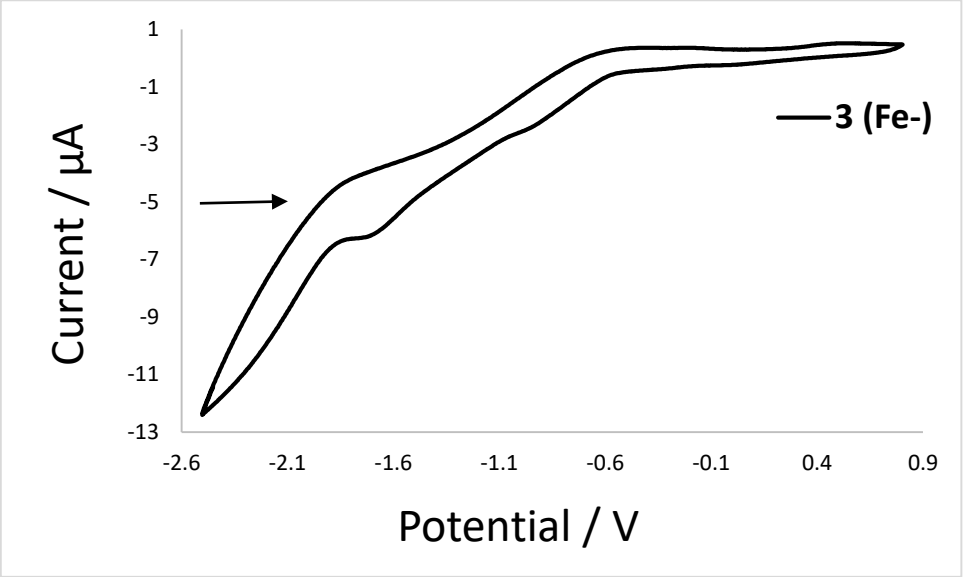

Figure S44. Cyclic voltammogram for complex **3** in THF (1 mM, 500 mV/s, 0.1 M [NBu$_4$][PF$_6$]).

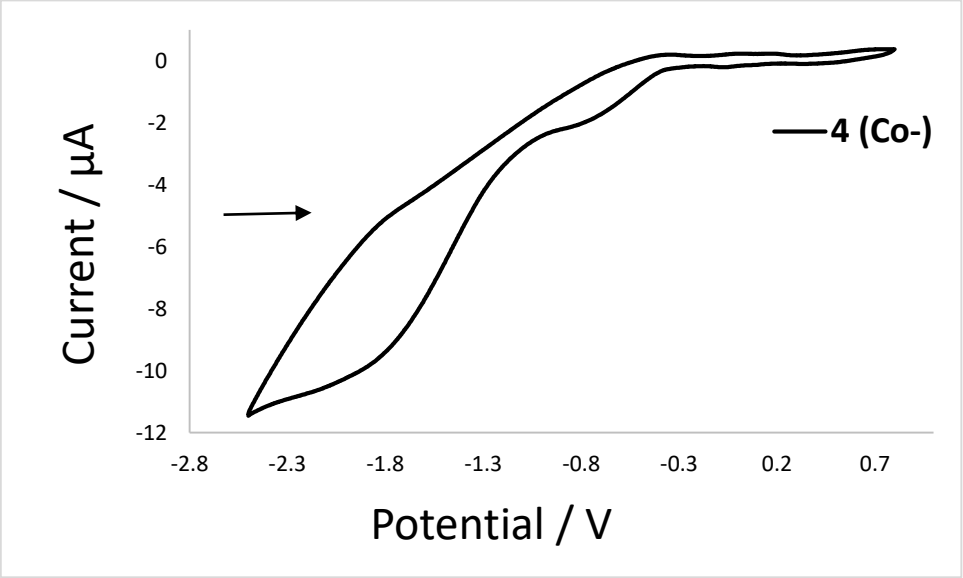

Figure S46. Cyclic voltammogram for complex **4** in THF (1 mM, 500 mV/s, 0.1 M [NBu$_4$][PF$_6$]).

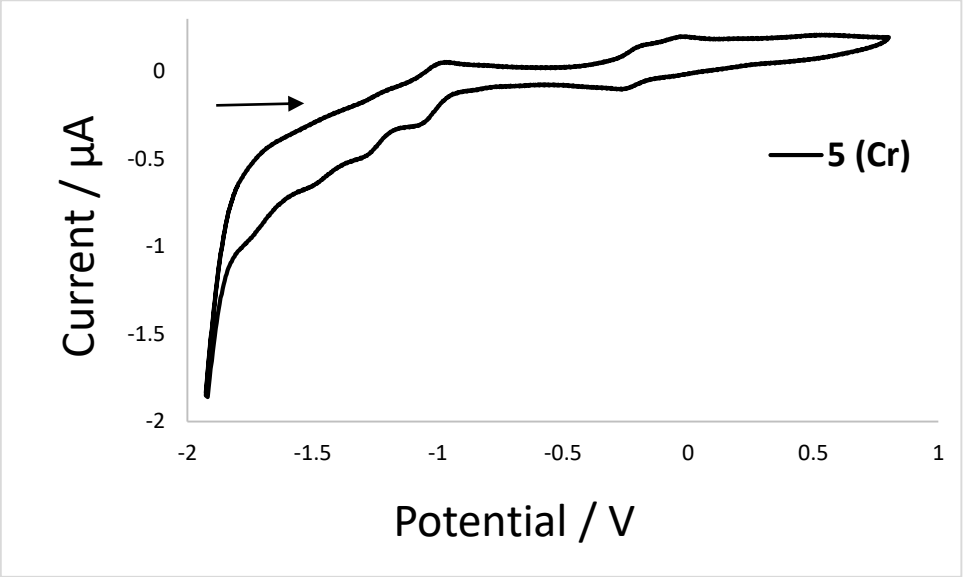

Figure S47. Cyclic voltammogram for complex **5** in THF (1 mM, 500 mV/s, 0.1 M [NBu$_4$][PF$_6$]).

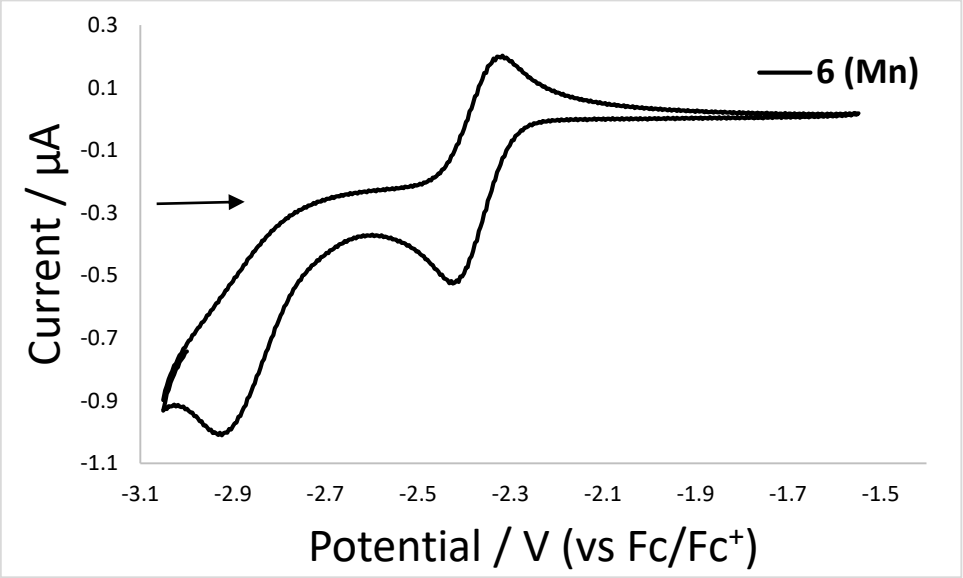

Figure S48. Cyclic voltammogram for complex **6** in THF (1 mM, 500 mV/s, 0.1 M [NBu$_4$][PF$_6$]).

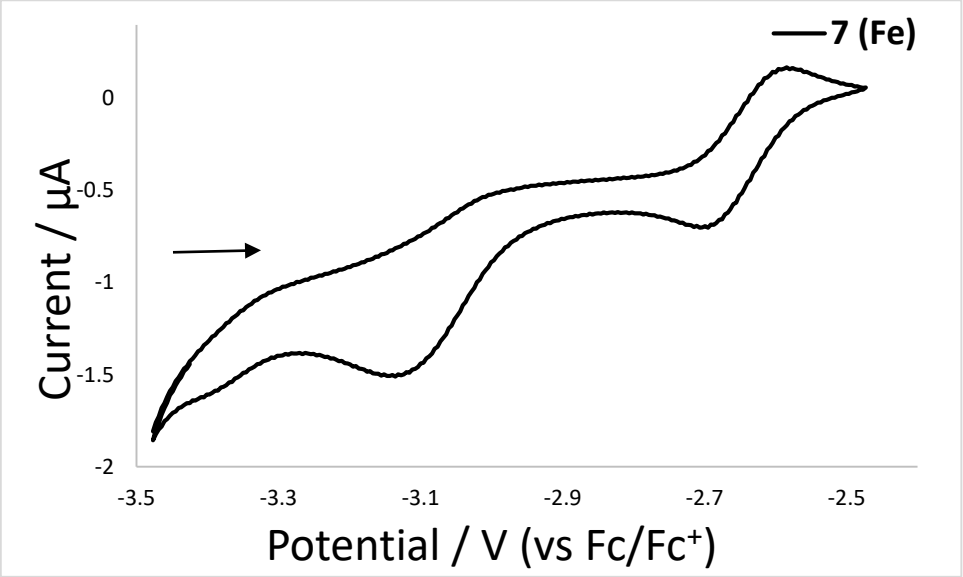

Figure S49. Cyclic voltammogram for complex **7** in THF (1 mM, 500 mV/s, 0.1 M [NBu_4][PF_6]).

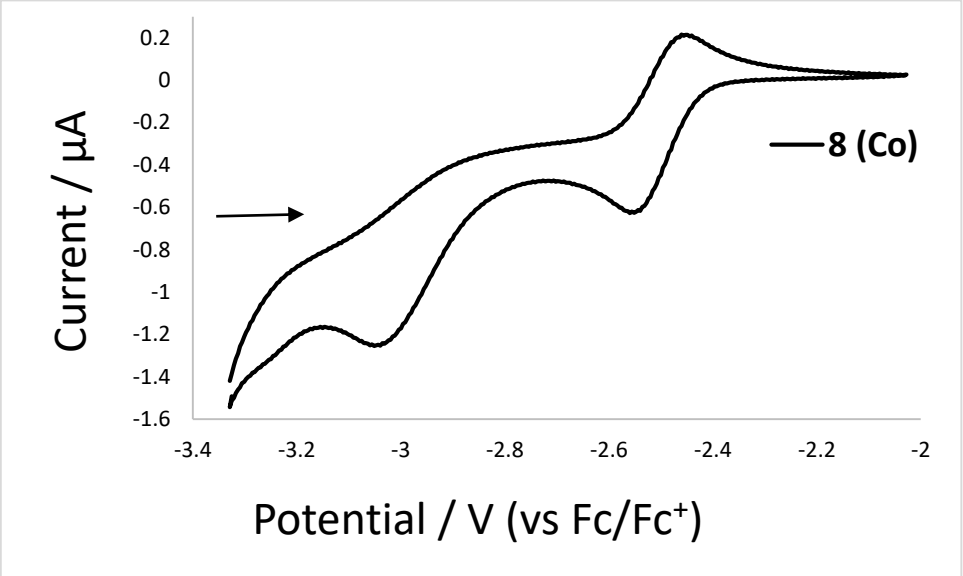

Figure S50. Cyclic voltammogram for complex **8** in THF (1 mM, 500 mV/s, 0.1 M [NBu_4][PF_6]).

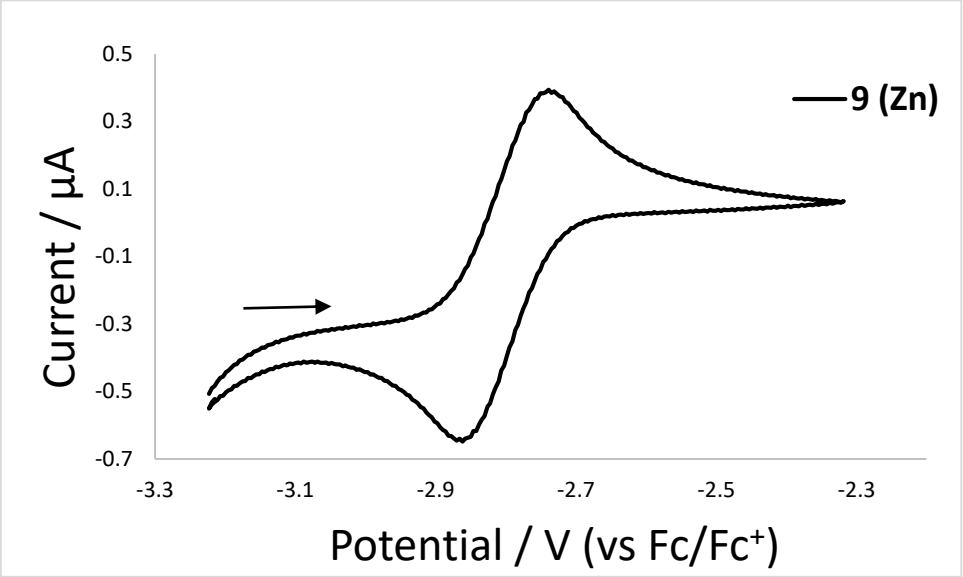

Figure S51. Cyclic voltammogram for complex **9** in THF (1 mM, 500 mV/s, 0.1 M [NBu_4][PF_6]).

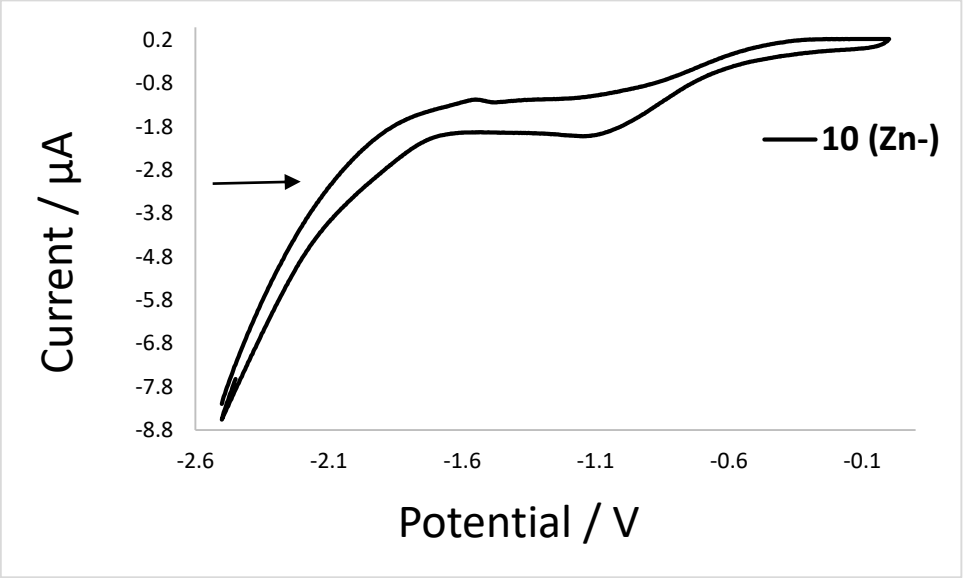

Figure S52. Cyclic voltammogram for complex **10** in THF (1 mM, 500 mV/s, 0.1 M [NBu_4][PF_6]).

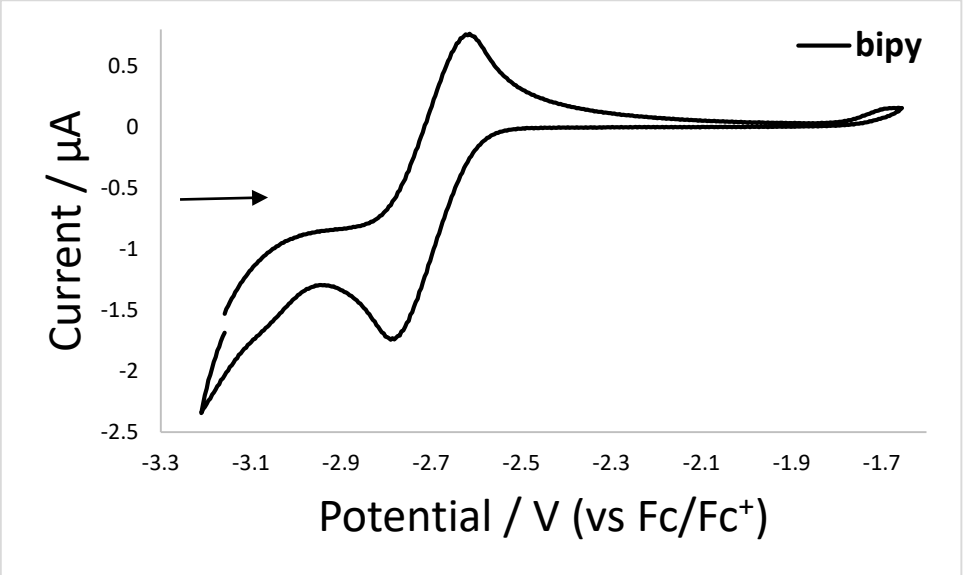

Figure S53. Cyclic voltammogram for 2,2′-bipyridine in THF (1 mM, 500 mV/s, 0.1 M [NBu_4][PF_6]).

6. X-Ray Diffraction Analysis and Molecular Structures

Data for **3** (CCDC 1918204), **4** (CCDC 1918205), **10** (CCDC 1918207) were collected at 100 K on a Bruker Quest D8 diffractometer using a graphite-monochromated Mo-Kα radiation and equipped with an Oxford Instrument Cooler Device. Data for **8** (CCDC 1918202), **1** (CCDC 1918208), **9** (CCDC 1918206) was collected at 100 K a STOE IPDS2 diffractometer and data for **2** (CCDC 1918203) were collected at 100 K a STOE IPDS2T diffractometer using a graphite-monochromated Mo-Kα radiation (λ = 0.71073 Å) and equipped with an Oxford Cryosystems Cryostream Cooler Device. The structures have been solved using either OLEX SHELXT V2014/1 [1] and refined by means of least-squares procedures on a F^2 with the aid of the program SHELXL-2016/6 [2] included in the software package WinGX version 1.63 [3] or using CRYSTALS [4].

The Atomic Scattering Factors were taken from International Tables for X-Ray Crystallography [5]. All non-hydrogen atoms were refined anisotropically. All hydrogens atoms were refined by using a riding model. Absorption corrections were introduced by using the MULTISCAN and X-Red program [6,7]. Drawings of molecules are performed with the program DIAMOND with 50% probability displacement ellipsoids for non-H atoms. Depiction of H atoms is omitted for clarity.

Table S1. Crystal data and structure refinement for **1**.

Identification Code	**K(18c6)Cr5**
Empirical formula	$C_{42}H_{84}CrKN_4O_8Si_4$
Formula weight	976.59
Temperature/K	100.0
Crystal system	triclinic
Space group	P−1
a/Å	11.6269(2)
b/Å	21.5546(4)
c/Å	21.8560(4)
α/°	95.633(2)
β/°	89.8920(10)
γ/°	90.377(2)
Volume/Å^3	5450.83(17)
Z	4
ρ_{calc} g/cm^3	1.190
μ/mm^{-1}	0.422
F(000)	2108.0
Crystal size/mm^3	0.3494 × 0.2903 × 0.2027
Radiation	Mo-Kα (λ = 0.71073)
2Θ range for data collection/°	3.504 to 50
Index ranges	−13 ≤ h ≤ 13, −25 ≤ k ≤ 25, −25 ≤ l ≤ 25
Reflections collected	88325
Independent reflections	19148 [R_{int} = 0.0630, R_{sigma} = 0.0368]
Data/restraints/parameters	19148/0/1112
Goodness-of-fit on F^2	1.073
Final *R* indexes [I>=2σ (I)]	R_1 = 0.0512, wR_2 = 0.1293
Final *R* indexes [all data]	R_1 = 0.0571, wR_2 = 0.1323
Largest diff. peak/hole/e Å^{-3}	0.79/−0.47

Table S2. Crystal data and structure refinement for **2**. The structure was refined as an inversion twin, twin ratio refined to 0.085(13).

Identification Code	**K(18c6)Mn6**
Empirical formula	$C_{34}H_{68}KMnN_4O_6Si_4$
Formula weight	835.32
Temperature/K	100.0
Crystal system	monoclinic
Space group	C2
a/Å	34.8403(17)
b/Å	18.4715(11)
c/Å	14.5302(8)
α/°	90
β/°	96.555(4)
γ/°	90
Volume/Å^3	9289.8(9)
Z	8
ρ_{calc} g/cm^3	1.194
μ/mm^{-1}	0.518
F(000)	3584.0
Crystal size/mm^3	0.27 × 0.18 × 0.07
Radiation	Mo-Kα (λ = 0.71073)
2Θ range for data collection/°	3.668 to 54.998
Index ranges	−45 ≤ h ≤ 43, −24 ≤ k ≤ 24, −18 ≤ l ≤ 18
Reflections collected	52126
Independent reflections	21354 [R_{int} = 0.0285, R_{sigma} = 0.0488]
Data/restraints/parameters	21354/1546/1264
Goodness-of-fit on F^2	0.917
Final *R* indexes [I>=2σ (I)]	R_1 = 0.0376, wR_2 = 0.0780
Final *R* indexes [all data]	R_1 = 0.0521, wR_2 = 0.0815
Largest diff. peak/hole / e Å^{-3}	0.81/−0.39

Table 3. Crystal data and structure refinement for **3**.

Identification Code	**K(18c6)Fe7**
Empirical formula	$C_{42}H_{83}FeKN_4O_8Si_4$
Formula weight	978.61
Temperature/K	100.0
Crystal system	triclinic
Space group	P−1
a/Å	10.8613(5)
b/Å	13.2627(6)
c/Å	19.8669(9)
α/°	77.5970(10)
β/°	80.062(2)
γ/°	83.452(2)
Volume/Å^3	2744.3(2)
Z	2
ρ_{calc} g/cm^3	1.184
μ/mm^{-1}	0.485
F(000)	1055.0
Crystal size/mm^3	0.21 × 0.2 × 0.11
Radiation	Mo-Kα (λ = 0.71073)
2Θ range for data collection/°	4.646 to 55.124
Index ranges	−14 ≤ h ≤ 14, −17 ≤ k ≤ 17, −25 ≤ l ≤ 25
Reflections collected	103782
Independent reflections	12642 [R_{int} = 0.0332, R_{sigma} = 0.0201]
Data/restraints/parameters	12642/276/683
Goodness-of-fit on F^2	1.054
Final *R* indexes [*I*>=2σ (*I*)]	R_1 = 0.0279, wR_2 = 0.0618
Final *R* indexes [all data]	R_1 = 0.0383, wR_2 = 0.0658
Largest diff. peak/hole/e Å^{-3}	0.34/−0.24

Table S4. Crystal data and structure refinement for **4**.

Identification Code	**K(18c6)Co8**
Empirical formula	$C_{42}H_{84}CoKN_4O_8Si_4$
Formula weight	983.52
Temperature/K	100.0
Crystal system	triclinic
Space group	P−1
a/Å	10.8097(5)
b/Å	13.2648(6)
c/Å	19.9051(10)
α/°	77.712(2)
β/°	80.199(2)
γ/°	83.606(2)
Volume/Å^3	2739.7(2)
Z	2
ρ_{calc} g/cm^3	1.192
μ/mm^{-1}	0.524
F(000)	1060.0
Crystal size / mm^3	0.23 × 0.14 × 0.07
Radiation	Mo-Kα (λ = 0.71073)
2Θ range for data collection/°	4.238 to 55.058
Index ranges	−14 ≤ h ≤ 14, −16 ≤ k ≤ 17, −25 ≤ l ≤ 25
Reflections collected	89930
Independent reflections	12549 [R_{int} = 0.0853, R_{sigma} = 0.0565]
Data/restraints/parameters	12549/57/584
Goodness-of-fit on F^2	1.017
Final *R* indexes [*I*>=2σ (*I*)]	R_1 = 0.0420, wR_2 = 0.0739
Final *R* indexes [all data]	R_1 = 0.0780, wR_2 = 0.0831
Largest diff. peak/hole/e Å^{-3}	0.29/−0.49

Table S5. Crystal data and structure refinement for **8**. The structure was refined as an inversion twin, twin ratio refined to 0.495(10).

Identification Code	**Co4**
Empirical formula	$C_{44}H_{88}Co_2N_8Si_8$
Formula weight	1071.80
Temperature/K	100
Crystal system	orthorhombic
Space group	$Pca2_1$
a/Å	18.7674(9)
b/Å	18.1030(8)
c/Å	17.5930(7)
α/°	90
β/°	90
γ/°	90
Volume/Å^3	5977.2(5)
Z	4
ρ_{calc} g/cm^3	1.191
μ/mm^{-1}	0.751
F(000)	2296.0
Crystal size/mm^3	0.31 × 0.2 × 0.2
Radiation	Mo K*α* (*λ* = 0.71073)
2Θ range for data collection/°	3.89 to 51.998
Index ranges	−23 ≤ h ≤ 21, −19 ≤ k ≤ 22, −19 ≤ l ≤ 21
Reflections collected	20518
Independent reflections	10939 [R_{int} = 0.0219, R_{sigma} = 0.0228]
Data/restraints/parameters	10939/1/588
Goodness-of-fit on F^2	1.014
Final *R* indexes [*I*>=2σ (*I*)]	R_1 = 0.0280, wR_2 = 0.0670
Final *R* indexes [all data]	R_1 = 0.0307, wR_2 = 0.0679
Largest diff. peak/hole/e Å^{-3}	0.45/−0.25

Table S6. Crystal data and structure refinement for **9**. The structure was refined as an inversion twin, twin ratio refined to 0.292(9).

Identification Code	**Zn9**
Empirical formula	$C_{44}H_{88}N_8Si_8Zn_2$
Formula weight	1084.68
Temperature/K	100
Crystal system	orthorhombic
Space group	P*ca*2$_1$
a/Å	18.8806(12)
b/Å	18.0560(13)
c/Å	17.6133(17)
α/°	90
β/°	90
γ/°	90
Volume / Å^3	6004.5(8)
Z	4
ρ_{calc} g/cm^3	1.200
μ/mm^{-1}	0.994
F(000)	2320.0
Crystal size/mm^3	0.254 × 0.189 × 0.085
Radiation	Mo-Kα (λ = 0.71073)
2Θ range for data collection/°	4.314 to 51.996
Index ranges	−23 ≤ h ≤ 23, −21 ≤ k ≤ 22, −21 ≤ l ≤ 21
Reflections collected	52603
Independent reflections	11789 [R_{int} = 0.0737, R_{sigma} = 0.0589]
Data/restraints/parameters	11789/1/584
Goodness-of-fit on F^2	0.969
Final *R* indexes [*I*>=2σ (*I*)]	R_1 = 0.0340, wR_2 = 0.0700
Final *R* indexes [all data]	R_1 = 0.0445, wR_2 = 0.0718
Largest diff. peak/hole/e Å^{-3}	0.58/−0.21

Table S7. Crystal data and structure refinement for **10**.

Identification Code	**K(18c6)Zn10**
Empirical formula	$C_{38}H_{78}KN_4O_7Si_4Zn$
Formula weight	919.87
Temperature/K	100.0
Crystal system	monoclinic
Space group	$P2_1/c$
a/Å	12.1899(7)
b/Å	18.4365(10)
c/Å	22.8273(13)
α/°	90
β/°	95.423(2)
γ/°	90
Volume/Å^3	5107.2(5)
Z	4
ρ_{calc} g/cm^3	1.196
μ/mm^{-1}	0.700
F(000)	1980.0
Crystal size / mm^3	0.492 × 0.383 × 0.15
Radiation	Mo Kα (λ = 0.71073)
2Θ range for data collection/°	4.268 to 49.998
Index ranges	−14 ≤ h ≤ 14, −21 ≤ k ≤ 21, −27 ≤ l ≤ 27
Reflections collected	96672
Independent reflections	8987 [R_{int} = 0.0946, R_{sigma} = 0.0427]
Data/restraints/parameters	8987/1293/603
Goodness-of-fit on F^2	1.077
Final R indexes [I>=2σ (I)]	R_1 = 0.1301, wR_2 = 0.2536
Final R indexes [all data]	R_1 = 0.1530, wR_2 = 0.2636
Largest diff. peak/hole/e Å^{-3}	1.75/−1.94

Table S 8. Crystal data and structure refinement for **1**-**4**, **10**.

Identification code	K(18c6)Cr5	K(18c6)Mn6	K(18c6)Fe7	K(18c6)Co8	K(18c6)Zn10
Empirical formula	$C_{42}H_{84}CrKN_4O_8Si_4$	$C_{34}H_{68}KMnN_4O_6Si_4$	$C_{42}H_{83}FeKN_4O_8Si_4$	$C_{42}H_{84}CoKN_4O_8Si_4$	$C_{38}H_{78}KN_4O_7Si_4Zn$
Formula weight	976.59	835.32	978.61	983.52	919.87
Temperature / *K*	100.0	100.0	100.0	100.0	100.0
Crystal system	triclinic	monoclinic	triclinic	triclinic	monoclinic
Space group	P−1	C2	P−1	P−1	$P2_1/c$
a/Å	11.6269(2)	34.8403(17)	10.8613(5)	10.8097(5)	12.1899(7)
b/Å	21.5546(4)	18.4715(11)	13.2627(6)	13.2648(6)	18.4365(10)
c/Å	21.8560(4)	14.5302(8)	19.8669(9)	19.9051(10)	22.8273(13)
α/°	95.633(2)	90	77.5970(10)	77.712(2)	90
β/°	89.8920(10)	96.555(4)	80.062(2)	80.199(2)	95.423(2)
γ/°	90.377(2)	90	83.452(2)	83.606(2)	90
Volume/Å^3	5450.83(17)	9289.8(9)	2744.3(2)	2739.7(2)	5107.2(5)
Z	4	8	2	2	4
ρ_{calc} g/cm^3	1.190	1.194	1.184	1.192	1.196
μ/mm^{-1}	0.422	0.518	0.485	0.524	0.700
F(000)	2108.0	3584.0	1055.0	1060.0	1980.0
Crystal size/mm^3	0.3494 × 0.2903 × 0.2027	0.27 × 0.18 × 0.07	0.21 × 0.2 × 0.11	0.23 × 0.14 × 0.07	0.492 × 0.383 × 0.15
Radiation	Mo Kα (λ = 0.71073)	Mo Kα (λ = 0.71073)	Mo Kα (λ = 0.71073)	Mo Kα (λ = 0.71073)	Mo Kα (λ = 0.71073)
2Θ range for data collection/°	3.504 to 50	3.668 to 54.998	4.646 to 55.124	4.238 to 55.058	4.268 to 49.998
Index ranges	−13 ≤ h ≤ 13, −25 ≤ k ≤ 25, −25 ≤ l ≤ 25	−45 ≤ h ≤ 43, −24 ≤ k ≤ 24, −18 ≤ l ≤ 18	−14 ≤ h ≤ 14, −17 ≤ k ≤ 17, −25 ≤ l ≤ 25	−14 ≤ h ≤ 14, −16 ≤ k ≤ 17, −25 ≤ l ≤ 25	−14 ≤ h ≤ 14, −21 ≤ k ≤ 21, −27 ≤ l ≤ 27
Reflections collected	88325	52126	103782	89930	96672
Independent reflections	19148 [R_{int} = 0.0630, R_{sigma} = 0.0368]	21354 [R_{int} = 0.0285, R_{sigma} = 0.0488]	12642 [R_{int} = 0.0332, R_{sigma} = 0.0201]	12549 [R_{int} = 0.0853, R_{sigma} = 0.0565]	8987 [R_{int} = 0.0946, R_{sigma} = 0.0427]
Data/restraints/parameters	19148/0/1112	21354/1546/1264	12642/276/683	12549/57/584	8987/1293/603
Goodness-of-fit on F^2	1.073	0.917	1.054	1.017	1.077
Final *R* indexes [I>=2σ (I)]	R_1 = 0.0512, wR_2 = 0.1293	R_1 = 0.0376, wR_2 = 0.0780	R_1 = 0.0279, wR_2 = 0.0618	R_1 = 0.0420, wR_2 = 0.0739	R_1 = 0.1301, wR_2 = 0.2536
Final *R* indexes [all data]	R_1 = 0.0571, wR_2 = 0.1323	R_1 = 0.0521, wR_2 = 0.0815	R_1 = 0.0383, wR_2 = 0.0658	R_1 = 0.0780, wR_2 = 0.0831	R_1 = 0.1530, wR_2 = 0.2636
Largest diff. peak/hole/e Å^{-3}	0.79/−0.47	0.81/−0.39	0.34/−0.24	0.29/−0.49	1.75/−1.94

Table S9. Crystal data and structure refinement for **4** and **9**.

Identification Code	**Co4**	**Zn9**
Empirical formula	$C_{44}H_{88}Co_2N_8Si_8$	$C_{44}H_{88}N_8Si_8Zn_2$
Formula weight	1071.80	1084.68
Temperature / *K*	100	100
Crystal system	orthorhombic	orthorhombic
Space group	P*ca*2$_1$	P*ca*2$_1$
a/Å	18.7674(9)	18.8806(12)
b/Å	18.1030(8)	18.0560(13)
c/Å	17.5930(7)	17.6133(17)
α/°	90	90
β/°	90	90
γ/°	90	90
Volume / Å^3	5977.2(5)	6004.5(8)
Z	4	4
ρ_{calc} g/cm^3	1.191	1.200
μ/mm^{-1}	0.751	0.994
F(000)	2296.0	2320.0
Crystal size / mm^3	0.31 × 0.2 × 0.2	0.254 × 0.189 × 0.085
Radiation	Mo Kα (λ = 0.71073)	Mo Kα (λ = 0.71073)
2Θ range for data collection/°	3.89 to 51.998	4.314 to 51.996
Index ranges	−23 ≤ h ≤ 21, −19 ≤ k ≤ 22, −19 ≤ l ≤ 21	−23 ≤ h ≤ 23, −21 ≤ k ≤ 22, −21 ≤ l ≤ 21
Reflections collected	20518	52603
Independent reflections	10939 [R_{int} = 0.0219, R_{sigma} = 0.0228]	11789 [R_{int} = 0.0737, R_{sigma} = 0.0589]
Data/restraints/parameters	10939/1/588	11789/1/584
Goodness-of-fit on F^2	1.014	0.969
Final *R* indexes [*I*>=2σ (*I*)]	R_1 = 0.0280, wR_2 = 0.0670	R_1 = 0.0340, wR_2 = 0.0700
Final *R* indexes [all data]	R_1 = 0.0307, wR_2 = 0.0679	R_1 = 0.0445, wR_2 = 0.0718
Largest diff. peak/hole/e Å^{-3}	0.45/−0.25	0.58/−0.21

References

1. O. V. Dolomanov, L. J. Bourhis, R. J. Gildea, J. A. K. Howard, H. Puschmann, OLEX2: A Complete Structure Solution, Re-finement and Analysis Program. *J. Appl. Crytallogr*. **2009**, *42*, 339–441.
2. G. M. Sheldrick, *Acta Cryst*. **2015**, *71*, 3–8.
3. L.Farrugia, J. Appl. *Crystallogr*., **1999**, *32*, 837–838.
4. P. W. Betteridge, J. R. Carruthers, R. I. Cooper, K. Prout, D. J. Watkin *J. Appl. Cryst*. **2003**, *36*, 1487.
5. International Tables for X-ray crystallography (Kynoch Press, Birmingham, England, **1974**) *Vol*. *IV*.
6. Bruker AXS Inc. SADABS, 2016/2; Bruker AXS Inc.: Madison, WI, USA, 2016.
7. Stoe & Cie. X-Area, X-Red 1.63.1.0, 2002; Stoe & Cie: Darmstadt, Germany, 2016.

8.2 Supporting Information zur Publikation „Reductive coupling of (Fluoro)-Pyridines by Quasi-Linear 3d-Metal(I) Silylamides of Cr –Co: A Tale of C–C bond formation, C–F bond cleavage and pyridyl radical anions"

Igor Müller und C. Gunnar Werncke, *Chem. Eu. J.* **2020**, *eingereichtes Manuskript*.

Reductive Coupling of (Fluoro)-Pyridines by Quasi-Linear 3d-Metal(I) Silylamides of Cr – Co: A Tale of C–C Bond Formation, C–F Bond Cleavage and Pyridyl Radical Anions

I. Müller and C. Gunnar Werncke[*,1]*

[1]Department of Chemistry, Philipps-University Marburg, Hans-Meerwein-Straße 4, 35043 Marburg, Germany; gunnar.werncke@chemie.uni-marburg.de, +49 6421 282 5627.

Table of Contents

1. General Considerations

All manipulations were carried out in a glovebox under a dry argon atmosphere, unless indicated otherwise. Used solvents were dried by continuous distillation over sodium metal for several days, degassed via three freeze-pump cycles and stored over molecular sieves 4 Å. Deuterated solvents were used as received, degassed via three freeze-pump cycles and stored over molecular sieves 4 Å. The ^{1}H-NMR spectra were recorded on a Bruker HD 250, Bruker AV 300 or a Bruker HD 500 NMR spectrometer (Bruker Corporation, Billerica, USA). Chemical shifts are reported in ppm relative to the residual proton signals of the solvent (for ^{1}H) or relative to the signal of the solvent itself (^{13}C). $w_{1/2}$ is the line width of a signal at half its maximum intensity. Integrals of the broad signals of the $N(SiMe_3)_2$ units were obtained directly or by peak fitting (in case of overlapping signals) using the MestreNova software package (Mestrelab, Santiago de Compostela, Spain). Solution magnetic susceptibilities were determined by the Evans method.[1,2] IR measurements were conducted on a Bruker Alpha ATR-IR spectrometer (Bruker Corporation, Billerica, USA). Elemental analyses were performed by the "in-house" service of the Chemistry Department of the Philipps University Marburg, Germany using a CHN(S) analyzer vario MICRO Cube (Elementar Analysensysteme GmbH, Langenselbold, Germany). UV/Vis-spectra were recorded on an AnalytikJena Specord S600 diode array spectrometer (AnalytikJena, Jena, Germany). $[M(N(SiMe_3)_2)_2]$ (Mn and Fe),[3,4] $[Cr(N(SiMe_3)_2)_2(thf)_2]$,[5], $[Co(N(SiMe_3)_2)_2(thf)]$,[3] $[K\{18c6\}[M(N(SiMe_3)_2)_2]$ (Fe and Co),[6,7] were prepared according to literature procedures. $K\{18c6\}[M(N(SiMe_3)_2)_2]$ (Cr and Mn) were synthesized *in situ* according the published procedure for $K\{18c6\}[Mn(N(SiMe_3)_2)_2]$ and used as such.[6]

2. Synthesis of Compounds

$[K\{18c6\}(py)_2]_2[(py)Cr(N(SiMe_3)_2)_2(py)]_2$ (1): $Cr(N(SiMe_3)_2)_2*(THF)_2$ (51.7 mg, 0.10 mmol, 1.0 eq) and 18-crown-6 (31.8 mg, 0.105 mmol, 1.05 eq) were dissolved in 3 mL of Et_2O. Addition of KC_8 (20.2 mg. 0.15 mmol, 1.5 eq) led to an immediate colour change to dark orangegreen. After stirring for 5 minutes, the mixture was filtered and the filtrate was given to pyridine (7.9 mg, 0.10 mmol, 1.0 eq), led to an immediate colour change to dark brown. The solution was stirring for 5 minutes and layered with 3 mL of pentane. Storing the solution at -35°C for days yielded a orange crystalline solid. The solution was removed via pipette, washing of the residue with 2x5 mL of pentane and drying it afforded **1** as a orange crystalline solid (30.4 mg, 0.036 mmol, 36%). ^{1}H-NMR ([D8]THF, 300.1 MHz, 298 K, ppm): 37.70 (bs, 72H, $w_{½}$ = 829.9 Hz $Si(CH_3)_3$), No useful signal attribution possible; IR (ATR, cm^{-1}): ν = 2939 (m), 2889 (m), 1625 (m), 1599 (w), 1473 (w), 1454 (w), 1351 (m), 1284 (w), 1231 (s), 1204 (m), 1101 (vs), 1015 (s), 998 (s), 960 (s), 870 (m), 818 (m), 749 (vs), 711 (m), 661 (m), 658 (m), 617 (m), 607 (m), 530 (w), 429 (w); elemental analysis calc. ($C_{68}H_{140}Cr_2K_2N_4O_{12}Si_8$ 1668.78 g/mol) C 48.94 H 8.46 N 6.71; exp. C 48.63 H 8.48 N 6.54. μ_{eff} = 5.88 μ_B (Evans, [D8]THF + 1% TMS, 500.1 MHz, 298 K). $\mu_{S.O.}$ = 6.92 μ_B. Crystals, suitable for X-Ray diffraction analysis, were obtained from a pentane layered solution of **1** in Et_2O at -35°C.

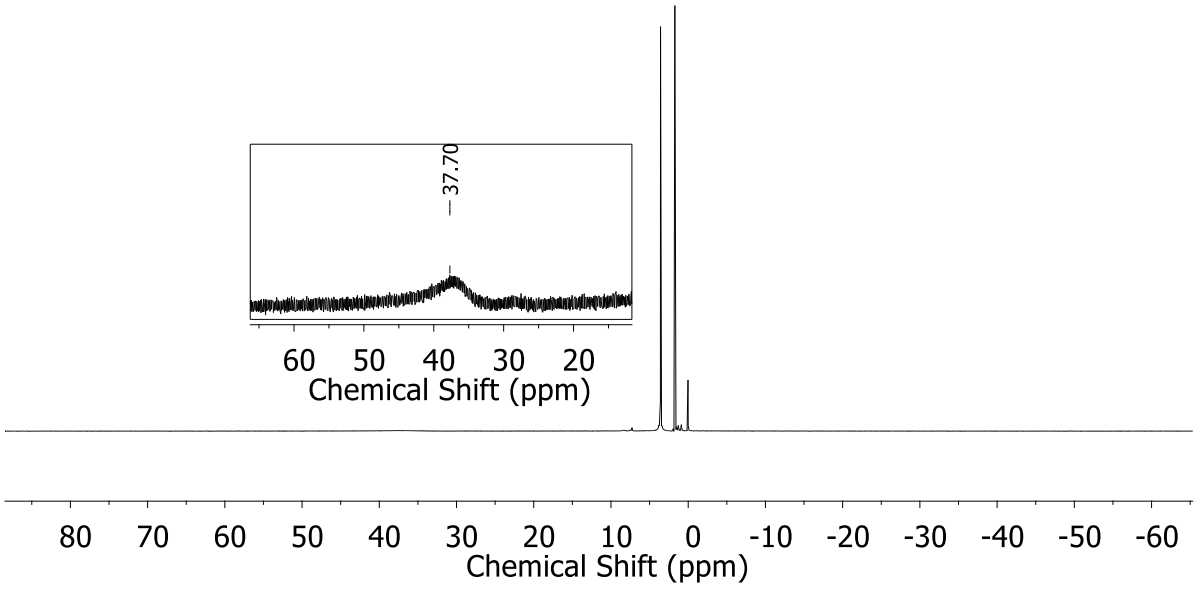

Figure S 1. ^{1}H NMR spectrum of **$[K\{18c6\}(py)_2]_2[(py)Cr(N(SiMe_3)_2)_2(py)]_2$** (**1**) in THF-$d_8$ (500.1 MHz).

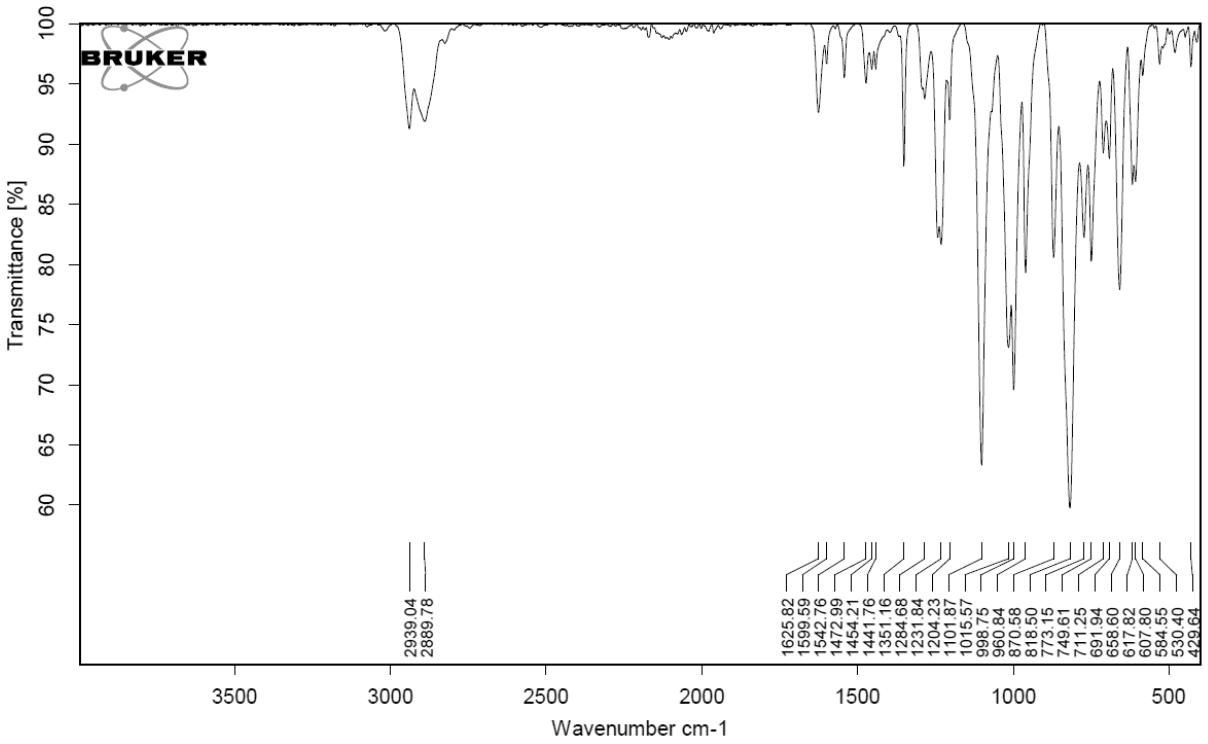

Figure S 2. IR spectrum of **[K{18c6}(py)$_2$]$_2$[(py)Cr(N(SiMe$_3$)$_2$)$_2$(py)]$_2$** (**1**).

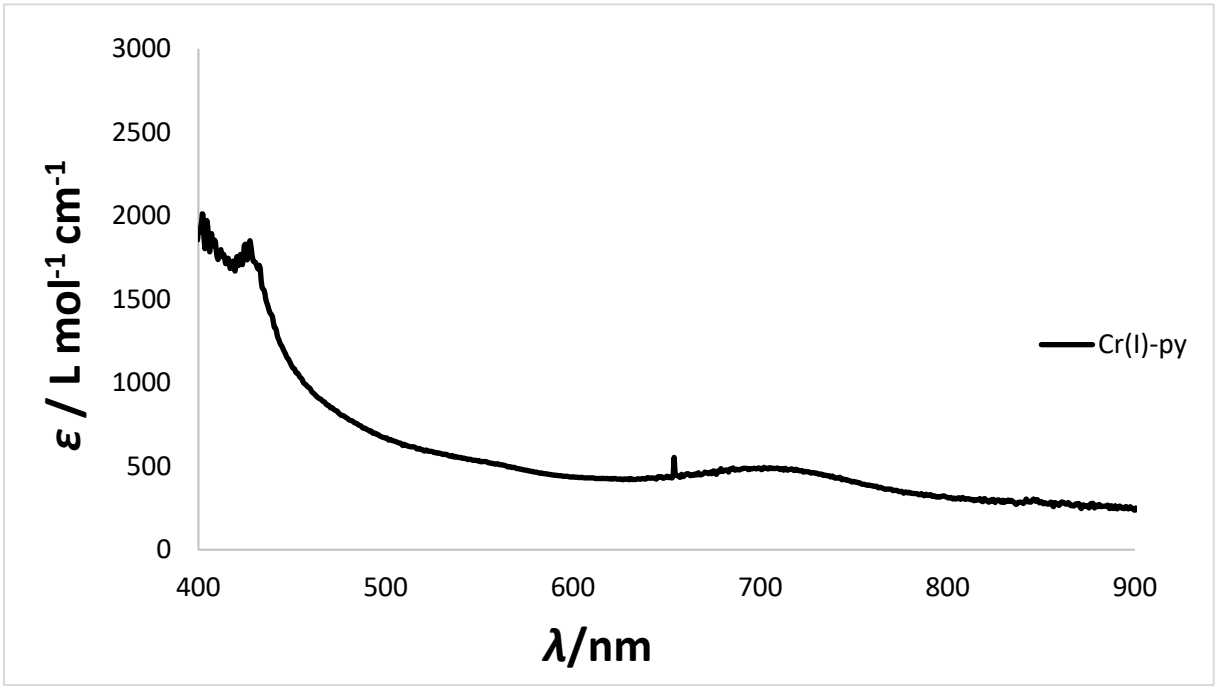

Figure S 3. UV/vis spectrum of **[K{18c6}(py)$_2$]$_2$[(py)Cr(N(SiMe$_3$)$_2$)$_2$(py)]$_2$** (**1**) in Et_2O.

[K{18c6}]$_2$[Mn(N(SiMe$_3$)$_2$)$_2$(py)]$_2$ (**2a**)**:** Mn(N(SiMe$_3$)$_2$)$_2$ (37.6 mg, 0.10 mmol, 1.0 eq) and 18-crown-6 (31.8 mg, 0.105 mmol, 1.05 eq) were dissolved in 3 mL of Et_2O. Addition of KC_8 (20.2 mg. 0.15 mmol, 1.5 eq) led to an immediate colour change to dark violet. After stirring for 5 minutes, the mixture was filtered and the filtrate was given to Pyridine (7.9 mg,

0.10 mmol, 1.0 eq), led to an immediate colour change to brown. The solution was stirring for 5 minutes and layered with 3 mL of pentane. Storing the solution at -35°C for days yielded a light yellow crystalline solid. The solution was removed via pipette, washing of the residue with 2x5 mL of pentane and drying it afforded **2a** as a light yellow crystalline solid. The yield **2a** and further analysis could not be determined due to contamination with the inseperable decomposition product [K{18c6}][Mn(N($SiMe_3$)$_2$)$_3$]. Crystals, suitable for X-Ray diffraction analysis, were obtained from a pentane layered solution of **2a** in Et_2O at -35°C.

[K{18c6}]$_2$[Mn(N($SiMe_3$)$_2$)$_2$(phpy)]$_2$ (2b): Mn(N($SiMe_3$)$_2$)$_2$ (37.6 mg, 0.10 mmol, 1.0 eq) and 18-crown-6 (31.8 mg, 0.105 mmol, 1.05 eq) were dissolved in 3 mL of Et_2O. Addition of KC_8 (20.2 mg. 0.15 mmol, 1.5 eq) led to an immediate colour change to dark violet. After stirring for 5 minutes, the mixture was filtered and the filtrate was given to 2-Phenylpyridine (15.5 mg, 0.10 mmol, 1.0 eq), led to an immediate colour change to dark blue. The solution was stirred for 5 minutes and layered with 3 mL of pentane. Storing the solution at -35°C for days yielded a greenish yellow crystalline solid. The solution was removed via pipette, washing of the residue with 2x5 mL of pentane and drying it afforded **2b** as a greenish yellow crystalline solid (37.1 mg, 0.044 mmol, 44%). ^{1}H-NMR ([D8]THF, 300.1 MHz, 298 K, ppm): No useful signal attribution possible; IR (ATR, cm^{-1}): ν = 2942 (m), 2893 (m), 1624 (m), 1594 (w), 1574 (w), 1557 (w), 1471 (w), 1452 (w), 1350 (m), 1283 (w), 1232 (s), 1106 (vs), 1057 (w), 1003 (vs), 961 (s),888 (m), 868 (m), 822 (vs), 774 (m), 746 (m), 701 (m), 661 (m), 608 (m),582 (m), 528 (w), 497 (w), 417 (w); elemental analysis calc. ($C_{70}H_{138}Mn_2K_2N_4O_{12}Si_8$ 1668.66 g/mol) C 50.39 H 8.34 N 5.04; exp. C 48.49 H 8.61 N 4.62. No matching C value could be obtained, even when using crushed, freshly prepared crystals; an approx. 3.5% lower value was always observed (>4 tries), an observation already made for other manganese silylamides.[6] μ_{eff} = 7.33 μ_B (Evans, [D8]THF + 1% TMS, 500.1 MHz, 298 K). $\mu_{S.O.}$ = 8.37 μ_B (for two non-coupling S = 5/2 ions). Crystals, suitable for X-Ray diffraction analysis, were obtained from a pentane layered solution of **2b** in Et_2O at -35°C.

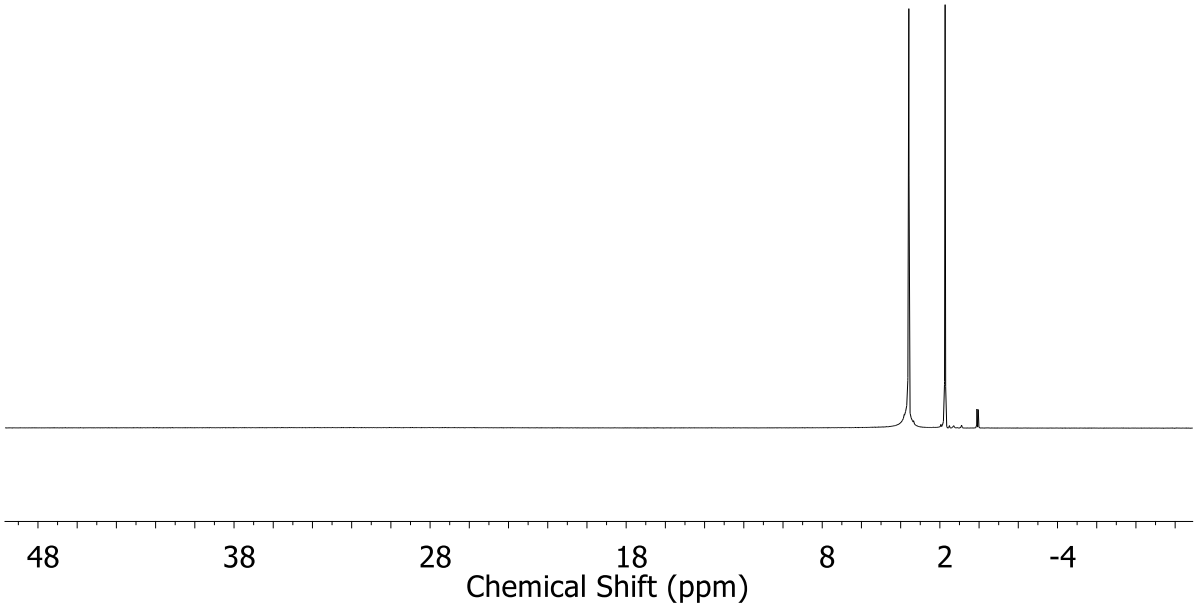

Figure S 4. ^{1}H NMR spectrum of **[K{18c6}]$_2$[Mn(N($SiMe_3$)$_2$)$_2$(phpy)]$_2$ (2b)** in THF-d_8 (500.1 MHz).

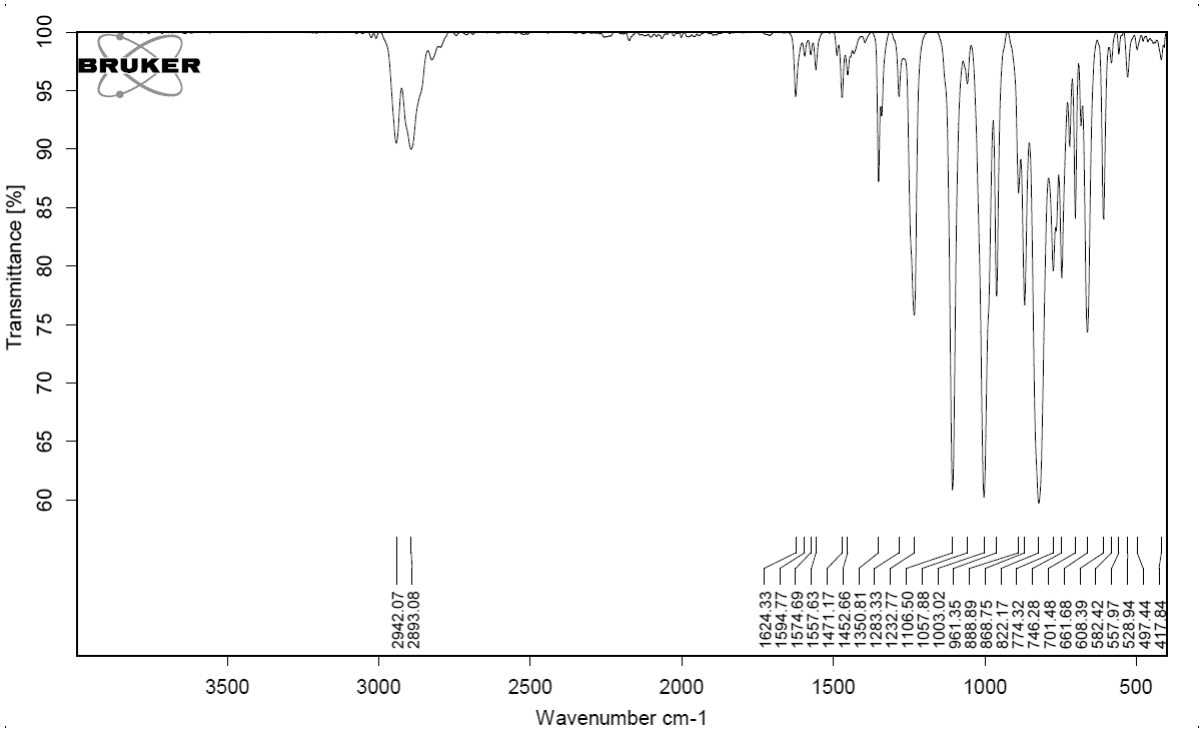

Figure S 5. IR spectrum of **[K{18c6}]$_2$[Mn(N(SiMe$_3$)$_2$)$_2$(phpy)]$_2$** (**2b**).

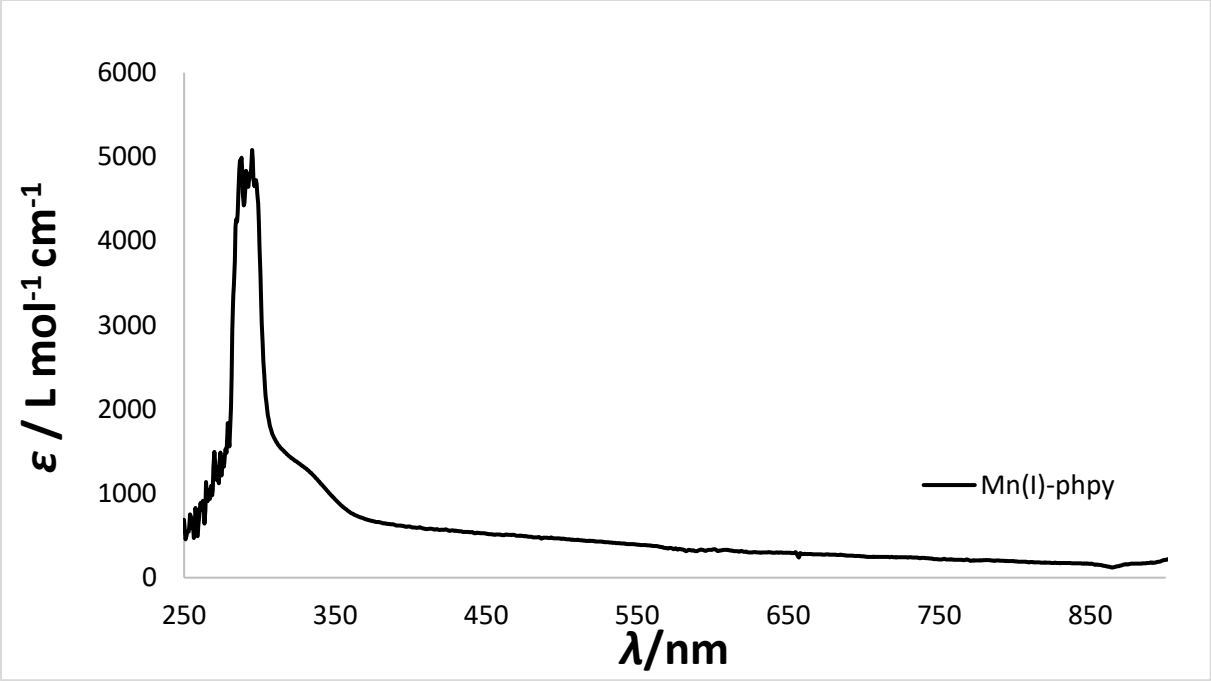

Figure S 6. UV/vis spectrum of **[K{18c6}]$_2$[Mn(N(SiMe$_3$)$_2$)$_2$(phpy)]$_2$** (**2b**) in Et_2O.

[K{18c6}]$_2$[Fe(N(SiMe$_3$)$_2$)$_2$(py)]$_2$ (**3a**)**:** [K{18c6}][Fe(N(SiMe$_3$)$_2$)$_2$] (68.0 mg, 0.10 mmol, 1.0 equiv.) and Pyridine (7.9 mg, 0.10 mmol, 1.0 eq) were dissolved in 3 mL of Et_2O and led to an immediate color change from brownish green to brown. After stirring for 5 minutes the

solution was layered with 3 mL of pentane. Storing the solution at −35°C for days yielded a light yellow crystalline solid. The solution was removed via a Pasteur pipette. Washing of the residue with 2x5 mL of pentane and drying it under reduced pressure afforded compound **3a** as a light yellow crystalline solid (21.6 mg, 0.028 mmol, 28%). ^{1}H-NMR ([D8]THF, 300.3 MHz, 298 K, ppm): δ = −4.50 (s, 72H, $w_{½}$ = 430 Hz, $Si(CH_3)_3$), 2.16 (s, 48H, $w_{½}$ = 140 Hz, OCH_2), No useful signal attribution possible; IR (ATR, cm^{-1}): ν = 2943 (m), 2891 (m), 1633 (m), 1562 (w), 1470 (w), 1452 (w), 1413 (m), 1350 (m), 1284 (w), 1246 (w), 1232 (s), 1204 (w), 1106 (vs), 1056 (w), 990 (vs), 960 (s),888 (m), 866 (m), 823 (vs), 780 (m), 747 (m), 722 (m), 663 (m), 624 (s), 609 (m), 589 (m), 527 (w), 409 (w); elemental analysis calc. ($C_{58}H_{130}Fe_2K_2N_6O_{12}Si_8$ + Et_2O/Pentane 1518.27 g/mol) C 48.35 H 9.20 N 5.05; exp. C 48.19 H 9.01 N 4.79. μ_{eff} = 7.35 μ_B (Evans, [D8]THF + 1% TMS, 500.1 MHz, 300 K). $\mu_{S.O.}$ = 6.93 μ_B (for two non-coupling S = 2 ions). Crystals, suitable for X-Ray diffraction analysis, were obtained from a pentane layered solution of compound **3a** in Et_2O at −35°C.

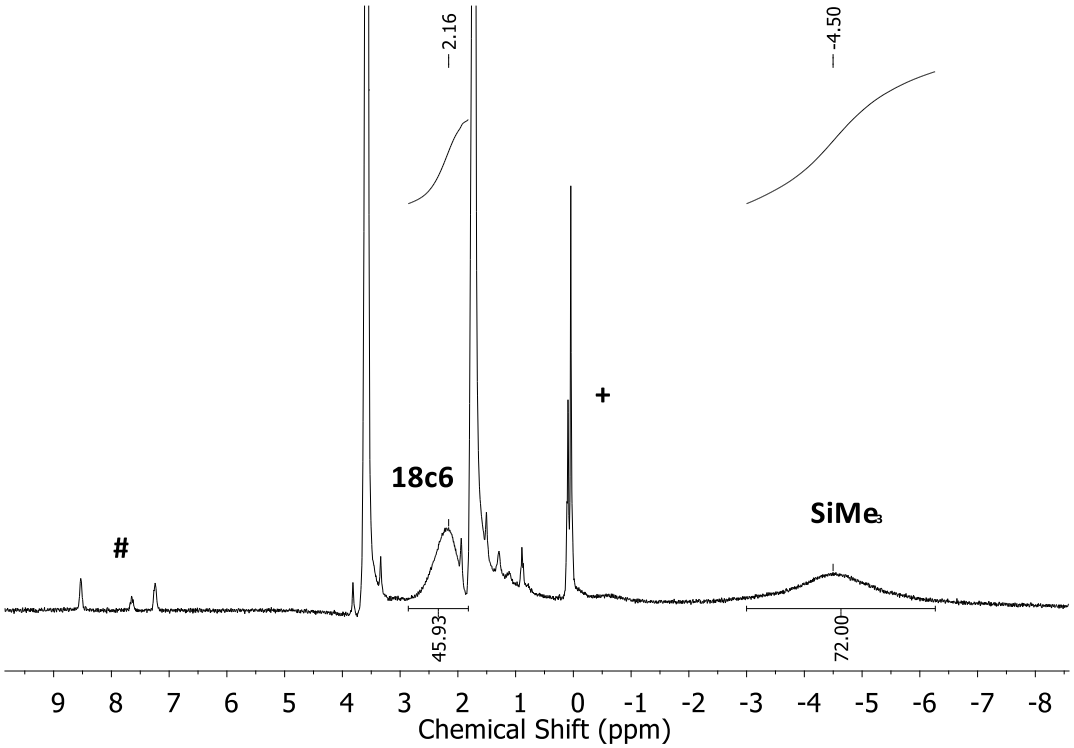

Figure S 7. ^{1}H NMR spectrum of **$[K\{18c6\}]_2[Fe(N(SiMe_3)_2)_2(py)]_2$** (**3a**) in THF-$d_8$ (500.1 MHz). # denotes free pyridine. + decomposition.

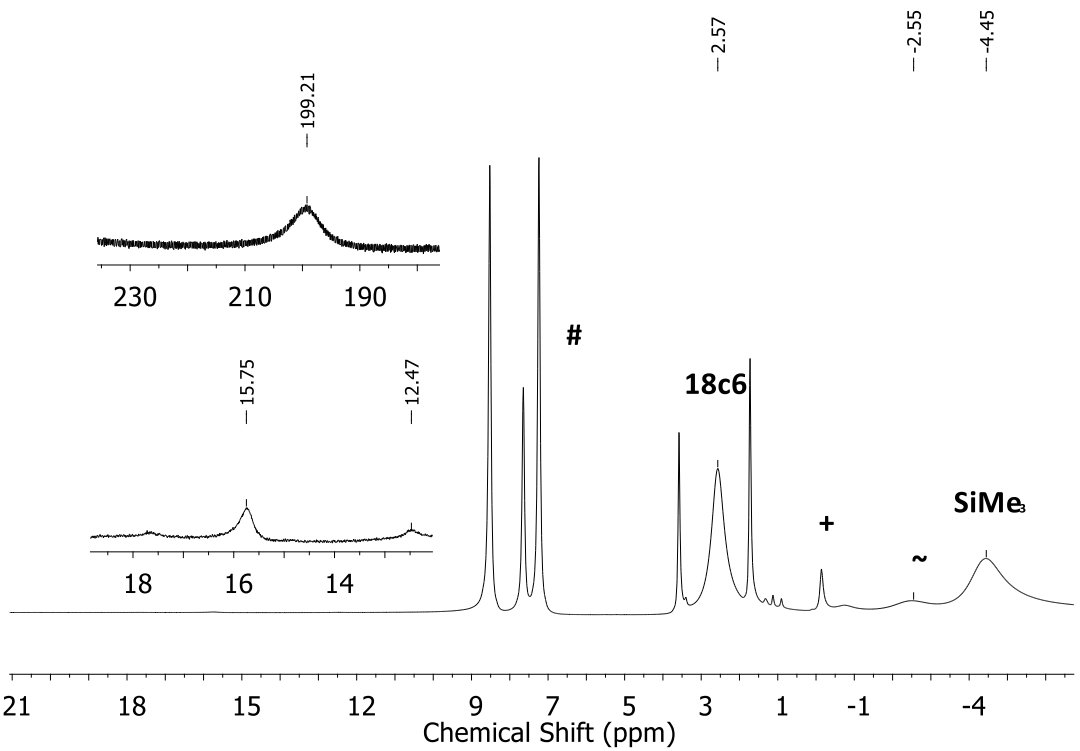

Figure S 8. ^{1}H NMR spectrum of the *in-situ* reaction of [K{18c6}][Fe(N(SiMe$_3$)$_2$)$_2$] (1.0 eq) and pyridine (5.0 eq) in THF-d$_8$ (500.1 MHz). # denotes free pyridine. + decomposition. ~ [Fe(N(SiMe$_3$)$_2$)$_3$]$^-$.

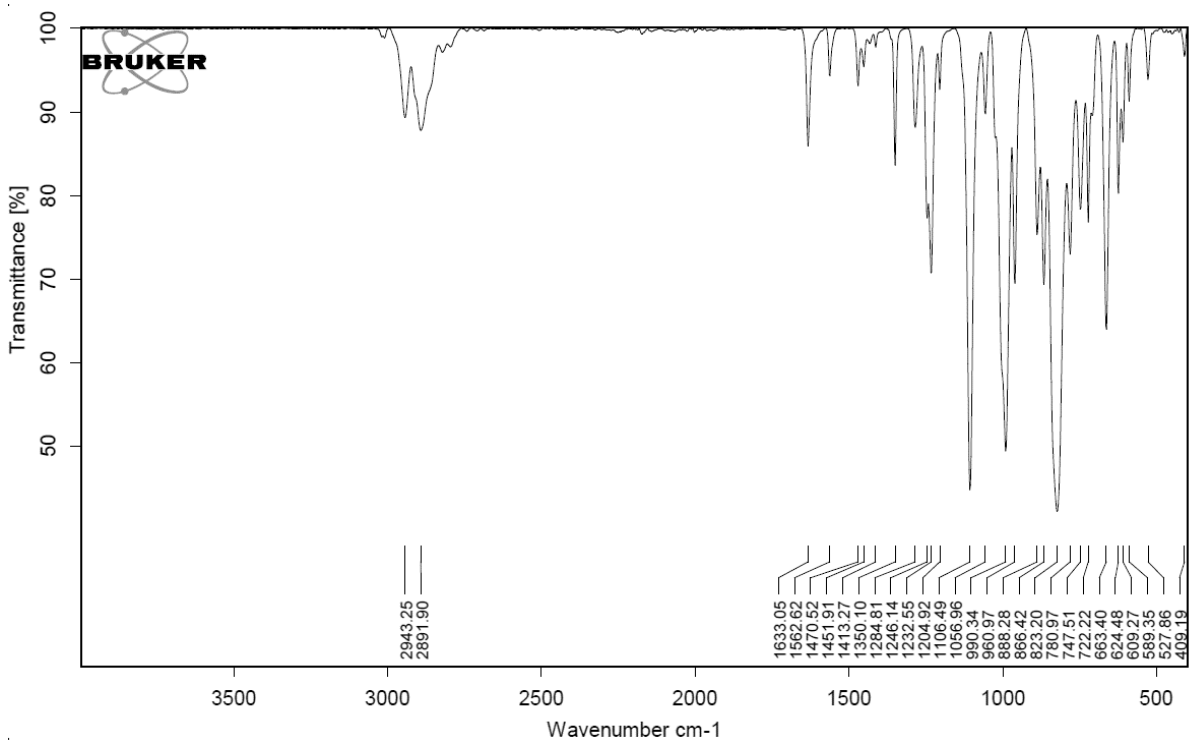

Figure S 9. IR spectrum of **[K{18c6}]$_2$[Fe(N(SiMe$_3$)$_2$)$_2$(py)]$_2$** (**3a**).

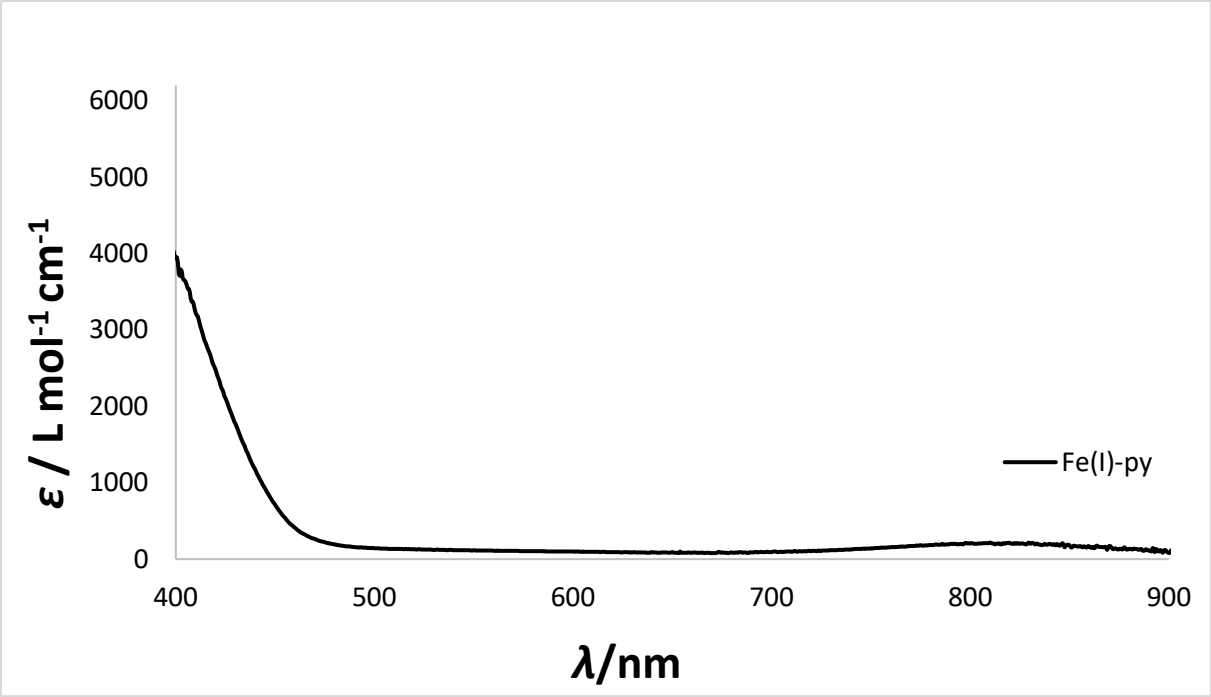

Figure S 10. UV/vis spectrum of **[K{18c6}]$_2$[Fe(N(SiMe$_3$)$_2$)$_2$(py)]$_2$** (**3a**) in Et_2O.

[K{18c6}]$_2$[Fe(N(SiMe$_3$)$_2$)$_2$(phpy)]$_2$ (**3b**)**:** [K{18c6}][Fe(N(SiMe$_3$)$_2$)$_2$] (68.0 mg, 0.10 mmol, 1.0 equiv.) and 2-phenylpyridine (15.5 mg, 0.10 mmol, 1.0 eq) were dissolved in 3 mL of Et_2O and led to an immediate color change from brownish green to brownish red. After stirring for 5 minutes the solution was layered with 3 mL of pentane. Storing the solution at −35°C for days yielded a dark red crystalline solid. The solution was removed via a Pasteur pipette. Washing of the residue with 2x5 mL of pentane and drying it under reduced pressure afforded compound **3b** as a dark red crystalline solid (45.6 mg, 0.055 mmol, 55%). ^{1}H-NMR ([D8]THF, 500.1 MHz, 298 K, ppm): No useful signal attribution possible due to equilibrium with the starting iron(I) compound; IR (ATR, cm^{-1}): ν = 2938 (m), 2888 (m), 1589 (m), 1482 (m), 1452 (m), 1350 (s), 1232 (s), 1101 (vs), 1004 (s), 959 (s), 868 (s), 817 (vs), 772 (s), 747 (s), 694 (s), 640 (s), 606 (s), 528 (m); elemental analysis calc. ($C_{70}H_{138}Fe_2K_2N_6O_{12}Si_8$ 1670.47 g/mol) C 50.39 H 8.07 N 5.04; exp. C 50.99 H 8.22 N 4.68. Crystals, suitable for X-Ray diffraction analysis, were obtained from a pentane layered solution of compound **3b** in Et_2O at −35°C.

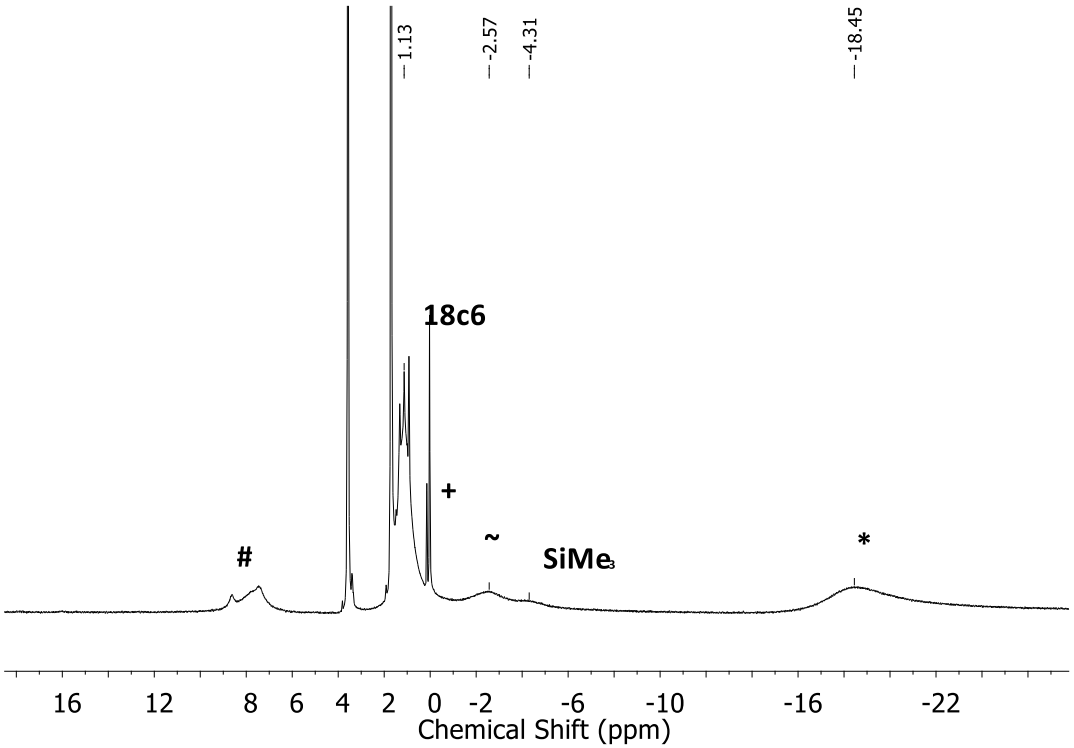

Figure S 11. ^{1}H NMR spectrum of **[K{18c6}]$_2$[Fe(N(SiMe$_3$)$_2$)$_2$(phpy)]$_2$** (**3b**) in THF-d$_8$ (500.1 MHz). # denotes free 2-phenylpyridine. + decomposition.*denotes free [Fe(N(SiMe$_3$)$_2$)$_2$]$^-$. ~[Fe(N(SiMe$_3$)$_2$)$_3$]$^-$.

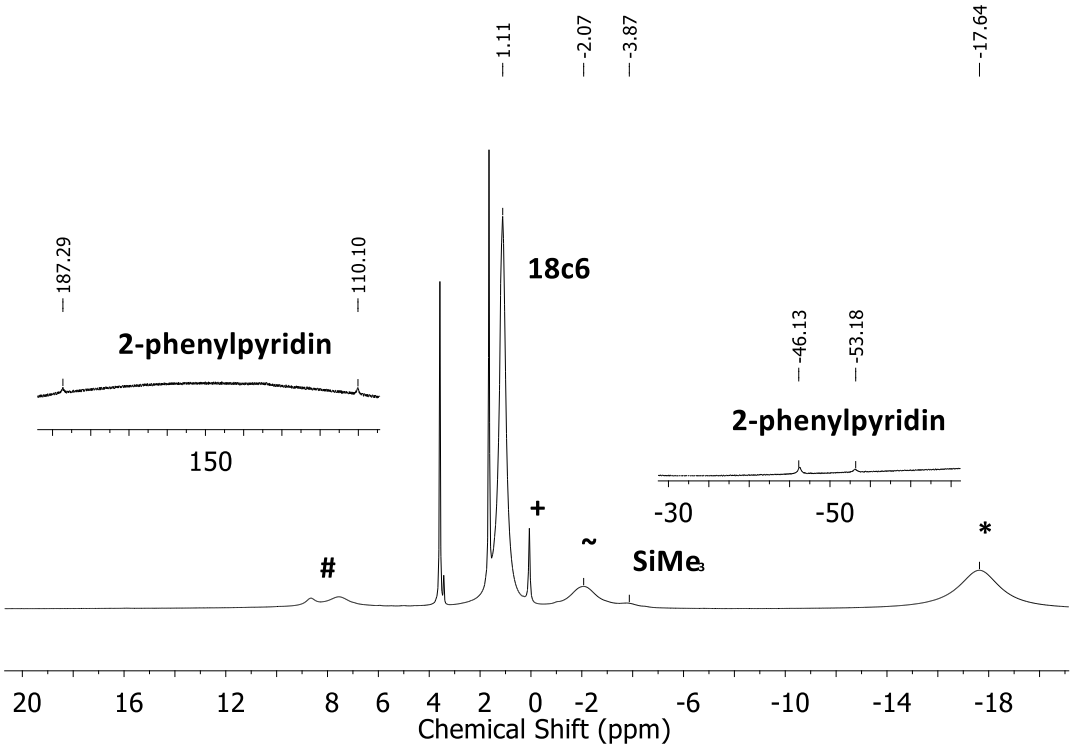

Figure S 12. ^{1}H NMR spectrum of the *in-situ* reaction of [K{18c6}][Fe(N(SiMe$_3$)$_2$)$_2$] (1.0 eq) and 2-phenylpyridine (0.5 eq) in THF-d$_8$ (500.1 MHz). # denotes free 2-phenylpyridine. + decomposition. * denotes free [Fe(N(SiMe$_3$)$_2$)$_2$]$^-$. ~ [Fe(N(SiMe$_3$)$_2$)$_3$]$^-$.

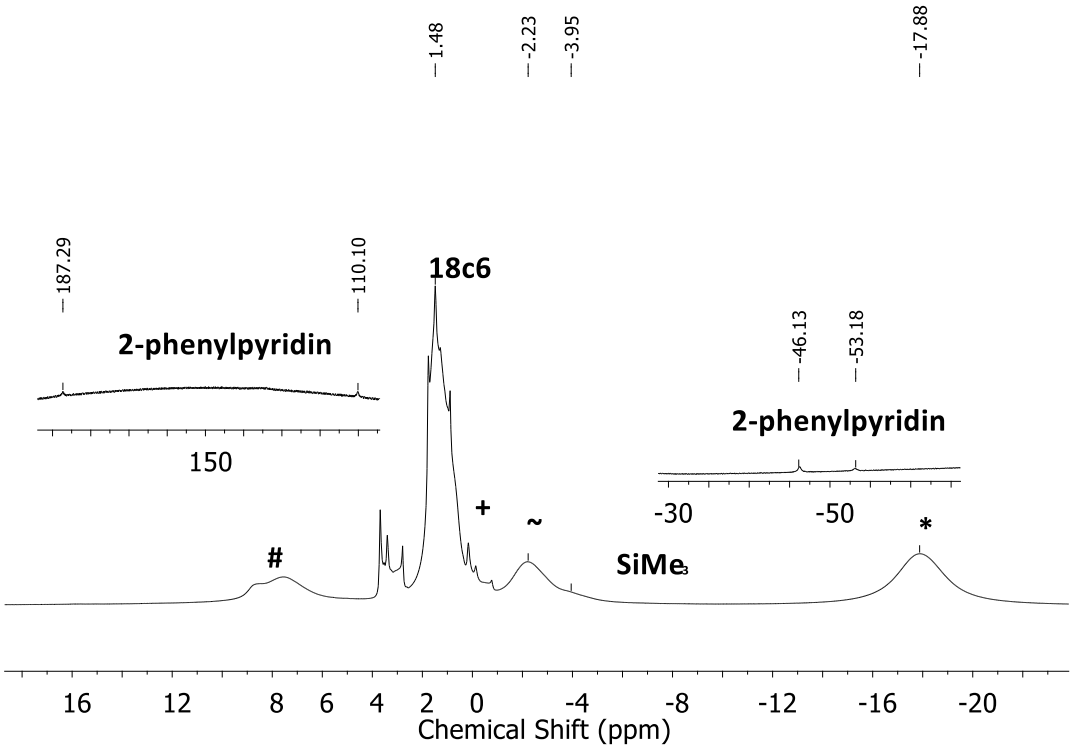

Figure S 13. ^{1}H NMR spectrum of the *in-situ* reaction of [K{18c6}][Fe(N(SiMe$_3$)$_2$)$_2$] (1.0 eq) and 2-phenylpyridine (1.0 eq) in THF-d$_8$ (500.1 MHz). # denotes free pyridine. + decomposition. * denotes free [Fe(N(SiMe$_3$)$_2$)$_2$]$^-$. ~ [Fe(N(SiMe$_3$)$_2$)$_3$]$^-$.

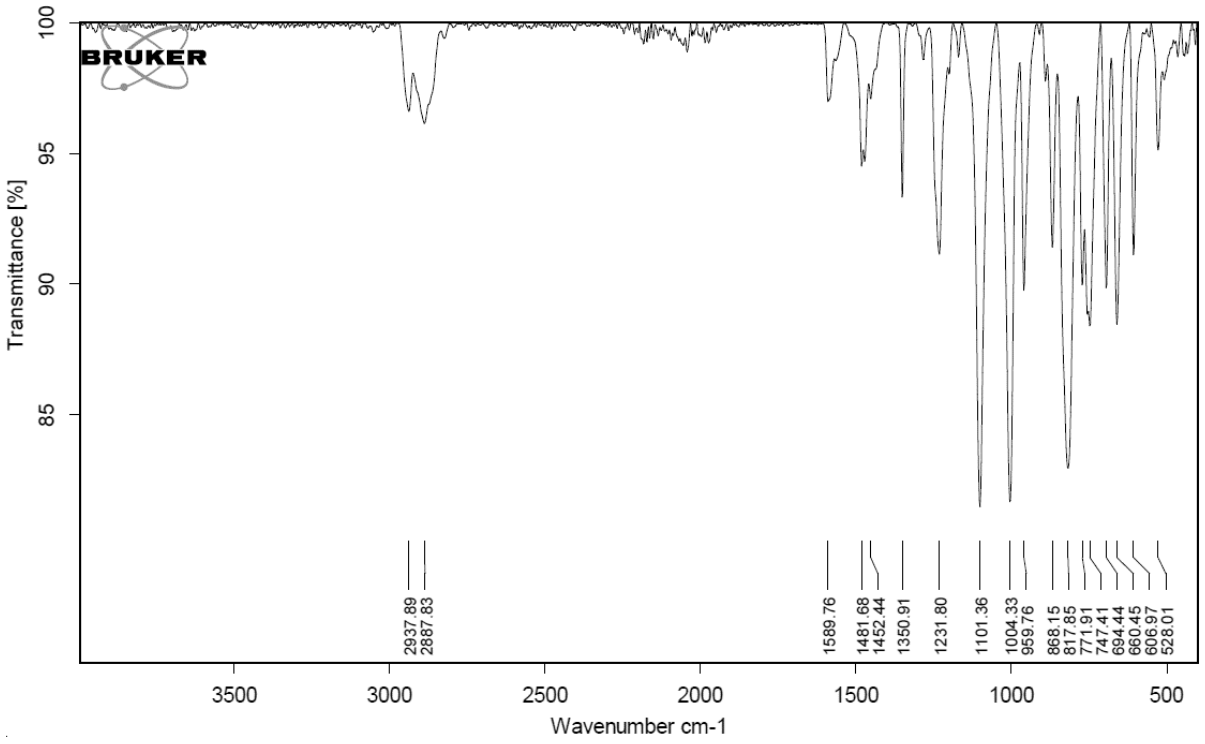

Figure S 14. IR spectrum of **[K{18c6}]$_2$[Fe(N(SiMe$_3$)$_2$)$_2$(phpy)]$_2$** (**3b**).

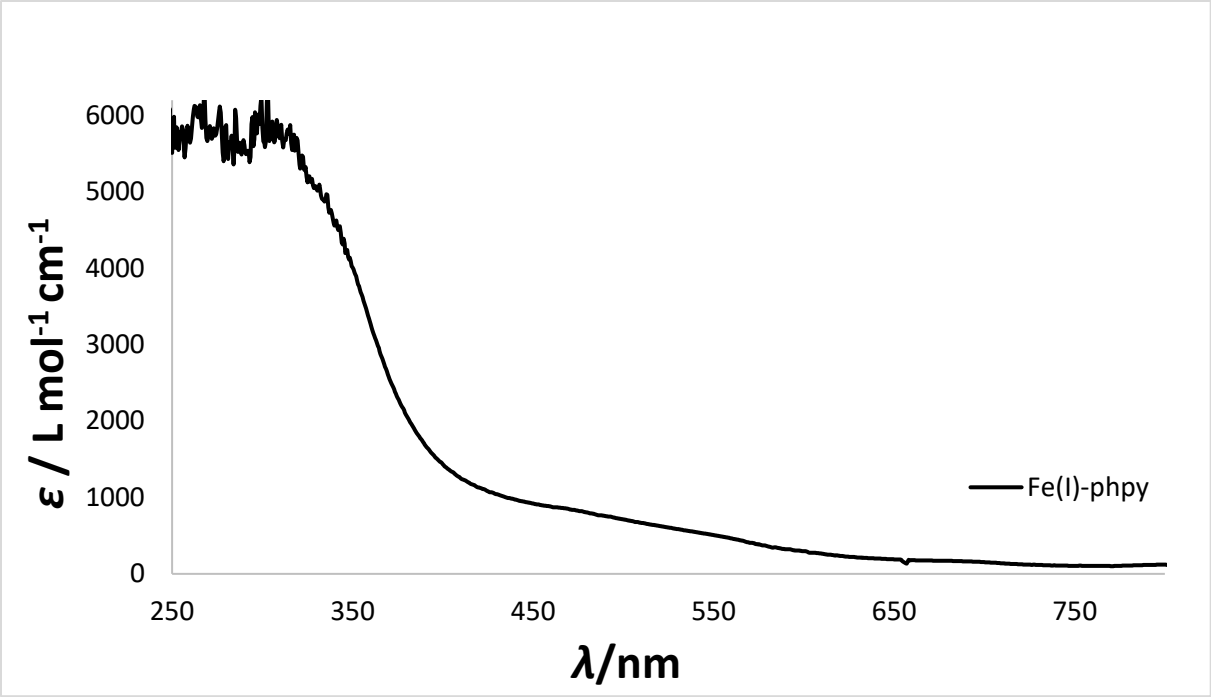

Figure S 15. UV/vis spectrum of **[K{18c6}]$_2$[Fe(N(SiMe$_3$)$_2$)$_2$(phpy)]$_2$** (**3b**) in Et_2O.

[K{18c6}]$_2$[Fe(N(SiMe$_3$)$_2$)$_2$(lut)]$_2$ (**3c**)**:** [K{18c6}][Fe(N(SiMe$_3$)$_2$)$_2$] (68.0 mg, 0.10 mmol, 1.0 equiv.) and 3,5-Lutidine (10.7 mg, 0.10 mmol, 1.0 eq) were dissolved in 3 mL of Et_2O and led to an immediate color change from brownish green to yellow. After stirring for 5 minutes the solution was layered with 3 mL of pentane. Storing the solution at −35°C for days yielded a yellowish green crystalline solid. The solution was removed via a Pasteur pipette. Washing of the residue with 2x5 mL of pentane and drying it under reduced pressure afforded compound **3c** as a yellowish green crystalline solid (46.6 mg, 0.059 mmol, 59%). ^{1}H-NMR ([D8]THF, 500.1 MHz, 298 K, ppm): No useful signal attribution possible due to equilibrium with the starting iron(I) compound; IR (ATR, cm^{-1}): ν = 2941 (m), 2889 (m), 1651 (w), 1597 (m), 1472 (m), 1453 (m), 1351 (s), 1283 (w), 1232 (s), 1103 (vs), 982 (vs), 960 (s), 888 (m), 865 (s), 821 (vs), 779 (s), 748 (s), 660 (m), 608 (m), 529 (w); elemental analysis calc. ($C_{68}H_{138}Fe_2K_2N_6O_{12}Si_8$ + Et_2O 1574.38 g/mol) C 48.15 H 8.94 N 5.10; exp. C 48.06 H 8.46 N 5.46. Crystals, suitable for X-Ray diffraction analysis, were obtained from a pentane layered solution of compound **3c** in Et_2O at −35°C.

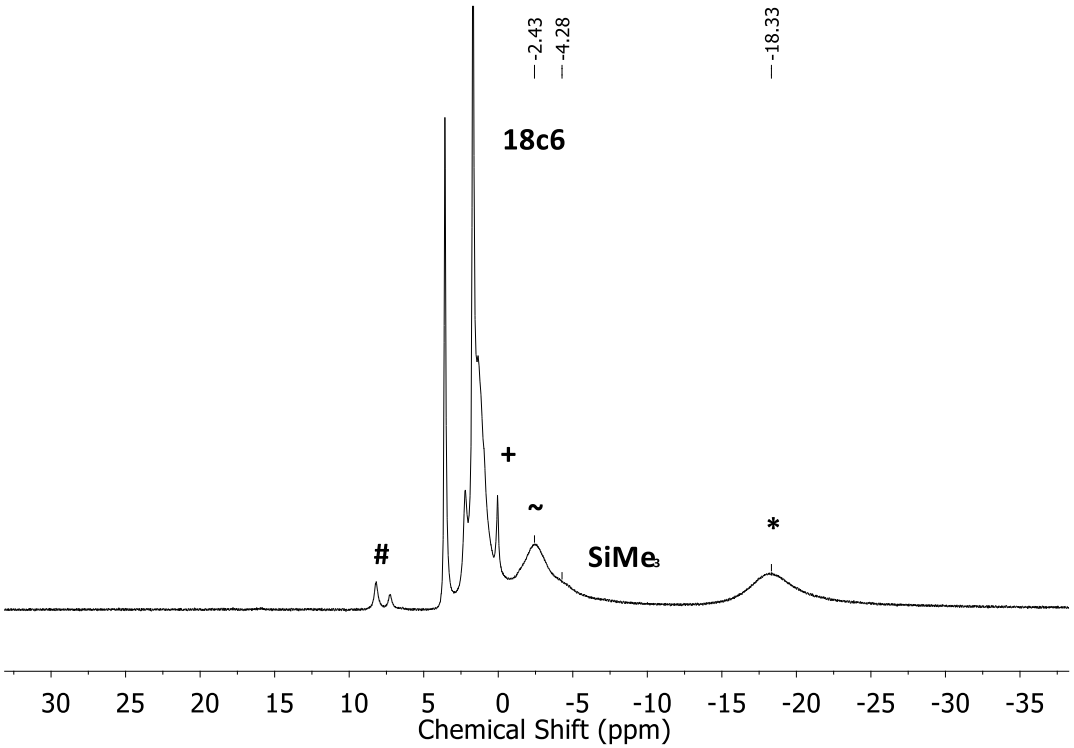

Figure S 16. ^{1}H NMR spectrum of **[K{18c6}]$_2$[Fe(N(SiMe$_3$)$_2$)$_2$(lut)]$_2$** (**3c**) in THF-d$_8$ (500.1 MHz). # denotes free 3,5-lutidine. + decomposition. * denotes free [Fe(N(SiMe$_3$)$_2$)$_2$]$^-$. ~ Decomposition product [Fe(N(SiMe$_3$)$_2$)$_3$]$^-$.

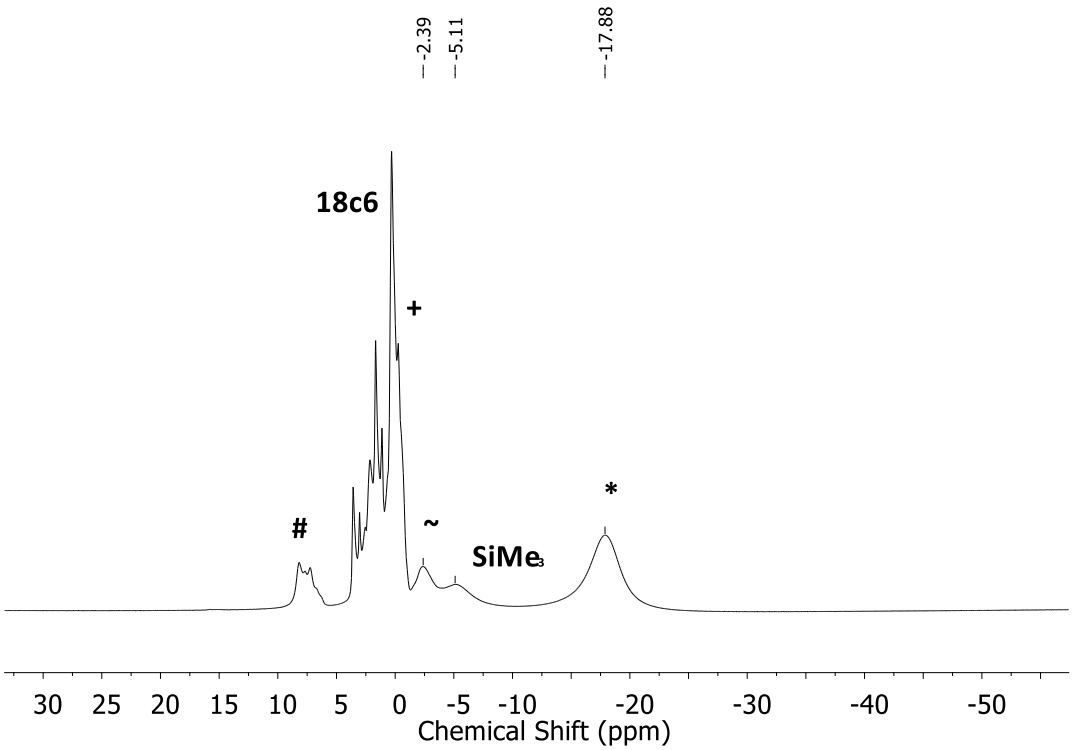

Figure S 17. ^{1}H NMR spectrum of the *in-situ* reaction of [K{18c6}][Fe(N(SiMe$_3$)$_2$)$_2$] (1.0 eq) and 3,5-lutidine (1.0 eq) in THF-d$_8$ (500.1 MHz). # denotes free pyridine. + decomposition. * denotes free [Fe(N(SiMe$_3$)$_2$)$_2$]$^-$. ~ Decomposition product [Fe(N(SiMe$_3$)$_2$)$_3$]$^-$.

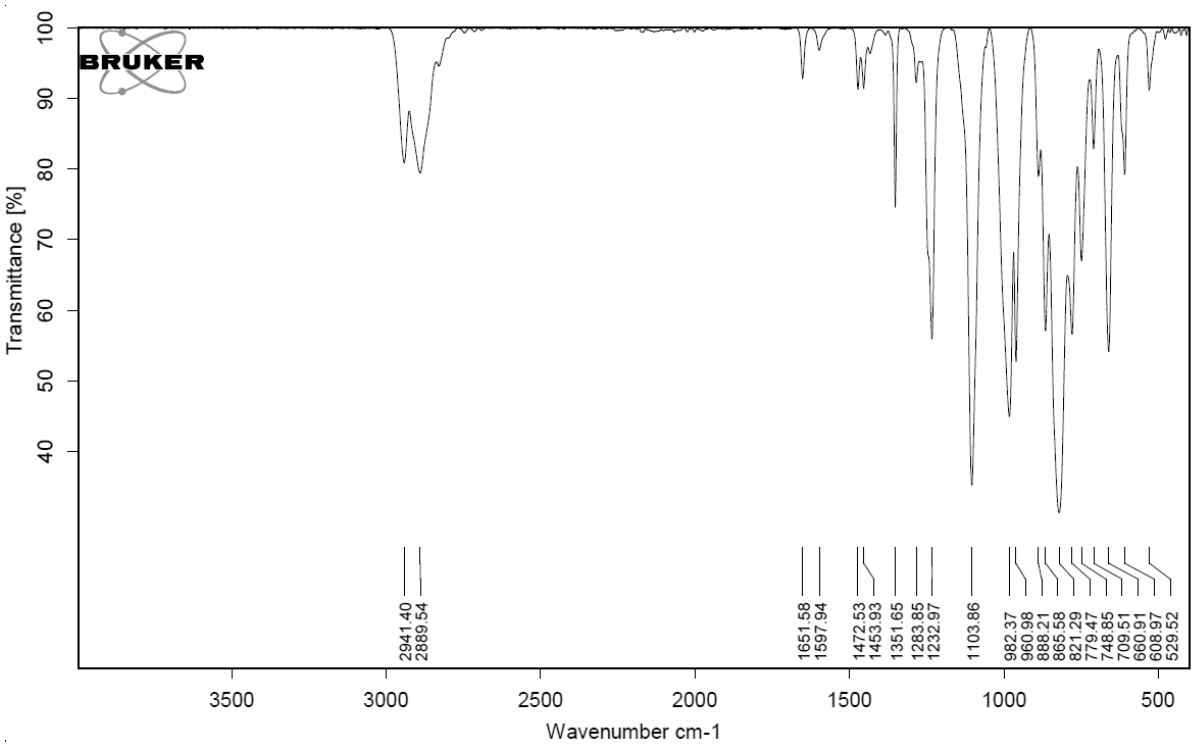

Figure S 18. IR spectrum of **[K{18c6}]$_2$[Fe(N(SiMe$_3$)$_2$)$_2$(lut)]$_2$** (**3c**).

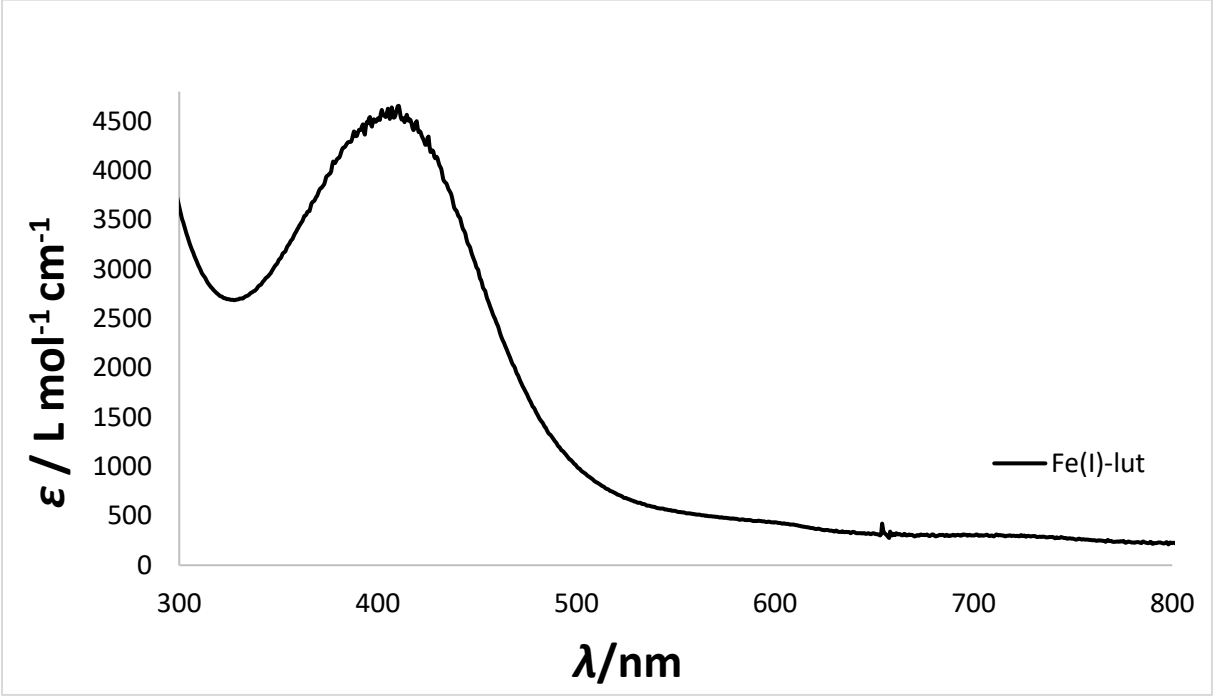

Figure S 19. UV/vis spectrum of **[K{18c6}]$_2$[Fe(N(SiMe$_3$)$_2$)$_2$(lut)]$_2$** (**3c**) in Et_2O.

[K{18c6}]$_2$[Mn(N(SiMe$_3$)$_2$)$_3$][Phpy] (**4**)**:** Mn(N(SiMe$_3$)$_2$)$_2$ (37.6 mg, 0.10 mmol, 1.0 eq) and 18-crown-6 (31.8 mg, 0.105 mmol, 1.05 eq) were dissolved in 3 mL of Et_2O. Addition of KC_8 (20.2 mg. 0.15 mmol, 1.5 eq) led to an immediate colour change to dark violet. After stirring for 5 minutes, the mixture was filtered and the filtrate was given to 2-Phenylpyridine (15.5 mg,

0.10 mmol, 1.0 eq), led to an immediate colour change to dark blue. The solution was stirring for 5 minutes and layered with 3 mL of pentane. Storing the solution at -35°C for days yielded a dark blue crystalline solid. Determination of the yield of **4** and further analysis was not possible because of complex sensitivity and presence of the (decomposition) products [K{18c6}][Mn(N(SiMe$_3$)$_2$)$_3$]. Crystals, suitable for X-Ray diffraction analysis, were directly obtained from the reaction mixture. Crystals, suitable for X-Ray diffraction analysis, were obtained from a pentane layered solution of **4** in Et_2O at -35°C.

[K{18c6}]$_2$[Mn(N(SiMe$_3$)$_2$)$_3$][phpy] (4): [K{18c6}][Mn(N(SiMe$_3$)$_2$)$_3$] (20.6 mg, 0.025 mmol, 1.0 eq), 18-crown-6 (6.6 mg, 0.025 mmol, 1.0 eq) and 2-phenylpyridine (3.8 mg, 0.025 mmol, 1.0 eq) were dissolved in 3 mL of Et_2O. Addition of KC_8 (4.1 mg. 0.025 mmol, 1.0 eq) led to an immediate colour change to dark blue. The mixture was filtered and the solution was layered with 3 mL of pentane. Storing the solution at -35°C for days yielded a pale brownish violet crystalline solid. Determination of the yield of **4** and further analysis was not possible because of complex sensitivity and presence of the (decomposition) products [K{18c6}][Mn(N(SiMe$_3$)$_2$)$_3$]. Crystals, suitable for X-Ray diffraction analysis, were directly obtained from the reaction mixture.

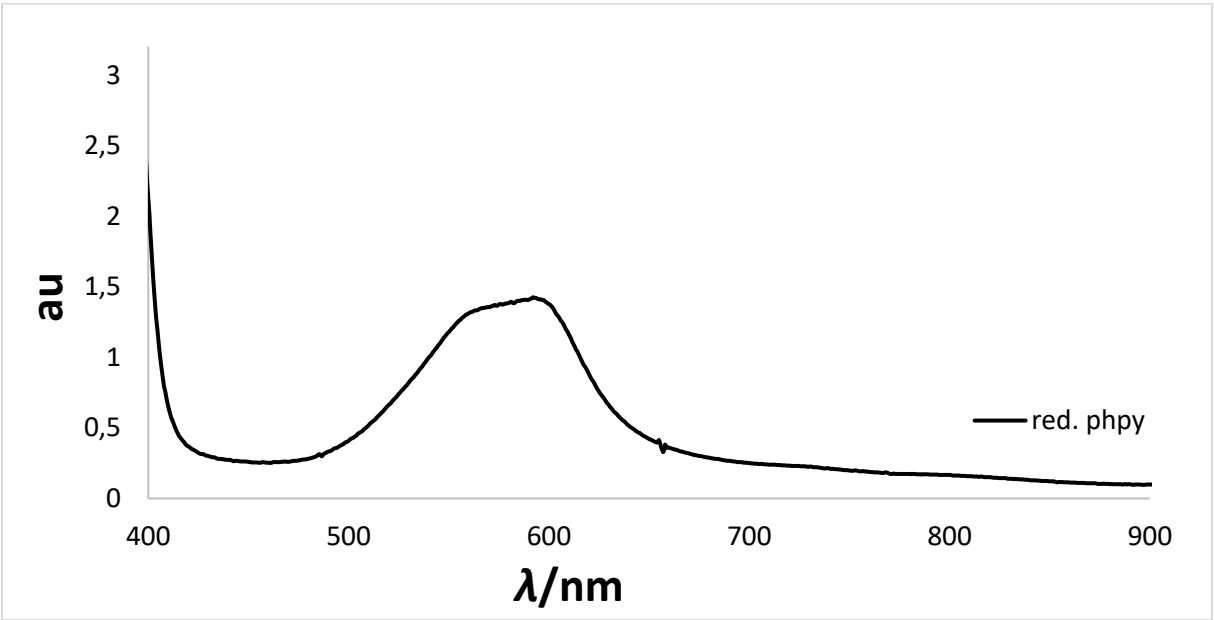

Figure S 20. UV/vis spectrum of the *in-situ* reaction of [K{18c6}][Mn(N(SiMe$_3$)$_2$)$_3$] (1.0 eq), KC_8 (1.0 eq), 18c6 (1.0) and 4-phenylpyridine (1.0 eq) in Et_2O.

[K{18c6}][Co(N(SiMe$_3$)$_2$)$_2$(F)] (5): [K{18c6}][Co(N(SiMe$_3$)$_2$)$_2$] (34.2 mg, 0.05 mmol, 1.0 equiv.) and Pentafluoropyridine (8.45 mg, 0.05 mmol, 1.0 eq) were dissolved in 3 mL of Et_2O and led to an immediate color change from light green to dark green. After stirring for 5 minutes the solution was layered with 3 mL of pentane. Storing the solution at −35°C for days yielded a

light green crystalline solid. The solution was removed via a Pasteur pipette. Washing of the residue with 2x5 mL of pentane and drying it under reduced pressure afforded compound **5** as a light green crystalline solid (31.3 mg, 0.045 mmol, 45%). Complex **5** was also obtained from the reaction with 2,3,5,6-Tetrafluoropyridine (7.55 mg, 0.05 mmol, 1.0 eq) and 2,3-Difluoropyridine (5.75 mg, 0.05 mmol, 1.0 eq). ^{1}H-NMR ([D8]THF, 300.3 MHz, 298 K, ppm): δ = -15.20 (s, 36H, $w_{½}$ = 48 Hz, $Si(CH_3)_3$), 9.71 (s, 24H, $w_{½}$ = 41 Hz, OCH_2); IR (ATR, cm^{-1}): ν = 2944 (m), 2905 (m),1601 (m), 1473 (w), 1453 (m), 1425 (w), 1343 (s), 1247 (m), 1234 (s), 1102 (vs), 1009 (s), 994 (s), 962 (s), 891 (m), 865 (vs), 823 (s), 780 (m), 749 (m), 718 (w), 703 (m), 662 (m), 620 (w), 609 (m), 529 (w), 495 (s), 410 (w); elemental analysis calc. ($C_{24}H_{60}CoKFN_2O_6Si_4$ 702.12 g/mol) C 41.06 H 8.61 N 3.99; exp. C 41.95 H 8.41 N 4.05. No matching C value could be obtained, even when using crushed, freshly prepared crystals; an approx. 1% lower value was always observed (>10 tries). μ_{eff} = 4.37 μ_B (Evans, [D8]THF + 1% TMS, 500.1 MHz, 300 K). $\mu_{S.O.}$ = 3.87 μ_B. Crystals, suitable for X-Ray diffraction analysis, were obtained from a pentane layered solution of compound **5** in Et_2O at −35°C.

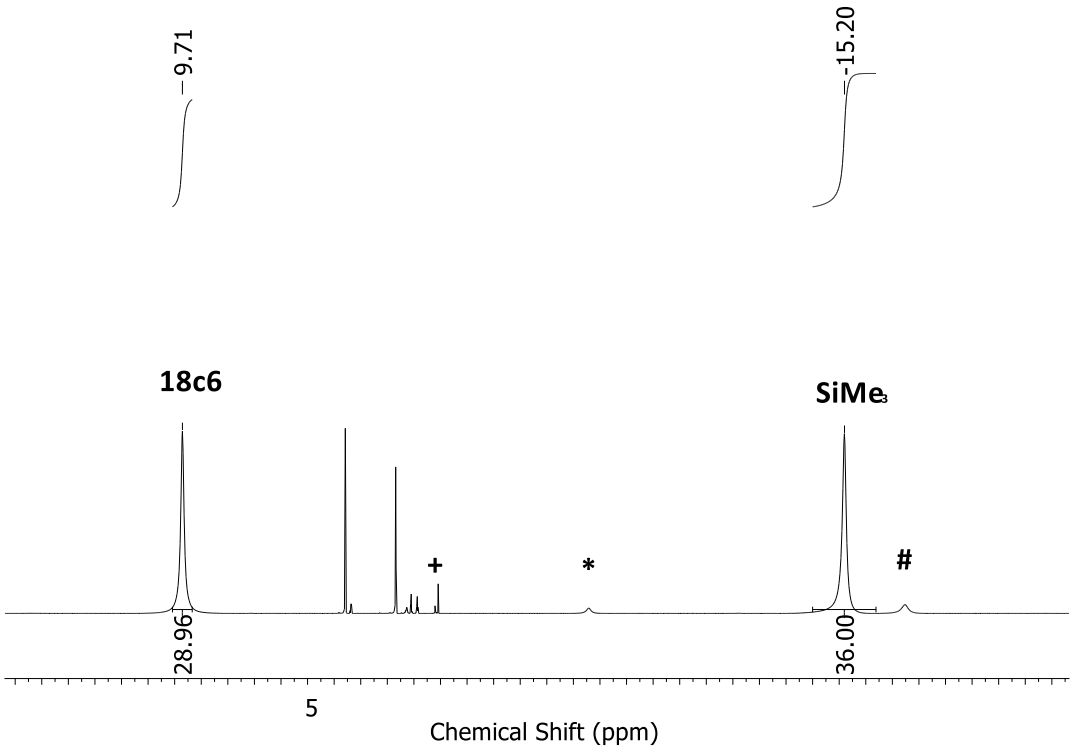

Figure S 21. ^{1}H NMR spectrum of **[K{18c6}][Co(N(SiMe$_3$)$_2$)$_2$(F)]** (**7**) in THF-d_8 (300.1 MHz). # $Co(N(SiMe_3)_2)_2$(thf). + decomposition. * denotes free $[Co(N(SiMe_3)_2)_2]^-$.

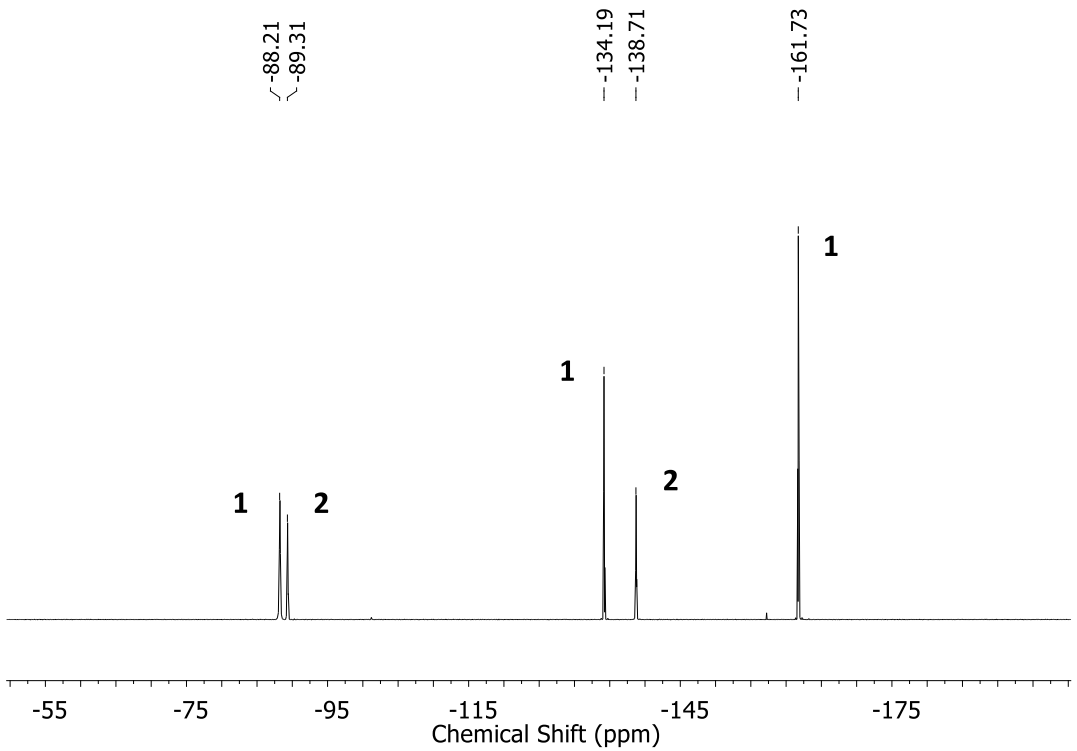

Figure S 22. ^{19}F NMR spectrum of the *in-situ* reaction of [K{18c6}][Co(N(SiMe$_3$)$_2$)$_2$] (1.0 eq) and pentafluoropyridine (1.0 eq) in THF-d$_8$ (300.1 MHz). 1 pentafluoropyridine. 2 perfluoro-4,4´bipyridine.

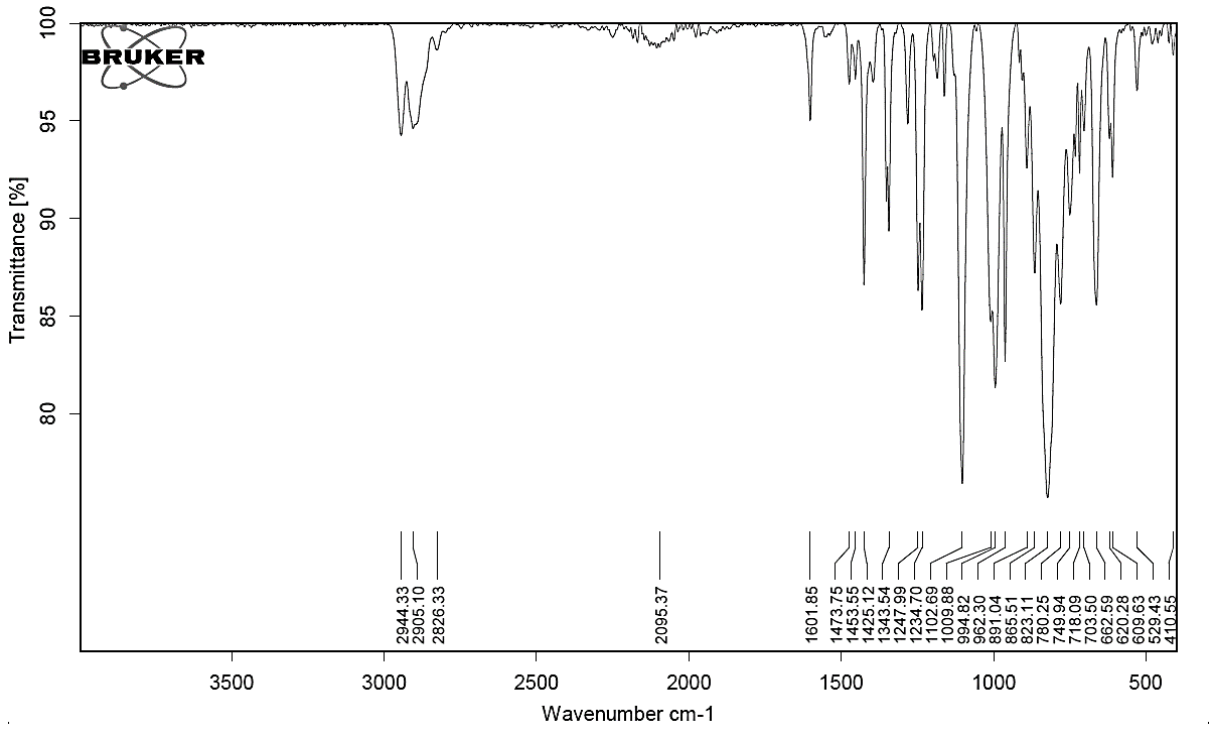

Figure S 23. IR spectrum of **[K{18c6}][Co(N(SiMe$_3$)$_2$)$_2$(F)]** (**5**).

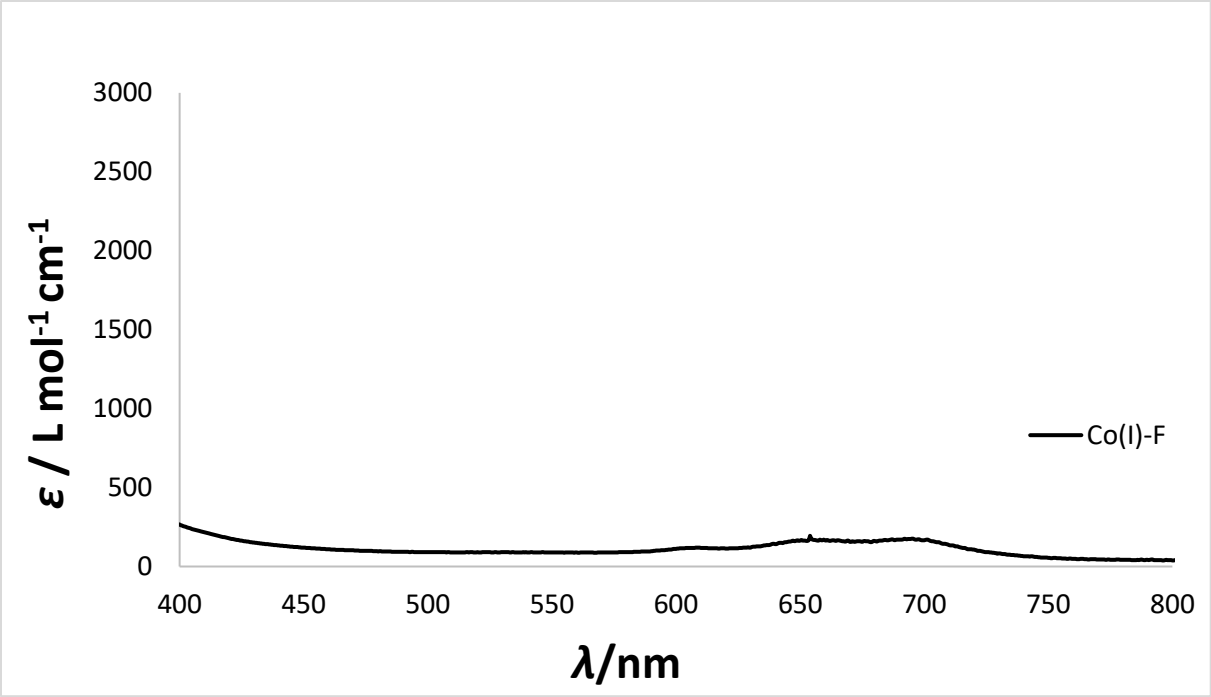

Figure S 24. UV/vis spectrum of **[K{18c6}][Co(N(SiMe$_3$)$_2$)$_2$(F)]** (**5**) in Et_2O.

[K{18c6}][Fe(N(SiMe$_3$)$_2$)$_2$(F)] (**6**)**:** [K{18c6}][Fe(N(SiMe$_3$)$_2$)$_2$] (68.0 mg, 0.10 mmol, 1.0 equiv.) and Pentafluoropyridine (16.9 mg, 0.10 mmol, 1.0 eq) were dissolved in 3 mL of Et_2O which led to an immediate color change from brownish green to dark yellow. After stirring for 5 minutes the solution was layered with 3 mL of pentane. Storing the solution at −35°C for days yielded a colorless crystalline solid. The solution was removed via a Pasteur pipette. Washing of the residue with 2x5 mL of pentane and drying it under reduced pressure afforded compound **6** as a colorless crystalline solid (49.3 mg, 0.071 mmol, 71%). Complex **6** was also obtained from the reaction with 2,3,5,6-Tetrafluoropyridine (15.1 mg, 0.10 mmol, 1.0 eq) and 2-Fluoropyridine (4.85 mg, 0.05 mmol, 1.0 eq). ^{1}H-NMR ([D8]THF, 300.3 MHz, 298 K, ppm): δ = -2.29 (bs, 36H, $w_{½}$ = 457 Hz, Si(CH_3)$_3$), 4.28 (s, 24H, $w_{½}$ = 216 Hz ,OCH_2); IR (ATR, cm^{-1}): ν = 2943 (m), 2887 (m), 1473 (w), 1452 (m), 1350 (s), 1282 (w), 1247 (m), 1234 (s), 1107 (vs), 1057 (w), 991 (w), 963 (s), 867 (s), 824 (vs), 781 (m), 752 (m), 708 (m), 665 (m), 622 (w), 528 (w), 495 (s), 409 (w); elemental analysis calc. ($C_{24}H_{60}FeFKN_2O_6Si_4$ 699.03 g/mol) C 41.24 H 8.65 N 4.01; exp. C 40.33 H 8.15 N 3.68. No matching C value could be obtained, even when using crushed, freshly prepared crystals; an approx. 1.0% lower value was always observed (>4 tries). μ_{eff} = 4.18 μ_B (Evans, [D8]THF + 1% TMS, 500.1 MHz, 300 K). $\mu_{S.O.}$ = 4.89 μ_B. Crystals, suitable for X-Ray diffraction analysis, were obtained from a pentane layered solution of compound **6** in Et_2O at −35°C. The crystal data is in line with the literature.[8]

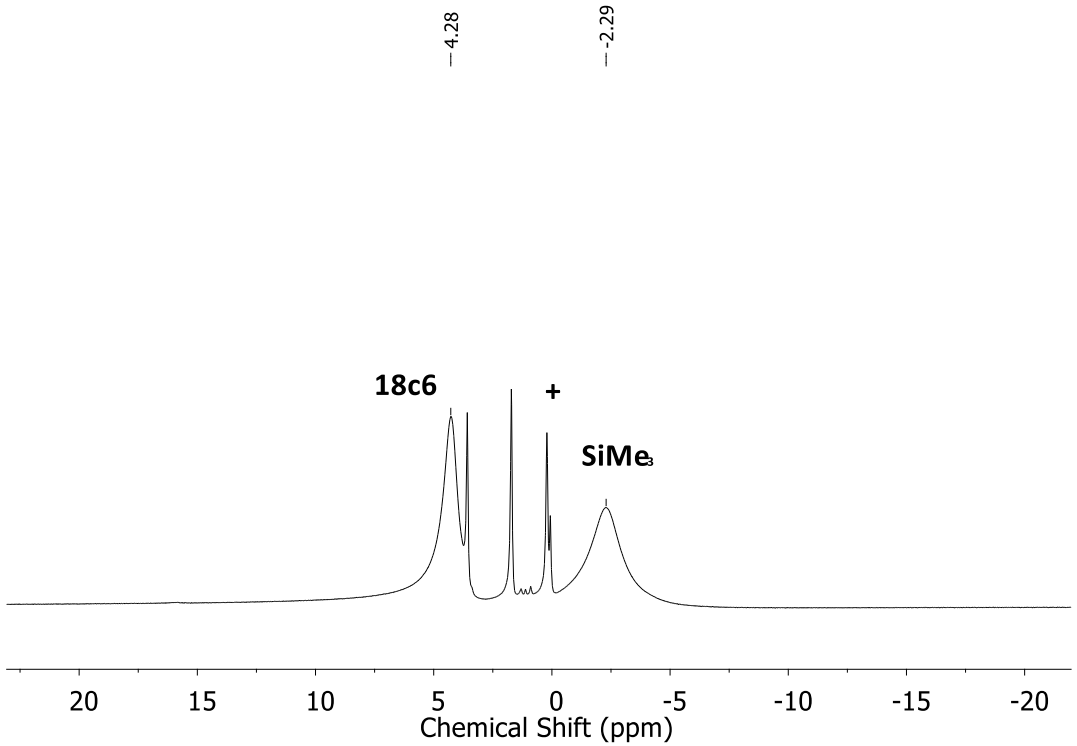

Figure S 25. ^{1}H NMR spectrum of **[K{18c6}][Fe(N(SiMe$_3$)$_2$)$_2$(F)]** (**6**) in THF-d$_8$ (500.1 MHz). + decomposition.

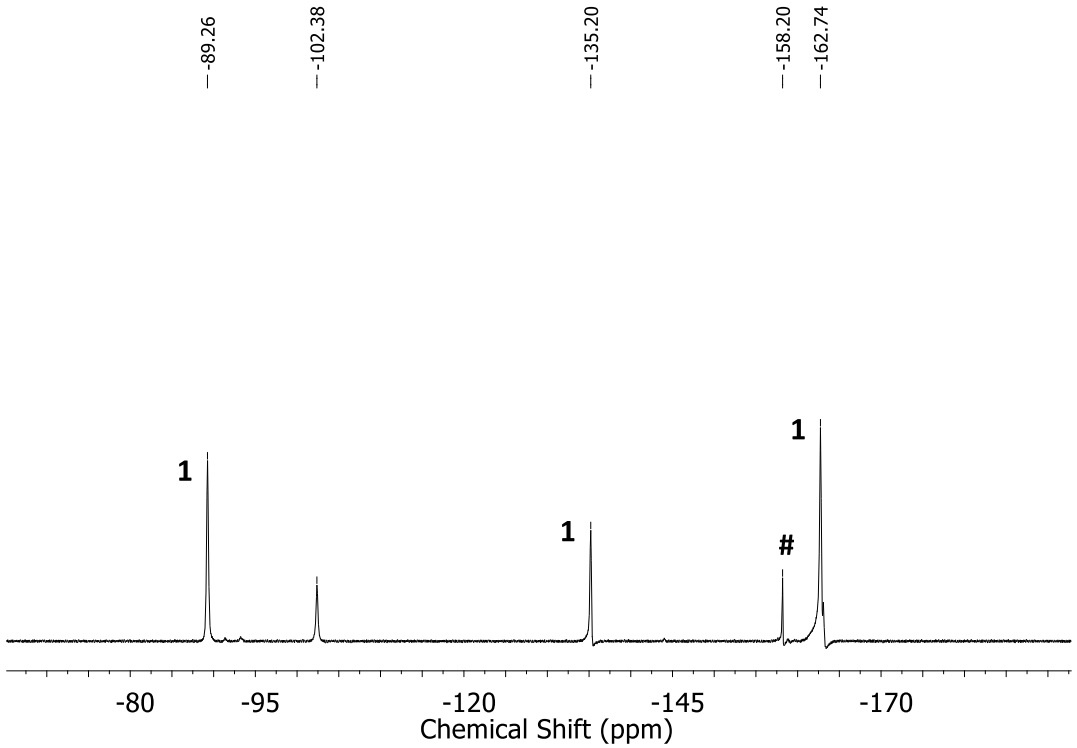

Figure S 26. ^{19}F NMR spectrum of the *in-situ* reaction of [K{18c6}][Fe(N(SiMe$_3$)$_2$)$_2$] (1.0 eq) and pentafluoropyridine (1.0 eq) in THF-d$_8$ (300.1 MHz). 1 pentafluoropyridine. # SiFMe$_3$.

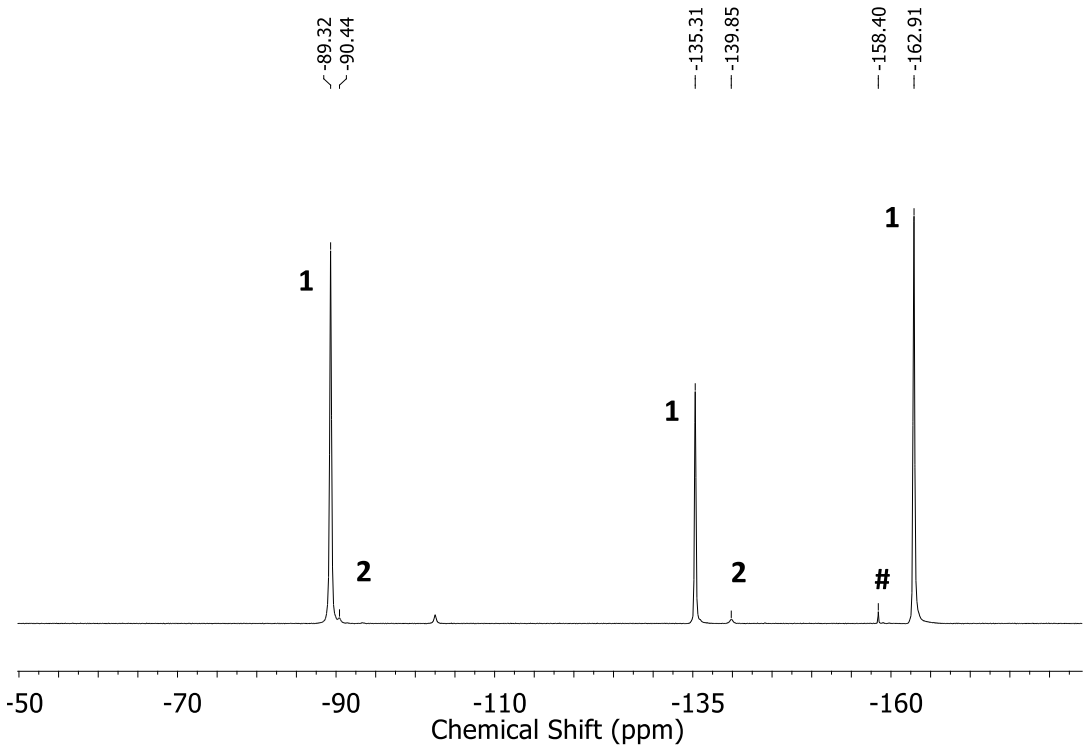

Figure S 27. ^{19}F NMR spectrum of the *in-situ* reaction of [K{18c6}][Fe(N(SiMe$_3$)$_2$)$_2$] (1.0 eq) and pentafluoropyridine (5.0 eq) in THF-d$_8$ (300.1 MHz). 1 pentafluoropyridine. 2 perfluoro-4,4´bipyridine. # SiFMe$_3$.

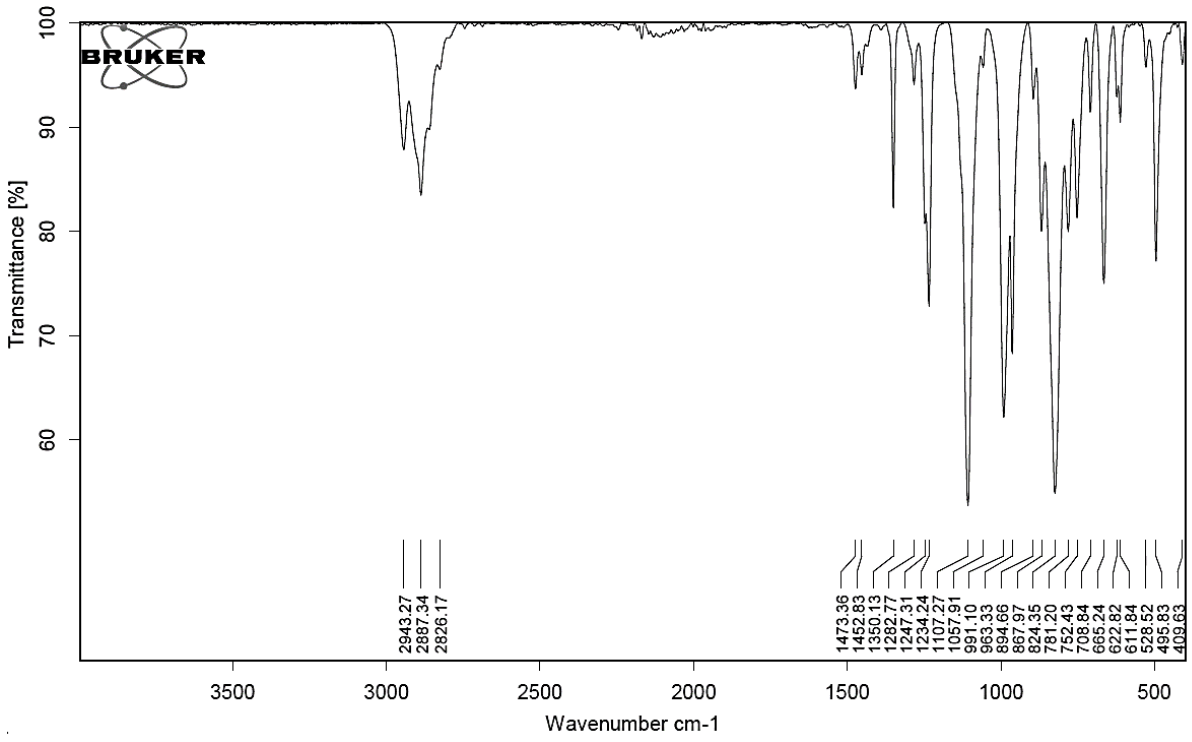

Figure S 28. IR spectrum of **[K{18c6}][Fe(N(SiMe$_3$)$_2$)$_2$(F)]** (**6**).

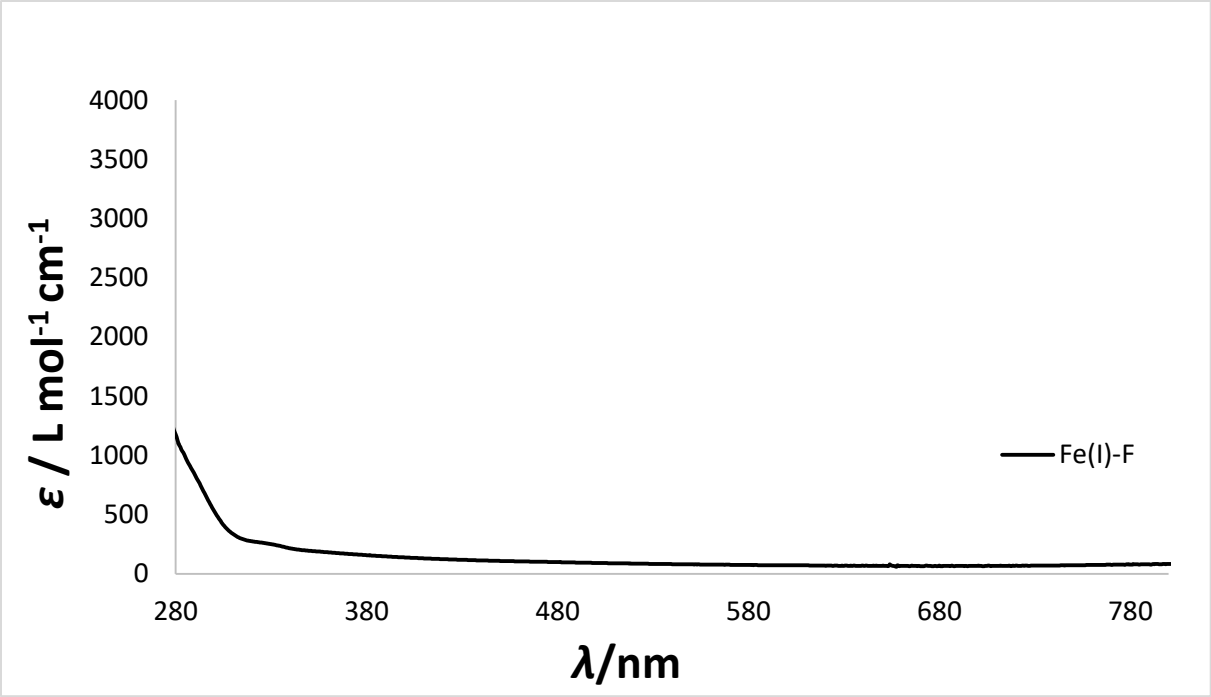

Figure S 29. UV/vis spectrum of **[K{18c6}][Fe(N(SiMe$_3$)$_2$)$_2$(F)]** (**6**) in Et_2O.

[K{18c6}][Mn(N(SiMe$_3$)$_2$)$_2$(F)] (**7**)**:** $Mn(N(SiMe_3)_2)_2$ (18.9 mg, 0.05 mmol, 1.0 eq) and 18-crown-6 (15.35 mg, 0.053 mmol, 1.05 eq) were dissolved in 3 mL of Et_2O. Addition of KC_8 (10.2 mg. 0.075 mmol, 1.5 eq) led to an immediate colour change to dark violet. After stirring for 5 minutes, the mixture was filtered and the filtrate was given to 2,3,5,6-Tetrafluoropyridine (7.55 mg, 0.05 mmol, 1.0 eq), led to an immediate colour change to brown. The solution was stirring for 5 minutes and layered with 3 mL of pentane. Storing the solution at -35°C for days yielded a colorless crystalline solid. The solution was removed via pipette, washing of the residue with 2x5 mL of pentane and drying it afforded **7** as a colorless crystalline solid. The yield **7** and further analysis could not be determined due to contamination with the decomposition product [K{18c6}][Mn(N(SiMe$_3$)$_2$)$_3$]. Crystals, suitable for X-Ray diffraction analysis, were obtained from a pentane layered solution of **7** in Et_2O at -35°C.

3. *In-situ* NMR Spectra of reactivity studies

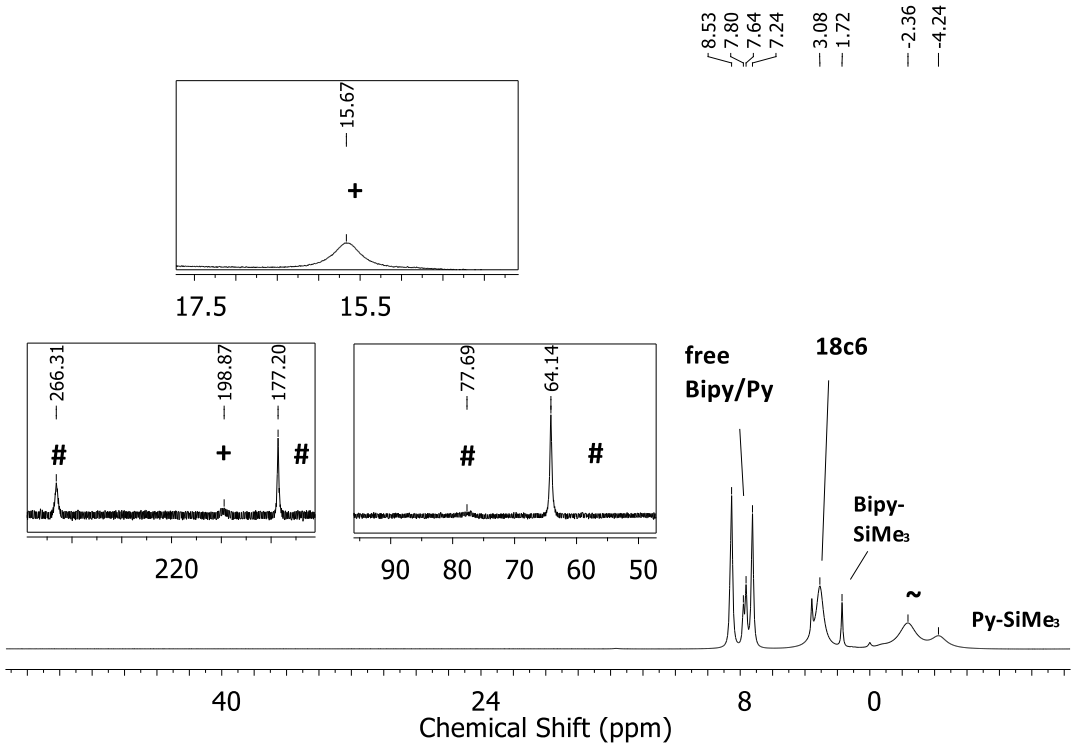

Figure S 30. ^{1}H NMR spectrum of the *in-situ* reaction of **[K{18c6}]$_2$[Fe(N(SiMe$_3$)$_2$)$_2$(py)]$_2$** (**3a**) (1.0 eq) and 2,2´bipyridine (1.0 eq) in THF-d$_8$ (500.1 MHz). ~ [Fe(N(SiMe$_3$)$_2$)$_3$]$^-$.# bipyridine complex.[9] + **3a**.

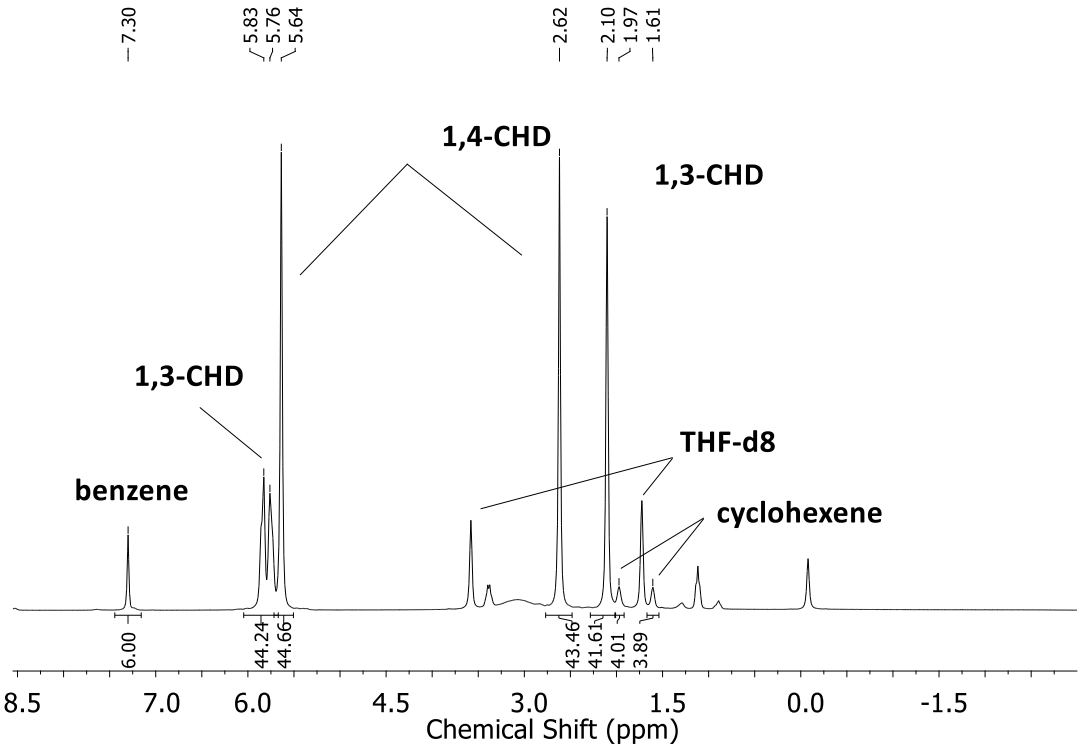

Figure S 31. ^{1}H NMR spectrum of the *in-situ* reaction of **[K{18c6}]$_2$[Fe(N(SiMe$_3$)$_2$)$_2$(py)]$_2$** (**3a**) (1.0 eq) and 1,4-cyclohexadiene = 1,4 CHD (5.0 eq) in THF-d$_8$ (500.1 MHz).

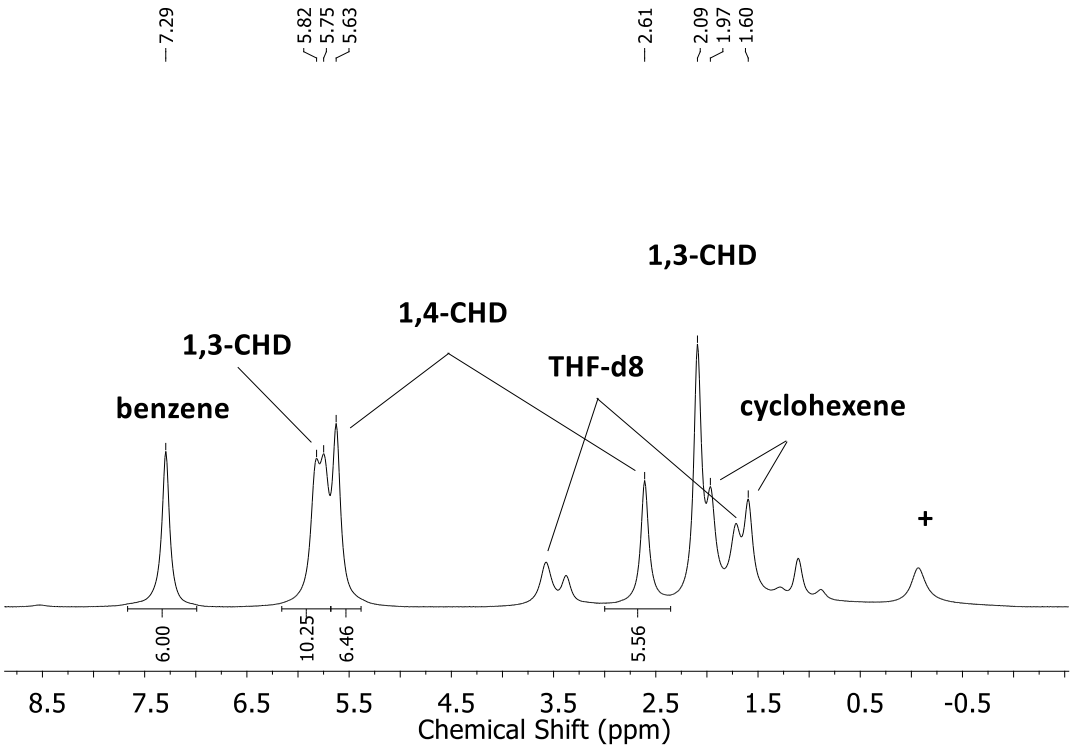

Figure S 32. ^{1}H NMR spectrum of the *in-situ* reaction of **[K{18c6}]$_2$[Fe(N(SiMe$_3$)$_2$)$_2$(py)]$_2$** (**3a**) (1.0 eq) and 1,4-cyclohexadiene (5.0 eq) after 12 h in THF-d$_8$ (500.1 MHz). + decomposition.

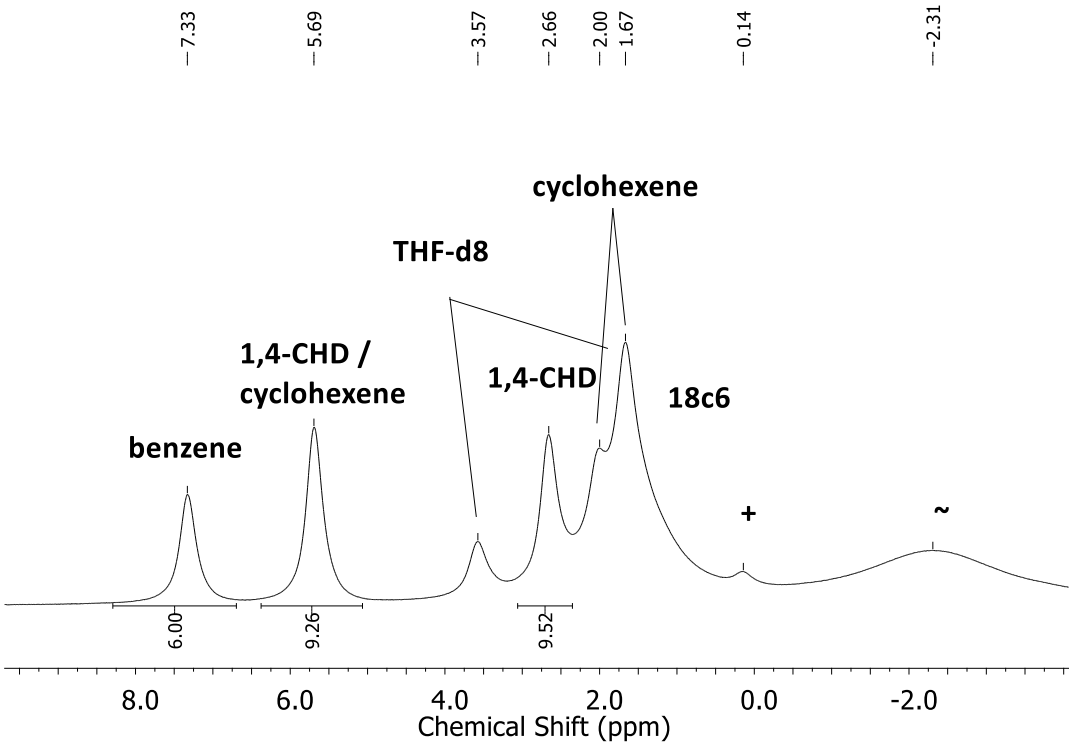

Figure S 33. ^{1}H NMR spectrum of the *in-situ* reaction of [K{18c6}][Fe(N(SiMe$_3$)$_2$)$_2$] (1.0 eq) and 1,4-cyclohexadiene (1.0 eq) in THF-d$_8$ (300.1 MHz) after 30 min. ~ [Fe(N(SiMe$_3$)$_2$)$_3$]$^-$. + decomposition.

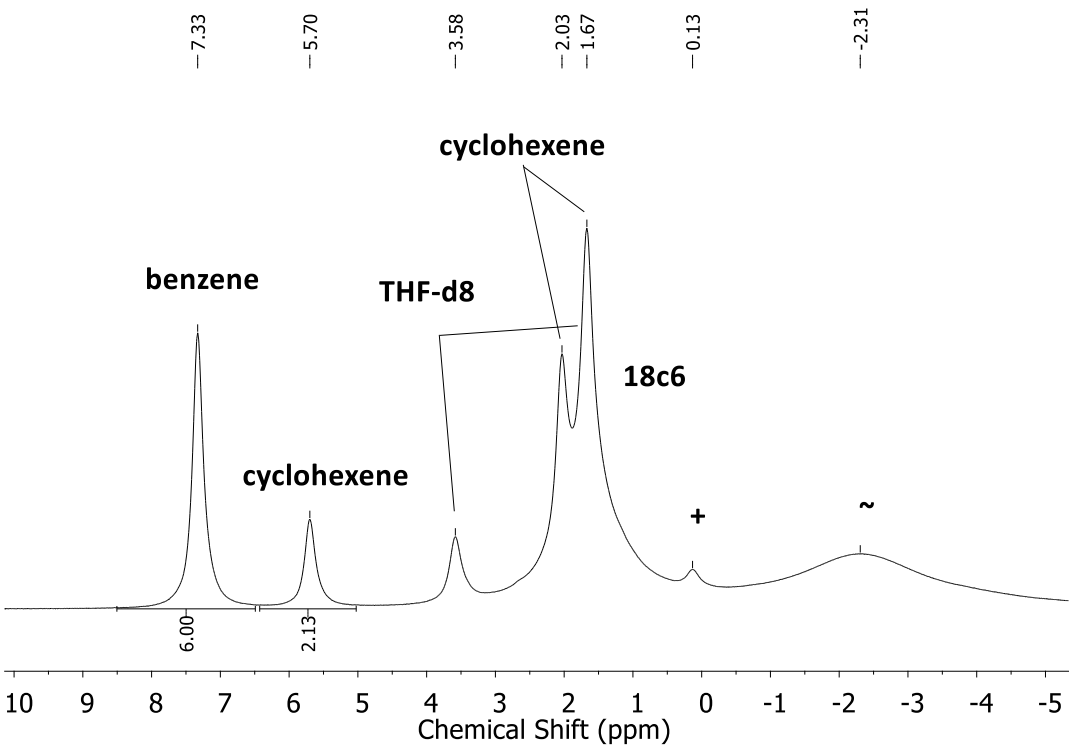

Figure S 34. ^{1}H NMR spectrum of the *in-situ* reaction of [K{18c6}][Fe(N(SiMe$_3$)$_2$)$_2$] (1.0 eq) and 1,4-cyclohexadiene (1.0 eq) after 12 h in THF-d$_8$ (300.1 MHz). ~ [Fe(N(SiMe$_3$)$_2$)$_3$]$^-$. + decomposition.

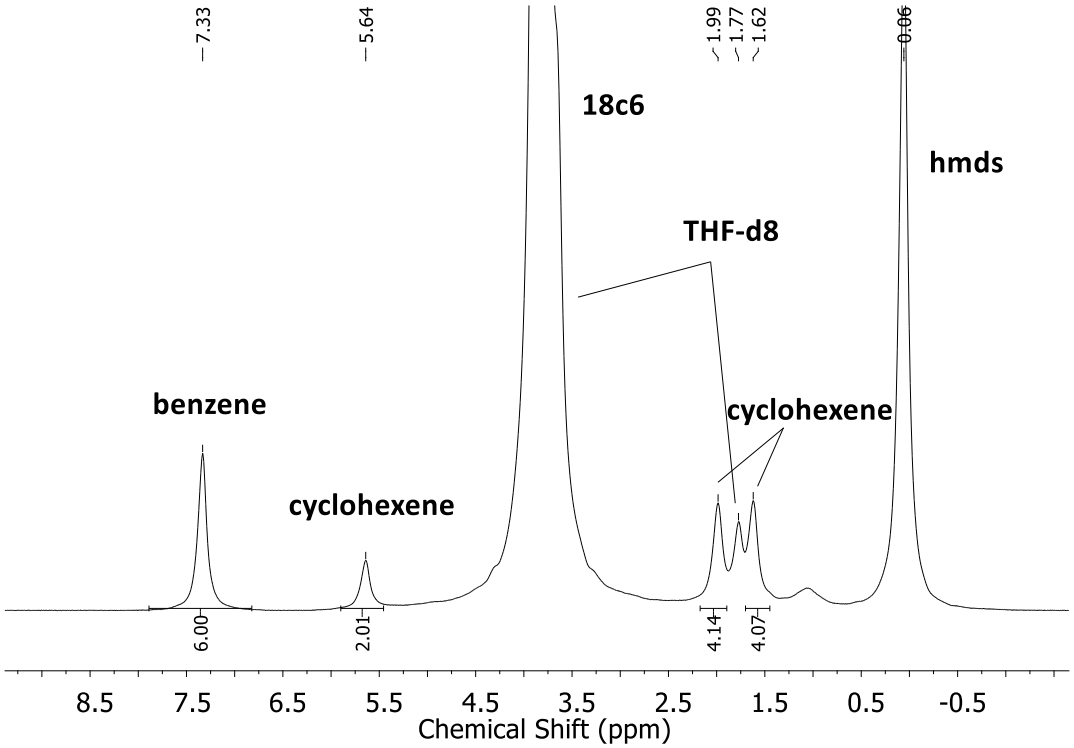

Figure S 35. ^{1}H NMR spectrum of the *in-situ* reaction of [K{18c6}][Fe(N(SiMe$_3$)$_2$)$_2$] (1.0 eq) and 1,4-cyclohexadiene (1.0 eq) after 12 h in THF-d$_8$. The solution was quenched with water and filtered through Celite (300.1 MHz). (hmds = HN(SiMe$_3$)$_2$).

***In-situ* $^{1}H/^{19}F$-NMR spectra of the reaction of fluoropyridines with $[Co(N(SiMe_3)_2)_2]^-$**

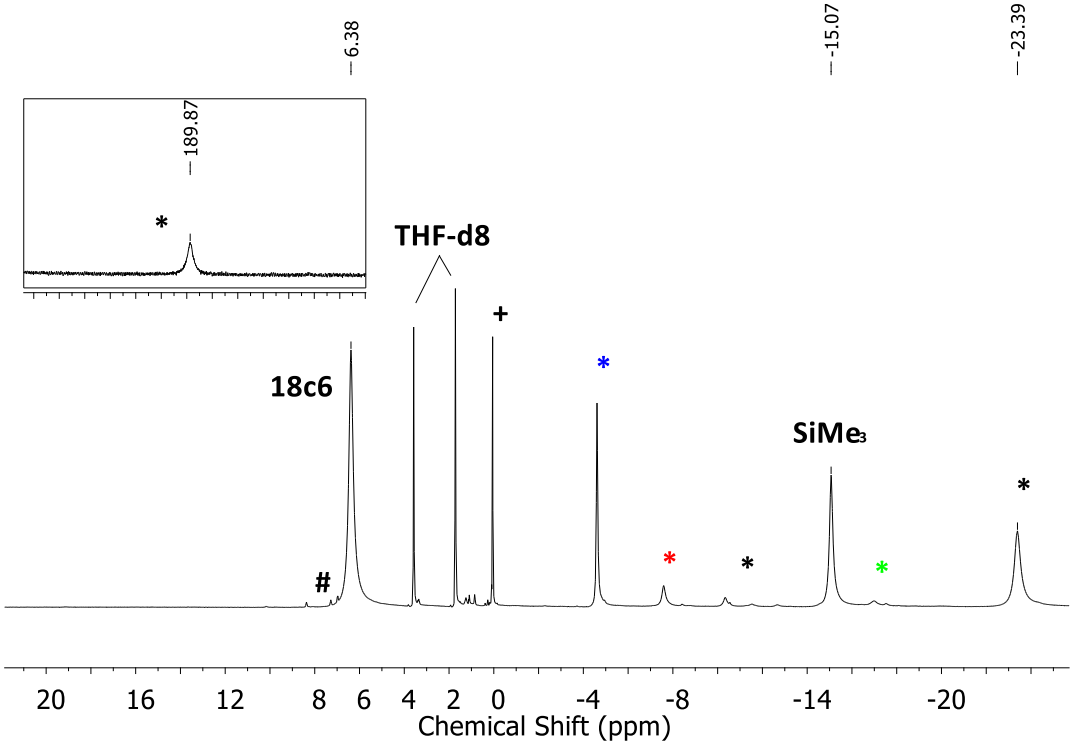

Figure S 36. ^{1}H NMR spectrum of the *in-situ* reaction of [K{18c6}][Co(N(SiMe$_3$)$_2$)$_2$] (1.0 eq) and 2,4-difluoropyridine (0.5 eq) in THF-d$_8$ (300.1 MHz). # denotes free 2,4-difluoropyridine. + decomposition. * pyridinylcomplexe. * Co(N(SiMe$_3$)$_2$)$_2$(thf). * [Co(N(SiMe$_3$)$_2$)$_3$]$^-$. * denotes free [Co(N(SiMe$_3$)$_2$)$_2$]$^-$.

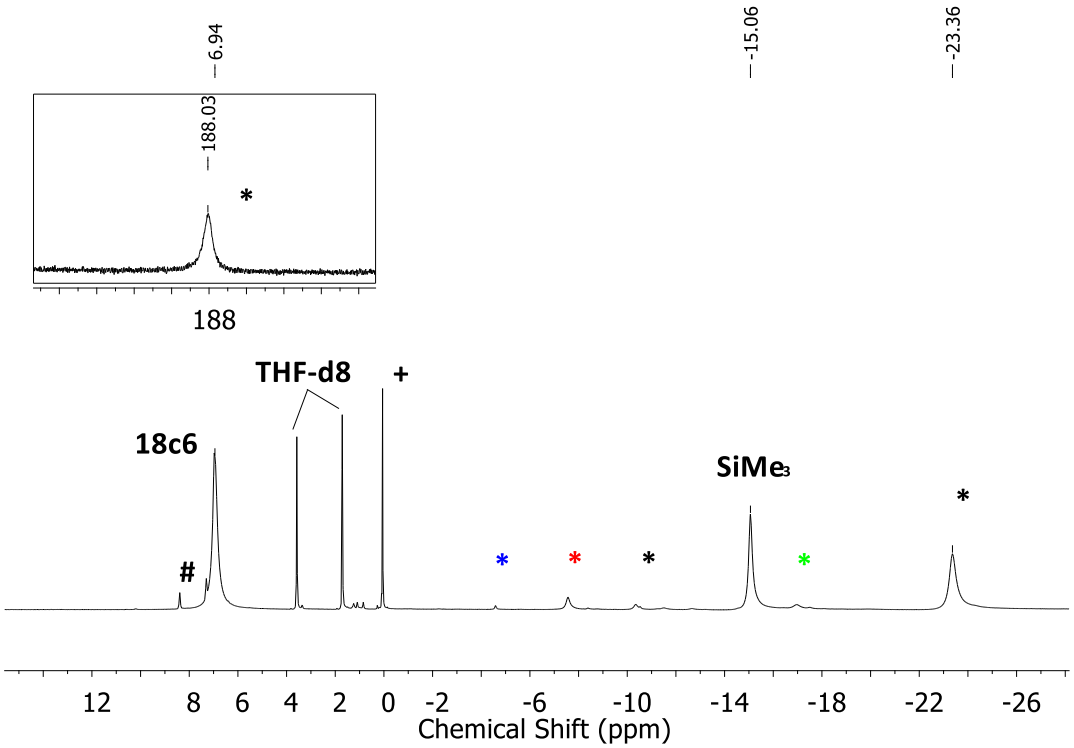

Figure S 37. ^{1}H NMR spectrum of the *in-situ* reaction of [K{18c6}][Co(N(SiMe$_3$)$_2$)$_2$] (1.0 eq) and 2,4-difluoropyridine (1.0 eq) in THF-d$_8$ (300.1 MHz). # denotes free 2,4-difluoropyridine. + decomposition. * pyridinylcomplexe. * Co(N(SiMe$_3$)$_2$)$_2$(thf). * [Co(N(SiMe$_3$)$_2$)$_3$]$^-$. * denotes free [Co(N(SiMe$_3$)$_2$)$_2$]$^-$.

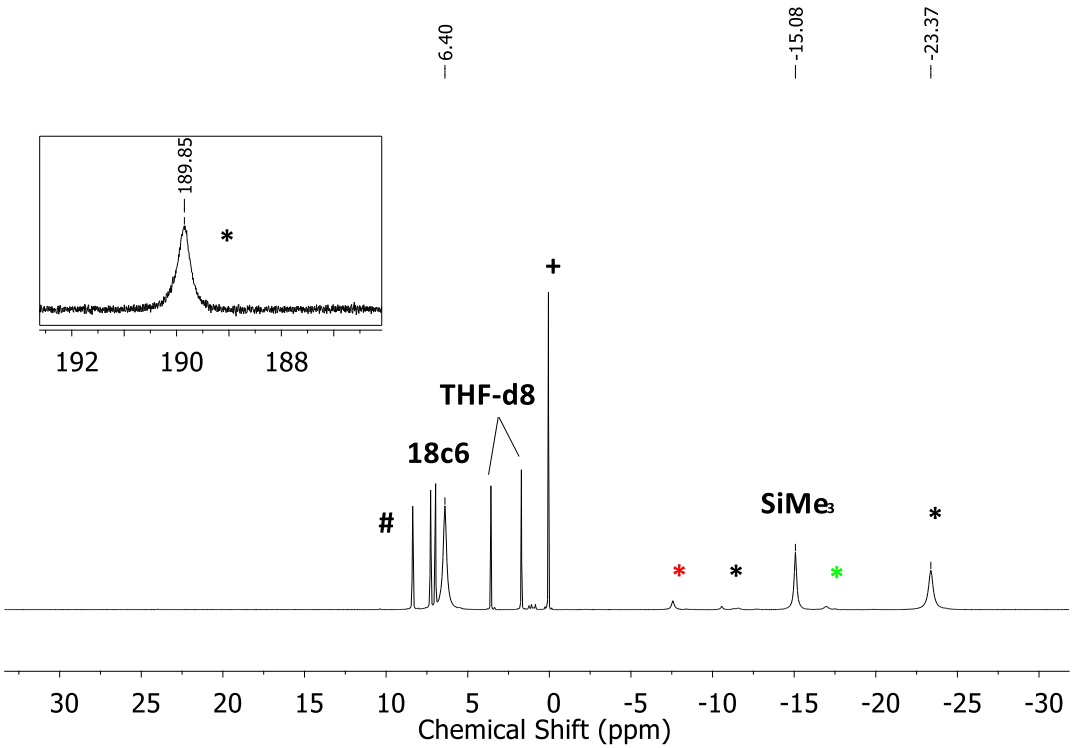

Figure S 38. ^{1}H NMR spectrum of the *in-situ* reaction of [K{18c6}][Co(N(SiMe$_3$)$_2$)$_2$] (1.0 eq) and 2,4-difluoropyridine (1.0 eq) in THF-d$_8$ (300.1 MHz). # denotes free 2,4-difluoropyridine. + decomposition. * pyridinylcomplexe. * Co(N(SiMe$_3$)$_2$)$_2$(thf). * [Co(N(SiMe$_3$)$_2$)$_3$]$^-$.

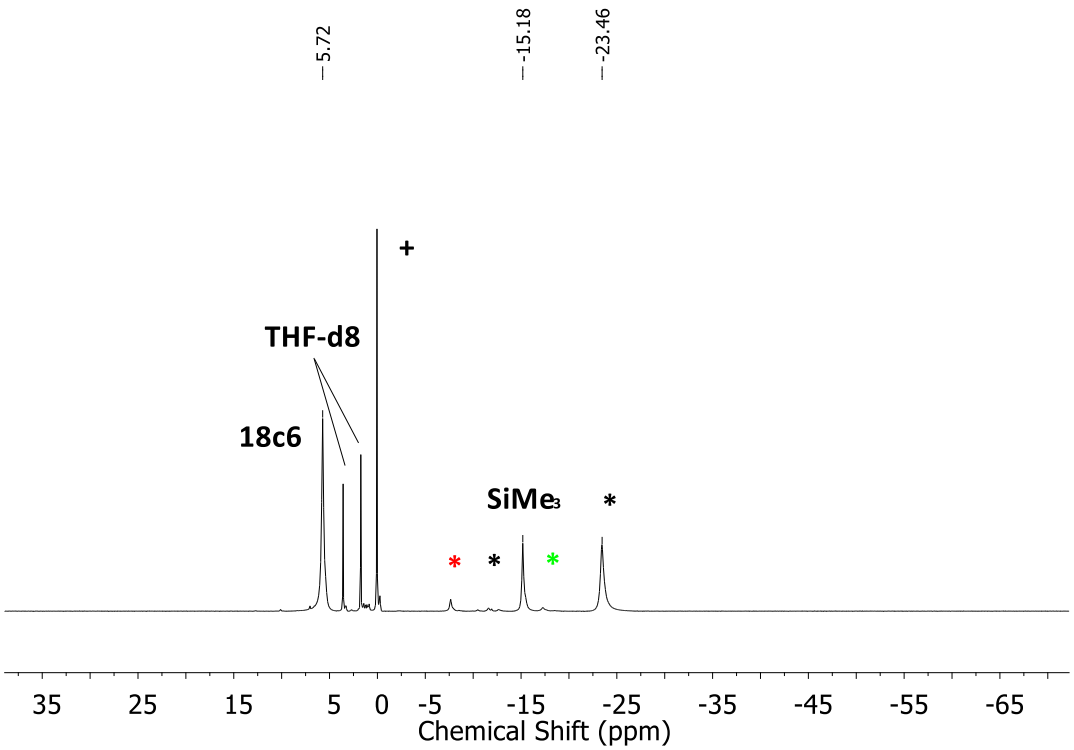

Figure S 39. ^{1}H NMR spectrum of the *in-situ* reaction of [K{18c6}][Co(N(SiMe$_3$)$_2$)$_2$] (1.0 eq) and 2,4,6-trifluoropyridine (0.5 eq) in THF-d$_8$ (300.1 MHz). # denotes free 2,4,6-trifluoropyridine. + decomposition. * pyridinylcomplexe. * Co(N(SiMe$_3$)$_2$)$_2$(thf). * [Co(N(SiMe$_3$)$_2$)$_3$]$^-$.

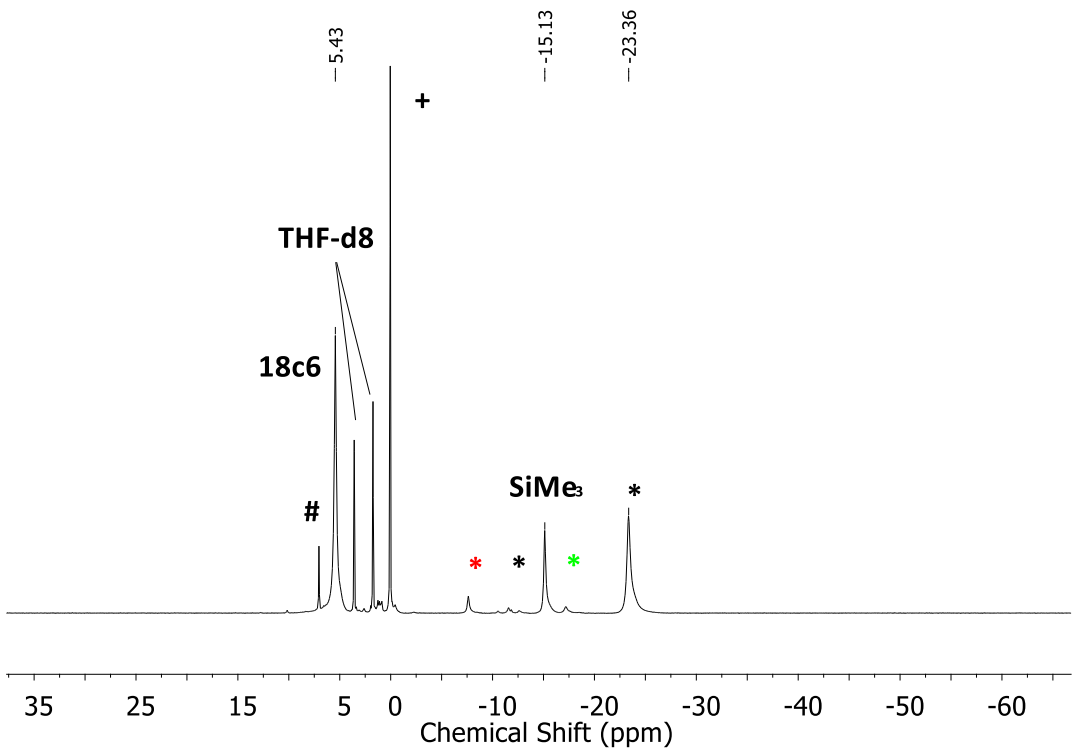

Figure S 40. ^{1}H NMR spectrum of the *in-situ* reaction of [K{18c6}][Co(N(SiMe$_3$)$_2$)$_2$] (1.0 eq) and 2,4,6-trifluoropyridine (1.0 eq) in THF-d$_8$ (300.1 MHz). # denotes free 2,4,6-trifluoropyridine. + decomposition. * pyridinylcomplexe. * Co(N(SiMe$_3$)$_2$)$_2$(thf). * [Co(N(SiMe$_3$)$_2$)$_3$]$^-$.

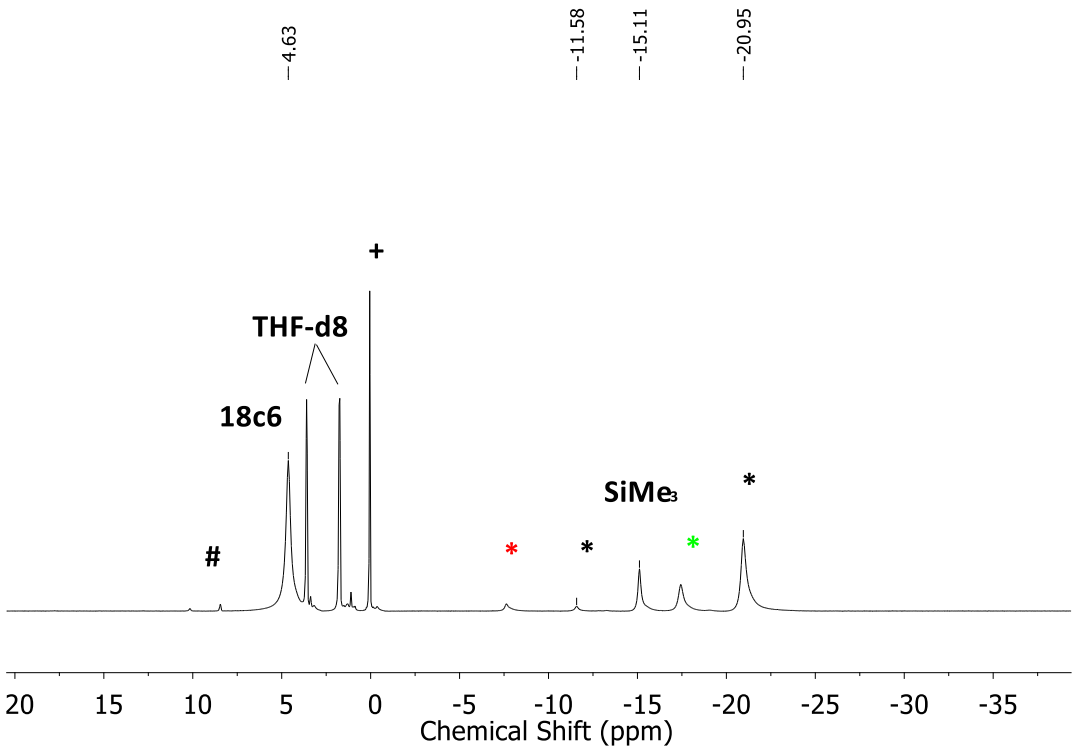

Figure S 41. ^{1}H NMR spectrum of the *in-situ* reaction of [K{18c6}][Co(N(SiMe$_3$)$_2$)$_2$] (1.0 eq) and 2,3,5,6-tetrafluoropyridine (0.5 eq) in THF-d$_8$ (300.1 MHz). # denotes free 2,3,5,6-tetrafluoropyridine. + decomposition. * pyridinylcomplexe. * Co(N(SiMe$_3$)$_2$)$_2$(thf). * [Co(N(SiMe$_3$)$_2$)$_3$]$^-$.

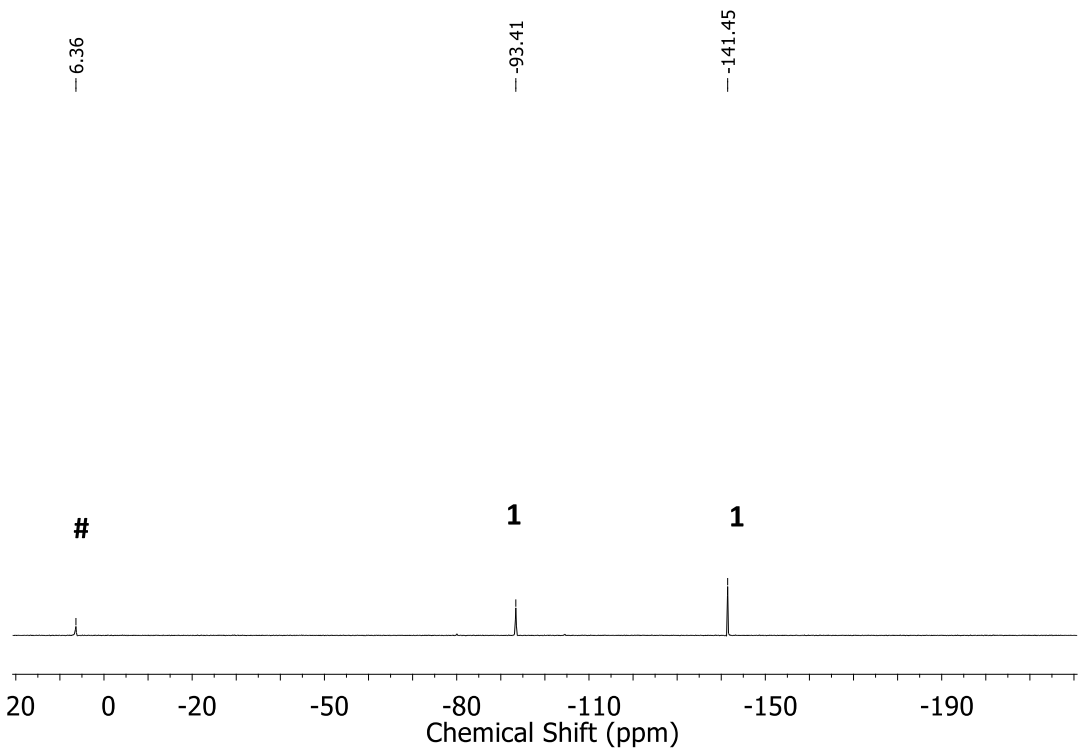

Figure S 42. ^{19}F NMR spectrum of the *in-situ* reaction of [K{18c6}][Co(N(SiMe$_3$)$_2$)$_2$] (1.0 eq) and 2,3,5,6-tetrafluoropyridine (0.5 eq) in THF-d$_8$ (300.1 MHz). 1 2,3,5,6-tetrafluoropyridine. # Signal cannot be assigned.

4. *In-situ* UV/Vis Spectra

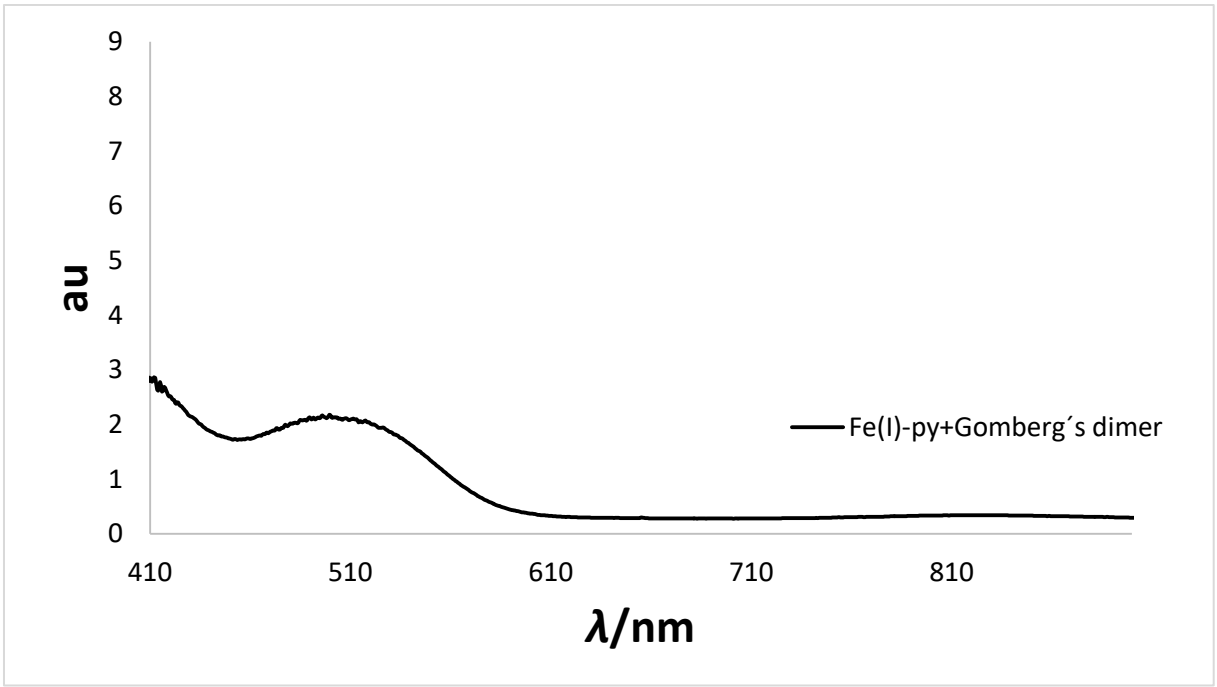

Figure S 43. UV/vis spectrum of the *in-situ* reaction of **[K{18c6}]$_2$[Fe(N(SiMe$_3$)$_2$)$_2$(py)]$_2$** (**3a**) (1.0 eq) and triphenylmethyl radical (Gomberg dimer) (1.0 eq) in Et$_2$O (λ_{max} = 501 nm).

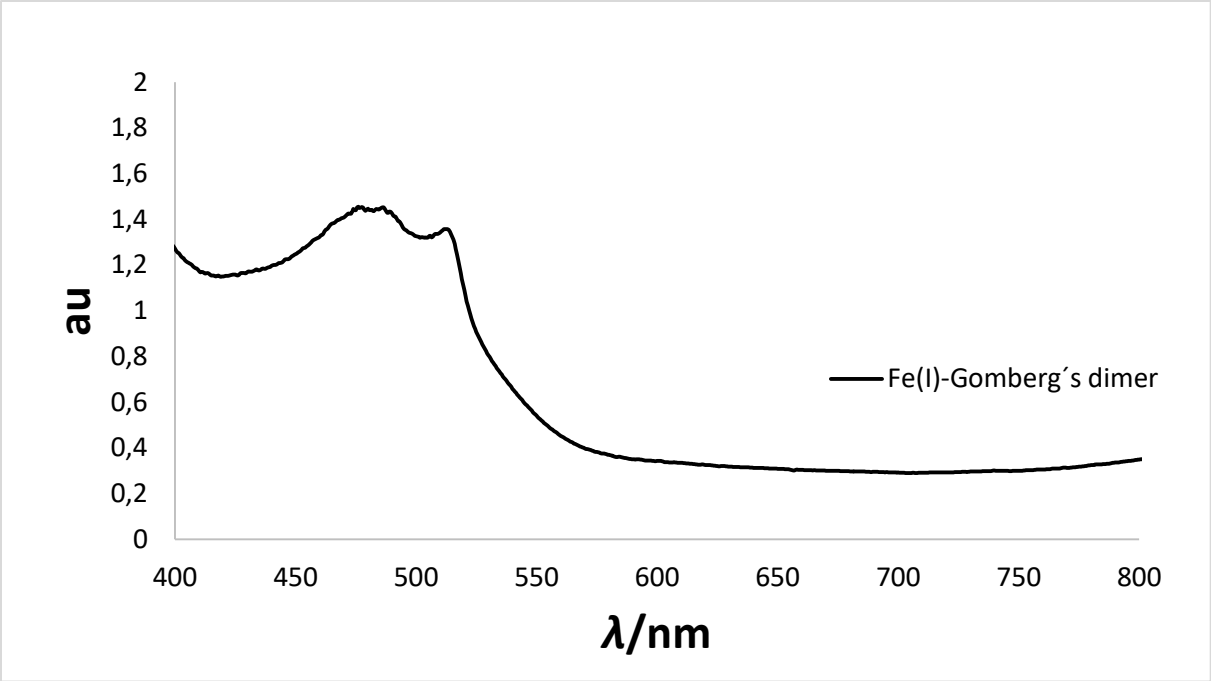

Figure S 44. UV/vis spectrum of the *in-situ* reaction of [K{18c6}][Fe(N(SiMe$_3$)$_2$)$_2$] (1.0 eq) and triphenylmethyl radical (Gomberg dimer) (1.0 eq) in Et$_2$O (λ_{max} = 492 nm).

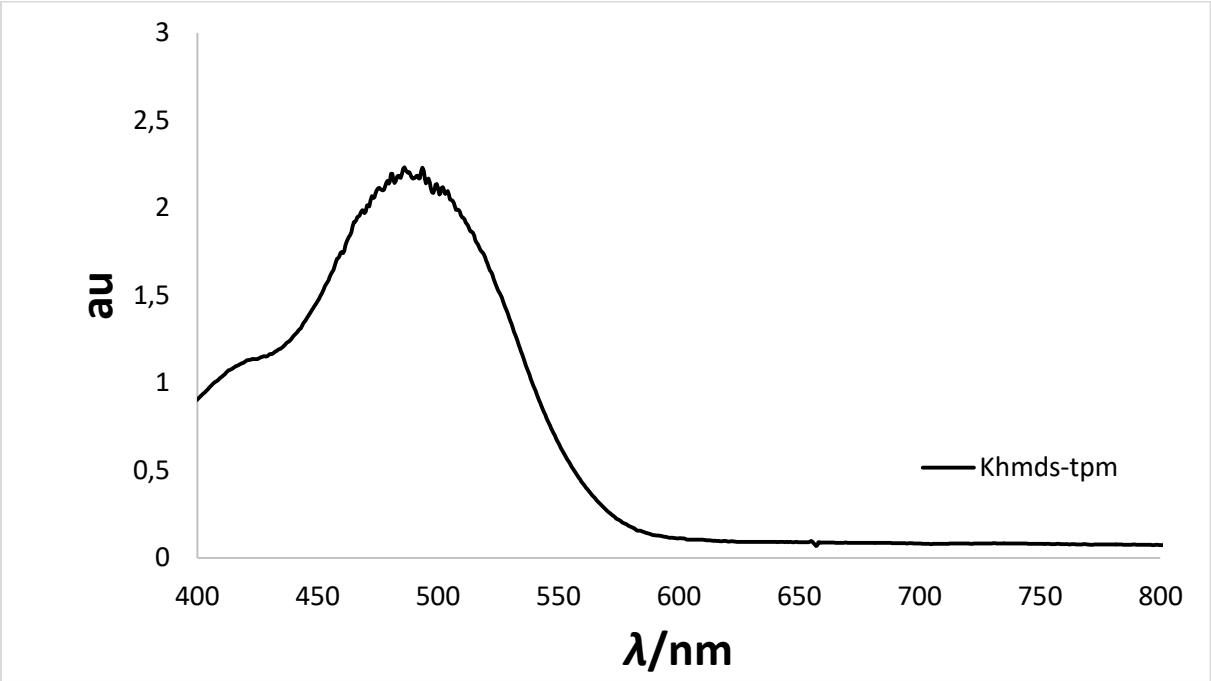

Figure S 45. UV/vis spectrum of the *in-situ* reaction of K(N(SiMe$_3$)) (Khmds) (1.0 eq) and triphenylmethane (tpm) (1.0 eq) in Et$_2$O (λ_{max} = 489 nm).

5. X-Ray diffraction analysis

Data for compounds **2a** (CCDC 2041120), **2b** (CCDC 2041121), **3b** (CCDC 2041123), **4** (CCDC 2041219), **6a** (CCDC 1858775) [12] were collected at 100 K on a Bruker Quest D8 diffractometer (Bruker Corporation, Billerica, USA) using a ncoatec Microfocus Source Mo-Kα radiation and equipped with an Oxford Instrument Cooler Device (Oxford Instruments, Abingdon, UK) and Photon 100 detector. Data for compounds **1** (CCDC 2041119) and **6b** (CCDC 1979606) (STOE & Cie GmbH, Darmstadt, Germany) and data for compound **4** (CCDC 1979595), **3a** (CCDC 2041122), **3c** (CCDC 2041124), **5** (CCDC 2041126) and **7** (CCDC 2041128) were collected at 100 K on a STOE IPDS-2T diffractometer using a graphite-monochromated Mo-Kα radiation (λ = 0.71073 Å) and equipped with an Oxford Instrument Cooler Device (Oxford Instruments, Abingdon, UK). The structures have been solved using either OLEX SHELXT V2014/1[10] and refined by means of least-squares procedures on an F^2 with the aid of the program SHELXL-2016/6[11] included in the software package WinGX version 1.63[12] or using CRYSTALS[13]. The atomic scattering factors were taken from International Tables for X-ray Crystallography[14]. All non-hydrogen atoms were refined anisotropically. All hydrogens atoms were refined by using a riding model. Absorption corrections were introduced by using the MULTISCAN and X-Red programs.[15,16] Drawings of molecules are performed with the program DIAMOND (Crystal Impact, Bonn, Germany) with 50% probability displacement ellipsoids for non-H atoms. Additional details are given in the Supporting Information.

Table S 1. Crystal data and structure refinement for **1**.

Identification code	Crpy_1
Empirical formula	$C_{102}H_{200}Cr_2K_2N_{10}O_{24}Si_8$
Formula weight	2353.65
Temperature / *K*	100.0
Crystal system	triclinic
Space group	P-1
a/Å	15.620(13)
b/Å	15.805(11)
c/Å	16.511(11)
α/°	113.15(6)
β/°	97.38(6)
γ/°	114.26(5)
Volume / Å^3	3206(4)
Z	1
ρ_{calc} g/cm^3	1.219
μ/mm^{-1}	0.375
F(000)	1270.0
Crystal size / mm^3	0.513 × 0.357 × 0.165
Radiation	MoKα (λ = 0.71073)
2Θ range for data collection /°	3.048 to 52.994
Index ranges	-19 ≤ h ≤ 19, -19 ≤ k ≤ 19, -20 ≤ l ≤ 20
Reflections collected	26341
Independent reflections	13256 [R_{int} = 0.0340, R_{sigma} = 0.0538]
Data/restraints/parameters	13256/1332/877
Goodness-of-fit on F^2	0.963
Final *R* indexes [I>=2σ (I)]	R_1 = 0.0445, wR_2 = 0.1077
Final *R* indexes [all data]	R_1 = 0.0804, wR_2 = 0.1167
Largest diff. peak/hole / e Å^{-3}	0.58/-0.22

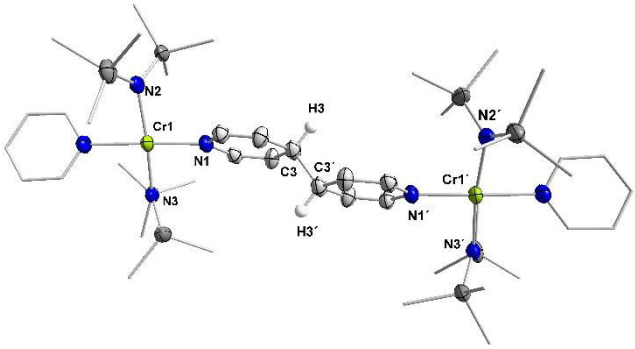

Figure S 46. Molecular structure of **1**. [K{18c6}]$^+$-cation is not shown and all hydrogen atoms are omitted for clarity. The disorder of the cation ([K18c6]) was divided into two parts, part 1 with 50% and part 2 with 50% occupation. Additionally an 18c6 molecule crystallizes in the elementary cell and is disordered too.

Table S 2. Crystal data and structure refinement for **2a**.

Identification code	Mnpy_2a
Empirical formula	$C_{66}H_{150}K_2Mn_2N_6O_{14}Si_8$
Formula weight	1664.71
Temperature / *K*	100.0
Crystal system	triclinic
Space group	P-1
a/Å	11.1700(5)
b/Å	14.7871(6)
c/Å	16.1471(7)
α/°	108.3960(10)
β/°	96.711(2)
γ/°	106.9290(10)
Volume / Å^3	2356.20(18)
Z	1
ρ_{calc} g/cm^3	1.173
μ/mm^{-1}	0.511
F(000)	900.0
Crystal size / mm^3	0.34 × 0.33 × 0.28
Radiation	MoKα (λ = 0.71073)
2Θ range for data collection /°	4.758 to 55.094
Index ranges	-14 ≤ h ≤ 14, -19 ≤ k ≤ 19, -20 ≤ l ≤ 20
Reflections collected	67628
Independent reflections	10857 [R_{int} = 0.0276, R_{sigma} = 0.0196]
Data/restraints/parameters	10857/49/512
Goodness-of-fit on F^2	1.021
Final *R* indexes [I>=2σ (I)]	R_1 = 0.0294, wR_2 = 0.0730
Final *R* indexes [all data]	R_1 = 0.0363, wR_2 = 0.0766
Largest diff. peak/hole / e Å^{-3}	0.41/-0.39

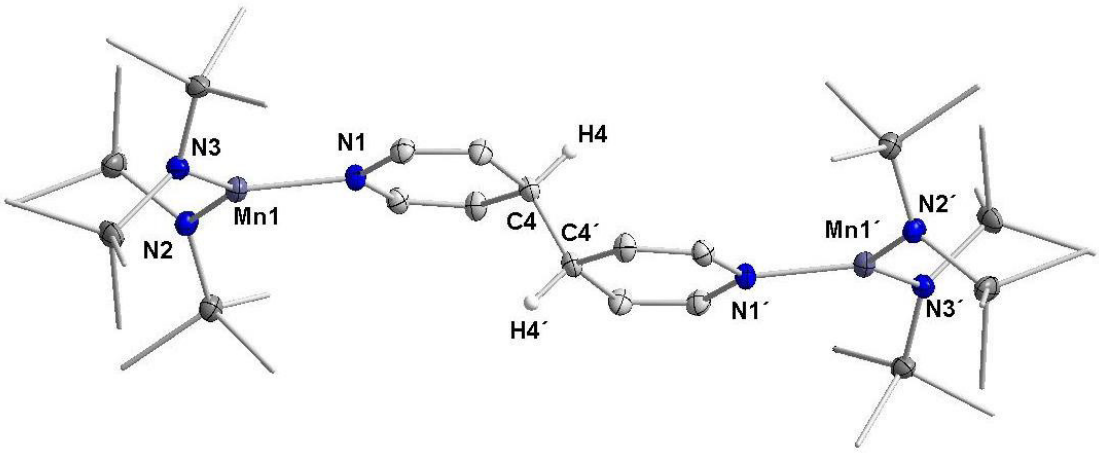

Figure S 47. Molecular structure of **2a**. [K{18c6}]$^+$-cation is not shown and all hydrogen atoms are omitted for clarity.

Table S 3. Crystal data and structure refinement for **2b**.

Identification code	Mnpy_2b
Empirical formula	$C_{78}H_{154}K_2Mn_2N_6O_{14}Si_8$
Formula weight	1812.86
Temperature / *K*	100.00
Crystal system	triclinic
Space group	P-1
a/Å	10.4609(7)
b/Å	12.0312(8)
c/Å	21.5168(14)
α/°	100.491(2)
β/°	96.709(2)
γ/°	105.181(2)
Volume / Å^3	2530.9(3)
Z	1
ρ_{calc} g/cm^3	1.189
μ/mm^{-1}	0.481
F(000)	976.0
Crystal size / mm^3	0.3 × 0.2 × 0.1
Radiation	MoKα (λ = 0.71073)
2Θ range for data collection /°	4.46 to 49.998
Index ranges	-12 ≤ h ≤ 12, -14 ≤ k ≤ 14, 0 ≤ l ≤ 25
Reflections collected	8214
Independent reflections	8214 [R_{int} = 0.0753, R_{sigma} = 0.0959]
Data/restraints/parameters	8214/1982/808
Goodness-of-fit on F^2	1.163
Final *R* indexes [I>=2σ (I)]	R_1 = 0.1008, wR_2 = 0.1949
Final *R* indexes [all data]	R_1 = 0.1286, wR_2 = 0.2047
Largest diff. peak/hole / e Å^{-3}	0.96/-0.60

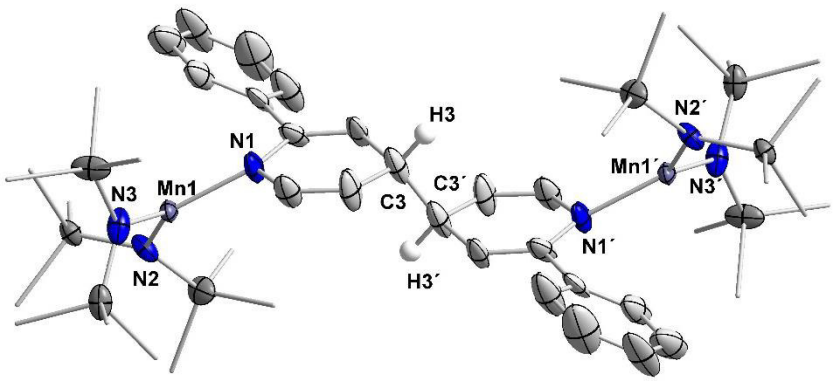

Figure S 48. Molecular structure of **2b**. $[K\{18c6\}(thf)_2]^+$-cation is not shown and all hydrogen atoms are omitted for clarity. One $SiMe_3$ group of a $–N(SiMe_3)_2$ ligand and the cation ($[K\{18c6\}(thf)_2]$) are disordered. Due to the twin integration the data set does not loss of completeness.

Table S 4. Crystal data and structure refinement for **3a**. The very high number of restraints is necessary to model the disorder of the K{18c6} cation.

Identification code	Fepy_3a
Empirical formula	$C_{58}H_{130}Fe_2K_2N_6O_{12}Si_8$
Formula weight	1518.29
Temperature / *K*	100.0
Crystal system	triclinic
Space group	P-1
a/Å	11.0151(17)
b/Å	12.877(2)
c/Å	16.445(3)
α/°	86.946(13)
β/°	76.533(12)
γ/°	70.538(12)
Volume / Å^3	2138.0(6)
Z	1
ρ_{calc} g/cm^3	1.179
μ/mm^{-1}	0.599
F(000)	818.0
Crystal size / mm^3	0.342 × 0.186 × 0.174
Radiation	MoKα (λ = 0.71073)
2Θ range for data collection /°	4.562 to 49.996
Index ranges	-13 ≤ h ≤ 13, -15 ≤ k ≤ 15, -19 ≤ l ≤ 19
Reflections collected	31819
Independent reflections	7453 [R_{int} = 0.1520, R_{sigma} = 0.0779]
Data/restraints/parameters	7453/671/580
Goodness-of-fit on F^2	1.170
Final *R* indexes [I>=2σ (I)]	R_1 = 0.0673, wR_2 = 0.1387
Final *R* indexes [all data]	R_1 = 0.0739, wR_2 = 0.1415
Largest diff. peak/hole / e Å^{-3}	0.39/-0.70

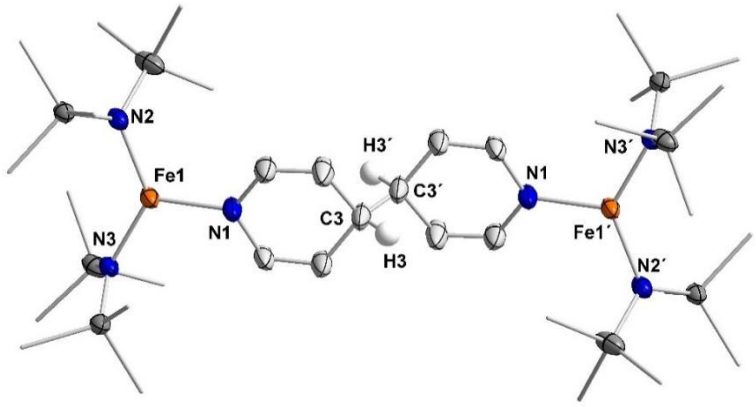

Figure S 49. Molecular structure of **3a**. [K{18c6}]$^+$-cation is not shown and all hydrogen atoms are omitted for clarity.

Table S 5. Crystal data and structure refinement for **3b**.

Identification code	Fephpy_3b
Empirical formula	$C_{70}H_{138}Fe_2K_2N_6O_{12}Si_8$
Formula weight	1670.48
Temperature / *K*	100.0
Crystal system	triclinic
Space group	P-1
a/Å	13.8561(8)
b/Å	18.7017(10)
c/Å	20.4776(11)
α/°	110.638(2)
β/°	99.747(2)
γ/°	103.096(2)
Volume / Å^3	4652.5(4)
Z	2
ρ_{calc} g/cm^3	1.192
μ/mm^{-1}	0.557
F(000)	1796.0
Crystal size / mm^3	0.295 × 0.289 × 0.212
Radiation	MoKα (λ = 0.71073)
2Θ range for data collection /°	4.478 to 50.904
Index ranges	-16 ≤ h ≤ 16, -22 ≤ k ≤ 21, 0 ≤ l ≤ 24
Reflections collected	17140
Independent reflections	17140 [R_{int} = 0.0689, R_{sigma} = 0.0532]
Data/restraints/parameters	17140/0/926
Goodness-of-fit on F^2	1.051
Final *R* indexes [I>=2σ (I)]	R_1 = 0.0494, wR_2 = 0.1302
Final *R* indexes [all data]	R_1 = 0.0698, wR_2 = 0.1425
Largest diff. peak/hole / e Å^{-3}	0.75/-0.62

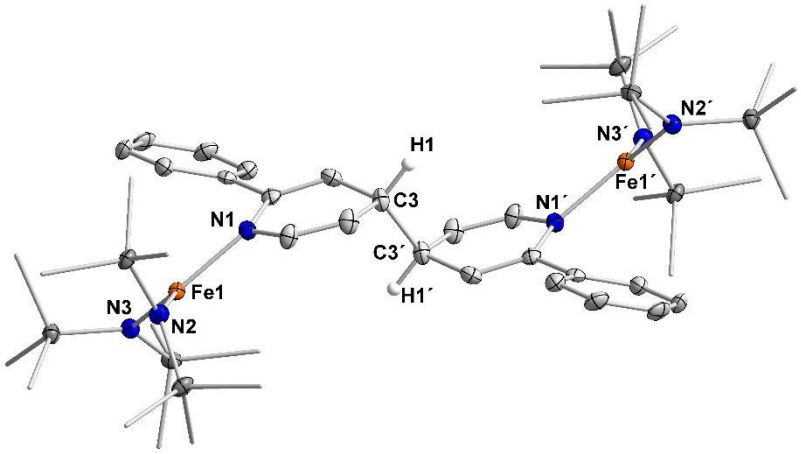

Figure S 50. Molecular structure of **3b**. [K{18c6}]$^+$-cation is not shown and all hydrogen atoms are omitted for clarity. The structure was refined as a twin, twin ratio refined to 0.4657(8).

Table S 6. Crystal data and structure refinement for **3c**.

Identification code	Felut_3c
Empirical formula	$C_{70}H_{158}Fe_2K_2N_6O_{14}Si_8$
Formula weight	1722.63
Temperature / *K*	100.0
Crystal system	monoclinic
Space group	C2/c
a/Å	21.140(4)
b/Å	21.337(3)
c/Å	22.709(4)
α/°	90
β/°	91.610(14)
γ/°	90
Volume / Å^3	10239(3)
Z	4
ρ_{calc} g/cm^3	1.117
μ/mm^{-1}	0.509
F(000)	3736.0
Crystal size / mm^3	0.851 × 0.788 × 0.513
Radiation	MoKα (λ = 0.71073)
2Θ range for data collection /°	3.222 to 50
Index ranges	-21 ≤ h ≤ 25, -22 ≤ k ≤ 25, -26 ≤ l ≤ 26
Reflections collected	24265
Independent reflections	9000 [R_{int} = 0.1262, R_{sigma} = 0.1189]
Data/restraints/parameters	9000/540/648
Goodness-of-fit on F^2	0.981
Final *R* indexes [I>=2σ (I)]	R_1 = 0.0711, wR_2 = 0.1740
Final *R* indexes [all data]	R_1 = 0.1380, wR_2 = 0.1972
Largest diff. peak/hole / e Å^{-3}	0.33/-0.57

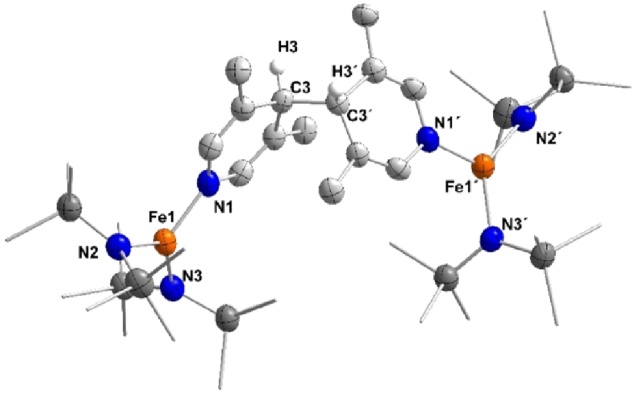

Figure S 51. Molecular structure of **3c**. [K{18c6}]$^+$-cation is not shown and all hydrogen atoms are omitted for clarity. Two Et_2O molecules were squeezed, because modeling of the disorder did not improve the data set. The disorder of the cation ([K18c6]) was divided into two parts, part 1 with 67% and part 2 with 33% occupation.

Table S 7. Crystal data and structure refinement for **4**.

Identification code	2phpy_4
Empirical formula	$C_{53}H_{111}K_2MnN_4O_{12}Si_6$
Formula weight	1298.13
Temperature / *K*	100.0
Crystal system	triclinic
Space group	P-1
a/Å	9.4269(9)
b/Å	19.659(2)
c/Å	21.971(3)
α/°	115.337(5)
β/°	92.181(5)
γ/°	93.061(3)
Volume / Å^3	3666.6(8)
Z	2
ρ_{calc} g/cm^3	1.176
μ/mm^{-1}	0.443
F(000)	1400.0
Crystal size / mm^3	0.282 × 0.178 × 0.096
Radiation	MoKα (λ = 0.71073)
2Θ range for data collection /°	4.112 to 53.74
Index ranges	-11 ≤ h ≤ 11, -24 ≤ k ≤ 24, -27 ≤ l ≤ 27
Reflections collected	65168
Independent reflections	15606 [R_{int} = 0.0614, R_{sigma} = 0.0550]
Data/restraints/parameters	15606/0/721
Goodness-of-fit on F^2	1.069
Final *R* indexes [I>=2σ (I)]	R_1 = 0.0544, wR_2 = 0.1255
Final *R* indexes [all data]	R_1 = 0.0765, wR_2 = 0.1344
Largest diff. peak/hole / e Å^{-3}	0.65/-0.42

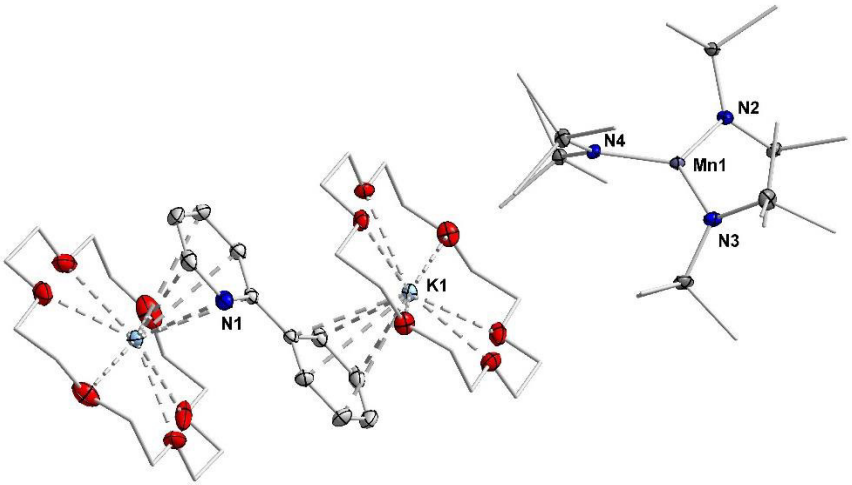

Figure S 52. Molecular structure of **4**. All hydrogen atoms are omitted for clarity.

Table S 8. Crystal data and structure refinement for **5**.

Identification code	Cof_5
Empirical formula	$C_{24}H_{60}CoFKN_2O_6Si_4$
Formula weight	702.13
Temperature / *K*	100
Crystal system	triclinic
Space group	P-1
a/Å	12.3897(4)
b/Å	16.1245(4)
c/Å	19.2411(5)
α/°	93.563(2)
β/°	90.205(2)
γ/°	90.589(2)
Volume / Å^3	3836.28(19)
Z	4
ρ_{calc} g/cm^3	1.216
μ/mm^{-1}	0.719
F(000)	1508.0
Crystal size / mm^3	0.614 × 0.243 × 0.125
Radiation	MoKα (λ = 0.71073)
2Θ range for data collection /°	4.6 to 51
Index ranges	-15 ≤ h ≤ 15, -19 ≤ k ≤ 19, -23 ≤ l ≤ 22
Reflections collected	26756
Independent reflections	14237 [R_{int} = 0.0857, R_{sigma} = 0.0739]
Data/restraints/parameters	14237/0/720
Goodness-of-fit on F^2	1.160
Final *R* indexes [I>=2σ (I)]	R_1 = 0.0877, wR_2 = 0.2469
Final *R* indexes [all data]	R_1 = 0.0985, wR_2 = 0.2777
Largest diff. peak/hole / e Å^{-3}	0.78/-1.25

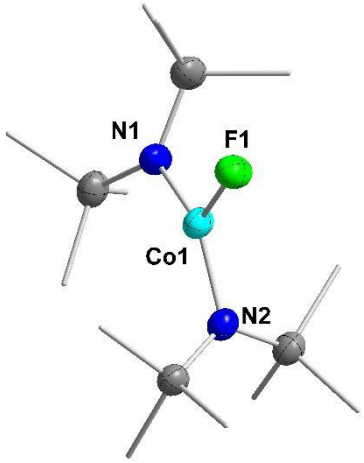

Figure S 53. Molecular structure of **5**. All hydrogen atoms are omitted for clarity. The structure was refined as an inversion twin, twin ratio refined to 0.1733(16). A disorder is found for a $SiMe_3$ groups of one of the –$N(SiMe_3)_2$ ligands.

Table S 9. Crystal data and structure refinement for **7**.

Identification code	Mnf_7
Empirical formula	$C_{24}H_{60}FKMnN_2O_6Si_4$
Formula weight	698.14
Temperature / *K*	100.00
Crystal system	monoclinic
Space group	$P2_1/c$
a/Å	19.206(5)
b/Å	12.7365(18)
c/Å	15.772(3)
α/°	90
β/°	92.087(19)
γ/°	90
Volume / Å^3	3855.7(14)
Z	4
ρ_{calc} g/cm^3	1.203
μ/mm^{-1}	0.613
F(000)	1500.0
Crystal size / mm^3	0.607 × 0.315 × 0.214
Radiation	MoKα (λ = 0.71073)
2Θ range for data collection /°	3.838 to 49.998
Index ranges	-22 ≤ h ≤ 22, -15 ≤ k ≤ 15, -17 ≤ l ≤ 18
Reflections collected	25513
Independent reflections	6785 [R_{int} = 0.0995, R_{sigma} = 0.0668]
Data/restraints/parameters	6785/29/374
Goodness-of-fit on F^2	1.112
Final *R* indexes [I>=2σ (I)]	R_1 = 0.0853, wR_2 = 0.2164
Final *R* indexes [all data]	R_1 = 0.1042, wR_2 = 0.2268
Largest diff. peak/hole / e Å^{-3}	1.55/-0.74

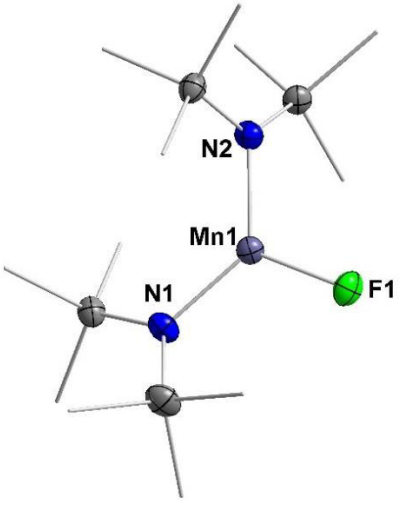

Figure S 54. Molecular structure of **7**. All hydrogen atoms are omitted for clarity. A disorder is found for a $SiMe_3$ groups of one of the $–N(SiMe_3)_2$ ligands.

References

[1] Schubert, E. M. *J. Chem. Educ.* **1992**, *69*, 62.
[2] Evans, A. G.; Evans, J. C.; Emes, P. J.; Haider, S. I. *J. Chem. Soc., Perkin Trans. 2* **1974**, 1121.
[3] Bürger, H.; Wannagat, U. *Monatsh. Chem.* **1963**, *94*, 1007–1012.
[4] Bürger, H.; Wannagat, U. *Monatsh. Chem.* **1964**, *95*, 1099–1102.
[5] Conley, M. P.; Delley, M. F.; Siddiqi, G.; Lapadula, G.; Norsic, S.; Monteil, V.; Safonova, O. V.; Copéret, C. *Angew. Chem. Int. Ed.* **2014**, *53*, 1872–1876.
[6] Werncke, C. G.; Suturina, E.; Bunting, P. C.; Vendier, L.; Long, J. R.; Atanasov, M.; Neese, F.; Sabo-Etienne, S.; Bontemps, S. *Chem. Eur. J.* **2016**, *22*, 1668–1674.
[7] Werncke, C. G.; Bunting, P. C.; Duhayon, C.; Long, J. R.; Bontemps, S.; Sabo-Etienne, S. *Angew. Chem. Int. Ed.* **2015**, *54*, 245–248.
[8] Werncke, C. G.; Pfeiffer, J.; Müller, I.; Vendier, L.; Sabo-Etienne, S.; Bontemps, S. *Dalton Trans.* **2019**, *48*, 1757–1765.
[9] Müller, I.; Schneider, C.; Pietzonka, C.; Kraus, F.; Werncke, C. G. *Inorganics* **2019**, *7*, 117.
[10] Dolomanov, O. V.; Bourhis, L. J.; Gildea, R. J.; Howard, J.; Puschmann, H. *J. Appl. Crystallogr.* **2009**, *42*, 339–341.
[11] Sheldrick, G. M. *Acta. Crystallogr. C* **2015**, *71*, 3–8.
[12] Farrugia, L. J. *J. Appl. Crystallogr.* **1999**, *32*, 837–838.
[13] Betteridge, P. W.; Carruthers, J. R.; Cooper, R. I.; Prout, K.; Watkin, D. J. *J. Appl. Crystallogr.* **2003**, *36*, 1487.
[14] *International tables for crystallography*, 1st online ed.; International Union of Crystallography; Springer: Chester, England, New York, 2006.
[15] SADABS-2016/2. *Bruker*, 2016.
[16] X-Area, X.-R. 1. *STOE*, 2016.

8.3 Supporting Information zur Publikation „Reactions of Alkynes with Quasilinear 3d-Metal(I) Silylamides of Chromium to Cobalt – A Comparative Study"

Igor Müller, Dominik Munz und C. Gunnar Werncke, *Inorg. Chem*. **2020**, *59*, 9521.

Reactions of Alkynes with Quasi-Linear 3d Metal(I) Silylamides of Chromium to Cobalt – A Comparative Study

Igor Müller,[1] Dominik Munz,[2,3] C. Gunnar Werncke[,1]*

[1]Department of Chemistry, Philipps-University Marburg, Hans-Meerwein-Straße 4, 35043 Marburg, Germany; gunnar.werncke@chemie.uni-marburg.de, +49 6421 282 5627; [2]Inorganic Chemistry: Coordination Chemistry, Saarland University, 66123 Saarbrücken Germany. [3]Inorganic and General Chemistry, Friedrich-Alexander University Erlangen-Nürnberg, Egerlandstr. 1, 91058 Erlangen, Germany.

Table of Contents

1. NMR Spectra

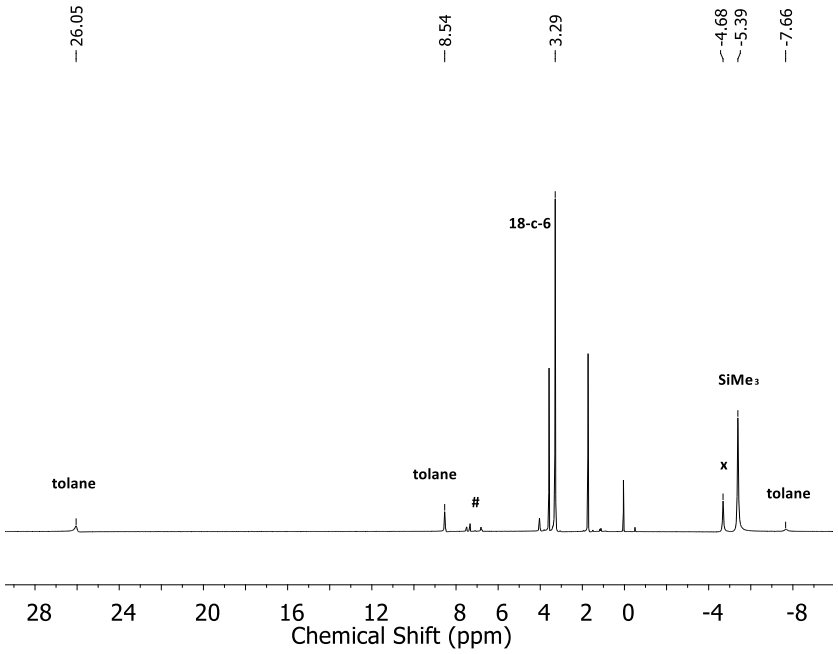

Figure S 1. ^{1}H NMR spectrum of **[K{18c6}][Co(N(SiMe$_3$)$_2$)$_2$(η^2-PhCCPh)]** (**1**) in THF-d$_8$ (500.1 MHz). *#* denotes free diphenylacetylene. *x* denotes free K{18c6}][Co(N(SiMe$_3$)$_2$)$_2$].

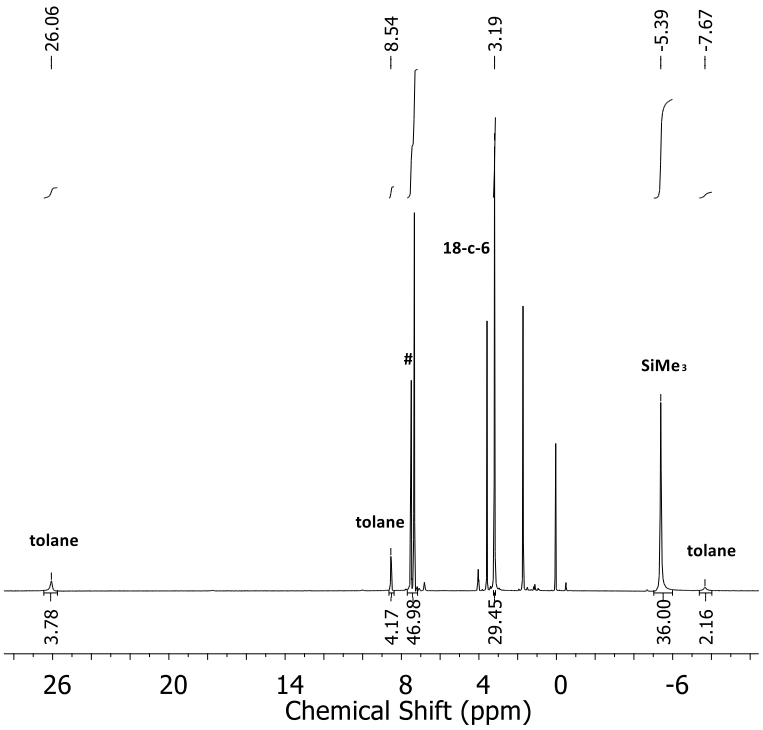

Figure S 2. ^{1}H NMR spectrum of **[K{18c6}][Co(N(SiMe$_3$)$_2$)$_2$(η^2-PhCCPh)]** (**1**) and fivefold surplus of diphenylacetylene in THF-d$_8$ (500.1 MHz). *#* denotes excess of free diphenylacetylene. *x* denotes free [K{18c6}][Co(N(SiMe$_3$)$_2$)$_2$].

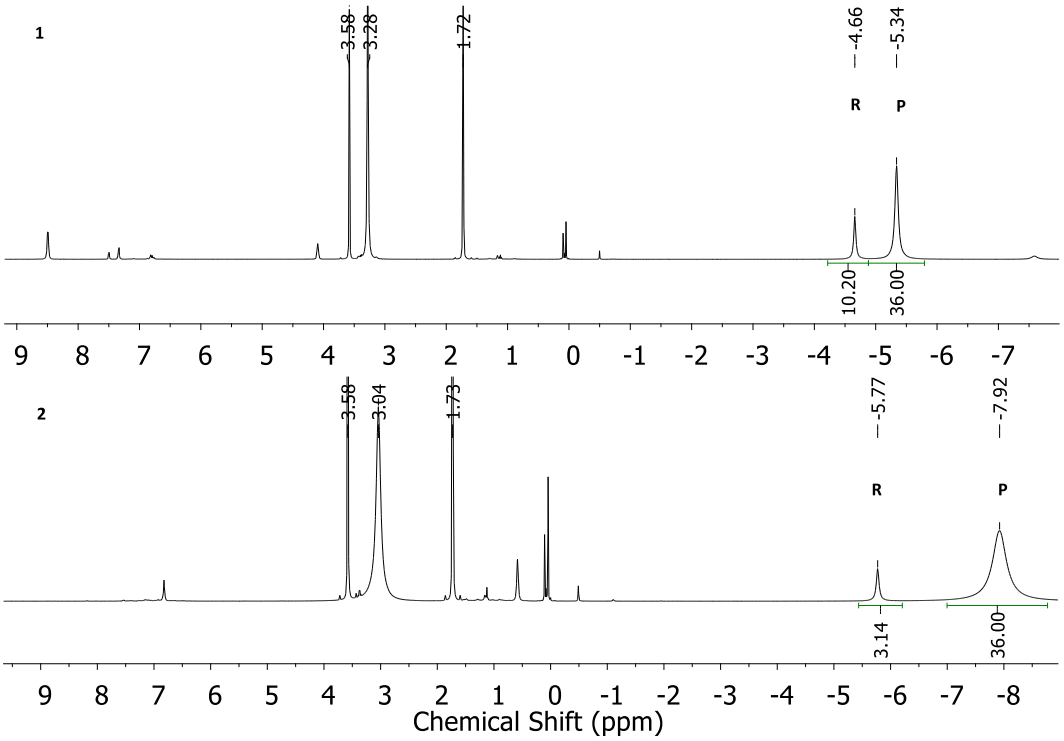

Figure S 3. Temperature dependent ^{1}H NMR Spectra of **[K{18c6}][Co(N(SiMe$_3$)$_2$)$_2$(η^2-PhCCPh)]** (**1**) at room temperature (top, *1*) and at 240 K (bottom, *2*). *R* denotes free [K{18c6}][Co(N(SiMe$_3$)$_2$)$_2$]. *P* denotes **1**.

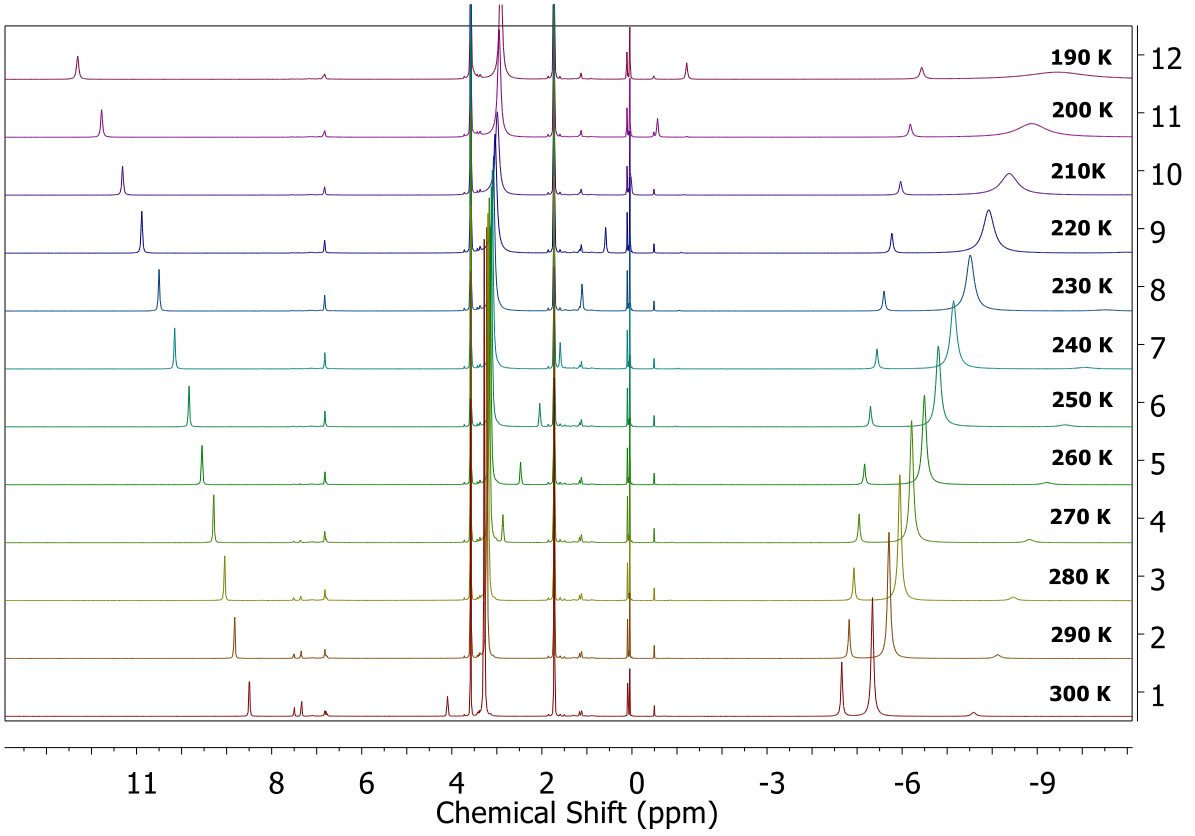

Figure S 4. Temperature dependent ^{1}H NMR Spectra of **[K{18c6}][Co(N(SiMe$_3$)$_2$)$_2$(η^2-PhCCPh)]** (**1**) in the range of 300 K to 190 K.

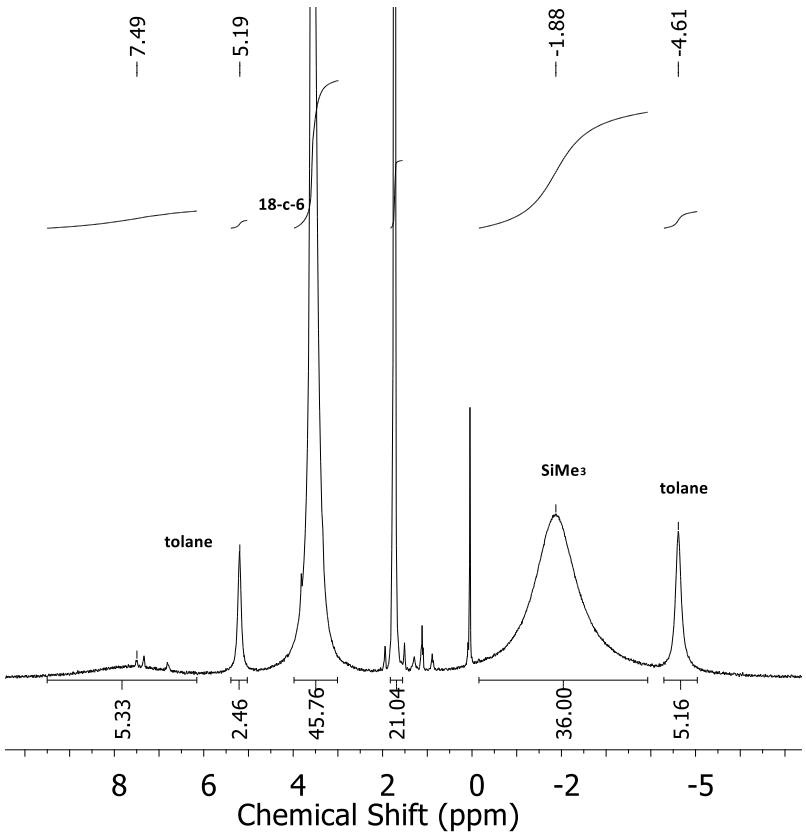

Figure S 5. ^{1}H NMR spectrum of **[K{18c6}][Fe(N(SiMe$_3$)$_2$)$_2$(η^2-PhCCPh)]** (**2a**) in THF-d$_8$ (500.1 MHz).

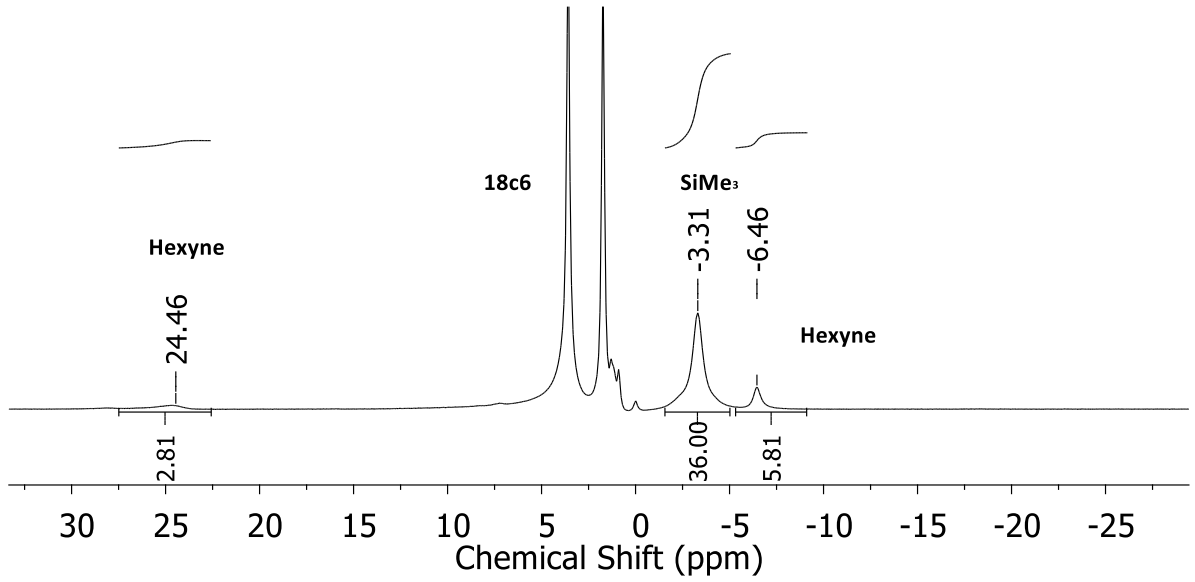

Figure S 6. ^{1}H NMR spectrum of **[K{18c6}][Fe(N(SiMe$_3$)$_2$)$_2$(η^2-EtCCEt)]** (**2b**) in THF-d$_8$ (500.1 MHz).

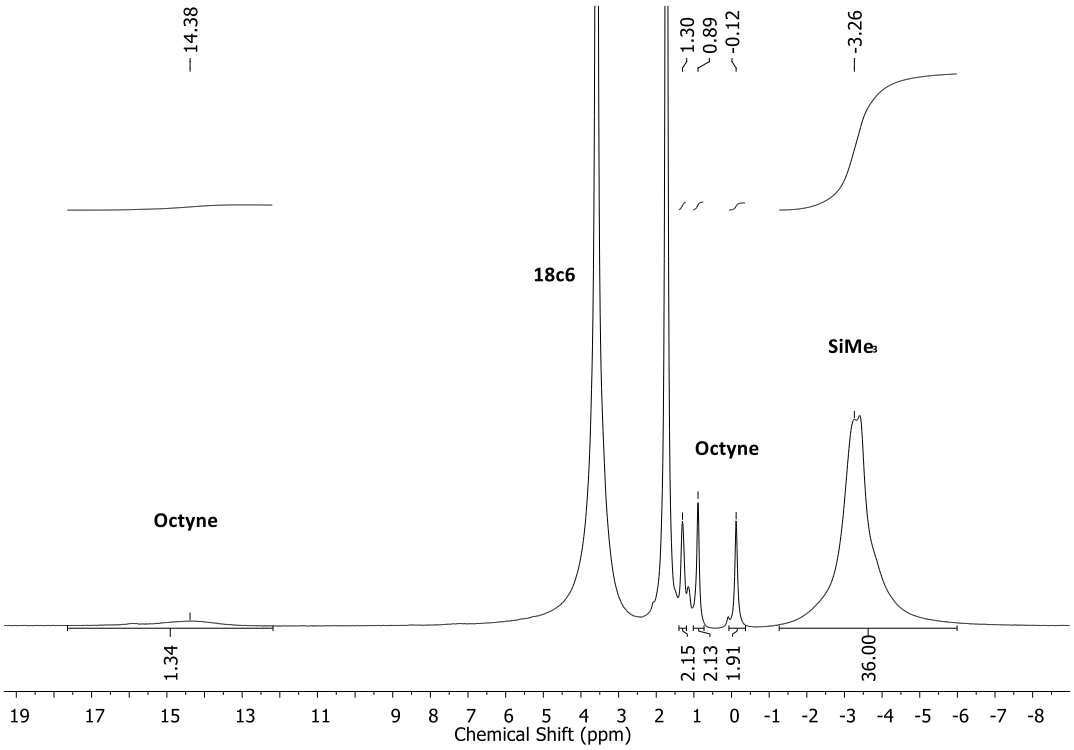

Figure S 7. ^{1}H NMR spectrum of **[K{18c6}][Fe(N(SiMe$_3$)$_2$)$_2$(η^2-^{n}PrCC^{n}Pr)]** (**2c**) in THF-d$_8$ (500.1 MHz).

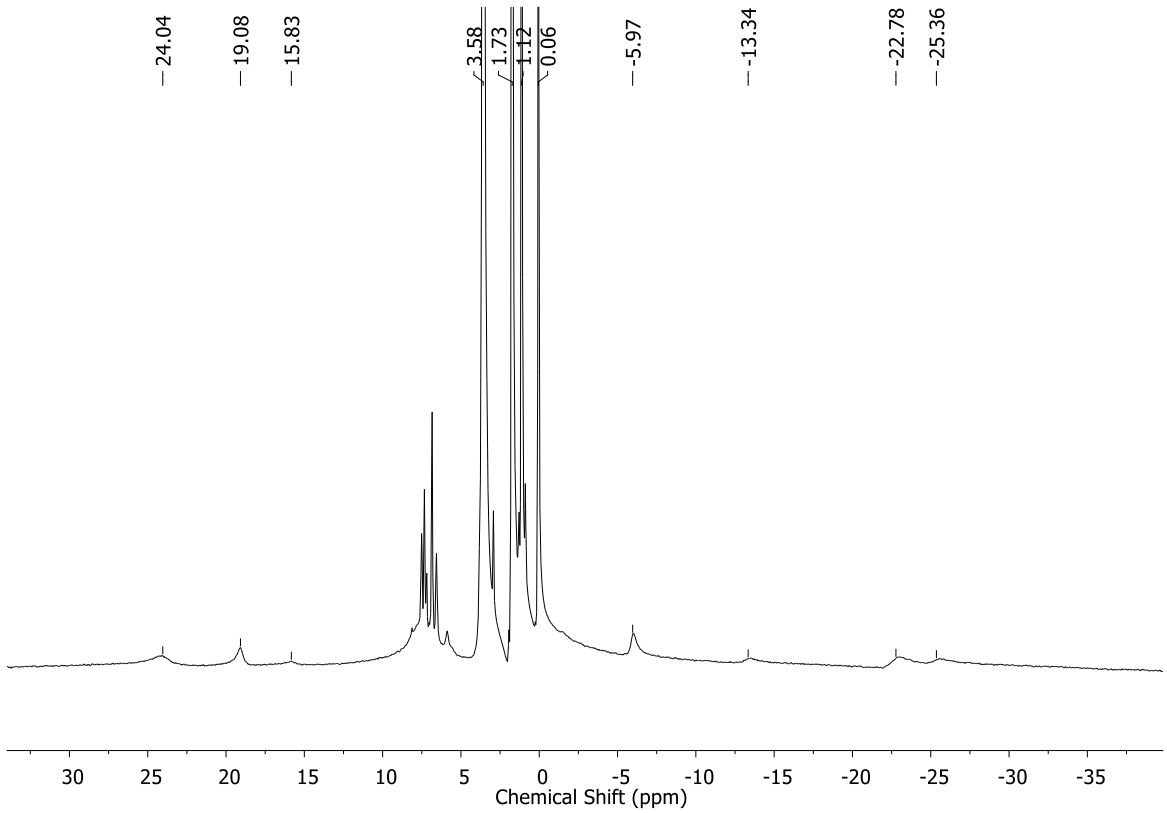

Figure S 8. ^{1}H NMR spectrum of **[K{18c6}][Mn(N(Dipp)(SiMe$_3$))$_2$(η^2-PhCCPh)]** (**3a**) in THF-d$_8$ (300.1 MHz).

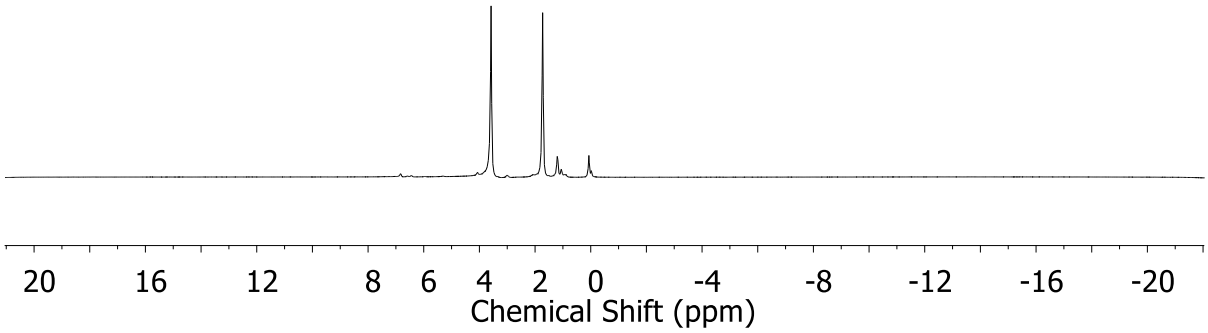

Figure S 9. ^{1}H NMR spectrum of **[K{18c6}][Mn(N(Dipp)(SiMe$_3$))$_2$(η^2-EtCCEt)]** (**3b**) in THF-d$_8$ (300.1 MHz).

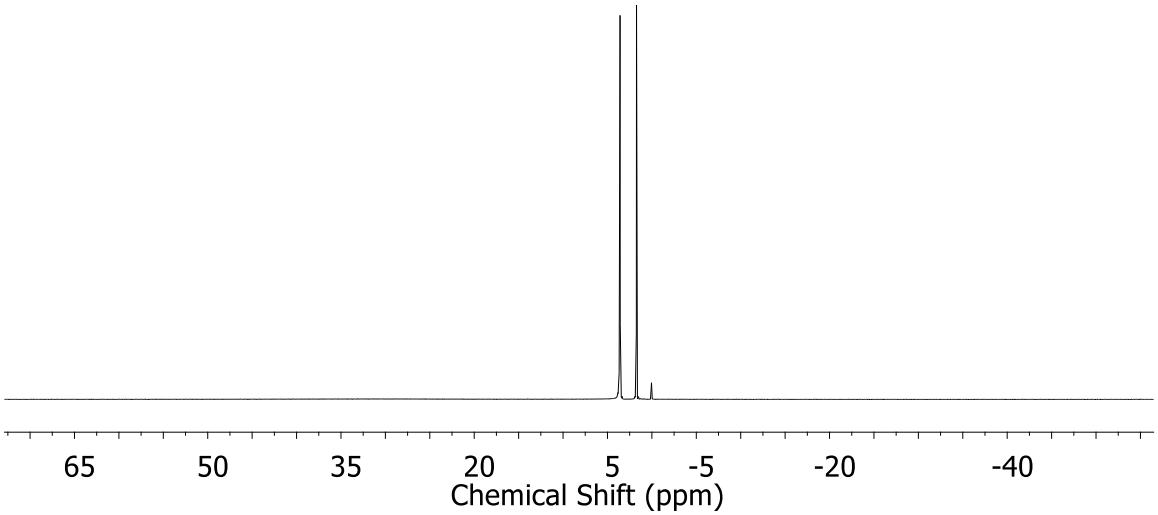

Figure S 10. ^{1}H NMR spectrum of **[K{18c6}][Mn(N(SiMe$_3$)$_2$)$_3$]** (**5**) in THF-d$_8$ (300.1 MHz).

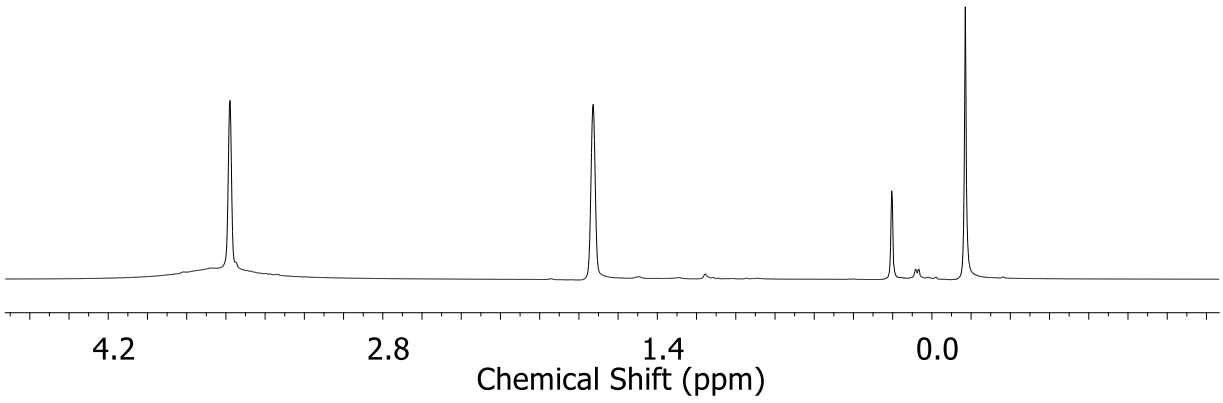

Figure S 11. ^{1}H NMR spectrum of **[K{18c6}][Cr(N(SiMe$_3$)$_2$)$_2$(η^2-Me$_3$SiCCSiMe$_3$)]** (**6a**) in THF-d$_8$ (500.1 MHz).

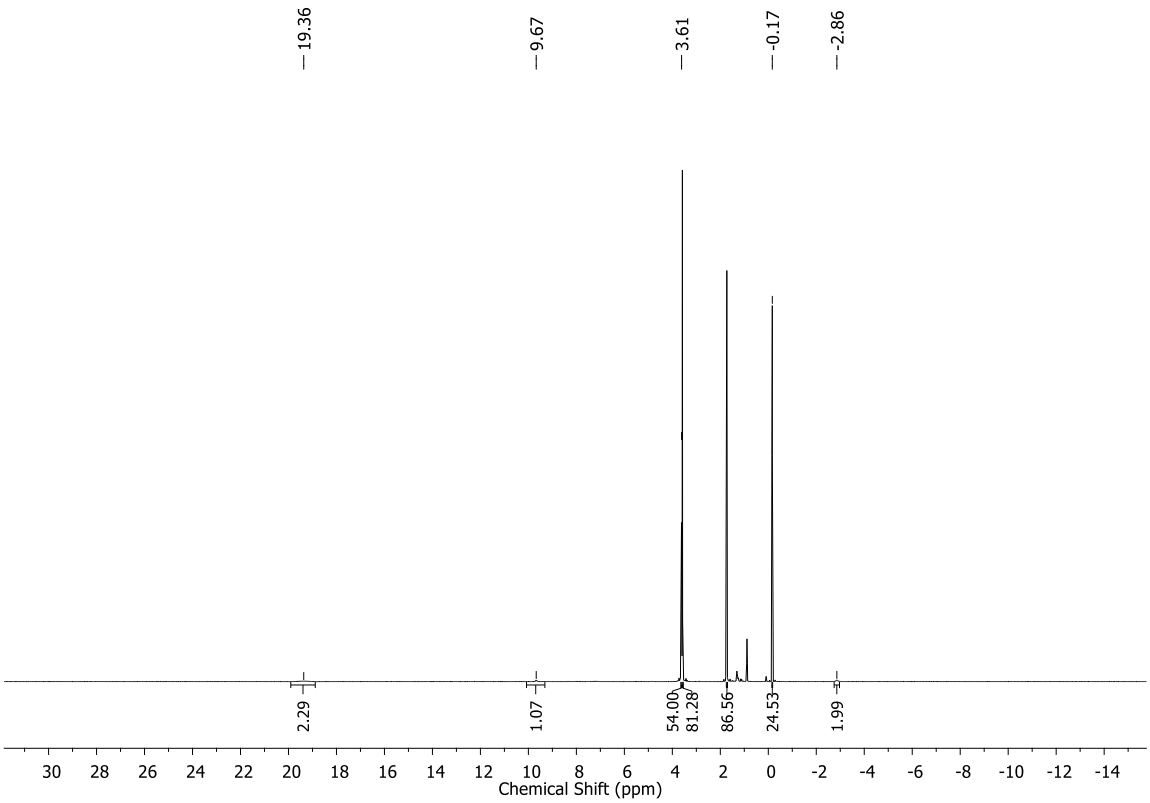

Figure S 12. ^{1}H NMR spectrum of **[K{18c6}]$_2$[Cr$_2$(N(SiMe$_3$)$_2$)$_2$(η^2-N(SiMe$_3$)$_2$)(μ-κ^1(C):κ^1(C)-Me$_3$SiCCSiMe$_3$)]** (**6b**) in THF-d$_8$ (500.1 MHz).

2. IR Spectra

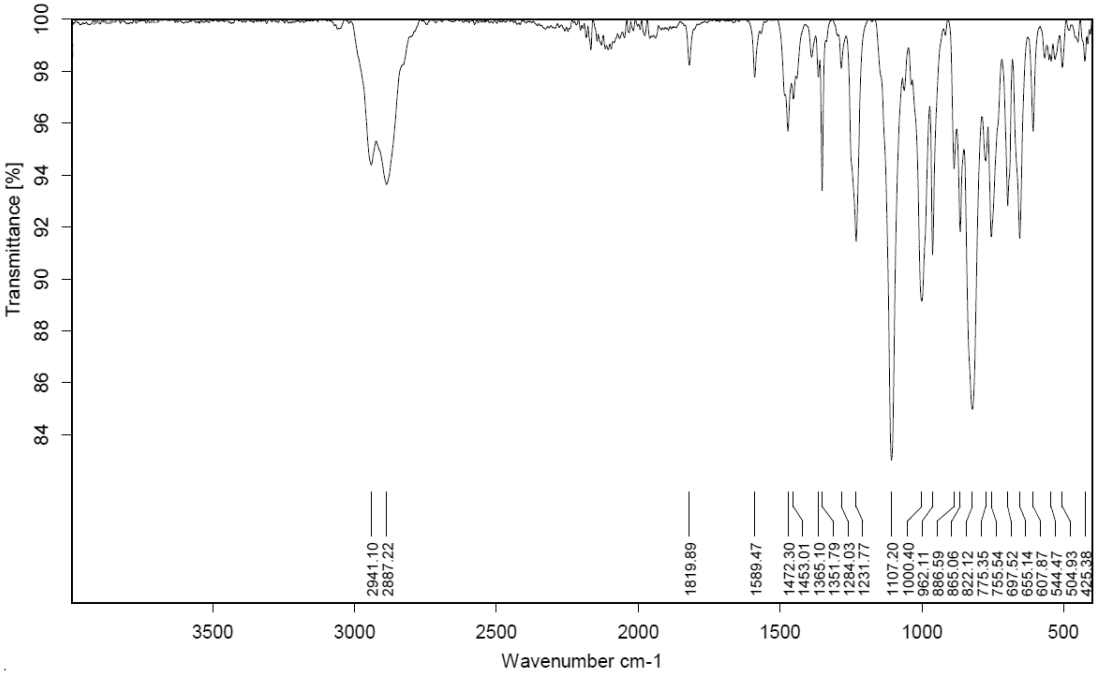

Figure S 13. IR spectrum of **[K{18c6}][Co(N(SiMe$_3$)$_2$)$_2$(η^2-PhCCPh)]** (**1**).

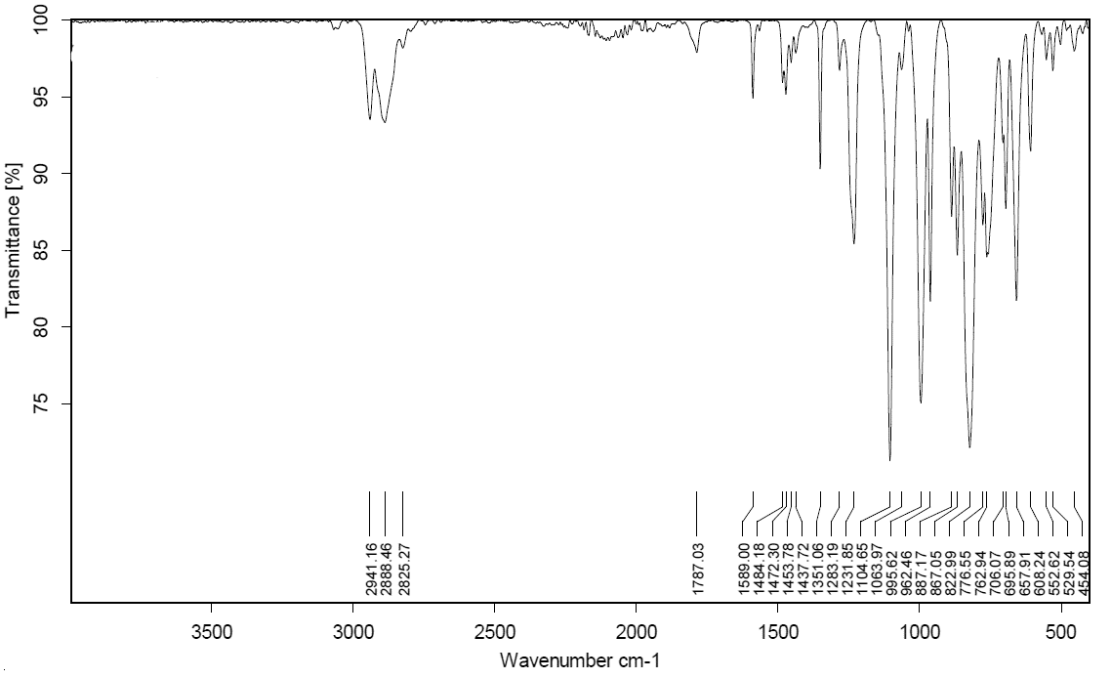

Figure S 14. IR spectrum of **[K{18c6}][Fe(N(SiMe$_3$)$_2$)$_2$(η^2-PhCCPh)]** (**2a**).

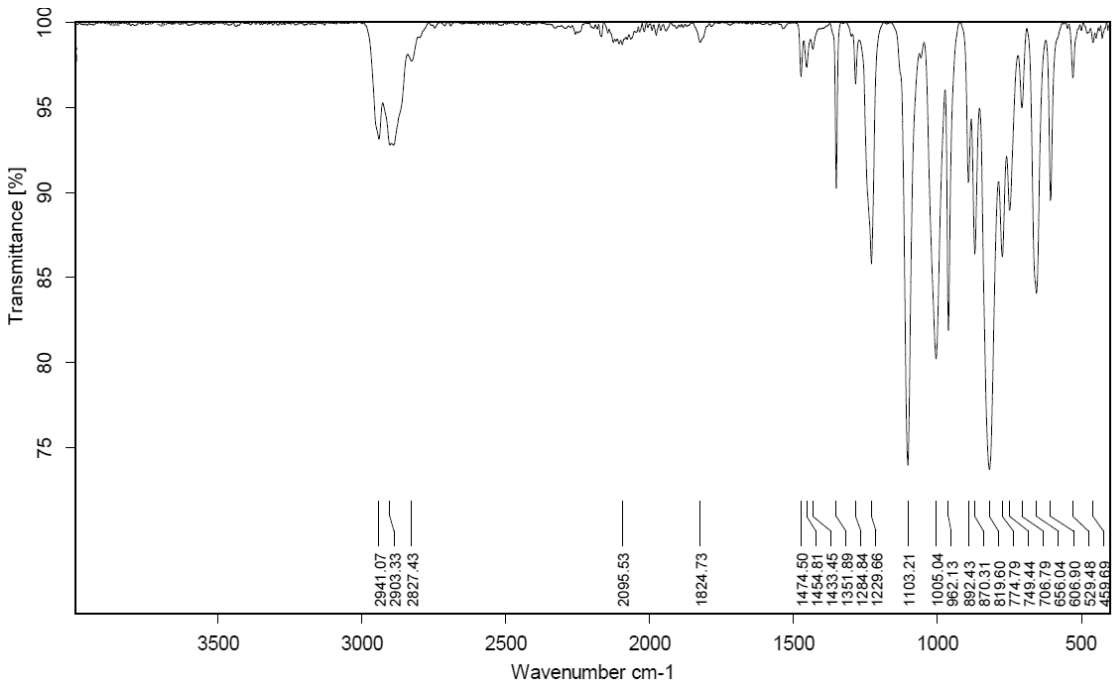

Figure S 15. IR spectrum of **[K{18c6}][Fe(N(SiMe$_3$)$_2$)$_2$(η^2-EtCCEt)]** (**2b**).

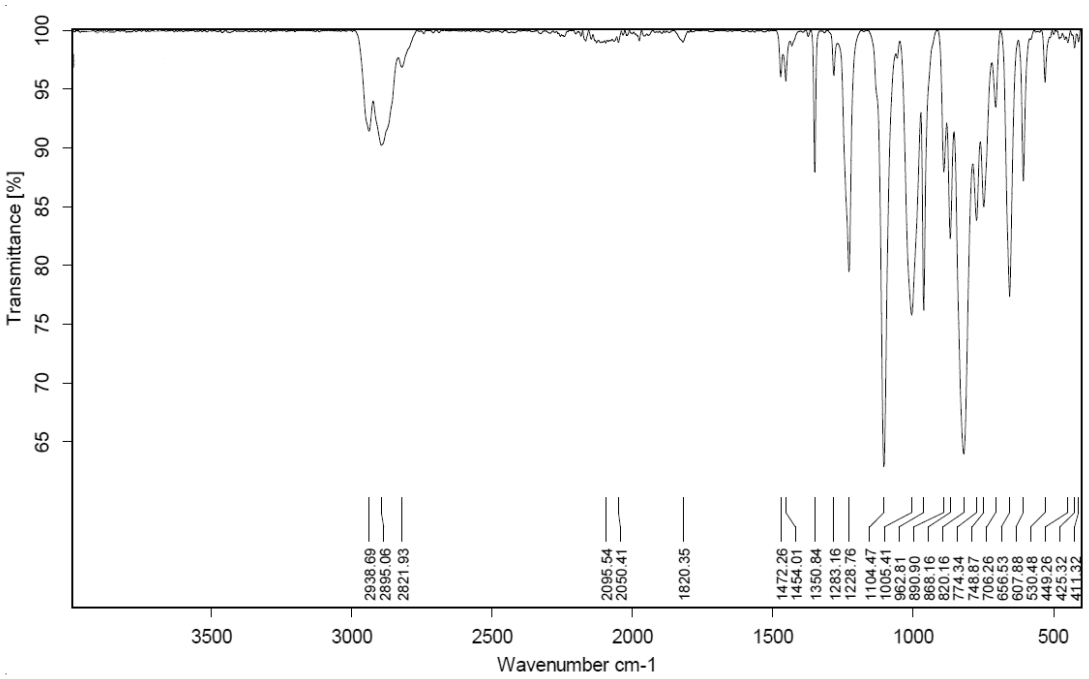

Figure S 16. IR spectrum of **[K{18c6}][Fe(N(SiMe$_3$)$_2$)$_2$(η^2-^{n}PrCC^{n}Pr)]** (**2c**).

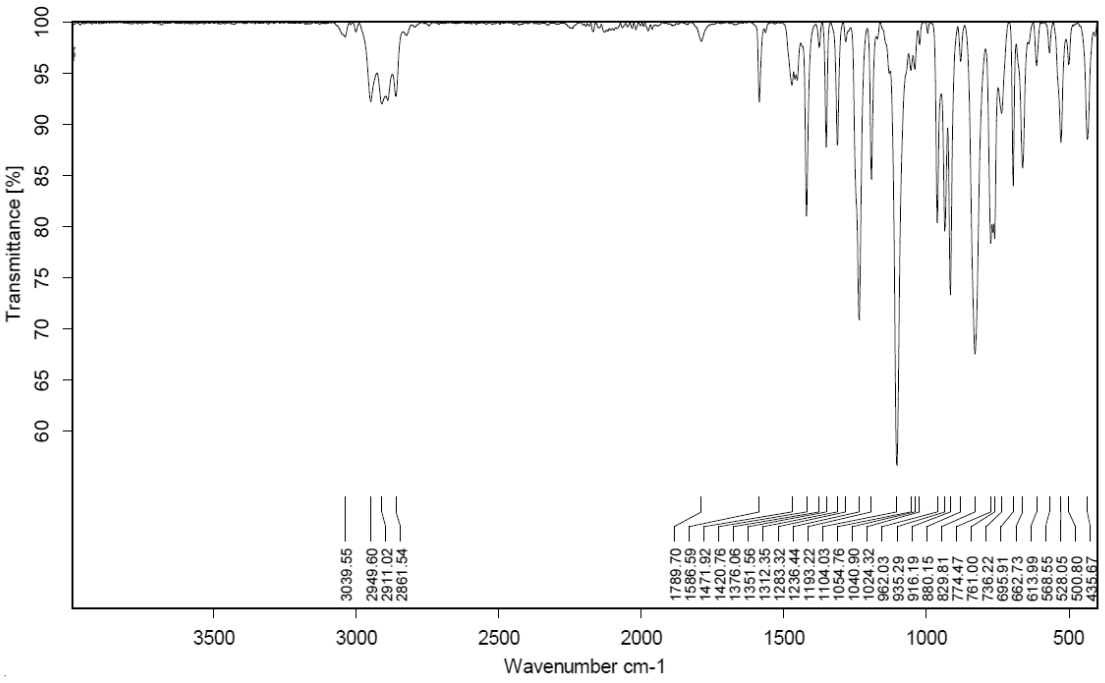

Figure S 17. IR spectrum of **[K{18c6}][Mn(N(Dipp)(SiMe$_3$))$_2$(η^2-PhCCPh)]** (**3a**).

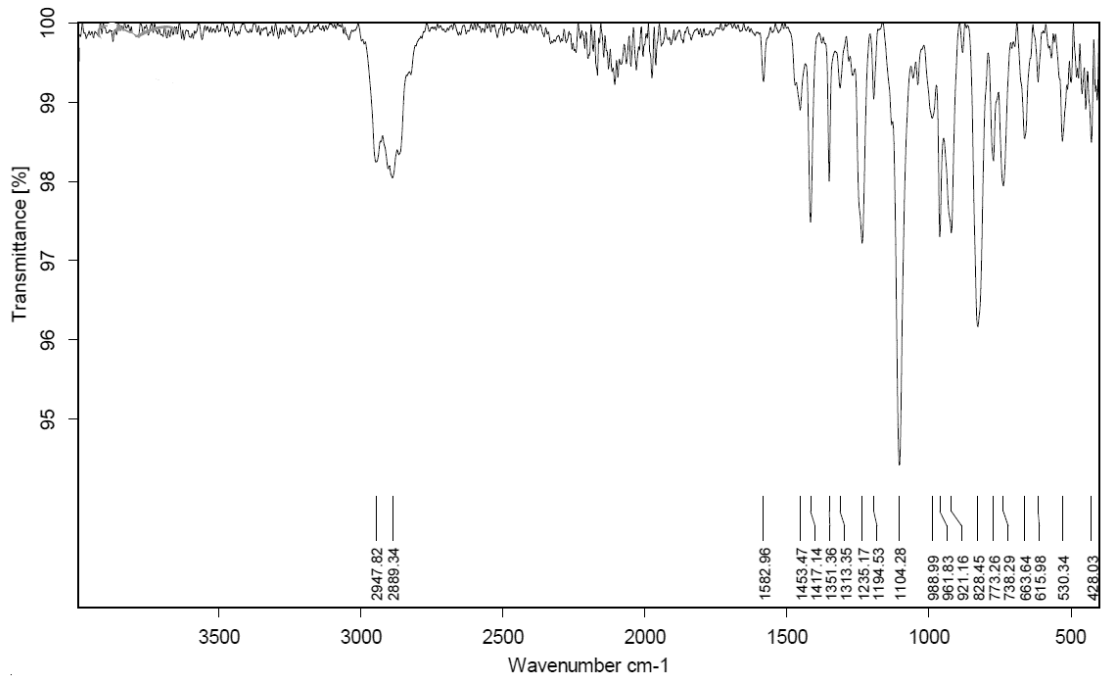

Figure S 18. IR spectrum of **[K{18c6}][Mn(N(Dipp)(SiMe$_3$))$_2$(η^2-EtCCEt)]** (**3b**).

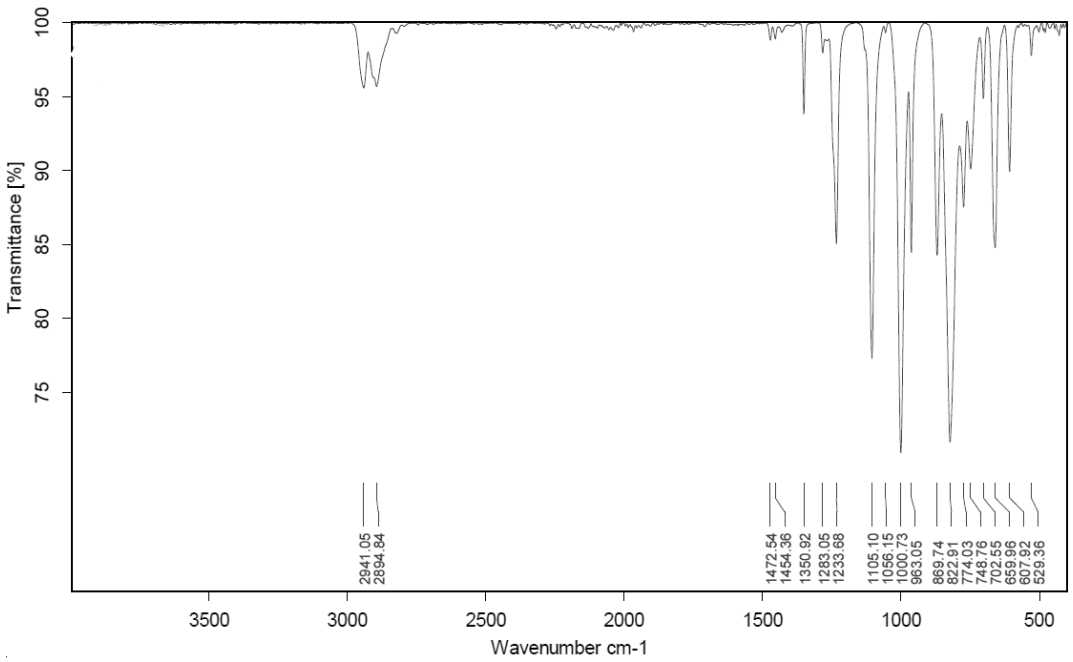

Figure S 19. IR spectrum of **[K{18c6}][Mn(N(SiMe$_3$)$_2$)$_3$]** (**5**).

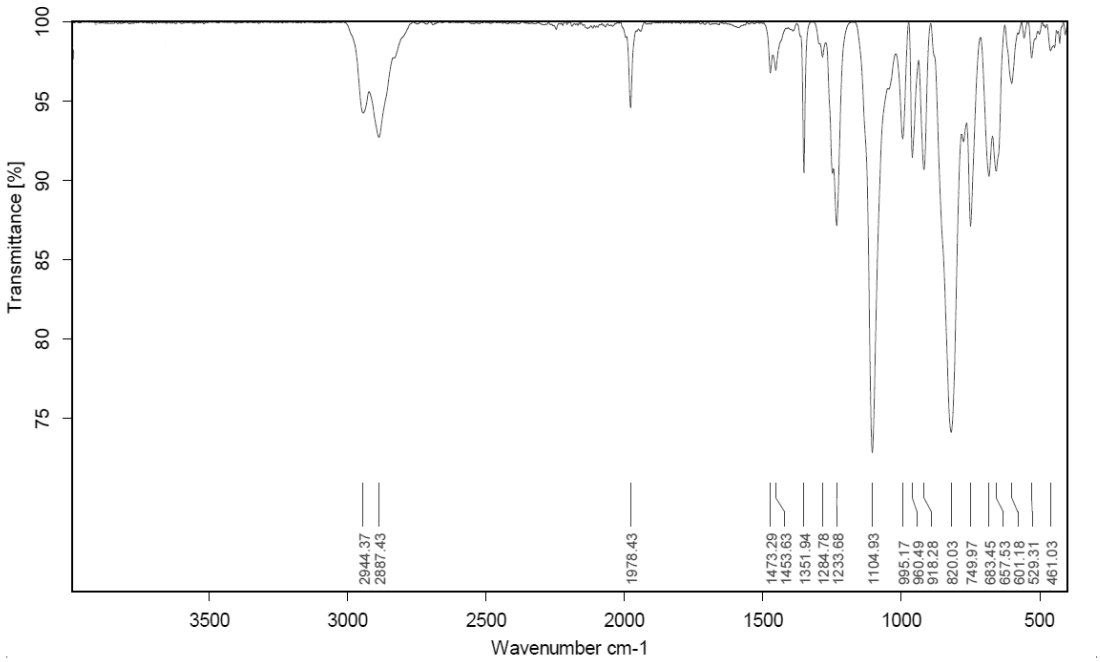

Figure S 20. IR spectrum of **[K{18c6}][Cr(N(SiMe$_3$)$_2$)$_2$(η^2-Me$_3$SiCCSiMe$_3$)]** (**6a**).

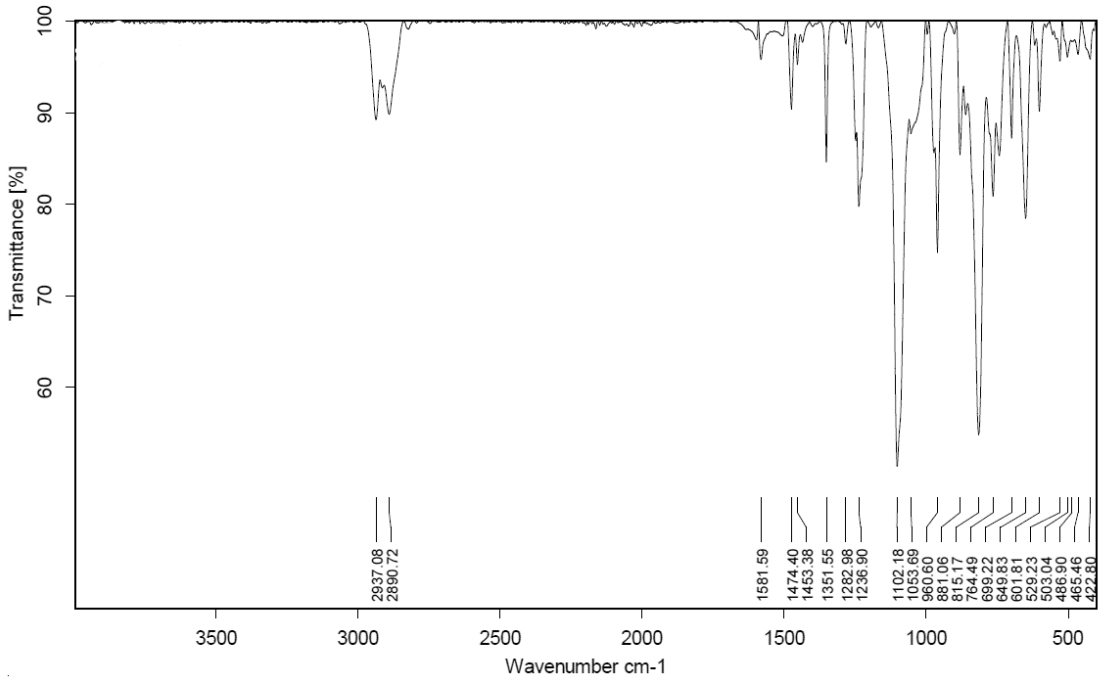

Figure S 21. IR spectrum of **[K{18c6}]$_2$[Cr$_2$(N(SiMe$_3$)$_2$)$_2$(η^2-N(SiMe$_3$)$_2$)(*μ*-*κ*^{1}(C):*κ*^{1}(C)-*η*^{2}-PhCCPh)]** (**6b**).

3. UV/Vis Spectra

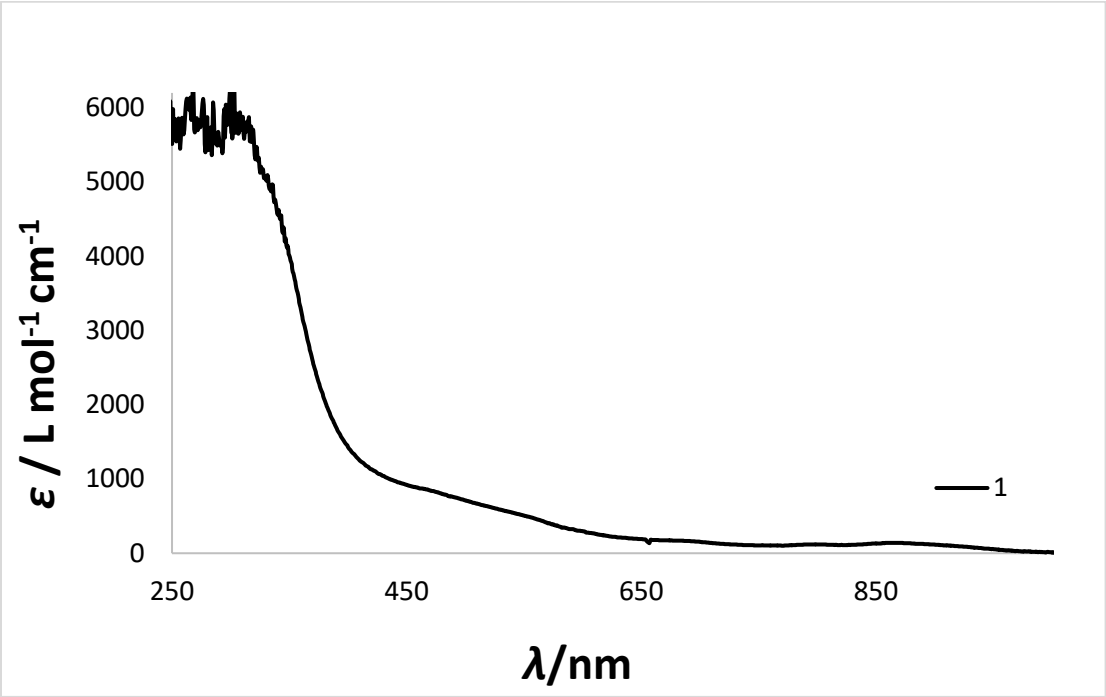

Figure S 22. UV/Vis spectrum of **[K{18c6}][Co(N(SiMe$_3$)$_2$)$_2$(η^2-PhCCPh)]** (**1**) in Et$_2$O.

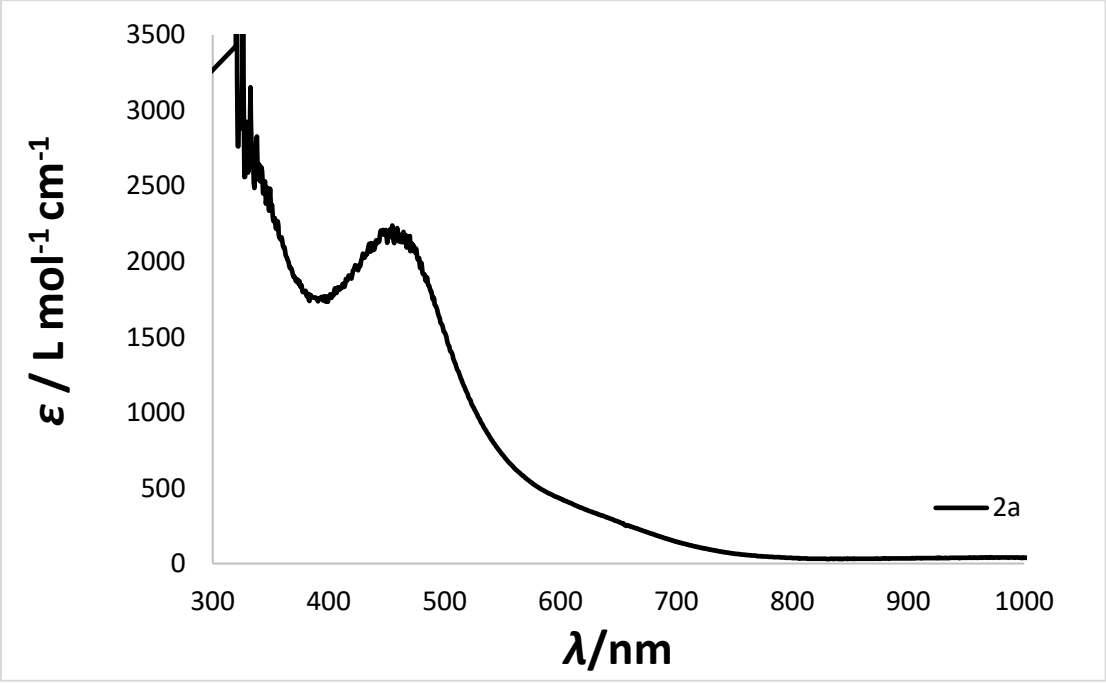

Figure S 23. UV/Vis spectrum of **[K{18c6}][Fe(N(SiMe$_3$)$_2$)$_2$(η^2-PhCCPh)]** (**2a**) in Et$_2$O.

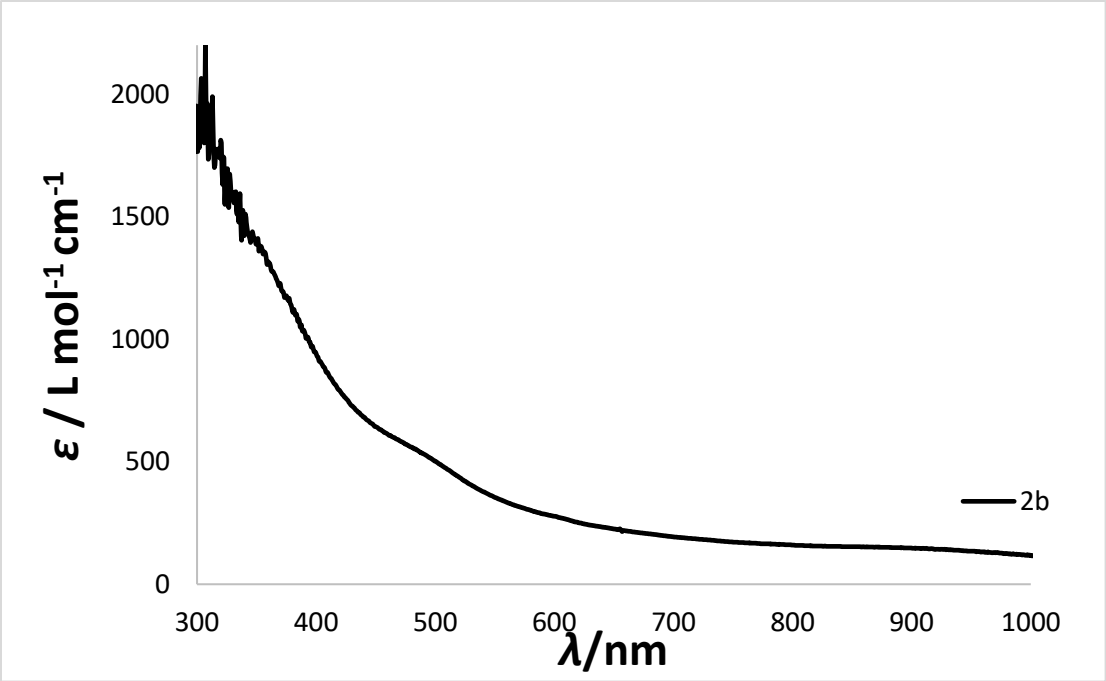

Figure S 24. UV/Vis spectrum of **[K{18c6}][Fe(N(SiMe$_3$)$_2$)$_2$(η^2-EtCCEt)]** (**2b**) in Et_2O.

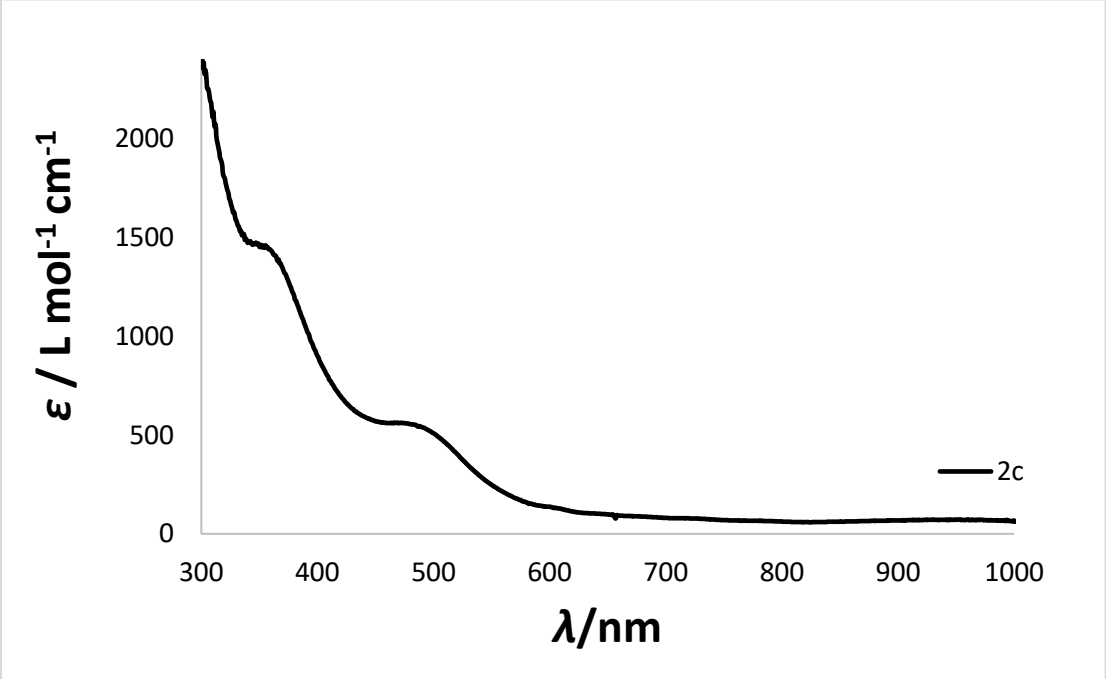

Figure S 25. UV/Vis spectrum of **[K{18c6}][Fe(N(SiMe$_3$)$_2$)$_2$(η^2-^{n}PrCC^{n}Pr)]** (**2c**) in Et_2O.

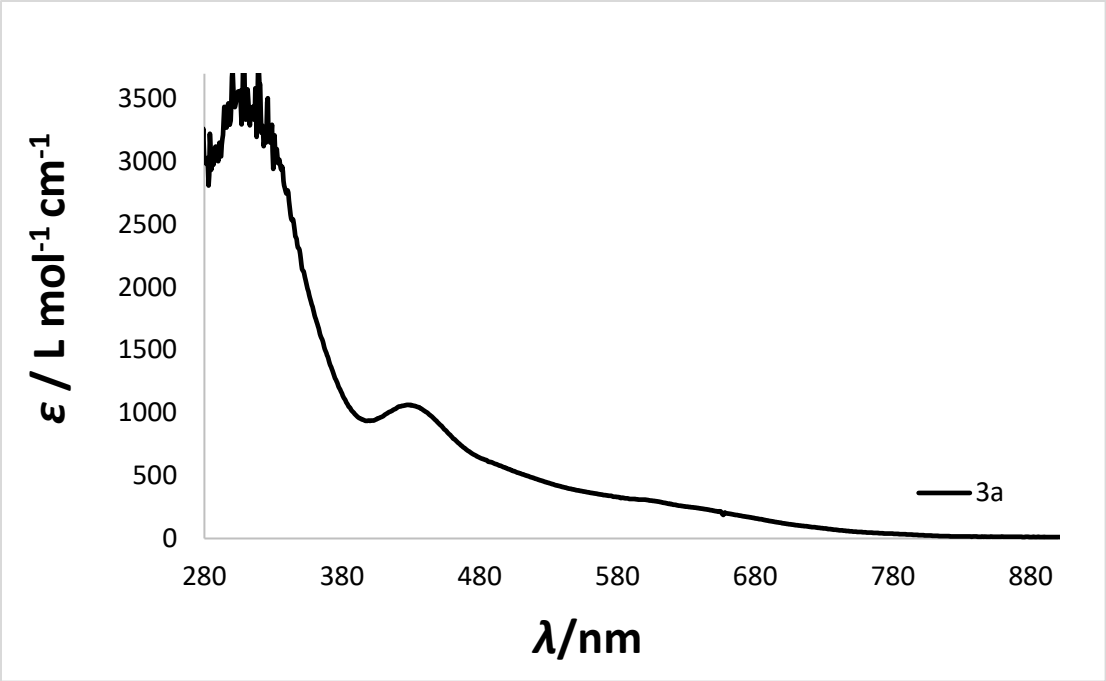

Figure S 26. UV/Vis spectrum of **[K{18c6}][Mn(N(Dipp)(SiMe$_3$))$_2$(η^2-PhCCPh)]** (**3a**) in THF.

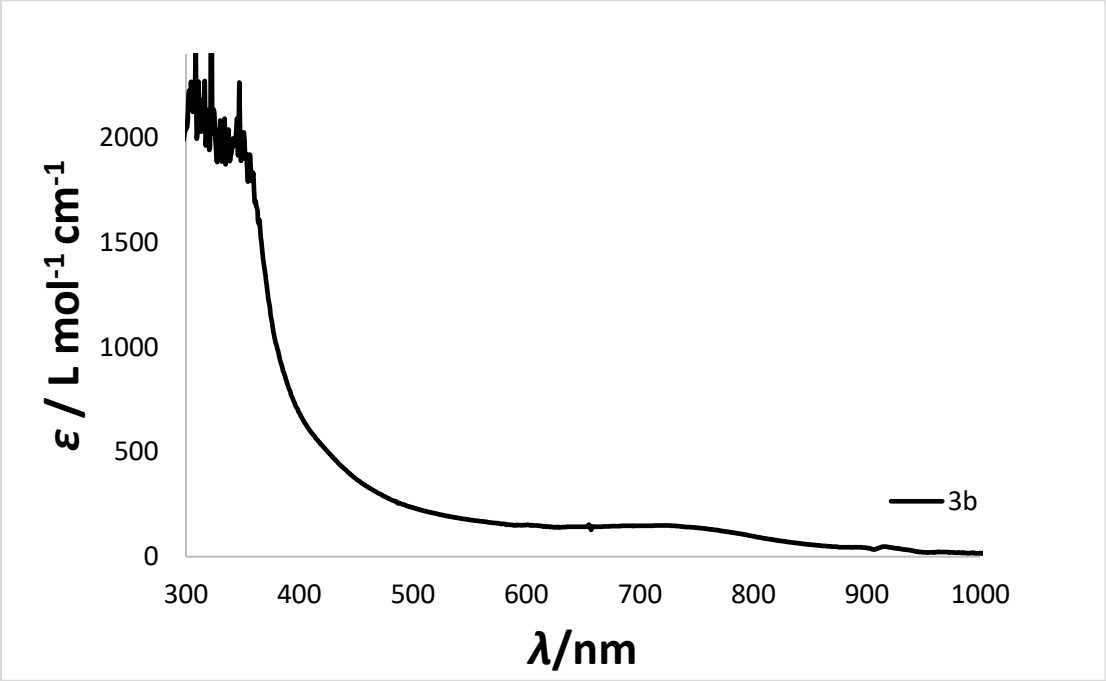

Figure S 27. UV/Vis spectrum of **[K{18c6}][Mn(N(Dipp)(SiMe$_3$))$_2$(η^2-EtCCEt)]** (**3b**) in THF.

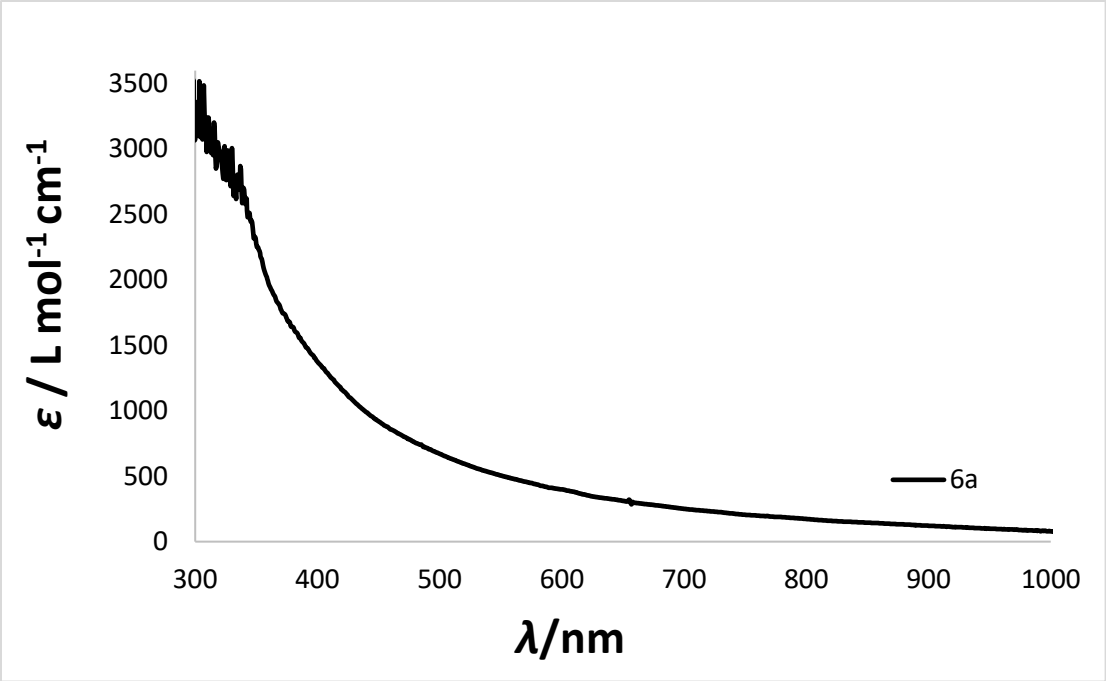

Figure S 28. UV/Vis spectrum of **[K{18c6}][Cr(N(SiMe$_3$)$_2$)$_2$(η^2-Me$_3$SiCCSiMe$_3$)]** (**6a**) in Et$_2$O.

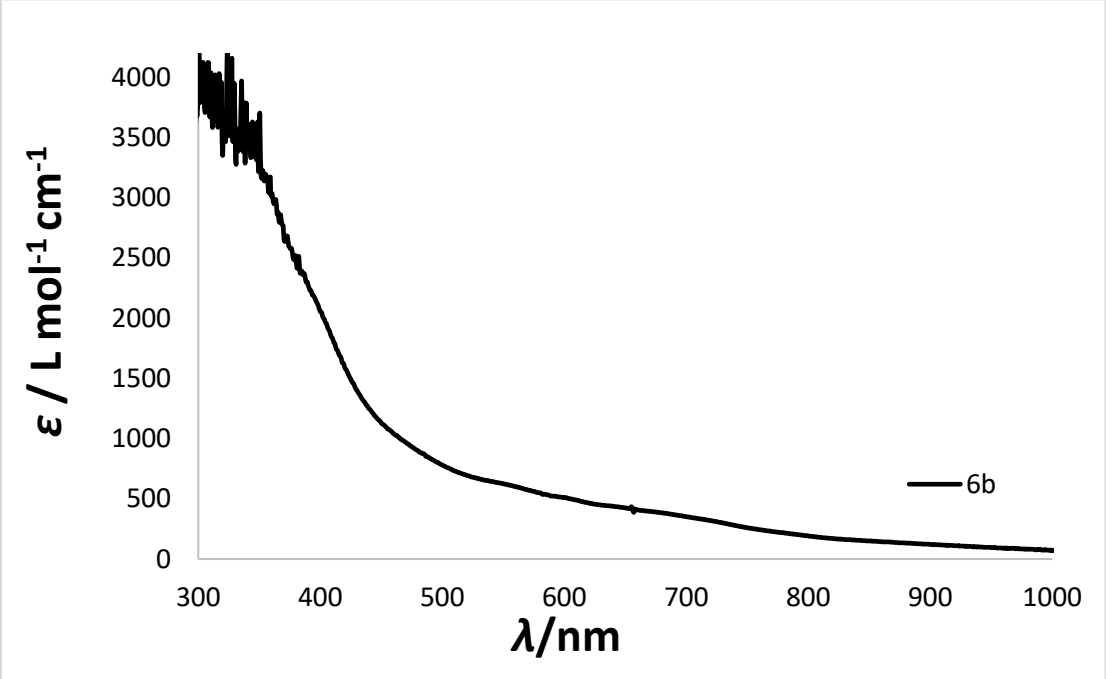

Figure S 29. UV/Vis spectrum of **[K{18c6}]$_2$[Cr$_2$(N(SiMe$_3$)$_2$)$_2$(η^2-N(SiMe$_3$)$_2$)(μ-κ^1(C):κ^1(C)-Me$_3$SiCCSiMe$_3$)]** (**6b**) in Et$_2$O.

4. X-Ray diffraction analysis and molecular structures

Table S 1. Crystal data and structure refinement for **1**. For **1** a disorder of one TMS group of the HMDS ligand.

Identification code	1_Co_tolane
Empirical formula	$C_{164}H_{310}Co_4K_4N_8O_{27}Si_{16}$
Formula weight	3667.74
Temperature / *K*	100.0
Crystal system	triclinic
Space group	P-1
a/Å	11.2698(5)
b/Å	11.6482(5)
c/Å	42.5344(18)
α/°	84.828(2)
β/°	86.155(2)
γ/°	66.747(2)
Volume / Å^3	5106.2(4)
Z	1
ρ_{calc} g/cm^3	1.193
μ/mm^{-1}	0.555
F(000)	1974.0
Crystal size / mm^3	0.336 × 0.132 × 0.062
Radiation	MoKα (λ = 0.71073)
2Θ range for data collection /°	4.296 to 49.998
Index ranges	-13 ≤ h ≤ 13, -13 ≤ k ≤ 13, -50 ≤ l ≤ 50
Reflections collected	78240
Independent reflections	17974 [R_{int} = 0.0861, R_{sigma} = 0.1074]
Data/restraints/parameters	17974/3/1078
Goodness-of-fit on F^2	1.216
Final *R* indexes [I>=2σ (I)]	R_1 = 0.0958, wR_2 = 0.1638
Final *R* indexes [all data]	R_1 = 0.1423, wR_2 = 0.1734
Largest diff. peak/hole / e Å^{-3}	1.70/-0.61

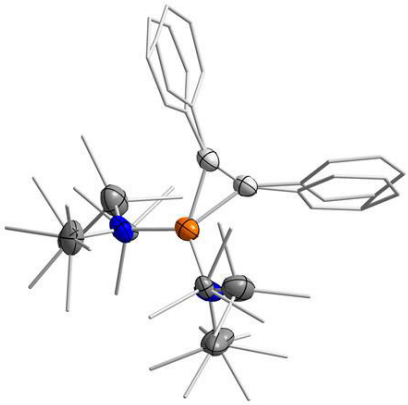

Figure S 30. Depiction of the disorder found for of **2a**. All H atoms are omitted. The disordered tolane ligand with similar bond metrics is twisted by approx. 7° around the carbon-ethylene axis. The hmds ligands and the cation ([K{18c6}]) are disordered too.

Table S 2. Crystal data and structure refinement for **2a**.

Identification code	2a_fe_tolane
Empirical formula	$C_{38}H_{70}FeKN_2O_6Si_4$
Formula weight	858.27
Temperature / *K*	100.0
Crystal system	monoclinic
Space group	C2/c
a/Å	18.583(4)
b/Å	17.246(2)
c/Å	16.431(3)
α/°	90
β/°	114.581(14)
γ/°	90
Volume / Å^3	4788.4(16)
Z	4
ρ_{calc} g/cm^3	1.191
μ/mm^{-1}	4.587
F(000)	1844.0
Crystal size / mm^3	0.213 × 0.208 × 0.186
Radiation	CuKα (λ = 1.54186)
2Θ range for data collection /°	7.324 to 133.958
Index ranges	-19 ≤ h ≤ 22, -10 ≤ k ≤ 20, -19 ≤ l ≤ 19
Reflections collected	22822
Independent reflections	4266 [R_{int} = 0.0603, R_{sigma} = 0.0750]
Data/restraints/parameters	4266/489/436
Goodness-of-fit on F^2	0.835
Final *R* indexes [I>=2σ (I)]	R_1 = 0.0435, wR_2 = 0.0820
Final *R* indexes [all data]	R_1 = 0.0884, wR_2 = 0.0908
Largest diff. peak/hole / e Å^{-3}	0.20/-0.27

Table S 3. Crystal data and structure refinement for **2b**. For **2b** a disorder of one methyl group of the hexyne ligand is found.

Identification code	2b_fe_hexyne
Empirical formula	$C_{30}H_{70}FeKN_2O_6Si_4$
Formula weight	762.19
Temperature / *K*	100.0
Crystal system	triclinic
Space group	P-1
a/Å	9.3374(14)
b/Å	14.817(2)
c/Å	16.695(3)
α/°	89.991(12)
β/°	100.494(12)
γ/°	103.488(12)
Volume / Å^3	2206.3(6)
Z	2
ρ_{calc} g/cm^3	1.147
μ/mm^{-1}	0.580
F(000)	826.0
Crystal size / mm^3	0.457 × 0.327 × 0.252
Radiation	MoKα (λ = 0.71073)
2Θ range for data collection /°	4.566 to 50
Index ranges	-10 ≤ h ≤ 11, -17 ≤ k ≤ 17, -19 ≤ l ≤ 19
Reflections collected	14468
Independent reflections	7731 [R_{int} = 0.0763, R_{sigma} = 0.0661]
Data/restraints/parameters	7731/125/453
Goodness-of-fit on F^2	1.089
Final *R* indexes [I>=2σ (I)]	R_1 = 0.0873, wR_2 = 0.2503
Final *R* indexes [all data]	R_1 = 0.0933, wR_2 = 0.2568
Largest diff. peak/hole / e Å^{-3}	2.46/-0.96

Table S 4. Crystal data and structure refinement for **2c**.

Identification code	2c_fe_octyne
Empirical formula	$C_{32}H_{74}FeKN_2O_6Si_4$
Formula weight	790.24
Temperature / *K*	100.0
Crystal system	triclinic
Space group	P-1
a/Å	10.473(5)
b/Å	11.775(4)
c/Å	19.255(10)
α/°	79.03(3)
β/°	79.55(4)
γ/°	79.35(3)
Volume / $Å^3$	2264.6(17)
Z	2
ρ_{calc} g/cm^3	1.159
μ/mm^{-1}	0.568
F(000)	858.0
Crystal size / mm^3	0.275 × 0.215 × 0.186
Radiation	MoKα (λ = 0.71073)
2Θ range for data collection /°	4.472 to 53.588
Index ranges	-13 ≤ h ≤ 13, -14 ≤ k ≤ 14, -24 ≤ l ≤ 24
Reflections collected	24835
Independent reflections	9569 [R_{int} = 0.0388, R_{sigma} = 0.0336]
Data/restraints/parameters	9569/0/432
Goodness-of-fit on F^2	1.047
Final *R* indexes [I>=2σ (I)]	R_1 = 0.0359, wR_2 = 0.0921
Final *R* indexes [all data]	R_1 = 0.0464, wR_2 = 0.0959
Largest diff. peak/hole / e $Å^{-3}$	0.47/-0.43

Table S 5. Crystal data and structure refinement for **3a**.

Identification code	3a_mn_tolane
Empirical formula	$C_{64}H_{102}KMnN_2O_8Si_2$
Formula weight	1177.69
Temperature / *K*	100.0
Crystal system	triclinic
Space group	P-1
a/Å	11.0549(8)
b/Å	13.4879(10)
c/Å	22.1575(16)
α/°	83.805(2)
β/°	88.175(2)
γ/°	88.092(2)
Volume / Å^3	3281.4(4)
Z	2
ρ_{calc} g/cm^3	1.192
μ/mm^{-1}	0.353
F(000)	1272.0
Crystal size / mm^3	0.398 × 0.387 × 0.056
Radiation	MoKα (λ = 0.71073)
2Θ range for data collection /°	4.708 to 50.168
Index ranges	-13 ≤ h ≤ 13, -16 ≤ k ≤ 16, -26 ≤ l ≤ 26
Reflections collected	74065
Independent reflections	11615 [R_{int} = 0.1250, R_{sigma} = 0.0798]
Data/restraints/parameters	11615/0/720
Goodness-of-fit on F^2	1.010
Final *R* indexes [I>=2σ (I)]	R_1 = 0.0516, wR_2 = 0.0851
Final *R* indexes [all data]	R_1 = 0.0984, wR_2 = 0.0935
Largest diff. peak/hole / e Å^{-3}	0.32/-0.34

Table S 6. Crystal data and structure refinement for **3b**. For **3b** a disorder of one methyl group of the hexyne ligand is found.

Identification code	3b_mn_hexyne
Empirical formula	$C_{56}H_{102}KMnN_2O_8Si_2$
Formula weight	1081.61
Temperature / *K*	100.0
Crystal system	monoclinic
Space group	$P2_1/c$
a/Å	27.8937(19)
b/Å	17.8243(12)
c/Å	26.7359(18)
α/°	90
β/°	110.002(2)
γ/°	90
Volume / Å^3	12490.9(15)
Z	8
ρ_{calc} g/cm^3	1.150
μ/mm^{-1}	0.365
F(000)	4704.0
Crystal size / mm^3	0.475 × 0.324 × 0.015
Radiation	MoKα (λ = 0.71073)
2Θ range for data collection /°	4.302 to 50
Index ranges	-33 ≤ h ≤ 33, -21 ≤ k ≤ 21, -31 ≤ l ≤ 31
Reflections collected	250504
Independent reflections	21975 [R_{int} = 0.1111, R_{sigma} = 0.0525]
Data/restraints/parameters	21975/1003/1168
Goodness-of-fit on F^2	1.044
Final *R* indexes [I>=2σ (I)]	R_1 = 0.0679, wR_2 = 0.1568
Final *R* indexes [all data]	R_1 = 0.1064, wR_2 = 0.1727
Largest diff. peak/hole / e Å^{-3}	1.19/-0.99

Table S 7. Crystal data and structure refinement for **4a**.

Identification code	4a_mn_btmsa
Empirical formula	$C_{38}H_{96}KMn_2N_3O_6Si_8$
Formula weight	1064.87
Temperature / *K*	100.0
Crystal system	triclinic
Space group	P-1
a/Å	9.8792(4)
b/Å	16.2013(7)
c/Å	19.3380(8)
α/°	85.370(2)
β/°	89.5430(10)
γ/°	75.2070(10)
Volume / Å^3	2982.5(2)
Z	2
ρ_{calc} g/cm^3	1.186
μ/mm^{-1}	0.692
F(000)	1148.0
Crystal size / mm^3	0.37 × 0.19 × 0.09
Radiation	MoKα (λ = 0.71073)
2Θ range for data collection /°	4.734 to 50.656
Index ranges	-11 ≤ h ≤ 11, -19 ≤ k ≤ 19, -23 ≤ l ≤ 23
Reflections collected	69931
Independent reflections	10864 [R_{int} = 0.0338, R_{sigma} = 0.0218]
Data/restraints/parameters	10864/292/720
Goodness-of-fit on F^2	1.067
Final *R* indexes [I>=2σ (I)]	R_1 = 0.0383, wR_2 = 0.0800
Final *R* indexes [all data]	R_1 = 0.0444, wR_2 = 0.0825
Largest diff. peak/hole / e Å^{-3}	1.71/-0.90

Table S 8. Crystal data and structure refinement for **4b**. Additionally an 18c6 molecule crystallizes between the two cations ([K {18c6}]).

Identification code	4b_mn_tolane
Empirical formula	$C_{88}H_{164}K_2Mn_2N_4O_{18}Si_8$
Formula weight	1979.02
Temperature / *K*	100.0
Crystal system	triclinic
Space group	P-1
a/Å	15.599(5)
b/Å	20.269(6)
c/Å	20.674(6)
α/°	99.02(2)
β/°	110.63(2)
γ/°	107.99(2)
Volume / Å^3	5553(3)
Z	2
ρ_{calc} g/cm^3	1.184
μ/mm^{-1}	0.447
F(000)	2128.0
Crystal size / mm^3	0.448 × 0.247 × 0.215
Radiation	MoKα (λ = 0.71073)
2Θ range for data collection /°	2.616 to 50
Index ranges	-18 ≤ h ≤ 18, -24 ≤ k ≤ 24, -24 ≤ l ≤ 24
Reflections collected	42309
Independent reflections	19527 [R_{int} = 0.1125, R_{sigma} = 0.0955]
Data/restraints/parameters	19527/1888/1123
Goodness-of-fit on F^2	1.042
Final *R* indexes [I>=2σ (I)]	R_1 = 0.0870, wR_2 = 0.2364
Final *R* indexes [all data]	R_1 = 0.1085, wR_2 = 0.2483
Largest diff. peak/hole / e Å^{-3}	1.30/-0.77

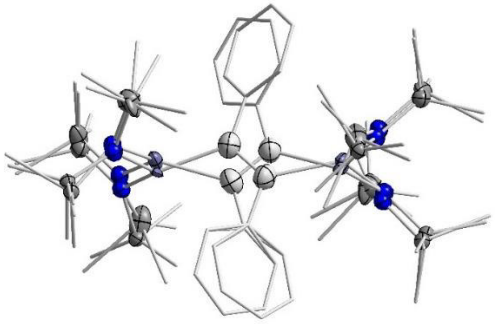

Figure S 31. Depiction of the disorder found for of **4c**. All H atoms are omitted. The disorder of dianion was divided into two parts, part 1 with 67% and part 2 with 33% occupation. Additionally a cation ([K18c6]) is disordered. The substrate tolane is disordered too, but the disorder have an occupation of 50%.

Table S 9. Crystal data and structure refinement for **4c**. Three molecules of Et_2O were squeezed.

Identification code	4c_mn_tolane
Empirical formula	$C_{31}H_{65}KMnN_2O_6Si_4$
Formula weight	767.37
Temperature / *K*	100.0
Crystal system	monoclinic
Space group	C2/c
a/Å	26.0194(17)
b/Å	13.0449(9)
c/Å	30.743(2)
α/°	90
β/°	97.801(2)
γ/°	90
Volume / Å^3	10338.1(12)
Z	8
ρ_{calc} g/cm^3	0.986
μ/mm^{-1}	0.460
F(000)	3300.0
Crystal size / mm^3	0.7 × 0.2 × 0.1
Radiation	MoKα (λ = 0.71073)
2Θ range for data collection /°	5.16 to 50
Index ranges	-30 ≤ h ≤ 30, -15 ≤ k ≤ 15, -36 ≤ l ≤ 36
Reflections collected	107973
Independent reflections	9091 [R_{int} = 0.1362, R_{sigma} = 0.0646]
Data/restraints/parameters	9091/702/811
Goodness-of-fit on F^2	1.051
Final *R* indexes [I>=2σ (I)]	R_1 = 0.0659, wR_2 = 0.1367
Final *R* indexes [all data]	R_1 = 0.1108, wR_2 = 0.1494
Largest diff. peak/hole / e Å^{-3}	0.38/-0.34

Table S 10. Crystal data and structure refinement for **4d**. The structure was refined as an inversion twin, twin ratio refined to 0.08(3). Three molecules of thf was squeezed. Two thf molecules were removed with the program squeeze because they are not fully occupied and they are slightly disordered. The third thf molecule war removed with program squeeze too, because it is disordered at a special position and on the symmetry element.

Identification code	4d_mn_tolane
Empirical formula	$C_{76}H_{75}KMnO_8$
Formula weight	1210.40
Temperature / *K*	100.0
Crystal system	orthorhombic
Space group	$P2_12_12$
a/Å	24.6553(12)
b/Å	28.1217(13)
c/Å	10.7076(5)
α/°	90
β/°	90
γ/°	90
Volume / Å^3	7424.1(6)
Z	4
ρ_{calc} g/cm^3	1.083
μ/mm^{-1}	0.283
F(000)	2556.0
Crystal size / mm^3	0.516 × 0.178 × 0.09
Radiation	MoKα (λ = 0.71073)
2Θ range for data collection /°	4.392 to 50
Index ranges	-29 ≤ h ≤ 29, -33 ≤ k ≤ 33, -12 ≤ l ≤ 12
Reflections collected	74212
Independent reflections	13067 [R_{int} = 0.0621, R_{sigma} = 0.0429]
Data/restraints/parameters	13067/1262/738
Goodness-of-fit on F^2	1.061
Final *R* indexes [I>=2σ (I)]	R_1 = 0.0636, wR_2 = 0.1453
Final *R* indexes [all data]	R_1 = 0.0690, wR_2 = 0.1479
Largest diff. peak/hole / e Å^{-3}	0.56/-0.49
Flack parameter	0.08(3)

Table S 11. Crystal data and structure refinement for **6a**.

Identification code	6a_cr_btmsa
Empirical formula	$C_{36}H_{88}CrKN_2O_7Si_6$
Formula weight	920.72
Temperature / *K*	100.0
Crystal system	triclinic
Space group	P-1
a/Å	14.928(4)
b/Å	20.242(5)
c/Å	27.765(7)
α/°	93.95(2)
β/°	96.09(2)
γ/°	92.57(2)
Volume / Å^3	8311(4)
Z	6
ρ_{calc} g/cm^3	1.104
μ/mm^{-1}	0.449
F(000)	3006.0
Crystal size / mm^3	0.392 × 0.188 × 0.174
Radiation	MoKα (λ = 0.71073)
2Θ range for data collection /°	2.748 to 50
Index ranges	-17 ≤ h ≤ 17, -24 ≤ k ≤ 24, -33 ≤ l ≤ 32
Reflections collected	55223
Independent reflections	28960 [R_{int} = 0.0717, R_{sigma} = 0.0940]
Data/restraints/parameters	28960/150/1498
Goodness-of-fit on F^2	1.035
Final *R* indexes [I>=2σ (I)]	R_1 = 0.0784, wR_2 = 0.2265
Final *R* indexes [all data]	R_1 = 0.1378, wR_2 = 0.2541
Largest diff. peak/hole / e Å^{-3}	0.96/-0.56

Table S 12. Crystal data and structure refinement for **6b**.

Identification code	6b_Cr_tolane
Empirical formula	$C_{44}H_{88}Cr_2KN_3O_6Si_6$
Formula weight	1066.81
Temperature / *K*	100.0
Crystal system	triclinic
Space group	P-1
a/Å	11.625(2)
b/Å	12.418(5)
c/Å	21.366(6)
α/°	92.29(3)
β/°	102.78(2)
γ/°	106.98(2)
Volume / Å^3	2858.9(15)
Z	2
ρ_{calc} g/cm^3	1.239
μ/mm^{-1}	0.622
F(000)	1144.0
Crystal size / mm^3	0.245 × 0.232 × 0.15
Radiation	MoKα (λ = 0.71073)
2Θ range for data collection /°	4.744 to 53.65
Index ranges	-12 ≤ h ≤ 14, -15 ≤ k ≤ 15, -26 ≤ l ≤ 26
Reflections collected	26880
Independent reflections	12044 [R_{int} = 0.0451, R_{sigma} = 0.0662]
Data/restraints/parameters	12044/0/577
Goodness-of-fit on F^2	0.914
Final *R* indexes [I>=2σ (I)]	R_1 = 0.0379, wR_2 = 0.0871
Final *R* indexes [all data]	R_1 = 0.0667, wR_2 = 0.0915
Largest diff. peak/hole / e Å^{-3}	0.57/-0.36

5. Calculations

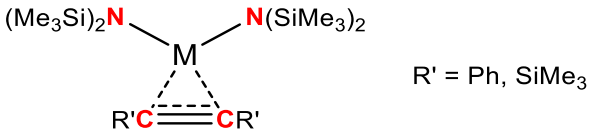

Table S 13. Deviation of calculated structural parameters and unscaled vibrational frequencies averaged for **1**, **2a**, **4b** and **6a** with the values obtained from the solid state structures and IR spectra.

	MC	**MN**	**CC**	**Average**	**R'CC**	**CC stretch**
	in [Å]	in [Å]	in [Å]	in [Å]	in [°]	in [cm^{-1}]
BP86	0.04466104	0.04488052	0.03417833	0.04123997	1.0855	100.75
PBE0	0.01533104	0.01504552	0.02117833	0.01718497	2.168	145
B3LYP	0.01708104	0.01292052	0.02117833	0.01705997	1.843	128.25
B3PW91	0.02891104	0.02325552	0.02192833	0.0246983	1.8805	141.25
PBEh-3c	0.02071396	0.01411427	0.02091333	0.01858052	1.46575	164
B97-3c	0.04341104	0.02988052	0.33751583	0.1369358	1.45325	105.5

Table S 14. Comparison of structural parameters of **2a** as obtained without or with diffuse functions (ma-).

	MC	**MN**	**CC**	**R'CC**	**CC stretch**
	in [Å]	in [Å]	in [Å]	in [°]	in [cm^{-1}]
ma-def2-SVP	1.916	1.945	1.320	149.1	1733
def2-SVP	1.955	1.990	1.300	148.0	1879
experimental	1.947	1.973	1.269	151.3	1787

Table S 15. Composition (reduced Löwdin) of IBOs as calculated with B3LYP.

B3LYP											
[Mn]	**C(alkyne)**	**Mn**	**Mn %**	**Avg. %**	**further d-electrons**	**All d-electrons**	**C(d,f)**	**C(s)**	**C(p)**	**Hybridi-zation $s^x p^3$**	**Avg.**
α IBO	21.2	72.7	77.4	77.4	4	4.8	2.9	1	7.4	0.40540	
							3	0.8	6.1	0.39344	0.39942
β IBO	53.3	27	33.6				0.8	9	43.5	0.62069	
	53	21.4	28.8	31.2			0.9	8.6	43.5	0.59310	0.60689

[Fe]	C(alkyne)	Fe	Fe %	Avg. %	further d-electrons	All d-electrons	C(d,f)	C(s)	C(p)	Hybridization s^xp^3	Avg.
α IBO	17	74.2	81.2	81.2	5	5.8	2.6	0.6	5.2	0.34615	
							2.7	0.6	5.3	0.33962	0.34288
β IBO	49.1	31.4	39.0				0.9	7.3	40.9	0.53545	
	49.2	31.3	38.9	38.9			0.9	7.4	40.9	0.54278	0.5391
[Co]	C(alkyne)	Co	Co %	Avg. %	further d-electrons	All d-electrons	C(d,f)	C(s)	C(p)	Hybridization s^xp^3	Avg.
α IBO	16.7	77.8	82.3	82.3	6	6.8	2.4	0.6	5.3	0.33962	
							2.5	0.6	5.3	0.33962	0.33962
β IBO	45.4	35.7	44.0				0.8	6.7	37.9	0.53034	
	44.3	36.6	45.2	44.6			0.7	5.9	37.7	0.46949	0.49992
[Cr^{TMS}]	C(alkyne)	Cr	Cr %	Avg. %	further d-electrons	All d-electrons	C(d,f)	C(s)	C(p)	Hybridization s^xp^3	Avg.
α IBO	39.5	44.4	52.9				0.7	2.3	36.5	0.18904	
	45.9	31	40.3	46.6	3	3.8	0.1	4.2	41.6	0.30288	0.24596
β IBO	53.8	26.4	32.9				0.4	11.2	42.2	0.79620	
	54.3	26.3	32.6	32.8			0.4	11.8	42.1	0.84085	0.81853
[Cr^{Ph}]	C(alkyne)	Cr	Cr %	Avg. %	further d-electrons	All d-electrons	C(d,f)	C(s)	C(p)	Hybridization s^xp^3	Avg.
α IBO	44.5	38.8	46.6				0.7	8.8	35	0.75428	
	48	31	39.2	42.9	3	3.8	0.3	9.1	38.6	0.70725	0.7308
β IBO	54.4	25.2	31.7				0.6	10.5	43.3	0.72748	
	54.1	27.4	33.6	32.6			0.8	10.5	42.8	0.73598	0.73173
Ni_alkyne	C(alkyne)	Ni	Ni %	Avg. %	further d-electrons	All d-electrons	C(d,f)	C(s)	C(p)	Hybridization s^xp^3	Avg.
	23	69.3	75.1	75.1	8	9.6	3.1	1	7.7	0.3896	
							3.2	0.9	7.1	0.38028	0.38495

Table S 16. Composition (reduced Löwdin) of IBOs as calculated with BP86.

BP86											
[Mn]	**C(alkyne)**	**Mn**	**Mn %**	**Avg. %**	**further d-electrons**	**All d-electrons**	**C(d,f)**	**C(s)**	**C(p)**	**Hybridi-zation s^xp^3**	**Avg.**
α IBO	25.2	67.4	72.7	72.7	4	4.7	2.7	1.8	12.8	0.421875	
							3.5	0.6	3.8	0.473684	0.44778
β IBO	50.6	29.8	37.0				0.6	8.7	41.3	0.631961	
	50.2	28.6	36.2	36.7			0.7	8.3	41.2	0.604369	0.618165
[Fe]	**C(alkyne)**	**Fe**	**Fe %**	**Avg. %**	**further d-electrons**	**All d-electrons**	**C(d,f)**	**C(s)**	**C(p)**	**Hybridi-zation s^xp^3**	**Avg.**
α IBO	20.1	74	78.6	78.6	5	5.8	3	0.8	6.3	0.380952	
							3	0.8	6.2	0.387097	0.384025
β IBO	45.7	35.3	43.5				0.7	6.8	38.2	0.534031	
	45.7	35.4	43.6	43.6			0.7	6.8	38.2	0.534031	0.534031
[Co]	**C(alkyne)**	**Co**	**Co%**	**Avg. %**	**further d-electrons**	**All d-electrons**	**C(d,f)**	**C(s)**	**C(p)**	**Hybridi-zation s^xp^3**	**Avg.**
α IBO	19.4	74	79.2	79.2	6	6.8	2.8	0.7	5.8	0.362069	
							2.8	0.7	6.6	0.318182	0.340125
β IBO	43.2	38.2	46.9				0.7	6.3	36.2	0.522099	
	43.1	37	46.1	46.6			0.9	5.5	36.7	0.449591	0.485845
Cr	**Löwdin**	**Löwdin**	**Cr %**	**Avg. %**	**further d-electrons**	**All d-electrons**	**Löwdin d/f**	**Löwdin**	**Löwdin**	**Hybridi-zation s^xp^3**	**Avg.**
α IBO	42.9	38.3	47.2				0.5	2.9	39.5	0.220253	
	48.9	34.1	41.1	44.1	3	3.8	2	10.1	36.8	0.82337	0.521811
β IBO	51.7	28.3	35.3				0.3	11.9	39.5	0.903797	
	52	27.8	34.8	35.1			0.2	12.6	39.2	0.964286	0.934042

[Cr^{Ph}]	C(alkyne)	Cr	Cr %	Avg. %	further d-electrons	All d-electrons	C(d,f)	C(s)	C(p)	Hybridi-zation s^xp^3	Avg.
α IBO	44.8	37.3	45.4				0.7	8.9	35.2	0.758523	
	46.8	32.2	40.7	43.1	3	3.8	0.3	9.2	37.3	0.739946	0.749235
β IBO	51.8	27.5	34.7				0.3	10.4	41.1	0.759124	
	51.8	29.6	36.3	35.5			0.7	10.4	40.7	0.766585	0.762854

Table S 17. Composition (reduced Löwdin) of IBOs as calculated with ωB97XD3.

wB97XD3											
[Mn]	**C(alkyne)**	**Mn**	**Mn %**	**Avg. %**	**further d-electrons**	**All d-electrons**	**C(d,f)**	**C(s)**	**C(p)**	**Hybridi-zation s^xp^3**	**Avg.**
α IBO	20.5	73.6	78.2	78.2	4	4.7	2.8	0.9	6.4	0.421875	
							2.7	0.9	6.8	0.397059	0.409467
β IBO	53.9	26.5	32.9				0.9	8.9	44.1	0.605442	
	53.5	25.8	32.5	32.7			0.9	8.4	44.2	0.570136	0.587789
[Fe]	**C(alkyne)**	**Fe**	**Fe %**	**Avg. %**	**further d-electrons**	**All d-electrons**	**C(d,f)**	**C(s)**	**C(p)**	**Hybridi-zation s^xp^3**	**Avg.**
α IBO	15.9	65.61	80.4	80.4	5	5.8	2.5	0.6	4.9	0.367347	
							2.4	0.6	4.9	0.367347	0.367347
β IBO	49.9	30.8	38.2				1	7.3	41.6	0.526442	
	49.8	30.9	38.2	38.2			1	7.3	41.5	0.527711	0.527077
[Co]	**C(alkyne)**	**Co**	**Co %**	**Avg. %**	**further d-electrons**	**All d-electrons**	**C(d,f)**	**C(s)**	**C(p)**	**Hybridi-zation s^xp^3**	**Avg.**
α IBO	17.4	79	81.9	81.9	6	6.8	2.2	0.6	5.1	0.352941	
							2.2	0.6	6.7	0.268657	0.310799
β IBO	46.9	34.7	42.5				4.4	12.2	30.3	1.207921	
	45.5	35.2	43.6	43.1			0.2	6.1	39.2	0.466837	0.837379

[Cr^{TMS}]	C(alkyne)	Cr	Cr %	Avg. %	further d-electrons	All d-electrons	C(d,f)	C(s)	C(p)	Hybridi-zation sxp3	Avg.
α IBO	39	52.4	57.3	57.3			1.2	2	30.7	0.19544	
					3	3.8	4.4	0.1	0.6	0.5	0.34772
β IBO	54.5	26.1	32.4				0.5	10.1	43.9	0.690205	
	54.8	26	21.0	32.3			0.4	10.7	43.7	0.734554	0.712379
[Cr^{Ph}]	**C(alkyne)**	**Cr**	**Cr %**	**Avg. %**	**further d-electrons**	**All d-electrons**	**C(d,f)**	**C(s)**	**C(p)**	**Hybridi-zation sxp3**	**Avg.**
α IBO	44.8	37.9	45.8				0.7	8.6	35.5	0.726761	
	48.7	31.6	39.3	42.6	3	3.8	0.7	8.9	39.1	0.682864	0.704813
β IBO	54.9	25.2	31.5				0.7	10.2	44	0.695455	
	54.2	27.4	33.5	32.5			0.7	10.3	43.2	0.715278	0.705366

Table S 18. Composition (reduced Löwdin) of IBOs as calculated with M06.

M06											
[Mn]	**C(alkyne)**	**Mn**	**Mn %**	**Avg. %**	**further d-electrons**	**All d-electrons**	**C(d,f)**	**C(s)**	**C(p)**	**Hybridi-zation s^xp^3**	**Avg.**
α IBO	17.7	76.3	81.2		4	4.8	2.3	0.8	5.9	0.40678	
							2.5	0.7	5.5	0.381818	0.394299
β IBO	54.4	25.6	32.0				0.8	8.8	44.8	0.589286	
	54	23.5	30.3	31.2			0.8	8.4	44.8	0.5625	0.575893
[Fe]	**C(alkyne)**	**Fe**	**Fe %**	**Avg. %**	**further d-electrons**	**All d-electrons**	**C(d,f)**	**C(s)**	**C(p)**	**Hybridi-zation s^xp^3**	**Avg.**
α IBO	13.9	82.2	85.5		5	5.9	2.3	0.5	4.2	0.357143	
							2.2	0.5	4.2	0.357143	0.357143
β IBO	49.8	30.6	38.1				0.7	7.2	41.9	0.515513	
	50	29.6	37.2	37.6			0.9	7.2	41.9	0.515513	0.515513

[Co]	C(alkyne)	Co	Co %	Avg. %	further d-electrons	All d-electrons	C(d,f)	C(s)	C(p)	Hybridi-zation s^xp^3	Avg.
α IBO	15.4	81.9	84.2	84.2	6	6.9	2.2	0.5	5.5	0.272727	
							2.1	0.5	4.6	0.326087	0.299407
β IBO	47.3	33.5	41.5				1.7	6.1	39.5	0.463291	
	46.8	33.8	41.9	41.7			0.6	6.9	39.3	0.526718	0.495004
[Cr^{TMS}]	C(alkyne)	Cr	Cr %	Avg. %	further d-electrons	All d-electrons	C(d,f)	C(s)	C(p)	Hybridi-zation s^xp^3	Avg.
α IBO	12.7	69.3	84.5	84.5	3	3.9	2.9	0.5	9.3	0.16129	
β IBO	55.1	25	31.2				0.4	10.6	44.1	0.721088	
	55.4	25.2	31.3	31.2			0.4	11.2	43.8	0.767123	0.744106
[Cr^{Ph}]	C(alkyne)	Cr	Cr %	Avg. %	further d-electrons	All d-electrons	C(d,f)	C(s)	C(p)	Hybridi-zation s^xp^3	Avg.
α IBO	41	52.2	56.0				0.8	7.5	32.7	0.688073	
	47.3	30.6	39.3	47.6	3	3.8	0.1	8.4	38.8	0.649485	0.668779
β IBO	55.5	24	30.2				0.7	10.3	44.5	0.694382	
	55.3	25.8	31.8	31.0			0.6	10.4	44.3	0.704289	0.699335

Table S 19. Composition (reduced Löwdin) of IBOs as calculated with TPSSh.

TPSSh											
[Mn]	C(alkyne)	Mn	Mn %	Avg. %	further d-electrons	All d-electrons	C(d,f)	C(s)	C(p)	Hybridi-zation s^xp^3	Avg.
α IBO	20.8	70.3	77.2	77.2	4	4.8	2.6	1	7.7	0.38961	
							1.7	1	6.8	0.441176	0.415393
β IBO	52.4	27.9	34.7				0.8	9.1	42.5	0.642353	
	52	27.1	34.2	34.5			0.9	8.7	42.4	0.615566	0.628959

[Fe]	**C(alkyne)**	**Fe**	**Fe %**	**Avg. %**	**further d-electrons**	**All d-electrons**	**C(d,f)**	**C(s)**	**C(p)**	**Hybridi-zation s^xp^3**	**Avg.**
	C(all)	Fe(all)	C(all)	C(all)			C(d,f)	C(s)	C(p)	sxp3	average
α IBO	18.4	75.7	80.4		5		2.6	0.7	5.9	0.355932	
							2.8	0.7	5.7	0.368421	0.362177
β IBO	42.3	32.6	43.5				1.5	13.7	27.1	1.516605	
	48	32.7	40.5	42.0			0.8	7.4	39.8	0.557789	1.037197
[Co]	**C(alkyne)**	**Co**	**Co %**	**Avg. %**	**further d-electrons**	**All d-electrons**	**C(d,f)**	**C(s)**	**C(p)**	**Hybridi-zation s^xp^3**	**Avg.**
	C(all)	Co(all)	C(all)	C(all)			C(d,f)	C(s)	C(p)	sxp3	average
α IBO	18.3	75.5	80.5		6	6.8	2.8	0.7	5.4	0.388889	
							2.6	0.7	6.1	0.344262	0.366576
β IBO	45.1	35.7	44.2				0.7	6.9	37.5	0.552	
	43.4	37	46.0	45.1			0.6	6	36.8	0.48913	0.520565
[Cr^{TMS}]	**C(alkyne)**	**Cr**	**Cr %**	**Avg. %**	**further d-electrons**	**All d-electrons**	**C(d,f)**	**C(s)**	**C(p)**	**Hybridi-zation s^xp^3**	**Avg.**
α IBO	42.6	39.1	47.9				0.5	2.6	39.5	0.197468	
	45.4	34.9	43.4	45.7	3	3.8	0.7	3.7	41	0.270732	0.2341
β IBO	53	27	33.8				0.3	11.7	41	0.856098	
	53.7	26.8	33.3	33.5			0.4	12.4	40.9	0.909535	0.882817
[Cr^{Ph}]	**C(alkyne)**	**Cr**	**Cr %**	**Avg. %**	**further d-electrons**	**All d-electrons**	**C(d,f)**	**C(s)**	**C(p)**	**Hybridi-zation s^xp^3**	**Avg.**
α IBO	45.1	37.5	45.4				0.7	9.1	35.3	0.773371	
	48.1	30.9	39.1	42.3	3	3.8	0.4	9.4	38.3	0.736292	0.754832
β IBO	53.8	25.7	32.1				0.6	10.7	42.5	0.755294	
	53.2	28.1	34.6	33.4			0.7	10.7	41.8	0.767943	0.761618

Table S 20. Composition (reduced Löwdin) of covalent QROs as calculated with B3LYP.

B3LYP										
[Mn]	**C(alkyne)**	**Mn**	**Mn %**	**Further d-electrons**	**All d-electrons**	**C(d,f)**	**C(s)**	**C(p)**	**Hybridization s^xp^3**	**Avg.**
QRO	27.9	37	57.0	d5	7.6	3.7	0.8	9	0.26666667	
						3.6	0.8	10	0.24	0.25333333
[Fe]	**C(alkyne)**	**Fe**	**Fe %**	**Further d-electrons**	**All d-electrons**	**C(d,f)**	**C(s)**	**C(p)**	**Hybridization s^xp^3**	**Avg.**
QRO	20.6	39.5	65.7	d6	7.7	2.8	0.5	6.9	0.2173913	
						3	0.5	6.9	0.2173913	0.2173913
[Co]	**C(alkyne)**	**Co**	**Co %**	**Further d-electrons**	**All d-electrons**	**C(d,f)**	**C(s)**	**C(p)**	**Hybridization s^xp^3**	**Avg.**
	C(all)	Co(all)	Co %		average		s	p	sxp3	average
QRO	18.7	39.4	67.8	d7	7.7	1.6	0.1	6.9	0.04347826	
						2	0.1	8	0.0375	0.04048913
[Cr^{TMS}]	**C(alkyne)**	**Cr**	**Cr %**	**Further d-electrons**	**All d-electrons**	**C(d,f)**	**C(s)**	**C(p)**	**Hybridization s^xp^3**	**Avg.**
	C(all)	Cr(all)	Cr %		average		s	p	sxp3	average
QRO	37.6	46.7	55.4	d4		4.6	0.2	13.5	0.04444444	
						4.4	0.6	14.3	0.12587413	0.08515929
[Cr^{Ph2}]	**C(alkyne)**	**Cr**	**Cr %**	**Further d-electrons**	**All d-electrons**	**C(d,f)**	**C(s)**	**C(p)**	**Hybridization s^xp^3**	**Avg.**
	C(all)	Cr(all)	Cr %		average		s	p	s^xp^3	average
QRO	33.7	37.5	52.7	d4		3.8	1.3	14.4	0.27083333	
						4.2	1	9	0.33333333	0.30208333

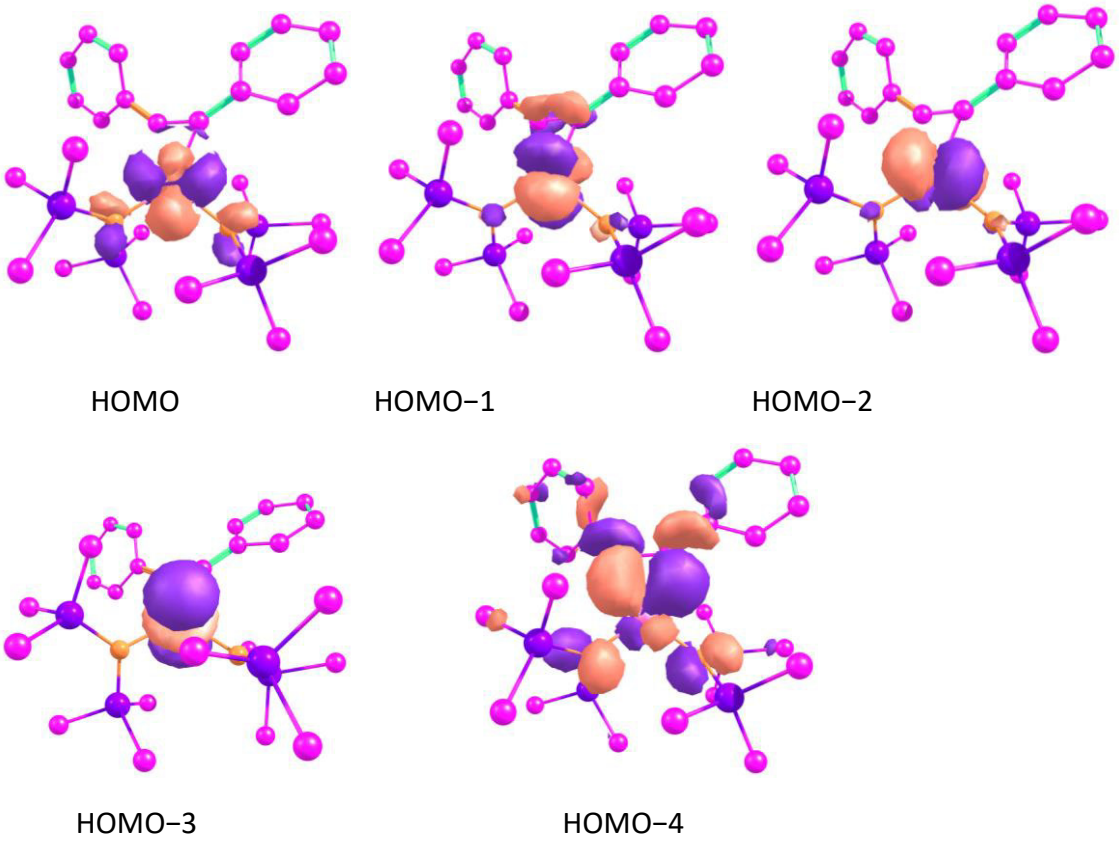

Figure S 32. QROs obtained for **4b** (hydrogen atoms omitted for clarity).

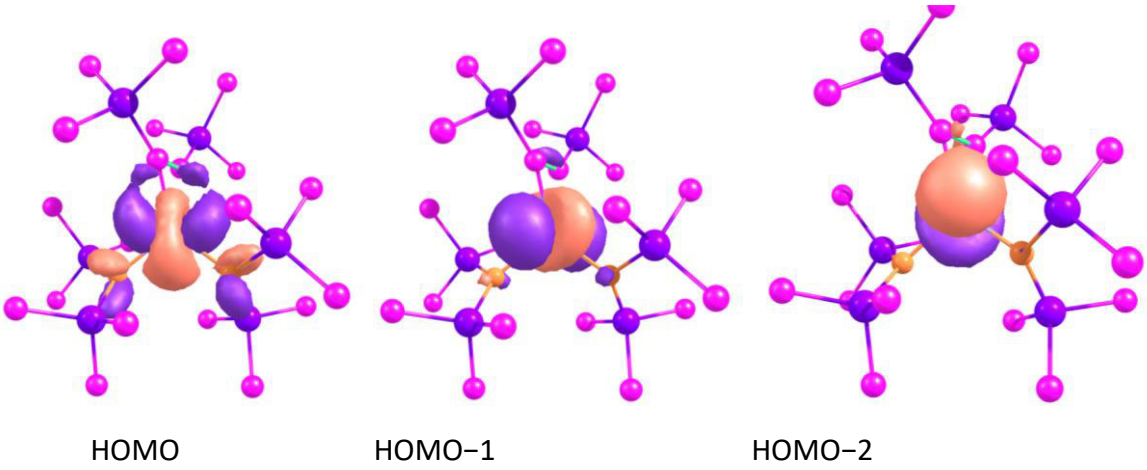

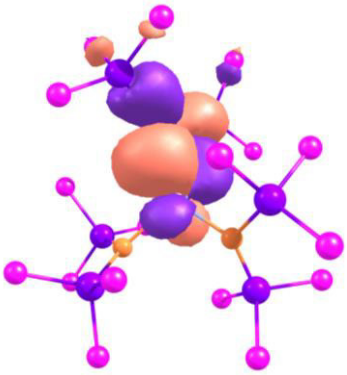

HOMO−3

Figure S 33. QROs obtained for **6a** (hydrogen atoms omitted for clarity).

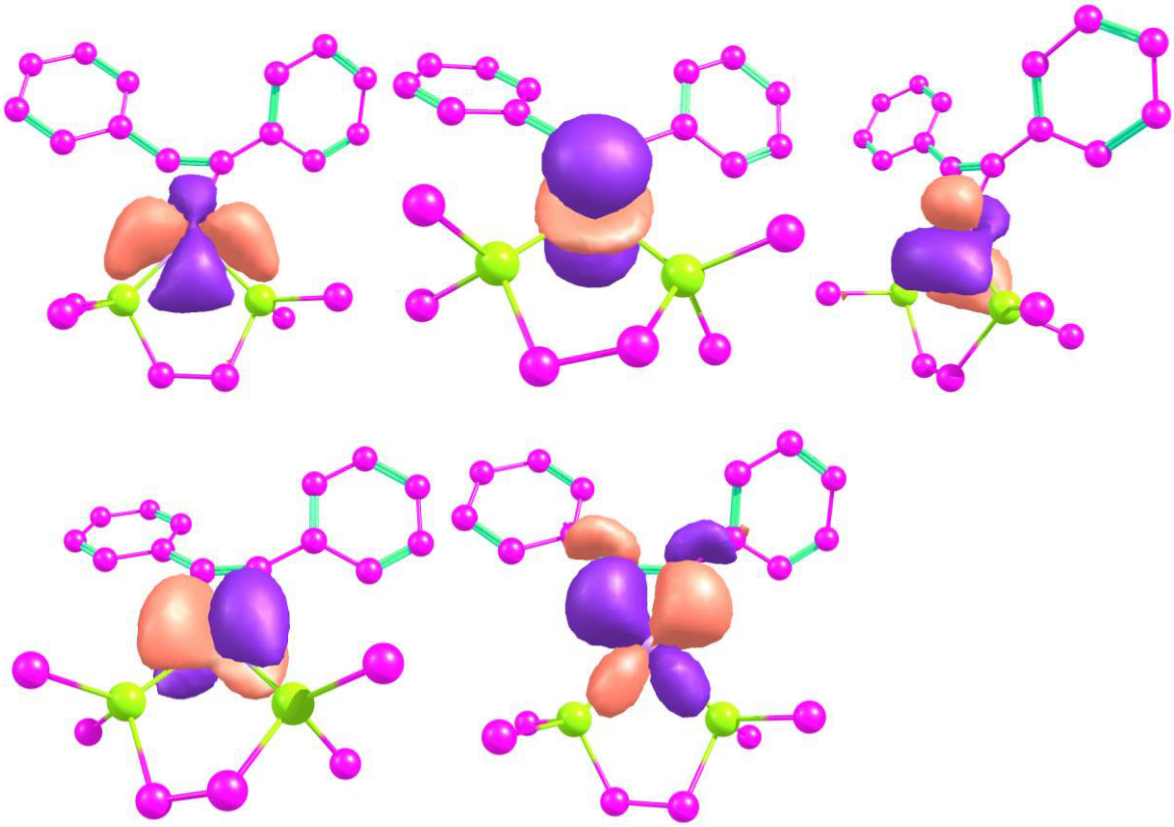

Figure S 34. IBOs for [Ni(dmpe)(C_2Ph_2)], which are associated with the metal's d-electrons (hydrogen atoms omitted for clarity).

Table S 21. Configurations for ground state of **1** as obtained from CAS(12,9).

0.76615 [1552]: 222221100

0.06788 [1519]: 222201120

0.02802 [1549]: 222220200

0.02408 [1553]: 222222000

0.01397 [1447]: 222021102

0.01233 [766]: 122221200

0.01193 [1352]: 221121111

0.00775 [1195]: 212222010

0.00666 [1187]: 212220210

0.00560 [1171]: 212211111

0.00443 [1491]: 222112110

0.00300 [1180]: 212212200

0.00272 [502]: 112222110

Table S 22. Configurations for ground state of **2a** as obtained from CAS(11,9).

0.79780 [1799]: 222211100

0.07194 [1745]: 222011120

0.06708 [1779]: 222111110

0.01415 [1601]: 220211102

0.01207 [1400]: 211211111

0.00920 [1003]: 122111111

0.00258 [1052]: 122211101

0.00252 [1345]: 211111121

Table S 23. Configurations for ground state of **4b** as obtained from CAS(10,9).

0.78483 [1520]: 222111100

0.09391 [1485]: 221111110

0.07269 [1425]: 220111120

0.01774 [1139]: 202111102

0.01440 [730]: 112111111

0.00307 [589]: 111111121

Table S 24. Configurations for ground state of **6a** as obtained from CAS(9,9).

0.83186 [0]: 222111000

0.05585 [114]: 220111200

0.04840 [35]: 221111100

0.01816 [505]: 202111020

0.01392 [1102]: 112111110

0.00970 [281]: 211111101

Table S 25. Configurations for ground state of **6b** as obtained from CAS(9,9).

0.86414 [0]: 222111000

0.03809 [114]: 220111200

0.03192 [35]: 221111100

0.01591 [505]: 202111020

0.01346 [1102]: 112111110

0.01197 [281]: 211111101

0.00252 [178]: 212111001

Table S 26. Energies as obtained with B3LYP.

B3LYP					
Compound	***E***	***G***	***E*(TZVPP)**	***E*(TZVPP, broken symmetry 4/1)**	**Overlap Corresponding Orbitals**
	[H]	**[H]**	**[H]**	**[H]**	**[H]**
1	-3667.06604	-3666.48966	-3668.68544		
2b	-3548.01515	-3547.43952	-3549.71054		
4b	-3435.30916	-3434.73461	-3437.0037		
6a	-3684.02303	-3683.41371	-3685.70617		0.95
6a_coplanar_sextet	-3684.00285	-3683.39533	-3685.68935	-3685.678208	0.47
6c*	-3328.7628	-3328.18829	-3330.45612		0.97
6c*_coplanar_sextet	-3328.74316	-3328.17177	-3330.43735	-3330.43282	0.38
6c*_coplanar_quart	-3328.76365	-3328.1895	-3330.45588		0.96
nickel_alkyne	-2967.54923	-2967.19863	-2968.64678		

Table S 27. Energies as obtained with BP86.

BP86	***E***	***E* (broken symmetry 4/1)**	***G***	**Overlap Corresponding Orbitals**
	[H]	**[H]**		
1	-3668.38911		-3667.8316	
2b	-3549.31345		-3548.75756	
4b	-3436.57485		-3436.01931	
6a	-3685.28015		-3684.69192	0.98
6a_coplanar_sextet	-3685.24962	-3685.24767	-3684.66133	0.94
6c*	-3330.01788		-3329.46229	0.99
6c*_coplanar_sextet	-3329.98616	-3329.9912	-3329.43341	0.85
6c*_coplanar_quart	-3330.01905		-3329.46352	

Table S 28. Energies as obtained with B97-3c.

B973c	***E***	***E* (broken symmetry 4/1)**	***G***	**Overlap Corresponding Orbitals**
	[H]	**[H]**		
1	-3668.66068		-3668.08987	
2b	-2035.41346		-3548.97485	
4b	-3436.76726		-3436.19978	
6a	-3685.41427		-3684.80596	0.96
6a_coplanar_sextet	-3685.39227	-3685.38245	-3684.78841	0.9
6c*	-3330.16609		-3329.59726	0.96
6c*_coplanar_sextet	-3330.14352	-3330.13547	-3329.57817	0.51
6c*_coplanar_quart	-3330.16643		-3329.59864	

Table S 29. Energies as obtained with PBEh-3c.

PBEh3c	***E***	***E* (broken symmetry 4/1)**	***G***	**Overlap Corresponding Orbitals**
	[H]	**[H]**		
1	-3664.33005		-3663.7323	
2b	-3545.33209		-3544.73437	
4b	-3432.68506		-3432.08955	
6a	-3681.21271		-3680.58029	0.83
6a_coplanar_sextet	-3681.20735	-3681.19151	-3680.57364	0.32
6c*	-3326.16032		-3325.56282	0.9
6c*_coplanar_sextet	-3326.15156	-3326.1445	-3325.55793	0.25
6c*_coplanar_quart	-3326.15962		-3325.56313	

Table S 30. Energies as obtained with B3PW91.

B3PW91	***E***	***E* (broken symmetry 4/1)**	***G***	**Overlap Corresponding Orbitals**
	[H]	**[H]**		
1	-3667.54545		-3666.96712	
2b	-3548.48938		-3547.91339	
4b	-3435.77976		-3435.20385	
6a	-3684.48669		-3683.87681	0.95
6a_coplanar_sextet	-3684.46803	-3684.45488	-3683.85798	0.48
6c*	-3329.22746		-3328.65052	0.96
6c*_coplanar_sextet	-3329.20655	-3329.20127	-3328.63282	0.5
6c*_coplanar_quart	-3329.2281		-3328.65247	

Table S 31. Energies as obtained with PBE0.

PBE0	***E***	***E* (broken symmetry 4/1)**	***G***	**Overlap Corresponding Orbitals**
	[H]	**[H]**		
1	-3665.90372		-3665.32412	
2b	-3546.86176		-3546.28311	
4b	-3434.16836		-3433.5911	
6a	-3682.85189		-3682.24071	0.93
6a_coplanar_sextet	-3682.83466	-3682.82208	-3682.22438	0.45
6c*	-3327.62445		-3327.04727	0.95
6c*_coplanar_sextet	-3327.60857	-3327.60341	-3327.03392	0.24
6c*_coplanar_quart	-3327.62436		-3327.04726	

8.4 Supporting Information zur Publikation „Catalytic Transformation of Alkynes by Low-Coordinate Iron Silylamides and the Surprising Role of Potassium"

Igor Müller und C. Gunnar Werncke, *Manuskript in der Vorbereitung*.

Reactions of Terminal Alkyne with Quasilinear Iron(I) Silylamides – A Comparative Study

Igor Müller,[1] C. Gunnar Werncke*[1]

[1]Department of Chemistry, Philipps-University Marburg, Hans-Meerwein-Straße 4, 35043 Marburg, Germany; gunnar.werncke@chemie.uni-marburg.de, +49 6421 282 5627;

Table of Contents

1. NMR Spectra

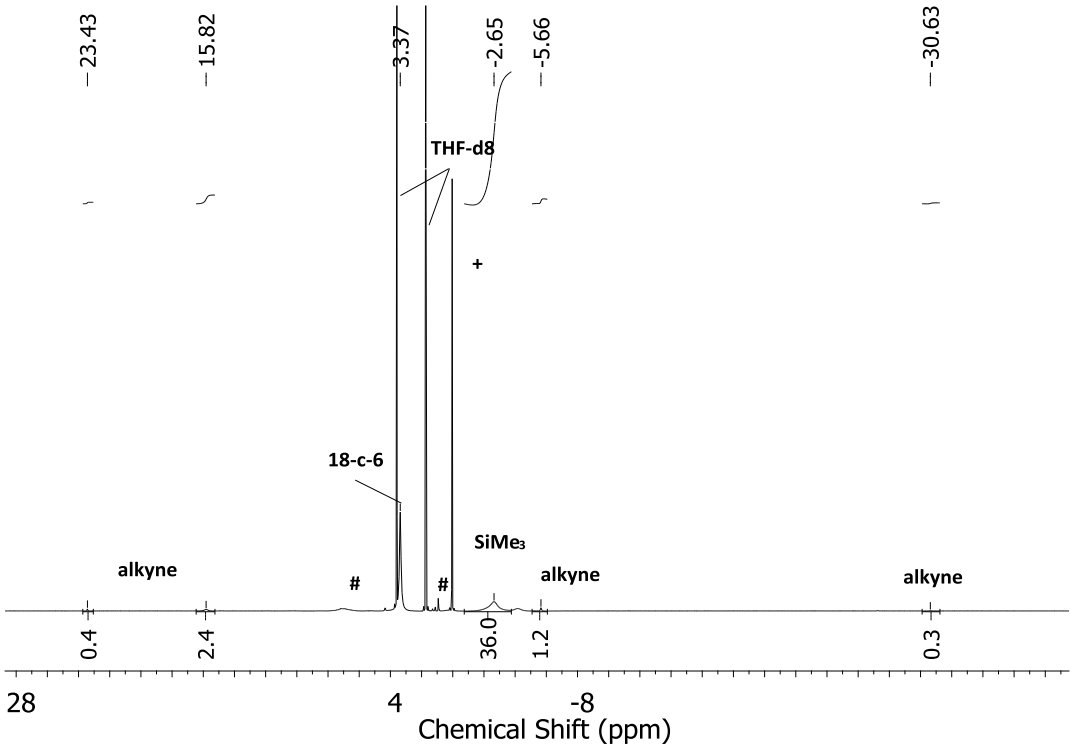

Figure S 1. ^{1}H NMR spectrum of **[K{18c6}][Fe(N(SiMe$_3$)$_2$)$_2$(η^2-PhCCH)]** (**1**) in THF-d$_8$ (500.1 MHz). # denotes free alkyne. + decomposition.

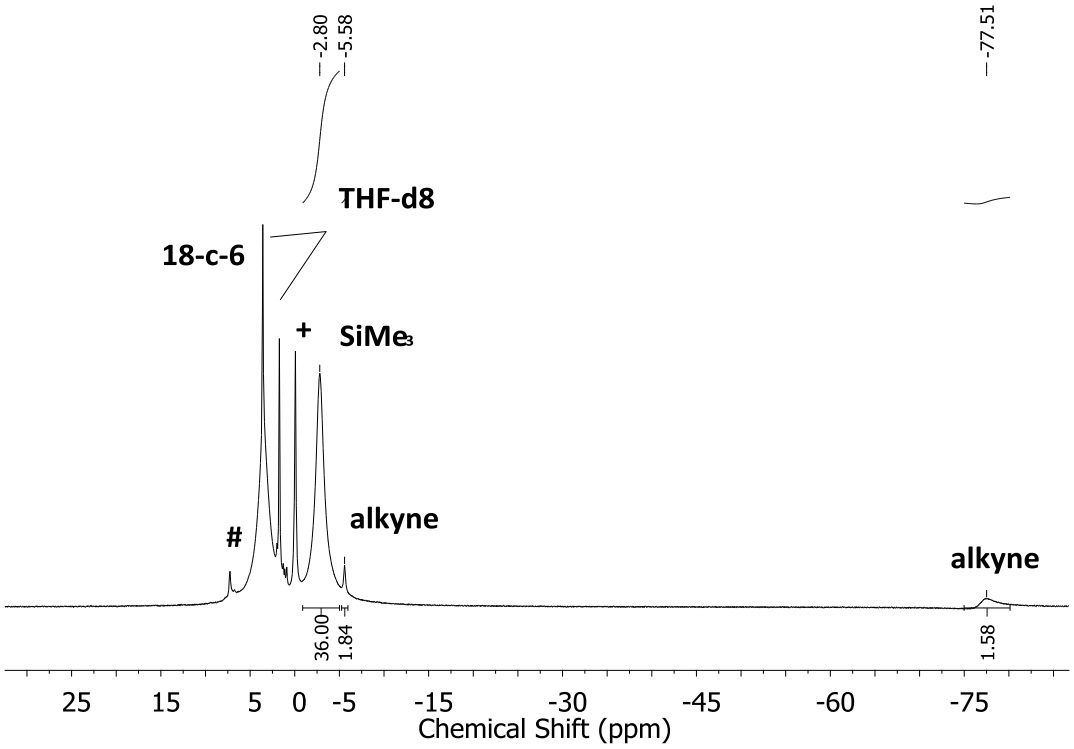

Figure S 2. ^{1}H NMR spectrum of **[K{18c6}][Fe(N(SiMe$_3$)$_2$)$_2$(η^2-PhCCMe)]** (**2**) in THF-d$_8$ (300.1 MHz). # denotes free alkyne. + decomposition.

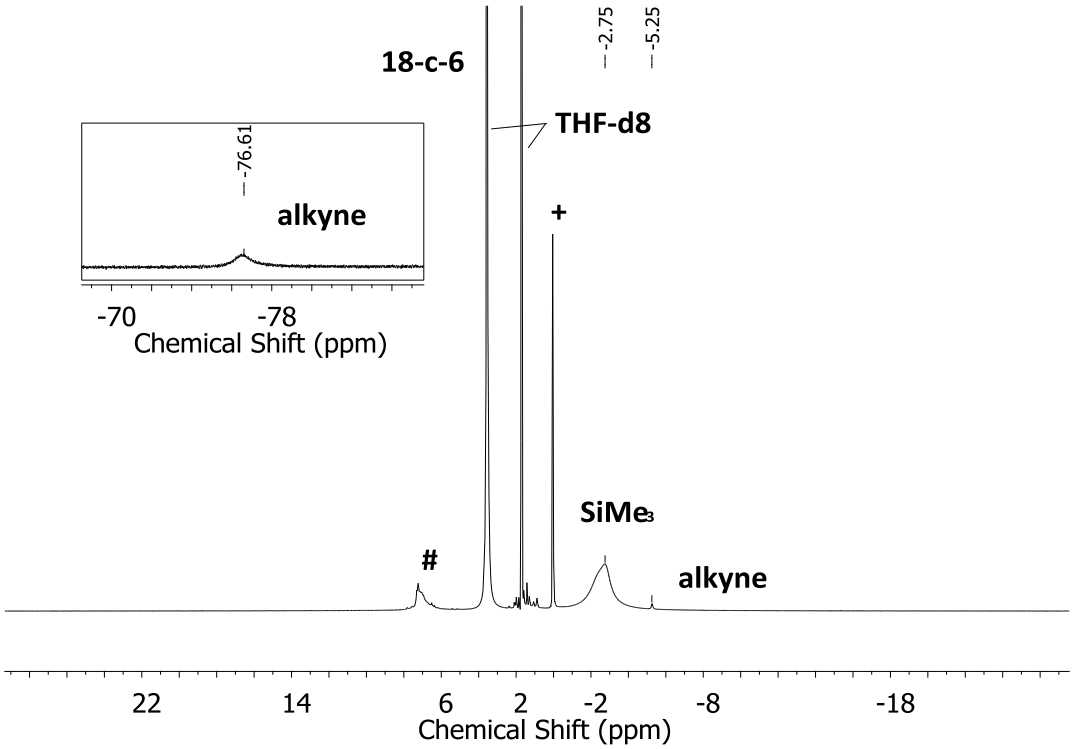

Figure S 3. ^{1}H NMR spectrum of **[K{18c6}][Fe(N(SiMe$_3$)$_2$)$_2$(η^2-PhCCMe)]** (**2**) in THF-d$_8$ (300.1 MHz). # denotes free alkyne. + decomposition.

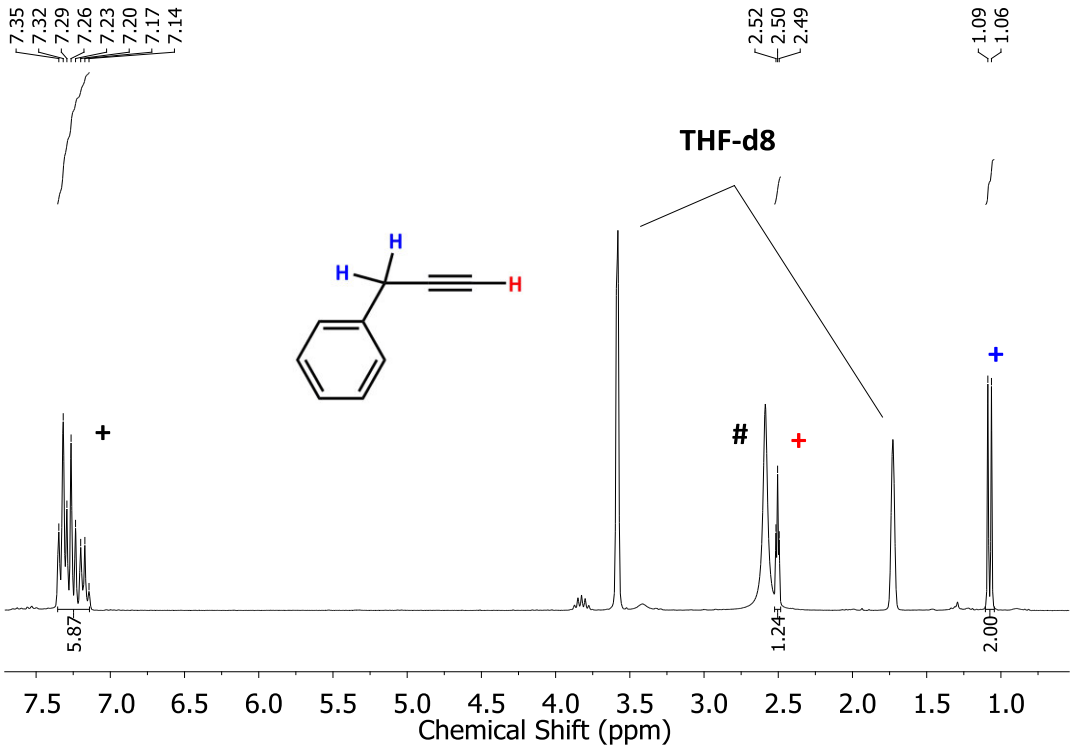

Figure S 4. ^{1}H NMR spectrum of **3-Phenyl-1-propyne** in THF-d$_8$ (300.1 MHz). # water. + alkyne.

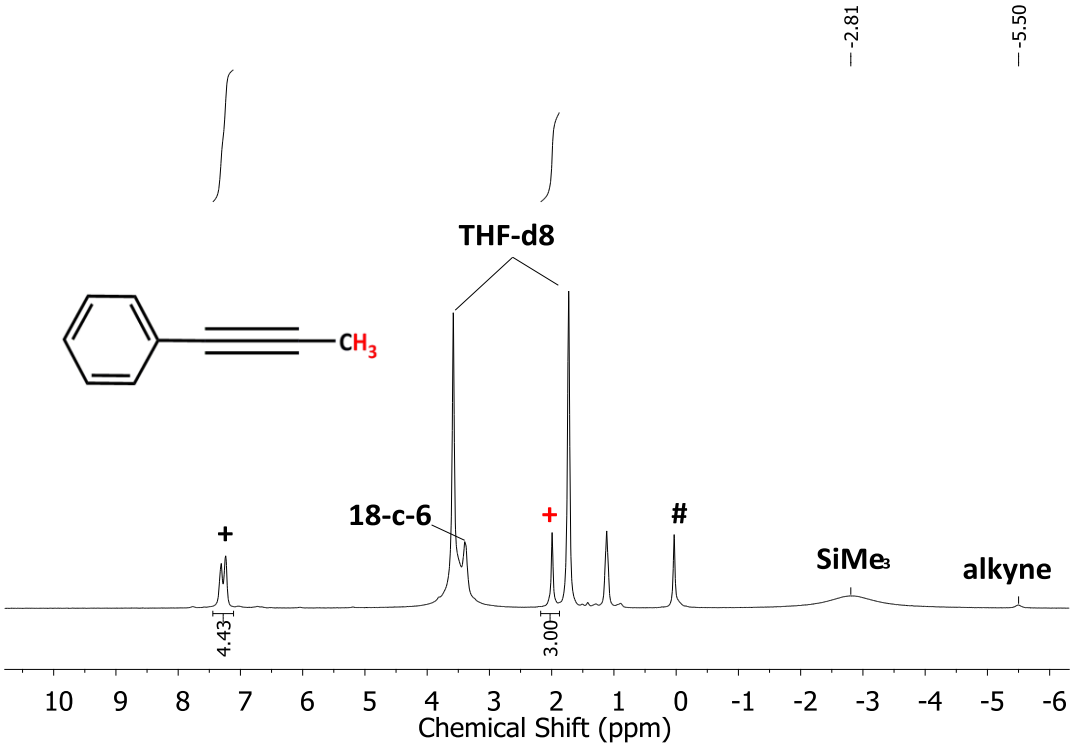

Figure S 5. ^{1}H NMR spectrum of the in situ reaction at room temperature and 5 min reaction time of [K{18c6}][Fe(N(SiMe$_3$)$_2$)$_2$] (1.0 eq) and 3-Phenyl-1-propyne (2.0 eq) in THF-d$_8$ (300.1 MHz). # decomposition. +/+ 1-Phenyl-1-propyne.

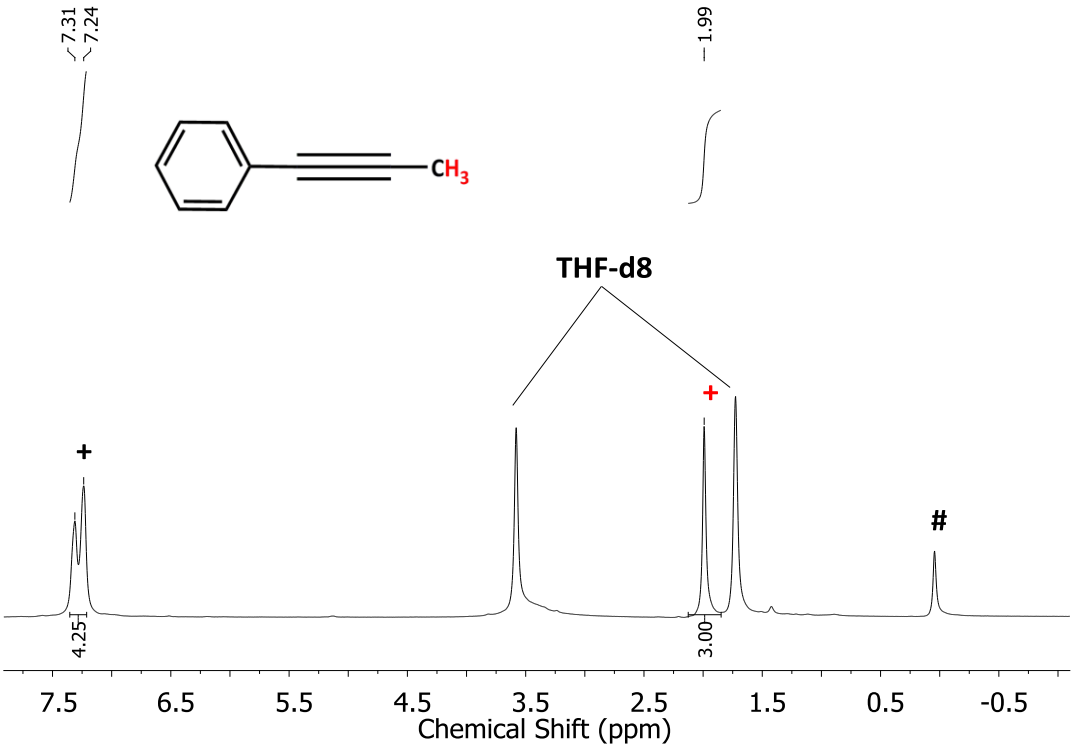

Figure S 6. ^{1}H NMR spectrum of the in situ reaction at room temperature and 5 min reaction time of [K{18c6}][Fe(N(SiMe$_3$)$_2$)$_2$] (1.0 eq) and 3-Phenyl-1-propyne (100.0 eq) in THF-d$_8$ (300.1 MHz). # decomposition. +/+ 1-Phenyl-1-propyne.

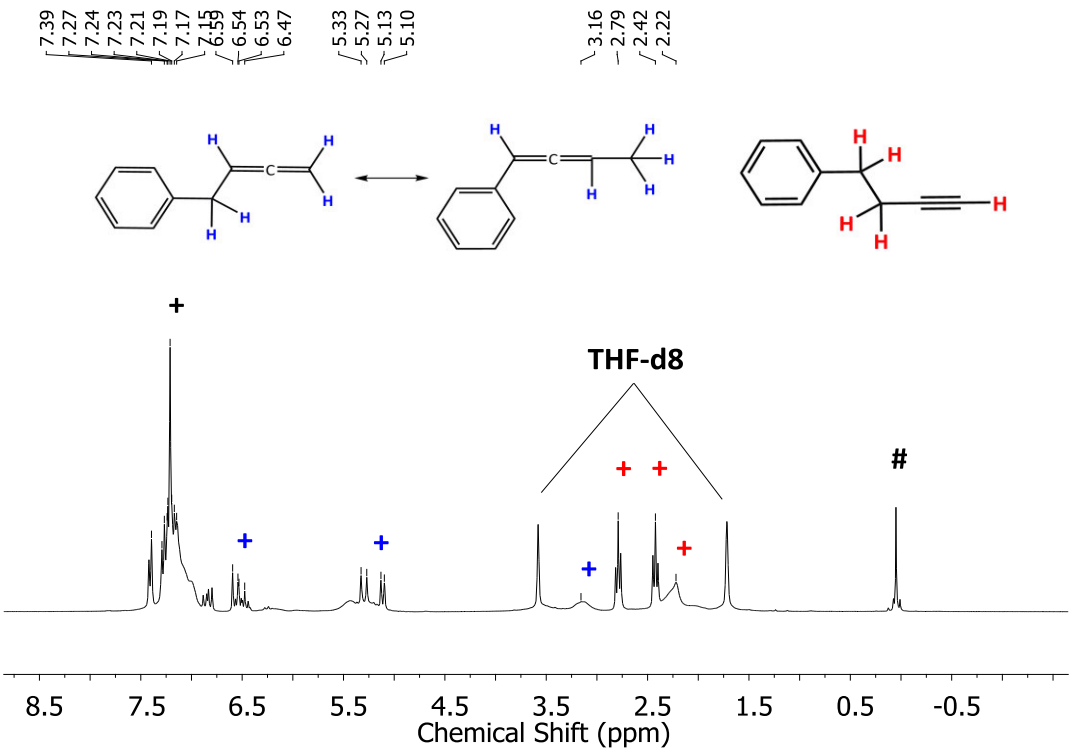

Figure S 7. ^{1}H NMR spectrum of the in situ reaction at room temperature and 5 min reaction time of [K{18c6}][Fe(N(SiMe$_3$)$_2$)$_2$] (1.0 eq) and 4-Phenyl-1-butyne (100.0 eq) in THF-d$_8$ (300.1 MHz). # decomposition. + 4-Phenyl-1-butyne. + Butadienylbenzene.

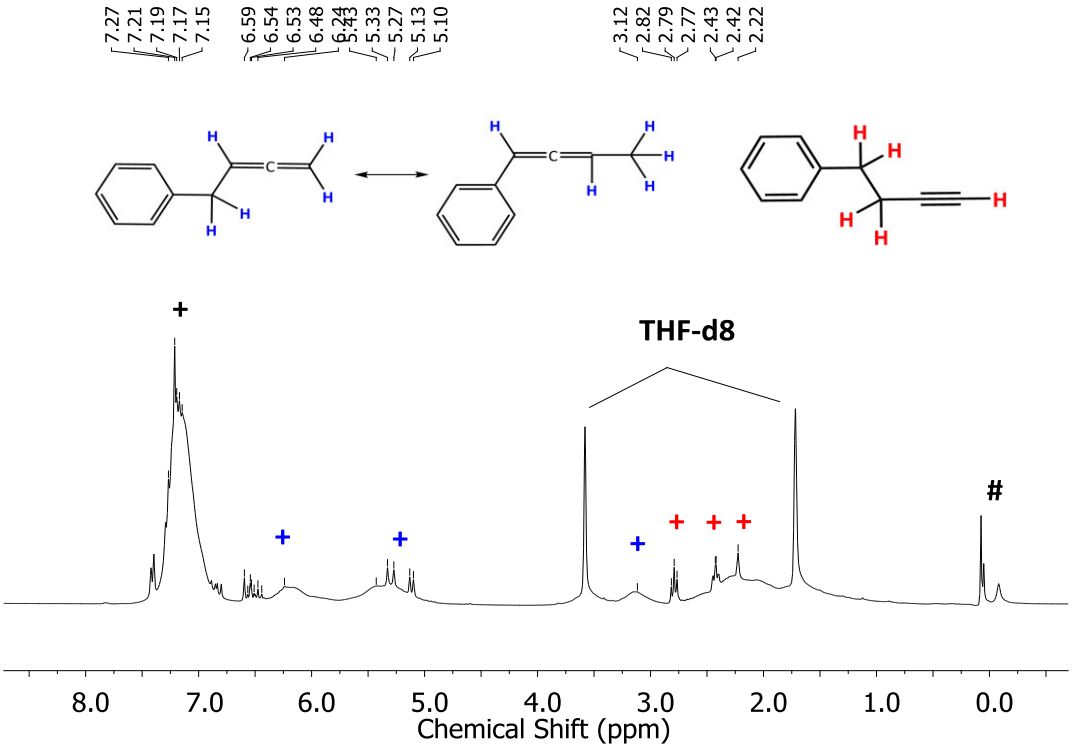

Figure S 8. ^{1}H NMR spectrum of the in situ reaction at room temperature and two weeks reaction time of [K{18c6}][Fe(N(SiMe$_3$)$_2$)$_2$] (1.0 eq) and 4-Phenyl-1-butyne (100.0 eq) in THF-d$_8$ (300.1 MHz). # decomposition. + 4-Phenyl-1-butyne. + Butadienylbenzene.

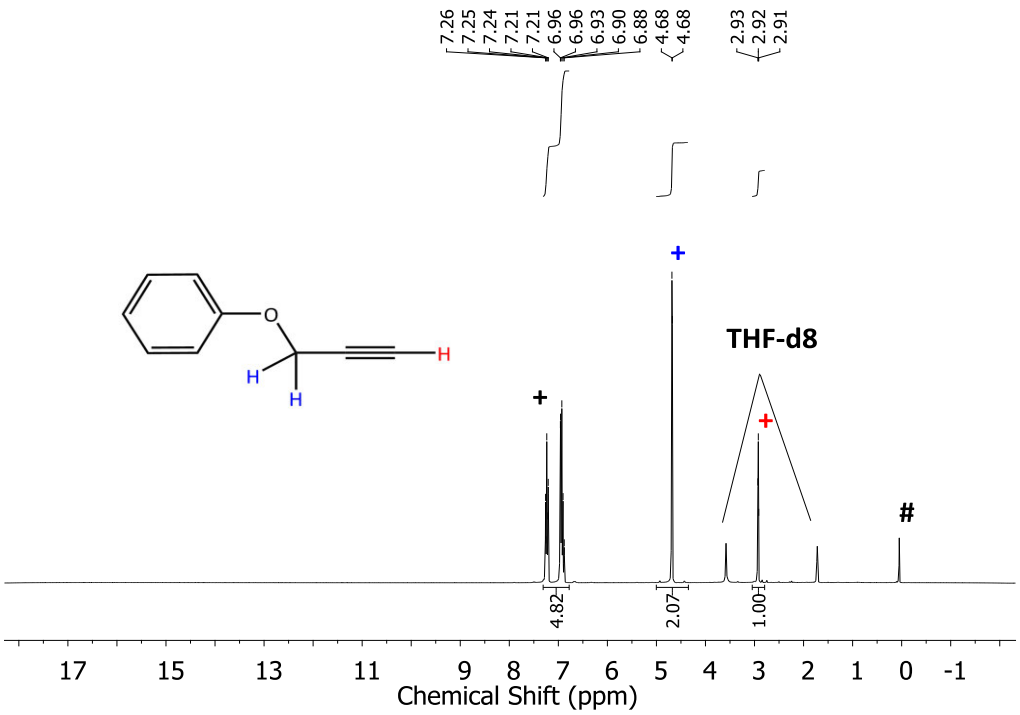

Figure S 9. ^{1}H NMR spectrum of the in situ reaction at room temperature after two weeks of [K{18c6}][Fe(N(SiMe$_3$)$_2$)$_2$] (1.0 eq) and 2-Propynyloxy-benzen (100.0 eq) in THF-d$_8$ (300.1 MHz). # decomposition. +/+/+ 2-Propynyloxy-benzene. [K{18c6}][Fe(N(SiMe$_3$)$_2$)$_2$] appeared no reactivity observe to this substrate.

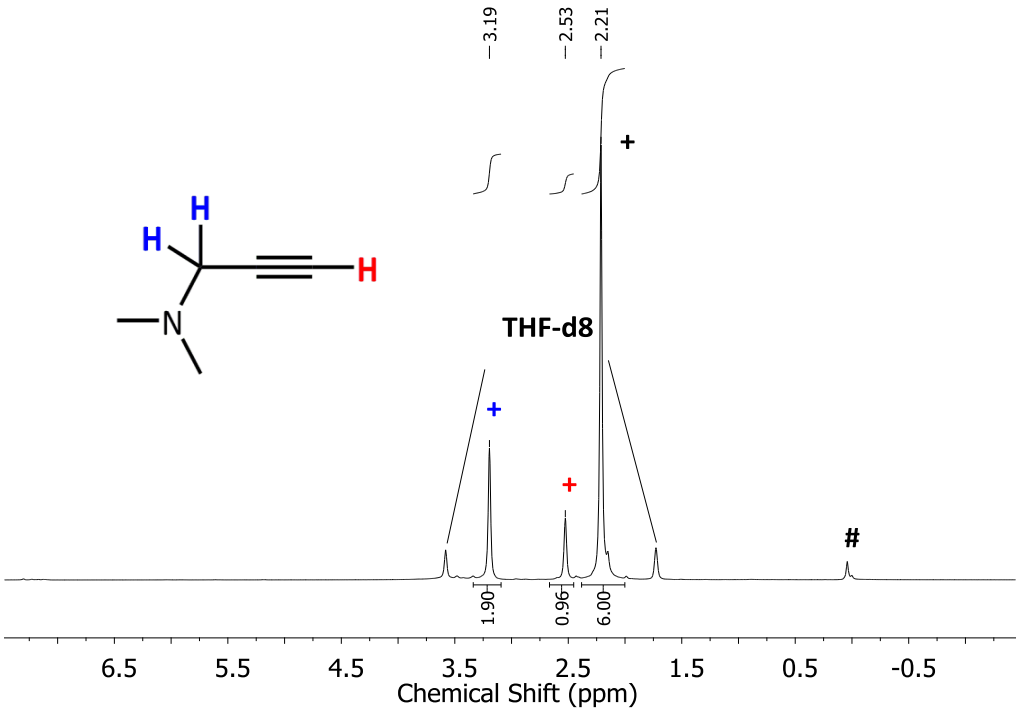

Figure S 10. ^{1}H NMR spectrum of the in situ reaction at room temperature and 5 min reaction time of [K{18c6}][Fe(N(SiMe$_3$)$_2$)$_2$] (1.0 eq) and *N*,*N*-Dimethylpropargulamine (100.0 eq) in THF-d$_8$ (300.1 MHz). # decomposition. +/+/+ *N*,*N*-Dimethylpropargulamine. [K{18c6}][Fe(N(SiMe$_3$)$_2$)$_2$] appeared no reactivity observe to this substrate .

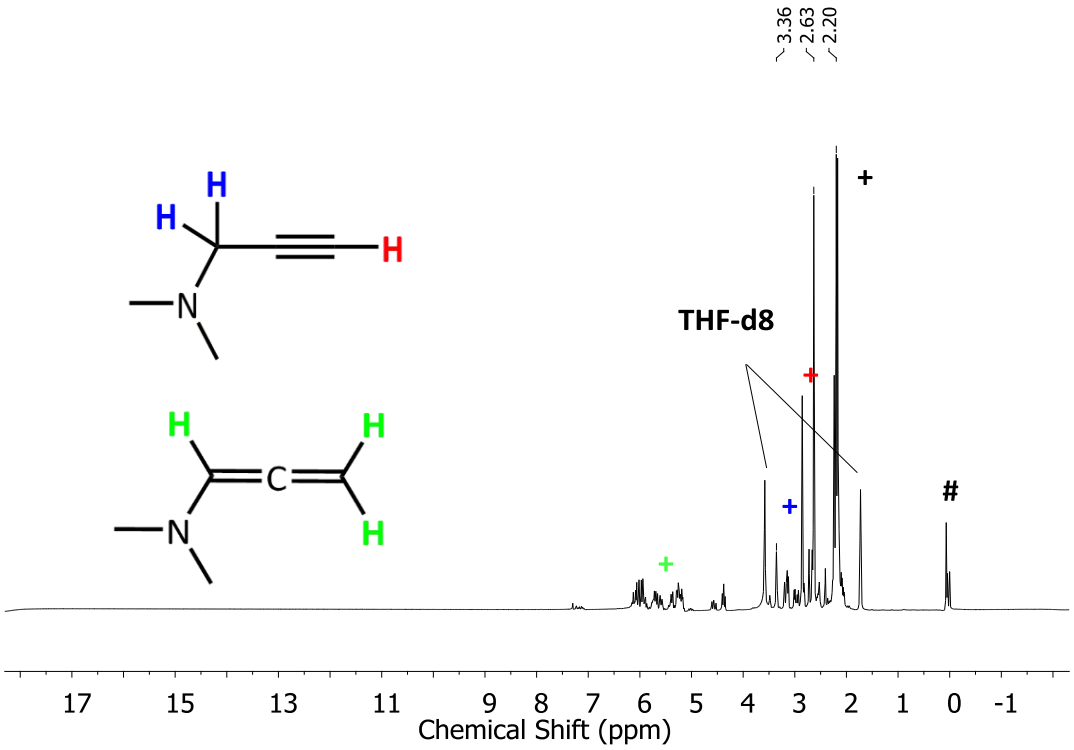

Figure S 11. ^{1}H NMR spectrum of the in situ reaction at room temperature after two weeks of [K{18c6}][Fe(N(SiMe$_3$)$_2$)$_2$] (1.0 eq) and *N*,*N*-Dimethylpropargulamine (100.0 eq) in THF-d$_8$ (300.1 MHz). # decomposition. +/+/+ *N*,*N*-Dimethylpropargulamine. [K{18c6}][Fe(N(SiMe$_3$)$_2$)$_2$] appeared reactivity observe to this substrate.

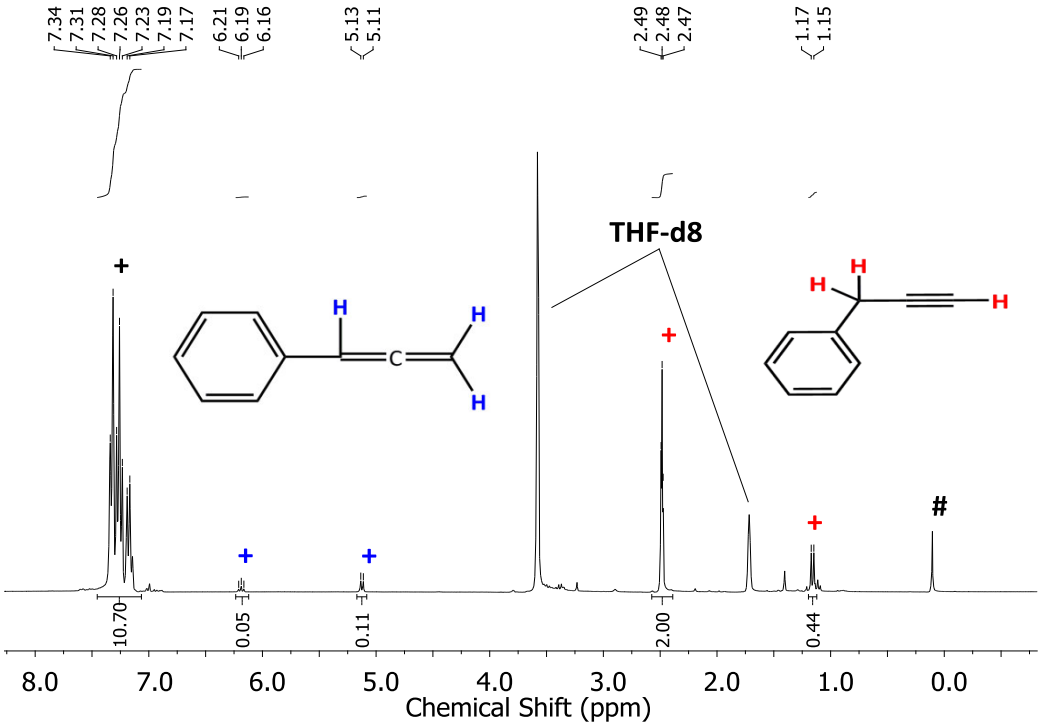

Figure S 12. ^{1}H NMR spectrum of the in situ reaction at room temperature and 5 min reaction time of [K{18c6}][Fe(N(DippTMS)$_2$] (1.0 eq) and 3-Phenyl-1-propyne (100.0 eq) in THF-d$_8$ (300.1 MHz). # decomposition. +/+ 3-Phenyl-1-propyne. +/+ Propa-1,2-dien-1-benzene.

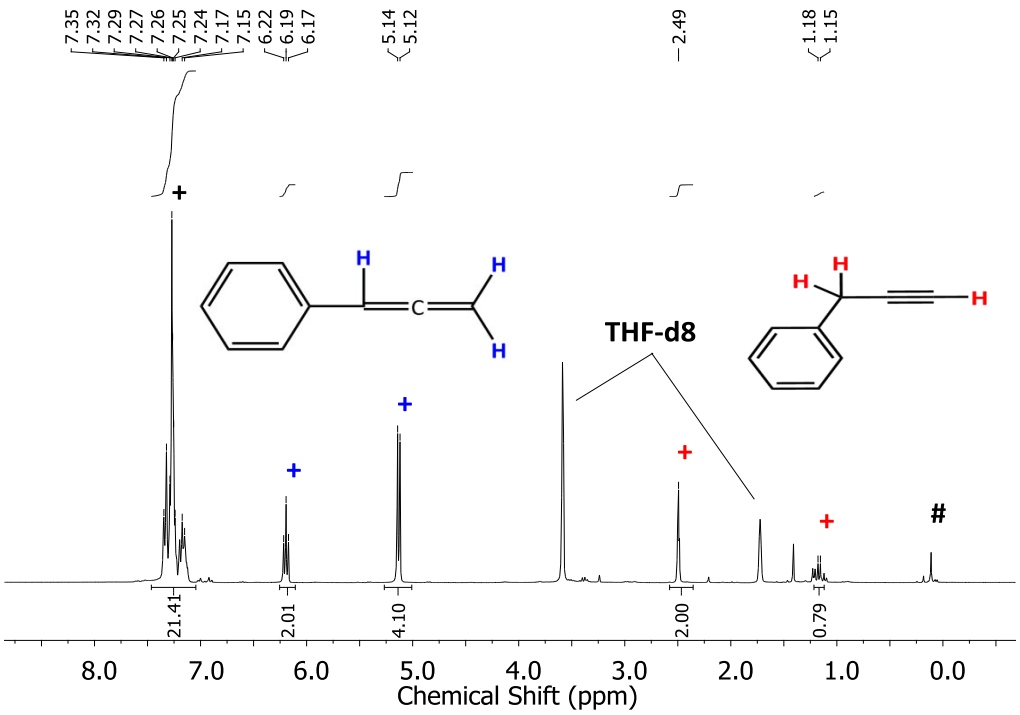

Figure S 13. ^{1}H NMR spectrum of the in situ reaction at room temperature and one week reaction time of [K{18c6}][Fe(N(DippTMS)$_2$] (1.0 eq) and 3-Phenyl-1-propyne (100.0 eq) in THF-d_8 (300.1 MHz). # decomposition. +/+ 3-Phenyl-1-propyne. +/+ Propa-1,2-dien-1-benzene.

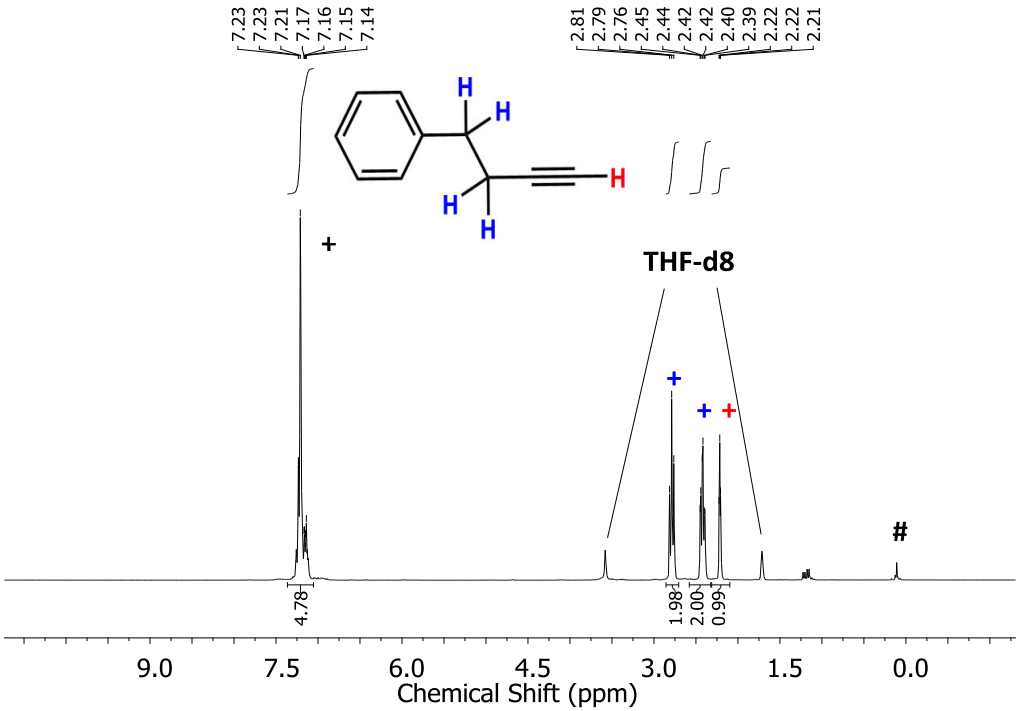

Figure S 14. ^{1}H NMR spectrum of the in situ reaction at room temperature and two weeks reaction time of [K{18c6}][Fe(N(DippTMS)$_2$] (1.0 eq) and 4-Phenyl-1-butyne (100.0 eq) in THF-d_8 (300.1 MHz). # decomposition. +/+/+ 4-Phenyl-1-butyne. [K{18c6}][Fe(N(DippTMS)$_2$] appeared no reactivity observe to this substrate.

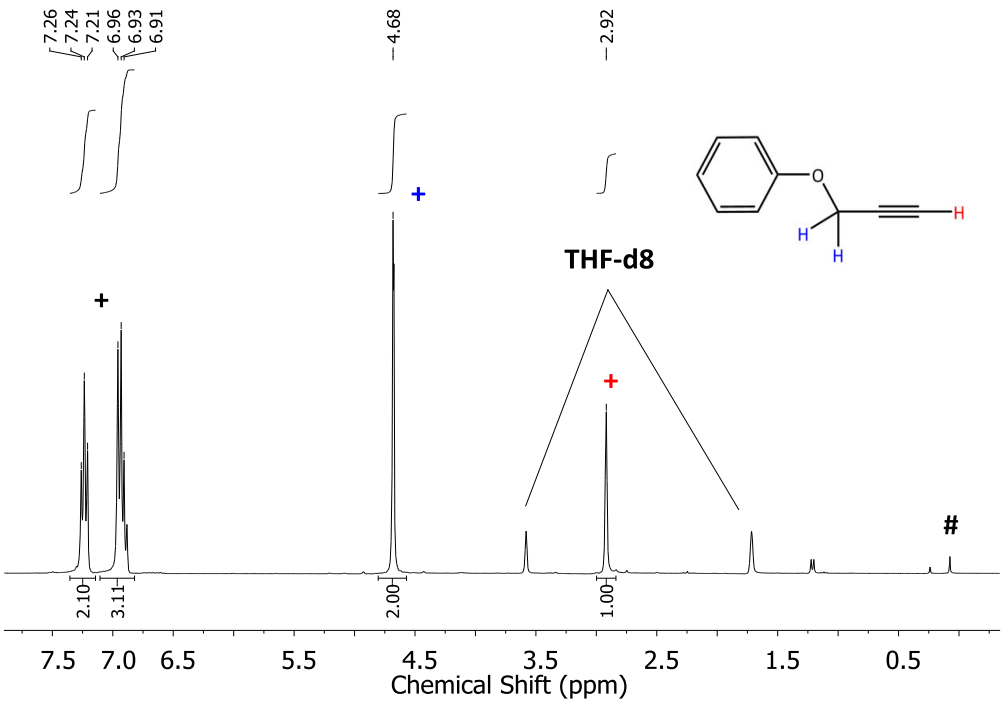

Figure S 15. ^{1}H NMR spectrum of the in situ reaction at room temperature after two weeks of [K{18c6}][Fe(N(DippTMS)$_2$] (1.0 eq) and 2-Propynyloxy-benzen (100.0 eq) in THF-d$_8$ (300.1 MHz). # decomposition. +/+/+ 2-Propynyloxy-benzene. [K{18c6}][Fe(N(DippTMS)$_2$] appeared no reactivity observe to this substrate.

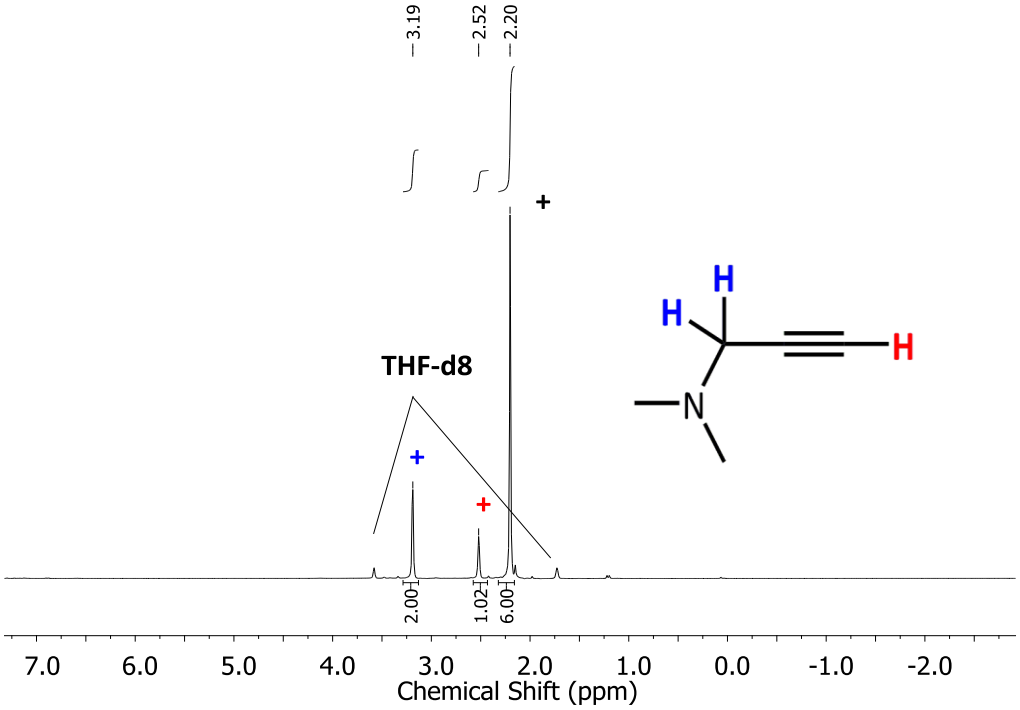

Figure S 16. ^{1}H NMR spectrum of the in situ reaction at room temperature and two weeks reaction time of [K{18c6}][Fe(N(DippTMS)$_2$] (1.0 eq) and *N*,*N*-Dimethylpropargulamine (100.0 eq) in THF-d$_8$ (300.1 MHz). +/+/+ *N*,*N*-Dimethylpropargulamine. [K{18c6}][Fe(N(DippTMS)$_2$] appeared no reactivity observe to this substrate.

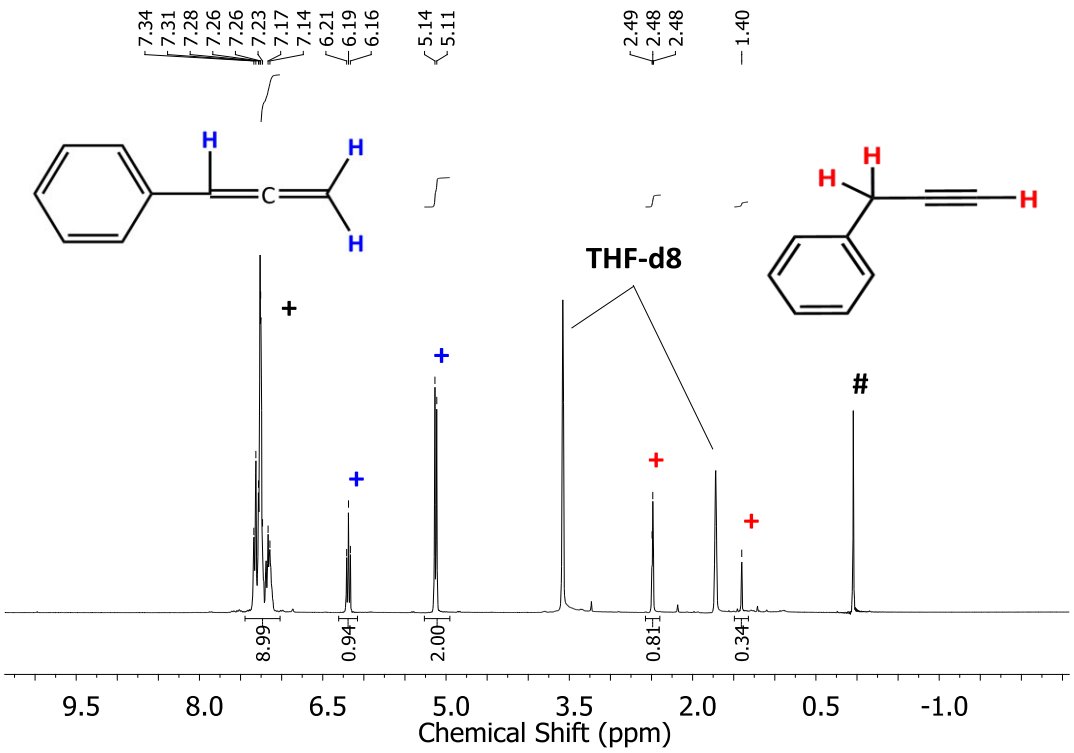

Figure S 17. ^{1}H NMR spectrum of the in situ reaction at room temperature and 5 min reaction time of [K{18c6}][Fe(N(SiMe$_3$)$_2$)$_3$] (1.0 eq) and 3-Phenyl-1-propyne (100.0 eq) in THF-d$_8$ (300.1 MHz). # decomposition. +/+ 3-Phenyl-1-propyne. +/+ Propa-1,2-dien-1-benzene.

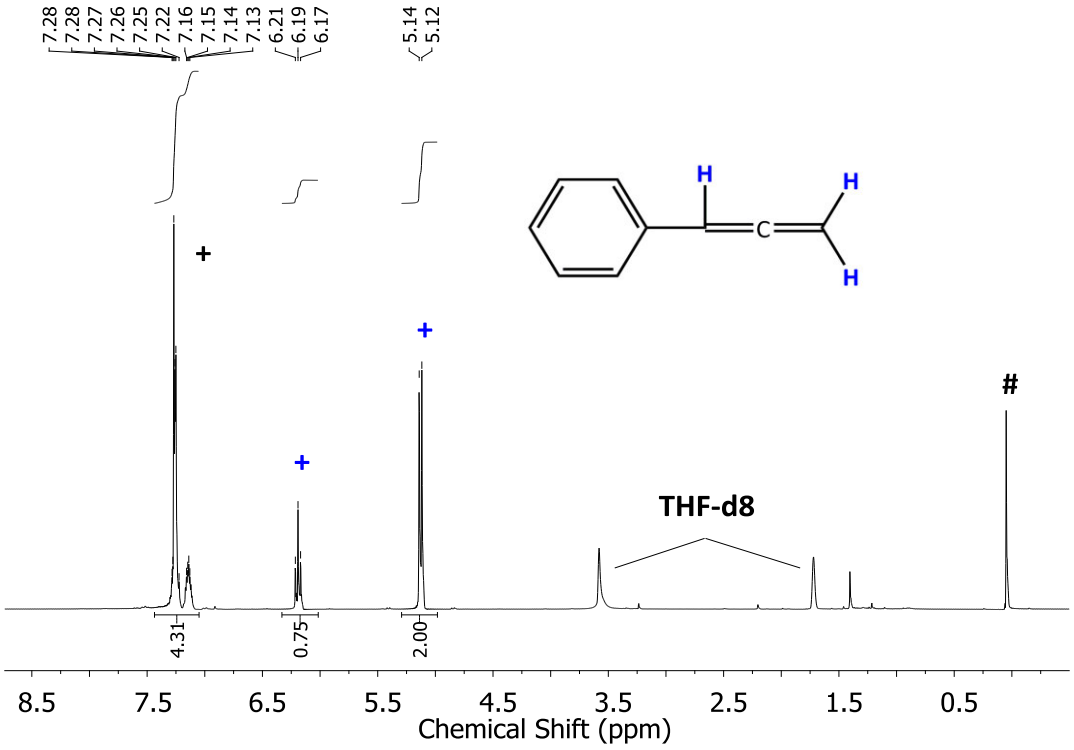

Figure S 18. ^{1}H NMR spectrum of the in situ reaction at room temperature and two weeks reaction time of [K{18c6}][Fe(N(SiMe$_3$)$_2$)$_3$] (1.0 eq) and 3-Phenyl-1-propyne (100.0 eq) in THF-d$_8$ (300.1 MHz). # decomposition. +/+ Propa-1,2-dien-1-benzene.

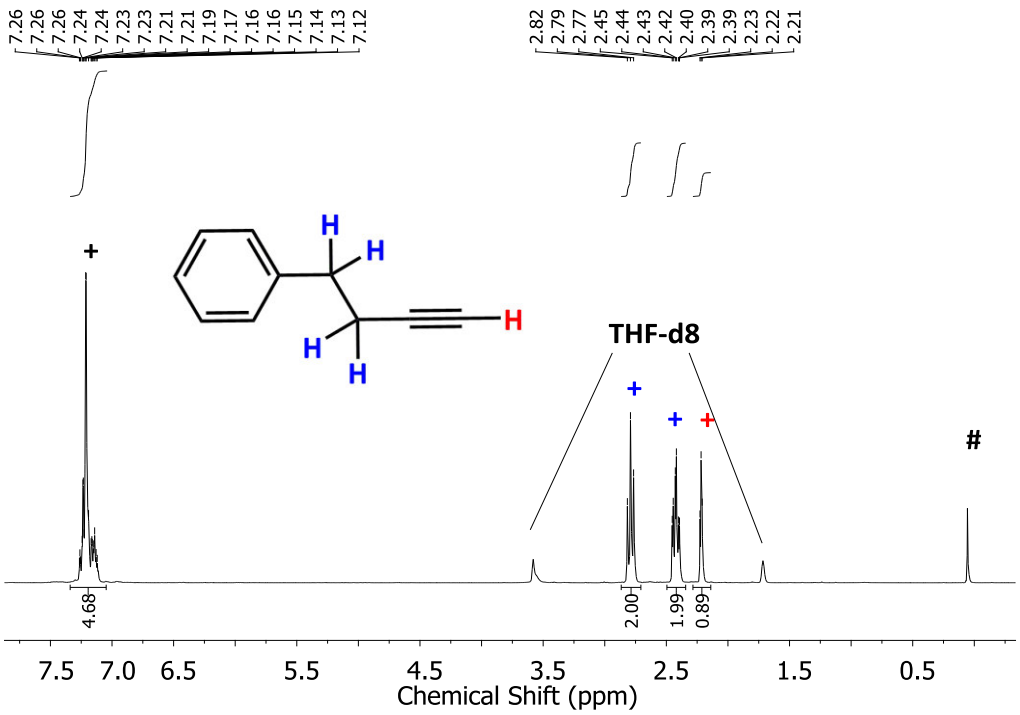

Figure S 19. ^{1}H NMR spectrum of the in situ reaction at room temperature and two weeks reaction time of [K{18c6}][Fe(N(SiMe$_3$)$_2$)$_3$] (1.0 eq) and 4-Phenyl-1-butyne (100.0 eq) in THF-d$_8$ (300.1 MHz). # decomposition. +/+/+ 4-Phenyl-1-butyne. [K{18c6}][Fe(N(SiMe$_3$)$_2$)$_3$] appeared no reactivity observe to this substrate.

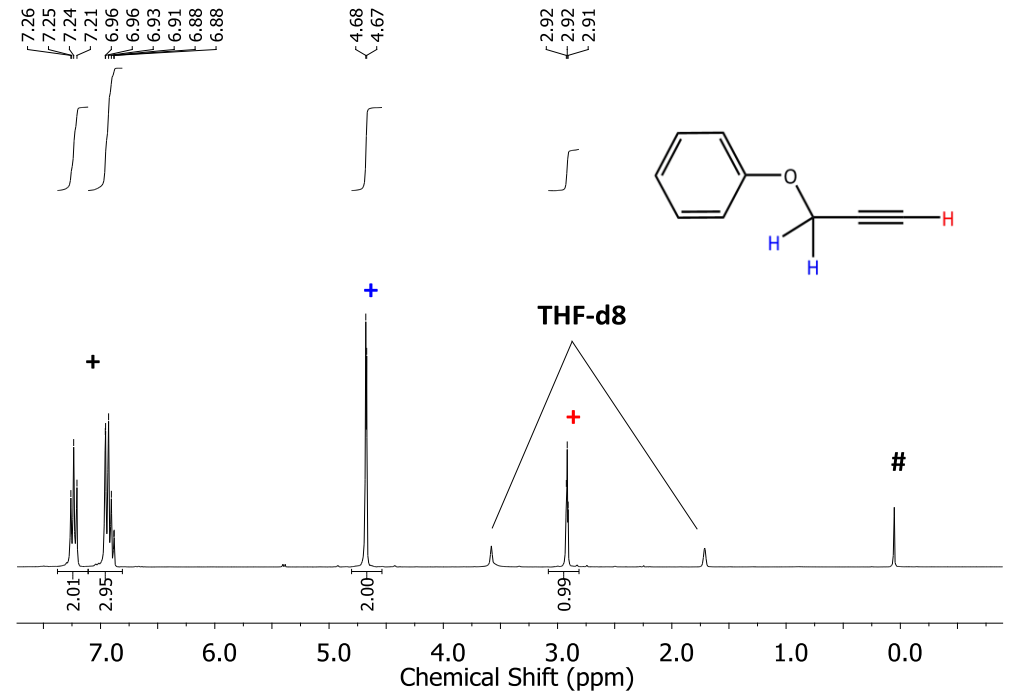

Figure S 20. ^{1}H NMR spectrum of the in situ reaction at room temperature and two weeks reaction time of [K{18c6}][Fe(N(SiMe$_3$)$_2$)$_3$] (1.0 eq) and 4-Phenyl-1-butyne (100.0 eq) in THF-d$_8$ (300.1 MHz). # decomposition. +/+/+ 2-Propynyloxy-benzene. [K{18c6}][Fe(N(SiMe$_3$)$_2$)$_3$] appeared no reactivity observe to this substrate.

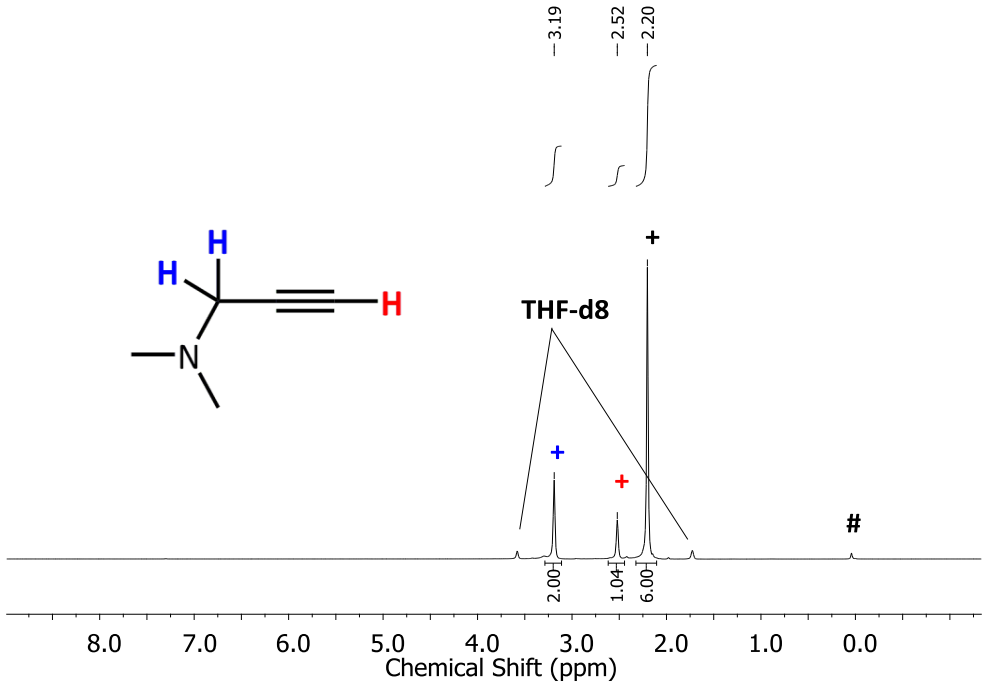

Figure S 21. ^{1}H NMR spectrum of the in situ reaction at room temperature and 5 min reaction time of [K{18c6}][Fe(N(SiMe$_3$)$_2$)$_3$] (1.0 eq) and *N*,*N*-Dimethylpropargulamine (100.0 eq) in THF-d$_8$ (300.1 MHz). # decomposition. +/+/+ *N*,*N*-Dimethylpropargulamine. [K{18c6}][Fe(N(SiMe$_3$)$_2$)$_3$] appeared no reactivity observe to this substrate.

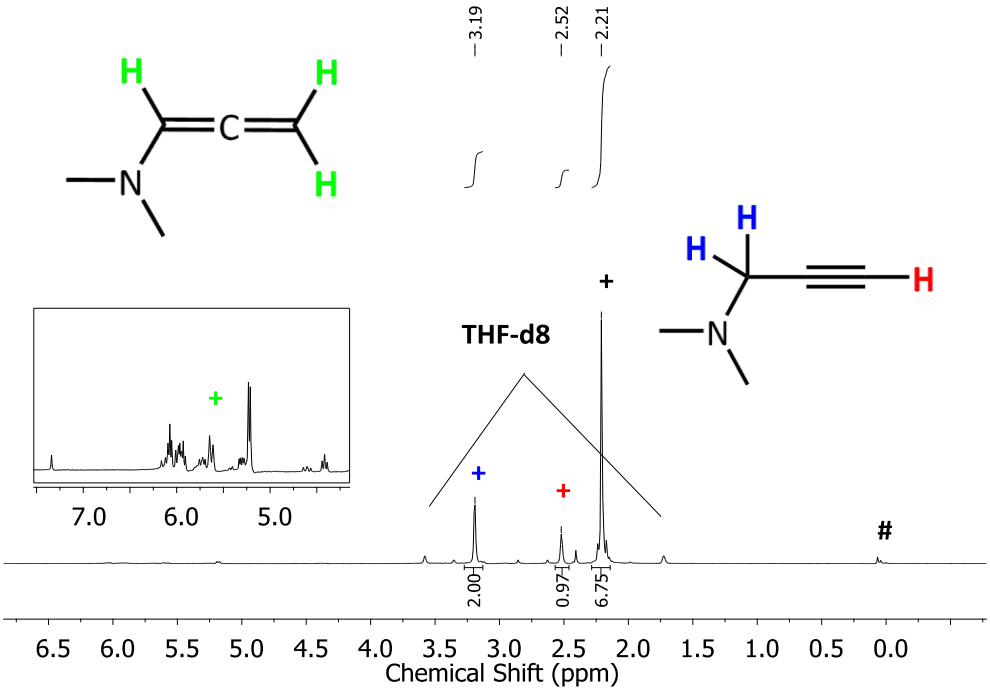

Figure S 22. ^{1}H NMR spectrum of the in situ reaction at room temperature and two weeks reaction time of [K{18c6}][Fe(N(SiMe$_3$)$_2$)$_3$] (1.0 eq) and *N*,*N*-Dimethylpropargulamine (100.0 eq) in THF-d$_8$ (300.1 MHz). # decomposition. +/+/+ *N*,*N*-Dimethylpropargulamine. [K{18c6}][Fe(N(SiMe$_3$)$_2$)$_3$] appeared reactivity observe to this substrate.

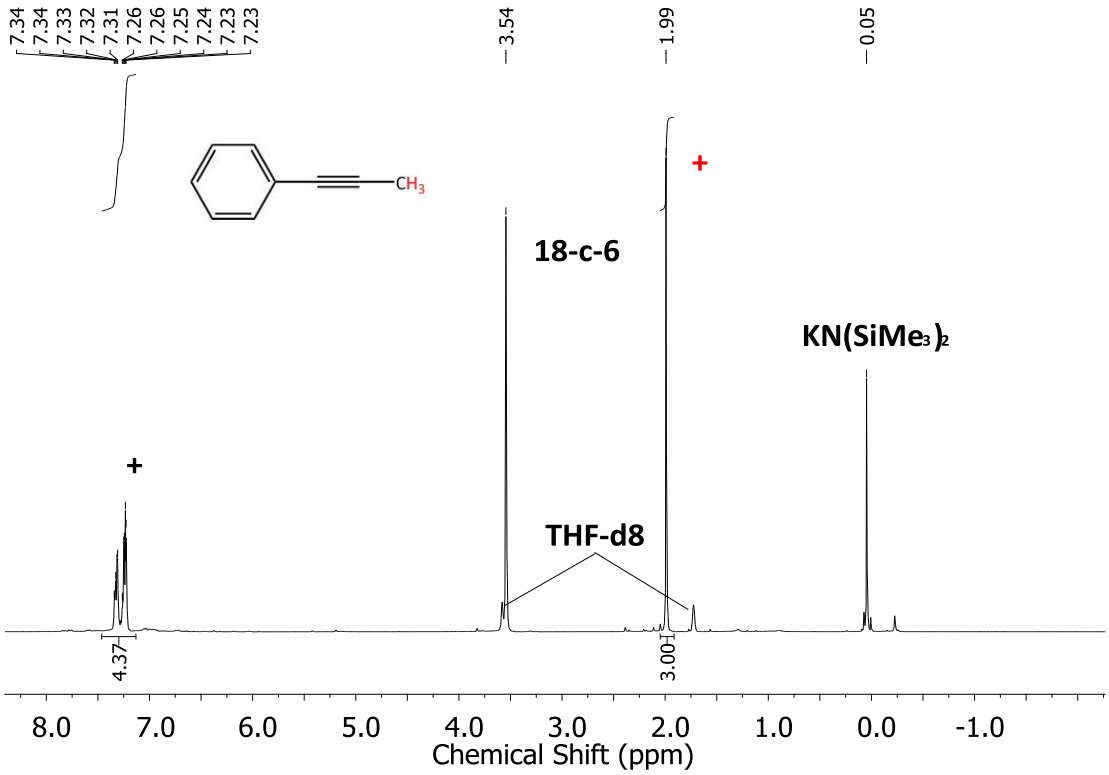

Figure S 23. ^{1}H NMR spectrum of the in situ reaction at room temperature and 5 min reaction time of $KN(SiMe_3)_2$ (10.0 eq) and 3-Phenyl-1-propyne (1.0 eq) in THF-d_8 (300.1 MHz). +/+ 1-Phenyl-1-propyne.

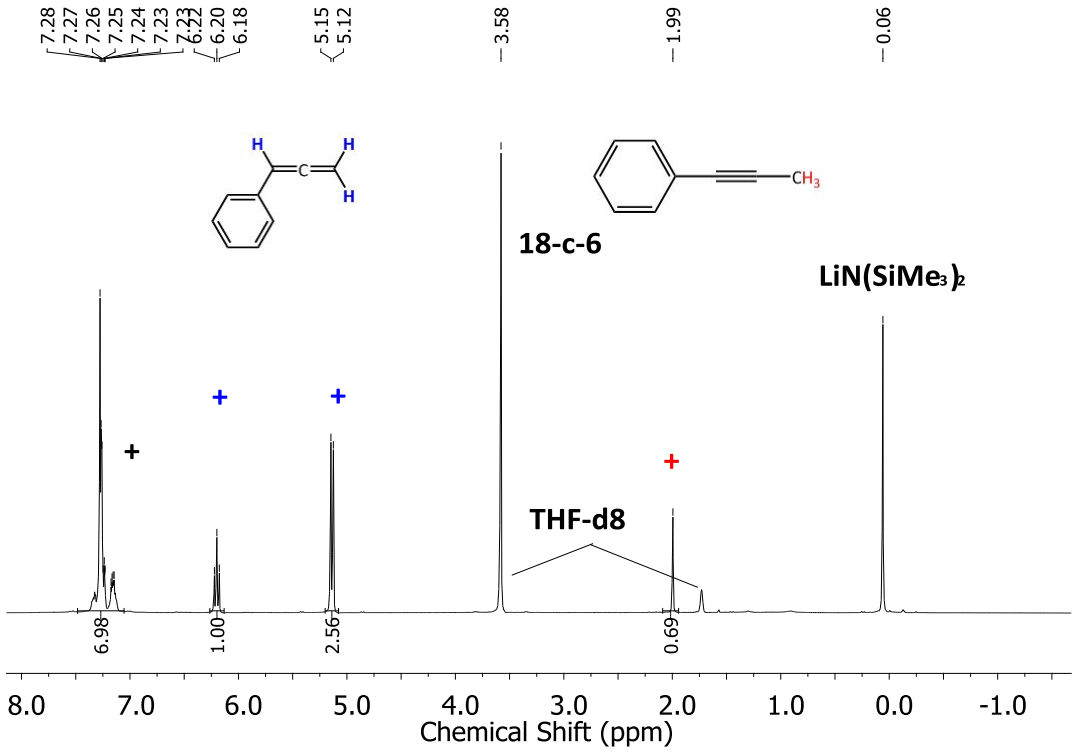

Figure S 24. ^{1}H NMR spectrum of the in situ reaction at room temperature and 5 min reaction time of $LiN(SiMe_3)_2$ (10.0 eq) and 3-Phenyl-1-propyne (1.0 eq) in THF-d_8 (300.1 MHz). +/+ 1-Phenyl-1-propyne. +/+ Propa-1,2-dien-1-benzene.

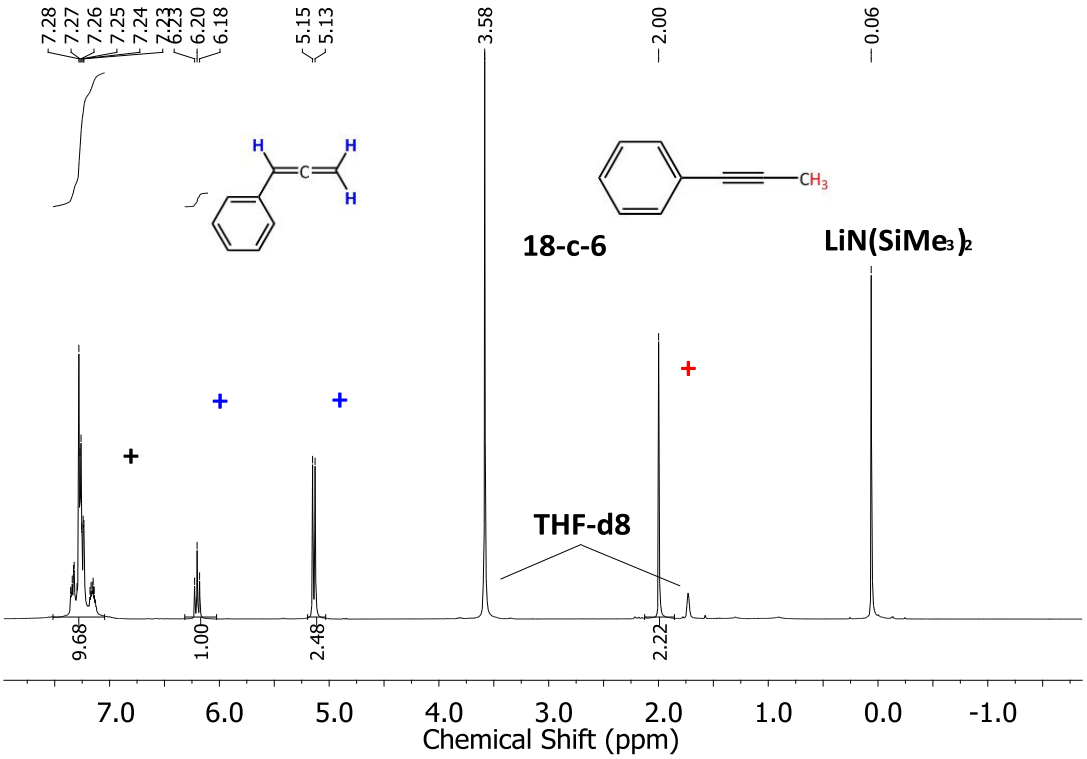

Figure S 25. ^{1}H NMR spectrum of the in situ reaction at room temperature and 24 h reaction time of $LiN(SiMe_3)_2$ (10.0 eq) and 3-Phenyl-1-propyne (1.0 eq) in THF-d_8 (300.1 MHz). +/+ 1-Phenyl-1-propyne. +/+ Propa-1,2-dien-1-benzene.

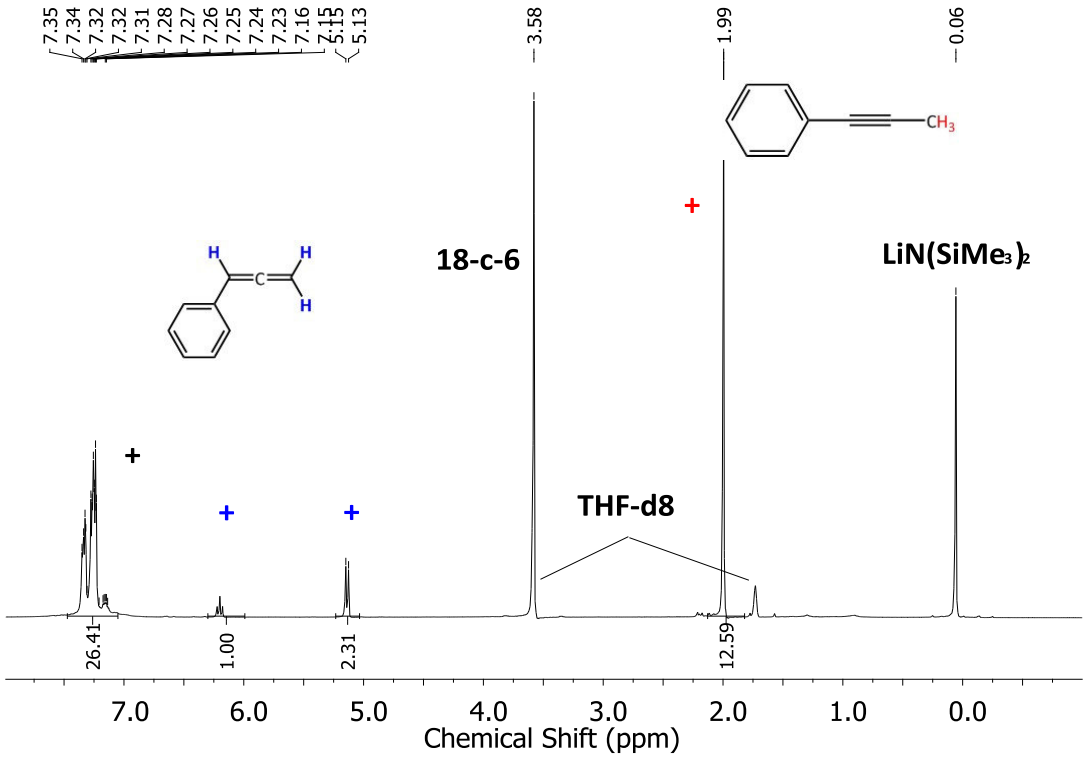

Figure S 26. ^{1}H NMR spectrum of the in situ reaction at room temperature and 7 d reaction time of $LiN(SiMe_3)_2$ (10.0 eq) and 3-Phenyl-1-propyne (1.0 eq) in THF-d_8 (300.1 MHz). +/+ 1-Phenyl-1-propyne. +/+ Propa-1,2-dien-1-benzene.

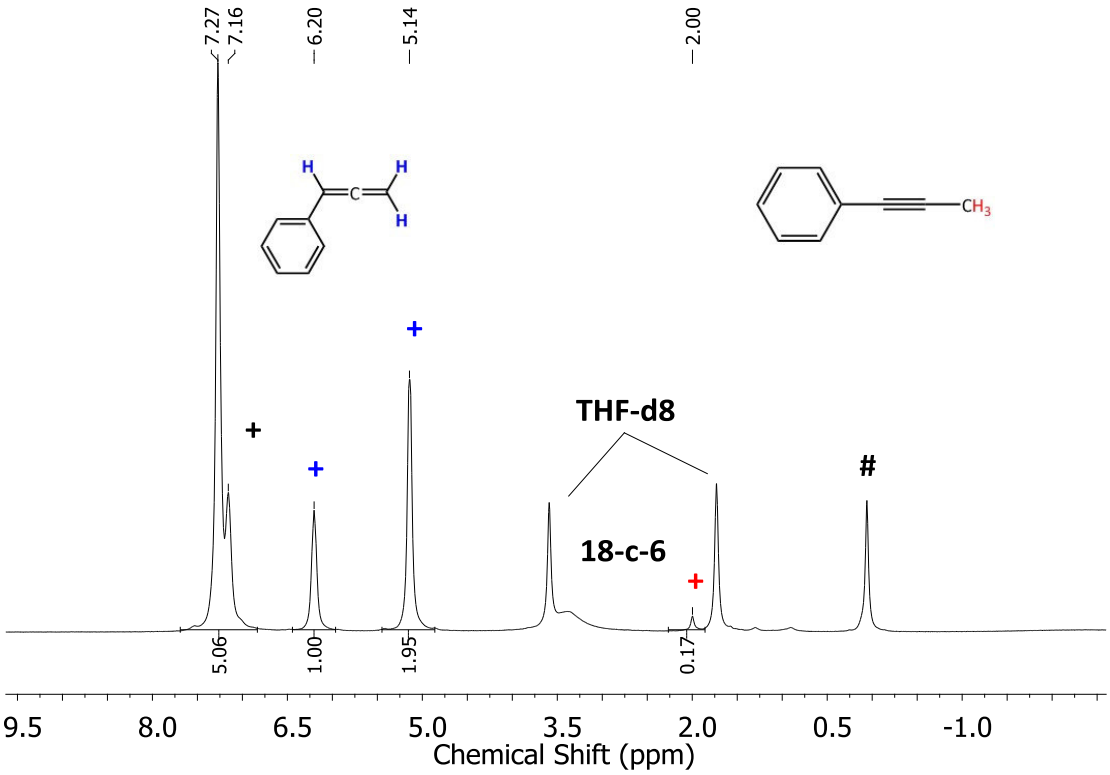

Figure S 27. ^{1}H NMR spectrum of the in situ reaction at room temperature and 5 min reaction time of [K{18c6}][Fe(N(SiMe$_3$)$_2$)$_3$] (1.0 eq), 3-Phenyl-1-propyne (100.0 eq) and[K{18c6}][Fe(N(SiMe$_3$)$_2$)$_2$] in THF-d$_8$ (300.1 MHz). # decomposition. +/+ 1-Pheynl-1-propyne. +/+ Propa-1,2-dien-1-benzene.

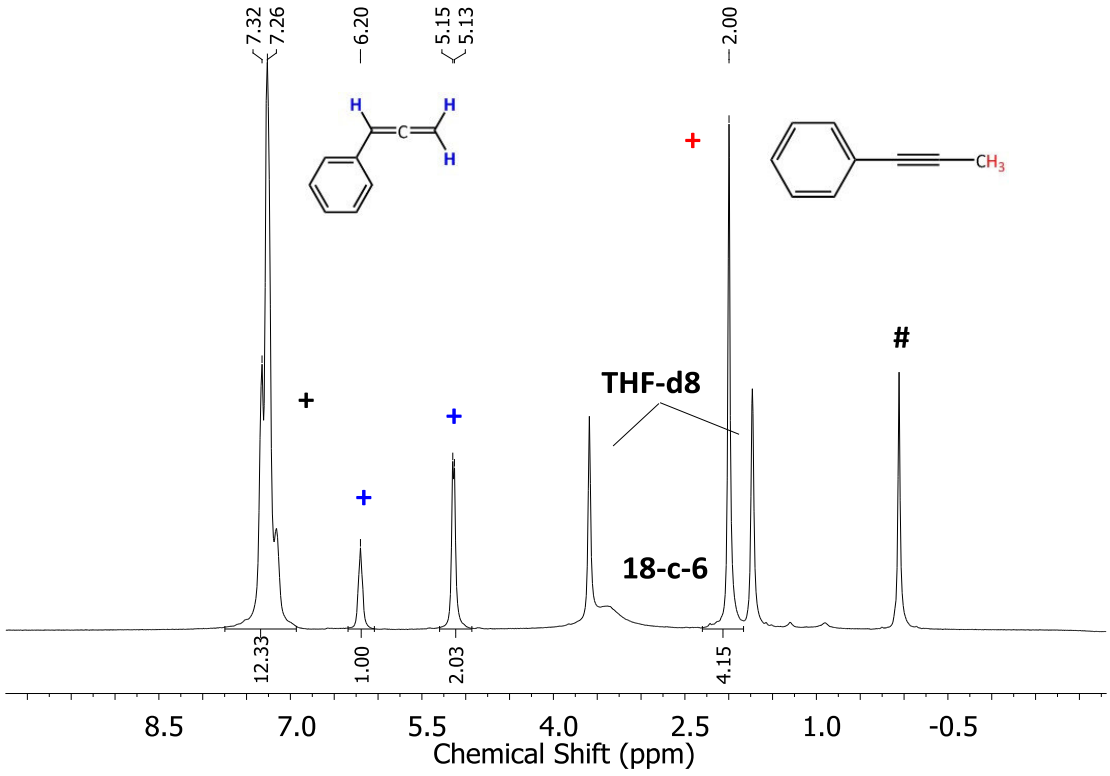

Figure S 28. ^{1}H NMR spectrum of the in situ reaction at room temperature and 12 h reaction time of [K{18c6}][Fe(N(SiMe$_3$)$_2$)$_3$] (1.0 eq), 3-Phenyl-1-propyne (100.0 eq)

and[K{18c6}][Fe(N(SiMe$_3$)$_2$)$_2$] in THF-d$_8$ (300.1 MHz). # decomposition. +/+ 1-Pheynl-1-propyne. +/+ Propa-1,2-dien-1-benzene.

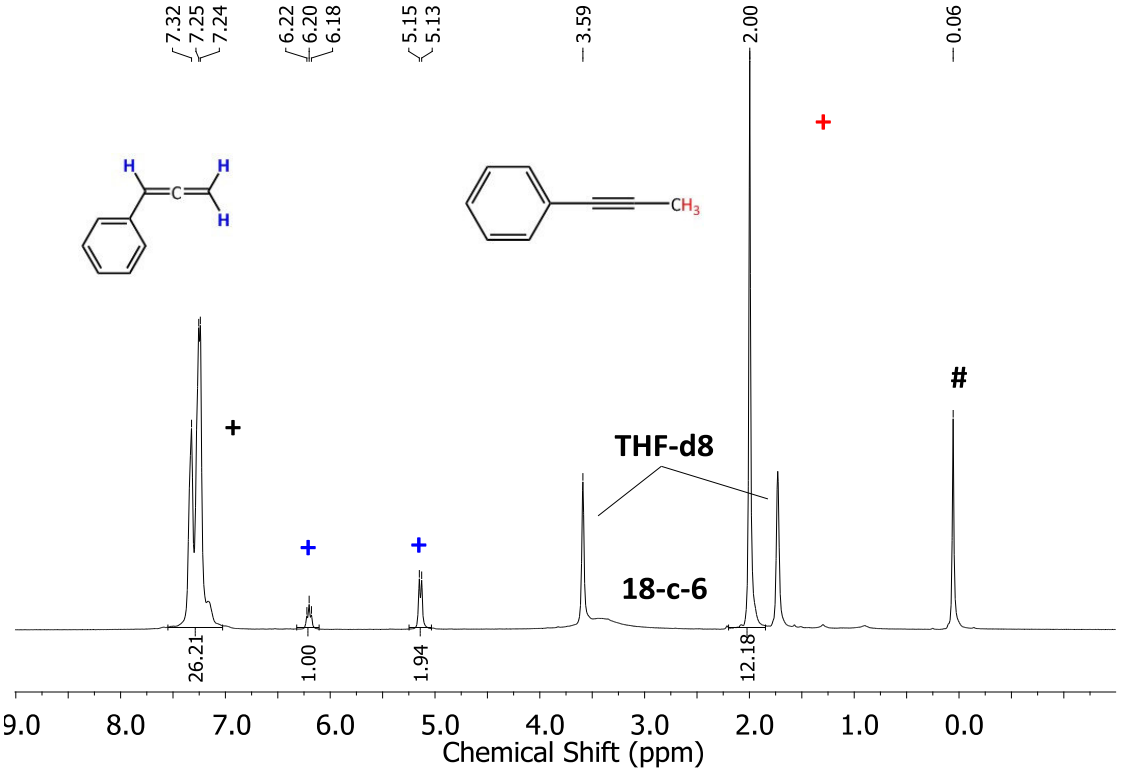

Figure S 29. ^{1}H NMR spectrum of the in situ reaction at room temperature and 48 h reaction time of [K{18c6}][Fe(N(SiMe$_3$)$_2$)$_3$] (1.0 eq), 3-Phenyl-1-propyne (100.0 eq) and[K{18c6}][Fe(N(SiMe$_3$)$_2$)$_2$] in THF-d$_8$ (300.1 MHz). # decomposition. +/+ 1-Pheynl-1-propyne. +/+ Propa-1,2-dien-1-benzene.

2. IR Spectra

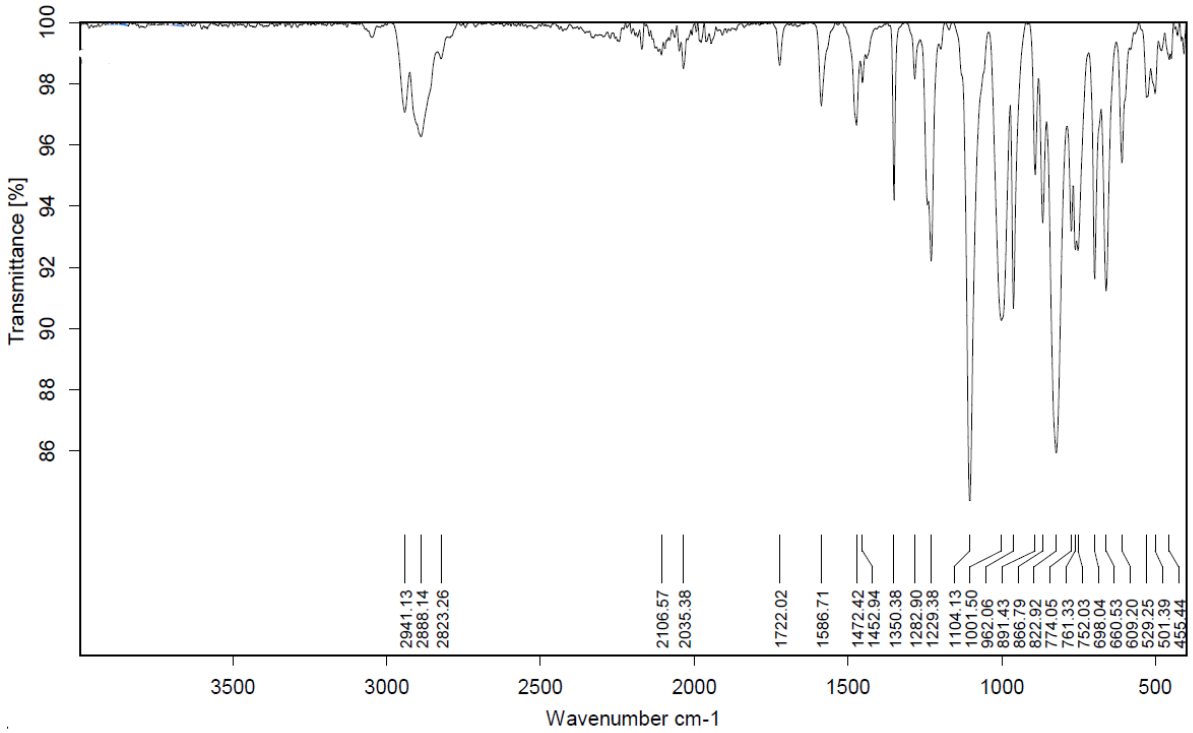

Figure S 30. IR spectrum of **[K{18c6}][Fe(N(SiMe$_3$)$_2$)$_2$(η^2-PhCCH)]** (**1**).

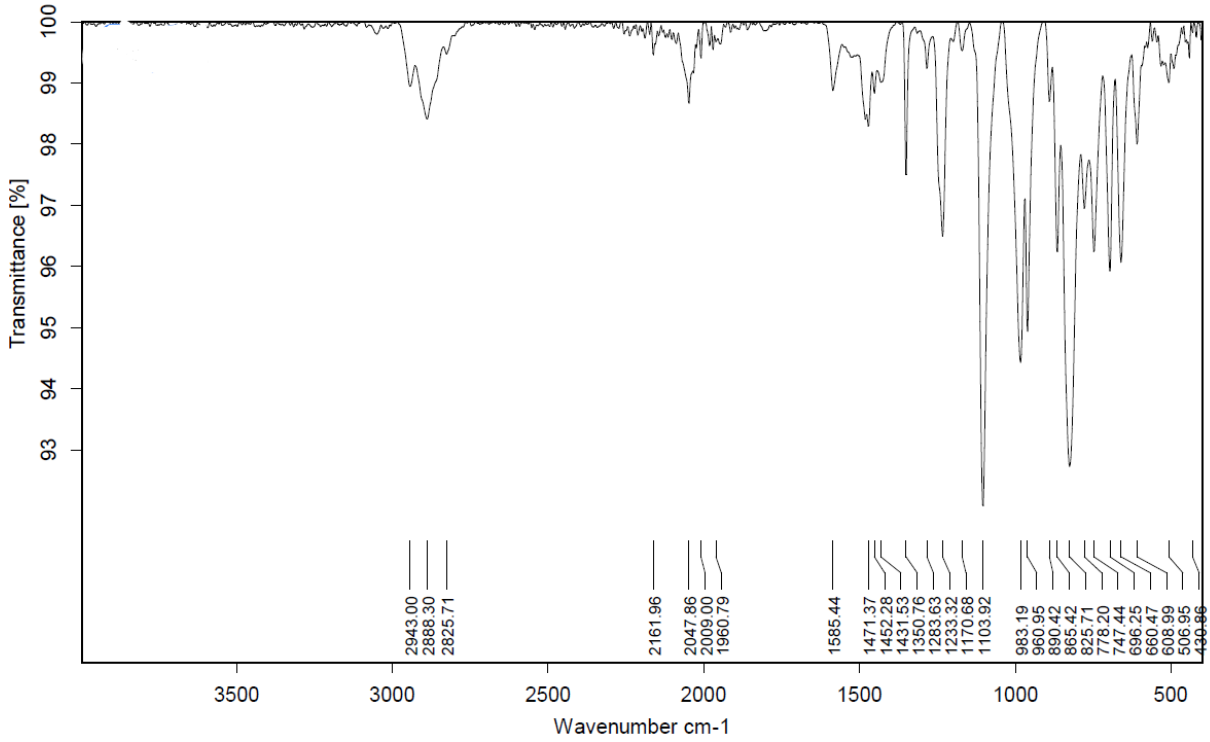

Figure S 31. IR spectrum of **[K{18c6}][Fe(N(SiMe$_3$)$_2$)$_2$(η^2-PhCCMe)]** (**2**).

3. UV/Vis Spectra

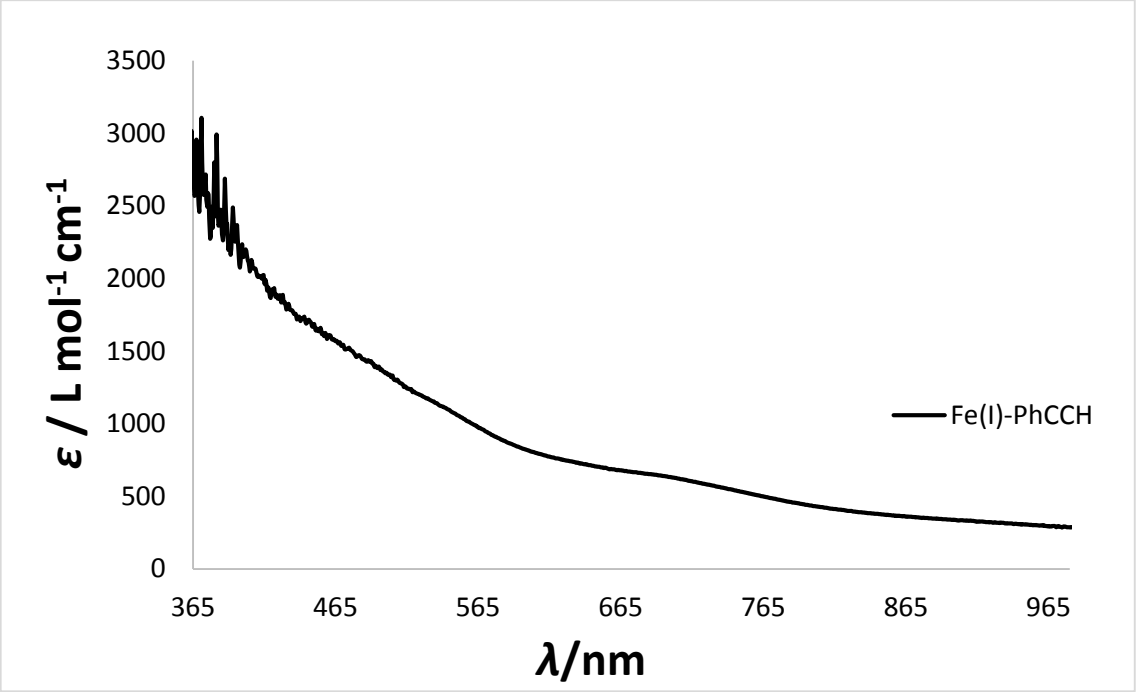

Figure S 32. UV/vis spectrum of **[K{18c6}][Fe(N(SiMe$_3$)$_2$)$_2$(η^2-PhCCH)]** (**1**) in Et$_2$O.

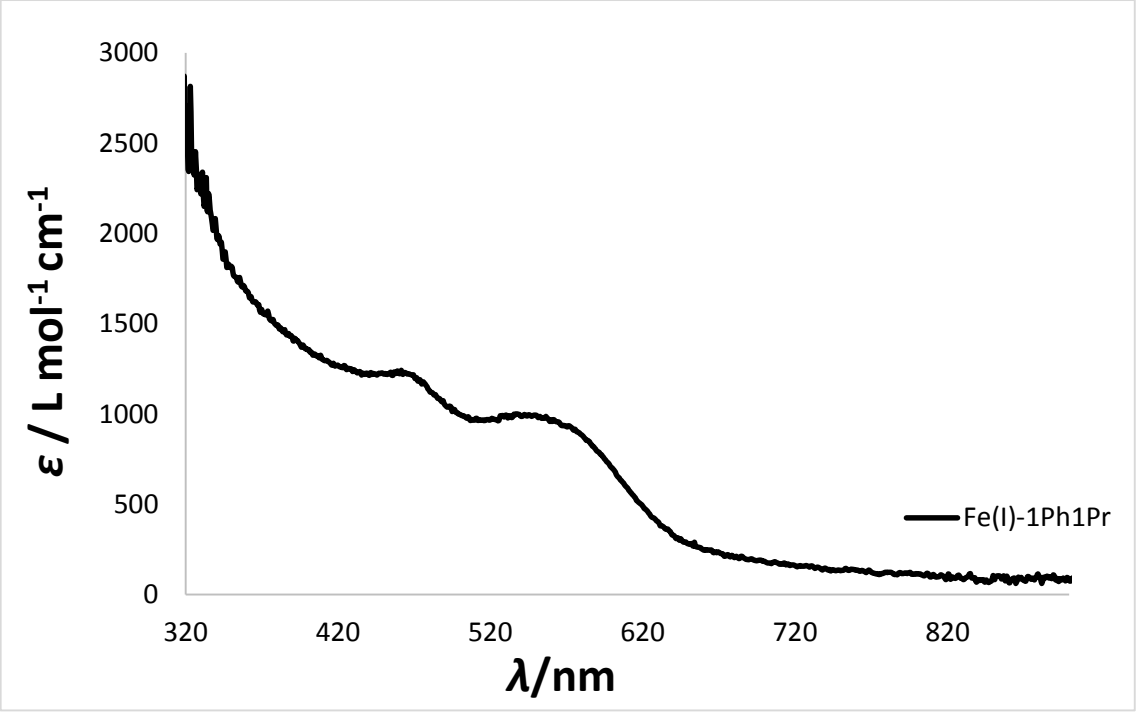

Figure S 33. UV/vis spectrum of **[K{18c6}][Fe(N(SiMe$_3$)$_2$)$_2$(η^2-PhCCMe)]** (**1**) in Et$_2$O.

4. X-Ray diffraction analysis and molecular structures

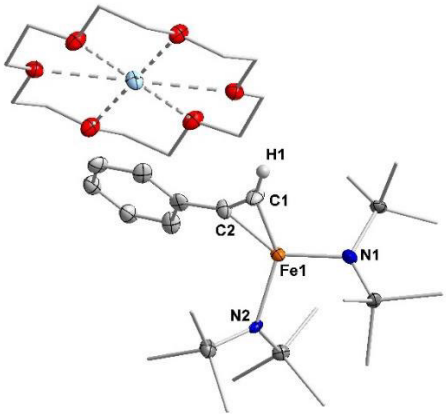

Figure S 34. Molecular structure of **1**. All hydrogen atoms are omitted for clarity. For **1** a disorder of the anionic ligand is found.

Table S 1. Crystal data and structure refinement for **1**.

Identification code	NHX05_0m
Empirical formula	$C_{32}H_{66}FeKN_2O_6Si_4$
Formula weight	782.17
Temperature / *K*	100.0
Crystal system	monoclinic
Space group	$P2_1/n$
a/Å	15.4733(14)
b/Å	13.1341(12)
c/Å	21.626(2)
α/°	90
β/°	94.876(3)
γ/°	90
Volume / Å^3	4379.1(7)
Z	4
ρ_{calc} g/cm^3	1.186
μ/mm^{-1}	0.587
F(000)	1684.0
Crystal size / mm^3	0.399 × 0.135 × 0.116
Radiation	MoKα (λ = 0.71073)
2Θ range for data collection /°	4.396 to 51
Index ranges	-18 ≤ h ≤ 18, -15 ≤ k ≤ 15, -26 ≤ l ≤ 26
Reflections collected	90751
Independent reflections	8146 [R_{int} = 0.1194, R_{sigma} = 0.0534]
Data/restraints/parameters	8146/109/687
Goodness-of-fit on F^2	1.041
Final *R* indexes [I>=2σ (I)]	R_1 = 0.0419, wR_2 = 0.0819
Final *R* indexes [all data]	R_1 = 0.0790, wR_2 = 0.0907

Largest diff. peak/hole / e Å^{-3}	0.41/-0.27

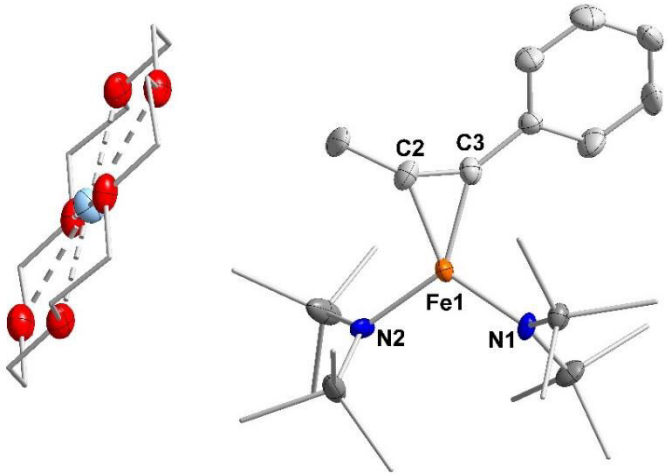

Figure S 35. Molecular structure of **2**. All hydrogen atoms are omitted for clarity.

Table S 2. Crystal data and structure refinement for **2**.

Identification code	PIM107_0m
Empirical formula	$C_{33}H_{68}FeKN_2O_6Si_4$
Formula weight	796.20
Temperature / *K*	100.0
Crystal system	monoclinic
Space group	$P2_1/n$
a/Å	16.4150(16)
b/Å	13.2604(12)
c/Å	20.7970(19)
α/°	90
β/°	98.928(3)
γ/°	90
Volume / Å^3	4472.0(7)
Z	4
ρ_{calc} g/cm^3	1.183
μ/mm^{-1}	0.576
F(000)	1716.0
Crystal size / mm^3	0.177 × 0.164 × 0.128
Radiation	MoKα (λ = 0.71073)
2Θ range for data collection /°	4.258 to 49.994
Index ranges	-19 ≤ h ≤ 19, -15 ≤ k ≤ 15, -24 ≤ l ≤ 24
Reflections collected	59594
Independent reflections	7854 [R_{int} = 0.1334, R_{sigma} = 0.0742]
Data/restraints/parameters	7854/0/440
Goodness-of-fit on F^2	1.170
Final *R* indexes [I>=2σ (I)]	R_1 = 0.1010, wR_2 = 0.2118
Final *R* indexes [all data]	R_1 = 0.1331, wR_2 = 0.2213

Largest diff. peak/hole / e $Å^{-3}$	1.09/-0.58

8.5 Supporting Information zur Publikation „The ambiguous behaviour of diphosphinestowards the quasilinear iron(I) complex $[Fe(N(SiMe_3)_2)_2]^-$ between inertness, P–C bondcleavage and C–C double bond isomerisation"

C. Gunnar Werncke und Igor Müller, *Chem. Commun.,* **2020**, *56*, 2268.

The Ambiguous Behaviour of Diphosphines Towards The Quasilinear Iron(I) Complex $[Fe(N(SiMe_3)_2)_2]^-$ – Between Inertness, P−C Bond Cleavage and C−C Double Bond Isomerisation

Christian Gunnar Werncke,*[a] and Igor Müller

a) Philipps-University Marburg, Hans-Meerwein-Straße 4, D-35032 Marburg, Germany

Table of Contents

General considerations

All manipulations were carried out in a glovebox or using Schlenk-type techniques under a dry argon atmosphere. Used solvents were dried by continuous distillation over sodium metal for several days, degassed via three freeze-pump-thaw cycles and stored over molecular sieves 4 Å. THF-d_8 was degassed via three freeze-pump-thaw cycles and stored over molecular sieves 4 Å. The ^{1}H NMR spectra were recorded on a *Bruker AV III 500* or *Bruker AV II 300* NMR spectrometers. Chemical shifts are reported in ppm relative to the residual proton signals of the solvent (for ^{1}H) or relative to the signal of the solvent itself (^{13}C). $w_{1/2}$ is the line width of a signal at half its maximum intensity. Integrals of the broad signals of the silylamide units were obtained directly or by peak fitting (in case of overlapping signals) using the MestreNova software package. IR measurements were conducted on a *Bruker Alpha ATR-IR* spectrometer. The UV/VIS measurement were recorded on an *Analytik Jena Specord S600* diode array UV/Vis spectrometer using the *WinASPECT* software. Elemental analysis was performed by the "in-house" service of the Chemistry Department of the Philipps University Marburg, Germany using a CHN(S) analyzer *vario MICRO Cube* (*Elementar)*. Solution magnetic susceptibilities were determined by the Evans method.[i] All substrates were obtained commercially (Sigma-Aldrich, Acros, Strem, Alfa Aesar) and - if not noted otherwise - used as received. Dimethoxy ethane, N-methyl-2-pyrrolidone, NEt_3, TMEDA and 4-tert-butylpyridine were degassed, transferred into the glovebox and stored over molecular sieves. 18-crown-6 was sublimed prior use to remove traces of water. [Fe{N(SiMe$_3$)$_2$}$_2$][ii] and K{18c6}[Fe{N(SiMe$_3$)$_2$}$_2$], **1**,[iii] were prepared according to literature procedures.

1. Synthesis of K{18-crown-6}[Fe(N(SiMe$_3$)$_2$)$_3$] (2)

A solution of 38 mg (0.1 mmol, 1 equiv.) Fe(N(SiMe$_3$)$_2$)$_2$ and 27 mg (0.1 mmol, 1 equiv.) 18-crown-6 in 2 ml Et$_2$O was treated with 20 mg (0.1 mmol 1 equiv.) KN(SiMe$_3$)$_2$. After 1 minute the colourless solution was filtered, layered with 3 ml pentane and stored at -35°C. After 16 h the supernatant solution was removed via a Pasteur pipette. The remaining colourless crystalline solid was washed with 2x2 ml pentane. Drying of the solid in vacuo yielded 74 mg (0.088 mmol, 88%) **K{18-crown-6}[Fe(N(SiMe$_3$)$_2$)$_3$]**, **2**. ^{1}H NMR (THF-d$_8$, 298 K, ppm, 500.1 MHz): δ = 3.38 (24 H, $w_{1/2}$ = 7.3 Hz, O-CH$_2$), -2.36 (54H, $w_{1/2}$ = 530 Hz, SiMe$_3$). IR (ATR, cm^{-1}): ν = 2944 (m), 2892 (m), 1471 (vw), 1454 (vw), 1351 (m), 1233 (s), 1105 (vs), 977 (vs), 960 (s), 866 (m), 824 (vs), 780 (m), 750 (m), 709 (m), 661 (s), 609 (m), 529 (w). Elemental analysis calcd. (%) for C$_{30}$H$_{78}$FeKN$_3$O$_6$Si$_6$ (840.42 g/mol): C 42.87, H 9.36, N 5.00; found: C 42.47, H 9.02, N 4.88. μ_{eff} = 5.15 μ_B (Evans, THF-d$_8$ + 1% Si(CH$_3$)$_4$), $\mu_{s.o.}$ = 4.90 μ_B).

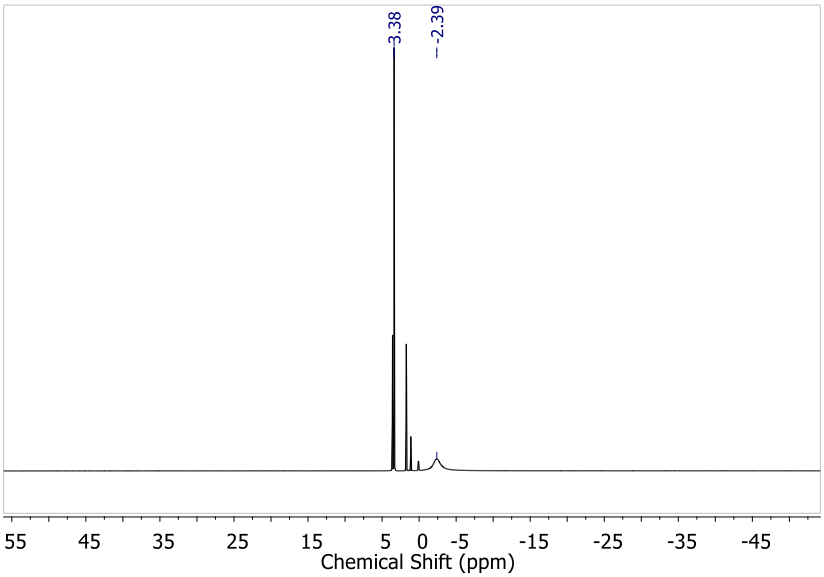

Figure S 1. ^{1}H NMR spectrum of K{18-crown-6}[Fe(N(SiMe$_3$)$_3$)] (**2**) in THF-d$_8$ (500.1 MHz).

2. Synthesis of K{18-crown-6}[Fe(Ph)(N(SiMe$_3$)$_2$)(ppbz*] (3)

A solution of 136 mg (0.2 mmol, 1 equiv.) **K{18-crown-6}[Fe(N(SiMe$_3$)$_2$)$_2$]** (**1**) in 5 ml Et$_2$O was treated with 45 mg dppbz (0.1 mmol, 0.5 equiv.). After stirring over night the blood red suspension was filtered, the dark red crystalline residue washed with 3 ml Et$_2$O and shortly dried *in vacuo* yielding 19 mg (0.017 mmol) of **K{18-crown-6}[Fe(Ph)(N(SiMe$_3$)$_2$)(ppbz]***2Et$_2$O (**3***2Et$_2$O). The combined filtrates were slightly reduced in volume *in vacuo* and kept at room temperature for several days to give a second crop of blood red crystals of **3***2Et$_2$O (45 mg, 0.041 mmol, combined yield 58%). ^{1}H NMR (THF-d$_8$, 298 K, ppm, 500.1 MHz): δ = 85.8, 27.6, 18.2, 15.6, 13.3, 7.1 ($w_{1/2}$ = 762 Hz, SiMe$_3$), 3.14 ($w_{1/2}$ = 120 Hz, O-C*H*$_2$), -11.34, -13.95, -22.65, -23.0, -53.0.). IR (ATR, cm^{-1}): ν = 3050 (vw), 2943 (w), 2891 (m), 1562 (w), 1469 (vw), 1433 (w), 1416 (w), 1350 (m), 1282 (m), 1235 (m), 1102 (vs), 1023 (m), 995 (s), 960 (s), 871 (m), 820 (s), 778 (s), 744 (m), 719 (s), 695 (s), 659 (m), 615 (m), 528 (m), 514 (m), 460 (m), 437 (w). Elemental analysis calcd. (%) for C$_{56}$H$_{84}$FeKNO$_8$P$_2$Si$_2$ (1110.45 g/mol): C 60.36, H 7.78, N 1.26; found: C 60.77, H 7.04, N 1.59. μ_{eff} = 5.29 μ_B (Evans, THF-d$_8$ + 1% Si(CH$_3$)$_4$), $\mu_{s.o.}$ = 4.90 μ_B).

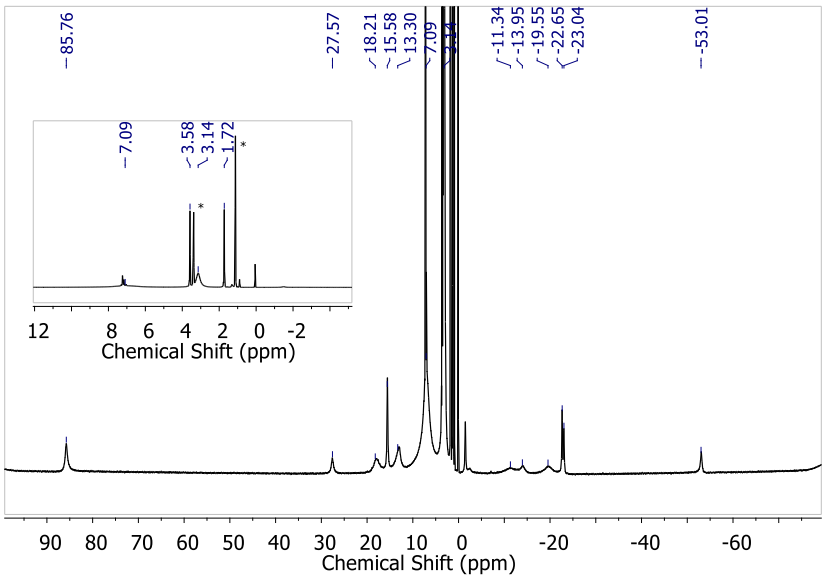

Figure S 2. ^{1}H NMR spectrum of K{18-crown-6}[Fe(Ph)(N(SiMe$_3$)$_2$)(ppbz*] (**3**) in THF-d$_8$ (500.1 MHz). (*) denotes Et$_2$O.

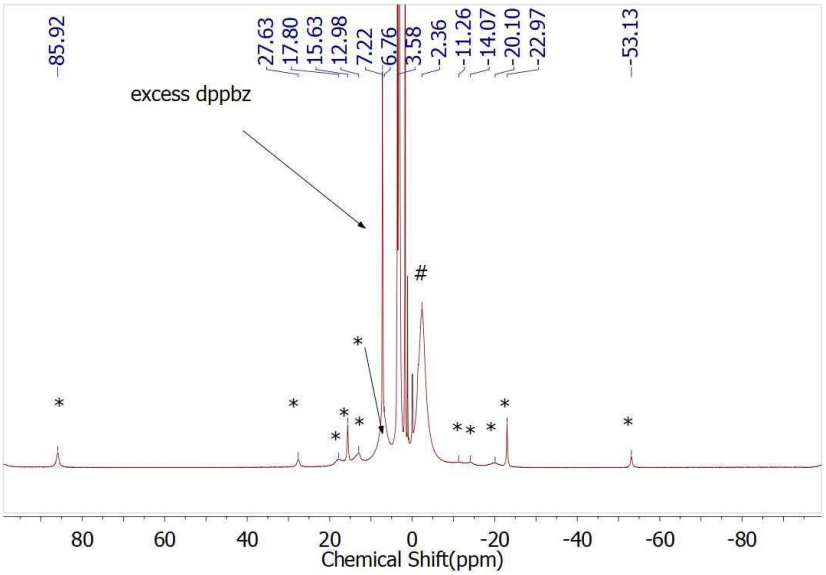

Figure S 3. *In-situ* ^{1}H NMR spectrum of the reaction of complex **1** with 1 equivalent dppbz (formally 0.5 equivalent excess). (*) signals belonging to complex **3**; (#) signal belonging to complex **2**. Integral ratio of the signals attributed to the respective SiMe$_3$ groups is 2.8 (complex **2**, signal at -2.36 ppm) : 1 (complex **3**, broad signal around 7 ppm). Deviation from the expected 3:1 integral ratio can be attributed to differences in paramagnetically induced line broadening and very short relaxation times.

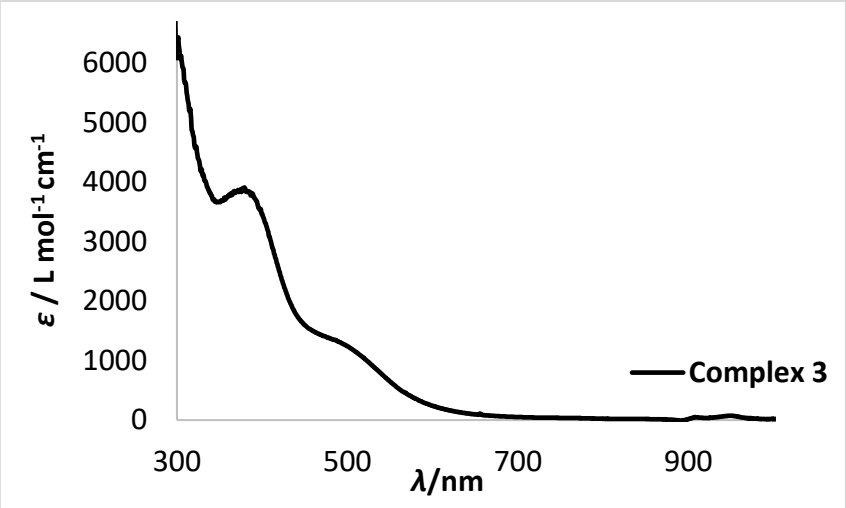

Figure S 4. UV/Vis spectrum of K{18-crown-6}[Fe(Ph)(N(SiMe$_3$)$_2$)(ppbz*] (**3**) in THF.

3. Synthesis of K{18-crown-6}[Fe(N(SiMe$_3$)$_2$)$_2$(*trans*-dppee)] (4)

Method A: A solution of 34 mg (0.05 mmol, 1 equiv.) **K{18-crown-6}[Fe(N(SiMe$_3$)$_2$)$_2$]** (**1**) in 3 ml THF was treated with 20 mg (0.05 mmol, 1 equiv.) *cis*-dppee. After stirring for 3 days, the brown red solution was stripped of all volatiles *in vacuo*. The residue was extracted with a mixture of 2 ml Et$_2$O and 0.5 ml THF, the filtrate layered with 3 ml pentane and stored at -40°C. After 2 days the supernatant solution was removed using a Pasteur pipette. The remaining brown crystals were rinsed with 2x2 ml pentane and dried *in vacuo* to yield 33 mg (0.031 mmol, 61%) of **K{18-crown-6}[Fe(N(SiMe$_3$)$_2$)(*trans*-dppee)]**, **4**.

Method B: A solution of 34 mg (0.05 mmol, 1 equiv.) **K{18-crown-6}[Fe(N(SiMe$_3$)$_2$)$_2$]** (**1**) in 3 ml THF was treated with 20 mg (0.05 mmol, 1 equiv.) *trans*-dppee. After stirring for 30 minutes, the brownish red solution was stripped of all volatiles *in vacuo*. The residue was extracted with a mixture of 2 ml Et$_2$O and 0.5 ml THF, the filtrate layered with 3 ml pentane and stored at -40°C. After 2 days the supernatant solution was removed using a Pasteur pipette. The remaining brown crystals were rinsed with 2x2 ml pentane and dried *in vacuo* to yield 51 mg (0.047 mmol, 94% yield) of **K{18-crown-6}[Fe(N(SiMe$_3$)$_2$)(*trans*-dppee)], 4**.

^{1}H NMR (THF-d$_8$, 298 K, ppm, 500.1 MHz): δ = 14.71 ($w_{1/2}$ = 303 Hz), 10.23 ($w_{1/2}$ = 57 Hz), 9.54 ($w_{1/2}$ = 51 Hz), 7.33 ($w_{1/2}$ = 52 Hz), 6.58 ($w_{1/2}$ = 52 Hz), 2.44 ($w_{1/2}$ = 65 Hz, O-C*H*$_2$), -4.53 ($w_{1/2}$ = 237 Hz, SiMe$_3$), -18.27 ($w_{1/2}$ = 52 Hz). IR (ATR, cm^{-1}): ν = 2939 (w), 2892 (w), 1583 (w), 1471 (w), 1451 (w), 1431 (w), 1351 (m), 1283 (w), 1244 (m), 1232 (m), 1105 (vs), 1053 (w), 989 (s), 959 (s), 885 (s), 864 (s), 819 (vs), 776 (m), 748 (m), 731 (s), 695 (s), 657 (s), 609 (s), 509 (m), 464 (s), 446 (m), 428 (m). Elemental analysis calcd. (%) for $C_{50}H_{82}FeKNO_8P_2Si_4$ (1076.44 g/mol): C 55.79, H 7.68, N 2.60; found: C 55.60, H 7.78, N 2.66. μ_{eff} = 4.38 μ_B (Evans, THF-d$_8$ + 1% Si(CH$_3$)$_4$), $\mu_{s.o.}$ = 3.87 μ_B).

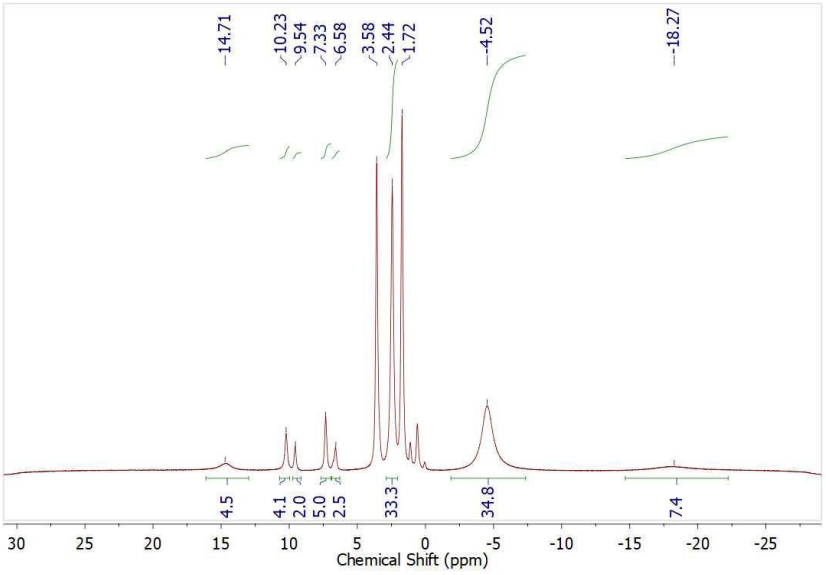

Figure S 5. ^{1}H NMR spectrum of K{18-crown-6}[Fe(N(SiMe$_3$)$_2$)$_2$(*trans*-dppee)] (**4**) in THF-d$_8$ (500.1 MHz).

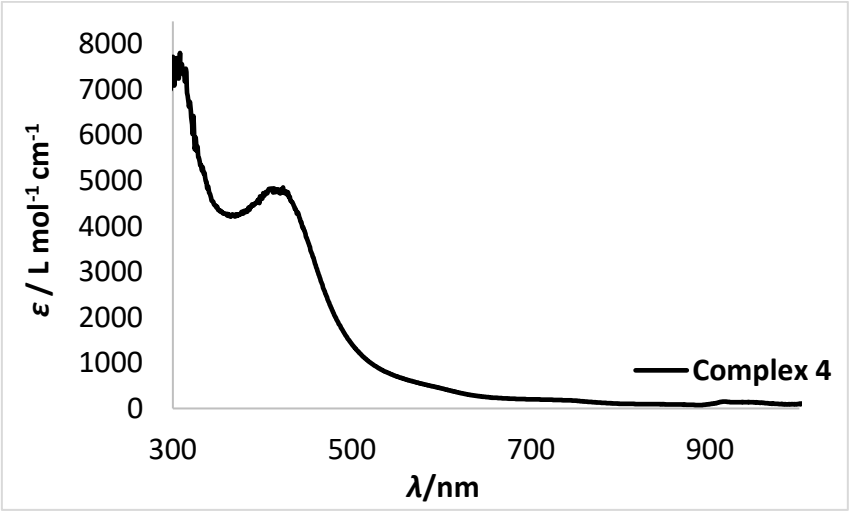

Figure S 6. UV/Vis spectrum of K{18-crown-6}[Fe(N(SiMe$_3$)$_2$)$_2$(*trans*-dppee)] (**4**) in THF.

4. Synthesis of K{18-crown-6}[Fe(N(SiMe$_3$)$_2$)$_2$)(*cis*-dppee)] (5)

A solution of 34 mg (0.05 mmol, 1 equiv.) **K{18-crown-6}[Fe(N(SiMe$_3$)$_2$)$_2$]** in 3 ml THF was treated with 20 mg (0.05 mmol, 1 equiv.) *cis*-dppee. After stirring for 1 minute, the brown red solution was stripped of all volatiles *in vacuo*. The residue was extracted with a mixture of 2 ml Et$_2$O and 0.5 ml THF and the filtrate layered with 3 ml pentane and stored at -40°C. After 2 days, the supernatant solution was removed using a Pasteur pipette. The remaining brown crystals were rinsed with 2x2 ml pentane and dried *in vacuo* to yield 33.6 mg (0.031 mmol, 62%) of **K{18-crown-6}[Fe(N(SiMe$_3$)$_2$)(*cis*-dppee)], 5**.

^{1}H NMR (THF-d$_8$, 298 K, ppm, 500.1 MHz): δ = 15.25 (4H, $w_{1/2}$ = 110 Hz), 12.40 (2H, $w_{1/2}$ = 80 Hz), 7.25 (8H, $w_{1/2}$ = 75 Hz), 3.81 (2H, $w_{1/2}$ = 140 Hz), 3.09 (24 H, $w_{1/2}$ = 110 Hz, O-CH_2), 2.11 (2H, $w_{1/2}$ = 100 Hz), –2.66 (36 H, $w_{1/2}$ = 500 Hz, SiMe$_3$). IR (ATR, cm^{-1}): ν = 2943 (w), 2891 (w), 1583 (w), 1472 (w), 1452 (w), 1431 (m), 1351 (w), 1283 (m), 1234 (m), 1104 (vs), 1026 (w), 960 (vs), 884 (m), 860 (m), 823 (vs),

779 (m), 735 (s), 691 (s), 657 (s), 609 (m), 533 (s), 509 (m), 480 (m). Elemental analysis calcd. (%) for $C_{50}H_{82}FeKNO_8P_2Si_4$ (1076.44 g/mol): C 55.79, H 7.68, N 2.60; found: C 55.37, H 7.62, N 2.58. μ_{eff} = 4.88 μ_B (Evans, THF-d_8 + 1% $Si(CH_3)_4$), $\mu_{s.o.}$ = 3.87 μ_B).

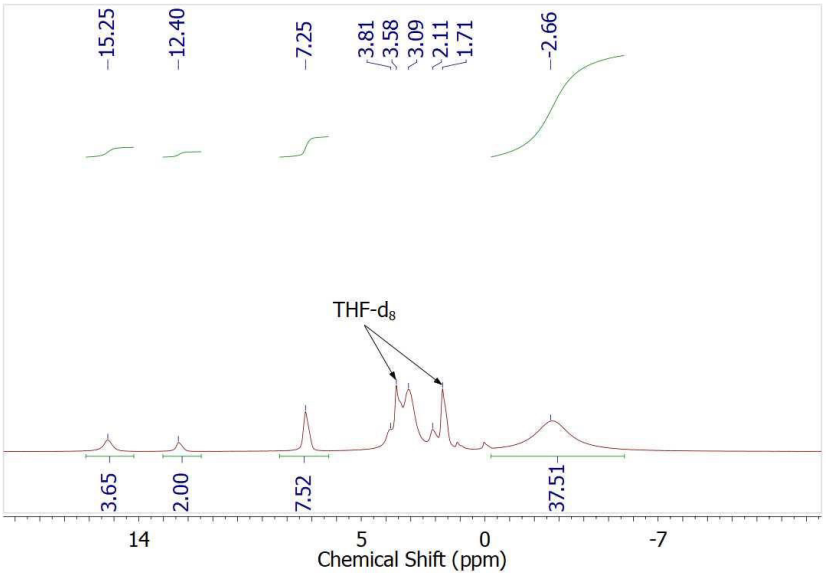

Figure S 7. ^{1}H NMR spectrum of K{18-crown-6}[Fe(N(SiMe$_3$)$_2$)$_2$(*cis*-dppee)] (**5**) in THF-d_8 (500.1 MHz).

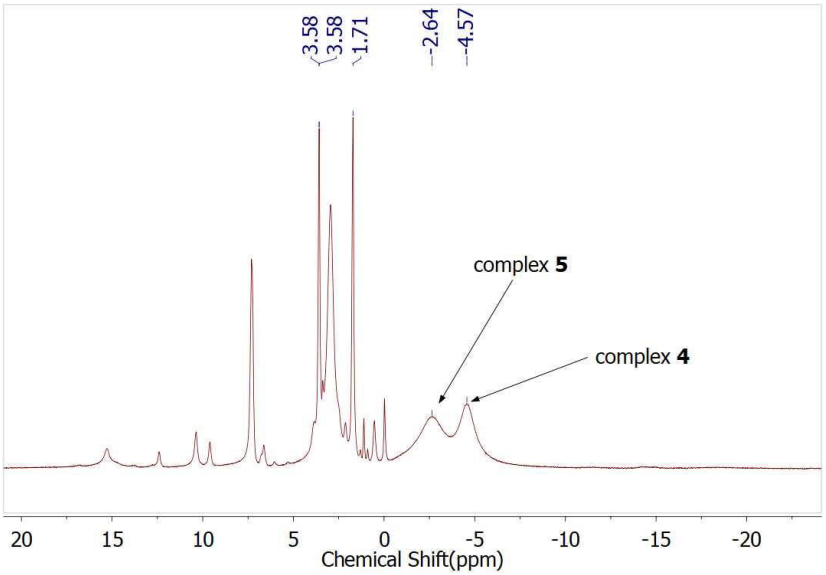

Figure S 8. ^{1}H NMR spectrum of K{18-crown-6}[Fe(N(SiMe$_3$)$_2$)$_2$(*cis*-dppee)] (**5**) in THF-d_8 after 16 h (500.1 MHz).

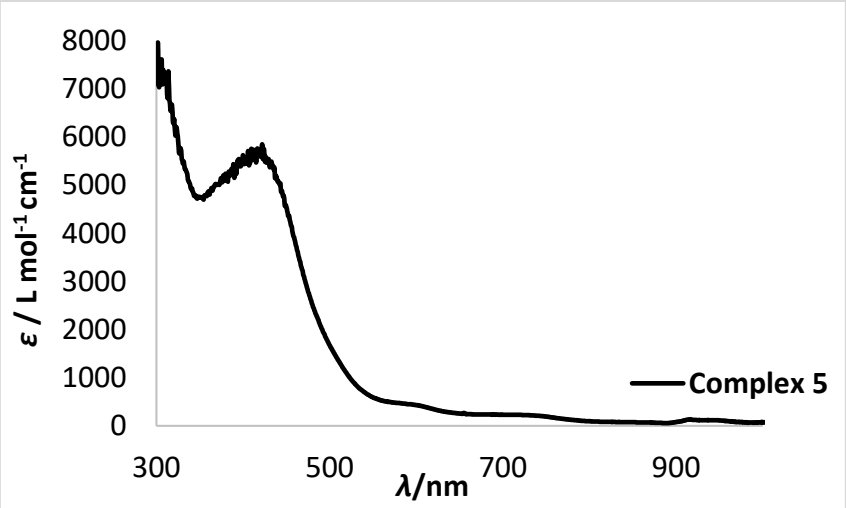

Figure S 9. UV/Vis spectrum of K{18-crown-6}[Fe(N(SiMe$_3$)$_2$)$_2$(*cis*-dppee)] (**5**) in THF.

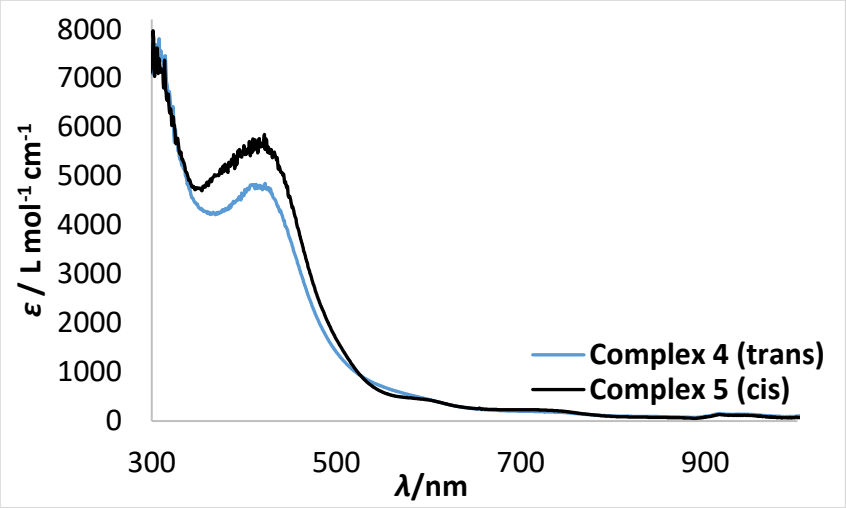

Figure S 10. Overlay of UV/Vis spectra of K{18-crown-6}[Fe(N(SiMe$_3$)$_2$)$_2$(*trans*-dppee)] **(4)** and K{18-crown-6}[Fe(N(SiMe$_3$)$_2$)$_2$(*cis*-dppee)] **(5)** in THF.

5. Catalytic *cis*->*trans* isomerization of *cis*-dppee mediated by 1

3.4 mg (0.005 mmol, 1 equiv.) K{18c6}[Fe(N(SiMe$_3$)$_2$)$_2$], **1**, and 20 mg (0.05 mmol, 10 equiv.) *cis*-dppee were dissolved in 0.7 mmol THF-d$_8$ and transferred into a Young NMR tube. The transformation was monitored via ^{31}P NMR spectroscopy.

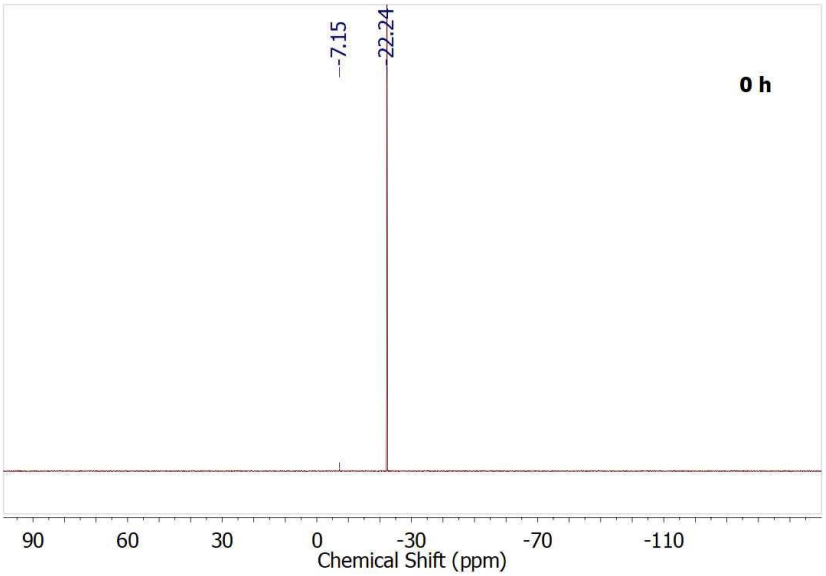

Figure S 11. Immediately taken ^{31}P{^{1}H} NMR spectrum of the reaction mixture of 5 µmol K{18-crown-6}[Fe(N(SiMe$_3$)$_2$)$_2$] (**1**) and 0.5 mmol *cis*-dppee in THF-d$_8$ (121.54 MHz).

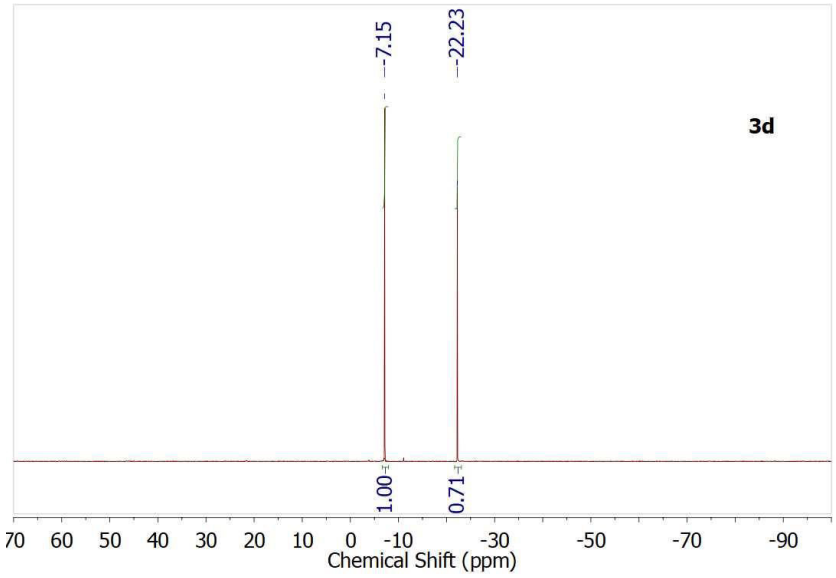

Figure S 12. ^{31}P{^{1}H} NMR spectrum of the reaction mixture of 5 µmol K{18-crown-6}[Fe(N(SiMe$_3$)$_2$)$_2$] (**1**) and 0.5 mmol *cis*-dppee in THF-d$_8$ after 72h (121.54 MHz).

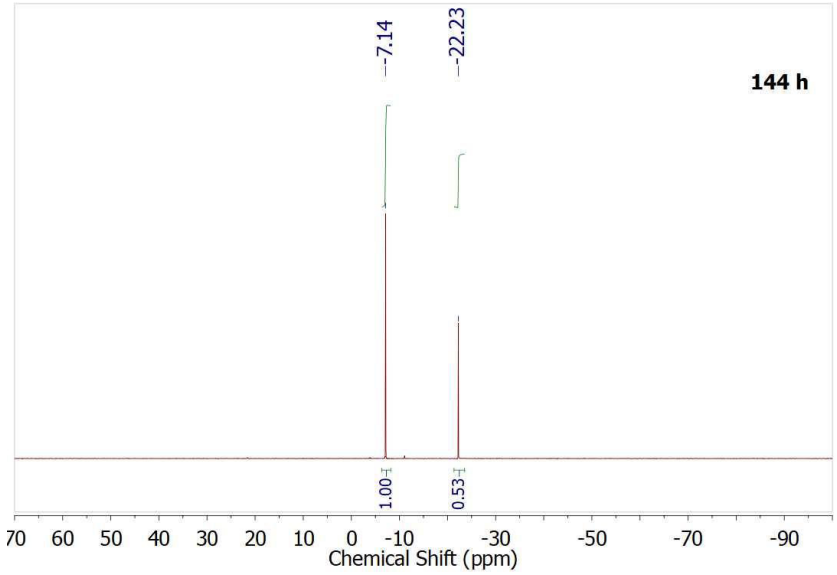

Figure S 13 $^{31}P\{^{1}H\}$ NMR spectrum of the reaction mixture of 5 μmol K{18-crown-6}[Fe(N(SiMe$_3$)$_2$)$_2$] (**1**) and 0.5 mmol *cis*-dppee in THF-d$_8$ after 144h (121.54 MHz).

6. X-Ray diffraction analysis and molecular structures

Data for **2** (CCDC 1858799), **3** (CCDC 1858802), **4** (CCDC 1964496), and **5** (CCDC 1964494) were collected at 100 K on a Bruker Quest D8 diffractometer using a graphite-monochromated Mo-Kα radiation and equipped with an *Oxford Instrument Cooler Device*. The structures have been solved using OLEX SHELXT V2014/1[iv] and refined by means of least-squares procedures on F^2 with the aid of the program SHELXL-2016/6[v] included in the softwares package WinGX version 1.63[vi] or using CRYSTALS.[vii]

The Atomic Scattering Factors were taken from *International Tables for X-Ray Crystallography*.[viii] All non-hydrogen atoms were refined anisotropically. All hydrogens atoms were refined by using a riding model. Absorption corrections were introduced by using MULTISCAN.[ix] Drawings of molecules are performed with the program DIAMOND with 50% probability displacement ellipsoids for non-H atoms. Depiction of H atoms is omitted for clarity.

Table S1. Crystal data and structure refinement for **2**. The high number of restraints is necessary in order to properly model a disorder of the potassium cation and the coordinated solvent (Et_2O).

Identification code	K18c6_Fehmds3
Empirical formula	$C_{38}H_{98}FeKN_3O_8Si_6$
Formula weight / g mol^{-1}	988.68
Temperature / K	110.0
Crystal system	monoclinic
Space group	$P2_1/n$
a / Å	15.4864(6)
b / Å	17.4686(7)
c / Å	21.7327(9)
α / °	90
β / °	92.3350(10)
k / °	90
V / Å^3	5874.4(4)
Z	4
ρ_{calc} / g cm^{-3}	1.118
μ / mm^{-1}	0.491
F(000)	2160.0
Crystal size / mm^3	0.37 × 0.3 × 0.19
Radiation	MoKα (λ = 0.71073)
2Θ range for data collection / °	4.418 to 55.142
Index ranges	-20 ≤ h ≤ 20, -22 ≤ k ≤ 22, -28 ≤ l ≤ 28
Reflections collected	160701
Independent reflections	13562 [R_{int} = 0.0512, R_{sigma} = 0.0251]
Data/restraints/parameters	13562/164/592
Goodness-of-fit on F^2	1.027
Final *R* indexes [*I*≥2σ (*I*)]	R_1 = 0.0367, wR_2 = 0.0839
Final *R* indexes [all data]	R_1 = 0.0539, wR_2 = 0.0913
Largest diff. peak/hole / e Å^{-3}	0.56/-0.49

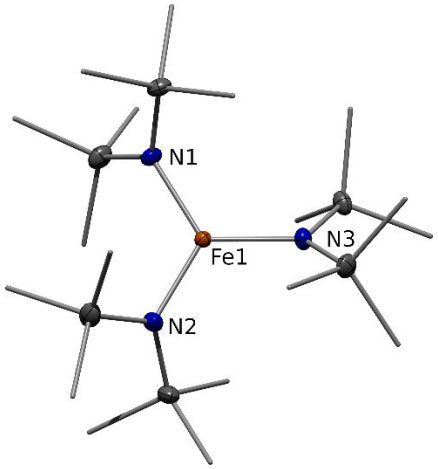

Figure S 14. Section of the crystal structure of **2**. The K{18-crown-6} cation and H atoms are omitted**.**

Table S2. Crystal data and structure refinement for 3.

Identification code	K18c6_Feppbz_hmds
Empirical formula	$C_{56}H_{82.48}FeKNO_8P_2Si_2$
Formula weight / g mol^{-1}	1110.77
Temperature/K	100.0
Crystal system	triclinic
Space group	P-1
a / Å	13.1704(6)
b / Å	15.3361(7)
c / Å	15.4398(7)
α / °	97.045(2)
β / °	103.248(2)
γ / °	95.214(2)
V / Å^3	2989.7(2)
Z	2
ρ_{calc} / g cm^{-3}	1.234
μ / mm^{-1}	0.465
F(000)	1185.0
Crystal size / mm^3	0.446 × 0.186 × 0.126
Radiation	MoKα (λ = 0.71073)
2Θ range for data collection / °	4.432 to 53.614
Index ranges	-16 ≤ h ≤ 16, -18 ≤ k ≤ 19, -19 ≤ l ≤ 19
Reflections collected	93235
Independent reflections	12781 [R_{int} = 0.0451, R_{sigma} = 0.0265]
Data/restraints/parameters	12781/0/674
Goodness-of-fit on F^2	1.024
Final *R* indexes [*I*≥2σ (*I*)]	R_1 = 0.0336, wR_2 = 0.0712
Final *R* indexes [all data]	R_1 = 0.0453, wR_2 = 0.0754
Largest diff. peak/hole / e Å^{-3}	0.56/-0.43

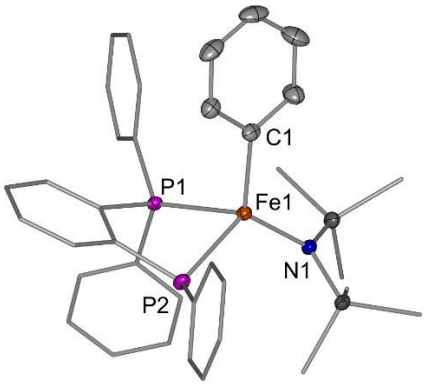

Figure S 15. Section of the crystal structure of **3**. K{18-crown-6} counter ion and H atoms are omitted.

Table S3. Crystal data and structure refinement for **4**. The high number of restraints stems from the modeling of the disorder of one of the phenyl groups.

Identification code	K18c6_Fehmds2_trans_dppe
Empirical formula	$C_{58}H_{98}FeKN_2O_8P_2Si_4$
Formula weight / g mol^{-1}	1220.63
Temperature/K	100.0
Crystal system	monoclinic
Space group	$P2_1/c$
a / Å	12.5633(5)
b / Å	35.5283(14)
c / Å	15.3551(7)
α / °	90
β / °	99.326(2)
γ / °	90
V / Å^3	6763.2(5)
Z	4
ρ_{calc} / g cm^{-3}	1.199
μ / mm^{-1}	0.451
F(000)	2620.0
Crystal size / mm^3	0.333 × 0.287 × 0.12
Radiation	MoKα (λ = 0.71073)
2Θ range for data collection / °	4.366 to 53.954
Index ranges	-16 ≤ h ≤ 16, -45 ≤ k ≤ 45, -19 ≤ l ≤ 19
Reflections collected	158557
Independent reflections	14674 [R_{int} = 0.0413, R_{sigma} = 0.0222]
Data/restraints/parameters	14674/231/751
Goodness-of-fit on F^2	1.064
Final *R* indexes [*I*≥2σ (*I*)]	R_1 = 0.0414, wR_2 = 0.0973
Final *R* indexes [all data]	R_1 = 0.0511, wR_2 = 0.1018
Largest diff. peak/hole / e Å^{-3}	1.10/-0.55

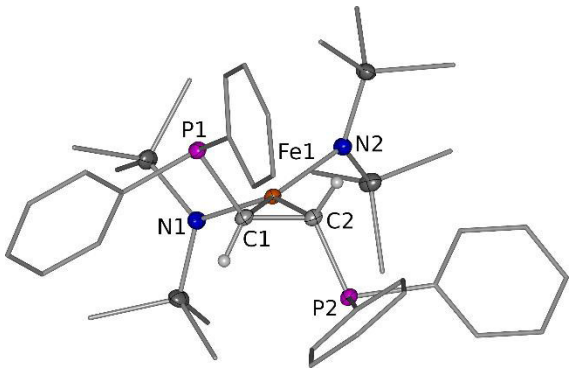

Figure S 16. Section of the crystal structure of **4**. The disorder found for the phenyl rings, the K{18-crown-6} counter ion and all H atoms except the ones at C1 and C2 are omitted.

Table S4. Crystal data and structure refinement for **5**. The very high number of restraints is necessary to model the disorder of the K{18c6} cation and of the coordinated dppee ligand. The disorder of the complex 5 is shown in figure S 18.

Identification code	K18c6_Fehmds2_cis_dppe
Empirical formula	$C_{50}H_{82}FeKN_2O_6P_2Si_4$
Formula weight / g mol^{-1}	1076.42
Temperature/K	100.0
Crystal system	triclinic
Space group	P-1
a / Å	11.660(2)
b /Å	13.061(2)
c / Å	20.875(4)
α / °	73.368(5)
β / °	74.116(6)
γ / °	75.985(5)
V / Å^3	2883.1(9)
Z	2
ρ_{calc} / g cm^{-3}	1.240
μ / mm^{-1}	0.518
F(000)	1150.0
Crystal size / mm^3	0.226 × 0.135 × 0.117
Radiation	MoKα (λ = 0.71073)
2Θ range for data collection / °	4.308 to 49.998
Index ranges	-13 ≤ h ≤ 13, -15 ≤ k ≤ 15, -24 ≤ l ≤ 24
Reflections collected	61411
Independent reflections	10137 [R_{int} = 0.1130, R_{sigma} = 0.0826]
Data/restraints/parameters	10137/2529/919
Goodness-of-fit on F^2	1.120
Final *R* indexes [*I*≥2σ (*I*)]	R_1 = 0.1185, wR_2 = 0.2694
Final *R* indexes [all data]	R_1 = 0.1565, wR_2 = 0.2835
Largest diff. peak/hole / e Å^{-3}	1.48/-0.92

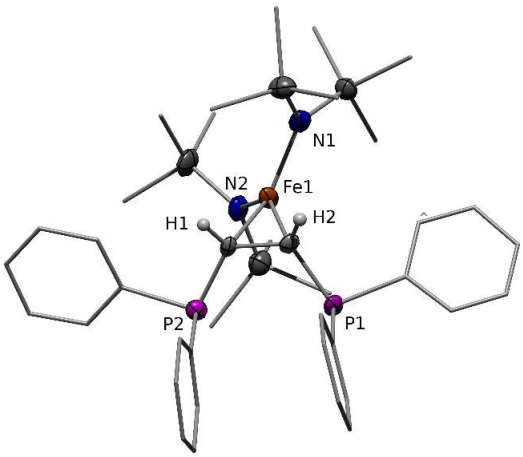

Figure S 17. Section of the crystal structure of **5**. K{18-crown-6} counter ion, disordered dppee ligand and all H atoms except the ones at C1 and C2 are omitted.

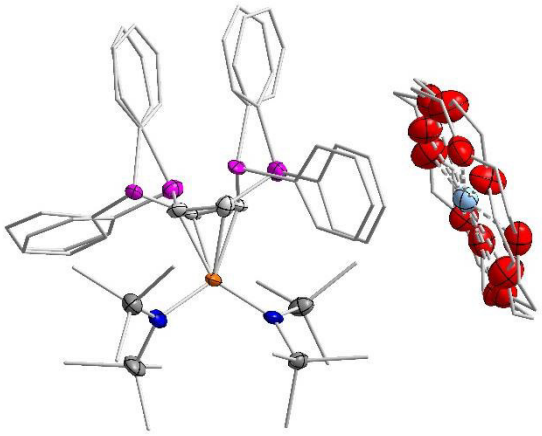

Figure S 18. Depiction of the disorder found for of **5**. All H atoms are omitted. The disordered *cis*-dppee ligand with 50% occupation with similar bond metrics is rotated by approx. 180° around the iron-ethylene axis. The crown ether of the K{18c6} cation is also disordered and rotated by 23° around the potassium ion.

References

[i] a) D. F. Evans *J. Chem. Soc.* **1959**, 2003; b) E. M. Schubert *J. Chem. Educ.* **1992**, *69*, 62.

[ii] A. M. Bryan, G. J. Long, F. Grandjean, P. P. Power; *Inorg*. *Chem.* **2013**, *52*, 12152-12160.

[iii] C. G. Werncke, P. C. Bunting, C. Duhayon, J. R. Long, S. Bontemps, S. Sabo-Etienne, *Angew*. *Chem*. *Int*. *Ed*. **2015**, *54*, 245-248.

[iv] O. V. Dolomanov, L. J. Bourhis, R. J. Gildea, J. A. K. Howard, H. Puschmann, *J. Appl. Crytallogr*. **2009**, *42*, 339-441.

[v] G. M. Sheldrick, *Acta Cryst*. **2015**, *71*, 3.

[vi] L. Farrugia, J. Appl. *Crystallogr.*, **1999**, *32*, 837.

[vii] P. W. Betteridge, J. R. Carruthers, R. I. Cooper, K. Prout, D. J. Watkin *J*. *Appl. Cryst*. **2003**, *36*, 1487.

[viii] *International Tables for X-ray crystallography* (Kynoch Press, Birmingham, England, **1974**) *Vol*. *IV*.

[ix] *SADABS-2016/2* (Bruker, **2016**).

8.6 Arbeitstechniken und Chemikalien

Alle durchgeführten Arbeiten wurden unter Argon-Atmosphäre mittels gängiger SCHLENK-Techniken oder mithilfe von Intergas-Gloveboxen (Fa. GS und M. BRAUN) verschiedener Art durchgeführt. Sämtliche Glasgeräte wurden zunächst in einem Trockenschrank bei 120 °C getrocknet und die Apparaturen im Feinvakuum evakuiert. Nach dem Ausheizen und Abkühlen der Apparaturen wurden diese mit Argon geflutet. Die verwendeten Lösungsmittel wurden nach Standard-Prozeduren absolutiert und über Molsieb 3Å (BASF AG) gelagert.[121] Lösungsmittel und Chemikalien wurden, falls nicht anders erwähnt von ACROS, ALFA-AESAR, FISHER SCIENTIFIC, FLUKA, MERCK oder SIGMA-ALDRICH bezogen. Die Metall(II)$(hmds)_2$ (M = Cr – Co) wurden nach der Vorschrift von BÜRGER und WANNAGAT dargestellt.[12,13] Die Metall(I)$(hmds)_2$ (M = Cr – Co) wurden nach der Synthesevorschrift von WERNCKE dargestellt.[50,51]

8.7 Analytische Methoden

8.7.1 Kernresonanzspektroskopie

Die NMR-Spektren wurden in den unten angegebenen deuterierten Lösungsmitteln an den Geräten des Typs Avance 300 und Avance 500 HD der Firma BRUKER in der Serviceabteilung für NMR-Spektroskopie des Fachbereiches Chemie der Philipps-Universität Marburg gemessen.
Die interne Kalibrierung der ^{1}H-NMR-Spektren erfolgte durch die Verwendung der Restprotonensignalen der Lösungsmittel als Referenz:[122]

THF-d_8: ^{1}H: 1.73 ppm und 3.58 ppm

Die Signale wurden anhand der chemischen Verschiebung, der Intergrale und Kopplungsmuster zugeordnet. Die Multiplizität aller Signale in dieser Arbeit wird mit den Abkürzungen *s* (Singulett), *d* (Dublett), *t* (Triplett) und *m* (Multiplett) angegeben.

8.7.2 Elementaranalyse

Elementaranalysen wurden in der Serviceabteilung für Massenspektrometrie und Elementaranalytik des Fachbereichs Chemie der Philipps-Universität Marburg an einem *vario* MICRO *cube* (Fa. ELEMENTAR) gemessen. Die Werte sind in Gewichtsprozent angegeben.

8.7.3 Infrarotspektroskopie

Infrarot-Spektren wurden mit einem Alpha ATR-FT-IR Spektrometer (Fa. BRUKER) in Substanz aufgenommen. Für die Auswertung der Spektren wurden folgende Abkürzung für die Bandenintensitäten verwendet: vs = sehr stark, s = stark, m = mittel, w = schwach.

8.7.4 Bestimmung der magnetischen Eigenschaften

Zur Bestimmung der magnetischen Suzeptibilität μ_{eff} [µB] mittels ^{1}H-NMR-Spektroskopie wurde die EVANS-Methode angewendet. Die Messungen wurden in THF-d_8 + 1% Tetramethylsilan bei Raumtemperatur (298K) und 500.1 MHz durchgeführt.[123]

8.7.5 Einkristallstrukturanalyse

Die Messungen wurden an einem IPDS 2T-, IPDS II- und StadiVari-Röntgendiffraktometer der Firma STOE und an einem D8-Quest-Röntgendiffraktometer der Firma BRUKER durchgeführt. Es wurde ein Standardgraphit-monochromator (Mo-K_α-Strahlung, λ = 71.073 pm) verwendet. Für die Datensammlung, die Zellverfeinerung und die Datenreduzierung wurden die Programme X-AREA[126], APEX3[131] und SAINT[132] verwendet. Die Lösungen der Kristallstrukturen wurden im Arbeitskreis von mir selbst mithilfe des Programmes SHELXL-97[127-130] durchgeführt, die ausführlichen Daten sind dem kristallographischen Anhang beigefügt. Die Molekülstrukturen wurden mit der Software DIAMOND[129] abgebildet. Geeignete Einkristalle für die Einkristallstrukturanalyse wurden aus einer Schichtlösung aus Diethylether und Pentan bei -35°C erhalten. Die Ellipsoide werden mit einer Aufenthaltswahrscheinlichkeit von 50% für alle Molekülstrukturen gezeigt.

8.8 Synthese der Verbindungen

8.8.1 Darstellung von [K{18c6}(thf)][(Fe(N(SiMe$_3$)$_2$)$_2$(η^2-styrol)] (1).

[K{18c6}(thf)][(Fe(N(SiMe$_3$)$_2$)$_2$(η^2-styrol)] (**1**).: [K{18c6}][Fe(N(SiMe$_3$)$_2$)$_2$)$_2$] (68.0 mg, 0.10 mmol, 1.0 eq) und Styrol (8.2 mg, 0.10 mmol, 1.0 eq) wurden in 3 mL Et_2O gelöst und führten zu einem sofortigen Farbumschlag von bräunlichgrün nach dunkelrot. Nach fünf Minuten Rühren wurde die Lösung mit 3 mL Pentan überschichtet. Nach einigen Tagen Lagerung der Lösung bei -35°C ergab es einen bräunlich-roten kristallinen Feststoff. Die Lösung wurde mit einer Pipette entfernt. Durch Waschen des Rückstands mit 2x5 mL Pentan und Trocknen unter reduziertem Druck entstand Verbindung **1** als bräunlich-roter kristalliner Feststoff

(33.9 mg, 0.043 mmol, 43%). Kristalle, die für die Röntgenbeugungsanalyse geeignet sind, wurden aus einer Lösung aus Et_2O und Pentan von **1** bei -35°C erhalten.

IR ATR, $\tilde{\nu}/cm^{-1}$ = 2938 (w), 2896 (w), 2176 (w), 1602 (w), 1589 (w), 1573 (w), 1350 (m), 1231 (s), 1104 (vs), 990 (s), 887 (m), 866 (m), 8206(vs), 749 (m), 659 (m), 611 (m), 576 (m), 530 (w), 514 (m), 449 (m), 430 (m), 421 (m), 406 (s).

Elementaranalyse $C_{32}H_{68}FeN_2KSi_4O_6$ (784.19 g/mol):
gef. (ber.): C: 48.49% (49.01%), H: 8.41% (8.74%), N: 3.55% (3.57%).

8.8.2 Darstellung von [K{18c6}][(Fe(N(SiMe$_3$)$_2$)$_2$(η^2-allylanisol)] (2).

[K{18c6}][(Fe(N(SiMe$_3$)$_2$)$_2$(η^2-allylanisol)] (**2**): [K{18c6}][Fe(N(SiMe$_3$)$_2$)$_2$)$_2$] (68.0 mg, 0.10 mmol, 1.0 eq) und 4-Allylanisol (14.8 mg, 0.10 mmol, 1.0 eq, but) wurden in 3 mL Et_2O gelöst und führten zu einem sofortigen Farbumschlag von bräunlichgrün nach dunkelrot. Nach fünf Minuten Rühren wurde die Lösung mit 3 mL Pentan überschichtet. Nach einigen Tagen Lagerung der Lösung bei -35°C ergab es einen bräunlich-roten kristallinen Feststoff. Die Lösung wurde mit einer Pipette entfernt. Durch Waschen des Rückstands mit 2x5 mL Pentan und Trocknen unter reduziertem Druck entstand Verbindung **2** als dunkelroter kristalliner Feststoff. Kristalle, die für die Röntgenbeugungsanalyse geeignet sind, wurden aus einer Lösung aus Et_2O und Pentan von **2** bei -35°C erhalten.

8.8.3 Darstellung von [K{18c6}]$_2$[1,1,4,4-Tetraphenlbutan-1,4-diyl)] (3).

[K{18c6}]$_2$[1,1,4,4-Tetraphenylbutan-1,4-diyl)] (**3**): Mn(N(SiMe$_3$)$_2$)$_2$ (37.6 mg, 0.10 mmol, 1.0 eq) und 18-Krone-6 (31.8 mg, 0.105 mmol, 1.05 eq) wurden in 3 mL Et2O gelöst. Die Zugabe von KC_8 (20.2 mg, 0.15 mmol, 1.5 eq) führte zu einem sofortigen Farbumschlag nach dunkelviolett. Nach fünf Minuten Rühren wurde die Mischung filtriert und das Filtrat in 1,1-Diphenylethylen (18.2 mg, 0.10 mmol, 1.0 eq) gegeben, was zu einem sofortigen Farbumschlag zu hellrot führte. Die Lösung wurde fünf Minuten lang gerührt und mit 3 mL Pentan überschichtet. Nach einigen Tagen Lagerung der Lösung bei -35°C ergab es einen hellroten kristallinen Feststoff. Die Lösung wurde mit einer Pipette entfernt, der Rückstand mit 2x5 mL Pentan gewaschen und getrocknet, sodass **3** als hellroter kristalliner Feststoff entstand. Kristalle, die für die Röntgenbeugungsanalyse geeignet sind, wurden aus einer Lösung aus Et_2O und Pentan von **3** bei -35°C erhalten.

IR ATR, $\tilde{\nu}/cm^{-1}$ = 2992 (w), 2960 (w), 2938 (w), 2922 (w), 2845 (w), 1601 (m), 1559 (m), 1477 (m), 1363(m), 1308(m), 1260(m), 1238(m), 1173(s), 1140(s), 1009(s), 970(s), 919(s), 874(s), 853(m), 807(m),

786(m), 767(m), 725(m), 702(m), 686(m), 634 (m), 554(m), 466 (m), 423(m).

8.8.4 Darstellung von [K{18c6}][Cr(N(SiMe$_3$)$_2$)(η^2-(Ph*C*HCH$_2$CH$_2$*C*HPh)] (4).

[K{18c6}(thf)$_2$][Cr(N(SiMe$_3$)$_2$)(η^2-(Ph***C***HCH$_2$CH$_2$***C***HPh)] (**4**): Cr(N(SiMe$_3$)$_2$)$_2$*(thf)$_2$ (51.7 mg, 0.10 mmol, 1.0 eq) und 18-Krone-6 (31.8 mg, 0.105 mmol, 1.05 eq) wurden in 3 mL Et$_2$O gelöst. Die Zugabe von KC$_8$ (20.2 mg, 0.15 mmol, 1.5 eq) führte zu einer sofortigen Farbveränderung zu dunklem Orange-Grün. Nach fünf Minuten Rühren wurde die Mischung filtriert und das Filtrat in Styrol (8.2 mg, 0.10 mmol, 1.0 eq) gegeben, was zu einem sofortigen Farbumschlag zu dunkelrot führte. Die Lösung wurde fünf Minuten lang gerührt und mit 3 mL Pentan überschichtet. Nach einigen Tagen Lagerung der Lösung bei -35°C ergab es ein roter kristalliner Feststoff. Die Lösung wurde mit einer Pipette entfernt, der Rückstand mit 2x5 mL Pentan gewaschen und getrocknet, wobei sich **4** als roter kristalliner Feststoff ergab (26.1 mg, 0.033 mmol, 33%). Kristalle, die für die Röntgenbeugungsanalyse geeignet sind, wurden aus einer Lösung aus Et$_2$O und Pentan von **4** bei -35°C erhalten.

IR ATR, ṽ/cm^{-1} = 2943 (w), 2889 (w), 1599 (m), 1581 (m), 1476 (w), 1449 (w), 1353 (m), 1251 (m), 1237 (s), 1204 (m), 1107 (s), 1055 (s), 1028 (m), 981 (vs), 957 (s), 863 (m), 817 (m), 776 (m), 742 (s), 700 (m), 662 (m), 607 (m), 513 (w), 465 (w), 440 (w).

8.8.5 Darstellung von [K{18c6}][Cr(N(SiMe$_3$)$_2$)(η^2-(Ph$_2$*C*CH$_2$CH$_2$*C*Ph$_2$)] (5).

[K{18c6}(thf)$_2$][Cr(N(SiMe$_3$)$_2$)$_2$(η^2-(Ph$_2$***C***CH$_2$CH$_2$***C***Ph$_2$)] (**5**): Cr(N(SiMe$_3$)$_2$)$_2$*(thf)$_2$ (51.7 mg, 0.10 mmol, 1.0 eq) und 18-Krone-6 (31.8 mg, 0.105 mmol, 1.05 eq) wurden in 3 mL Et$_2$O gelöst. Die Zugabe von KC$_8$ (20.2 mg, 0.15 mmol, 1.5 eq) führte zu einer sofortigen Farbveränderung zu dunklem Orange-grün. Nach fünf Minuten Rühren wurde die Mischung filtriert und das Filtrat in 1,1-Diphenylethylen (18.2 mg, 0.10 mmol, 1.0 eq) gegeben, was zu einem sofortigen Farbumschlag zu dunkelrot führte. Die Lösung wurde fünf Minuten lang gerührt und mit 3 mL Pentan überschichtet. Nach einigen Tagen Lagerung der Lösung bei -35°C ergab es einen dunkelroten kristallinen Feststoff. Die Lösung wurde mit einer Pipette entfernt, der Rückstand mit 2x5 mL Pentan gewaschen und getrocknet, wobei sich **5** als dunkelroter kristalliner Feststoff ergab. Kristalle, die für die Röntgenbeugungsanalyse geeignet sind, wurden aus einer Lösung aus Et$_2$O und Pentan von **5** bei -35°C erhalten.

IR ATR, ṽ/cm^{-1} = 2992 (w), 2975 (w), 2926 (w), 2878 (w), 2849 (w), 2780 (m), 1581 (s), 1481 (s), 1443 (m), 1364 (m), 1346 (m), 1278 (m), 1254 (m), 1239 (s), 1186 (s), 1150 (s), 1033(s), 996 (s), 970 (s), 917 (s),

875 (s), 854 (s), 806 (m), 782 (m), 758 (s), 699 (s), 689 (s), 639 (s), 583 (m), 539 (m), 501 (m), 479 (m), 448 (m), 434 (m).

8.8.6 Darstellung von [K{18c6}][Cr(N(SiMe$_3$)$_2$)$_2$(η^2-(*trans*-β-methylstyrol)] (6).

[K{18c6}][Cr(N(SiMe$_3$)$_2$)$_2$(η^2-(*trans*-β-methylstyrol)] (**6**): Cr(N(SiMe$_3$)$_2$)$_2$*(thf)$_2$ (51.7 mg, 0.10 mmol, 1.0 eq) und 18-Krone-6 (31.8 mg, 0.105 mmol, 1.05 eq) wurden in 3 mL Et$_2$O gelöst. Die Zugabe von KC$_8$ (20.2 mg, 0.15 mmol, 1.5 eq) führte zu einer sofortigen Farbveränderung zu dunklem orange-grün. Nach fünf Minuten Rühren wurde die Mischung filtriert und das Filtrat in *cis*-β-Methylstyrol (11.8 mg, 0.10 mmol, 1.0 eq, but) gegeben, was zu einem sofortigen Farbumschlag zu dunkelrot führte. Die Lösung wurde fünf Minuten lang gerührt und mit 3 mL Pentan überschichtet. Nach einigen Tagen Lagerung der Lösung bei -35°C ergab es einen dunkelroten kristallinen Feststoff. Die Lösung wurde mit einer Pipette entfernt, der Rückstand mit 2x5 mL Pentan gewaschen und getrocknet, wobei sich **6** als dunkelroter kristalliner Feststoff ergab Kristalle, die für die Röntgenbeugungsanalyse geeignet sind, wurden aus einer Lösung aus Et$_2$O und Pentan von **6** bei -35°C erhalten.

IR ATR, $\tilde{\nu}$/cm^{-1} = 2973 (w), 2950 (w), 2942(w), 2891(w), 2836 (w), 2822 (w), 2164 (w), 1600(s), 1574(s), 1490.2 (w), 1474 (w), 1415 (w), 1354 (w), 1302 (w), 1253 (w), 1238(s), 1162 (w), 1112 (m), 999 (s), 959 (s), 874 (s), 846 (m), 813(s), 768 (m), 738 (m), 702 (m), 689 (m), 653 (m), 606 (m), 579 (m), 509 (m), 433(m).

EVANS μ_{eff} = 4.64 μ_B ([D8]THF + 1% TMS, 500.1 MHz, 300 K). $\mu_{S.O.}$ = 5.91 μ_B.

8.8.7 Darstellung von [K{18c6}][Cr(N(SiMe$_3$)$_2$)$_2$(η^2-(*trans*-stilben)] (7).

[K{18c6}][Cr(N(SiMe$_3$)$_2$)$_2$(η^2-(*trans*-stilben)] (**7**): Cr(N(SiMe$_3$)$_2$)$_2$*(thf)$_2$ (51.7 mg, 0.10 mmol, 1.0 eq) und 18-Krone-6 (31.8 mg, 0.105 mmol, 1.05 eq) wurden in 3 mL Et$_2$O gelöst. Die Zugabe von KC$_8$ (20.2 mg, 0.15 mmol, 1.5 eq) führte zu einer sofortigen Farbveränderung zu dunklem orange-grün. Nach fünf Minuten Rühren wurde die Mischung filtriert und das Filtrat in *cis*-Stilben (18.0 mg, 0.10 mmol, 1.0 eq, but) gegeben, was zu einem sofortigen Farbumschlag zu dunkelviolett führte. Die Lösung wurde fünf Minuten lang gerührt und mit 3 mL Pentan überschichtet. Nach einigen Tagen Lagerung der Lösung bei -35°C ergab es einen weinroten kristallinen Feststoff. Die Lösung wurde mit einer Pipette entfernt, der Rückstand mit 2x5 mL Pentan gewaschen und getrocknet, wobei sich **7** als weinroter kristalliner Feststoff ergab. Kristalle, die für die Röntgenbeugungsanalyse geeignet sind, wurden aus einer Lösung aus Et$_2$O und Pentan von **7** bei -35°C erhalten.

IR ATR, $\tilde{\nu}/cm^{-1}$ = 3049 (w), 2943 (w), 2889 (m), 1600 (w), 1578 (m), 1479 (m), 1451 (w), 1352 (m), 1239 (s), 1201 (w), 1170 (s), 1109 (m), 1063 (m), 1029 (s), 975 (m), 929 (m), 877(s), 839 (s), 766 (s), 743 (s), 693 (s), 663 (m), 616 (m), 606 (s), 552 (w), 515 (m), 466(w), 420 (w).

EVANS μ_{eff} = 3.97 μ_B ([D8]THF + 1% TMS, 500.1 MHz, 300 K). $\mu_{S.O.}$ = 5.91 μ_B.

8.8.8 Darstellung von [K{18c6}][Mn(N(SiMe$_3$)$_2$)$_2$(η^2-(*trans*-β-methylstyrol)] (8).

[K{18c6}][Mn(N(SiMe$_3$)$_2$)$_2$(η^2-(*trans*-β-methylstyrol)] (**8**): Mn(N(SiMe$_3$)$_2$)$_2$ (37.6 mg, 0.10 mmol, 1.0 eq) und 18-Krone-6 (31.8 mg, 0.105 mmol, 1.05 eq) wurden in 3 mL Et_2O gelöst. Die Zugabe von KC_8 (20.2 mg, 0.15 mmol, 1.5 eq) führte zu einem sofortigen Farbumschlag nach dunkelviolett. Nach fünf Minuten Rühren wurde die Mischung filtriert und das Filtrat in *cis*-β-Methylstyrol (18.0 mg, 0.10 mmol, 1.0 eq, but) gegeben, was zu einem sofortigen Farbumschlag zu braunrot führte. Die Lösung wurde fünf Minuten lang gerührt und mit 3 mL Pentan überschichtet. Nach einigen Tagen Lagerung der Lösung bei -35°C ergab es einen braunroten kristallinen Feststoff. Die Lösung wurde mit einer Pipette entfernt, der Rückstand mit 2x5 mL Pentan gewaschen und getrocknet, so dass **8** als braunroter kristalliner Feststoff entstand. Kristalle, die für die Röntgenbeugungsanalyse geeignet sind, wurden aus einer Lösung aus Et_2O und Pentan von **8** bei -35°C erhalten.

IR ATR, $\tilde{\nu}/cm^{-1}$ = 2973 (w), 2950 (w), 2942(w), 2891(w), 2836 (w), 2822 (w), 2164 (w), 1600(s), 1574(s), 1490.2 (w), 1474 (w), 1415 (w), 1354 (w), 1302 (w), 1253 (w), 1238(s), 1162 (w), 1112 (m), 999 (s), 959 (s), 874 (s), 846 (m), 813(s), 768 (m), 738 (m), 702 (m), 689 (m), 653 (m), 606 (m), 579 (m), 509 (m), 433(m).

EVANS μ_{eff} = 4.69 μ_B ([D8]THF + 1% TMS, 500.1 MHz, 300 K). $\mu_{S.O.}$ = 4.89 μ_B.

8.8.9 Darstellung von [K{18c6}][Fe(N(SiMe$_3$)$_2$)$_2$(η^2-(*cis*-β-methylstyrol)] (9).

K{18c6}][Fe(N(SiMe$_3$)$_2$)$_2$(η^2-(*cis*-β-methylstyrol)] (**9**): [K{18c6}][Fe(N(SiMe$_3$)$_2$)$_2$)$_2$] (68.0 mg, 0.10 mmol, 1.0 eq) und *cis*-β-Methylstyrol (11.8 mg, 0.10 mmol, 1.0 eq) wurden in 3 mL Et_2O gelöst und führten zu einem sofortigen Farbumschlag von bräunlichgrün nach dunkelrot. Nach fünf Minuten Rühren wurde die Lösung mit 3 mL Pentan überschichtet. Nach einigen Tagen Lagerung der Lösung bei -35°C ergab es einen bräunlich-roten kristallinen Feststoff. Die Lösung wurde mit einer Pipette entfernt. Durch Waschen des Rückstands mit 2x5 mL Pentan und Trocknen unter reduziertem Druck entstand Verbindung **9** als dunkelroter kristalliner Feststoff. Kristalle, die für die Röntgenbeugungsanalyse geeignet sind, wurden aus einer Lösung aus Et_2O und Pentan von **9** bei -35°C erhalten.

^{1}H-NMR	300.1 MHz, 300 K, [D8]THF: δ/[ppm] = -4.13 (s, $Si(CH_3)_3$), 1.72 (s, OCH_2), es konnten keine weiteren sinnvollen Signale zugeordnet werden.
IR	ATR, $\tilde{\nu}/cm^{-1}$ = 2940 (m), 2888 (m), 2829 (w), 1473 (w), 1453 (w), 1352 (m), 1284 (s), 1231 (s), 1105 (vs), 995 (s), 962 (s), 868 (m), 823 (vs), 777 (m), 748 (m), 658 (m), 609 (m), 582 (m), 531 (w).
Elementaranalyse	$C_{54}H_{130}Fe_2N_4K_2Si_8O_{12}$ (879.21 g/mol): gef. (ber.): C: 49.31% (49.66%), H: 8.67% (8.84%), N: 3.78% (3.61%).

8.8.10 Darstellung von [K{18c6}][Fe(N(SiMe$_3$)$_2$)$_2$(η^2-(*trans*-stilben)] (10).

[K{18c6}][Fe(N(SiMe$_3$)$_2$)$_2$(η^2-(*trans*-stilben)] (**10**): [K{18c6}][Fe(N(SiMe$_3$)$_2$)$_2$)$_2$] (68.0 mg, 0.10 mmol, 1.0 eq) und *cis*-Stilben (12.8 mg, 0.10 mmol, 1.0 eq, but) wurden in 3 mL Et_2O gelöst und führten zu einem sofortigen Farbumschlag von bräunlichgrün nach dunkelrot. Nach fünf Minuten Rühren wurde die Lösung mit 3 mL Pentan überschichtet. Nach einigen Tagen Lagerung der Lösung bei -35°C ergab es einen dunkelroten kristallinen Feststoff. Die Lösung wurde mit einer Pipette entfernt. Durch Waschen des Rückstands mit 2x5 mL Pentan und Trocknen unter reduziertem Druck entstand Verbindung **10** als dunkelroter kristalliner Feststoff. Kristalle, die für die Röntgenbeugungsanalyse geeignet sind, wurden aus einer Lösung aus Et_2O und Pentan von **10** bei -35°C erhalten.

^{1}H-NMR	300.1 MHz, 300 K, [D8]THF: δ/[ppm] = -3.99 (s, $Si(CH_3)_3$), 1.72 (s, OCH_2), es konnten keine weiteren sinnvollen Signale zugeordnet werden.
IR	ATR, $\tilde{\nu}/cm^{-1}$ = 2995(w), 2966(w), 2921(w), 2891(w), 2838(w), 2161(w), 1578(m), 1428(w), 1267(m), 1239(m), 1123(s), 1031(s), 976(s), 951(s), 881(s), 856(s), 808(s), 783(m), 724(m), 690(s), 650(m) ,586(m),466(m), 422(s).
EVANS	μ_{eff} = 4.81 μ_B ([D8]THF + 1% TMS, 500.1 MHz, 300 K). $\mu_{S.O.}$ = 3.87 μ_B.

8.8.11 Darstellung von [K{18c6}]$_2$[(Mn(N(SiMe$_3$)$_2$)$_3$)(*trans*-stilben)] (11).

[K{18c6}]$_2$[(Mn(N(SiMe$_3$)$_2$)$_3$)(*trans*-stilben)] (**11**): Mn(N(SiMe$_3$)$_2$)$_2$ (37.6 mg, 0.10 mmol, 1.0 eq) und 18-Krone-6 (31.8 mg, 0.105 mmol, 1.05 eq) wurden in 3 mL Et2O gelöst. Die Zugabe von KC_8 (20.2 mg, 0.15 mmol, 1.5 eq) führte zu einem sofortigen Farbumschlag nach dunkelviolett. Nach fünf Minuten Rühren wurde die Mischung filtriert und das Filtrat in cis-Stilben (18.0 mg, 0.10 mmol, 1.0 eq, but) gegeben, was zu einem sofortigen Farbumschlag zu bräunlich-rot führte. Die Lösung wurde fünf Minuten lang gerührt und mit 3 mL Pentan überschichtet. Nach einigen Tagen Lagerung der Lösung bei -35°C ergab es einen dunkelviolttten kristallinen Feststoff. Die Lösung wurde mit einer Pipette entfernt, der Rückstand mit 2x5 mL Pentan gewaschen und getrocknet, so dass **11** als dunkelvioletter kristalliner Feststoff entstand. Kristalle,

die für die Röntgenbeugungsanalyse geeignet sind, wurden aus einer Lösung aus Et_2O und Pentan von **11** bei -35°C erhalten.

8.8.12 Darstellung von [K{18c6}(thf)$_2$][Cr(N(SiMe$_3$)$_2$)$_2$(η^4-but)] (12).

[K{18c6}(thf)$_2$][Cr(N(SiMe$_3$)$_2$)$_2$(η^4-but)] (**12**): Cr(N(SiMe$_3$)$_2$)$_2$*(thf)$_2$ (51.7 mg, 0.10 mmol, 1.0 eq) und 18-Krone-6 (31.8 mg, 0.105 mmol, 1.05 eq) wurden in 3 mL Et_2O gelöst. Die Zugabe von KC_8 (20.2 mg, 0.15 mmol, 1.5 eq) führte zu einer sofortigen Farbveränderung zu dunklem Orange-grün. Nach fünf Minuten Rühren wurde die Mischung filtriert und das Filtrat in 2,3-Dimethyl-1,3-butadien (8.2 mg, 0.10 mmol, 1.0 eq, but) gegeben, was zu einem sofortigen Farbumschlag zu dunkelorange führte. Die Lösung wurde fünf Minuten lang gerührt und mit 3 mL Pentan überschichtet. Nach einigen Tagen Lagerung der Lösung bei -35°C ergab es einen orangefarbenen kristallinen Feststoff. Die Lösung wurde mit einer Pipette entfernt, der Rückstand mit 2x5 mL Pentan gewaschen und getrocknet, wobei sich **12** als orangefarbener kristalliner Feststoff ergab (30.4 mg, 0.036 mmol, 36%). Kristalle, die für die Röntgenbeugungsanalyse geeignet sind, wurden aus einer Lösung aus Et_2O und Pentan von **12** bei -35°C erhalten.

8.8.13 Darstellung von [K{18c6}][Mn(η^4-but)$_2$] (13).

[K{18c6}][Mn(η^4-but)$_2$] (**13**): Mn(N(SiMe$_3$)$_2$)$_2$ (37.6 mg, 0.10 mmol, 1.0 eq) und 18-Krone-6 (31.8 mg, 0.105 mmol, 1.05 eq) wurden in 3 mL Et2O gelöst. Die Zugabe von KC_8 (20.2 mg, 0.15 mmol, 1.5 eq) führte zu einem sofortigen Farbumschlag nach dunkelviolett. Nach fünf Minuten Rühren wurde die Mischung filtriert und das Filtrat in 2,3-Dimethyl-1,3-butadien (8.2 mg, 0.10 mmol, 1.0 eq, but) gegeben, was zu einem sofortigen Farbumschlag zu bräunlichrot führte. Die Lösung wurde fünf Minuten lang gerührt und mit 3 mL Pentan überschichtet. Nach einigen Tagen der Lösung bei -35°C ergab es einen hellgelben kristallinen Feststoff. Die Lösung wurde mit einer Pipette entfernt, der Rückstand mit 2x5 mL Pentan gewaschen und getrocknet, so dass **13** als hellgelber kristalliner Feststoff (30.1 mg, 0.058 mmol, 58%) entstand. Kristalle, die für die Röntgenbeugungsanalyse geeignet sind, wurden aus einer Lösung aus Et_2O und Pentan von **13** bei -35°C erhalten.

IR ATR, $\tilde{\nu}/cm^{-1}$ = 2940 (m), 2892 (m), 2826 (w), 1472 (w), 1454 (w), 1351 (m), 1283 (w), 1233 (s), 1104 (vs), 1057 (w), 999 (vs), 961 (s), 869 (m), 821 (vs), 773 (m), 747 (m), 702 (m), 659 (m), 607 (m), 529 (w).

8.8.14 Darstellung von [K{18c6}][(Fe(N(SiMe$_3$)$_2$)$_2$)$_2$(but)] (14).

[K{18c6}]$_2$[(Fe(N(SiMe$_3$)$_2$)$_2$)$_2$(but)] (**14**): [K{18c6}][Fe(N(SiMe$_3$)$_2$)$_2$] (68.0 mg, 0.10 mmol, 1.0 eq) und 2,3-Dimethyl-1,3-butadien (8.2 mg, 0.10 mmol, 1.0 eq, but) wurden in 3 mL Et_2O gelöst und führten zu einem sofortigen Farbumschlag von bräunlichgrün nach dunkelrot. Nach fünf Minuten Rühren wurde die Lösung mit 3 mL Pentan überschichtet. Nach einigen Tagen Lagerung der Lösung bei -35°C ergab es einen bräunlich-roten kristallinen Feststoff. Die Lösung wurde mit einer Pipette entfernt. Durch Waschen des Rückstands mit 2x5 mL Pentan und Trocknen unter reduziertem Druck entstand Verbindung **14** als bräunlich-roter kristalliner Feststoff (48.5 mg, 0.034 mmol, 68%). Kristalle, die für die Röntgenbeugungsanalyse geeignet sind, wurden aus einer Lösung aus Et_2O und Pentan von **14** bei -35°C erhalten.

^{1}H-NMR	300.1 MHz, 300 K, [D8]THF: δ/[ppm] = -4.21 (s, Si(CH$_3$)$_3$), 1.72 (s, OCH$_2$), es können keine weiteren sinnvollen Signale zugeordnet werden.
IR	ATR, $\tilde{\nu}$/cm^{-1} = 2940 (m), 2888 (m), 2829 (w), 1473 (w), 1453 (w), 1352 (m), 1284 (s), 1231 (s), 1105 (vs), 995 (s), 962 (s), 868 (m), 823 (vs), 777 (m), 748 (m), 658 (m), 609 (m), 582 (m), 531 (w).
Elementaranalyse	$C_{54}H_{130}Fe_2N_4K_2Si_8O_{12}$ (1442.22 g/mol): gef. (ber.): C: 44.79% (44.97%), H: 8.86% (9.09%), N: 4.28% (3.88%).

8.9 Kristallographischer Anhang

8.9.1 [K{18c6}(thf)][(Fe(N(SiMe$_3$)$_2$)$_2$(η^2-styrol)] (1).

Tabelle 3. Kristallographische Daten von **1**.

Identification code	K19_0m	
Habitus, colour	block, dark red	
Crystal size	0.470 × 0.396 × 0.302 mm^3	
Crystal system	monoclinic	
Space group	$P2_1/n$	Z = 4
Unit cell dimensions	a = 15.4531(9) Å b = 18.0396(11) Å c = 17.4090(10) Å	α = 90.0° β = 92.158(2)° γ = 90.0°
Volume	4849.6(5) Å^3	
Empirical formula	$C_{36}H_{76}FeKN_2O_7Si_4$	
Formula weight	856.29 g/mol	
Density (calculated)	1.173 g/cm^3	
Absorption coefficient	0.537 mm^{-1}	
F(000)	1852.0	
Diffractometer type	Bruker D8 QUEST	
Wavelength	0.71073 Å	
Temperature	100 K	
2Θ range for data collection/°	4.478 to 50.904	
Index ranges	-19 ≤ h ≤ 19, -22 ≤ k ≤ 22, -21 ≤ l ≤ 21	
Data collection software	APEX3 (Bruker AXS Inc., 2015)[131]	
Cell refinement software	SAINT V8.37A (Bruker AXS Inc., 2015)[132]	
Data reduction software	SAINT V8.37A (Bruker AXS Inc., 2015)[132]	
Reflections collected	105009	
Independent reflections	10013 [R_{int} = 0.0487, R_{sigma} = 0.0240]	
Reflections used for refinement	10013	
Absorption correction	Semi-empirical from equivalents[133]	
Max. and min. transmission	0.7454 and 0.6809	
Solution	dual space algorithm	
Refinement	Full-matrix least-squares on F^2	
Treatment of hydrogen atoms	Calculated positions, constr. ref.	
Programs used	XT V2014/1 (Bruker AXS Inc., 2014)[127] SHELXL-2016/6 (Sheldrick, 2016)[128] DIAMOND (Crystal Impact)[129] ShelXle (Hübschle, Sheldrick, Dittrich, 2011)[130]	
Data/restraints/parameters	10013/0/472	
Goodness-of-fit on F^2	1.026	
Final R indexes [I>=2σ (I)]	wR_2 = 0.0778	
Final R indexes [all data]	R_1 = 0.0435	
Largest diff. peak/hole / e Å^{-3}	0.48/-0.34	

8.9.2 [K{18c6}][(Fe(N(SiMe$_3$)$_2$)$_2$(η^2-allylanisol)] (2).

Tabelle 4. Kristallographische Daten von **2**.

Identification code	GWX052_0m
Habitus, colour	block, dark red
Crystal size	0.232 × 0.313 × 0.422 mm^3
Crystal system	tetragonal
Space group	$P4_32_12$ Z = 8
Unit cell dimensions	a = 15.9718(7) Å α = 90.0° b = 15.9718(7) Å β = 90.0° c = 39.7910(17) Å γ = 90.0°
Volume	10.150.6(10) Å^3
Empirical formula	$C_{34}H_{71}FeKN_2O_7Si_4$
Formula weight	826.73 g/mol
Density (calculated)	1.082 g/cm^3
Absorption coefficient	0.511 mm^{-1}
F(000)	3654.0
Diffractometer type	Bruker D8 QUEST
Wavelength	0.71073 Å
Temperature	100 K
2Θ range for data collection/°	4.738 to 49.994
Index ranges	-18 ≤ h ≤ 18, -18 ≤ k ≤ 18, -47 ≤ l ≤ 47
Data collection software	APEX3 (Bruker AXS Inc., 2015)[131]
Cell refinement software	SAINT V8.37A (Bruker AXS Inc., 2015)[132]
Data reduction software	SAINT V8.37A (Bruker AXS Inc., 2015)[132]
Reflections collected	79540
Independent reflections	8921 [R_{int} = 0.0514, R_{sigma} = 0.0336]
Reflections used for refinement	8921
Absorption correction	Semi-empirical from equivalents[133]
Max. and min. transmission	0.7454 and 0.6767
Solution	dual space algorithm
Refinement	Full-matrix least-squares on F^2
Treatment of hydrogen atoms	Calculated positions, constr. ref.
Programs used	XT V2014/1 (Bruker AXS Inc., 2014)[127] SHELXL-2016/6 (Sheldrick, 2016)[128] DIAMOND (Crystal Impact)[129] ShelXle (Hübschle, Sheldrick, Dittrich, 2011)[130]
Data/restraints/parameters	8921/265/388
Goodness-of-fit on F^2	0.990
Final R indexes [I>=2σ (I)]	wR_2 = 0.0867
Final R indexes [all data]	R_1 = 0.2291
Largest diff. peak/hole / e Å^{-3}	1.61/-0.58
Flack parameter	0.06(5)

8.9.3 [K{18c6}]$_2$[1,1,4,4-Tetraphenlbutan-1,4-diyl)] (3).

Tabelle 5. Kristallographische Daten von **3**.

Identification code	GWX040_0ma
Habitus, colour	Block, dark red
Crystal size	0.238 × 0.280 × 0.304 mm^3
Crystal system	othorhombic
Space group	Pbca Z = 4
Unit cell dimensions	a = 15.3348(12) Å α = 90.0° b = 12.3843(10) Å β = 90.0° c = 26.193(2) Å γ = 90.0°
Volume	4974.3(7) Å^3
Empirical formula	$C_{52}H_{72}K_2O_{12}$
Formula weight	967.29 g/mol
Density (calculated)	1.292 g/cm^3
Absorption coefficient	0.252 mm^{-1}
F(000)	2072.0
Diffractometer type	Bruker D8 QUEST
Wavelength	0.71073 Å
Temperature	100 K
2Θ range for data collection/°	4.504 to 50
Index ranges	-18 ≤ h ≤ 16, -14 ≤ k ≤ 14, -31 ≤ l ≤ 31
Data collection software	APEX3 (Bruker AXS Inc., 2015)[131]
Cell refinement software	SAINT V8.37A (Bruker AXS Inc., 2015)[132]
Data reduction software	SAINT V8.37A (Bruker AXS Inc., 2015)[132]
Reflections collected	42408
Independent reflections	4368 [R_{int} = 0.0593, R_{sigma} = 0.0301]
Reflections used for refinement	4368
Absorption correction	Semi-empirical from equivalents[133]
Max. and min. transmission	0.7454 and 0.6523
Solution	dual space algorithm
Refinement	Full-matrix least-squares on F^2
Treatment of hydrogen atoms	Calculated positions, constr. ref.
Programs used	XT V2014/1 (Bruker AXS Inc., 2014)[127] SHELXL-2016/6 (Sheldrick, 2016)[128] DIAMOND (Crystal Impact)[129] ShelXle (Hübschle, Sheldrick, Dittrich, 2011)[130]
Data/restraints/parameters	4368/678/461
Goodness-of-fit on F^2	1.065
Final R indexes [I>=2σ (I)]	wR_2 = 0.0826
Final R indexes [all data]	R_1 = 0.0374
Largest diff. peak/hole / e Å^{-3}	0.28/-0.23

8.9.4 [K{18c6}][Cr(N(SiMe$_3$)$_2$)(η^2-(Ph*C*HCH$_2$CH$_2$*C*HPh)] (4).

Tabelle 6. Kristallographische Daten von **4**.

Identification code	PIM862_0m
Habitus, colour	plank, light green
Crystal size	0.124 × 0.243 × 0.514 mm^3
Crystal system	monoclinic
Space group	C2/c Z = 4
Unit cell dimensions	a = 12.646(2) Å α = 90.0° b = 12.635(2) Å β = 97.782(5)° c = 24.140(4) Å γ = 90.0°
Volume	3821.6(11) Å^3
Empirical formula	$C_{34}H_{58}CrKNO_6Si_2$
Formula weight	724.09 g/mol
Density (calculated)	1.259 g/cm^3
Absorption coefficient	0.512 mm^{-1}
F(000)	1552.0
Diffractometer type	Bruker D8 QUEST
Wavelength	0.71073 Å
Temperature	100 K
2Θ range for data collection/°	4.578 to 50.192
Index ranges	-15 ≤ h ≤ 13, -14 ≤ k ≤ 15, -28 ≤ l ≤ 27
Data collection software	APEX3 (Bruker AXS Inc., 2015)[131]
Cell refinement software	SAINT V8.37A (Bruker AXS Inc., 2015)[132]
Data reduction software	SAINT V8.37A (Bruker AXS Inc., 2015)[132]
Reflections collected	7693
Independent reflections	3265 [R_{int} = 0.0661, R_{sigma} = 0.1060]
Reflections used for refinement	3265
Absorption correction	Semi-empirical from equivalents[133]
Max. and min. transmission	0.7452 and 0.5945
Solution	dual space algorithm
Refinement	Full-matrix least-squares on F^2
Treatment of hydrogen atoms	Calculated positions, constr. ref.
Programs used	XT V2014/1 (Bruker AXS Inc., 2014)[127] SHELXL-2016/6 (Sheldrick, 2016)[128] DIAMOND (Crystal Impact)[129] ShelXle (Hübschle, Sheldrick, Dittrich, 2011)[130]
Data/restraints/parameters	3265/125/248
Goodness-of-fit on F^2	1.056
Final R indexes [I>=2σ (I)]	wR_2 = 0.1926
Final R indexes [all data]	R_1 = 0.0884
Largest diff. peak/hole / e Å^{-3}	1.54/-0.95

8.9.5 [K{18c6}][Cr(N(SiMe$_3$)$_2$)(η^2-(Ph$_2$*C*CH$_2$CH$_2$*C*Ph$_2$)] (5).

Tabelle 7. Kristallographische Daten von **5**.

Identification code	PIMX056a
Habitus, colour	needle, light green
Crystal size	0.173 × 0.336 × 0.368 mm^3
Crystal system	triclinic
Space group	P-1 Z = 1
Unit cell dimensions	a = 14.4300(13) Å α = 69.825(7)° b = 14.3830(14) Å β = 68.260(7)° c =14.9788(14) Å γ = 72.458(7)°
Volume	2656.2(5) Å^3
Empirical formula	$C_{100}H_{152}Cr_2K_2N_2O_{14}Si_4$
Formula weight	1900.79 g/mol
Density (calculated)	1.188 g/cm^3
Absorption coefficient	0.385 mm^{-1}
F(000)	1020.0
Diffractometer type	STOE IPDS-2
Wavelength	0.71073 Å
Temperature	100 K
2Θ range for data collection/°	3.034 to 53.484
Index ranges	-18 ≤ h ≤ 18, -18 ≤ k ≤ 18, -18 ≤ l ≤ 18
Data collection software	STOE X-Area[124]
Cell refinement software	STOE X-Area[124]
Data reduction software	STOE X-Area[124,125]
Reflections collected	25003
Independent reflections	11186 [R_{int} = 0.0329, R_{sigma} = 0.0613]
Completeness to theta = 25.242°	100 %
Reflections used for refinement	11186
Absorption correction	Semi-empirical from equivalents[126]
Max. and min. transmission	0.9165 and 0.7204
Solution	dual space algorithm
Refinement	Full-matrix least-squares on F^2
Treatment of hydrogen atoms	Calculated positions, constr. ref.
Programs used	XT V2014/1 (Bruker AXS Inc., 2014)[127] SHELXL-2016/6 (Sheldrick, 2016)[128] DIAMOND (Crystal Impact)[129] ShelXle (Hübschle, Sheldrick, Dittrich, 2011)[130]
Data/restraints/parameters	11186/0/570
Goodness-of-fit on F^2	0.920
Final R indexes [I>=2σ (I)]	wR_2 = 0.0887
Final R indexes [all data]	R_1 = 0.0385
Largest diff. peak/hole / e Å^{-3}	0.45/-0.28

8.9.6 [K{18c6}][Cr(N(SiMe$_3$)$_2$)$_2$(η^2-(*trans*-β-methylstyrol)] (6).

Tabelle 8. Kristallographische Daten von **6**.

Identification code	PIMX057a
Habitus, colour	block, light red
Crystal size	0.015 × 0.245 × 0.637 mm^3
Crystal system	triclinic
Space group	P-1 Z = 2
Unit cell dimensions	a = 11.5756(18) Å α = 81.196(12)° b = 12.1437(19) Å β = 84.161(13)° c =16.288(3) Å γ = 77.880(13)°
Volume	2207.96(6) Å^3
Empirical formula	$C_{33}H_{70}CrKN_2O_6Si_4$
Formula weight	794.37 g/mol
Density (calculated)	1.195 g/cm^3
Absorption coefficient	0.501 mm^{-1}
F(000)	858.0
Diffractometer type	STOE IPDS-2T
Wavelength	0.71073 Å
Temperature	100 K
2Θ range for data collection/°	2.536 to 53.474
Index ranges	-14 ≤ h ≤ 13, -15 ≤ k ≤ 15, -19 ≤ l ≤ 20
Data collection software	STOE X-Area[124]
Cell refinement software	STOE X-Area[124]
Data reduction software	STOE X-Area[124,125]
Reflections collected	19647
Independent reflections	9285 [R_{int} = 0.0639, R_{sigma} = 0.0850]
Reflections used for refinement	11186
Absorption correction	Semi-empirical from equivalents[126]
Max. and min. transmission	0.9449 and 0.7942
Solution	dual space algorithm
Refinement	Full-matrix least-squares on F^2
Treatment of hydrogen atoms	Calculated positions, constr. ref.
Programs used	XT V2014/1 (Bruker AXS Inc., 2014)[127] SHELXL-2016/6 (Sheldrick, 2016)[128] DIAMOND (Crystal Impact)[129] ShelXle (Hübschle, Sheldrick, Dittrich, 2011)[130]
Data/restraints/parameters	9285/0/437
Goodness-of-fit on F^2	0.927
Final R indexes [I>=2σ (I)]	wR_2 = 0.0747
Final R indexes [all data]	R_1 = 0.0370
Largest diff. peak/hole / e Å^{-3}	0.46/-0.39

8.9.7 [K{18c6}][Cr(N(SiMe$_3$)$_2$)$_2$(η^2-(*trans*-stilben)] (7).

Tabelle 9. Kristallographische Daten von **7**.

Identification code	GWX040_0mneu
Habitus, colour	Block, dark red
Crystal size	0.168 × 0.219 × 0.268 mm^3
Crystal system	Monoclinic
Space group	C2/c Z = 4
Unit cell dimensions	a = 28.1826(11) Å α = 90.0° b = 11.6627(5) Å β = 96.8280(10)° c = 31.0498(11) Å γ = 90.0°
Volume	10133.2(7) Å^3
Empirical formula	$C_{80}H_{154}Cr_2K_2N_4O_{13}Si_8$
Formula weight	1786.98 g/mol
Density (calculated)	1.171 g/cm^3
Absorption coefficient	0.444 mm^{-1}
F(000)	3856.0
Diffractometer type	Bruker D8 QUEST
Wavelength	0.71073 Å
Temperature	100 K
2Θ range for data collection/°	4.514 to 55.552
Index ranges	-32 ≤ h ≤ 36, -15 ≤ k ≤ 15, -40 ≤ l ≤ 40
Data collection software	APEX3 (Bruker AXS Inc., 2015)[131]
Cell refinement software	SAINT V8.37A (Bruker AXS Inc., 2015)[132]
Data reduction software	SAINT V8.37A (Bruker AXS Inc., 2015)[132]
Reflections collected	120108
Independent reflections	11946 [R_{int} = 0.0361, R_{sigma} = 0.0202]
Reflections used for refinement	11946
Absorption correction	Semi-empirical from equivalents[133]
Max. and min. transmission	0.7456 and 0.7232
Solution	dual space algorithm
Refinement	Full-matrix least-squares on F^2
Treatment of hydrogen atoms	Calculated positions, constr. ref.
Programs used	XT V2014/1 (Bruker AXS Inc., 2014)[127] SHELXL-2016/6 (Sheldrick, 2016)[128] DIAMOND (Crystal Impact)[129] ShelXle (Hübschle, Sheldrick, Dittrich, 2011)[130]
Data/restraints/parameters	11946/0/505
Goodness-of-fit on F^2	1.067
Final R indexes [I>=2σ (I)]	wR_2 = 0.0695
Final R indexes [all data]	R_1 = 0.0310
Largest diff. peak/hole / e Å^{-3}	0.41/-0.38

8.9.8 [K{18c6}][Mn(N(SiMe$_3$)$_2$)$_2$(η^2-(*trans*-β-methylstyrol)] (8).

Tabelle 10. Kristallographische Daten von **8**.

Identification code	GWX038_0m
Habitus, colour	plate, dark brown
Crystal size	0.17 × 0.188 × 0.262 mm^3
Crystal system	Monoclinic
Space group	$P2_1/c$ Z = 4
Unit cell dimensions	a = 17.526(2) Å α = 90.0° b = 13.8454(11) Å β = 113.277(4)° c = 19.908(2) Å γ = 90.0°
Volume	4437.6(8) Å^3
Empirical formula	$C_{33}H_{70}MnKN_2O_6Si_4$
Formula weight	797.31 g/mol
Density (calculated)	1.193 g/cm^3
Absorption coefficient	0.538 mm^{-1}
F(000)	1720.0
Diffractometer type	Bruker D8 QUEST
Wavelength	0.71073 Å
Temperature	100 K
2Θ range for data collection/°	4.454 to 50.136
Index ranges	-20 ≤ h ≤ 20, -16 ≤ k ≤ 16, -21 ≤ l ≤ 23
Data collection software	APEX3 (Bruker AXS Inc., 2015)[131]
Cell refinement software	SAINT V8.37A (Bruker AXS Inc., 2015)[132]
Data reduction software	SAINT V8.37A (Bruker AXS Inc., 2015)[132]
Reflections collected	119271
Independent reflections	7855 [R_{int} = 0.0656, R_{sigma} = 0.0226]
Reflections used for refinement	7855
Absorption correction	Semi-empirical from equivalents[133]
Max. and min. transmission	0.7452 and 0.6897
Solution	dual space algorithm
Refinement	Full-matrix least-squares on F^2
Treatment of hydrogen atoms	Calculated positions, constr. ref.
Programs used	XT V2014/1 (Bruker AXS Inc., 2014)[127] SHELXL-2016/6 (Sheldrick, 2016)[128] DIAMOND (Crystal Impact)[129] ShelXle (Hübschle, Sheldrick, Dittrich, 2011)[130]
Data/restraints/parameters	7855/497/495
Goodness-of-fit on F^2	1.060
Final R indexes [I>=2σ (I)]	wR_2 = 0.0672
Final R indexes [all data]	R_1 = 0.0421
Largest diff. peak/hole / e Å^{-3}	0.36/-0.34

8.9.9 [K{18c6}][Fe(N(SiMe$_3$)$_2$)$_2$(η^2-(*cis*-β-methylstyrol)] (9).

Tabelle 11. Kristallographische Daten von **9**.

Identification code	PIMX054a
Habitus, colour	block, dark red
Crystal size	0.412 × 0.524 × 0.984 mm^3
Crystal system	monoclinic
Space group	$P2_1/c$ Z = 4
Unit cell dimensions	a = 12.1227(8) Å α = 90.0° b = 18.3502(12) Å β = 104.6(5)° c = 21.0291(14) Å γ = 90.0°
Volume	4526.1(5) Å^3
Empirical formula	$C_{33}H_{70}FeKN_2O_6Si_4$
Formula weight	2069.12 g/mol
Density (calculated)	1.171 g/cm^3
Absorption coefficient	0.569 mm^{-1}
F(000)	1724.0
Diffractometer type	STOE IPDS-2
Wavelength	0.71073 Å
Temperature	100 K
2Θ range for data collection/°	2.988 to 58.508
Index ranges	-16 ≤ h ≤ 16, -22 ≤ k ≤ 25, -28 ≤ l ≤ 26
Data collection software	STOE X-Area[124]
Cell refinement software	STOE X-Area[124]
Data reduction software	STOE X-Area[124,125]
Reflections collected	30974
Independent reflections	12149 [R_{int} = 0.0459, R_{sigma} = 0.0488]
Reflections used for refinement	12149
Absorption correction	Semi-empirical from equivalents[126]
Max. and min. transmission	0.8403 and 0.6648
Solution	dual space algorithm
Refinement	Full-matrix least-squares on F^2
Treatment of hydrogen atoms	Calculated positions, constr. ref.
Programs used	XT V2014/1 (Bruker AXS Inc., 2014)[127] SHELXL-2016/6 (Sheldrick, 2016)[128] DIAMOND (Crystal Impact)[129] ShelXle (Hübschle, Sheldrick, Dittrich, 2011)[130]
Data/restraints/parameters	12149/0/437
Goodness-of-fit on F^2	0.951
Final R indexes [I>=2σ (I)]	wR_2 = 0.0944
Final R indexes [all data]	R_1 = 0.0607
Largest diff. peak/hole / e Å^{-3}	0.74/-0.37

8.9.10 [K{18c6}][Fe(N(SiMe$_3$)$_2$)$_2$(η^2-(*trans*-stilben)] (10).

Tabelle 12. Kristallographische Daten von **10**.

Identification code	K38a
Habitus, colour	plank, dark red
Crystal size	0.438 × 0.419 × 0.285 mm^3
Crystal system	monoclinic
Space group	C2/c Z = 4
Unit cell dimensions	a = 37.416(5) Å α = 90.0° b = 13.2067(15) Å β = 133.663(7)° c = 28.584(4) Å γ = 90.0°
Volume	10218(2) Å^3
Empirical formula	$C_{80}H_{154}Fe_2K_2N_4O_{13}Si_8$
Formula weight	1794.68 g/mol
Density (calculated)	1.167 g/cm^3
Absorption coefficient	0.512 mm^{-1}
F(000)	3872.0
Diffractometer type	STOE IPDS-2
Wavelength	0.71073 Å
Temperature	100 K
2Θ range for data collection/°	2.864 to 53.62
Index ranges	-47 ≤ h ≤ 46, -15 ≤ k ≤ 16, -35 ≤ l ≤ 36
Data collection software	STOE X-Area[124]
Cell refinement software	STOE X-Area[124]
Data reduction software	STOE X-Area[124,125]
Reflections collected	24901
Independent reflections	10544 [R_{int} = 0.0663, R_{sigma} = 0.0586]
Reflections used for refinement	10544
Absorption correction	Semi-empirical from equivalents[126]
Max. and min. transmission	0.9503 and 0.7902
Solution	dual space algorithm
Refinement	Full-matrix least-squares on F^2
Treatment of hydrogen atoms	Calculated positions, constr. ref.
Programs used	XT V2014/1 (Bruker AXS Inc., 2014)[127] SHELXL-2016/6 (Sheldrick, 2016)[128] DIAMOND (Crystal Impact)[129] ShelXle (Hübschle, Sheldrick, Dittrich, 2011)[130]
Data/restraints/parameters	10544/387/675
Goodness-of-fit on F^2	1.108
Final R indexes [I>=2σ (I)]	wR_2 = 0.01722
Final R indexes [all data]	R_1 = 0.0712
Largest diff. peak/hole / e Å^{-3}	0.50/-0.51

8.9.11 $[K\{18c6\}]_2[(Mn(N(SiMe_3)_2)_3)(\textit{trans}\text{-stilben})]$ (11).

Tabelle 13. Kristallographische Daten von **11**.

Identification code	PIMX058c
Habitus, colour	block, dark violet
Crystal size	0.155× 0.161 × 0.209 mm^3
Crystal system	triclinic
Space group	P-1 Z = 2
Unit cell dimensions	a = 13.5653(14) Å α = 90.039(8)° b = 13.5595(15) Å β = 89.991(8)° c = 20.4105(19) Å γ = 91.469(8)°
Volume	3753.0(7) $Å^3$
Empirical formula	$C_{56}H_{114}MnK_2N_3O_{12}Si_6$
Formula weight	1323.18 g/mol
Density (calculated)	1.171 g/cm^3
Absorption coefficient	0.434 mm^{-1}
F(000)	1428.0
Diffractometer type	STOE IPDS-2T
Wavelength	0.71073 Å
Temperature	100 K
2Θ range for data collection/°	3.606 to 50
Index ranges	$-15 \leq h \leq 16$, $-16 \leq k \leq 16$, $-24 \leq l \leq 24$
Data collection software	STOE X-Area[124]
Cell refinement software	STOE X-Area[124]
Data reduction software	STOE X-Area[124,125]
Reflections collected	25974
Independent reflections	12437 [R_{int} = 0.0493, R_{sigma} = 0.0467]
Reflections used for refinement	12437
Absorption correction	Semi-empirical from equivalents[126]
Max. and min. transmission	0.9619 and 0.9351
Solution	dual space algorithm
Refinement	Full-matrix least-squares on F^2
Treatment of hydrogen atoms	Calculated positions, constr. ref.
Programs used	XT V2014/1 (Bruker AXS Inc., 2014)[127] SHELXL-2016/6 (Sheldrick, 2016)[128] DIAMOND (Crystal Impact)[129] ShelXle (Hübschle, Sheldrick, Dittrich, 2011)[129]
Data/restraints/parameters	12437/1369/1190
Goodness-of-fit on F^2	1.074
Final R indexes [I>=2σ (I)]	wR_2 = 0.01155
Final R indexes [all data]	R_1 = 0.054
Largest diff. peak/hole / e $Å^{-3}$	0.71/-0.48

8.9.12 [K{18c6}][Cr(N(SiMe$_3$)$_2$)$_2$(η^4-but] (12).

Tabelle 14. Kristallographische Daten von **12**.

Identification code	PIMX045a
Habitus, colour	block, dark red
Crystal size	0.186 × 0.522 × 0.590 mm^3
Crystal system	triclinic
Space group	P-1 Z = 2
Unit cell dimensions	a = 11.008(3) Å α = 111.855(19)° b = 16.180(4) Å β = 105.32(2)° c = 16.353(4) Å γ = 96.66(2)°
Volume	2531.5(12) Å^3
Empirical formula	$C_{38}H_{86}CrKN_2O_8Si_4$
Formula weight	2353.71 g/mol
Density (calculated)	1.184 g/cm^3
Absorption coefficient	0.447 mm^{-1}
F(000)	982.0
Diffractometer type	STOE IPDS-2T
Wavelength	0.71073 Å
Temperature	100 K
2Θ range for data collection/°	3.952 to 50
Index ranges	-13 ≤ h ≤ 13, -19 ≤ k ≤ 19, -19 ≤ l ≤ 19
Data collection software	STOE X-Area[124]
Cell refinement software	STOE X-Area[124]
Data reduction software	STOE X-Area[124,125]
Reflections collected	29658
Independent reflections	29658 [R_{int} = 0.1173, R_{sigma} = 0.0098]
Reflections used for refinement	29658
Absorption correction	Semi-empirical from equivalents[126]
Max. and min. transmission	0.885 and 0.779
Solution	dual space algorithm
Refinement	Full-matrix least-squares on F^2
Treatment of hydrogen atoms	Calculated positions, constr. ref.
Programs used	XT V2014/1 (Bruker AXS Inc., 2014)[127] SHELXL-2016/6 (Sheldrick, 2016)[128] DIAMOND (Crystal Impact)[129] ShelXle (Hübschle, Sheldrick, Dittrich, 2011)[130]
Data/restraints/parameters	29658/0/502
Goodness-of-fit on F^2	1.381
Final R indexes [I>=2σ (I)]	wR_2 = 0.2918
Final R indexes [all data]	R_1 = 0.1138
Largest diff. peak/hole / e Å^{-3}	1.57/-0.74

8.9.13 [K{18c6}][Mn(η⁴-but)₂] (13).

Tabelle 15. Kristallographische Daten von **13**.

Identification code	PIMX043b
Habitus, colour	block, dark red
Crystal size	0.423 × 0.467 × 0.574 mm^3
Crystal system	monoclinic
Space group	$P2_1/n$ Z = 4
Unit cell dimensions	a = 12.0776(17) Å α = 90.0° b = 13.7289(12) Å β = 90.304(11)° c = 16.508(2) Å γ = 90.0°
Volume	2737.2(6) $Å^3$
Empirical formula	$C_{24}H_{44}MnKO_6$
Formula weight	522.63 g/mol
Density (calculated)	1.268 g/cm^3
Absorption coefficient	0.668 mm^{-1}
F(000)	1120.0
Diffractometer type	STOE IPDS-2T
Wavelength	0.71073 Å
Temperature	100 K
2Θ range for data collection/°	4.936 to 49.998
Index ranges	-13 ≤ h ≤ 14, -16 ≤ k ≤ 14, -19 ≤ l ≤ 19
Data collection software	STOE X-Area[124]
Cell refinement software	STOE X-Area[124]
Data reduction software	STOE X-Area[124,125]
Reflections collected	12470
Independent reflections	4820 [R_{int} = 0.069, R_{sigma} = 0.0699]
Reflections used for refinement	4820
Absorption correction	Semi-empirical from equivalents[126]
Max. and min. transmission	0.8113 and 0.7417
Solution	dual space algorithm
Refinement	Full-matrix least-squares on F^2
Treatment of hydrogen atoms	Calculated positions, constr. ref.
Programs used	XT V2014/1 (Bruker AXS Inc., 2014)[127] SHELXL-2016/6 (Sheldrick, 2016)[128] DIAMOND (Crystal Impact)[129] ShelXle (Hübschle, Sheldrick, Dittrich, 2011)[130]
Data/restraints/parameters	4819/0/293
Goodness-of-fit on F^2	0.952
Final R indexes [I>=2σ (I)]	wR_2 = 0.1202
Final R indexes [all data]	R_1 = 0.0932
Largest diff. peak/hole / e $Å^{-3}$	1.58/-0.42

8.9.14 [K{18c6}][(Fe(N(SiMe$_3$)$_2$)$_2$)$_2$(but)] (14).

Tabelle 16. Kristallographische Daten von **14**.

Identification code	PIMX016e
Habitus, colour	block, yellowish red
Crystal size	0.909 × 0.447 × 0.287 mm^3
Crystal system	monoclinic
Space group	$P2_1$ Z = 2
Unit cell dimensions	a = 10.2951(6) Å α = 90.0° b = 29.2772(18) Å β = 90.646(5)° c = 15.3322(11) Å γ = 90.0°
Volume	4621.0(5) Å^3
Empirical formula	$C_{62}H_{150}Fe_2K_2N_4O_{14}Si_{18}$
Formula weight	1590.47 g/mol
Density (calculated)	1.143 g/cm^3
Absorption coefficient	0.558 mm^{-1}
F(000)	1728.0
Diffractometer type	STOE IPDS-2T
Wavelength	0.71073 Å
Temperature	100 K
2Θ range for data collection/°	4.742 to 50.996
Index ranges	-12 ≤ h ≤ 12, -35 ≤ k ≤ 35, -18 ≤ l ≤ 18
Data collection software	STOE X-Area[124]
Cell refinement software	STOE X-Area[124]
Data reduction software	STOE X-Area[124,125]
Reflections collected	32148
Independent reflections	17181 [R_{int} = 0.0386, R_{sigma} = 0.0452]
Reflections used for refinement	32148
Absorption correction	Semi-empirical from equivalents[126]
Max. and min. transmission	0.9296 and 0.6857
Solution	dual space algorithm
Refinement	Full-matrix least-squares on F^2
Treatment of hydrogen atoms	Calculated positions, constr. ref.
Programs used	XT V2014/1 (Bruker AXS Inc., 2014)[127] SHELXL-2016/6 (Sheldrick, 2016)[128] DIAMOND (Crystal Impact)[129] ShelXle (Hübschle, Sheldrick, Dittrich, 2011)[130]
Data/restraints/parameters	17181/224/1242
Goodness-of-fit on F^2	1.037
Final R indexes [I>=2σ (I)]	wR_2 = 0.0913
Final R indexes [all data]	R_1 = 0.0389
Largest diff. peak/hole / e Å^{-3}	0.46/-0.56
Flack parameter	0.378(14)

8.10 NMR-Spektren

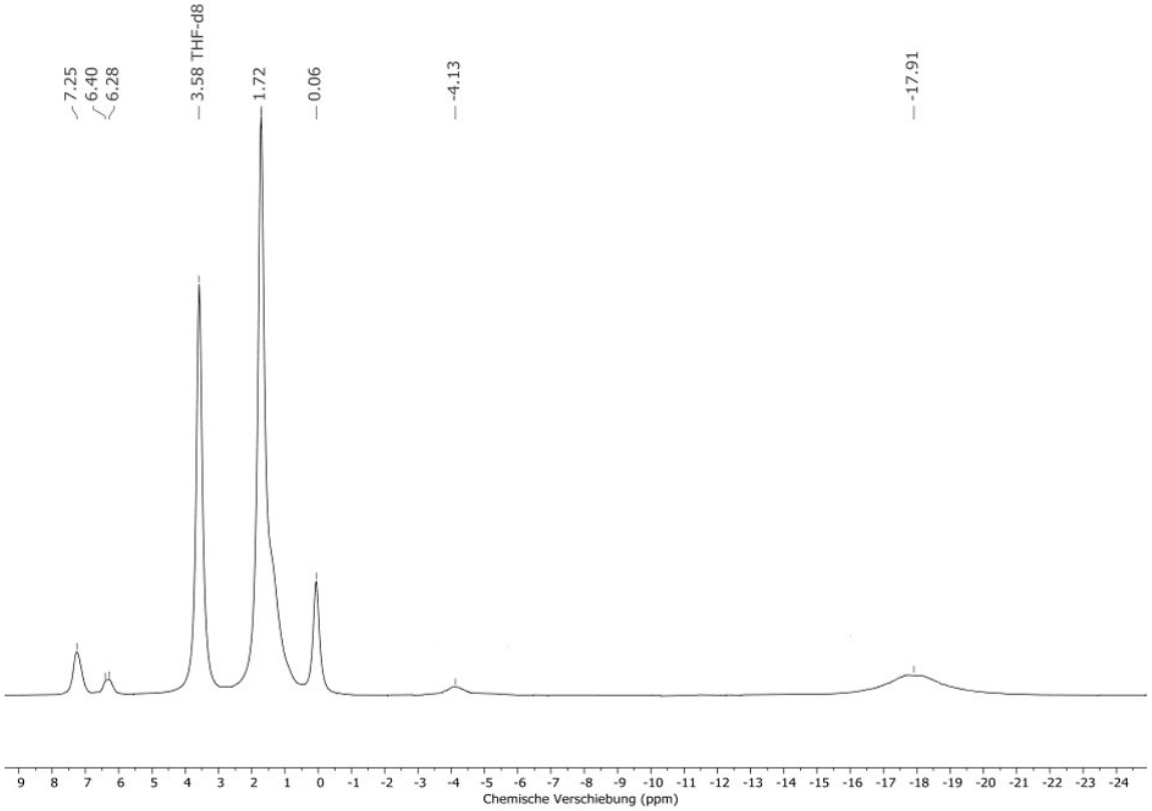

Abbildung 29. ^{1}H-NMR-Spektrum von **[K{18c6}][Fe(N(SiMe$_3$)$_2$)$_2$(η^2-(*cis*-β-methylstyrol)] (9)** in THF-d$_8$ (300.1 MHz).

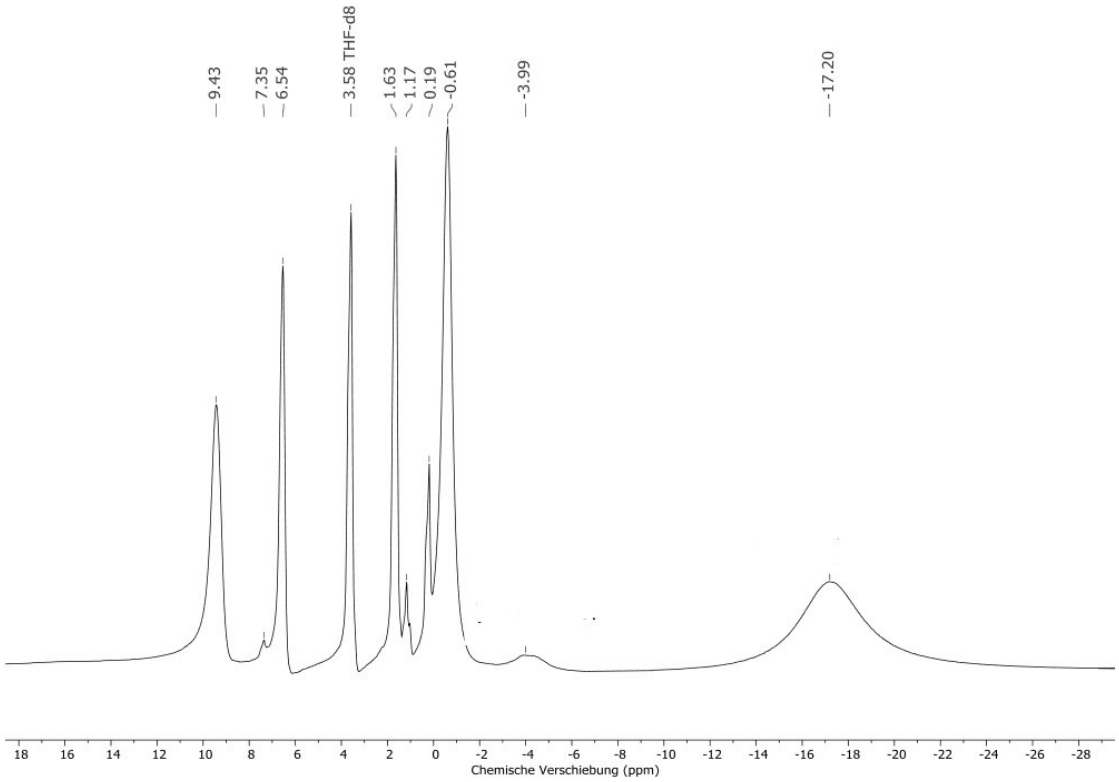

Abbildung 30. ^{1}H-NMR-Spektrum von **[K{18c6}][Fe(N(SiMe$_3$)$_2$)$_2$(η^2-(*trans*-stilben)] (10)** in THF-d$_8$ (300.1 MHz).

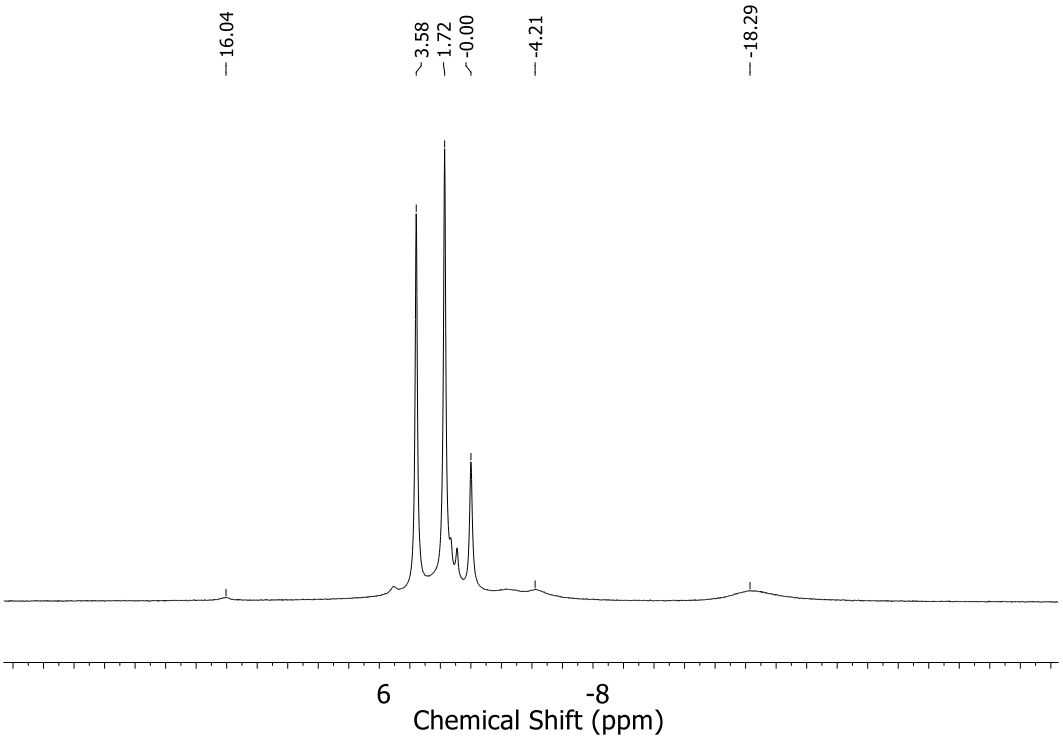

Abbildung 31. ^{1}H-NMR-Spektrum von **[K{18c6}]$_2$[(Fe(N(SiMe$_3$)$_2$)$_2$)$_2$(but)]** (**14**) in THF-d$_8$ (300.1 MHz).

8.11 IR-Spektren

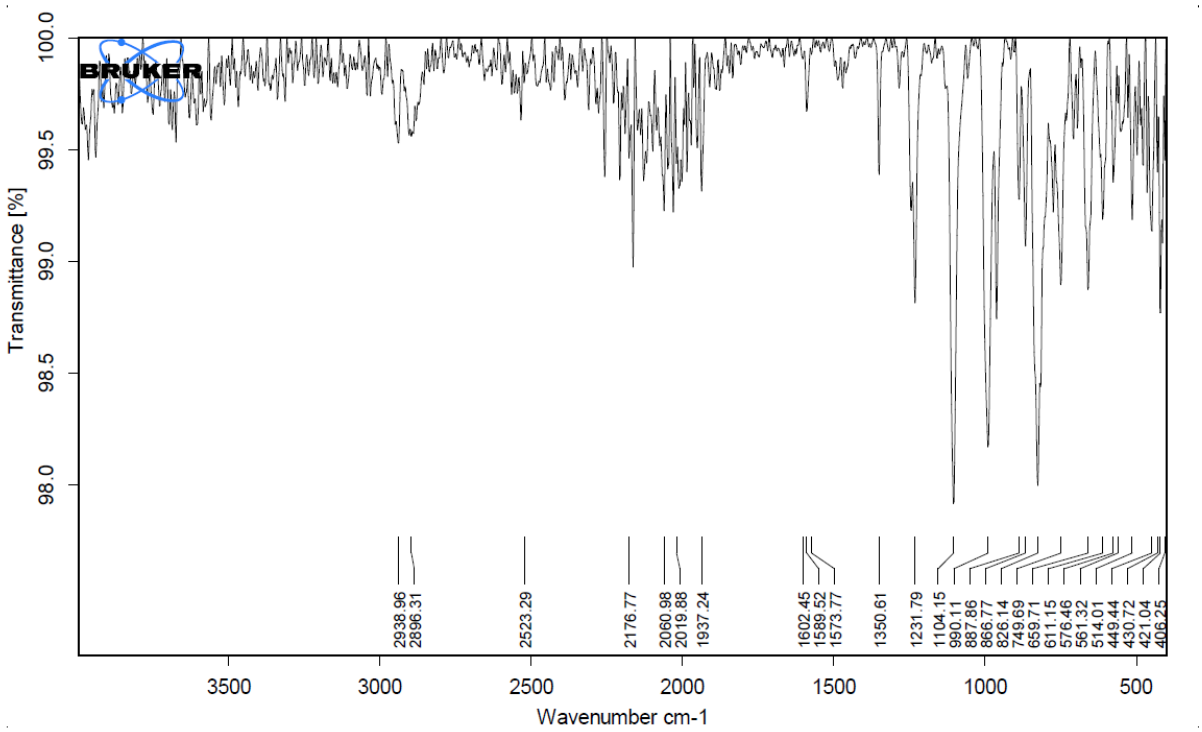

Abbildung 32. IR-Spektrum von **[K{18c6}(thf)][(Fe(N(SiMe$_3$)$_2$)$_2$(η^2-styrol)] (1)**.

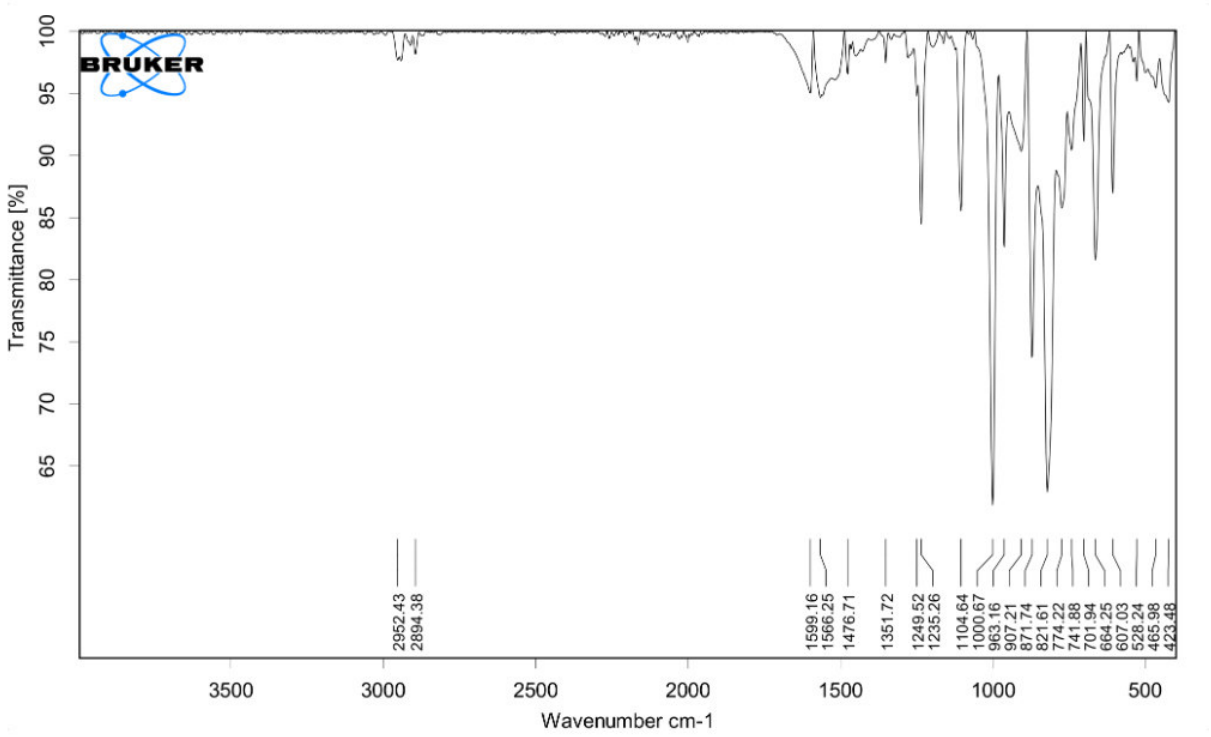

Abbildung 33. IR-Spektrum von **[K{18c6}]$_2$[1,1,4,4-Tetraphenlbutan-1,4-diyl)] (3)**.

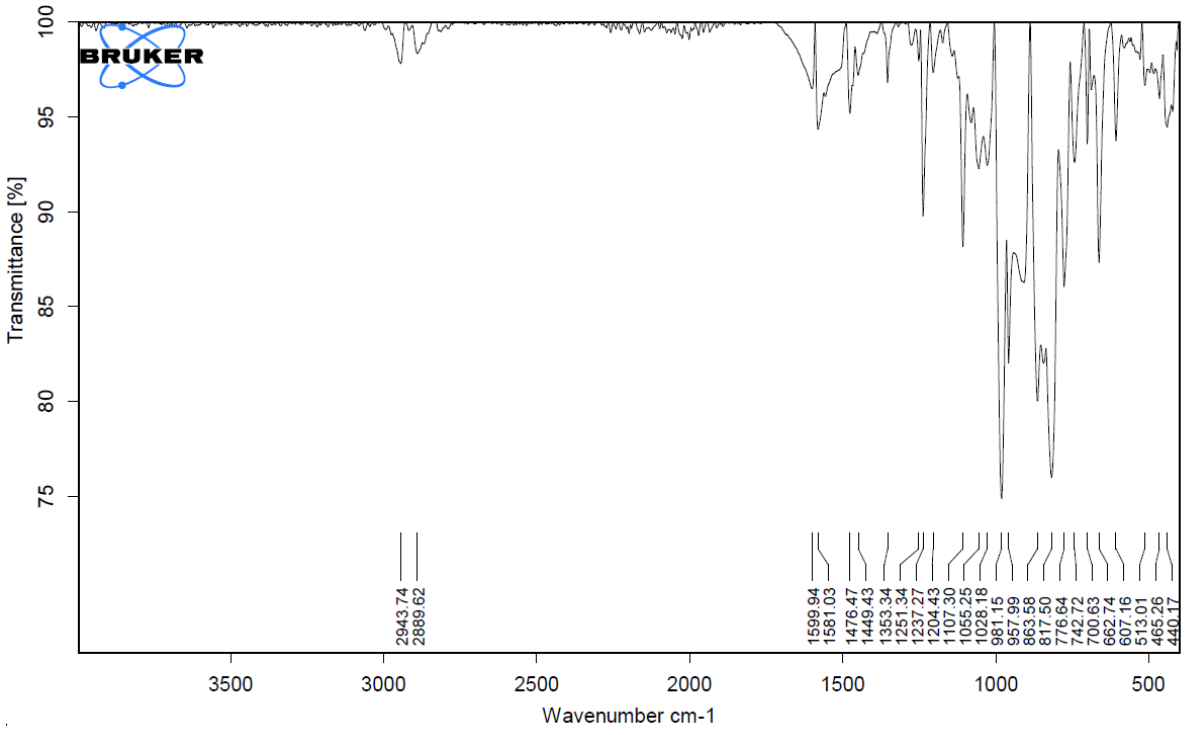

Abbildung 34. IR-Spektrum von **[K{18c6}][Cr(N(SiMe$_3$)$_2$)(η^2-(Ph*C*HCH$_2$CH$_2$*C*HPh)] (4)**.

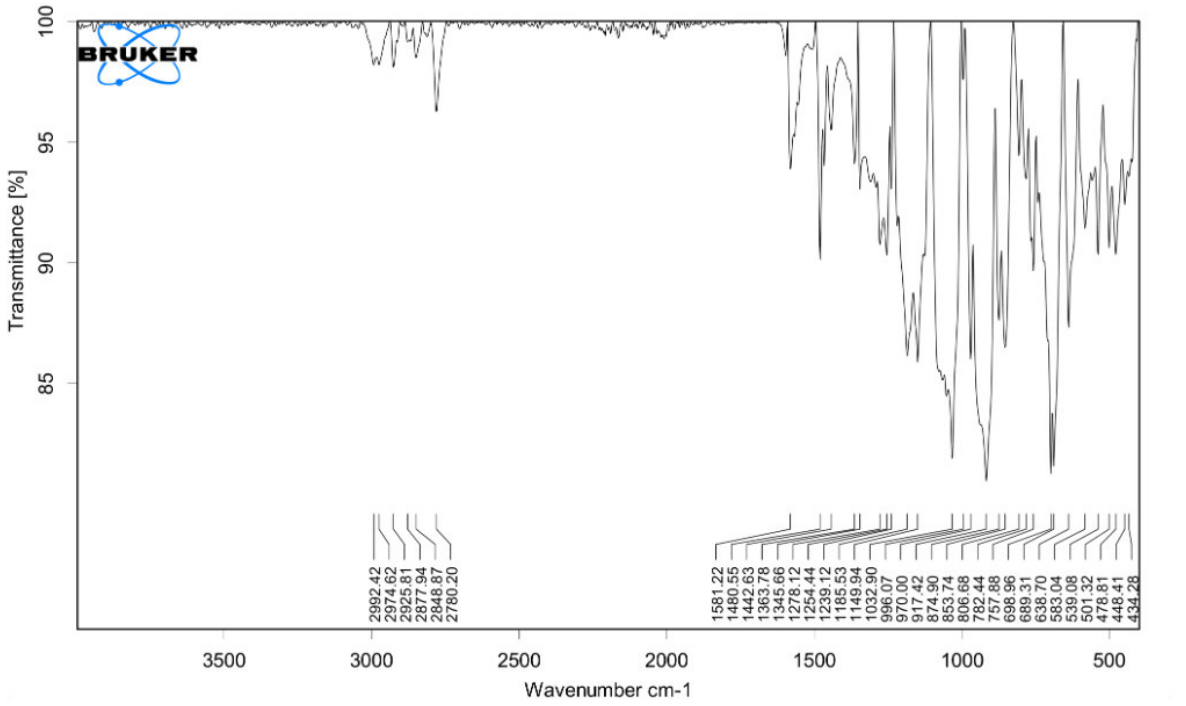

Abbildung 35. IR-Spektrum von **[K{18c6}][Cr(N(SiMe$_3$)$_2$)(η^2-(Ph$_2$*C*CH$_2$CH$_2$*C*Ph$_2$)] (5)**.

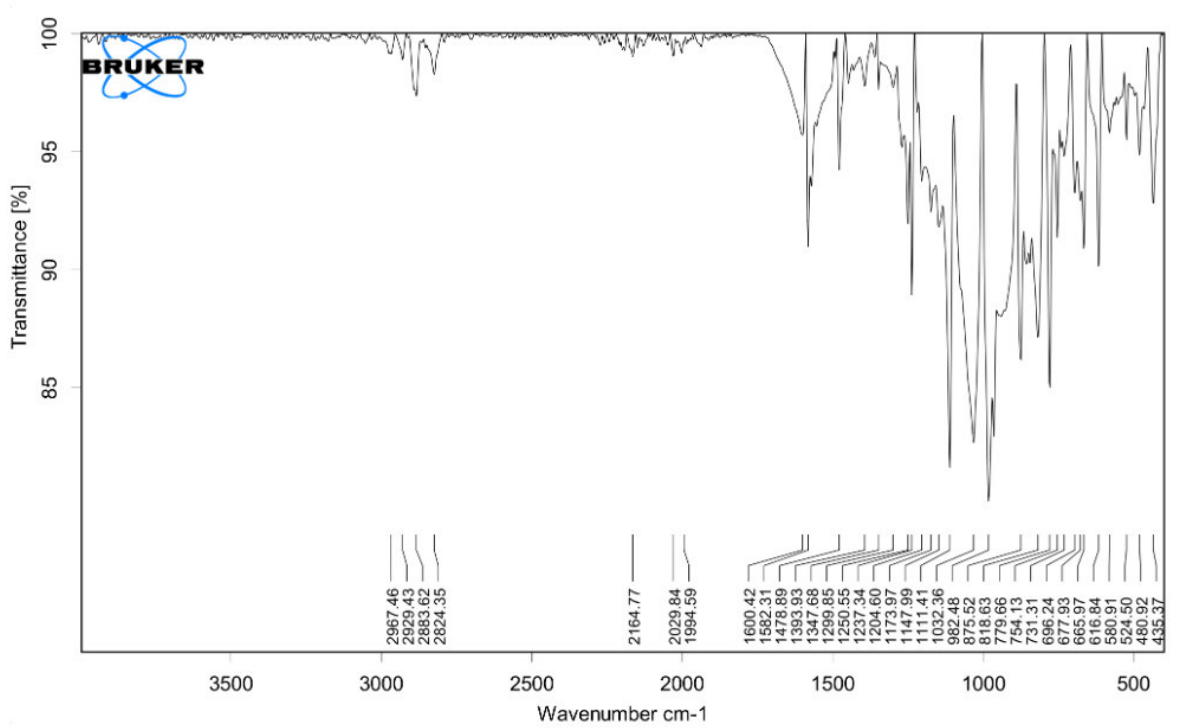

Abbildung 36. IR-Spektrum von **[K{18c6}][Cr(N(SiMe$_3$)$_2$)$_2$(η^2-(*trans*-β-methylstyrol)] (6)**.

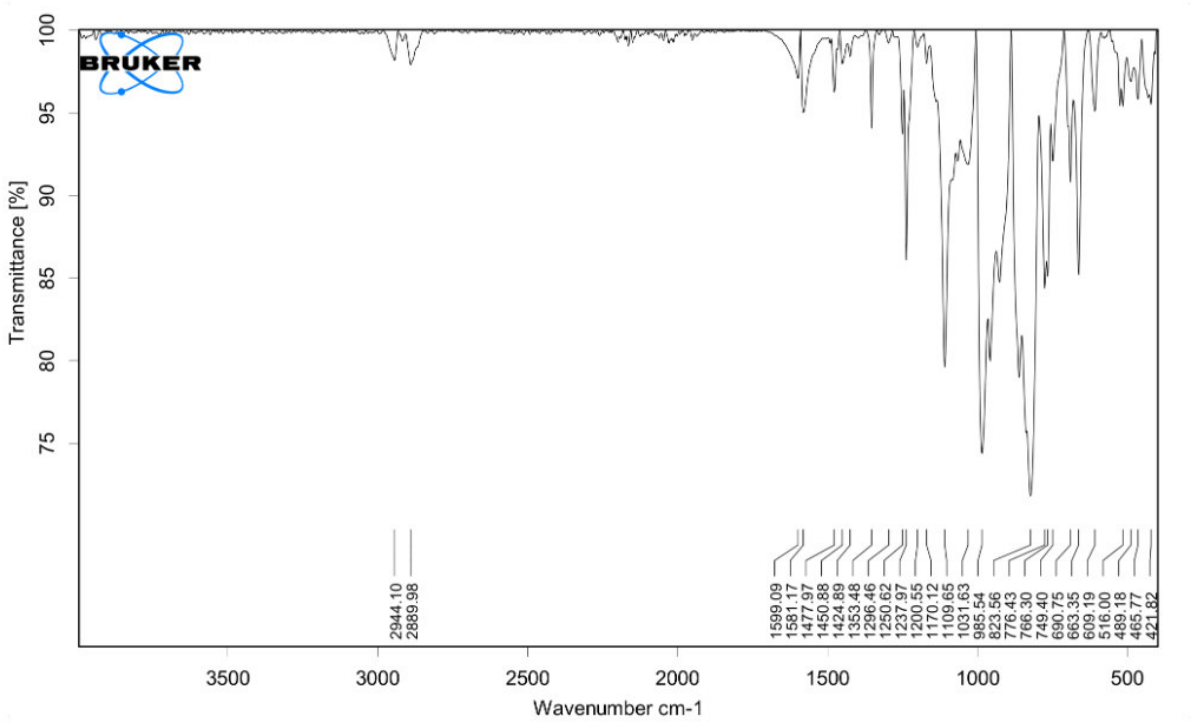

Abbildung 37. IR-Spektrum von **[K{18c6}][Cr(N(SiMe$_3$)$_2$)$_2$(η^2-(*trans*-stilben)] (7)**.

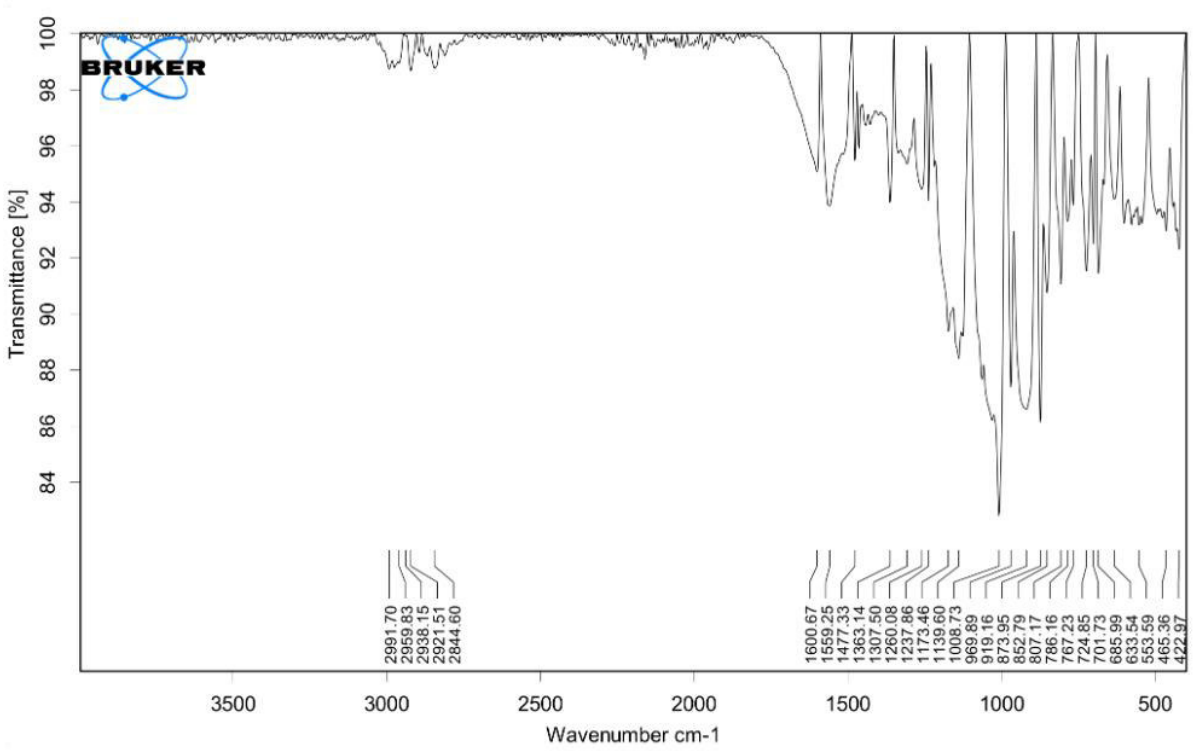

Abbildung 38. IR-Spektrum von **[K{18c6}][Mn(N(SiMe$_3$)$_2$)$_2$(η^2-(*trans*-*β*-methylstyrol)] (8)**.

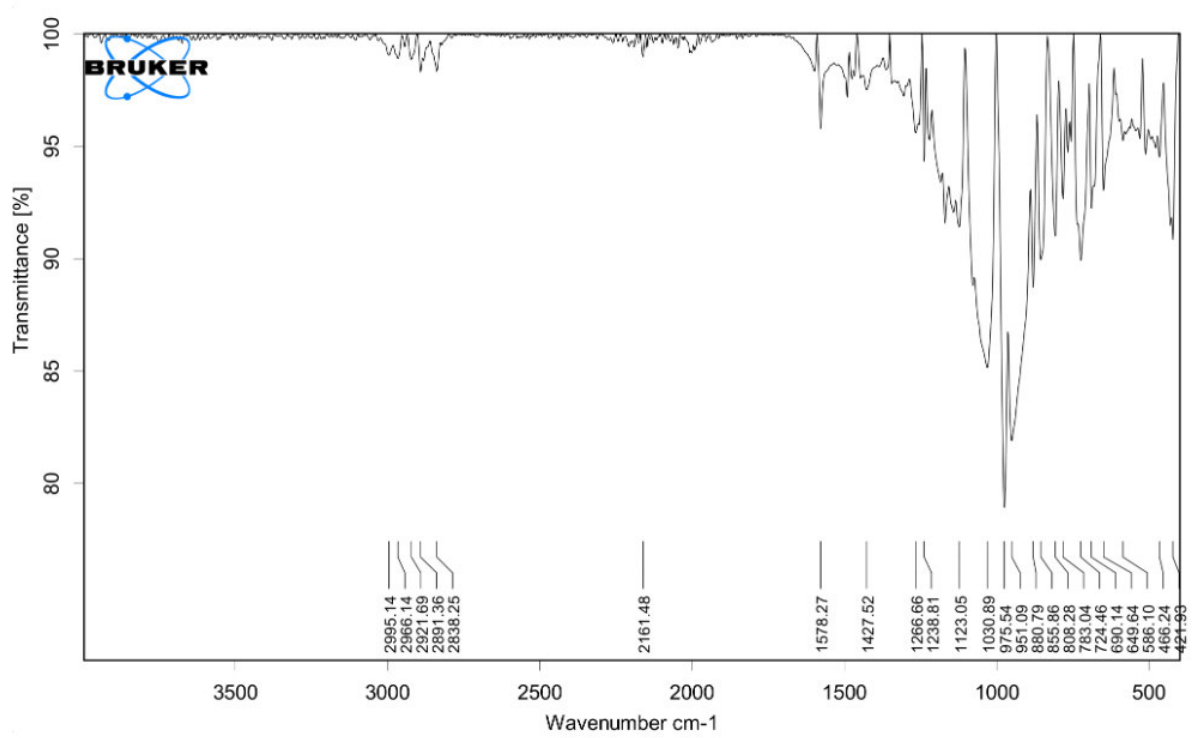

Abbildung 39. IR-Spektrum von **[K{18c6}][Fe(N(SiMe$_3$)$_2$)$_2$(η^2-(*cis*-β-methylstyrol)] (9)**.

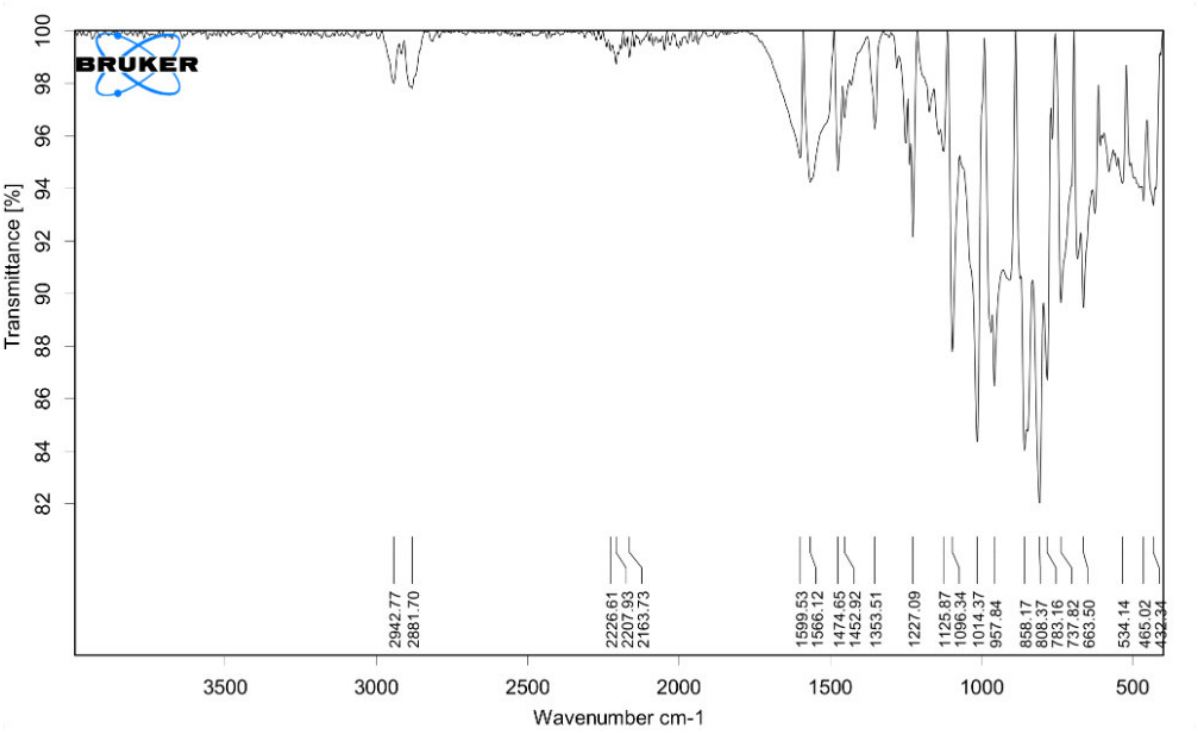

Abbildung 40. IR-Spektrum von **[K{18c6}][Fe(N(SiMe$_3$)$_2$)$_2$(η^2-(*trans*-stilben)] (10)**.

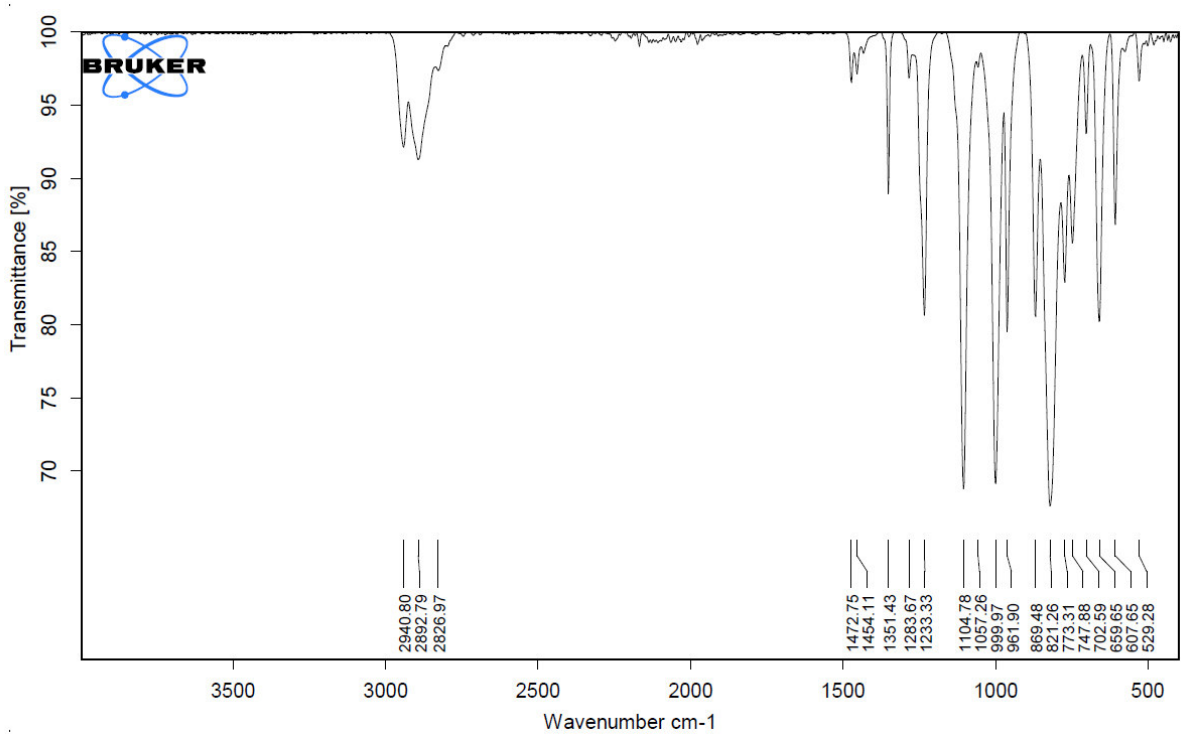

Abbildung 41. IR-Spektrum von **[K{18c6}][Mn(η^4-but)$_2$] (13)**.

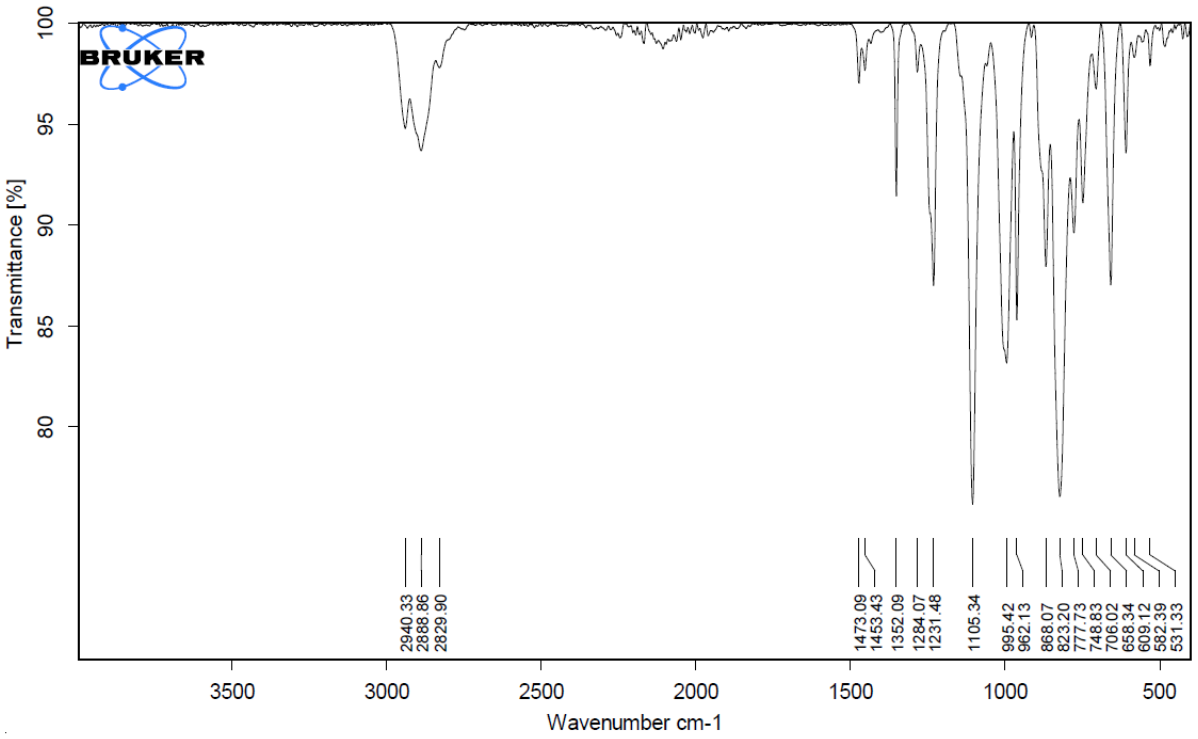

Abbildung 42. IR-Spektrum von **[K{18c6}]$_2$[(Fe(N(SiMe$_3$)$_2$)$_2$)$_2$(but)]** (**14**).

9 Publikationsliste

Publikationen

Die in dieser Arbeit enthaltenen Publikationen sind durch fett gedruckten Titel gekennzeichnet.

5. **„Reductive coupling of (Fluoro)-Pyridines by Quasi-Linear 3d-Metal(I) Silylamides of Cr–Co: A Tale of C-C bond formation, C-F bond cleavage and pyridyl radical anions"**

Igor Müller und C. Gunnar Werncke, *Chem. Eu. J.* **2020**, eingereichtes Manuskript.

4. **„Reaction of Alkynes with Quasilinear Metal(I) Silylamides of Chromium to Cobalt – A Comparative Study"**

I. Müller, D. Munz, C. G. Werncke, *Inorg. Chem*. **2020**, *59*, 9521.

3. **„The Ambiguous Behaviour of Diphosphines Towards the Quasilinear Iron(I) Complex [Fe(N(SiMe3)2)2]- – Between Inertness, P–C Bond Cleavage and C–C Double Bond Isomerisation"**

C. G. Werncke, I. Müller, *Chem. Comm.* **2020**, *56*, 2268.

2. **„Reduction of 2,2'-Bipyridine by Quasi-Linear 3d-Metal(I) Silylamides – A Structural and Spectroscopic Study"**

I. Müller, C. Pietzonka, F. Kraus, C. G. Werncke, *Inorganics* **2019**, *7*, 117.

1. „C-Halide Bond Cleavage by a Two-Coordinate Iron(I) Complex"

C. G. Werncke, J. Pfeiffer, I. Müller, L. Vendier, S. Sabo-Etienne, S. Bontemps, *Dalton Trans.* **2019**, *48*, 1757–1765.

Präsentationen

Poster

KCT Heidelberg März 2018

„Aktivierung von C-C-Mehrfachbindungen und C-F-Einfachbinden durch zweifach-koordinierte Metall(I)-Komplexe"

ICOMC Florenz Juli 2018

„Activation of C/C- and C/N-Multiple Bonds by Two-Coordinate 3d-Metal(I) Complexes"

Wöhler Tagung Regensburg September 2018

„Activation of C/C- and C/N-Multiple Bonds by Two-Coordinate 3d-Metal(I) Complexes”

Vorträge

Doktorandenkolloquium Februar 2020

„Über das Verhalten von quasi-linearen 3d-Metall(I)-Komplexen gegenüber C/N-Mehrfachbindungen und aromatischen Systemen“

KCT München 2018

„Aktivierung von C/C-Mehrfachbindungen durch zweifach koordinierte Metall(I)-Komplexe“

Hirschegg August 2017

„Behavior of Two Coordinate 3d-Metal(I) Complexes toward C/N-Multiple Bonds”

10 Wissenschaftlicher Lebenslauf

Persönliche Daten
Name: Igor Müller
Geburtsdatum: 12.07.1988
Geburtsort: Barnaul (Russland)

Januar 2017 – Dezember 2020
Promotion an der Philipps-Universität Marburg
Abschluss voraussichtlich im Januar 2021: Dr. rer. Nat.
Thema der Promotion: *„Verhalten linearer 3d-Metall(I)-Komplexen gegenüber C/N-Mehrfachbindungen und aromatischen Systemen“*

April 2014 – August 2016
Chemiestudium an der Philipps-Universität Marburg
Abschluss: Master of Science
Thema der Master-Thesis: *„Untersuchungen zur Synthese anionischer Thio-Phosphate, Thiostannate und Thiozinkate über Sulfid-basierte Ionische Flüssigkeiten“*

Oktober 2010 – März 2014
Chemiestudium an der Philipps-Universität Marburg
Abschluss: Bachelor of Science
Thema der Bachelor-Thesis: *„Synthese und Charakterisierung von Übergangsmetallkomplexen auf Basis von N,-Dimethylamino-N´,N´´-trimethylguanidin“*

August 2009 – Juni 2010
Adolf-Reichwein-Schule Marburg
Abschluss: Chemisch-Technischer-Assistent

August 2006 – Juli 2009
Adolf-Reichwein-Schule Marburg
Abschluss: Allgemeine Hochschulreife

Danksagung

In erster Linie möchte ich Herrn *Dr. C. Gunnar Werncke* meinem Doktorvater, für die Möglichkeit der Promotion in seinem Arbeitskreis und für die interessante Themenstellung meinen Dank aussprechen.

Ebenso möchte ich mich bei Herrn Prof*. Dr. J. Sundermeyer* für die Bereitstellung seiner Zeit und das Zweitgutachten bedanken.

Herrn *Prof. Dr. Paultheo von Zezschwitz* und *Prof. Dr. Michael Gottfried* danke ich für die Mitwirkung in der Prüfungskommission.

Weiter danke ich Herrn *Dr. Carsten Donsbach* für die Einführung in die Röntgenstrukturanalyse und die Hilfestellung beim Lösen und Verfeinerung der Datensätze.

Alexander Reckziegel, *Niklas Rinn*, *Ruth Weller, Nina Müller, Laura Cerny* und *Dr. Bastian Weinert* danke ich für die kritische Durchsicht des Manuskripts.

Den aktuellen und ehemaligen Mitgliedern der Arbeitskreise Werncke, Dehnen, Heine, Kuzu und Tamborino: *Christian* Schneider, *Ruth* Weller, *Gregoire Sieg*, *Alexander Reckziegel*, *Andres Gonzales*, *Prof. Dr. Stefanie Dehnen*, *Dr. Bastian Weinert*, *Dr. Chris Hosier*, *Dr. Irán Rojas León*, *Dr. Niklas Rinn*, *Dr. Lukas Guggolz*, *Dr. Fu-Xing Pan*, *Dr. Carsten Donsbach*, *Eugenie Geringer*, *Katharina Hanau*, *Bertram* Peters, *Marc Duchardt*, *Simon Nier*, *Shangxin Wie*, *Uwe Justus*, *Stephanie Göbeler-Scheuer*, *Andrea Tschirch*, *Katrin Beuthert, Felix Fischer*, *Ursula Siepe*, *Dr. Johanna Heine*, *Bettina Wagner*, *Natalie Dehnardt*, *Jakob Möbs*, *Dr. Istemi Kuzu*, *Kimon Flosdorf*, *Jörn Münzer*, *Dr. Frank Tamborino* und *Jonathan Pfeiffer* danke ich für die angenehme Arbeitsatmosphäre, die ständige Diskussionsbereitschaft und viele schöne Stunden im Rahmen gemeinsamer Feiern oder sportlicher Aktivitäten.

Allen Mitarbeitern der Serviceabteilungen des Fachbereichs danke ich für die Bearbeitung der Aufträge sowie für die generelle Hilfsbereitschaft bei Fragen, dabei gilt ein besonderer Dank der NMR- und der Röntgenabteilung, namentlich *Cornelia Mischke, Klaus Harms, Sergej Ivlev, Radostan Riedel, Michael Marsch*, und *Clemens Pietzonka* für die PPMS-Messungen an meinen Substanzen. Ich danke auch dem externen Kooperationspartner *Dominik Munz* für die quantenchemischen Rechnungen meiner Verbindungen.

Natürlich danke ich auch meinen Bachelor- und Vertiefungsstudenten *Lifang Zhou*, *Andreas Schwabauer, Nikolas Hecht*, *Katrin Beuthert*, *Shen Chen* und *Leonard Kersting* für die Unterstützung im Labor.

Ebenso möchte ich *Jörn Münzer* für die sportliche Unterstützung bei verschiedenen Aktivitäten wie beispielsweise StrongViking in der Promotion danken. Meiner Bürokollegin „Laborehefrau“ *Bettina Wagner* möchte ich für die Hilfe und Organisation im Labor und Büro danken.

Meiner Frau *Nina* danke ich für ihre Unterstützung, ihr Verständnis und ihre aufbauenden Worte in einer stressigen Zeit.

Mein größter Dank gilt meiner Familie für ihre Liebe und ihre kompromisslose Unterstützung. Ohne Euch wäre weder der Beginn und erfolgreichen Abschluss des Studiums, noch die Promotion möglich gewesen.